

Marc R. Knecht · Tiffany R. Walsh *Editors*

# Bio-Inspired Nanotechnology

From Surface Analysis to Applications

 Springer

# Bio-Inspired Nanotechnology

Marc R. Knecht · Tiffany R. Walsh  
Editors

# Bio-Inspired Nanotechnology

From Surface Analysis to Applications

 Springer

*Editors*

Marc R. Knecht  
Department of Chemistry  
University of Miami  
Coral Gables, FL  
USA

Tiffany R. Walsh  
Institute for Frontier Materials  
Deakin University  
Geelong, VIC  
Australia

ISBN 978-1-4614-9445-4                      ISBN 978-1-4614-9446-1 (eBook)

DOI 10.1007/978-1-4614-9446-1

Springer New York Heidelberg Dordrecht London

Library of Congress Control Number: 2014936425

© Springer Science+Business Media New York 2014

This work is subject to copyright. All rights are reserved by the Publisher, whether the whole or part of the material is concerned, specifically the rights of translation, reprinting, reuse of illustrations, recitation, broadcasting, reproduction on microfilms or in any other physical way, and transmission or information storage and retrieval, electronic adaptation, computer software, or by similar or dissimilar methodology now known or hereafter developed. Exempted from this legal reservation are brief excerpts in connection with reviews or scholarly analysis or material supplied specifically for the purpose of being entered and executed on a computer system, for exclusive use by the purchaser of the work. Duplication of this publication or parts thereof is permitted only under the provisions of the Copyright Law of the Publisher's location, in its current version, and permission for use must always be obtained from Springer. Permissions for use may be obtained through RightsLink at the Copyright Clearance Center. Violations are liable to prosecution under the respective Copyright Law. The use of general descriptive names, registered names, trademarks, service marks, etc. in this publication does not imply, even in the absence of a specific statement, that such names are exempt from the relevant protective laws and regulations and therefore free for general use.

While the advice and information in this book are believed to be true and accurate at the date of publication, neither the authors nor the editors nor the publisher can accept any legal responsibility for any errors or omissions that may be made. The publisher makes no warranty, express or implied, with respect to the material contained herein.

Printed on acid-free paper

Springer is part of Springer Science+Business Media ([www.springer.com](http://www.springer.com))

# Preface

The research encompassing the screening, selection, characterization, and exploitation of peptides capable of recognizing and binding inorganic materials is rapidly growing; however, it remains far from maturity. In the space of two decades, this area has exploded with activity, driving innovations in both the experimental and theory arenas. With the strong encouragement of the team at Springer, we considered this an ideal point to reflect on the enormous progress that has been made thus far, to consolidate these accomplishments, and to highlight some of the new applications and research directions emerging in this new field.

One of the key audiences for this book is the scientist or scholar who is new to the research area. The inherently multidisciplinary nature of this research field that embraces chemistry, physics, surface science, structural and molecular biology, genetics, materials science, computational modeling, and informatics, makes a comprehensive entry a challenging prospect. The earlier chapters of this book detail the foundational aspects of this scientific field, to assist those getting started. Another key audience for this volume is the established practitioner in bio-inspired technologies, who is interested in expanding the horizons of the possible applications of their research. The latter chapters in this volume highlight applications that are currently emerging and could potentially have significant opportunities for growth. This includes the expansion of bio-inspired methodologies and applications that could have important implications in sustainability, which is important for future scientific progression.

We are grateful to all of our authors for their outstanding contributions. We would also like to thank Merry Stuber, Allison Waldron, and the team at Springer for their hard work, enthusiasm, organization, support, persistence, and patience. And finally, we would like to thank our colleagues, friends, and especially families, for their support and encouragement.

Marc R. Knecht  
Tiffany R. Walsh

# Contents

<b>1</b>	<b>Peptide-Nanoparticle Strategies, Interactions, and Challenges . . .</b>	<b>1</b>
	Joseph M. Slocik and Rajesh R. Naik	
<b>2</b>	<b>Fundamentals of Peptide-Materials Interfaces . . . . .</b>	<b>17</b>
	Tiffany R. Walsh	
<b>3</b>	<b>Experimental Characterization of Peptide–Surface Interactions . . . . .</b>	<b>37</b>
	Marion J. Limo, Carole C. Perry, A. A. Thyparambil, Yang Wei and Robert A. Latour	
<b>4</b>	<b>Interfacial Structure Determination . . . . .</b>	<b>95</b>
	Peter A. Mirau	
<b>5</b>	<b>Understanding Biomineral Growth and Assembly for Engineering Novel Green Nanomaterials . . . . .</b>	<b>127</b>
	Siddharth Patwardhan	
<b>6</b>	<b>Understanding Molecular Recognition on Metallic and Oxidic Nanostructures from a Perspective of Computer Simulation and Theory . . . . .</b>	<b>141</b>
	Hendrik Heinz	
<b>7</b>	<b>Bio-Inspired Nanocatalysis . . . . .</b>	<b>173</b>
	Ryan Coppage and Marc R. Knecht	
<b>8</b>	<b>Addressable Biological Functionalization of Inorganics: Materials-Selective Fusion Proteins in Bio-nanotechnology. . . . .</b>	<b>221</b>
	Banu Taktak Karaca, Marketa Hnilova and Candan Tamerler	

<b>9</b>	<b>Environmental Interactions of Geo- and Bio-Macromolecules with Nanomaterials</b> . . . . .	257
	Navid B. Saleh, Jamie R. Lead, Nirupam Aich, Dipesh Das and Ifthekeer A. Khan	
<b>10</b>	<b>Mimicking Biomineral Systems: What have we Achieved and Where do we go from Here?</b> . . . . .	291
	James J. De Yoreo	

# Chapter 1

## Peptide-Nanoparticle Strategies, Interactions, and Challenges

Joseph M. Slocik and Rajesh R. Naik

**Abstract** The ability to control and manipulate peptide-nanoparticle interactions is an important goal in achieving biofunctionalized materials with enhanced properties and precise nanostructures for use in sensing, catalysis, and biomedical applications. However, currently, there are many challenges to overcome in order to obtain better design and create these peptide-based functional nanomaterials. These include a need to better our understanding of the mechanisms/forces which drive peptide-nanomaterial interactions, improve characterization techniques to probe the peptide-nanoparticle interfaces, to design and identify new nanomaterial-binding peptides with greater affinities using a combination of advanced combinatorial techniques and next-gen sequencing, and to effectively utilize computational modeling to guide/predict peptide-nanomaterial binding. In this chapter, we describe these technical challenges and highlight recent examples of peptide-nanoparticle interactions, their resultant properties, and how some of these challenges are being addressed.

### 1.1 Introduction

Nature has evolved molecules that possess functional properties in the form of self-assembly, signaling, sensing, catalysis, motion, and storage. In addition, nature hybridizes materials (organic and inorganic) in order to produce sophisticated structures and materials. This is best exemplified by the biogenesis of multiscale silica exoskeletons of marine diatoms (Fig. 1.1) and the organic-inorganic composite material of nacre from molluscs (Skowronski et al. 2007; Dickerson et al. 2008), the highly orchestrated synthesis and assembly of magnetic nanoparticle

---

J. M. Slocik · R. R. Naik (✉)

Soft Matter Materials Branch, Materials and Manufacturing Directorate, Air Force Research Lab, Wright-Patterson Air Force Base, Dayton OH 45433-7750, USA

e-mail: rajesh.naik@us.af.mil



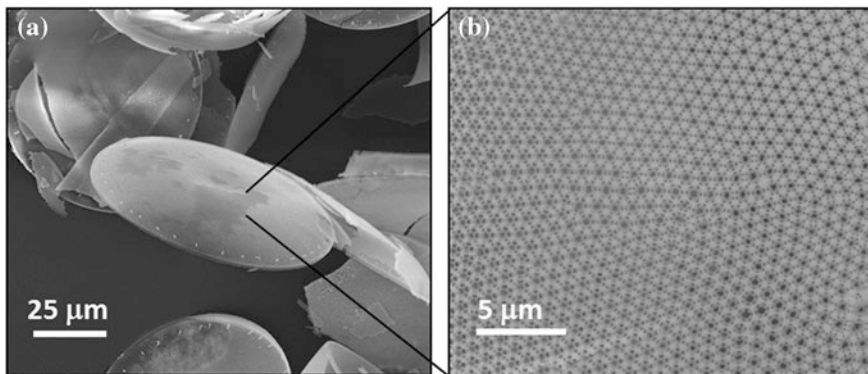


**Fig. 1.1** Biological Inspiration Organisms, such as diatoms, produce minerals of defined composition and structure under cellular conditions and genetic control (**a** and **b**). An example of nature's mastery of mineralization is depicted above in a SEM images of a (*cleaned*) silica cell wall (i.e., frustule) grown by the diatom *Coscinodiscus granii*. (Image by M. B. Dickerson, Diatom cultured by Y. Fang)

(NP) chains (Bazylinski et al. 2007), and the formation of self-assembled protein cages for the storage of inorganic materials (Flenniken et al. 2008). In all of these cases, nature has created unique biomolecules with specific functions that represents the ultimate paradigm of control, chemical specificity, geometrical complementarity, and assembly of well-defined nanostructures. The ability to replicate the structures and functions of biomolecules with regard to how they assemble and interact with inorganic materials is highly desired for a range of applications in medicine, sensors, and catalysis. With current advancements in nanotechnology, there have been many breakthroughs in using biomolecules to fabricate and/or functionalize inorganic nanoparticles (NPs) that exhibit new material functionality when combined with the electronic, optical, and magnetic properties of nanomaterials (Pelaz et al. 2012). To date, these include using biomolecules (e.g., peptides, DNA) for the synthesis of different materials (inorganic and carbon-based), to alter NP properties and structure, and more importantly, impart biological activity and molecular recognition function to nanomaterials.

Peptides and proteins are an integral part of materials synthesis, assembly, and functionalization due to their rich chemical variability (hydrophobic/hydrophilic, aromatic, acidic, basic residues), presence of short segments of secondary structural elements (helices,  $\beta$ -sheets, turns), can be synthesized using standard coupling strategies, and available screening methods in place for identifying material-specific peptides from large combinatorial libraries (Briggs and Knecht 2012). These qualities are appealing given that they are easier to control and manipulate as compared to larger proteins, but provide a lot more chemical and structural diversity unlike single amino acids or DNA bases. Also, a common characteristic of most, if not all, proteins with known biomineralization activity is the presence of multiple repeating peptide domains (Dickerson et al. 2008).

This has provided a means to isolate and study the activity of these domains in a single peptide repeat without the complexity of the full protein structure. This was first demonstrated by the use of a silica precipitating peptide R5 identified from silaffins contained in diatoms to replicate the biosilification reaction under laboratory conditions (Kroger et al. 1999). In addition to biologically derived peptide sequences for the synthesis and assembly of materials, peptides with specific material-binding sequences isolated through combinatorial screening approaches have been used as synthetic templates to synthesize, functionalize, and assemble a wide variety of NP types (Song et al. 2013; Nam et al. 2008; Coppage et al. 2011). For example, platinum-binding and silica-binding peptides isolated from phage displayed peptide libraries were reported to control the morphology and shape of platinum (Li and Huang 2010) and silica particles (Patwardhan et al. 2012).

Peptide-nanoparticle interactions have been exploited for the synthesis and assembly of higher order complex inorganic structures using protein scaffolds or lipid-like molecules. Using protein scaffolds, peptides are locally/spatially arranged in a 3-D geometry around the protein to display multiple repeating peptide sequences with NP templating activity. For example, proteins such as  $\beta$ -silk, S-layer proteins from bacteria, chaperonin proteins, viral capsids, and ferritin protein cages have all been modified with functional peptides for materials synthesis and in the assembly of unique nanostructure geometries (Coordination Chemistry 2013). The protein scaffold also imparts added stability to the displayed peptides, enhanced solubility in aqueous environments, and diminished immunogenic or toxicity effects in regards to therapeutic treatments; while the conjugated peptide modifies the size of the protein scaffold and adds new functionality. The iron storage protein of ferritin is an example of a biologically important protein scaffold which offers these benefits. Notably, ferritin forms a cage-like nanostructure with external and internal diameters being 12 nm and 8 nm, respectively, and contains numerous repeating residues at fivefold or sixfold symmetry sites for genetic or chemical addition of peptides (Coordination Chemistry 2013). As a result, there is much interest in ferritin for not only a therapeutic use but also as a scaffold for biomaterial applications. We have previously shown that self-assembled ferritin cages can be generated through engineering recombinant human light chain ferritin with a silver-binding peptide (Kramer et al. 2004). Consequently, the peptide modified ferritin allowed for inorganic NP growth of silver within the interior protein cavity and only at the sites where peptides were displayed. Interestingly, bacterial cells that expressed protein cages with silver-binding peptide were resistant to increased concentrations of  $\text{Ag}^+$  ions. Modified ferritin can also be assembled on the surface of aluminum NPs to generate bio-thermite materials with enhanced kinetic and energetic properties (Slocik et al. 2013). Also, peptides have been conjugated with amphiphilic molecules in the form of short carbon chains ( $\text{C}_{12}$ ) for the self-assembly of new peptide-gold nanostructures. In recent studies by Rosi and coworkers, scaffolds of gold-binding peptide-based conjugates were created through rational design principles for the preparation of complex plasmonic materials with tailorable optical properties (Chen et al. 2008). The use of peptides allowed for manipulating the helical content in the scaffold to

optimize the optical properties needed. Alternatively, Mirkin and others have used DNA hybridization to control the placement of NPs into programmable 3-D structures (Macfarlane et al. 2011).

Because of the influence of biomolecules, and of peptides in particular, on material properties, there have been many studies on probing peptide interactions with nanomaterials in order to understand fundamental principles that control binding and structure at this dynamic interface. Together, this insight can lead to the improved design of peptides with tunable binding affinities and the ability to impart functionality to both the peptide and NP for the goal of biosensor fabrication, catalysis development, and/or implementation in biomedical applications such as in drug delivery and bioimaging (Slocik and Naik 2010). For biosensors, for example, it's imperative to gain a detailed understanding of the binding interactions/structure effects between the peptide sensing element, nanomaterial, and the biomolecule/chemical target of interest. Each interaction is necessary to enhance sensor responses, optimize sensitivity and specificity to target, and to achieve low detection limits. Alternatively, this is also true for interactions with nonbiological ligands (polymers, organic ligands), simple peptide analogs such as peptoids, and Peptide Nucleic Acids (PNA). Consequently, there are many challenges to overcome in understanding and exploiting peptide-nanoparticle interactions.

## 1.2 Grand Challenges in Bionanotechnology

Incorporation of biomolecules with nanomaterials leads to synergistic effects that combine the ability of biomolecules to control, shape, manipulate, and enhance the physiochemical properties of nanomaterials. As a result, this is technologically important for the development of advanced multifunctional materials as described above and throughout the remaining chapters. Nanomaterials have benefited from using biomolecules, and the combination of biomolecules with nanomaterials can lead to properties that are of interest to the materials, medical, and engineering communities (Fig. 1.2). However, significant challenges still exist and, to date, we do not fully understand what dictates biotic-abiotic interactions or what the most effective biomolecular elements are to be used (DNA, peptides, proteins) to elicit strong binding interactions.

Improvements in the design and selection of nanoparticle-binding peptides are needed much in the same way that nature has optimized/evolved biomolecules for specific functions. The mechanisms/interactions/forces that drive peptide-material binding and peptide structure, characterization techniques which directly analyze and quantify both peptide and nanomaterial with atomic and molecular level resolution, and reliable theoretical modeling/dynamics/simulations capable of validating and guiding experimental data and design, are all important technical challenges that need to be addressed. In the following section, we will highlight a few of these challenges which are relevant to peptide synthesized or assembled

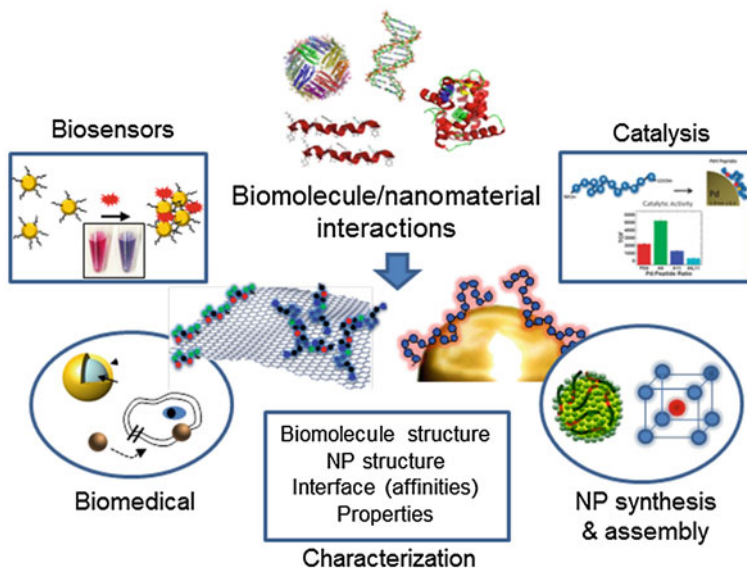


**Fig. 1.2** Biomolecule-nanomaterial interactions, characterization, and applications. Catalysis image (*upper right panel*) is reproduced from Ref #13 with permission from The Royal Society of Chemistry

materials and provide examples of what is currently being done to understand and design better peptide-nanoparticle interactions as well as determine binding interactions.

### ***1.2.1 Design and Selection of Nanoparticle/Material-Binding Peptides***

The design and selection of nanoparticle-binding peptides remains a major challenge due in part to a lack of high-throughput methods, rational design principles, an absence of complete data sets for existing nanoparticle-peptide-binding pairs, and in many cases a lack of accurate computational models. There is an increasing need for methods capable of identifying nanoparticle-peptide interactions with high binding affinity and specificity. New high-throughput techniques should offer the ability to rapidly explore and screen large libraries of random peptides against any material target (soluble and insoluble), a desired function (catalytic activity), or nanomaterial property (size, crystallinity, morphology). Currently, the state of the art method for selecting nanoparticle-binding peptides either involves the use of a limited number of biologically derived material-specific peptide sequences with known biomineralization activity (i.e., R5 peptide discovered from diatoms); peptide or protein templates with no known mineralization function such as

antibodies that can be adapted for NP binding and/or synthesis; or by a combinatorial based approach in the form of phage displayed, cell displayed, or resin displayed peptide libraries (Tamerler and Sarikaya 2009). The largest of these combinatorial libraries sample a small subset of sequences ( $10^9$ ), only address primary peptide structure, and have sequence biases (Derda et al. 2011). These techniques have been extensively used over the past decade with great success in the identification of strong peptide binders and have been the focus of numerous comprehensive reviews (Dickerson et al. 2008; Tamerler and Sarikaya 2009). Phage or cell displayed approaches have become powerful and reliable tools for rapidly screening large populations of random peptides against an assortment of endless nanomaterials, polymers, and biomolecules (Dickerson et al. 2008; Tamerler and Sarikaya 2009), although, there have been minimal improvements or advancements over the past 5–10 years in either the technique or off-the-shelf commercial libraries. In the case of the latter, typical phage displayed peptide libraries available are heavily biased in amino acid composition with several amino acids severely underrepresented or not present at all in the total population (i.e., cysteine) (Derda et al. 2011; Matochko et al. 2012). Additional limitations include high background interference from nonspecific peptide binders, the faster growth of certain phage clones after negative selection, and the absence of dominant sequences. In terms of the technique, they are time and labor intensive (weeks), require specialized instrumentation (incubators, DNA sequencers, PCR), and until recently was restricted to use on immobilized or insoluble NP targets which could be separated from unbound phage by centrifugation. In a few recent cases, phage display has been used to screen small soluble dipeptide targets or NP precursors for catalytic peptides by assaying for an insoluble end product (Wei et al. 2011). This represents a new capability of phage display which has otherwise been limited to insoluble or immobilized targets.

Alternative emerging technologies are likely positioned to address some of these challenges as well as offer new platforms to complement existing high-throughput combinatorial approaches. For example, new printing techniques (i.e., Inkjet printing, dip pen nanolithography, nanoprint<sup>TM</sup> microarrays) have made it economically feasible to print biomolecules in massive parallel microarrays (Swartz et al. 2010; Uttamchandani and Yao 2008). This has enabled the development of peptide microarrays consisting of  $10^2$ – $10^4$  random peptide sequences and has been successfully used by the biomedical community for the rapid identification of potential drug candidates, peptide-peptide interactions, and antibody/peptide pairs (Uttamchandani and Yao 2008). Similarly, we envision the use of peptide microarrays with different nanomaterial targets for screening peptides with high binding affinity or NP templating activity. This preliminary concept is illustrated in Fig. 1.3 and shows the synthesis of Au NPs on a peptide microarray consisting of 100 peptides after incubation with buffered  $\text{Au}^{3+}$  salts. The presence of dark purple spots indicates potential peptide sequences specific for gold NP synthesis. Ideally, this platform will significantly reduce processing/screening time from weeks to hours, eliminate the need for specialized instrumentation (cell incubators, PCR, DNA sequencers) except for an optical

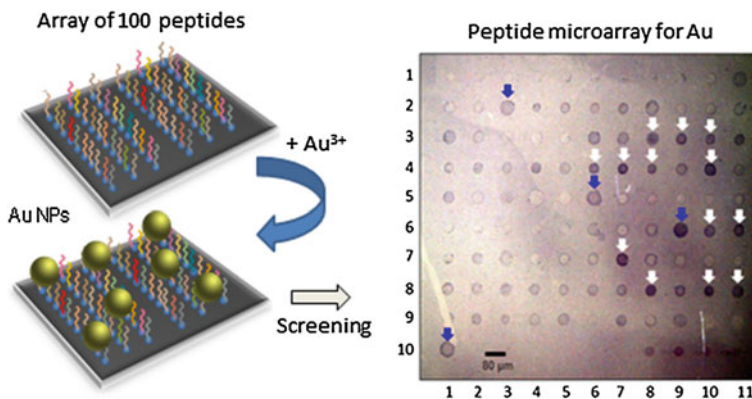


**Fig. 1.3** Screening of peptide microarray for gold NP binding and synthesis. Peptide microarray was constructed by Thinkpeptides<sup>®</sup> to contain a 10 × 10 peptide array of random and selected dodecamer gold-binding peptides with a Gly-Gly-Gly spacer at C-terminus immobilized on a glass slide in triplicate sets. For screening peptides which are capable of synthesizing gold NPs, the microarray was incubated with an aqueous solution of 1 mM HAuCl<sub>4</sub> in 0.1 M HEPES buffer pH 7.4 for 2 h. Peptide microarray was removed from gold salt solution and washed with double deionized water for 10 min repeatedly. Peptide microarray was characterized for gold NP synthesis and imaged using a Leica stereomicroscope at 20× magnification under *white light* illumination (unpublished). *Blue arrows* indicate a consensus sequence (TSNAVAPTLRHL) and *white arrows* indicate selected peptide sequences which exhibited enhanced gold NP synthesis

microscope/flatbed color scanner, can be adapted for any soluble nanomaterial target, and will allow for the monitored in situ synthesis of NPs. In another example, phage display has been integrated with a microfluidic device to form a multiplexed automated platform for peptide selection. In this platform configuration, the microfluidic chip offers the capability to screen a phage library against multiple targets in a single round without the need for bacterial infection for multiplex panning (Cung et al. 2012). This level of automation decreases the amount of time from weeks to hours to obtain a set of peptide-binding sequences for each target. Also, miniaturization of the screening platform reduces the amount of sample needed from mg to μg which is beneficial when dealing with precious rare sample targets. However, fluid flow rates have to be optimized to ensure isolation of the highest affinity binders and there's a need for better sequencing tools in terms of high-throughput and next-gen sequencing.

Achieving the goal of identifying strong peptide binders using a high-throughput technique is only part of the challenge, but being able to maximize, tune, and enhance material properties through modulating peptide-binding affinity and processing conditions is highly desired. Ultimately, maximizing NP properties is entirely empirical and involves testing many different peptide sets identified from phage display by trial and error for a given binding quality in addition to the strongest peptide binders. Nevertheless, this approach has resulted in the creation of new chiro-optical properties in gold using a gold-binding peptide (Slocik et al. 2011), a 40 % gain in the hardness of stainless steel upon functionalization with a

short synthetic peptide identified from bacteria (Chiu et al. 2011), and improved NP catalysts with high activities by a palladium-binding peptide as described in a later chapter (Coppage et al. 2013). These examples highlight the potential benefits of balancing peptide-nanoparticle-binding interactions with material properties; although with the caveat that strong peptide-binding does not always produce NPs with the highest activity or enhanced properties. Hence, the goal of identifying strong peptide-binding achieved by the phage display process is not necessarily a suitable metric into whether a peptide will be capable of templating NP synthesis or imparting the largest property enhancements. Consequently, many strong peptide-binding sequences isolated from phage displayed peptide libraries suffer from a lack of templating activity or less than optimal properties. However, these peptides provide an initial sequence for further refinement in order to tune and enhance properties and binding. On the other hand, higher peptide-binding affinity and specificity for its biological target is necessary for applications such as biosensor development or surface immobilization of NP agents.

The ability to manipulate and control the arrangement, assembly, localization, surface density, and structure of these peptides on nanomaterial surfaces on demand without the use of a patterning technique is also challenging. For example, we have identified peptide sequences which preferentially bind to either the edges or planes of graphene (Kim et al. 2011). Here, the localization of peptides at different regions (edges or planes) on a graphene substrate resulted in different electronic surface states and resistivity. In a similar example, the influence of peptide-binding on the electronic properties of semiconductor surfaces was examined by Ashkenasy et al. (2012). They demonstrated that dodecameric peptides can enhance the electronic properties of Gallium-Arsenide (GaAs) by dipolar and charge redistribution effects based on the position and type of amino acid residue present within the surface bound peptide. Also, through rational substitution of a graphitic binding peptide, different extents of self-assembled peptide structures were obtained on graphite with varying surface chemistries (So et al. 2012). In this study, peptide-binding was used to control the surface chemistry on graphene and could be changed from hydrophilic to hydrophobic by modifying the amino acid sequence accordingly (Khatayevich et al. 2012).

### ***1.2.2 Control of Nanoparticle Structure and Composition Over Multiple Length Scales***

In nature, biological systems effortlessly control synthesis and assembly across multiple length scales using genetic and molecular level control. For years, we have admired and tried to mimic the unparalleled level of control and organization. Unfortunately, achieving this is much more difficult using biomimetic approaches by comparison and typically involves bottom-up or top-down approaches, combinations of different sized templates (i.e., peptides conjugated to larger proteins, DNA origami patterns), and/or peptides which are inclined to self-assembly such

as amphiphilic peptides as described earlier. For example, the biomolecules responsible for biogenic silica found in diatoms have been extensively studied, but the ability to mimic biosilica structures *ex vivo* at the same length scales created by nature has largely been unsuccessful. This begs the question whether along with specific biomolecules, the physio-chemical environment is equally important in the development of specific morphologies seen in diatoms and other biological systems. However, the first challenge is to unscramble the role of amino acids, peptide sequence, molecular weight, and context in material binding and/or templating. For example, different molecular weights of poly-L-lysine (PLL) were shown to affect the morphology of silica structures, whereby high molecular weight PLL produced hexagonal silica platelets while low molecular weight PLL yielded spherical particles (Tomczak et al. 2005). Single unassembled material-binding peptides are optimally effective in the nanometer size scale regime and are mainly used to bias the growth of nanocrystal facets along a preferred orientation, control NP sizes by restricting growth, and impart a biological function to the NP surface. Generally, the ability of small peptides to control NP structures and compositions over several different length scales (nano to micro and beyond) is prohibitive due to the intrinsic lack of a 3-D structure. This is evident in the many NP products templated by specific peptides.

### ***1.2.3 Characterizing Biotic-Abiotic Interface***

Another limitation to the design of new nanoparticle-binding peptides has been a lack of understanding and characterizing the mechanisms and binding interactions which guide the assembly and structure of the biotic-abiotic interface. These limitations are significantly apparent by comparing the qualities and structures of laboratory grown inorganic materials with equivalent biominerals produced in nature. For example, marine organisms are able to synthesize and control the mineralization of highly oriented  $\text{CaCO}_3$  crystals with defined facets and geometries, while the comparable laboratory grown NP counterparts exhibit random orientations and geometries and do not share the same physical properties and superior qualities (optical, mechanical, catalytic). Although several significant advances have been made in gaining insight into the mechanisms of crystal orientation *in vivo* (Killian et al. 2009) as well as the specialized macromolecules and conditions necessary for calcite growth (Aizenberg et al. 2002; Wang et al. 2009), we don't fully understand how biomolecules template the synthesis of nanomaterials or organize on their surface. Several studies by groups around the world including the authors of chapters in this book are attempting to get a handle on these rules that govern recognition and templating of biogenic materials. The reasons for this shortcoming include the vast complexity of the biomolecule-crystal interface, differences in sequence and structure between peptides, variability, influences from processing conditions (temperature, buffers), and the absence of appropriate characterization tools discussed below (Slocik and Naik 2010).



The complexity of the interface develops from having peptides or biomolecules with variable conformations, structures, chemistries, polarities, chiralities, electrostatic charges, and binding affinities in combination with diverse nanocrystal surfaces which possess different facets, oxidation states, surface charges, crystallographic orientations, and defects (Fig. 1.4) (Nel et al. 2009; Sapsford et al. 2012). Each of these characteristics and properties has been shown to affect the degree of binding whereby simply changing one property will circumvent or enhance binding. For example, by changing the surface charge densities of a gold surface electrochemically, a gold-binding peptide elicited different binding behaviors (Donatan et al. 2012). In this regard, switching the surface charges can be used to attenuate peptide adsorption and potentially to clean the surface of biological materials. This feature is particularly attractive for biosensors and presents a quick means to reconfigure a sensor for different targets simply by changing the peptide recognition elements. Also, the molecular conformations of peptides have been shown to significantly impact binding in a number of examples. For instance, a cyclic gold-binding peptide (GBP1) with a constrained conformation exhibited lower binding to a planar gold surface as opposed to its conformationally free linear peptide analog which can adopt many different binding conformations on the gold surface (Hnilova et al. 2008). This increased flexibility was also determined computationally to be an important driving force for strong binding; and as a result, should be included in design of nanoparticle-binding peptides (Heinz et al. 2009). Finally, to add to the complexity, the assembled interface is dynamic in nature such that peptides are in constant motion and diffuse along the surface to adopt the lowest energy structures. Peptide diffusion along a (111) gold surface was recently observed with a different gold-binding peptide (A3) by monitoring the formation of a self-assembled peptide coil over time using Atomic Force Microscopy (AFM) (Nergiz et al. 2013). Altogether, understanding peptide-nanoparticle interactions represents an overwhelming task even when utilizing the most advanced characterization techniques; although some techniques such as solution NMR spectroscopy (discussed in later chapters) have successfully exploited the dynamic nature of peptides going on and coming off the NP surface to produce an averaged NP bound peptide structure (Mirau et al. 2011). To date, the biomimetic materials community at large has made progress in providing a partial picture of what guides peptide-nanoparticle interactions on a peptide per peptide basis, but has struggled in establishing a general set of guidelines or rules relating to different NP binding-peptides.

Collectively, characterization techniques used for studying peptide-nanomaterial interactions were borrowed from materials science (electron microscopy, atomic force microscopy (AFM), X-ray scattering/diffraction), biochemistry (electrophoresis, NMR, Circular dichroism spectroscopy (CD)), and the remaining physical sciences (Fourier transform infrared spectroscopy (FT-IR), UV-Vis spectroscopies) (Slocik and Naik 2010). Qualitatively, most of these techniques offer insight into either the surface bound peptides or the nanomaterial itself and often indirectly measure a single property or physical feature as highlighted in upcoming chapters. For example, FT-IR and CD spectroscopies measure changes in

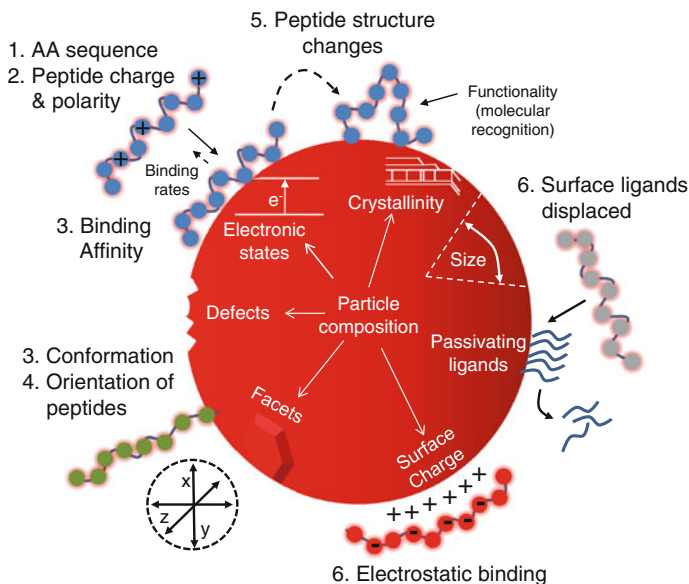


**Fig. 1.4** Variables affecting biomolecule-nanomaterial interactions. These include binding affinity, orientation of biomolecules on surface, distance from surface, biomolecular structure/conformation, and surface density

the global peptide structure exclusively; while electron microscopy and X-ray techniques probe the nanomaterial's physical structure and attributes (i.e., crystallinity, morphology, size). In a recent study, Knecht et al. showed how the CD structures of palladium-binding peptides with cysteine and/or alanine substitutions contributed to large differences in the catalytic activity of peptide capped NPs (Coppage et al. 2013). The peptide structure in this case plays a larger role in defining NP activity as opposed to requiring strong binding affinities to palladium. This illustrates the importance of balancing molecular structure with binding affinity in order to achieve enhanced nanomaterial properties. Additionally, there is a great need to quantify peptide-nanomaterial interactions in terms of equilibrium binding data (quartz crystal microbalance (QCM) and surface plasmon resonance spectroscopy (SPR)), kinetics (on/off binding rates), forces associated with binding (atomic force spectroscopy), and thermodynamics of binding using isothermal titration calorimetry (ITC). Recently, atomic force spectroscopy has been used to gain insight into the different adhesion forces (electrostatic, hydrophobic) associated with single molecule binding of amino acids to silicon substrates (Razvag et al. 2013). Here, the average adhesion forces were on the average of 20–300 pN for single amino acids but are expected to be much higher for peptides that exhibit multivalent binding to NP or surfaces. This binding data set is valuable in determining the binding interaction strengths of amino acids and peptides for a set of inorganic substrates, assessing their ability to effectively functionalize surfaces, and in providing a quantifiable means of comparison for examining the effects of site

specific sequence mutations on binding or evaluating the potential binding other peptides. This last aspect alone has provided much detail about key residues necessary for binding based on calculated equilibrium binding constants ( $K_{eq}$ ,  $k_a$  and  $k_d$  constants) and how they affect nanomaterial properties. In total, these techniques and instrumentation have provided significant detail about peptide-binding, but, unfortunately have limited availability in a typical research laboratory or departmental inventory. As a result, analysis is restricted to either examining the peptide or nanomaterial using available resources. Most nanoparticle-binding peptides have only been partially characterized, and offer an incomplete picture of corresponding peptide-binding interactions. To date, only a handful of gold- and carbon nanotube-binding peptides have been extensively characterized using both molecular modeling simulations and experimental analysis techniques to elucidate a detailed understanding through many years of collective research among collaborative efforts (Briggs and Knecht 2012; Corni 2013).

It is equally important to understand how the structure, properties, and activity of biomolecules or nanoparticle-binding peptides are affected by nanomaterial interactions. This is critical to the successful implementation of peptide-functionalized NPs for biomedical uses and in assessing their potential toxicity and biocompatibility. In complex biological environments such as in biological fluids or in living cells; NPs are exposed to high ionic strengths (150 mM), oxidizing environments, numerous physical forces (hydrodynamic, osmotic pressures), an infinite matrix of different competing biomolecules to interact with and to displace surface proteins (enzymes, albumin, immunoglobulins), and/or macrophage cells trying to engulf and eliminate NPs (Nel et al. 2009). These secondary interactions could likely alter the peptide structure and function on the NP surface. Also, upon intimate contact with proteins, NPs act as catalysts by exposing new antigenic epitopes and protein interaction domains through unfolding of the protein structure on the NP surface leading to an adsorption layer of proteins around the nanomaterial, the so-called "protein corona." The physiochemical parameters (size, shape, surface charges) of the nanomaterial have a large influence on the composition and structure of the protein corona (Lundqvist et al. 2011). For example,  $\beta$ 2-microglobulin fibrillation occurs on the surface of carbon nanotubes or cerium oxide NPs due to protein unfolding and exposure of new domains which induce aggregation of promote formation of fibrils. These effects have severe biochemical and toxicological implications which require complete characterization of potential biological interactions in vivo. Alternatively, for nonmedical uses, the structure and activity of peptides altered by a NP surface and/or by the binding of a chemical or biological target determines sensing efficiency, catalytic and biological activity, and functionality of the NP system. This concept was recently exploited by using peptide-functionalized gold NPs as a sensing material for the selective detection of multiple vapors with similar dielectric constants (Nagraj et al. 2013). In this sensing structure, the diverse amino acid composition of peptides on gold when exposed to different vapors yielded unique vapor-peptide interactions which affected the impedance output of the NPs. As demonstrated by

this example, the utility and effectiveness of peptide capped NPs for sensing depends on not only gaining insight into peptide-nanoparticle interactions but also understanding multiple fundamental interactions occurring with the peptide coat in terms of both target specific binding and interfering environmental agents present (humidity, nonspecific targets, temperature). The adsorption of molecules on nanoscale objects, in principle, can then be used to control assembly, function, and the structure of the adsorbed species. This ultimately can result in the formation of sophisticated nanostructures with adaptable/smart features or conversely have adverse effects on biomolecules.

### ***1.2.4 Computational Modeling of Peptide-Nanomaterial Interactions***

Current computational modeling efforts have provided much needed atomic, molecular, and structural level detail on peptide-inorganic surface interactions. Computational tools are getting better at dealing with more complex nanosystems and larger biomolecules due to the progression of computing power (faster processors), development of new force fields for molecular modeling, and newer software packages. For instance, only a few years ago, computer simulations were restricted to a single peptide on a flat planar surface consisting of several hundred atoms; but have recently been expanded to include various shapes of nanostructured metal surfaces and many more peptides or larger proteins (Feng et al. 2012). The various geometrical surfaces have provided a starting structure more closely resembling those obtained experimentally. Modeling has also provided insight into key residues and peptide structural parameters such as conformational flexibility important in NP binding. This has led to refinement of peptide-binding and enhancements in properties as discussed in upcoming chapters. Although from its inception, molecular modeling/simulations have served in a passive supporting role with the goal of complementing experimental data/structures. Additionally, one of many challenges to overcome is the lack of open communication and dialog between experimentalists and the computational community. In order for modeling to make an impact, there is a need to facilitate more of these interactions and work closely on a routine basis. Also, to date, there is a lack of predictive mesoscale coarse grain models which can accommodate particles and not just atoms, minimal force fields limited to a few types of materials (Au and SiO<sub>2</sub>), poor computational efficiency associated with biomaterials modeling, and a need to analyze/mine large collections of data for the purpose of identifying/assessing sequences/patterns which would be overlooked by human operators. These hidden data links will ensure and expand the materials genome at a tremendous pace. In the coming years, computational modeling is expected to rapidly accelerate the discovery of new nanomaterial-binding peptides, provide predictive tools for structure and function, offer rapid exploration of biomolecule and nanomaterial parameter space (sequence, structure, chirality, physical properties), and operate independently of

experimentally collected data. Ideally, modeling will be used to generate and identify new nanoparticle-binding peptides, validate and maximize binding, evaluate NP properties as a result of peptide-binding, and perhaps even anticipate material related problems of the future.

### 1.3 Visions/Possibilities in The Future

The future of bio-nanomaterials science holds great promise for enabling the development of sensors that can emulate their biological counterparts, materials that have adaptable self-repairing properties, and devices that can perform like biological machinery. These efforts will heavily rely on computational resources for automation, discovery of new peptide ligands, and prediction of material properties. There have been many new applications found for existing proteins and biologically derived inorganic materials such as in the areas of protein-based optical coatings, hybrid structures, and in bioenergetics. Also, as discussed earlier, the advent of emerging technologies especially in the areas of 3-D printing and patterning in general, will revolutionize how materials and biomolecules will be processed and assembled into highly intricate structures comparable to those observed in nature. Ultimately, this type of application could possibly one day rival those created in nature and lead to multiscale structures. While nature has perfected the synthesis of a variety of nanostructures, the formation of novel NPs not found in nature is currently a challenge using biological systems. Although, even this concept is quickly becoming antiquated as the limits of biology are constantly being expanded through advancements in genetic engineering and synthetic biology. In the near future, factories of microbial communities will be able to synthesize and create any artificial inorganic nanomaterial on demand using synthetic biology to achieve precise control over properties. Additionally, Mirkin's group has already demonstrated the assembly of NP superlattice structures that adopt various crystal structures using DNA. Using gold NPs as the core, DNA conjugated to the metal NP allows for the independent control of three important design parameters (particle size, lattice parameters, and crystallographic symmetry) to create the nanostructure lattice of choice (Macfarlane et al. 2011). This has resulted in the creation of binary NP lattices and new crystal lattice structures never before observed in nature. Similarly, using protein cages or peptide-functionalized NPs to form assemblies can also be a useful tool in biomedical applications. Ultimately, the ability to control and predict biomolecule structure and orientation on NP surfaces through ongoing studies and improvement of peptide or DNA nanomaterial interactions will result in catalysts with greater activity and efficiency, better sensing and recognition of targets, effective antibody binding, assembly of multicomponent materials and development of smart materials for drug delivery, and other therapeutic applications. Moreover, the knowledge base acquired from studying peptide-nanomaterial interactions will also provide the framework for understanding and exploiting interactions with nonbiologically based molecules such as various polymers and simpler peptide analogs (peptoids).

**Acknowledgements** The authors would like to thank several colleagues and members of the AFRL/RX bio-research team for useful discussions. AFRL/RX and AFOSR is acknowledged for financial support.

## References

- Aizenberg J, Lambert G, Weiner S, Addadi L (2002) *J Am Chem Soc* 124:32
- Bazyllinski DA, Frankel RB, Konhauser KO (2007) *Geomicrobiol J* 24:456
- Briggs BD, Knecht MR (2012) *J Phys Chem Lett* 3:405
- Chen C-L, Zhang P, Rosi NL (2008) *J Am Chem Soc* 130:13555
- Chiu CY, Li YJ, Ruan LY, Ye XC, Murray CB, Huang Y (2011) *Nat Chem* 3:393
- Coordination Chemistry in Protein Cages: Principles, Design, and Applications (2013). In: Ueno T, Watanabe Y (eds) Vol. 1. John Wiley & Sons, New Jersey
- Coppage R, Slocik JM, Briggs BD, Frenkel AI, Heinz H, Naik RR, Knecht MR (2011) *J Am Chem Soc* 133:12346
- Coppage R, Slocik JM, Ramezani-Dakhel H, Bedford NM, Heinz H, Naik RR, Knecht MR (2013) *J Am Chem Soc* 135:11048
- Corni S, Hnilova M, Tamerler C, Sarikaya M (2013) *J Phys Chem C* 117:16990
- Cung K, Slater RL, Cui Y, Jones SE, Ahmad H, Naik RR, McAlpine MC (2012) *Lab Chip* 12:562
- Derda R, Tang SKY, Li SC, Ng S, Matochko W, Jafari M (2011) *Molec* 16:1776
- Dickerson MB, Sandhage KH, Naik RR (2008) *Chem Rev* 108:4935
- Donatan S, Sarikaya M, Tamerler C, Uergen M (2012) *J R Soc Interface* 9:2688
- Feng J, Slocik JM, Sarikaya M, Naik RR, Farmer BL, Heinz H (2012) *Small* 8:1049
- Flenniken ML, Liepold L, Kang S, Uchida M, Young MJ, Douglas T (2008) *Curr Opin Microbiol Immunol* 327:71
- Heinz H, Farmer BL, Pandey RB, Slocik JM, Patnaik S, Pachter R, Naik RR (2009) *J Am Chem Soc* 131:9704
- Hnilova M, Oren EE, Seker UOS, Wilson BR, Collino S, Evans JS, Tamerler C, Sarikaya M (2008) *Langmuir* 24:12440
- Khatayevich D, So CR, Hayamizu Y, Gresswell C, Sarikaya M (2012) *Langmuir* 28:8589
- Killian CE, Metzler RA, Gong YUT, Olson IC, Aizenberg J, Polit Y, Wilt FH, Scholl A, Young A, Doran A, Kunz M, Tamura N, Coppersmith SN, Gilbert PUPA (2009) *J Am Chem Soc* 131:18404
- Kim SN, Kuang ZF, Slocik JM, Jones SE, Cui Y, Farmer BL, McAlpine MC, Naik RR (2011) *J Am Chem Soc* 133:14480
- Kramer RM, Li C, Carter DC, Stones MO, Naik RR (2004) *J Am Chem Soc* 126:13282
- Kroger N, Deutzmann R, Sumper M (1999) *Science* 286:1129
- Li Y, Huang Y (2010) *Adv Mater* 22:1
- Lundqvist M, Stigler J, Cedervall T, Berggard T, Fanagan MB, Lynch I, Elia G, Dawson K (2011) *ACS Nano* 5:7503
- Macfarlane RJ, Lee B, Jones MR, Harris N, Schatz GC, Mirkin CA (2011) *Science* 14:204
- Matmor M, Ashkenasy N (2012) *J Am Chem Soc* 134:20403
- Matochko W, Chu K, Jin B, Lee S-W, Whitesides G, Derda R (2012) *Methods* 58:47
- Mirau PA, Naik RR, Gehring P (2011) *J Am Chem Soc* 133:18243
- Nagraj N, Slocik JM, Phillips DM, Kelley-Loughnane N, Naik RR, Potyrailo RA (2013) *Analyst* 138:4334
- Nam KT, Lee YJ, Kottmann S, Krauland E, Liao F, Belcher AM (2008) *ACS Nano* 2:1480
- Nel AE, Madler L, Velegol D, Xia T, Hoek EMV, Somasundaran P, Klaessig F, Castranova VT (2009) *M. Nat Mater* 8:543
- Nergiz SZ, Slocik JM, Naik RR, Singamaneni S (2013) *Phys Chem Chem Phys* 15:11629

- Patwardhan SV, Emami FS, Berry RL, Jones SE, Naik RR, Deschaume O, Heinz H, Perry CC (2012) *J Am Chem Soc* 134:6244
- Pelaz B, Jaber S, de Aberasturi D, Wulf V, Aida T, de la Fuente JM, Feldman J, HGaub HE, Josephson L, Kagan CR, Kotov NA, Liz-Marzan LM, Mattoussi H, Mulvaney P, Murray CB, Rogach AL, Weiss PS, Willner I, Parak W (2012) *ACS Nano* 6:8468
- Razvag Y, Gutkin V, Reches M (2013) *Langmuir* 29:10102
- Sapsford KE, Algar WR, Berti L, Gemmill KB, Casey BJ, Oh E, Stewart MH, Medintz IL (2012) *Chem Rev* 113:1904
- Skowronski M, DeYoreo JJ, Wang C (eds) (2007) *Perspectives on inorganic, organic, and biological crystal growth: from fundamentals to applications*, vol 916. American Institute of Physics, New York
- Slocik JM, Naik RR (2010) *Chem Soc Rev* 39:3454
- Slocik JM, Govorov AO, Naik RR (2011) *Nano Lett* 11:701
- Slocik JM, Crouse CA, Spowart JE, Naik RR (2013) *Nano Lett* 13:2535
- So CR, Hayamizu Y, Yazici H, Gresswell C, Khatayevich D, Tamerler C, Sarikaya M (2012) *ACS Nano* 6:1648
- Song C, Blaber MG, Zhao G, Zhang P, Fry C, Schazt GC, Rosi NL (2013) *Nano Lett* 13:3256
- Swartz JD, Deravi LF, Wright DW (2010) *Adv Func Mater* 20:1488
- Tamerler C, Sarikaya M (2009) *ACS Nano* 3:1606
- Tomczak MM, Glawe DD, Drummy LF, Lawrence CG, Stones MO, Perry CC, Pochan DJ, Deming TJ, Naik RR (2005) *J Am Chem Soc* 127:12577
- Uttamchandani M, Yao SQ (2008) *Curr Pharmaceutical Des* 14:1
- Wang D, Wallace AF, DeYoreo JJ, Dove PM (2009) *Proc Natl Acad Sci USA* 106:21511
- Wei ZY, Maeda Y, Matsui H (2011) *Angewandte Chemie (International Edition)* 50:10585

# Chapter 2

## Fundamentals of Peptide-Materials Interfaces

Tiffany R. Walsh

**Abstract** The investigation of the binding, dynamics and properties of peptides adsorbed on inorganic surfaces is an inherently multidisciplinary endeavor. This chapter is primarily aimed at new researchers in this field, to introduce the basic concepts that span physical chemistry, surface science, structural biology, computational techniques, and materials science; all of which are necessary for gaining a comprehensive overview of peptide-materials interfaces. What are the key insights that can be determined from these interfaces? Usually, this will comprise a blend of thermodynamics, kinetics and structural characterizations. Typically, we might wish to compare the binding strength of a peptide, and concomitantly, the structure(s) assumed by the peptide upon adsorption. We might also seek to characterize the surface diffusion, and/or aggregation (or assembly) of these surface-adsorbed biomolecules. These observations serve to facilitate connections between the composition and sequence of the peptide, and its behavior and properties at the interface. Such connections could be subsequently exploited in bioinformatics models to enable the prediction of new peptide sequences, with designed, predictable interfacial properties.

### 2.1 Introduction and Background

Peptides and proteins are workhorses in the natural world, carrying out a variety of roles, including: recognizers, connectors, transporters, messengers/reporters, and structural support, just to name a few (Whitford 2005). Peptides and proteins are also closely associated with biominerals in Nature, such as in shells, bone, sponge spicules, and tooth enamel (Sarikaya et al. 2003; Crookes-Goodson et al. 2008;

---

T. R. Walsh (✉)

Institute for Frontier Materials, Deakin University, Geelong, VIC 3216, Australia  
e-mail: tiffany.walsh@deakin.edu.au



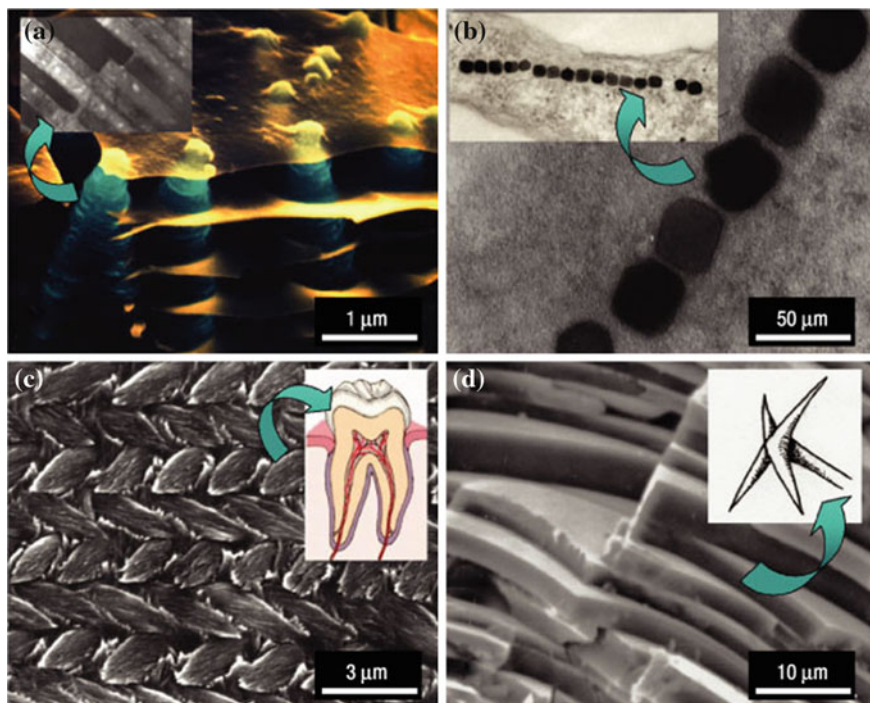


**Fig. 2.1** Scanning electron microscopy images of naturally-occurring high-performance bioorganic composite materials. **a** Aragonite platelets in the growth edge of an abalone shell (*inset* transmission electron microscope, TEM, image); **b** crystallographically-aligned magnetite nanoparticles formed by magnetotactic bacteria (*inset* TEM image); **c** woven nanocrystals of hydroxyapatite in tooth enamel; **d** layered silica of a sponge spicule. Reproduced with permission of the copyright holder, from Sarikaya et al. (2003)

Dickerson et al. 2008a), see Fig. 2.1 for example. Biomineral-associated proteins and peptides are thought to have evolved to play a key role in the nucleation, growth, and organization of nanostructured biocomposite materials. They are thought to do so via specific, noncovalent interactions with the aqueous materials interface. Research in this area spans the investigation of naturally occurring biogenic minerals through to the search and identification of new peptide sequences, associated with artificial hard materials. It is the latter, that of selected peptide sequences that recognize materials through specific noncovalent interfacial interactions, that we will focus on herein in this chapter.

The pioneering work of Stanley Brown, employing cell surface display, first identified peptide sequences that recognized the gold surface (Brown 1997). Since this pioneering work, the research field encompassing the identification and characterization of materials-binding peptide sequences grew rapidly (see, e.g., Whaley et al. 2000; Naik et al. 2002a; Sarikaya et al. 2004); to date these selection data cover peptide sequences identified to bind, for example, metals (Naik et al. 2002b; Forbes et al. 2010; Li et al. 2009; Hnilova et al. 2008; Heinz et al. 2009;

Chiu et al. 2010), oxides (Naik et al. 2002a; Oren et al. 2007; Patwardhan et al. 2012; Sano and Shiba 2003; Dickerson et al. 2008b; Fang et al. 2008; Thai et al. 2004; Nygaard et al. 2002; Rothenstein et al. 2012), semi-conductors (Whaley et al. 2000; Lee et al. 2002; Estephan et al. 2011), nanostructured carbon such as carbon nanotubes and graphite (Kulp et al. 2005; Wang et al. 2003; Cui et al. 2010; Pender et al. 2006), polymers (Serizawa et al. 2007), carbohydrates (Guo et al. 2013), as well as naturally-occurring minerals (Li et al. 2002; Roy et al. 2008, Gungormus et al. 2008). These peptide sequences were typically selected from libraries via an iterative binding process referred to as biopanning (Sarıkaya et al. 2003). The final set of selected sequences resulting from the biopanning process are those deemed to confer the strongest *binding affinity* (i.e., adsorption strength) for a target material. In addition to these identification studies, peptide sequences have been reported that exhibit a discrimination in terms of surface recognition, sometimes referred to as *binding selectivity*: discrimination between two (or more) material surfaces (compositional selectivity) (Tamerler et al. 2006; Fang et al. 2008); discrimination between different crystallographic surface orientations of the same material (facet selectivity) (Wright and Walsh 2012; Ruan et al. 2013), and discrimination between two (or more) polymorphs of the same material (polymorph selectivity). Exploitation of this binding selectivity is poised to play a pivotal role in the future adoption of materials-binding peptides into the mainstream deployment of nucleation, growth, and assembly approaches for making novel, synthetic, nanostructured bioinorganic hybrid materials with designed and predictable properties, under ambient conditions.

However, identification of peptide sequences is only the first, albeit crucial, step in the successful utilization of materials-binding selective peptides in realizing this goal. Currently, isolation and identification of materials-binding peptide sequences, per se, do not form the bottleneck in advancing this research field; rather, it is the generation of understanding, and the distillation of *generalizable* principles, derived from this understanding, that at present hinders progress toward these goals. Key unanswered questions remain, and resolution of these questions is central to enabling the incorporation of materials-binding peptides into the toolbox of reliable materials synthesis approaches that can be realized for a variety of different inorganic components, and furthermore, enable the *versatile* creation of novel, multimaterials nanostructured assemblies.

Some of these questions are concerned with experimental approaches, ranging from the fundamental conditions for biopanning and the impact of this on the selected sequences (Puddu and Perry 2012) through to how to directly determine the adsorbed peptide structure(s) at the interface (Mirau et al. 2011). However, one of the more imperative questions in this research topic is associated with interpretation—how can we relate the materials-binding behavior to the peptide sequence (and not just the residue content of the peptide)? This question concerns not only how to interpret outcomes from peptide selection experiments, but also is pivotal to understanding how to systematically preserve the materials-recognition properties of these selected peptides upon conjugation into larger molecular constructs.

## 2.2 Basic Key Concepts: Surface Science and Physical Chemistry

### 2.2.1 Introductory Surface and Interface Science

Characterization of the surface of the target material is as important to gaining insight into the adsorption behaviors of materials-binding peptides as the conformations of the peptides themselves. Relevant questions regarding the state of the surface include: is the surface crystalline or amorphous? If crystalline, is the surface single crystal or polycrystalline? What is the charged state of the surface, under aqueous conditions, and at a range of pH values? The process history of the surface samples can be pivotal to understanding the behavior of the surface (particularly for silica) (Patwardhan et al. 2012); is the surface clean—e.g., are there problems with adventitious carbon? If so, is there a way to clean the surface without destroying or modifying the desired surface structure? If the surface is already coated (e.g., with a stabilizing ligand such as citrate, in the case of nanoparticles), how does the presence of the ligand and its distribution on the surface affect peptide binding? Moreover, the shape of the aqueous materials interface could also conceivably play a role in controlling adsorption of peptides, in addition to the consideration of steps and kinks that may be present on planar materials surfaces. For some materials (such as oxides) it can be challenging to separate out the dependencies between surface curvature and surface chemistry for small nanoparticle surfaces (Patwardhan et al. 2012). The propensity of the material surface to oxidize may also create challenges; while some oxide surfaces are well understood from a structural perspective, other materials, e.g., semiconductor surfaces such as GaAs and CdSe, may possess very complex oxide surface structures that are not necessarily well resolved at the atomistic level, thus potentially hindering our understanding of how peptides recognize these materials. Finally, all of these factors regarding the materials surface structure can also play a critical role in determining the structuring of the solvent (usually aqueous solution) at the interface. The impact of this interfacial solvent structuring on the adsorption propensity of materials-binding peptides will be subsequently discussed in more detail (*vide infra*).

Before doing so, we give a brief summary of some common terms and concepts associated with the surface science of crystalline materials. In brief, if a material is crystalline, then the bulk material will feature a regular patterning in three-dimensional (3-D) space in terms of the constituents of the crystal, i.e., the atoms and/or molecules in the material. By cutting the 3-D bulk crystal along a given plane (defined by three noncolinear points in the crystal lattice) different crystal-line *surfaces* can be generated, thus presenting different, two-dimensional arrangements of surface atoms—e.g., see Fig 2.2. Types of surfaces are characterized by three numbers known as the Miller indices ( $h$ ,  $k$ ,  $l$ )—e.g., the (111) surface or the (100) surface (as in Fig. 2.2). The vector normal to the Miller Plane is the vector  $[h, k, l]$ . (see, for example, Atkins and de Paula 2010, for more

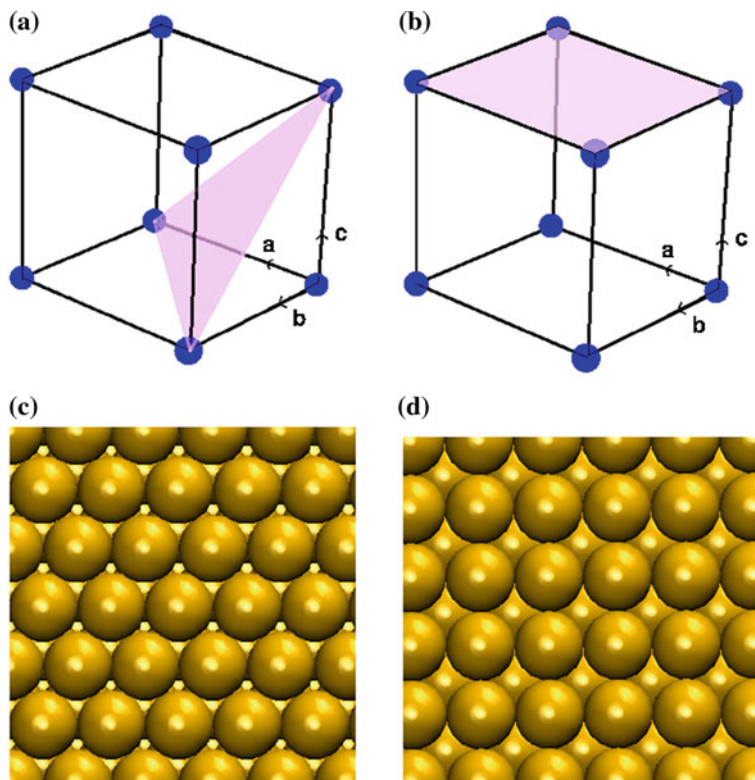


**Fig. 2.2** Illustration of different crystallographic orientations of surfaces. **a** and **b** Indicate two lattice planes of a simple cubic lattice, the (111) and (001) planes, respectively. The three principal axes are indicated as  $\vec{a}$ ,  $\vec{b}$ , and  $\vec{c}$ . **c** and **d** Give the atomistic-level structure of two different example crystallographic orientations of the ideal gold surface, the (111) and (100) planes, respectively

details). Crystalline surfaces can depart from ideality via the incorporation of defects; e.g., vacancy defects; and through the presence of steps, kinks, and adatoms on the surface. These features may exhibit very different propensities for interaction with adsorbed peptides, compared with the ideal surface. One other point of distinction for crystalline surfaces is the consideration whether the surface is single crystal (e.g., a single crystal Au(111) surface), or, a polycrystalline surface (one that presents an ensemble of different low-energy planes).

A further complication arises in the consideration of crystalline surfaces in terms of surface reconstruction. If we consider cleaving the bulk crystal along a given plane orientation, then the newly generated surface exposes atoms on the surface that are *under-coordinated* in comparison with the atoms underneath the surface layers. This under-coordination may lead to a rearrangement of the surface atoms such that the potential dangling bonds at the surface can be satisfied, a

classic example of which is the  $(7 \times 7)$  reconstruction of the Si(111) surface (Binnig et al. 1983). While this definition may suggest that covalently bonded network solids are prone to surface reconstruction, it is also possible for other types of materials, e.g., noble metals, to support surface reconstruction. The favorable reconstructions of a surface should be considered, since the subsequent arrangement of the surface atoms could impact substantially on adsorption behavior at the aqueous interface, not only through spatial registry of the collective interactions between the peptide atoms and the surface atoms per se, but also via any changes of the solvent structuring at the reconstructed surface.

Structuring (both spatial and orientational) of interfacial solvent is thought to highly influential on the adsorption structure(s) of the peptide. Part of this influence is possibly due to the changes in the solvent hydrogen-bonded network in the interfacial region, thus perhaps modifying the opportunities for the peptide interact via hydrogen-bonds with this interfacial solvent. In addition, the thermodynamics of peptide adsorption can be influenced by how tightly the solvent is bound to the surface itself, given that the peptide will displace solvent in the first solvation layer if the peptide makes direct surface contact, i.e., non solvent-mediated surface contact (Skelton et al. 2009; Schneider and Colombi-Ciacchi 2012). In free energy terms, there will be a trade-off between the loss of enthalpy of the released first-layer solvent molecules, the gain in enthalpy for the adsorbed peptide groups, the gain in entropy of the interfacial waters released into the bulk—due to the footprint of the parts of the peptide that make direct contact, and thus displace the waters, and the loss in peptide conformational entropy upon adsorption onto the surface. Additional complications arise in the interfacial solvent structuring due to the presence of solvated ions, particularly due to structuring of the electrical double layer for interfacial salt solutions. The influence of salt concentration on the interfacial adsorption of functional groups analogous to peptides has been recently investigated using atomic force microscopy (AFM) (Hassenkam et al. 2012). Finally, the sharpness of the interface between the solvent and the materials surface could potentially exert a significant influence on peptide adsorption; very sharp interfaces (such as for the aqueous noble-metal interface), might show differences in adsorption with the slowly dissolving interface of some materials surfaces (e.g., for silica). However, both of these examples could differ substantially with some carbohydrate surfaces, where ingress of water into the upper surface layers of the material may instead result in a diffuse interfacial layer instead of a sharp interface, thus potentially modulating the binding behaviors of the peptide.

If the target material is amorphous, we cannot know the local arrangement of the atoms on the surface in precise detail. However, we can make statistical inference regarding some average structural characteristics. This is important not only for the bulk material—e.g., in terms of determining the radial distribution function between pairs of atoms in the bulk—but also for the surface structure, such as the average distances between moieties presented on the surface. Average surface densities of relevant groups are also valuable information; e.g., for hydroxylated surfaces, it may be possible to identify the average surface density of hydroxyl groups, as well as the types of hydroxyl (germinal *vs* vicinal) on the surface. Further details

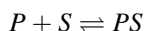
regarding the distribution of these sites, while desirable, are typically not available from experimental data. This creates a challenge for interpreting adsorption data, since many distribution models of the sites can admit the same average site density. The atomistic scale surface topography of the amorphous surface may also be much more rugged compared with an ideal single-crystal surface.

In closing, often one of the most challenging aspects related to surface characterization for materials-binding peptide systems is related to consistency. In other words, is it not uncommon that the target surface against which the peptide library was screened was not, for reasons of practicality, the same surface that was used for subsequent characterization experiments. For example, a peptide may be selected to recognize the quartz(100) surface (crystalline  $\text{SiO}_2$ ), but the peptide-binding characterization may be performed on the amorphous  $\text{SiO}_2$  surface. This apparent inconsistency can perhaps be attributed to the common quantitative characterization techniques currently available (quartz crystal microbalance, and, surface plasmon resonance) where the required material surface under study must first be deposited as a thin film on top of the surface of, e.g., the surface plasmon resonance chip. Thin-film deposition of amorphous or polycrystalline materials is viable for a range of materials—deposition of crystalline materials, at present, is not.

### 2.2.2 Physical Chemistry

Two key viewpoints from which to survey any interfacial process are thermodynamics and kinetics. Thermodynamics is concerned with the state of the system at a given state point (in temperature and pressure) at chemical equilibrium. The reaction kinetics concern the rates at which both peptide adsorption and desorption take place, as well as the rates of interconversion between different peptide conformations in the adsorbed state.

Consider the following chemical equation for peptide adsorption on a surface (Wei and Latour 2008):



where  $P$ ,  $S$  and  $PS$  represent the peptide in solution, the available surface sites for adsorption, and the peptide in the surface-adsorbed state, respectively.  $k_{\text{ads}}$  is the forward rate coefficient for the adsorption process, while  $k_{\text{des}}$  is the reverse rate coefficient for the desorption of the peptide, assuming that the binding process is reversible. The forward and backward rates of reaction can be expressed assuming elementary reaction steps in both instances:

$$\frac{d[P]}{dt} = -k_{\text{ads}}[P][S]$$

$$\frac{d[PS]}{dt} = -k_{\text{des}}[PS].$$

In simplified terms (Pilling and Seakins 2001), the equilibrium constant,  $K_{\text{ads}}$ , for this reaction can therefore be expressed as:

$$K_{\text{ads}} = \frac{[PS]}{[P][S]}.$$

Equilibrium is dynamic, with both adsorption and desorption taking place, but *at equal rates* such that the concentrations  $[PS]$ ,  $[P]$  and  $[S]$  are maintained at constant values. This leads to a further expression, relating the ratio of the rate coefficients for both the forwards and backwards reactions to the equilibrium constant:

$$\frac{k_{\text{ads}}}{k_{\text{des}}} = K_{\text{ads}}.$$

At equilibrium, changes in thermodynamic properties (such as the change in free energy), between an initial state and a final state, depend only on the differences in these properties at these state points, and are independent of the pathway taken to proceed from the initial state to the final state (Atkins and de Paula 2010). The key thermodynamic quantity of interest is the change in free energy upon adsorption, although associated quantities, such as the fractional surface coverage are also often reported in adsorption studies. The change in Gibbs free energy corresponding to adsorption of the peptide,  $\Delta G_{\text{ads}}$ , is measured to be the change in free energy at constant temperature and pressure, for an initial state where the peptide is located far from the interface, in bulk solution, and for a final state where the peptide is adsorbed on the surface. In terms of experimental measurements, the free energy of adsorption is usually derived for the standard state (Wei and Latour 2008).

Typically, the experimentally determined binding free energy is inferred from the binding constant, via use of the expression:

$$\Delta G_{\text{ads}} = -RT \ln(K_{\text{ads}}).$$

However, inference of the free energy of adsorption, derived from experimental techniques such as quartz crystal microbalance (QCM), or surface plasmon resonance (SPR) measurements, via fitting of the raw data to the Langmuir isotherm (see Atkins and de Paula 2010, for more details), may also implicitly include contributions from peptide–peptide interactions (in the surface adsorbed state), in addition to the peptide–surface interactions under investigation. Corrections for this effect have been proposed (Wei and Latour 2008) to address this challenging problem.

## 2.3 Basic Key Concept: Energy Landscapes

To interpret physical chemistry observations, we need to establish links between entities such as free energy and reaction rates (in our case, e.g., rates for surface adsorption and desorption), and the structure and dynamics of the peptide, at the atomistic level. Here, we introduce and elaborate on the concept of energy landscape theory (Wales 2003; Wales et al. 1998), to reveal and interpret these links. Energy landscape theory is a unifying framework for understanding and interpreting both thermodynamic and kinetic behaviors of a system at the atomistic level. Herein, we outline the basic concepts in energy landscape theory and relate this to peptide-materials interactions.

The potential energy of a chemical system comprises the total of all inter-atomic interactions, between all atoms in the system. Typically, these potential energy contributions vary with the inter-atomic distances between all atoms in the system. Therefore, we can express the potential energy of our system as a function of the positions, e.g., in three-dimensional Cartesian space, of all atoms in this system. The position of each atom can be expressed as three scalars (numbers), e.g., corresponding to the coordinates of the atom in space ( $x$ ,  $y$ ,  $z$ ). It is usual to simplify this further, and express the potential energy in terms of the number of vibrational degrees of freedom of the system. Consider a general system comprising a single, nonlinear molecule with  $N$  atoms. This system has  $3N-6$  vibrational degrees of freedom (see Atkins and de Paula 2010, for more details); 3 degrees of freedom are subtracted for bulk translation along the  $x$ ,  $y$  and  $z$  principal axes, and a further three are subtracted for bulk rotations around the  $x$ ,  $y$  and  $z$  principal axes. This is because the potential energy captures the interactions between all atoms in the system, and the bulk translation and rotations of the system do not alter the inter-atomic distances in the system. For example, the molecule butane  $C_4H_{10}$  has 14 atoms, and thus has 36 vibrational degrees of freedom. We can therefore represent the potential energy of butane as a 36-dimensional function, and thus the potential energy surface has 37 dimensions. In order to process such a multidimensional surface, it is usual to take lower-dimensional “slices” through this surface—e.g., see Fig. 2.3 for an example of a two-dimensional slice taken from a three-dimensional potential energy surface, for a complex biomolecular system. Returning to our butane example, we can take a two-dimensional slice through the 37-dimensional surface that corresponds to the change in potential energy of butane as a function of torsion about the central carbon–carbon bond. Therefore, in general, the abscissa associated with a two-dimensional slice through a multidimensional potential energy surface corresponds to a conflation of the  $3N-6$  degrees of freedom, projected onto this single variable. This abscissa variable is typically referred to as a “reaction coordinate.”

The key features of the potential energy surface are the stationary points—these are points on the surface where the gradient of the surface is zero. Minima on the potential energy surface are those stationary points that are convex with respect to all positions of the atoms (see Fig. 2.3). Minima on the potential energy surface



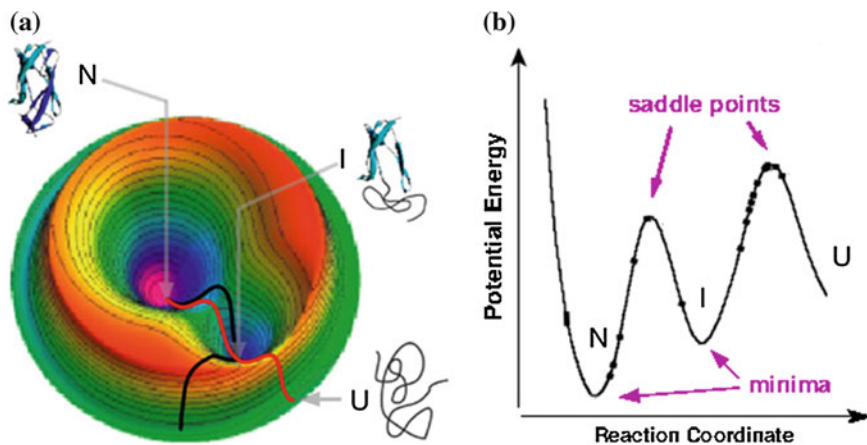


**Fig. 2.3** Example of a three-dimensional potential energy surface and a two-dimensional “slice.” **a** Three-dimensional surface, where stationary points *N* and *I* correspond to different stable structures. **b** The two-dimensional projection of the black pathway from the three-dimensional surface, with minima and saddle points indicated. Adapted from Schwaiger et al. (2004) EMBO reports. 6:46–51. Reproduced with permission of the copyright holder

correspond with experimentally-observable structures. The other relevant type of stationary point is the saddle point, where the potential energy is concave with respect to at least 1 degree of freedom (see Fig. 2.3). First-order saddles correspond with transition-states. Transition from one minimum to another (i.e., interconversion between two structures) can proceed via transition-states or, less directly, via higher-order saddle points (Wales 2003).

It is well-known that the number of atoms in the system is broadly connected to the number of minima supported on the potential energy surface (Wales 2003). The minimum of lowest energy on the potential energy surface is denoted the global minimum. Therefore, for a large, complex system—such as the aqueous peptide-inorganic interface—it is more likely that individual minima are many in number and comprise very small details in the overall scale of the relevant features of the potential energy surface. In this instance, collections of individual minima, grouped into *basins* (on a coarser spatial resolution) are a more appropriate level of description—and instead, we refer to the broader *potential energy landscape* (PEL).

The distribution of minima/basins in the PEL allows the prediction (or interpretation) of the equilibrium thermodynamic properties of the system. In other words, if we can determine the number of basins as a function of potential energy of these basins, as well as the shape of these basins, we can gain insight into the equilibrium properties of the system, such as the relative free energy corresponding to different configurations of the system, as a function of a (typically small) set of relevant “reaction coordinates.” In the case of the aqueous peptide-inorganic interface, the distance between the peptide (say, the center of mass) and the materials surface is an appropriate reaction coordinate. The distribution of

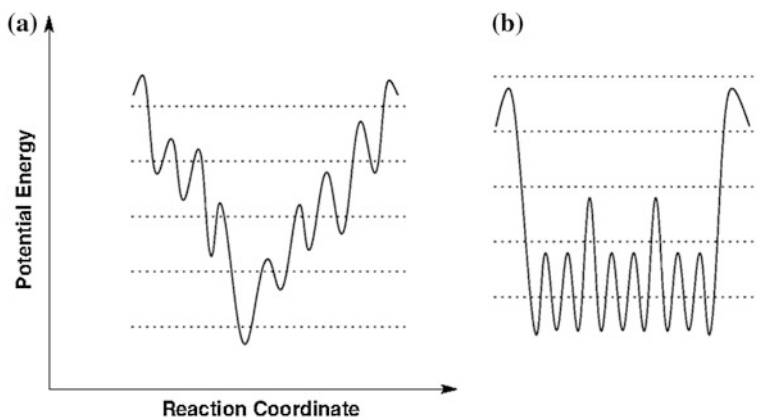
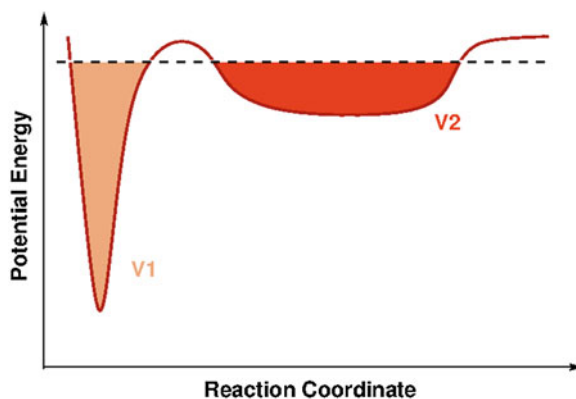


**Fig. 2.4** Two exemplar potential energy landscapes projected into two dimensions. **a** Landscape corresponding to a steep funnel with moderate energy barriers between minima. **b** Landscape corresponding to a frustrated system with large barriers located between roughly iso-energetic minima. The ensemble of surface-adsorbed states for a typical materials-binding peptide could resemble example (b). Adapted from Wales et al. (1998). Reproduced with permission from the copyright owner

energetic barriers between basins on the PEL—in other words, the distribution of saddle points, and the minima/basins they connect, as a function of potential energy—gives us insight into the kinetics of the system. In particular, the identification of large barriers between basins can indicate basins (including those not necessarily very low in energy) that correspond with metastable configurations of the system. This information about kinetic barriers and possible metastable states is particularly important for ensuring reliable descriptions of the system using molecular simulation techniques (see Sect. 2.5). Representative, exemplar PELs, and their corresponding equilibrium and kinetic properties, are well documented (Wales et al. 2003), see Fig. 2.4. Perhaps the most well-recognized exemplar PEL is that of the protein-folding “funnel” (Bryngelson et al. 1995). On the other hand, of relevance to the aqueous peptide-materials interface is the “frustrated” or “rugged” energy landscape, characterized by large numbers of approximately iso-energetic minima/basins, separated by barriers of height much greater than  $k_B T$  (where  $k_B$  is Boltzmann’s constant and  $T$  is the system temperature) (Wales et al. 1998)—see Fig. 2.4 and Sect. 2.4 for more details.

The distribution of basins/minima on the PEL, and the relative volume of these basins (in multidimensional space) can be used to roughly gauge the relative free energy of the configurations associated with these basins. Consider an example of a hypothetical PEL that features two basins: one is broad and shallow, one is narrow and deep—see Fig. 2.5. We could, for instance, relate the volume of the basin to the relative population of this basin, with respect to the total ensemble of basins, at a given temperature. Using an arbitrary energy cut-off for evaluation of the relative volume of each basin, indicated by the dashed line in Fig. 2.5. it is entirely plausible that the two basins, while having very different well-depths in

**Fig. 2.5** Schematic of a hypothetical potential energy landscape projected into two dimensions. The volume of each basin, relative to a given cut-off (black dashed line) is indicated by the filled areas in 2-D, with the deep narrow basin corresponding with volume  $V1$ , and the shallow broad basin corresponding with volume  $V2$

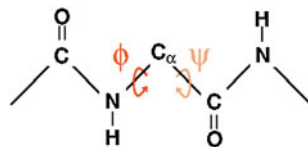


terms of potential energy, could support very similar volumes ( $V1$  and  $V2$  in Fig. 2.5), and thus, be roughly equivalent in terms of relative free energy, for that given energetic cut-off. In terms of interpreting peptide-materials adsorption, consider three hypothetical cases. In Case 1, a peptide that features a strong materials-binding affinity (i.e., a large and negative free energy of adsorption) is attributed to a multitude of relatively-weakly-bound adsorbed peptide configurations (i.e., a multitude of broad, shallow basins). In Case 2, a different peptide sequence also showing strong materials-binding affinity, is ascribed to a relatively fewer number relatively-strongly bound adsorbed peptide configurations; i.e., corresponding to a smaller number of deeper, narrow basins, where the collective volume of these narrow basins is roughly equivalent to the collective volume of the greater number of shallow basins in Case 1. Conversely, in Case 3, one could propose a peptide with a relatively weaker binding affinity, ascribed to a PEL with, say, just one single deep, narrow basin, with a volume smaller than that of the collective volumes in Cases 1 and 2. In summary, the binding affinity of a peptide is not just about the lowest-energy configuration (as illustrated by Case 3), but instead can be attributed to a combination of (1) the shape (breadth and depth) of the basins corresponding to adsorbed states, and (2) the relative numbers of each type of basin (e.g., in *very* simple terms, the number of narrow and deep basins, vs the number of broad and more shallow basins).

## 2.4 Basic Key Concept: Structure-Function Relationships at the Bio-Interface

Secondary structural motifs for peptide and proteins are defined by the positions of the backbone atoms in the peptide/protein possessing a regular pattern in space. This pattern of backbone atom positions is reflected in repetitive patterning in the values of two (of the possible three) backbone dihedral angles,  $\phi$  and  $\psi$  (see Fig. 2.6). The third backbone dihedral angle,  $\omega$ , describes the twist about the amide bond, and is thus typically considered to be rather rigid under ambient

**Fig. 2.6** Illustration of the two relevant dihedral angles for the peptide backbone; *phi* (defined by the C'-N-C $\alpha$ -C dihedral),  $\phi$ , and *psi* (defined by the N-C $\alpha$ -C-N' dihedral),  $\psi$



conditions. Some examples of secondary-structure classifications include  $\alpha$ -helix,  $\beta$ -sheet,  $\beta$ -turn, and polyproline II helix (PPII). The term *random coil* does not correspond with one single secondary structure, but in its most fundamental definition, based on ideal polymer models, the Flory random coil (Flory 1969), refers to the conditions under which the backbone dihedral angles of each residue in a peptide sequence are independent of their neighbors in the sequence (Mao et al. 2013), and thus, in principle (but not usually truly in practice), should represent an ensemble of conformations where all possible conformations are sampled. On the whole, many materials-binding peptides, identified from peptide selection experiments have been found to be lacking in well-defined secondary-structure, both when free in solution and when adsorbed at the aqueous materials interface (Collino and Evans 2008; Hnilova et al. 2008; Oren et al. 2010; Slocik et al. 2011), with random coil and PPII being dominant structural assignments. In some instances, chiefly those derived from naturally occurring mineral-binding proteins (Keene et al. 2010; Delak et al. 2009), the peptide is thought to gain structural ordering upon adsorption to the target material. These structural data have led to the proposal that some materials-binding peptides could be classified as intrinsically disordered (Collino and Evans 2008).

The relationship between the well-defined three-dimensional (3-D) structure of a protein or peptide, and its function, is a paradigm that is evolving. It is now established that well-defined 3-D structure is a sufficient, but not a necessary condition for conferring function. In other words, there exist a significant number of proteins, over 40 % of the human proteome (Jensen et al. 2010), that either fully lack a well-defined folded structure, or are partially unstructured, in their *functional* form. These proteins and peptides form a class known as Intrinsically Disordered Proteins/Peptides, IDPs (Dunker et al. 2008; Tompa 2012). IDPs are thus thought to be conformationally labile; and in many (but not all) instances may show propensity to fold upon exposure to an external stimulus—such as binding to a target (Xie et al. 2007). Not only may an IDP fold upon binding to a target, the IDP also may be amenable to binding multiple targets, and the resultant conformation may also be target-dependent (Keene et al. 2010).

It is challenging to characterize the conformational heterogeneity inherent to IDP systems. This structural characterization is necessary, however, in order to construct required links between the protein/peptide sequence, the ensemble of conformations supported by this sequence, and the functionality of this sequence—namely the materials-binding affinity and/or selectivity. The techniques for this

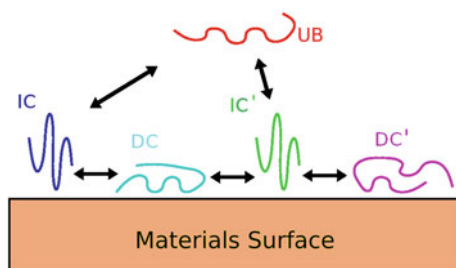


**Fig. 2.7** Schematic of the proposed interconversion between various configurations in the peptide-materials interfacial system. IC and IC' denote “indirect contact” states, where the peptide may interact with the surface via a structured solvent layer. DC and DC' represent “direct contact” states where the peptide-materials interaction is not solvent mediated. UB represents the ensemble of configurations where the peptide is not bound at the materials surface

task in widespread use are nuclear magnetic resonance (NMR) spectroscopy and circular dichroism (CD) spectroscopy, although other techniques such as small angle X-ray scattering (SAXS), electron spin resonance (ESR) and fluorescence correlation spectroscopy (FCS) have also been extensively employed in the study of IDPs in general (Eliezer 2009). Given that most materials-binding peptide sequences identified from peptide selection experiments are not long (typically 7 or 12 residues), NMR, and particularly CD spectroscopy, have comprised the principal characterization tools (Collino and Evans 2008; Hnilova et al. 2008; Oren et al. 2010), and furthermore, have been applied chiefly to the characterization of the peptide structures free in solution (i.e., not bound at the interface). There is still a good deal that is unknown regarding the archetypal structure of potential energy landscape(s) associated with IDPs in general (Fisher and Stultz 2011), and materials-binding peptides in particular.

The ensemble of peptide conformations in the presence of the aqueous materials interface is anticipated to be complex. In addition to the equilibrium partitioning of the peptide between the adsorbed and desorbed states, interconversion between different adsorbed peptide conformations may also take place (see schematic in Fig. 2.7), in addition to peptide diffusion and subsequent structural change due to peptide-peptide interactions (So et al. 2009; Nergiz et al. 2013). Therefore, gaining direct structural information of materials-binding peptides adsorbed at the materials interface, under aqueous conditions, at the atomistic level, remains a significant challenge. Despite these challenges, recent advances in NMR show promise in this area (Mirau et al. 2011).

The hypothesized interplay between a peptide sequence, the ensemble of structures that is supported by this sequence, and the binding propensity and selectivity conferred by the peptide, is pivotal to understanding, and ultimately, predicting and designing materials-binding sequences with tailored interfacial properties. Due to the challenges in obtaining direct structural data, the basis for this hypothesis has been compiled from indirect evidence from experimental sources. Compelling evidence exists regarding the impact of peptide sequence on binding

selectivity; for example, the sequence AQNPSDNNTHTH was found to bind with high affinity to GaAs, but with low affinity to silica (Goede et al. 2004). Random scrambling of this sequence to TNHDHSNAPTQ was shown to abolish this binding selectivity, such that the sequence adsorbed to both materials with similar binding strengths (Goede et al. 2004). This finding clearly underscores the idea that the binding affinity cannot be a mere additive function of a number of strongly binding residues alone. While data such as these are helpful in developing our understanding, at present, the complex relationship between sequence, structure(s), and materials binding for these bio interfaces is still not well-defined to date. For example, for a range of materials that have been previously studied (e.g., titania, silica, gold, and so forth), there is not necessarily a clear, consensus pattern in the sequences that have identified as the strong-binding peptides, *vs* the weak binding sequences. Bioinformatics approaches are one promising route to identifying such nonobvious patterns in sequence similarity—see Sect. 2.5 for more details.

Given the experimental challenges in direct structural determination of these systems, links between peptide sequence and materials-binding affinity/selectivity can be further elucidated, in partnership with indirect experimental observations, by using computational modeling at the atomistic level. In addition, bioinformatics approaches have the potential to harness existing experimental data to identify sequence motifs with predictable binding behaviors, potentially paving the way for tailored sequence design in future.

## 2.5 Links to Computational Approaches

While a detailed overview of molecular simulation methods is provided in a later chapter, we conclude this introductory chapter with some brief comments relating computational approaches to both energy landscapes and structure-function relationships, in relation to the study of peptide-materials interfaces. Herein, we will briefly touch on aspects of two computational approaches; molecular simulation from the viewpoint of the potential energy landscape, and bioinformatics approaches from the viewpoint of the structure-function relationships for materials-binding peptides.

We start with a discussion of molecular simulation approaches, with particular attention on the challenge of recovering the ensemble of conformations inherent to an IDP system. The archetypal structure of potential energy landscapes (PEL) that are typical of materials binding peptide behavior have not yet been mapped out. However, for other IDP systems, initial discussions of the PEL and how this relates to the structure(s) and dynamics of these peptides and proteins is appearing in the literature (Fisher and Stultz 2011).

Because any molecular simulation approach for IDPs must be able to locate all of the relevant stable conformations (some of which may be separated by high energy barriers) and thus recover the Boltzmann-weighted ensemble of conformations, the clear need for advanced conformational sampling approaches in

modeling IDP systems is now well established (Ostermeir and Zacharias 2013). A variety of simulation strategies as applied to IDP modeling have been reported. Replica-Exchange-based approaches (Ostermeir and Zacharias 2013; Narayanan et al. 2012; Wright and Walsh 2013; Schneider and Colombi-Ciacchi 2012; Mittal et al. 2013; Knott and Best 2012; Vellore et al. 2010; Wang et al. 2008), ‘divide and conquer’ approaches (Sethi et al. 2012), extreme long-timescale simulation (hundreds of  $\mu$ sec of continuous trajectory) (Lindorff-Larsen et al. 2012), multi-scale enhanced sampling (Moritsugu et al. 2012), multiscale ensemble modeling (Terakawa and Takada 2011), multicanonical MD (Higo et al. 2011). While extreme long-timescale simulations may be accessible to a fortunate few, replica-exchange-based approaches and variants thereof may provide a promising route that is more accessible to a wider range of researchers in this field. The few instances of advanced sampling approaches applied to materials binding peptides have employed replica-exchange-based approaches (Wang et al. 2008; Vellore et al. 2010; Schneider and Colombi-Ciacchi 2012; Wright and Walsh 2013). Methods development and testing of advanced sampling approaches for IDPs, including materials binding peptides, are expected to be a rapidly growing aspect of this research area, with many of the simulation studies cited here appearing in the past 1–2 years.

Another emerging computational approach that is poised for promising future growth is related to knowledge-based design and bioinformatics. In these approaches, a direct link can be made between the materials-binding propensity of a peptide sequence and the sequence itself, thus connecting nonobvious patterns in sequence to predictable binding behaviors. One such example of this approach is RosettaSurface (Masica and Gray 2009), which, for example has been used to design protein-biomineralization systems for calcite (Masica et al. 2010). In an alternative approach, a large dataset of experimental binding data for quartz-binding peptide sequences was successfully exploited to adapt common bioinformatics scoring matrices (Oren et al. 2007). This led to the prediction and verification of new silica-binding sequences with tailored binding affinity (both strong and weak), including sequences that bound stronger than the strongest binding peptide in the experimental dataset (Oren et al. 2007). Subsequent analysis of common sequence motifs (sequence dyads, triads, and tetrads) in the predicted silica-binding sequences was also compared against motifs identified from molecular simulation data, with very good agreement found between the two (Oren et al. 2010). However, the success of this approach hinged on the availability of a large set of experimentally determined binding data (Oren et al. 2007). This obstacle notwithstanding, a combination of experiment, informatics and molecular simulation could further prove to be an effective future direction for generating broader insights into sequence $\leftrightarrow$ structure(s) $\leftrightarrow$ binding interplay for a wide range of peptide-materials interfaces.

**Acknowledgments** TRW gratefully recognizes the enormously valuable contributions from members of her research group past and present, who have worked in this research field: Dr. Adam Skelton, Dr. Taining Liang, Dr. Rebecca Notman, Dr. Susana Tomasio, Simon Friling,

Louise Wright, Aaron Brown, Jasmine Desmond, Dr J. Pablo Palafox-Hernandez, Dr Zak Hughes, Kurt Drew, Anas Sultan and Andrew Church. TRW also acknowledges helpful discussions with colleagues and collaborators, from both experiment and theory, in the field of peptide-surface interactions: M. R. Knecht, R. R. Naik, R. A. Latour, J. S. Evans, S. Corni, L. Colombi-Ciacchi, S. Monti, M. Sarikaya, C. Tamerler, E. E. Oren, C. C. Perry, C. L. Freeman, P. M. Rodger, M. P. Allen, J. D. Gale, S. L. S. Stipp, J. H. Harding, M. T. Swihart and P. N. Prasad. Funding from the EPSRC, AFOSR, Deakin University and the AOARD is gratefully acknowledged. TRW thanks **veski** for an Innovation Fellowship.

## References

- Atkins PW, de Paula J (2010) *Physical chemistry*, 9th edn. OUP, Oxford
- Binnig G, Rohrer H, Gerber CH, Weibel E (1983)  $7 \times 7$  Reconstruction on Si(111) resolved in real space. *Phys Rev Lett* 50:120–123
- Brown S (1997) Metal-recognition by repeating polypeptides. *Nat Biotechnol* 15:269–272
- Bryngelson JD, Onuchic JN, Socci ND, Wolynes PG (1995) Funnels pathways, and the energy landscape of protein-folding—a synthesis. *Proteins* 21:167–195
- Crookes-Goodson WJ, Slocik JM, Naik RR (2008) Bio-directed synthesis and assembly of nanomaterials. *Chem Soc Rev* 37:2403–2412
- Chiu CY, Li Y, Huang Y (2010) Size-controlled synthesis of Pd nanocrystals using a specific multifunctional peptide. *Nanoscale* 2:927–930
- Collino S, Evans JS (2008) Molecular specifications of a mineral modulation sequence derived from the aragonite-promoting protein n16. *Biomacromolecules* 9:1909–1918
- Cui Y, Kim SN, Jones SE, Wissler LL, Naik RR, McAlpine MC (2010) Chemical functionalization of graphene enabled by phage displayed peptides. *Nano Lett* 10:4559–4565
- Delak K, Harcup C, Lakshminarayanan R, Sun Z, Fan YW, Moradian-Oldak J, Evans JS (2009) The tooth enamel protein, porcine amelogenin, is an intrinsically disordered protein with an extended molecular configuration in the monomeric form. *Biochemistry* 48:2272–2281
- Dickerson MB, Sandhage KH, Naik RR (2008a) Protein- and peptide-directed syntheses of inorganic materials. *Chem Rev* 108:4935–4978
- Dickerson MB, Jones SJ, Cai Y, Ahmad G, Naik RR, Kroeger N, Sandhage KH (2008b) Identification and design of peptides for the rapid, high-yield formation of nanoparticulate  $\text{TiO}_2$  from aqueous solutions at room temperature. *Chem Mater* 20:1578–1584
- Dunker AK, Silman I, Uversky VN, Sussman JL (2008) Function and structure of inherently disordered proteins. *Curr Opin Struct Biol* 18:756–764
- Eliezer D (2009) Biophysical characterization of intrinsically disordered proteins. *Curr Opin Struct Biol* 19:23–30
- Estephan E, Saab MB, Martin M, Larroque C, Cuisinier FJG, Briot O, Ruffenach S, Moret M, Gergely C (2011) Phages recognizing the indium nitride semiconductor surface via their peptides. *J Pept Sci* 17:143–147
- Fang Y, Poulsen N, Dickerson MB, Cai Y, Jones SJ, Naik RR, Kroeger N, Sandhage KH (2008) Identification of peptides capable of inducing the formation of titania but not silica via a subtractive bacteriophage display approach. *J Mater Chem* 18:3871–3875
- Fisher CK, Stultz CM (2011) Constructing ensembles for intrinsically disordered proteins. *Curr Opin Struct Biol* 21:426–431
- Flory PJ (1969) *Statistical Mechanics of Chain Molecules*. OUP, New York
- Forbes LM, Goodwin AP, Cha JN (2010) Tunable size and shape control of platinum nanocrystals from a single peptide sequence. *Chem Mater* 24:6524–6528
- Goede K, Busch P, Grundmann M (2004) Binding specificity of a peptide on semiconductor surfaces. *Nano Lett* 4:2115–2120



- Gungormus M, Fong H, Kim IW, Evans JS, Tamerler C, Sarikaya M (2008) Regulation of in vitro calcium phosphate mineralization by combinatorially selected hydroxyapatite-binding peptides. *Biomacromolecules* 9:966–973
- Guo J, Catchmark JM, Mohamed MNA, Benesi AJ, Tien M, Kao TH, Watts HD, Kubicki JD (2013) Identification and characterization of a cellulose binding heptapeptide revealed by phage display. *Biomacromolecules* 14:1795–1805
- Hassenkam T, Mitchell AC, Pedersen CS, Skovbjerg LL, Bovet N, Stipp SLS (2012) The low salinity effect observed on sandstone model surfaces. *Colloid Surf A* 403:79–86
- Heinz H, Farmer BL, Pandey RB, Slocik JM, Patnaik SS, Pachter R, Naik RR (2009) Nature of molecular interactions of peptides with gold, palladium and pd-au bimetal surfaces in aqueous solution. *J Am Chem Soc* 131:9704–9714
- Higo J, Nishimura Y, Nakamura H (2011) A free energy landscape for coupled folding and binding of an intrinsically disordered protein in explicit solvent from detailed all-atom simulations. *J Am Chem Soc* 133:10448–10458
- Hnilova M, Oren EE, Seker UOS, Wilson BR, Collino S, Evans JS, Tamerler C, Sarikaya M (2008) Effect of molecular conformations on the adsorption behavior of gold-binding peptides. *Langmuir* 24:12440–12445
- Jensen MR, Salmon L, Nodet G, Blackledge M (2010) Defining conformational ensembles of intrinsically disordered and partially folded proteins directly from chemical shifts. *J Am Chem Soc* 132:1270–1272
- Keene EC, Evans JS, Estroff LA (2010) Matrix interactions in biomineralization: aragonite nucleation by an intrinsically disordered nacre polypeptide, n16N, associated with a beta-chitin substrate. *Cryst Growth Des* 10:1383–1389
- Knott M, Best RB (2012) A preformed binding interface in the unbound ensemble of an intrinsically disordered protein: evidence from molecular simulations. *PLoS Comp Biol* 8:e1002605-1-10
- Kulp JL, Shiba K, Evans JS (2005) Probing the conformational features of a phage display polypeptide sequence directed against single-walled carbon nanohorn surfaces. *Langmuir* 21:11907–11914
- Lee SW, Mao C, Flynn CE, Belcher AM (2002) Ordering of quantum dots using genetically engineered viruses. *Science* 296:892–895
- Li CM, Botsaris GD, Kaplan DL (2002) Selective in vitro effect of peptides on calcium carbonate crystallization. *Cryst Growth Des* 2:387–393
- Li YJ, Whyburn GB, Huang Y (2009) Specific peptide regulated synthesis of ultrasmall platinum nanocrystals. *J Am Chem Soc* 131:15998–15999
- Lindorff-Larsen K, Trbovic N, Maragakis P, Piana S, Shaw DE (2012) Structure and dynamics of an unfolded protein examined by molecular dynamics simulation. *J Am Chem Soc* 134:3787–3791
- Mao AH, Lyle N, Pappu RV (2013) Describing sequence-ensemble relationships for intrinsically disordered proteins. *Biochem J* 449:307–318
- Masica DL, Gray JJ (2009) Solution- and adsorbed-state structural ensembles predicted for the statherin-hydroxyapatite system. *Biophys J* 96:3082–3091
- Masica DL, Schrier SB, Specht EA, Gray JJ (2010) De novo design of peptide-calcite biomineralization systems. *J Am Chem Soc* 132:12252–12262
- Mirau PA, Naik RR, Gehring P (2011) Structure of peptides on metal oxide surfaces probed by NMR. *J Am Chem Soc* 133:18243–18248
- Mittal J, Yoo TH, Georgiou G, Truskett TM (2013) Structural ensemble of an intrinsically disordered peptide. *J Phys Chem B* 117:118–124
- Morisugu K, Terada T, Kidera A (2012) Disorder-to-order transition of an intrinsically disordered region of sortase revealed by multiscale enhanced sampling. *J Am Chem Soc* 134:7094–7101
- Naik RR, Brott L, Carlson SJ, Stone MO (2002a) Silica precipitating peptides isolated from a combinatorial phage display library. *J Nanosci Nanotechnol* 2:95–100

- Naik RR, Stringer SJ, Agarwal G, Jones SE, Stone MO (2002b) Biomimetic synthesis and patterning of silver nanoparticles. *Nat Mater* 1:169–172
- Narayanan C, Weinstock DS, Wu KP, Baum J, Levy RM (2012) Investigation of the polymeric properties of  $\alpha$ -synuclein and comparison with NMR experiments: a replica exchange molecular dynamics study. *J Chem Theory Comput* 8:3929–3942
- Nergiz SZ, Slocik JM, Naik RR, Singamaneni S (2013) *Phys Chem Chem Phys* 15:11629–11633
- Nygaard S, Wendelbo R, Brown S (2002) Surface-specific zeolite-binding proteins. *Adv Mater* 14:1853–1856
- Oren EE, Tamerler C, Sahin D, Hnilova M, Seker UOS, Sarikaya M, Samudrala R (2007) A novel knowledge-based approach to design inorganic binding peptides. *Bioinformatics* 23:2816–2822
- Oren EE, Notman R, Kim IW, Evans JS, Walsh TR, Samudrala R, Tamerler C, Sarikaya M (2010) Probing the molecular mechanisms of quartz-binding peptides. *Langmuir* 26:11003–11009
- Ostermeir K, Zacharias M (2013) Advanced replica-exchange sampling to study the flexibility and plasticity of peptides and proteins. *Biochim Biophys Acta* 1834:847–853
- Patwardhan SV, Emami FS, Berry RJ, Jones SE, Naik RR, Deschaume O, Heinz H, Perry CC (2012) Chemistry of aqueous silica nanoparticle surfaces and the mechanism of selective peptide adsorption. *J Am Chem Soc* 134:6244–6246
- Pender MJ, Sowards LA, Hartgerink JD, Stone MO, Naik RR (2006) Peptide-mediated formation of single-wall carbon nanotube composites. *Nano Lett* 6:40–44
- Pilling MJ, Seakins PW (2001) Reaction kinetics. OUP, Oxford
- Puddu V, Perry CC (2012) Peptide adsorption on silica nanoparticles: evidence of hydrophobic interactions. *ACS Nano* 6:6356–6363
- Rothenstein D, Claasen B, Omiecienski B, Lammel P, Bill J (2012) Isolation of ZnO-Binding 12-mer peptides and determination of their binding epitopes by NMR spectroscopy. *J Am Chem Soc* 134:12547–12556
- Roy MD, Stanley SK, Amis EJ, Becker ML (2008) Identification of a highly specific hydroxyapatite-binding peptide using phage display. *Adv Mater* 20:1830–1836
- Ruan LY, Ramezani-Dakheel H, Chiu CY, Zhu E, Li YJ, Heinz H, Huang Y (2013) Tailoring molecular specificity toward a crystal facet: a lesson from biorecognition toward Pt{111}. *Nano Lett* 13:840–846
- Sano KI, Shiba K (2003) A hexapeptide motif that electrostatically binds to the surface of titanium. *J Am Chem Soc* 125:14234–14235
- Sarikaya M, Tamerler C, Jen A-K, Schulten K, Baneyx F (2003) Molecular biomimetics: nanotechnology through biology. *Nat Mater* 2:577–585
- Sarikaya M, Tamerler C, Schwartz DT, Baneyx F (2004) Materials assembly and formation using engineered polypeptides. *Annu Rev Mater Res* 34:373–408
- Schneider J, Colombi Ciacchi L (2012) Specific material recognition by small peptides mediated by the interfacial solvent structure. *J Am Chem Soc* 134:2407–2413
- Serizawa T, Techawanitchai P, Matsuno H (2007) Isolation of peptides that can recognize syndiotactic polystyrene. *ChemBioChem* 8:989–993
- Sethi A, Tian J, Vu DM, Gnanakaran S (2012) Identification of minimally interacting modules in an intrinsically disordered protein. *Biophys J* 103:748–757
- Skelton AA, Liang TN, Walsh TR (2009) Interplay of sequence, conformation, and binding at the peptide-titania interface as mediated by water. *ACS Appl Mater Interfaces* 1:1482–1491
- Slocik JM, Govorov AO, Naik RR (2011) Plasmonic circular dichroism of peptide-functionalized gold nanoparticles. *Nano Lett* 11:701–705
- So CR, Kulp JL, Oren EE, Zareie H, Tamerler C, Evans JS, Sarikaya M (2009) Molecular recognition and supramolecular self-assembly of a genetically engineered gold binding peptide on Au{111}. *ACS Nano* 3:1525–1531
- Tamerler C, Duman M, Oren EE, Gungormus M, Xiong X, Kacar T, Parviz BA, Sarikaya M (2006) Materials specificity and directed assembly of a gold-binding peptide. *Small* 2:1372–1378

- Terakawa T, Takada S (2011) Multiscale ensemble modelling of intrinsically disordered proteins: p53 N-terminal domain. *Biophys J* 101:1450–1458
- Thai CK, Dai H, Sastry MSR, Sarikaya M, Schwartz DT, Baneyx F (2004) Identification and characterization of Cu<sub>2</sub>O- and ZnO-binding polypeptides by Escherichia coli cell surface display. *J Biotech Bioeng* 87:129–137
- Tompa P (2012) Intrinsically disordered proteins: a 10-year recap. *Trends Biochem Sci* 37:509–516
- Vellore NA, Yancey JA, Collier G, Latour RA, Stuart SJ (2010) Assessment of the transferability of a protein force field for the simulation of peptide-surface interactions. *Langmuir* 26:7396–7404
- Wales DJ (2003) *Energy landscapes*. CUP, Cambridge
- Wales DJ, Miller MA, Walsh TR (1998) Archetypal energy landscapes. *Nature* 394:758–760
- Wang SQ, Humphreys ES, Chung SY, Delduco DF, Lustig SR, Wang H, Parker KN, Rizzo NW, Subramoney S, Chiang YM, Jagota A (2003) Peptides with selective affinity for carbon nanotubes. *Nat Mater* 2:196–200
- Wang F, Stuart SJ, Latour RA (2008) Calculation of adsorption free energy for solute-surface interactions using biased replica-exchange molecular dynamics. *Biointerphases* 3:9–18
- Wei Y, Latour RA (2008) Determination of the adsorption free energy for peptide-surface interactions by SPR spectroscopy. *Langmuir* 24:6721–6729
- Whaley SR, English DS, Hu EL, Barbara PF, Belcher AM (2000) Selection of peptides with semiconductor binding specificity for directed nanocrystal assembly. *Nature* 405:665–668
- Whitford D (2005) *Proteins: structure and function*. Wiley, Chichester
- Wright LB, Walsh TR (2012) Facet selectivity of binding on quartz surfaces: free energy calculations of amino-acid analogue adsorption. *J Phys Chem C* 116:2933–2945
- Wright LB, Walsh TR (2013) Efficient conformational sampling of peptides adsorbed onto inorganic surfaces: insights from a quartz binding peptide. *Phys Chem Chem Phys* 15:4715–4726
- Xie HB, Vucetic S, Iakoucheva LM, Oldfield CJ, Dunker AK, Uversky VN, Obradovic Z (2007) Functional anthology of intrinsic disorder. 1. Biological processes and functions of proteins with long disordered regions. *J Proteome Res* 6:1882–1898

# Chapter 3

## Experimental Characterization of Peptide–Surface Interactions

Marion J. Limo, Carole C. Perry, A. A. Thyparambil,  
Yang Wei and Robert A. Latour

**Abstract** Interactions between peptides and proteins with material surfaces are fundamental to a broad range of applications in biotechnology and biomedical engineering. Many different methods have been developed to measure a range of properties that quantify these types of interactions. In this chapter, three of these methods are presented for the determination of thermodynamic parameters that characterize peptide adsorption behavior, each of which is based on a different type of measurement. These three methods are surface plasmon resonance spectroscopy (SPR; spectroscopic-based method), atomic force microscopy (AFM; force-based method), and isothermal titration calorimetry (ITC; thermal-based method). The fundamental principles underlying each of these methods are presented followed by examples of their application for the determination of thermodynamic properties for specific peptide/protein-surface systems. The SPR method is presented for the determination of the standard-state adsorption free energy from adsorption isotherms characterizing the amount of peptide adsorbed as a function of solution concentration. This method, however, is limited to materials that can be used to form nanoscale-thick films about 100 nm thick or less on a gold biosensor substrate. For materials that are not easily formed into thin films, thus not being conducive for use with SPR, an AFM method is presented that can be used with any macroscopically flat surface through the correlation of peptide desorption force measured by AFM with adsorption free energy measurements by SPR. The third approach, ITC, measures thermal energy changes on adsorption with the method being applicable to the interaction of peptides/proteins with particles suspended in solution. The combined set of methods provides the

---

M. J. Limo · C. C. Perry (✉)

Interdisciplinary Biomedical Research Centre, Department of Chemistry and Forensic Science, School of Science and Technology, Nottingham Trent University, Clifton Lane, Nottingham NG11 8NS, UK  
e-mail: carole.perry@ntu.ac.uk

A. A. Thyparambil · Y. Wei · R. A. Latour

Department of Bioengineering, 501 Rhodes Engineering Research Center, Clemson University, Clemson, SC 29634, USA

means to quantitatively determine thermodynamic properties characterizing peptide and protein adsorption behavior for materials in either their bulk or particulate form, with important application to the broad range of technologies that involve contact between biological solutions and synthetic material surfaces.

### 3.1 Introduction

The interactions of proteins with material surfaces is of critical importance in many areas of biotechnology and biomedical engineering, including implant biocompatibility (Kasemo and Gold 1999; Bryers et al. 2012), tissue engineering and regenerative medicine (Garcia 2006; Mahmood et al. 2006; Gandavarapu et al. 2013), biosensors (Wisniewski et al. 2000; Geelhood et al. 2007), drug delivery systems (Liu and Webster 2010; Gref et al. 2012), enzyme-based technologies (Knowles 1991; Blankschien et al. 2013; Wu et al. 2013), and biodefense (Bramwell et al. 2005; Herr 2009). Proteins are, of course, made up of unique linear sequences of amino acids that form polypeptide chains, which constitute a protein's primary structure. These polypeptide chains then fold to form secondary, tertiary, and possibly quaternary levels of structure. The resulting geometric shape, dynamics, and surface chemistry of these hierarchical structures subsequently create bioactive sites that enable proteins to perform their designated functions, such as cell signaling, biosensing, biotransport, or biocatalysis. Due to the extreme complexity of proteins, it can be very difficult to quantitatively determine and understand the molecular-level interactions that occur in proteins when they come in contact with synthetic material surfaces, either through nonspecific or specific adsorption from solution, physical entrapment, or through direct covalent linkage. However, molecular-level insights into protein-surface interactions can be obtained by studying the interactions of small portions of a protein, i.e., short sequences of amino acids (or peptides), which can be isolated from a given protein once its structure has been determined. Furthermore, many peptides have substantial bioactivity themselves apart from being integrated within a larger protein structure, such that an understanding of their interactions with material surfaces is important in its own right.

Given the importance of the behavior of peptides when they come in contact with material surfaces, experimental methods are needed to quantitatively characterize peptide-surface interactions. Over the past few decades, several experimental techniques have been developed to study peptide adsorption behavior on material surfaces. These methods include atomic force microscopy (AFM), ellipsometry, isothermal titration calorimetry (ITC), optical waveguide lightmode spectroscopy (OWLS), quartz crystal microbalance (QCM), sum-frequency generation (SFG), and surface plasmon resonance spectroscopy (SPR). In this chapter, we focus on just three of these methods, which the authors have been applying and

further developing in their own laboratories to study the thermodynamics of peptide–surface interactions. These three methods are AFM, SPR, and ITC. The principles by which binding information is obtained for all three experimental approaches requires measurement of the ‘force’ of interaction (AFM), ‘spectroscopic’ measurement of interaction (SPR), and direct ‘thermal’ measurement of the thermodynamics of interaction (ITC). In all cases irrespective of the mode of measurement, thermodynamic data relating to the ‘strength’ of interaction can be obtained. In the subsequent sections of this chapter, details are presented on each of these three experimental methods along with an overview of methods used for analysis of the experimental data obtained by implementation of these methods. Examples are then provided to demonstrate how these techniques have been applied to characterize the behavior of a broad range of peptide–surface systems.

## 3.2 Surface Plasmon Resonance Spectroscopy

### 3.2.1 Surface Plasmons

Surface plasmons are guided electron oscillations confined to a thin layer of the interface between two materials with negative and positive real parts of permittivity (e.g., a metal–dielectric interface). The principle of SPR occurs when the incident light wave-vector component parallel to the interface matches the propagation constant of the surface plasmon (Pitarke et al. 2007).

This condition is only satisfied at distinct angles of incidence, appearing as a drop in the reflectivity of incident light from which the optical energy is dissipated into a guided electromagnetic wave along the interface (Homola et al. 1999). As the extent of energy transfer is sensitive to any coupling conditions close to the interface, SPR biosensing relies on the principle that changes in the local index of refraction near the dielectric sensing surface, which can be brought about by changes in solution concentration local to the sensor surface (e.g., from mass adsorption to the surface), will cause a shift in the angle of reflectivity, which can be sensed by a suitable detector. This serves as the basis for various SPR sensors used in either qualitative or quantitative mode to determine the molecular binding events or kinetics and affinity parameters of molecular interactions (Jung et al. 1999; Green et al. 2000; Zhang et al. 2003; Taylor et al. 2008; Chen and Ming 2012).

### 3.2.2 SPR Spectroscopy

The use of optical sensors based on SPR has become one of the most important tools in molecular interaction analysis in the past decade due to its real-time monitoring capability with high sensitivity (Chen and Ming 2012). For these reasons, SPR

spectroscopy has also been recognized as one of the most directly applicable methods to characterize adsorption/desorption behavior to determine kinetic and thermodynamic parameters, such as the rates of adsorption/desorption and adsorption free energies, respectively (Haruki et al. 1997; Loomans et al. 1997; Li and Husson 2006; Tamerler et al. 2006). This technique is particularly well suited for use with Au-alkanethiol self-assembled monolayers (SAMs) because of gold's ability to exhibit a strong plasmon resonance signal, and has been widely applied in recent years to study both peptide and protein adsorption behavior on these types of model surfaces (Silin et al. 1997; Vernekar and Latour 2005).

However, whereas SPR is a useful technique for measuring peptide-SAM surface interactions, its usefulness is limited to materials that can form high-quality uniform nanoscale-thick films (e.g., <100 nm) on a metallic surface that can be used to generate an SPR signal (Wei and Latour 2010). Many materials, including most polymers, ceramics, and inorganic glasses, are thus not readily suitable for use with SPR spectroscopy. Therefore, alternative methods are needed to characterize peptide-surface interactions for these types of materials.

### 3.3 Atomic Force Microscopy

Compared with SPR, AFM has also been widely applied to characterize biological molecular recognition processes because of its high force sensitivity and the capability of operating under different physiological conditions and on any material with a macroscopically flat surface (Lal and John 1994; Willemsen et al. 2000; Allison et al. 2002; Kidoaki and Matsuda 2002). However, the use of AFM for these applications can result in difficulties in interpreting molecular force data (e.g., adsorption behavior) for peptide-surface interactions due to the absence of a direct way to determine the actual number of interacting molecules for a corresponding force measurement (Blanchette et al. 2008). One approach to overcome this problem is to correlate AFM results for peptide-surface interactions using a standardized AFM methodology to thermodynamic measurements for the same systems obtained by another surface sensitivity technique, such as SPR spectroscopy (Wei and Latour 2010). This approach then enables the same probe tip density to be consistently used for the measurements even though the actual number of tethered chains is unknown.

### 3.4 Combined SPR and AFM Methods

It has been shown that desorption forces ( $F_{\text{des}}$ ) obtained using a standardized AFM method correlate linearly with  $\Delta G_{\text{ads}}^{\circ}$  values measured from SPR for peptide-surface interactions under a range of different solvent conditions, including both

potassium phosphate buffer (PPB) and phosphate buffered saline (PBS) at pH 7.4 for salt concentrations below about 150 mM (Thyparambil et al. 2012; Wei et al. 2012). This combined set of approaches thus provide a means to directly determine  $\Delta G_{\text{ads}}^{\circ}$  for peptide adsorption to surfaces that can be used with SPR, or to indirectly determine  $\Delta G_{\text{ads}}^{\circ}$  for any macroscopically flat material surface that is not conducive to SPR by using this correlated AFM technique. In this section, we introduce the combined SPR and AFM methods that we have developed to characterize peptide adsorption behavior and show how they can be used to experimentally provide  $\Delta G_{\text{ads}}^{\circ}$  values (by SPR) and effective  $\Delta G_{\text{ads}}^{\circ}$  values (by AFM) for a wide variety of peptide–surface combinations using a relatively simple, straightforward adsorption system.

### ***3.4.1 Surface Preparation and Characterization: Self-Assembled Monolayers on Gold and Material Surfaces Not Conducive to SPR***

#### **3.4.1.1 Surface Preparation**

For both SPR and AFM studies, we have used alkanethiol SAM surfaces on gold with the structure of Au–S(CH<sub>2</sub>)<sub>11</sub>–Y, with Y representing functional groups contained in a wide range of organic polymers, such as: Y = OH, CH<sub>3</sub>, OC<sub>6</sub>H<sub>5</sub>, NH<sub>2</sub>, COOH, NHCOCH<sub>3</sub>, COOCH<sub>3</sub>, and EG<sub>3</sub>OH (EG: ethylene glycol segment (–O–CH<sub>2</sub>–CH<sub>2</sub>–)). We have also investigated material surfaces that are not conducive for SPR, including fused silica glass and quartz (Chemglass Life Sciences, Vineland, NJ), high-density polyethylene (HDPE) (MW = 125,000 Da, Sigma Chemical Co., St. Louis, MO), and poly(methyl-methacrylate) (PMMA) (MW=350,000 Da, Sigma Chemical Co., St. Louis, MO). HDPE and PMMA surfaces are spin-coated from dodecalin (0.5 % (w/w) at 1,500 rpm for 60 s) and chloroform solutions (1.5 % (w/w) at 1,000 rpm for 60 s), respectively, onto fused silica glass slides, although bulk material surfaces can also be used.

#### **3.4.1.2 Surface Characterization**

Surface characterization is an extremely important component of any adsorption study in order to obtain as much quantitative information as possible regarding the physical and chemical structure of the surface. For our studies, surface characterization was performed to determine the static air–water contact angle, atomic composition, film thickness, and surface roughness of the substrates used. For all the surfaces, the static air–water contact angle values were analyzed using a CAM 200 optical contact angle goniometer (KSV Instruments Inc., Monroe, CT) and the atomic compositions were verified via X-ray photoelectron spectroscopy



**Table 3.1** Surface characterization: Atomic composition for each surface

Surface moiety	C (%)	S (%)	N (%)	O (%)
–OH	56.7 (0.8)	2.8 (0.6)	*	7.5 (0.2)
–CH <sub>3</sub>	64.9 (0.7)	2.8 (0.2)	*	*
–(EG) <sub>3</sub> OH	54.8 (0.3)	2.3 (0.1)	*	13.2 (0.6)
–NH <sub>2</sub>	54.0 (0.9)	2.0 (0.2)	4.0 (0.3)	3.3 (0.3)
–COOH	47.6 (1.8)	1.6 (0.1)	*	7.6 (0.3)
–OC <sub>6</sub> H <sub>5</sub>	56.2 (0.9)	2.4 (0.2)	*	5.3 (0.9)
–NHCOCH <sub>3</sub>	48.6 (0.6)	1.7 (0.1)	4.0 (0.1)	6.0 (0.7)
–COOCH <sub>3</sub>	45.4 (4.3)	2.5 (0.2)	*	10.8 (0.6)
Fused Glass**	25.0 (2.0)	*	<1.0	49.0 (2.0)
Quartz (100)**	15.0 (2.0)	<1.0	<2.0	53 (1.0)
PMMA	76.0 (1.0)	*	*	24.0 (1.0)
HDPE	96.0 (3.0)	*	*	3.0 (3.0)

An asterisk (\*) indicates negligible value for atomic composition data. (Mean  $\pm$  95 % confidence interval (C.I.),  $N = 3$ ). Reprinted from Thyparambil et al. (2012) with permission

\*\* Glass slide also contains Zn (<1 %), Al (<1 %) and Si ( $22.0 \pm 1.0$  %) while the quartz surface of specific orientation (100) contains Si ( $30.0 \pm 3.0$  %) in atomic composition by XPS (not shown). The presence of extra carbon composition is believed to be originating from surface contamination due to the exposure of samples to air after the cleaning procedure. These are the typical adventitious and unavoidable hydrocarbon impurities that adsorb spontaneously from ambient air onto the glass and quartz surfaces

(NESAC/BIO, University of Washington, Seattle, WA). Average surface roughness was analyzed using MFP-3D AFM (Asylum Research, Santa Barbara, CA) over an area of  $5 \times 5$   $\mu\text{m}$ . The film thicknesses of the SAMs and polymer films were characterized using a GES-5 variable angle spectroscopic ellipsometer (Sopra Inc., Palo Alto, CA). Tables 3.1 and 3.2 present results obtained for our surfaces by these characterization methods.

### 3.4.2 Host–Guest Peptide Model

The host–guest model peptides that we designed for our studies (synthesized by Biomatik, Wilmington, DE; characterized by analytical HPLC and mass spectral analysis with 98 % purity) have the amino acid sequence of TGTG-X-GTGT (for SPR studies) and TGTG-X-GTCT (for AFM studies) with zwitterionic end groups, where G, T, and C are glycine (–H side chain), threonine (–CH(CH<sub>3</sub>)OH side chain), and cysteine (–CH<sub>2</sub>SH side chain), respectively. *X* represents a “guest” amino acid residue, which can be any of the 20 naturally occurring amino acid types. This residue is placed in the middle of the peptide to represent the characteristics of a mid-chain amino acid in a protein by positioning it relatively far from the zwitterionic end groups of the peptide. The threonine (T) residues and the zwitterionic end groups were selected to enhance aqueous solubility and to provide additional molecular weight for SPR detection while the non-chiral glycine

**Table 3.2** Surface characterization: Static water contact angle, film thickness, and surface roughness analyses for each surface

Surface moiety	Roughness (nm)	Contact angle (°)	Thickness (Å)
–OH	<0.5	16 (2)	13.0 (1.0)
–CH <sub>3</sub>	<0.5	110 (3)	11.0 (1.0)
–(EG) <sub>3</sub> OH	<0.5	32 (3)	19.0 (3.0)
–NH <sub>2</sub>	<0.5	48 (2)	14.7 (2.5)
–COOH	<0.5	18 (1)	15.8 (2.0)
–OC <sub>6</sub> H <sub>5</sub>	<0.5	80 (4)	14.4 (4.0)
–NHCOCH <sub>3</sub>	<0.5	48 (2)	17.0 (2.0)
–COOCH <sub>3</sub>	<0.5	63 (2)	11.0 (4.8)
Fused glass	<10.0	23 (4)	**
Quartz (100)	<1.5	13 (3)	**
PMMA	<1.5	63 (3)	90 (10) in nm
HDPE	<8.0	97 (5)	100 (10) in nm

Mean  $\pm$  95 % confidence interval (C.I.),  $N = 3$ . Reprinted from Thyparambil et al. (2012) with permission

\*\*Custom cut glass slides (0.375''  $\times$  1.625''  $\times$  0.0625'', Chemglass Life Sciences, NJ) and custom cut quartz (100) (0.375''  $\times$  1.625''  $\times$  0.0625'', MTI Corporation, Richmond, CA)

residues were selected to inhibit the formation of secondary structure, thus simplifying its adsorption behavior. The cysteine (C) residue was required for the AFM studies as the linker to connect our host–guest peptide sequences to the AFM probe tip (Wei and Latour 2010). Preliminary SPR studies that we have conducted using both of these peptide models have indicated that the TGTG-X-GTCT peptide can be used in AFM studies as an equivalent system for comparison with the TGTG-X-GTGT peptide model used by SPR (Wei and Latour 2010; Thyparambil et al. 2012).

### 3.4.3 Solvent Environment

All peptide–surface interactions were investigated either in phosphate-buffered saline (PBS; Fisher Scientific, Fair Lawn, NJ) or in 10 mM potassium phosphate buffer (PPB; Sigma Chemical Co., St. Louis, MO) at a bulk solution pH of 7.4. PBS is a complex mixture of salts in aqueous solution (140 mM sodium chloride, 10 mM sodium phosphate, 2.7 mM potassium chloride, and 1.8 mM potassium phosphate). The PPB buffer used here is a homogenous simple minimum salt solution that contains only 10 mM phosphate salts of potassium (Fisher Scientific, Fair Lawn, NJ) as needed for pH control. All buffer solutions were filtered and degassed prior to use.

### 3.4.4 Determination of $\Delta G_{\text{ads}}^{\circ}$ by SPR Spectroscopy

To determine  $\Delta G_{\text{ads}}^{\circ}$  accurately for peptide adsorption using SPR, two key issues must be addressed: the need to account for (i) “bulk-shift” effects and (ii) the influence of solute–solute interactions on the surface.

Because SPR measures the refractive index change of the medium within a distance of about 300 nm of the plasmon-producing surface, it is sensitive to both the molecules adsorbed at the interface and the molecules suspended in the medium within this 300 nm distance (de Mol and Fischer 2010). This latter contribution, known as the “bulk effect,” introduces a component into the SPR signal that is linearly proportional to the mass concentration of the analyte in the solution. Therefore, to determine the amount of SPR signal that is due to the adsorption process, the bulk-shift contribution must be subtracted from the raw SPR signal that is obtained during the adsorption experiment (Wei and Latour 2008).

Peptide–peptide interactions present another problem that can greatly skew the shape of the adsorption isotherm and result in erroneous calculated values of  $\Delta G_{\text{ads}}^{\circ}$ .  $\Delta G_{\text{ads}}^{\circ}$  is determined from the equilibrium constant,  $K_{\text{eq}}$ , of a reversible adsorption process, which represents the partition coefficient for the concentration of the solute on a surface versus its concentration in bulk solution. Ideally, the value of  $K_{\text{eq}}$  could be determined as the initial slope in the linear region of the adsorption isotherm, which represents infinite dilution conditions, in order to minimize effects from solute–solute interactions at the surface (Charles and Abraham 2003). Unfortunately, this requires the measurement of adsorption events for solution concentrations that typically extend well below the detection limit of currently available commercial SPR instruments. To get around this problem, an adsorption model, such as the Langmuir model, is generally used to calculate  $\Delta G_{\text{ads}}^{\circ}$  on the basis of the overall shape of the isotherm. This, however, creates additional complications because solute–solute interactions may occur on the surface as the surface sites become filled, which can substantially influence the shape of the isotherm and invalidate the application of the Langmuir adsorption model. If the Langmuir model is still used despite the occurrence of solute–solute interactions, then substantial error will be introduced into the calculated value of  $\Delta G_{\text{ads}}^{\circ}$  (Wei and Latour 2008).

To address both of these problems, we conduct peptide adsorption experiments with SPR using a Biacore X SPR spectrometer (Biacore, Inc., Piscataway, NJ) in either PPB or PBS, pH 7.4, using the following methods (Wei and Latour 2008, 2009). Briefly, SPR sensorgrams for peptide adsorption are recorded in the form of resonance units [RU; 1 RU = 1.0 pg/mm<sup>2</sup> (Stenberg et al. 1991)] as a function of time for six independent runs of varied peptide concentrations over each SAM surface at 25 °C. The data obtained are then used to generate isotherm curves by plotting the raw SPR signal (i.e., the signal from both surface adsorption and solution bulk-shift effects) as a function of peptide solution concentration.

The equation that we use for the determination of  $\Delta G_{\text{ads}}^o$  from the adsorption isotherms was derived based on the chemical potential of the peptide in its adsorbed versus bulk solution state (Wei and Latour 2009). During an SPR experiment to measure the adsorption of a peptide to a surface, the overall change in the SPR signal (i.e., the raw SPR signal) reflects both of the excess amount of adsorbed peptide per unit area,  $q$  (measured in RU), and the bulk-shift response, which is linearly proportional to the concentration of the peptide in solution. This relationship can be expressed as:

$$\text{SPR} = q + mC_b = \frac{QC_b}{C_b + C^oK^{-1}} + mC_b \quad (3.2)$$

where  $C_b$  (mol/L, M) is the concentration of the peptide in bulk solution,  $C^o$  is the peptide solution concentration under standard-state conditions (taken as 1.0 M),  $m$  (RU/M) is the proportionality constant between the bulk shift in the SPR response and the peptide molar concentration in the bulk solution,  $K$  (unitless) is the effective equilibrium constant for the peptide adsorption reaction, and  $Q$  (RU) is amount of peptide adsorbed at surface saturation. Each isotherm plot of the raw SPR response versus  $C_b$  is fit with Eq. (3.2) by nonlinear regression to solve for the parameters  $Q$ ,  $K$ , and  $m$  using a nonlinear statistical analysis software program (e.g., SAS Institute, Cary, NC). However, it should be understood that the values of  $Q$  and  $K$  determined by this fit may be substantially influenced by peptide–peptide interactions on the surface. In order to measure peptide adsorption behavior with minimal influence from peptide–peptide interactions, we use the premise that peptide–peptide interactions are minimized at very low solution concentrations, but then influence the isotherm shape (and thus the values of  $Q$  and  $K$ ) as the surface becomes crowded at higher values of  $C_b$ . The initial slope of the isotherm where  $C_b$  approaches zero should thus be minimally influenced by peptide–peptide interactions. Based on this principle, we have derived the relationship shown in Eq. (3.3), which enables  $\Delta G_{\text{ads}}^o$  to be determined from an adsorption isotherm that is generated by SPR with minimal influence of peptide–peptide interactions. Readers are referred to our initial publication of this method for details on this derivation (Wei and Latour 2008), with the derivation basically involving the use of the fitted parameters (i.e.,  $Q$  and  $K$ ) to estimate the slope of the isotherm as  $C_b$  approaches zero. Accordingly,  $\Delta G_{\text{ads}}^o$  (kcal/mol) is calculated from the parameters obtained from our raw SPR sensorgrams as:

$$\Delta G_{\text{ads}}^o = -RT \ln \left[ \left( \frac{C_s}{C_b} \right)_{C_b \rightarrow 0} \right] = -RT \ln \left( \frac{QK}{\delta C^o} + 1 \right) \quad (3.3)$$

where the theoretically defined parameter  $\delta$  is the thickness of the adsorbed layer of the peptide (calculated to be about 1.2 nm),  $R$  (kcal/mol·K) is the ideal gas constant, and  $T$  (K) is the absolute temperature.

We have applied these methods to characterize the adsorption response of a large range of peptide–surface systems for the determination of  $\Delta G_{\text{ads}}^o$ . Figure 3.1 shows

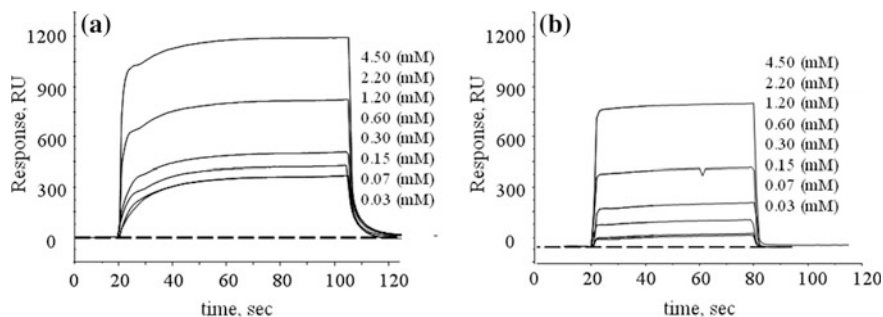


**Fig. 3.1** Response curves (SPR signal (RU) versus time for TGTG-V-GTGT on **a** SAM-CH<sub>3</sub> and **b** SAM-OH surface (not all of the concentration curves are listed for clarity sake because some of the low concentration curves overlap one another and are thus not separately distinguishable). Reprinted from Thyparambil et al. (2012) with permission

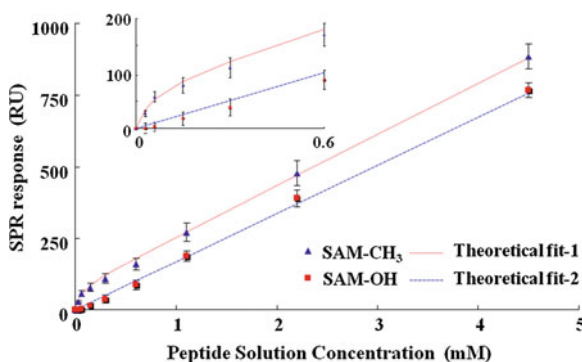


**Fig. 3.2** Corresponding raw data adsorption isotherm for TGTG-V-GTGT on both of the SAM-CH<sub>3</sub> surfaces (*Triangle* experimental data fitted by Eq. (3.2): theoretical curve-1, *upper dotted line*  $Q = 79$  (RU),  $K = 19,300$  (unitless), and  $m = 177,800$  (RU/M)) and SAM-OH [*white square* experimental data fitted by Eq. (3.2): theoretical curve-2, *lower dotted line*  $Q = 0.24$  (RU),  $K = 14$  (unitless), and  $m = 168,000$  (RU/M)]. Note that the adsorption response plotted on the y axis includes bulk-shift effects, which are linearly related to solution concentration (*error bar* represents 95 % C.I.,  $N = 6$  in PBS.). Reprinted from Thyparambil et al. (2012) with permission

examples of sensorgrams from a set of SPR experiments for TGTG-V-GTGT peptides on a SAM surface, with the resulting adsorption isotherms from the raw sensorgram data presented in Fig. 3.2.  $\Delta G_{\text{ads}}^{\circ}$  values for a set of peptides with 12 different X residues over a set of nine different functionalized SAM surfaces are presented in Table 3.3.

This SPR method could then be applied to investigate (i) the correlation between peptide adsorption affinity for SAM surfaces, as indicated by  $\Delta G_{\text{ads}}^{\circ}$ , and the hydrophobicity characteristics of the SAM surfaces involved, and (ii) the influence of salt concentration on adsorption free energy. Figure 3.3 presents a plot of the of  $\Delta G_{\text{ads}}^{\circ}$  values from Table 3.3 versus the respective cosine of the water

**Table 3.3** Values of  $\Delta G_{\text{ads}}^{\circ}$  (kcal/mol) for peptide-SAM combinations

-X-	-OH	-COOH	-EC <sub>3</sub> OH	-NH <sub>2</sub>	-NHCOCH <sub>3</sub>	-COOCH <sub>3</sub>	-OC <sub>6</sub> H <sub>5</sub>	-OCH <sub>2</sub> CF <sub>3</sub>	-CH <sub>3</sub>
<i>Nonpolar guest residues</i>									
-L-	-0.003 (0.001)	-1.30 (0.43)	-0.40 (0.28)	-2.34 (0.80)	-1.04 (0.30)	-2.06 (0.31)	-2.68 (0.72)	-3.09 (0.31)	-3.87 (0.69)
-F-	*	-1.11 (0.31)	-0.30 (0.13)	*	-2.44 (0.40)	*	*	-3.97 (0.24)	4.16 (0.16)
-V-	-0.002 (0.001)	-1.11 (0.31)	-0.26 (0.06)	-3.90 (0.12)	-0.16 (0.10)	*	*	-3.99 (0.22)	4.40 (0.31)
-A-	*	-1.14 (0.52)	-0.97 (0.36)	*	*	*	*	*	*
-W-	-0.001 (0.001)	-1.14 (0.52)	-1.72 (0.33)	-2.71 (0.32)	-1.94 (0.45)	-0.92 (0.36)	-1.65 (0.60)	-3.42 (0.27)	-3.89 (0.34)
<i>Polar guest residues</i>									
-T-	-0.001(0.001)	-0.87 (0.46)	-0.28 (0.15)	-3.15 (0.50)	-0.16 (0.09)	-0.40 (0.14)	-2.89 (0.75)	-2.81 (0.40)	-2.76 (0.28)
-G-	-0.001 (0.001)	-0.68 (0.36)	-0.30 (0.20)	-2.56 (0.32)	-1.86 (0.20)	-1.18 (0.30)	-3.51 (0.22)	-3.30 (0.37)	-3.40 (0.39)
-S-	002 (0.001)	-1.10 (0.10)	-0.34 (0.11)	-2.09 (0.98)	-1.49 (0.47)	-1.55 (0.26)	-3.20 (0.28)	-3.22 (0.24)	-2.75 (0.23)
-N-	-0.004 (0.003)	-0.86 (0.38)	-0.59 (0.11)	-3.22 (0.41)	-1.64 (0.23)	-1.37 (0.68)	-3.02 (0.16)	-3.41 (0.32)	4.33 (0.62)
<i>Charged guest residues</i>									
-R-	-0.002(0.001)	-1.53 (0.19)	-0.20 (0.10)	-3.03 (0.31)	-1.60 (0.80)	-1.17 (0.35)	-2.26 (0.82)	-3.45 (0.31)	4.15 (0.55)
-K-	-0.001 (0.001)	-1.71 (0.19)	-0.19 (0.07)	-3.14 (0.20)	-0.12 (0.07)	-1.77 (0.07)	-3.35 (0.25)	-3.54 (0.45)	-3.34 (0.39)
-D-	-0.003 (0.001)	-1.06 (0.09)	-0.44 (0.14)	-3.75 (0.20)	-1.93 (0.52)	-1.34 (0.50)	-3.89 (0.23)	-3.59 (0.37)	-3.54 (0.60)

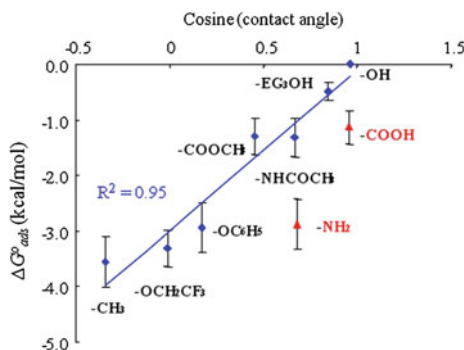


**Fig. 3.3**  $\Delta G_{\text{ads}}^{\circ}$  (kcal/mol) versus cosine (contact angle) for TGTG-X-GTGT on SAM surfaces with various functionalities in PBS. The  $\Delta G_{\text{ads}}^{\circ}$  values represent the average value of all of the host–guest peptides that exhibited reversible adsorption behavior on each SAM surface (i.e., peptides with  $X = A, F,$  and  $V,$  which tended to adsorb effectively irreversibly, were excluded from these average values). The blue line shows the linear regression for the noncharged SAM surfaces with  $R^2 = 0.95$  (the error bar represents 95 % C.I. with  $N = 6.$ ) Reprinted from Wei and Latour (2009) with permission

contact angle values for each SAM surface (contact angle values are presented in Table 3.2). The  $\Delta G_{\text{ads}}^{\circ}$  values shown in Fig. 3.3 represent the mean ( $\pm 95$  % C.I.) of the  $\Delta G_{\text{ads}}^{\circ}$  values from all of the host–guest peptides that exhibited reversible adsorption behavior on each SAM surface (i.e., peptides with  $X = A, F,$  and  $V,$  which tended to adsorb effectively irreversibly, were excluded from these average values). The cosine of contact angle values here, which can be related to the free energy of displacement of water from the surface, provide an energetic scale for the peptide adsorption behavior on the different surfaces.

As clearly indicated in Fig. 3.3, the lowest mean  $\Delta G_{\text{ads}}^{\circ}$  value (i.e., greatest adsorption affinity) was obtained on the SAM-CH<sub>3</sub> surface with the highest contact angle value and the highest mean  $\Delta G_{\text{ads}}^{\circ}$  value (i.e., least adsorption affinity) was obtained on the SAM-OH surface with the lowest contact angle value (with greater cosine value). These results also clearly show that this general relationship holds for each of the neutrally charged SAM surfaces, with peptide adsorption affinity increasing (i.e.,  $\Delta G_{\text{ads}}^{\circ}$  gets more negative) in a manner that strongly correlates in a linear manner with the hydrophobicity of the SAM surfaces over the full range of contact angles. The physical meaning behind this linear relationship can then be understood as reflecting a thermodynamic benefit for the transition of interfacial water from the surface to the bulk water phase and a reduction in solvent accessible surface area of the system as the peptide adsorbs as the surface energy decreases (i.e., becomes more hydrophobic), resulting in a decrease in free energy (more negative  $\Delta G_{\text{ads}}^{\circ}$ ). However, in addition to this general linear trend shown in Fig. 3.3, the substantial amount of scatter around each data point from this trend line suggests that specific functional group interactions also substantially influence the adsorption behavior. This same general trend is apparent for the charged SAM

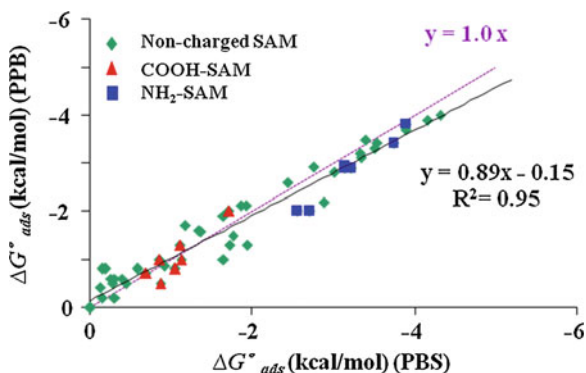


**Fig. 3.4** Plot of  $\Delta G_{\text{ads}}^{\circ}$  under PPB versus PBS solution conditions for 64 different peptide-SAM systems (peptides with  $X = \text{V, G, F, W, K, D, T, \text{ and } N}$ , on eight different SAM surfaces [SAM- $Y$  with  $Y = \text{OH, CH}_3, \text{OC}_6\text{H}_5, \text{NH}_2, \text{COOH, NHCOCH}_3, \text{COOCH}_3, \text{ and EG}_3\text{OH}$ ]). The *solid line* represents a linear regression of the data points (regression equation in *black text*). The *dotted line* represents what the linear regression should be for perfect agreement between the two data sets (regression line in *purple text* with slope = 1.0 and  $y$ -intercept = 0.0). Reprinted from Wei et al. (2012) with permission

surfaces, but with an additional contribution of adsorption affinity due to the presence of relatively strong electrostatic interactions, which was expected based on the zwitterionic nature of each of the peptides.

To evaluate the influence of salt concentration on adsorption free energy, we then compared  $\Delta G_{\text{ads}}^{\circ}$  values for peptide adsorption in PPB with our prior results obtained in PBS (Fig. 3.3). The resulting  $\Delta G_{\text{ads}}^{\circ}$  comparisons between peptide adsorption in PPB versus PBS from SPR are presented in Fig. 3.4. As shown in Fig. 3.4, two lines are plotted in this figure: a solid line, which represents the linear regression of the experimental data points and a dotted line, which represents what the regression line would be if perfect agreement existed between the  $\Delta G_{\text{ads}}^{\circ}$  values obtained in PPB compared with PBS, with a slope of 1.0 and  $y$ -intercept of zero. Statistical comparison between these two lines using a Student's  $t$ -test at the 95 % confidence level shows no significant difference in either the slope ( $p = 0.12$ ) or the  $y$ -intercept ( $p = 0.33$ ), thus indicating that the differences in salt composition and concentration between PPB and PBS do not substantially influence peptide adsorption behavior for this set of 64 different peptide–surface systems. Of particular interest, this finding holds for both the charged SAM surfaces (i.e., negatively charged COOH-SAM, red-triangle data points; and the positively charged  $\text{NH}_2$ -SAM, blue-square data points) as well as for the noncharged SAM surfaces (green diamond data points). This observation primarily indicates that the presence of monovalent  $\text{Na}^+$  and  $\text{Cl}^-$  salt ions in solution from 0 to 140 mM concentration in the presence of 10 mM phosphate buffer has negligible influence on peptide adsorption behavior.

These results provide a quantitative measure of peptide adsorption behavior at a liquid–solid interface as a function of amino acid type and surface functionality,



thus providing fundamental insights for understanding peptide and protein adsorption behavior for applications in bionanotechnology and biomedical engineering.

### ***3.4.5 Determination of Effective $\Delta G^{\circ}_{\text{ads}}$ ads Using a Standardized AFM Method***

As noted above, the use of experimental techniques such as SPR for the determination of  $\Delta G^{\circ}_{\text{ads}}$ , is limited to use for materials that can readily form nanoscale-thick layers over sensor surfaces, thus limiting these techniques to a relatively small set of materials. In order to provide a means of obtaining values of  $\Delta G^{\circ}_{\text{ads}}$  for a much broader set of materials (i.e., surfaces that are not conducive for use with techniques such as SPR), we have developed a standardized AFM method that can be applied to any macroscopically smooth surface for the determination of effective  $\Delta G^{\circ}_{\text{ads}}$  values by correlating the force of desorption measured by AFM with  $\Delta G^{\circ}_{\text{ads}}$  values measured by SPR.

The desorption force for peptide–surface interactions ( $F_{\text{des}}$ ) is measured from force curves using an AFM instrument (MFP-3D instrument, Asylum Research, Santa Barbara, CA) with DNP-10 silicon nitride cantilevers (Veeco Nanofabrication Center, Camarillo, CA) at room temperature in a fluid cell filled with droplets of either PPB or PBS, pH 7.4. For this technique, our TGTG-X-GTGT host–guest peptides are modified to TGTG-X-GTCT to provide a cysteine amino acid that is used to link the peptides to the AFM tips. The modified host–guest peptide sequences are tethered to AFM tips via a heterobifunctional PEG tether (3.4-kDa pyridyl dithio propionate-poly(ethylene glycol)-*N*-Hydroxyl succinimidyl ester (PDP-PEG-NHS), Creative PEGWorks, Winston Salem, NC), the specific details of which have been published (Wei and Latour 2010). Tips with PEG–OH (i.e., without the peptide) are then also used as controls. Although there is uncertainty in the areal density of tethered peptides on the probe tip, as long as the AFM force measurements for peptide–surface interactions are obtained using a standardized methodology, similar probe tip densities (although unknown) can be expected (Thyparambil et al. 2012). The functionalized tip with the peptide is then brought in contact with a selected substrate surface for one second of surface delay and then retracted at a constant vertical scanning speed of 0.1  $\mu\text{m/s}$ . The peptide–surface interaction force is then recorded as a function of the tip-to-sample separation distance on approach and retraction. From this data for each peptide–surface combination, the unbinding force that is measured during the plateau region ending right at the separation distance (max sep), which corresponds to the contour length of the PEG spacer and the peptide sequence, is taken as the  $F_{\text{des}}$ , as illustrated in Fig. 3.5 (Horinek et al. 2008; Pirzer et al. 2009).

In order to apply this method for the determination of effective values of  $\Delta G^{\circ}_{\text{ads}}$ , AFM studies were first conducted to measure  $F_{\text{des}}$  for a set of eight different types

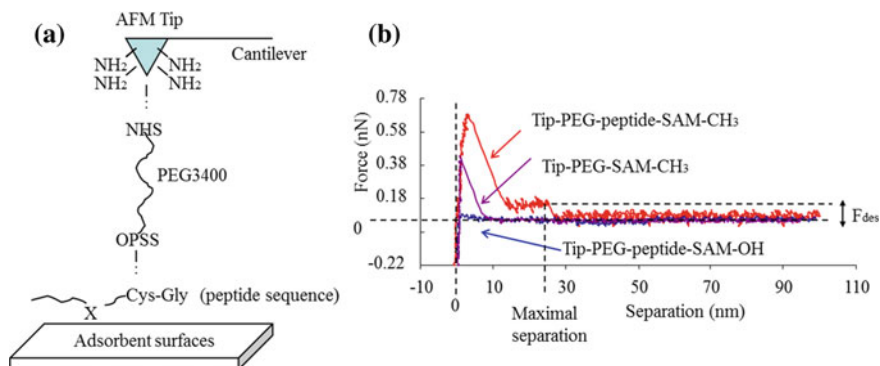


**Fig. 3.5** **a** AFM tip linkage. Peptide sequences are coupled to AFM tips via a 3.4 kDa polyethylene glycol (PEG) crosslinker. **b** AFM force–separation curves recorded during adsorption–desorption of TGTG-V-GTCT peptide on a SAM-CH<sub>3</sub> (*upper red curve*) and an SAM-OH (*bottom blue curve*). The *middle (purple)* curve represents a control group with the AFM tip without the peptide (only covered with PEG) on a SAM-CH<sub>3</sub> surface. Reprinted from Wei and Latour (2010) with permission

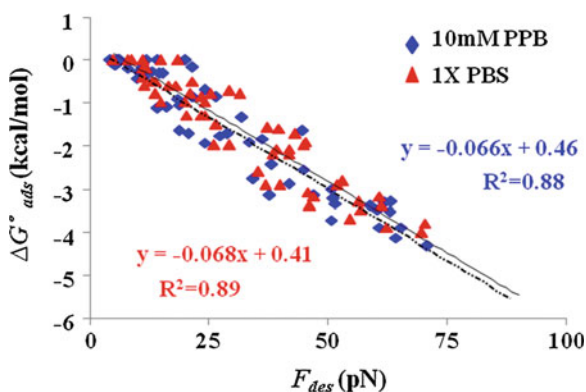


**Fig. 3.6** Correlation between  $\Delta G_{\text{ads}}^{\circ}$  by SPR and  $F_{\text{des}}$  by AFM for an equivalent set of 64 peptide-SAM systems in PBS (*lower dashed trend line with  $R^2 = 0.89$ ; red triangle data points and red regression equation*) and 10 mM PPB (*upper solid trend line with  $R^2 = 0.88$ ; blue diamond data points and blue regression equation*); pH = 7.4, 25 °C. Reprinted from Wei et al. (2012) with permission

of peptides on a set of eight different types of SAM surfaces in PBS and 10 mM PPB that were also evaluated by SPR (Fig. 3.4).

As shown in Fig. 3.6, a strong linear correlation (dashed trend line with  $R^2 = 0.88$ ; blue-diamond data points) is observed for the 64 peptides-SAM systems in PPB in a manner that is essentially indistinguishable with the linear relationship found with the dataset in PBS (solid trend line with  $R^2 = 0.89$ ; red-triangle data points). Comparison between regression lines for the datasets in PBS and PPB

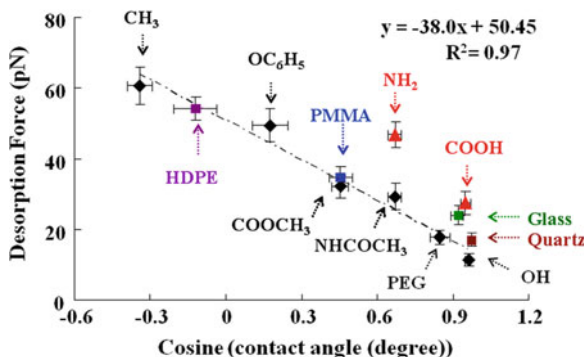


**Fig. 3.7**  $F_{\text{des}}$  versus cosine (static water contact angle) for SAMs with specific functionalities and the selected material (Snyder et al. 2012; Thyparambil et al. 2012; Wei et al. 2012). The trend line shows the linear regression for the noncharged surfaces (i.e., excluding the charged SAM and material surfaces at pH 7.4: SAM-NH<sub>2</sub> (pK ~6.5) (Fears et al. 2008) and -COOH (pK ~5.5) (Jiang et al. 2002) and the glass and quartz surfaces which were expected to be negatively charged (Sabia and Ukrainczyk 2000). The error bars represent the 95 % C.I. with  $N = 48$  for  $F_{\text{des}}$  and  $N = 3$  for contact angle measurements

again shows no significant difference in either the slopes ( $p = 0.68$ ) or intercepts ( $p = 0.19$ ) at the 95 % confidence level ( $\alpha = 0.05$ ), thus indicating negligible influence of the differences in the salt compositions and concentrations between these two solution environments along with consistency in the correlation between  $F_{\text{des}}$  measured by AFM and  $\Delta G_{\text{ads}}^{\circ}$  determined by SPR using the applied experimental methods. A combination of these two datasets provides an overall correlation equation (Eq. (3.4)) with  $R^2 = 0.89$ .

$$\Delta G_{\text{ads}}^{\circ} = -0.067 F_{\text{des}} + 0.44 \quad (3.4)$$

Equation (3.4) thus provides the means to determine effective values of  $\Delta G_{\text{ads}}^{\circ}$  for material surfaces that are not readily amenable for use with SPR by conducting measurements using our standardized AFM method to measure  $F_{\text{des}}$  and then applying this correlation equation to estimate  $\Delta G_{\text{ads}}^{\circ}$  for these systems in either PPB or PBS solution. This capability is of interest to provide a common basis for comparing peptide interactions for a broad range of material surfaces that can be tested by either SPR (e.g., SAMs, some thin polymer films) or AFM (e.g., glass, quartz (100), HDPE, and PMMA).

The reasonableness of applying this newly developed  $F_{\text{des}} : \Delta G_{\text{ads}}^{\circ}$  correlation to estimate the  $\Delta G_{\text{ads}}^{\circ}$  for peptide–surface systems can be generally assessed by plotting the measured  $F_{\text{des}}$  values to the cosine of the static water contact angle of these surfaces along with the SAM surfaces as an additional check on the validity of these results (Fig. 3.7) (Thyparambil et al. 2012). As shown, the relationship between the cosine of the static water contact angle and  $F_{\text{des}}$  for this set of additional material surfaces (HDPE and PMMA) agrees extremely well with the

data for the noncharged SAM surfaces. A strong correlation exists between  $F_{\text{des}}$  and the water contact angle for each of the neutrally charged SAM surfaces, with peptide adsorption affinity increasing in a linear manner with the hydrophobicity of the SAM surfaces over the full range of contact angles. For the charged SAM surfaces (e.g., SAM-NH<sub>2</sub> and –COOH) and the silica glass and quartz samples, the strength of adsorption is substantially higher than the correlation line for the noncharged surfaces, reflecting the additional attraction considered to be provided by electrostatic interactions between the peptides and the surfaces, similar to what we have observed from our previous SPR data set shown in Fig. 3.3. The correlation between the peptide desorption force and the cosine of the static water contact angle thus provides an additional means of qualitatively assessing the reasonableness of the AFM desorption force results prior to using the data to estimate  $\Delta G_{\text{ads}}^{\circ}$  for a given peptide–surface system.

These synergistically combined methods thus provide the ability to make quantitative measurements of peptide–surface interactions for any macroscopically flat surface, including surfaces that are not amenable for use with SPR. Importantly for our specific interests in the development of methods to accurately predict peptide and protein adsorption behavior, these methods also provide a means to obtain experimental data that are useful for the evaluation, modification, and validation of interfacial force field parameters that are required to enable peptide and protein adsorption behavior to be accurately represented by molecular simulation (Latour 2008; Vellore et al. 2010; Snyder et al. 2012).

### ***3.4.6 Concluding Remarks for SPR and AFM Methods***

The above-described combined SPR and AFM methods provide experimental approaches to obtain thermodynamic properties for the characterization of peptide–surface interactions that can be used with any macroscopically flat material surface. If appropriately applied, these methods are able to generate very accurate and reproducible determinations of adsorption free energy. While these techniques have utility for a broad range of applications, they are limited in terms of not being applicable for the characterization of peptide interactions with nano- and micro-sized particles, which are of particular interest in the general area of nanobiotechnology and for drug delivery systems in biomedical engineering. Fortunately, alternative methods are available for the determination of thermodynamic parameters for these types of systems. One of the most powerful methods for this type of application is ITC. Using ITC, the change in energy due to peptide–surface interactions can be directly measured over a range of temperatures, from which adsorption-induced changes in enthalpy, entropy, and free energy can be readily determined. The fundamentals of ITC and its application for a range of molecular systems are addressed in the following section of this chapter.

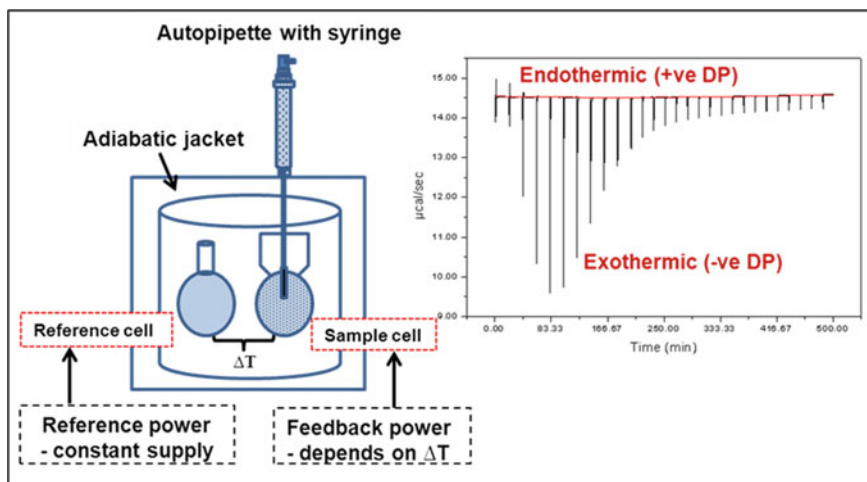


**Fig. 3.8** A simplified diagram of an ITC instrument showing its components and a representation of raw data

### 3.5 Isothermal Titration Calorimetry

The chemical or physical interaction of any two components forming a complex is accompanied by an exchange of heat with the environment, with heat either being absorbed (endothermic) or released (exothermic). The complex may also further undergo a physical change forming a product in a process which also produces a heat change. Modern ITC instruments are powerful precision devices designed to use power compensation to monitor heat changes that occur when two components interact. An ITC consists of a reference cell and a sample cell which are enclosed in an adiabatic outer shield jacket (Fig. 3.8). The cells are made using chemically inert and thermal conducting material such as Hastelloy alloy used in VP-ITC MicroCal instruments (MicroCal 2003). The reference cell should contain the solvent in which the component in the sample cell (i.e., macromolecule) is dissolved or suspended in. An important component of the instrument is its automated pipette containing a syringe which is filled with a second component (i.e., ligand) dissolved in the same solvent used to fill the reference cell and containing the component in the sample cell.

At the start of a measurement, the temperature of the reference cell and the sample cell is at equilibrium. A reference power which is defined by the user is constantly supplied to the reference cell offset heater to maintain a positive differential power (DP) feedback system also acknowledged as the baseline setting (thermal equilibrium). The positive DP can be used to supply compensating power to the sample cell whose temperature changes when a component from the syringe is titrated into the sample cell containing another component with which it is expected to interact. Differences in temperature between the sample cell and the

reference cell are monitored using a sensitive thermocouple circuit throughout the experiment. The extent of heat change depends on whether an interaction occurs or not. If no interaction takes place, only heat change as a result of titrating the syringe component into the sample cell component is measured which may be similar to the dilution heat change of titrating the syringe component into the sample cell containing only the solvent. However, if an interaction occurs forming a complex, a greater heat change than dilution heat change occurs causing the sample cell to be either hotter or cooler than the reference cell. If the sample cell is hotter than the reference cell (exothermic reaction) less power will be required to maintain thermal equilibrium between the two cells thus a negative DP ( $\mu\text{cal/s}$ ) will be registered. The opposite happens if the sample cell is cooler than the reference cell (endothermic reaction), more power will be required to maintain thermal equilibrium hence a positive DP will be recorded. The heat signal/power required to return to thermal equilibrium is integrated with respect to time and is directly proportional to the amount of interaction that occurs (Cliff et al. 2004).

The total volume of the component in the syringe can all be injected slowly and continuously into the sample cell component in what is known as the single injection method (SIM). However, the conventional ITC method involves the injection of the total syringe volume in several small aliquots of known volume. With continuous addition of the syringe component into the sample cell component, the cell component eventually becomes saturated at which point the heat signal decreases until only dilution heats are observed (Liang 2008; Thomson and Ladbury 2004). The extent of the reaction can, therefore, be probed per injected aliquot and this heat signal can be described as apparent  $\Delta H$  ( $\Delta H_{\text{app}}$ ) or observed  $\Delta H$  ( $\Delta H_{\text{obs}}$ ) heat change which is a global response as it includes the sum total of all heat changes. Total heat change is attributed to (i) noncovalent (hydrogen bonding, electrostatic interactions, hydrophobic interactions and van der Waals forces) binding/interaction ( $\Delta H_{\text{bind}}$ ) which principally reflects the strength of the interaction (ii) other contributions to heat change such as protonation/deprotonation events ( $\Delta H_{\text{ion}}$ ), and (iii) conformational changes as well as the incorporation or displacement of solvent both of which are reflected in the  $\Delta S$  of the interaction (Ababou and Ladbury 2006; Cliff et al. 2004; Leavitt and Freire 2001).

Data analysis can be carried out with the help of software such as Origin to plot and fit data using suitable binding models made available by MicroCal that use a nonlinear least-squares algorithm. After subtracting the baseline experiment (dilution heat change) from the ligand binding experiment, data is plotted as normalized integrated heat change in kcal/mole of injectant against the molar ratio of ligand to macromolecule to obtain the binding isotherm. The equilibrium binding constant ( $K_{\text{B}}$ ) can then be determined from precise knowledge of the concentration of free and bound ligand. The accuracy of  $K_{\text{B}}$  can be evaluated based on a measurement known as the critical parameter ( $C$ ) which determines the shape of the isotherm and is a product of the total concentration of the cell component,  $K_{\text{B}}$  and the stoichiometry ( $n$ ) and should ideally lie between 10 and 100 (Cliff et al. 2004). The stoichiometry value ( $n$ ) represents the number of binding sites per particle or macromolecule for a specific ligand. Figure 3.9 shows the effect of

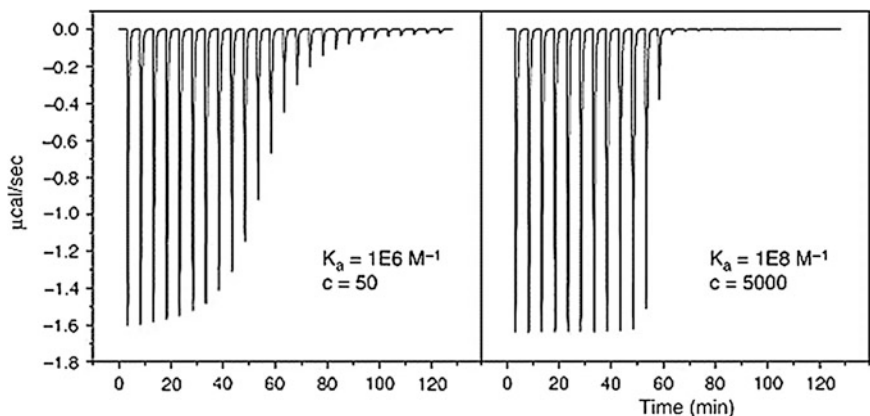


**Fig. 3.9** Illustration of the interaction between a protein and a ligand showing the effect of increasing the binding affinity measured in ITC experiments. Critical parameter ( $C$ ) =  $K_B \times$  protein concentration  $\times n$ . Experiment parameters used were: cell volume of 1.4 ml, 10  $\mu$ l injection aliquots, protein concentration of 0.05 mM, ligand concentration of 0.6 mM,  $\Delta H_{\text{bind}} = -10$  kcal/mol, and  $n = 1$ . Where  $C = 50$  in the first panel,  $K_B$  and  $\Delta H$  can be determined accurately but in the second panel where  $C = 5,000$  only  $\Delta H$  can be determined accurately. Reprinted with permission from Leavitt and Freire (2001) Elsevier

increasing the binding affinity hence the  $C$  value on the shape of isothermal profiles obtained using an ITC (Leavitt and Freire 2001).  $C$  values lower than 10 have featureless curves to almost straight lines which imply that there is very little change in enthalpy from one injection to the next hence determining the concentration of bound and free ligand becomes erroneous. On the other extreme scenario where  $C$  values are higher than 100, the shape of the isotherm tends toward an angular form as saturation occurs too fast in the first few injections equally precluding accurate determination of  $K_B$  (Cliff et al. 2004; Leavitt and Freire 2001; Thomson and Ladbury 2004; Wiseman et al. 1989).

From  $\Delta H$  and  $K_B$ , other thermodynamic parameters of interaction; entropy ( $\Delta S$ ) and Gibbs free energy ( $\Delta G$ ) can then be determined using Eq. (3.5) below where  $T$  is the experimental temperature and  $R$  is the gas constant (Cliff et al. 2004; Karlsen et al. 2010; Thomson and Ladbury 2004).

$$\Delta G = \Delta H - T\Delta S = -RT\ln K_B \quad (3.5)$$

ITC is, therefore, a powerful technique able to determine all thermodynamic parameters of interaction from one experiment and is the only direct measure of molar enthalpy (Cliff et al. 2004). It is a highly sensitive tool that can measure as little as 0.1  $\mu$ cal heat change and can determine binding constants in the millimolar to picomolar range ( $10^2$ – $10^9$   $M^{-1}$ ). Additional advantages are that ITC does not require labeling or immobilization of the interacting components. These features make it superior to other conventional techniques used to measure binding constants of interaction such as SPR, quartz crystal microbalance with dissipation

monitoring (QCM-D), nuclear magnetic resonance (NMR), spectroscopy, analytical ultracentrifugation (AUC), stopped-flow, and radioligand binding assays; many of which would require a series of experiments at different concentrations and temperatures before thermodynamic parameters can be determined using Van't Hoff's equation (Ababou and Ladbury 2006; Chaid et al. 2009). All the above techniques have advantages and disadvantages outlined elsewhere in the literature but a combination of complementary techniques is highly beneficial (Chaid et al. 2009; Mahmoudi et al. 2011).

### ***3.5.1 ITC and Peptide–Surface Interactions***

ITC was initially developed for the study of biological binding interactions mainly biopolymer interactions such as protein–enzyme interactions and DNA (deoxyribonucleic acid)–protein interactions (Ababou and Ladbury 2006; Biltonen and Langerman 1979; Wiseman et al. 1989). Over the years, commercial instruments have been designed with improvements in sensitivity, controlled and accurate automation of experiment, faster response, and advanced data analysis software (Freyer and Lewis 2008; Perozzo et al. 2004). Its applications are continuously being expanded and it is now being used in other fields such as in materials science to study thermodynamics of interfacial interactions between various inorganic and organic components (Ababou and Ladbury 2006; Chiad et al. 2009; Joshi et al. 2004).

Biomolecules such as carbohydrates, proteins, and lipids are known to play significant roles in biomineralization processes (Dujardin and Mann 2002; Kroger et al. 1999). Proteins in particular have sparked great interest due to their exceptional properties of specificity, biofabrication, self-assembly, recognition, and their ability to control the biosynthesis of soft through to hard biomaterials having detailed structural motifs at the nanoscale (Davis et al. 2003; Perry et al. 2009; Sanford and Kumar 2005). Peptide sequences which can interact specifically with any target surfaces, not just biomaterials have been identified using combinatorial methods such as the phage display technique and more recently, computational tools are also being employed (Dickerson et al. 2008; Naik et al. 2002; Oren et al. 2005; Sarikaya et al. 2003). In some cases, these peptide sequences not only interact with the target surface but have also been seen to modify the structure of the material which is believed to occur through modification of energy barriers at the peptide–surface interface (Cedervall et al. 2007; Dickerson et al. 2008; Naik et al. 2002; Perry et al. 2009; Whyburn et al. 2008). The exact nature of the interactions between inorganic materials and peptides remains largely elusive. Understanding the changes that occur at the interface during peptide–inorganic interactions and correlating these to structural modifications of the inorganic materials could be the key to advancing material synthesis and design.

In general, peptide adsorption on inorganic surfaces may be influenced by three overriding factors: (i) the intrinsic properties of the peptide (ii) the physico-chemical properties of the inorganic surface, and (iii) the media/environment



where the interaction takes place. Interaction may occur through specific counterparts (reactive groups) that allow only certain peptide sequences to interact specifically with certain inorganic surfaces and not others as demonstrated using the phage display technique. The inherent characteristics of the peptide sequence that may play a role in determining whether an interaction takes place with a substrate are mainly its charge, hydrophathy, and conformation. The overall net charge of the peptide mainly influences the occurrence of electrostatic interactions or repulsion with a surface that may also be charged. Many studies have attributed electrostatic interactions as the principle driving force behind peptide–inorganic interactions (Lynch and Dawson 2008; Chen et al. 2011). However, other non-covalent interactions such as hydrophilic or hydrophobic interactions, van der Waals forces, and hydrogen bonding between peptides and a surface are equally significant and may singlehandedly drive interactions in conditions where peptides have no net charge or even under repulsive charge conditions (Lynch and Dawson 2008; Rezwan et al. 2005). The media in which the interaction is taking place influences the conformation and stability of the peptide which may structure itself depending on its properties, mainly the hydrophathy of individual amino acids and/or the specific alignment of amino acids in the sequence relative to the polarity of the media. The overall binding activity of the peptide against the surface may depend on a contribution from various chemical and physical parameters. Ultimately, the interaction may be reversible or irreversible attained through a contribution from many weak interactions. Hence, some questions that need to be explored in the study of peptide–inorganic interactions include:

- What are the intrinsic properties of the peptide sequence and what are the differences between the free and bound states of the peptide?
- What are the surface properties of the inorganic material in solution (media) and what changes take place on the surface before a peptide molecule adsorbs onto it?
- What forces drive the interaction between a specific peptide and an inorganic material? What is the strength and reversibility of the interaction, how do these interactions modify the energy barriers at the peptide–inorganic interface and eventually lead to morphology modification of inorganic materials?

ITC is potentially the most ideal technique to study peptide–surface interactions as it can be used to directly determine all thermodynamic parameters of interaction. However, its application to study peptide–surface interactions is at its infancy with few documented studies in literature to date. This approach has its challenges which cannot go unmentioned.

In a typical ITC experiment to characterize the interaction of a ligand with a receptor, an interaction occurs forming a ligand–receptor complex described by E. Fisher as a lock and key mechanism. The formation of the complex is accompanied by a heat change as a result of binding but may also include a contribution from solvation entropy and structural changes (i.e., conformational change of the ligand in solution before it interacts with the receptor, structural changes of the

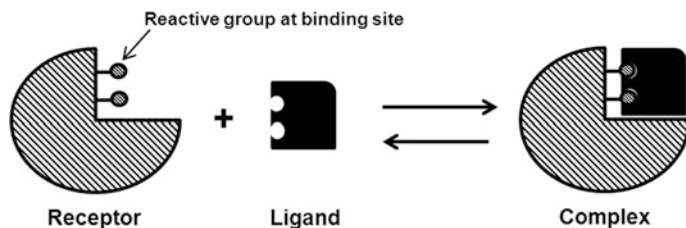


**Fig. 3.10** A simplified model of a specific interaction between a ligand and a receptor forming a complex

receptor to accept the ligand and the final ligand-receptor complex may also undergo conformational changes). The receptor-binding site is specific as it is defined by a precise geometry/recognition motif and the interaction is achieved through chemical functions at the binding site through which it can complex to the ligand (Ball and Maechline 2009). This interaction is at a reversible equilibrium hence the free energy change can be measured experimentally through determination of the  $K_B$  (Fig. 3.10).

ITC studies of peptide–inorganic interactions differ from typical ITC experiments. For example, here the inorganic material is a solid entity, therefore, any conformational entropy that may contribute to the measured heat change can only result from differences between the free and bound peptide. Also determination of  $K_B$  requires that precise concentrations of the initial free peptide and binding site on the inorganic surface to be known. The peptide concentration can be determined accurately if all quantified peptide is pure and active; however, clearly defining and quantifying the binding site on the inorganic surface is more challenging. For instance, synthesis studies of inorganic materials in the presence of peptides showing morphology modification via the adsorption growth inhibition mechanism have demonstrated that in some cases, peptides adsorb preferentially or solely to specific crystal planes (Chiu et al. 2011; Liang et al. 2011; Togashi et al. 2011). Adsorption of proteins on a surface of an inorganic material is described by some as nonspecific as there may be no clearly defined recognition pattern on the surface of the inorganic material similar to the lock and key mechanism (Ball and Maechline 2009). However, few studies have defined recognition patterns in peptide–inorganic surface interactions such as in studies of interaction between platinum (Pt) binding peptides with Pt crystallographic surfaces (Oren et al. 2005; Ruan et al. 2013). Computational analysis suggested the occurrence of physical recognition when platinum metal-binding peptides came into contact with the crystallographic metal surfaces (Oren et al. 2005; Ruan et al. 2013). The binding site can, therefore, be defined as the physicochemical characteristics of the inorganic material surface that can be recognized by the reactive groups present on the peptide sequence that form the “hot spot” regions through

which the interaction can take place. The importance of thorough characterization of peptides and inorganic materials used in such studies, therefore, becomes paramount and will be discussed hereafter.

### ***3.5.2 Characterization of Peptides and Inorganic Particles for ITC Experiments***

Peptide sequences identified from combinatorial methods or computational tools can be synthesized using microwave-assisted solid phase peptide synthesis protocol and their concentration, purity, and molecular weight can be ascertained using High performance liquid chromatography (HPLC), UV spectrophotometry, and Mass spectrometry. Circular dichroism (CD) and computational tools such as GROMACS, NAMD, Tripos SYBYL, and Accelrys Materials studio can be used to study the conformation and stability of peptide sequences. Dynamic light scattering (DLS) and zeta potential measurements can be used to study the size, dispersity, and net charge of peptides in solution. The net charge and isoelectric point of the peptides can also be calculated using the Henderson–Hasselbalch equation.

Inorganic particles can be synthesized using various techniques including: hydrothermal synthesis, template-directed approach, sol–gel process, electrospinning, electrodeposition, chemical vapor deposition, vapor phase transport process, and pyrolysis. Hydrothermal synthesis is carried out under ambient reaction conditions and is therefore commonly used in biomimetic studies. Physicochemical properties of inorganic surfaces that need to be determined include the surface charge, hydrophilicity/hydrophobicity, nanotopography, surface chirality, surface curvature, reactive sites, and stability of the surface/dissolution. These aspects have been covered in detail in a recent review (Fenoglio et al. 2011). Inorganic particles can be functionalized using different ligands and various organic capping agents including peptides are used to control the growth and morphology of inorganic particles. In circumstances where the interest is to study interactions of molecules with functionalized nanoparticles, the characteristics of the nanoparticles imparted by the ligand used to modify them should be known (Huang et al. 2013; You et al. 2008). Where the interest is to thermodynamically characterize interactions of molecules with bare nanoparticles, ideal particles should be pure, monodisperse, and homogeneous, having identical morphology of controlled shape and size. Attaining such particles is challenging and continues to be pursued by many researchers including ourselves. In this case, if capping agents were used during synthesis they have to be removed.

In our studies, we applied ITC to study the interaction of metal oxide and metal surfaces with peptides that had been shown to modify the morphology of the inorganic materials during synthesis studies (Chiu et al. 2011; Liang et al. 2011; Tomczak et al. 2009). As an example, we have monitored interactions between

ZnO crystals and ZnO-binding peptides using ITC. ZnO crystals used in ITC experiments were synthesized in the presence of organic matter either as precursors, solutes such as bases or growth modifying additives like peptides which can tightly adsorb to ZnO crystal planes. It was, therefore, crucial to characterize the organic content of the material before use in interaction studies with peptides. ZnO is known to decompose at a temperature of about 1,975 °C (Oka et al. 2002). ZnO-based materials can therefore be safely calcined to 900 °C to remove all organic materials. At 900 °C, there was also little risk of phase transformation of the ZnO crystals as this is known to require temperatures above 1,300 °C (Mazaheri et al. 2008). Synthesized particles were calcined up to 900 °C and weight loss was monitored by thermogravimetric analysis (TGA). Even though the crystals had been washed after synthesis, TGA analysis showed that ZnO crystals, even those formed without additives still contained a small amount of surface adsorbed organic matter (1.64 %  $\pm$  0.21). In our syntheses, the organic matter was identified to be an intermediate compound, layered basic zinc salt formed during the synthesis process. Calcined ZnO precipitates were again characterized using scanning electron microscopy (SEM) and appeared to have maintained their structure. X-ray diffraction (XRD) analysis confirmed that no phase transformation had taken place.

In another study within our group of the interaction of platinum-binding peptides and platinum nanoparticles, monodisperse cubic Pt nanoparticles with the {100} phase crystal structure were needed. Pt nanoparticles were prepared from a precursor using a growth modifying capping agent poly(vinylpyrrolidone) (PVP) along with trace levels of silver ions to enhance the rate of crystal growth along the desired plane (Song et al. 2005). The synthesized Pt nanoparticles cleaned according to the protocol described by Song et al. (2005) showed a significant amount of organic matter greater than 10 % weight content which was not desired for interaction experiments of Pt with Pt-binding peptides. As it is known that strongly bound PVP or any other capping agent can be challenging to remove (Rioux et al. 2006) an alternate approach to nanoparticle cleaning including calcination (not ideal for unencapsulated Pt nanoparticles as it leads to aggregation), plasma, or UV–ozone cleaning and the use of chemical cleaning methods for nanoparticles was required (Crespo-Quesada et al. 2011; Monzó et al. 2012). Most chemical cleaning methods are specific for a particular capping agent. For the removal of PVP from Pt nanoparticles, a method using a mixture of H<sub>2</sub>O<sub>2</sub> and H<sub>2</sub>SO<sub>4</sub> described by Monzó et al. (2012) was similarly used in our studies. TGA analysis was then used to confirm removal of the unwanted organic matter and the free-flowing state of the nanoparticulate (required for ITC analysis) confirmed using transmission electron microscopy (TEM). Any effects of contamination from Ag species was assessed by a combination of energy-dispersive X-ray spectroscopy (EDX), inductively coupled optical emission spectroscopy (ICP-OES), and XRD analysis of the treated platinum nanoparticles.

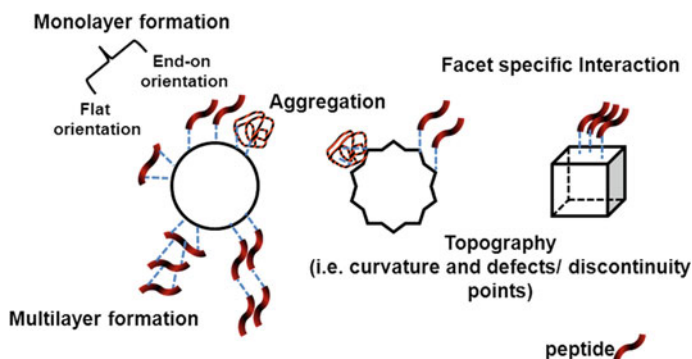


**Fig. 3.11** Illustration of some possible peptide–surface and peptide–peptide modes of interaction. Peptides may interact with the inorganic materials using specific functional groups of the amino acids in the sequence which may recognize chemical/physical surface features of the inorganic material. Image is not drawn to scale

In brief, some techniques that can be used to characterize the nanoparticulates include the use of imaging tools such TEM and SEM to characterize the morphology (shape, size, and aggregation) of the inorganic material. X-ray photoelectron spectroscopy (XPS) and EDX can be used to determine the samples' elemental composition. X-ray diffraction can be used to structurally characterize samples distinguishing between amorphous and crystalline samples. DLS and zeta potential measurements can be used to determine the hydrodynamic radius and surface charge of nanoparticles. The surface area of inorganic materials can be determined using nitrogen gas adsorption with analysis of the data using the Brunauer–Emmett–Teller (BET) method or calculated from dimensions obtained from image analysis such as SEM and TEM.

Quantifying the binding sites on the inorganic particles is complicated by the possible different adsorption orientations of peptide molecules (i.e., end-on surface adsorption, flat-on surface adsorption, adsorption as a monolayer, or multilayers and aggregates formed through possible peptide–peptide interactions) and possible surface specific adsorption whereby peptides adsorb to specific sites and not the total surface area (Fig. 3.11). These parameters are challenging to determine and require a combination of several complementary techniques and methodologies to ascertain. Once more, questions arise about the stability of the peptide–inorganic particle adduct; How dynamic or static is the adsorbed layer, whether a soft (weak and reversible interaction) or a hard (strong and irreversible) peptide layer adsorbs? The binding process is driven by kinetic and thermodynamic factors and may also vary depending on the properties of the peptide, the inorganic surface, the concentrations used, and temperature of the interaction environment as well as the influence of other molecules, including other ions and buffers present in the media.

### ***3.5.3 Basic Steps to Planning and Conducting an ITC Experiment***

This section has been written as a practical guide for ITC users. Herein, the instrument referred to is a MicroCal VP–ITC developed by GE Healthcare but the principles can be transferred for use with other similar ITC instruments. Before setting up an ITC experiment, the conditions under which the experiment should be conducted should be considered. VP–ITC has been set up to allow the user to alter a number of experimental parameters to optimize an experiment. These are the total number of injections, cell temperature ( $^{\circ}\text{C}$ ), reference power ( $\mu\text{cal/s}$ ), initial delay (s), syringe concentration (mM), cell concentration (mM), and stirring speed (rpm). Optimization is conducted to (i) attain saturation (which indicates the endpoint of the reaction), (ii) to minimize dilution heats in order to avoid interference in heats measured, and (iii) to attain sufficient measurements between baseline and saturation for prediction of curve shape. The importance of curve shape will be highlighted shortly.

#### **3.5.3.1 Experimental Parameters**

For the study of peptide–inorganic particle interactions using ITC, when working with a suspension of particles, it is best to have the nanoparticles in the sample cell as opposed to the syringe to avoid obstructing the flow and dispelling incorrect volumes into the sample cell during the experiment or completely blocking and damaging the syringe. Additionally, it is beneficial to have the particle suspension in the sample cell as the entire assembly of the syringe can be rotated continuously throughout the experiment maintaining the particles in suspension, availing all possible binding sites for the ligand. A stirring speed of 270–310 rpm (revolutions per minute) is usually optimal. However, when working with particles or if the solutions being mixed are viscous, it is recommended by MicroCal that the stirring speed should be fast enough to reduce error that can be encountered at the equivalence point of extremely tight interactions if the injected ligand is not evenly mixed throughout the cell component but should not be too fast to the point where the baseline becomes too noisy.

For a VP–ITC instrument, the user can choose to maintain the cell temperature between 2 and 80  $^{\circ}\text{C}$ . The temperature of the reaction affects the heat of binding and the binding constant. The instrument should be in a temperature controlled environment as fluctuation in room temperature may influence its performance and maintenance of cell temperature. At the start of the experiment, a thermal equilibrium is established which is the baseline of the experiment and falls around the value of the chosen reference power. MicroCal recommends a reference power of about 15–20  $\mu\text{cal/s}$  for systems where there is no prior knowledge of the expected heat change. For large endothermic heat changes, a low reference power ( $\sim 2 \mu\text{cal/s}$ ) is sufficient whereas for large exothermic heat changes, a large

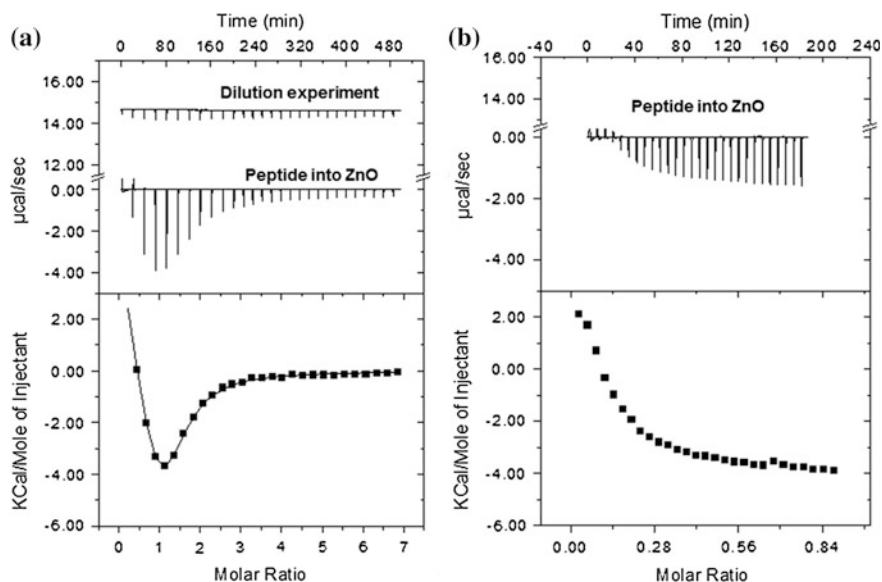


**Fig. 3.12** ITC isotherms representing heat changes that occur as a result of peptide GT-16 (GLHVMHKVAPPR-GGGC) interacting with ZnO hexagonal rods of wurtzite crystal structure,  $L/DAvg\ 8.92 \pm 3.26$ . **a** Above, raw data profile of titrating 280  $\mu\text{l}$  of 3.125 mM GT-16 peptide in 10  $\mu\text{l}$  aliquots into a cell containing 1.4 ml of ddH<sub>2</sub>O producing heats of dilution. Below, raw data profile of titrating the peptide into a cell containing a suspension of 0.1 mM ZnO rods (0.1 mM Zn<sup>2+</sup> determined using ICP-OES). Saturation is reached and both endothermic and exothermic heat change is measured. Dilution heat change has been subtracted. **b** GT-16 (1.25 mM) into an ITC cell containing a suspension of 0.3 mM ZnO rods. Saturation is not attained and heat measured is predominantly endothermic. A constant cell temperature of 298 K was maintained in all experiments. (Unpublished data)

reference power ( $\sim 30\ \mu\text{cal/s}$ ) may be required. An Initial delay (s) is required before the first injection to collect the baseline data.

The shape of the titration curve is important for determining  $K_B$  and is controlled by the concentration of the interacting components in the cell (molar ratio of ligand and macromolecules). Figure 3.12 illustrates how the molar ratio of the syringe and sample cell component determines the observed heat change and curve shape in an interaction where there are two thermodynamic events, an endothermic and an exothermic interaction.

The autopipette functions allow the user to control injection parameters such as the volume ( $\mu\text{l}$ ) dispensed from the syringe into the cell per injection, the duration (s) it takes for each injection to be made, the spacing (s) in between two subsequent injections which should be sufficient to allow thermal equilibrium to be re-established after each injection and the filter period (s), which is the period in which data collected is averaged and a single data point produced and plotted.

### 3.5.3.2 Sample Preparation and Running an ITC Experiment

The desired peptide concentration and nanoparticles required for each experiment are prepared in the chosen media. When choosing the media, the operator should be aware of the material used to make the ITC cell. For a MicroCal VP–ITC instrument, the cell is made using Hastelloy<sup>®</sup> C-276 alloy which is a robust material capable of withstanding corrosion by strong bases. However, strong acids can destroy the material and should therefore not be used. Hence any nonacidic solvent can be used in ITC experiments. The user should choose the most suitable solvent (it can be a mixture of solvents) that best dissolve the ligand/macromolecule and/or best disperse the inorganic particles (Chiad et al. 2009).

Generally, ITC experiments are conducted in aqueous media i.e., water and buffer (Bouchemal and Mazzaferro 2012). However, if nonaqueous or organic solvents is required, one has to ensure that the heat of dilution is minimal not to interfere with the accuracy of the binding experiment especially where the heat change of binding is comparatively minute (Thomson and Ladbury 2004). When buffers are used, buffer related contributions to the observed heat change should be considered (Leavitt and Freire 2001; Thomson and Ladbury 2004). Buffers containing reactive components such as reducing agents especially those with high heats of oxidation like dithiothreitol (DDT) should be avoided as they may cause artifacts in the raw data baseline. Buffers with low ionization enthalpy such as phosphate and citrate buffer are recommended as they cause few artifacts compared to those with high ionization enthalpy like Tris buffer (Pierce et al. 1999). However, in some cases, buffers with high ionization enthalpy may be used to enhance the signal strength of interactions involving protonation events (Ladbury and Doyle 2005; Perozzo et al. 2004). Matching the composition of the components in the sample cell and syringe such as concentration of salts used, pH and buffers may help to minimize dilution heat changes that may plausibly override binding signals (Freyer and Lewis 2008). Any media chosen must be of high purity and components can be dialyzed, centrifuged, or filtered to ensure no contaminants are present (Thomson and Ladbury 2004; Martinez et al. 2013). Prepared samples should also be degassed for at least 7 min using the thermovac or sonication to ensure no air bubbles are present that can interfere with the calorimetric readings.

Reproducibility of the sample preparation protocol for inorganic particles is essential for comparison between experiments. A dissolution study can be carried out to establish whether this has been achieved, whereby replicate samples containing inorganic particles as prepared for ITC experiments are dissolved in a suitable media and the ionic concentration of elements present in each quantified using inductively coupled plasma–optical emission spectroscopy (ICP-OES). The molar concentration of the nanoparticles can then be derived from its mass concentration (Huang et al. 2013).

To begin the experiment, the reference cell is filled with the solution in which the components to be studied are suspended or dissolved in hereafter referred to as the buffer. Component A is loaded into the ITC autopipette/syringe and the sample cell is filled with component B. Air bubbles that may be formed during the loading



process are expelled with the help of the loading syringe and the purging function of the control panel for the autopipette. Detailed explanation on loading of the autopipette and filling of the reference and sample cell can be found in the instrument manual and may vary depending on the instrument model and manufacturer. The syringe which has a twisted paddle on its end is then carefully placed inside the sample cell. The instrument equilibrates the temperature of the sample and the reference cell then the syringe begins to rotate and a final baseline about the chosen reference power is established. The syringe component is then periodically injected into the sample cell in predetermined aliquot volume and injection numbers.

Dilution experiments are principally conducted in order to subtract the heat changes that occur as a result of titrating the component in the syringe into the buffer. Other dilution experiments that should be considered are dilution of the buffer into the buffer and dilution of the buffer into component B in the cell which usually have negligible heat measurements (Freyer and Lewis 2008). The heat changes measured in the dilution experiment are then subtracted from the data obtained from the titration of component A into component B. The normalized heat change in kcal/mole of injectant is then plotted against the molar ratio of component A and component B. Data analysis and fitting can then be carried out using a nonlinear least-squares algorithm and suitable binding models made available by MicroCal.

The specific approach used in ITC experiments is determined by the objective of the user. For certain applications, only an accurate determination of  $\Delta H$  is required and not the binding constant. Here  $\Delta H$  does not need to be obtained as a fitting parameter in which case a  $C$  value greater than 100 is acceptable and the SIM can be used. If complex formation is occurring through protonation/deprotonation events, the heat signal measured may also include a contribution from buffer ionization. The experiment may, therefore, need to be performed at the same pH using buffers with different ionization enthalpies for comparison and thorough investigation of binding energetics (Cliff et al. 2004; Leavitt and Freire 2001). Where there is no buffer contributed protonation event accompanying the binding event, there will be no difference in  $\Delta H_{\text{obs}}$  using the different buffers (Leavitt and Freire 2001; Perozzo et al. 2004). Different strategies are employed to measure interactions with high affinities above the upper limit of binding constants (about  $10^9 \text{ M}^{-1}$ ) measurable using ITC. An example is a displacement/competition assay where the protein of interest is initially saturated with a ligand that interacts weakly before titrating with the high affinity ligand (Sigurskjold et al. 2000; Velazquez-Campoy et al. 2001). The thermodynamic linkage to temperature can also be evaluated by carrying out experiments at constant conditions and only varying the temperature within the limit of the instrument (2–80 °C). The change in heat capacity ( $\Delta C_p$ ) can then be determined which can be used to determine changes in hydrophobic interactions associated with binding (Cliff et al. 2004; Leavitt and Freire 2001). Standardized experimental parameters need to be applied in studies where comparisons need to be made between interactions of different ligands with the same macromolecule, i.e., mutagenesis studies to identify residues of an enzyme important for interaction with a ligand or mutants versus wild-type proteins with an inorganic material (De et al. 2007; Goobes G et al. 2007; Perozzo et al. 2004).

### 3.5.4 Data Analysis: Data Fitting Models Used in ITC Studies

Mathematical models are used to best fit integrated ITC data to obtain thermodynamic parameters using a curve-fitting process that applies a nonlinear regression procedure. Initial estimates of the parameters are made to generate a theoretical curve that is compared to and fit to the experiment data. This is achieved using an algorithm through an iteration process that minimizes the error function. MicroCal provides a data fitting software using Origin with three different binding models: one set of identical sites model, two sets of independent sites model, and sequential binding sites model. The relevant binding model is chosen based on information that may be known about the system being studied from other parallel studies. Where limited to no information is available, the model may be chosen based on the characteristics of the isothermal profile obtained. The main aim is to fit the data with preferably the fewest adjustable parameters which is synonymous to selecting the simplest binding model that can be used to most relevantly describe the biological, physical, or chemical process (Schmidtchen 2012). For more complicated analysis, users would need to develop their own mathematical models. The statistical significance of more complicated models with increased fitting parameters can be tested using a Monte Carlo analysis (Freyer and Lewis 2008).

From our discussion of the theory behind ITC experiments, we elaborated that the instrument operates using the heat compensation principle. For each aliquot of ligand ( $X$ ) injected into the ITC cell containing a macromolecule ( $M$ ), when a complex is formed ( $MX$ ), there is a release or absorption of heat ( $Q$ ). After subtraction of dilution heat changes, the area under each peak is equated to an interaction. Also considered is, with addition of ligand into the cell, the total volume of the mixture with the macromolecule exceeds the volume of the sample cell spilling into the tube above the sample cell. Since the instrument can only detect the heat change within the sample cell (active/working volume), equations to account for the displaced volume have been formulated to conserve the mass and correct for the measured heat change. The corrected bulk concentration of macromolecule and ligand is, therefore, expressed as  $M_t$  and  $X_t$ , respectively. The mass balance expression and equilibrium constant for the three models used by MicroCal<sup>®</sup> ITC Origin<sup>™</sup> are as follows:

- (i) One set of identical sites model: Applied where all binding sites have the same  $\Delta H$  and  $K$  values

$$K = \frac{\Theta}{(1 - \Theta)[X]} \quad (3.6)$$

where 1 represents total number of binding sites of the macromolecule available and unoccupied (unbound macromolecule),  $\Theta$  represents the fraction of sites that are occupied by ligand  $X$  and the concentration of free/unbound ligand is represented as  $[X]$ . From this binding model, the output gives one value for  $n$ ,  $K$ ,  $\Delta H$ , and  $\Delta S$ .

- (ii) Two sets of independent sites model: For independent interactions where macromolecules have two different binding sites with separate values of  $K$  and  $\Delta H$ . Therefore, two values are obtained for each parameter  $n$ ,  $K$ ,  $\Delta H$ , and  $\Delta S$  relating to the first and the second binding site.

$$K_1 = \frac{\Theta_1}{(1 - \Theta_1)[X]} \quad \text{and} \quad K_2 = \frac{\Theta_2}{(1 - \Theta_2)[X]} \quad (3.7)$$

Each binding site being independent means that where  $n_1 = 1$  and  $n_2 = 2$ , one ligand binds to the first site and two ligands of equivalent thermodynamics bind to the second site. For interactions that have independent binding sites,  $n$  being a nonintegral value is an indicator of errors to do with concentration (Freyer and Lewis 2008). The equilibrium constant is in actuality defined from the activities of interacting species rather than their concentration therefore errors in determination of concentration could arise especially when working with larger macromolecules like proteins which could be pure but not correctly folded hence inactive (Ball and Maechling 2009).

- (iii) Sequential binding sites model: Used where an interaction at one binding site influences a subsequent interaction at another binding site (negative or positive cooperativity). In this model, the binding sites could be identical or nonidentical and there is no clear distinction as to which specific binding sites are saturated. Only the total number of saturated binding sites can be known thus the binding constant is defined relative to the evolution of saturation. For interactions that are dependent, the  $n$  value is excluded as a fitting parameter because nonintegral values of no physical sense would be obtained. Unique parameters for  $K$ ,  $\Delta H$ , and  $\Delta S$  are obtained for each number of sites which is determined by the user.

$$K_1 = \frac{[MX]}{[M][X]}, \quad K_2 = \frac{[MX_2]}{[MX][X]} \quad \text{and} \quad K_3 = \frac{[MX_3]}{[MX_2][X]} \quad (3.8)$$

Detailed descriptions of the mathematical formulae corresponding to ITC models have been elaborated in the instrument user manual provided by MicroCal and in the literature (Chilom et al. 2004; Martinez et al. 2013; Perozzo et al. 2004; Poon 2010). In the following section, we will further describe how thermodynamic parameters can be determined using the simplest model, one set of identical sites model and later discuss how the model can be modified to more suitably portray peptide–inorganic interactions using proposed changes discussed in the section on the literature studies (Goobes G et al. 2007).

### 3.5.5 Determination of Thermodynamic Parameters Using One Set of Identical Sites Model

The equilibrium constant ( $K$ ) and the total ligand concentration ( $X_t$ ) can be expressed using the following equations;

$$K = \frac{\Theta}{(1 - \Theta)[X]} \quad (3.9)$$

$$X_t = [X] + n\Theta M_t \quad (3.10)$$

Combining Eqs. (3.9) and (3.10) gives a quadratic equation that is solved as follows:

$$K = \frac{\Theta}{(1 - \Theta)[X_t - n\Theta M_t]} \quad (3.11)$$

$$\Theta^2 - \Theta \left( 1 + \frac{X_t}{nM_t} + \frac{1}{nKM_t} \right) + \frac{X_t}{nM_t} = 0 \quad (3.12)$$

$$\Theta = \frac{-\left(1 + \frac{X_t}{nM_t} + \frac{1}{nKM_t}\right) \pm \sqrt{\left(1 + \frac{X_t}{nM_t} + \frac{1}{nKM_t}\right)^2 - \frac{4X_t}{nM_t}}}{2} \quad (3.13)$$

The total heat content ( $Q$ ) in the sample cell is proportional to the number of binding sites ( $n$ ), the fraction of the sites that have been occupied by the ligand ( $\Theta$ ), the molar heat of binding for the ligand ( $\Delta H$ ), and the total macromolecule concentration ( $M_t$ ) in the volume of the sample cell where the heat change is detectable ( $V_o$ ).

$$Q = n\Theta M_t \Delta H V_o \quad (3.14)$$

Substituting  $\Theta$  into the above equation gives

$$Q = \frac{nM_t \Delta H V_o}{2} \left[ 1 + \frac{X_t}{nM_t} + \frac{1}{nKM_t} - \sqrt{\left(1 + \frac{X_t}{nM_t} + \frac{1}{nKM_t}\right)^2 - \frac{4X_t}{nM_t}} \right] \quad (3.15)$$

The heat change of each injection,  $\Delta Q$  (i) taking into account correction of displaced volume can be expressed as

$$\Delta Q(i) = Q(i) + \frac{dV_i}{V_o} \left( \frac{Q(i) + Q(i-1)}{2} \right) + Q(i-1) \quad (3.16)$$

### 3.5.6 Case Studies on the Use of ITC in Materials Science

Applications of ITC have evolved from conventional biomolecular recognition reactions into diverse areas of interest in both academic and industrial laboratories. The exploration into novel systems equally drives the development and improvement of experiment strategies and data analysis. ITC protocols are developing in other fields including drug design, polymer chemistry, and nanotechnology hence studies where ITC has been successfully used to probe interactions between different ligand molecules with inorganic/organic materials continue to emerge. Some of these studies and research directions mainly involving interactions with suspensions of metals and metal oxide particles as well as metal ions have been highlighted in this chapter to provide a snapshot of the evolving applications of ITC in materials science and particularly interactions at the biotic–abiotic interface.

Among the pioneering studies applying ITC to investigate ligand–nanoparticle interactions was a study to characterize interactions between amino acids and the surface of gold nanoparticles (Joshi et al. 2004). Gold nanoparticles can be modified and functionalized through binding of specific ligands, i.e., thiols and amine groups (Jana et al. 2001; Kumar et al. 2003). Joshi et al. (2004) specifically endeavored to use ITC to investigate the interactions between gold nanoparticles with a basic (lysine) and an acidic (aspartic acid) amino acid. They observed that amine groups bind strongly with gold nanoparticles in their unprotonated state (Joshi et al. 2004). At physiological pH, lysine was found to interact weakly with gold nanoparticles compared to aspartic acid. This was thought to occur because at pH 7, amine groups in lysine (pI 9.4) may have been protonated while the amine groups of aspartic acid (pI 2.77) remained unprotonated (Joshi et al. 2004). When the experiments were repeated at pH 11, the amine group of lysine could interact more strongly with gold nanoparticles as they were unprotonated (Joshi et al. 2004). From TEM studies of nanoparticles used in the ITC experiments, the authors observed variable degrees of particle aggregation and concluded that accurate reproducibility of the surface area available for interaction with amino acids between experiments could not be attained.

In a similar study, ITC was used to characterize the energetics of interaction of deoxyribonucleic acid (DNA) and peptide nucleic acids (PNA) base monomers with gold nanoparticles (Gourishankar et al. 2004). Their aim was to design oligonucleotides that can complex with gold nanoparticles based on their different binding strengths without the need of thiolation. Gold nanoparticles modified using DNA and PNAs are of interest for applications such as sensors, biodiagnostics, chips, imaging, drug/DNA delivery, and structured nanoparticle assemblies with electronic properties (Gourishankar et al. 2004). In another study, surface modified gold nanoparticles were used to template the growth of hydroxyapatite crystals which are of interest for biomedical applications (Rautaray et al. 2005). Here, ITC was used to characterize interactions between gold nanoparticles capped with aspartic acid which can bind to calcium ions and induce crystal growth. In this

study, the authors also concluded that it was not possible to accurately determine the concentration of aspartic acid bound to gold nanoparticles as the total surface area of the gold nanoparticles could only be estimated (Rautaray et al. 2005). In all the above mentioned studies, binding isotherms were plotted against the total volume of the component injected into the cell instead of the molar ratio of interacting components; thus thermodynamic parameters of the interactions were not determined. However, the nature of the interaction and qualitative trends in the binding behavior of the amino acids could be identified (Gourishankar et al. 2004; Joshi et al. 2004, Rautaray et al. 2005). From the above studies, ITC showed great potential in its use to monitor the interactions between ligands and nanoparticles and the development of its application into new fields was encouraged.

ITC has been used in the advancement of novel hybrid materials that can specifically target a protein–protein interaction that would otherwise not occur in nature but could have beneficial applications (De et al. 2007; You et al. 2008). Artificial protein receptors can be created using nanoparticles whose surface can be modified to become surface receptors that can be recognized by proteins (De et al. 2007; You et al. 2008). ITC was successfully used to determine the selectivity and binding thermodynamics of the interactions between gold nanoparticles functionalized with amino acids/dipeptides (bearing leucine and/or phenylalanine residues) and target proteins; cytochrome *c* (CytC) and  $\alpha$ -chymotrypsin (ChT) (You et al. 2008). Because the nanoparticles were functionalized, the interaction is essentially a peptide–protein interaction but may be distinctively different from the mechanism through which the free amino acid/dipeptide interacts with the protein. This study has been specifically highlighted to illustrate how circular dichroism (CD) can be used to determine the arrangement of dipeptides and amino acids on the surface of gold nanoparticles (Huang et al. 2013; You et al. 2008). This approach can similarly be transferred to aid interpretation of thermodynamic data where direct interactions of molecules, i.e., peptides with nanoparticles is conducted. By determining the density of surface coverage using CD one may be able to deduce whether the adsorbed molecules form monolayers or multilayers through ligand–ligand self-recognition interactions. In this study, from CD analysis, no significant interaction between adjacent amino acid/dipeptide functionalities was detected which could otherwise occur through hydrogen bonding (You et al. 2008). For the enantiomeric dipeptides used to functionalize the gold nanoparticles, mirror CD signals suggested equal load on particles and ca. 100 amino acids were estimated to be bound to each nanoparticle. The concentration of nanoparticles was determined based on their average molecular weights considering the gold core’s size dispersion. Heat change was measured for the complexation of ChT and CytC with the functionalized nanoparticles (Fig. 3.13).

Data obtained was fit using a single set of identical sites model for the interaction with ChT based on the sigmoid shape of the curve obtained and the interaction with CytC was fit using both the single set of identical sites and two sets of independent sites model (Table 3.4). A compensatory relationship was observed between enthalpy and entropy during the complexation process. The authors state that the bimodal binding observed with CytC is unknown but may

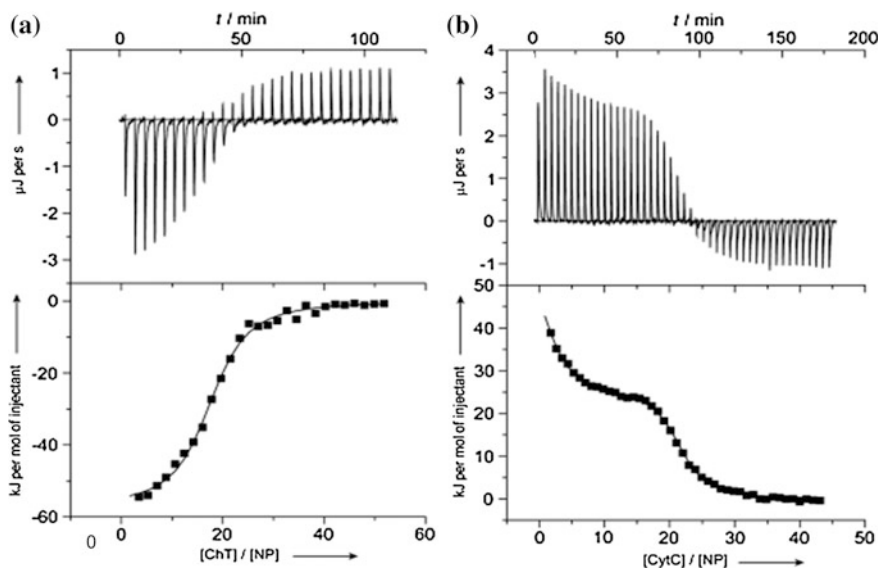


**Fig. 3.13** ITC isotherms showing the heat changes measured during the interaction of **a** ChT with gold nanoparticles functionalized with a dipeptide L-phenylalanine- D phenylalanine fit using one set of identical sites model **b** CytC with gold nanoparticles functionalized with dipeptide L-leucine-L-leucine fit using two sets of independent sites model. Experiments were conducted in sodium phosphate buffer pH 7.4. Reprinted with permission from You et al. (2008) John Wiley and Sons

arise from the particle's potential anisotropy or through possible variations in the binding geometry of CytC via protein–protein interactions (You et al. 2008). They proposed that complexation may occur through hydrophobic interactions and charge complementary interaction. They also highlighted the effect of amino acid/dipeptide chirality on complex stability. They concluded that with further investigation, knowledge gained could be used to manipulate protein recognition, specificity, affinity, and stability of the interactions formed paving the way for advances in creation of novel hybrid materials (You et al. 2008).

Another study of hybrid materials that employed ITC was conducted by Chiad et al. (2009) in which surface modification of SiO<sub>2</sub> via interaction with amphiphilic monomers and copolymers was investigated. The formation of these organic–inorganic hybrid systems occur through noncovalent adsorption of amphiphilic compounds to the surface of inorganic particles and the strength and irreversibility of the interaction is of great interest (Chiad et al. 2009; Hoffmann et al. 2006). The amphiphilic compounds used were monomers, i.e., 2-ethylhexyl methacrylate (EHMA), poly(ethylene oxide) methacrylate having 5 (PEOMA<sup>n</sup> ≈ 5), and 9 (PEOMA<sup>n</sup> ≈ 9) ethylene oxide units, poly(propylene oxide) methacrylate (PPOMA), 2-hydroxyethyl methacrylate (HEMA) (ethyl glycol) methacrylate phosphate (EGMP), 4-vinyl-1-(3-sulforopyl)pyridinium inner salt

**Table 3.4** Thermodynamic parameters (in  $\text{kJ mol}^{-1}$ ), dissociation constants ( $K_D$ ), and binding stoichiometry ( $n$ ) obtained through ITC measurements of the interaction between CHT and CytC with functionalized gold nanoparticles in phosphate buffer pH 7.4 at 30 °C

Protein	Nanoparticle <sup>b</sup>	First binding event				Second binding event				
		$K_D$ [ $\mu\text{M}$ ]	$\Delta G$	$\Delta H$	$T\Delta S$	$n$	$K_D$ [ $\mu\text{M}$ ]	$\Delta G$	$\Delta H$	$T\Delta S$
CHT <sup>a</sup>	NP_Gly-Gly	2.14 ± 0.20	-32.9	-37.1 ± 1.9	-4.2	11.6	-	-	-	-
	NP_L-Leu	2.45 ± 0.34	-32.6	-46.6 ± 25	-14.0	8.8	-	-	-	-
	NP_D-Leu	138 ± 0.07	-34.0	-47.0 ± 03	-13.0	9.2	-	-	-	-
	NP_L-Phe	229 ± 0.05	-32.7	-54.9 ± 2-8	-22.2	13.2	-	-	-	-
	NP_D-Phe	1.12 ± 0.16	-34.5	-59.3 ± 0.9	-24.7	17.2	-	-	-	-
	NP_L-Leu-L-Leu	132 ± 0.12	-34.1	-36.0 ± 0.6	-1.9	15.2	-	-	-	-
	NP_L-Leu-D-Leu	1.05 ± 0.12	-34.7	-47.6 ± 1.6	-12.9	12.8	-	-	-	-
	NP_L-Leu-L-Phe	0.81 ± 0.02	-35.3	-56.0 ± 1.0	-20.7	18.0	-	-	-	-
	NP_L-Leu-D-Phe	0.58 ± 0.05	-36.2	-49.1 ± 05	-12.9	20.0	-	-	-	-
	NP_L-Phe-D-Phe	0.82 ± 0.07	-35.3	-55.1 ± 1.6	-19.8	17.0	-	-	-	-
	NP_D-Phe-L-Phe	1.17 ± 0.15	-34.5	-46.9 ± 3.6	-12.4	11.2	-	-	-	-
	NP_D-Phe-D-Phe	0.44 ± 0.05	-36.9	-44.4 ± 13	-7.6	22.8	-	-	-	-
	NP_Gly-Gly	0.023 ± 0.004	-44.3	12.3 ± 2.0	56.6	1.8	1.78 ± 0.34	-33.4	4.9 ± 1.2	38.2
	NP_L-Leu	0.251 ± 0.012	-38.3	189.6 ± 3.0	227.9	2.0	1.95 ± 0.09	-33.1	2.3 ± 0.2	35.4
	NP_D-Leu	0.044 ± 0.008	-42.7	116.0 ± 0.1	158.5	1.6	1.12 ± 0.31	-34.5	6.6 ± 0.6	41.2
	NP_L-Phe	0.068 ± 0.006	-41.6	28.8 ± 0.1	70.4	2.2	1.51 ± 0.21	-33.8	13.1 ± 1.0	46.9
NP_D-Phe	0.015 ± 0.005	-45.5	55.0 ± 45	100.6	2.6	3.02 ± 0.98	-32.0	13.8 ± 0.5	45.8	
NP_L-Leu-L-Leu	0.107 ± 0.015	-40.4	59.1 ± 1.6	99.5	2.2	1.29 ± 0.42	-34.2	25.5 ± 0.8	59.7	
NP_L-Leu-D-Leu	0.692 ± 0.034	-35.7	31.4 ± 1.6	67.2	1.8	1.74 ± 0.24	-33.4	21.7 ± 0.2	55.2	
NP_L-Leu-L-Phe	0.025 ± 0.003	-44.2	34.8 ± 0.7	78.9	2.9	1.62 ± 0.22	-33.6	24.6 ± 0.9	58.2	
NP_L-Leu-D-Phe	0.525 ± 0.097	-36.4	34.9 ± 0.7	71.4	2.0	1.48 ± 0.41	-33.8	21.2 ± 0.2	55.1	
NP_L-Phe-D-Phe	0.251 ± 0.077	-38.3	49.2 ± 32	87.6	2.2	0.98 ± 0.23	-34.9	25.7 ± 1.7	60.6	
NP_D-P he- L-Phe	0.245 ± 0.114	-38.4	40.7 ± 4.7	79.1	1.8	1.00 ± 0.28	-34.8	21.2 ± 0.2	56.0	
NP_D-Phe-D-Phe	0.022 ± 0.004	-44.4	36.0 ± 2.6	80.3	2.6	0.79 ± 0.26	-35.4	21.7 ± 0.3	57.1	

Reprinted with permission from You et al. (2008) John Wiley and Sons

<sup>a</sup> Refers to the differences between binding constants determined using ITC and those previously determined using enzyme activity assays (You et al. 2005a, You et al. 2005b) which may have been due to differences in experiments conditions.

<sup>b</sup> The concentration of nanoparticles in ITC experiments was determined as an average of molecular weights taking into consideration the size dispersion of gold cores. This was different from previous determination of NP concentration using UV absorbance hence the differences in binding stoichiometries obtained.



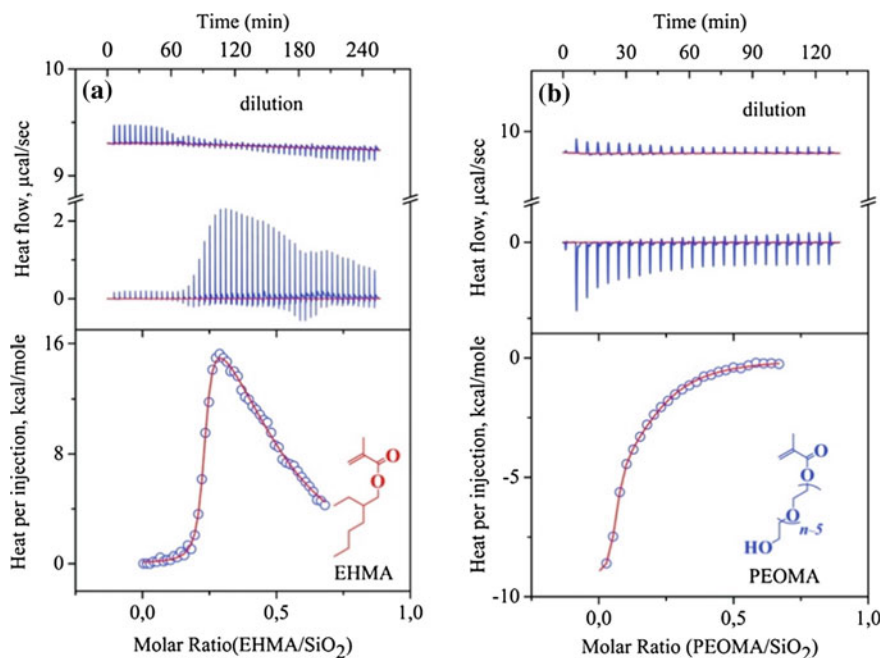


**Fig. 3.14** ITC isotherms showing the titration of **a** hydrophobic monomer EHMA and **b** hydrophilic PEOMA<sup>*n* ≈ 5</sup> into a suspension of SiO<sub>2</sub> in the chosen solvent mixture 1,4-dioxane/ethanol/H<sub>2</sub>O. Reprinted with permission from Chiad et al. (2009) American Chemical Society

(4VPSB), and copolymers PEHMA-*co*-PEGMP, PEHMA-*co*-PPEOMA<sup>*n* ≈ 5</sup>, and PEHMA-*co*-P4VPSB. The titration of hydrophobic EHMA and hydrophilic PEOMA<sup>*n* ≈ 5</sup> into suspensions of SiO<sub>2</sub> nanoparticles are shown in Fig. 3.14.

The Thermodynamic parameters of interaction ( $\Delta H$ ,  $\Delta S$ ,  $K_B$ , and  $\Delta G$ ) were determined (Table 3.2). The authors inferred that the low  $\Delta H$  value obtained in the titration of EHMA with SiO<sub>2</sub> indicates that there was no significant interaction of the polymer with the surface. They also attributed the observed endothermic heat changes to the collapse of the structure of water molecules surrounding the hydrophobic EHMA molecules. An enthalpically driven interaction was registered in the interaction of hydrophilic PEOMA with SiO<sub>2</sub> that was attributed to possible hydrogen bonding or van der Waals interactions. The authors stated that changes in conformational entropy of PEOMA and solvation entropy could also have occurred during the adsorption reflected by  $\Delta S$  values (Table 3.5). In conclusion, they stated that the approach of studying the thermodynamic changes occurring at interfaces could possibly allow one to directly correlate adsorption strength to the structure of inorganic particles allowing materials engineering to be conducted using more rational and optimized methods (Chiad et al. 2009).

**Table 3.5** Thermodynamic parameters of the interaction of amphiphilic monomers and copolymers with SiO<sub>2</sub> nanoparticles determined using ITC

Surface-active compound	$K_B$ (mol L <sup>-1</sup> )	$\Delta H$ (kcal mol <sup>-1</sup> )	T $\Delta S$ (kcal mol <sup>-1</sup> )	$\Delta G$ (kcal mol <sup>-1</sup> )
EHIB <sup>a</sup>	$1.10 \times 10^7 \pm 4.30 \times 10^6$	$0.25 \pm 0.18$	10.19	-9.94
	$1.00 \times 10^5 \pm 1.50 \times 10^4$	$63.46 \pm 2.70$	70.36	-6.88
PEOIB <sup>a</sup>	$3.87 \times 10^4 \pm 1.33 \times 10^4$	$-13.60 \pm 9.99$	-7.33	-6.25
EHMA <sup>a</sup>	$1.90 \times 10^7 \pm 3.00 \times 10^6$	$0.04 \pm 0.01$	9.98	-9.94
	$5.70 \times 10^4 \pm 6.20 \times 10^3$	$25.50 \pm 1.43$	31.90	-6.40
PEOMA <sup>n ≈ 5a</sup>	$6.10 \times 10^4 \pm 6.50 \times 10^3$	$-25.13 \pm 4.23$	-18.60	-6.53
HEMA <sup>b</sup>	$8.26 \times 10^4 \pm 2.27 \times 10^4$	$-0.19 \pm 0.04$	6.49	-8.20
PEOMA <sup>n ≈ 5b</sup>	$6.35 \times 10^3 \pm 0.04 \times 10^3$	$-43.50 \pm 0.20$	-38.16	-5.34
PEOMA <sup>n ≈ 9b</sup>	$1.15 \times 10^5 \pm 2.03 \times 10^4$	$-69.87 \pm 0.54$	-62.90	-6.97
PEOMA <sup>n ≈ 5b</sup>	$1.5S \times 10^5 \pm 0.92 \times 10^4$	$-0.05 \pm 0.007$	7.04	-6.98
4VPSB <sup>a</sup>	$1.74 \times 10^4 \pm 3.05 \times 10^4$	$-27.57 \pm 2.24$	-20.42	-7.14
EGMP <sup>a</sup>	$4.33 \times 10^4 \pm 2.35 \times 10^3$	$-39.85 \pm 0.8$	-33.39	-6.46
PEHM A-co-PPEOMA <sup>n ≈ 5</sup>	$2.50 \times 10^5 \pm 4.40 \times 10^4$	$-10.01 \pm 0.53$	-2.77	-7.33
PEHMA-co-P4VPSB	$5.70 \times 10^5 \pm 3.29 \times 10^5$	$-8.77 \pm 0.20$	-0.92	-7.86
PEHM A-co-PEGMP	$4.78 \times 10^5 \pm 0.00$	$-10.26 \pm 0.16$	-2.51	-7.75

Reprinted with permission from Chiad et al. (2009) American Chemical Society

<sup>a</sup> Concentration of the hydrophilic monomer = 55 mM

<sup>b</sup> Concentration of the hydrophilic monomer = 278 mM

In biomineralization studies, ITC has been used to study the thermodynamics of biomolecule interactions with biominerals. Statherin is an oral cavity protein that regulates the nucleation and growth of hydroxyapatite (HAP) and serves as a receptor for bacterial adhesion to enamel. Extensive studies on the interaction of statherin to HAP have been carried out to identify the underlying molecular mechanisms (Goobes R et al. 2007; Raj et al. 1992; Wikiel et al. 1994). The wild-type sequence of statherin consists of 43 amino acid residues. The first five residues are negatively charged and have been identified to directly participate in binding to hydroxyapatite (Goobes R et al. 2007; Raj et al. 1992; Wikiel et al. 1994). The acidic amino acids are followed by a basic amino acid rich segment whose role was unknown. The roles of the positively charged residues were determined by carrying out single and multiple point mutations replacing the basic residues with alanine amino acid (Goobes R et al. 2007). The interaction of the wild-type and mutant protein with HAP crystals was then studied using ITC and equilibrium adsorption binding isotherms (AI) as shown in Table 3.6 (Goobes R et al. 2007). Synthesized proteins were all labeled at specific positions for studies on the structure of the adsorbed protein using solid-state NMR rotational echo double resonance (ss-NMR REDOR) and dynamics measurements (Goobes R et al. 2007).

To attain the above thermodynamic parameters, Goobes R et al. (2007) proposed that when studying peptide–inorganic interactions, the equilibrium constant

**Table 3.6** Thermodynamic parameters of the interaction of statherin and its mutants with HAP determined using equilibrium adsorption isotherms and ITC

Protein	$N_{\max}$ ( $10^{-7}$ mol/ $m^2$ )	$K$ ( $10^5/M$ )	$\Delta G^0$ (kcal/ mol)	$\Delta\Delta G^0$ (kcal/ mol)	$\Delta H_{\text{initial}}^b$ (kcal/mol adsorbed)
stalh (WT)	$6.2 \pm 0.7$	$7.0 \pm 0.9$	$-7.9 \pm 0.1$		$-3.3 \pm 0.4$ , 90 %
stathik6A1	$7.3 \pm 0.9$	$2.8 \pm 0.6$	$-7.4 \pm 0.1$	$0.5 \pm 0.1$	$-3.7 \pm 0.5$ , 85 %
stath (R9A)	$6.8 \pm 0.3$	$2.8 \pm 0.5$	$-7.4 \pm 0.1$	$0.5 \pm 0.1$	$-3.2 \pm 0.3$ , 85 %
stath (RIOA)	$5.7 \pm 0.8$	$4.5 \pm 1.2$	$-7.6 \pm 0.2$	$0.3 \pm 0.2$	$-3.8 \pm 0.4$ , 85 %
stath (R 13 A)	$6.4 \pm 0.8$	$4.0 \pm 1.0$	$-7.6 \pm 0.2$	$0.3 \pm 0.2$	$-3.1 \pm 0.3$ , 85 %
stath (KRA)	$3.0 \pm 1.2$	$1.5 \pm 0.8$	$-7.0 \pm 0.3$	$0.9 \pm 0.3$	$-3.7 \pm 0.4$ , 45 %

$N_{\max}$ ,  $K$ ,  $\Delta G^0$  and  $\Delta\Delta G^0$  were determined from AI measurements and from ITC experiments,  $\Delta H_{\text{initial}}^b$  was determined which was the initial enthalpy change which corresponded to direct protein interaction with the surfaces of HAP. Experiments were conducted in phosphate buffer pH 7.4 at 25 °C. Reprinted with permission from Goobes R et al. (2007) American Chemical Society

( $K$ ) and the total ligand concentration ( $X_t$ ) can be expressed as previously described in the section on data analysis but  $M_t$  should be redefined.  $M_t$  can be modified to express the surface area of the inorganic particle which is the binding site as the effective concentration of sites on the surface ( $M'_t$ ) that are available for interaction with the peptide using the following expression;

$$M'_t = N_{\max} \left( \frac{\text{moles}}{m^2} \right) \times SA \left( \frac{m^2}{\text{gr}} \right) \times D \left( \frac{\text{gr}}{L} \right) \quad (3.17)$$

Equilibrium adsorption isotherm measurements (AI) can be used to quantify the maximum number of peptide interaction sites ( $N_{\max}$ ) per unit surface area of the inorganic particle. In AI measurements if centrifugation is used to separate the supernatant with free protein from the pellet-containing particles with adsorbed peptide, this may perturb the peptide–nanoparticle complex leading to inaccurate quantification of bound and free peptide (Klein et al. 2007). The total surface area (SA) of the inorganic particles can be determined from BET measurements although there may be discrepancies between the surface sites that are accessible to small gaseous molecules such as nitrogen used in BET experiments compared to the size of interacting molecules being studied (Goobes R et al. 2007). The density (D) of the inorganic particles in the ITC cell is obtained by dividing its mass by the volume of the cell (Goobes R et al. 2007).

The binding affinity of the single point mutant protein to the surfaces of HAP was lowered compared to the wild-type protein but the adsorption enthalpy, dynamic properties, structural properties, and the maximal surface coverage was not altered. The multiple point mutation of the wild-type protein replacing all basic residues with alanine simultaneously resulted in a fivefold reduction of the binding constant and a twofold reduction of the surface coverage despite no observed changes in the structure and dynamics of the *N*-terminal acidic segment. They deduced that the surface coverage of the multiple point mutant may have been

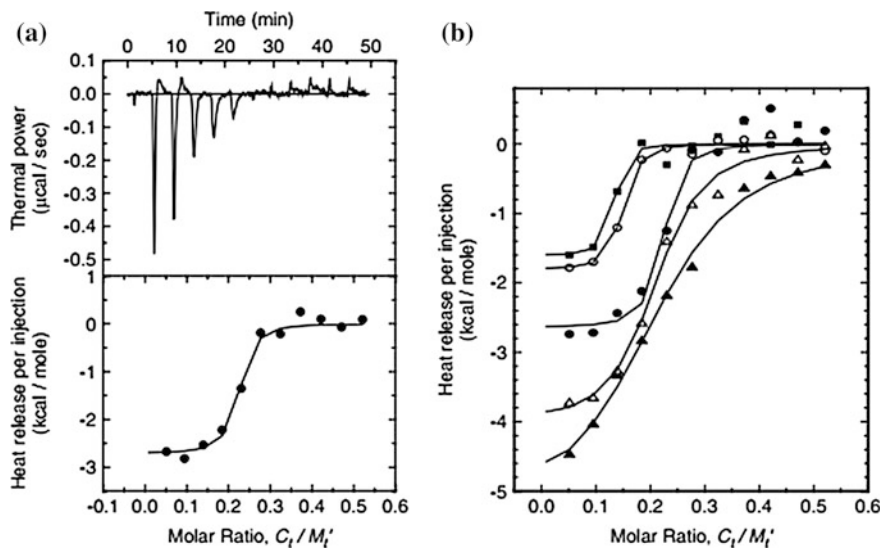


**Fig. 3.15** ITC profiles of the interaction of statherin with HAP **a** experiment conducted at 25 °C **b** experiment carried out at different temperatures, i.e., 15 °C (black triangle), 20 °C (white triangle), 25 °C (black circle), and 30 °C (white circle), 37 °C (black square). Reprinted with permission from Goobes G et al. (2007) John Wiley and Sons

decreased due to unfavored protein–protein interaction as a result of stronger repulsive charge between the higher negative net charge compared to the wild-type protein and single point mutants. In consistency with their previous studies, the authors proposed two binding sites for statherin on HAP surface; the first eliciting an exothermic heat change that can be correlated to statherin interacting with the crystal faces and step edges of HAP and the second that does not cause a measurable heat change and can be attributed to release of bound water and protein–protein interaction. The second binding site is therefore best characterized using binding models based on determination of surface coverage which can give a clearer indication of the occurrence of protein–protein interaction. For the measurable heat change in the initial interaction, all mutants and the wild-type possessed comparable binding entropy when studied using ITC. Any possible changes in enthalpy of the mutants compared to the wild-type may have been below the detection limit of the ITC instrument used. For the second interaction, the enthalpy contribution may be canceled by other events or may also be below the ITC’s detection limit. The authors concluded that the basic amino acids do not significantly contribute to the protein’s enthalpy of adsorption but influence the packing density of the protein at saturation (Goobes R et al. 2007).

In another study, statherin was titrated into a suspension of HAP crystals in a calorimetry cell at different temperature between 15 and 37 °C (Goobes G et al. 2007). The integrated heat change was plotted against the ratio of total protein concentration ( $C_T$ ) after each injection and the effective concentration of binding

**Table 3.7** Thermodynamic parameters of the interaction of statherin with HAP in phosphate buffer pH 7.4 determined using ITC

Temp (°C)	$\alpha$	$\Delta H$ (kcal/mole)	$T\Delta S^0$ (kcal/mole)	$\Delta G^0$ (kcal/mole)	$K$ (1/M)
15	0.21	$-5.4 \pm 0.4$	$2.1 \pm 0.3$	$-7.4 \pm 0.1$	$(4.3 \pm 0.8) \times 10^5$
20	0.18	$-4.0 \pm 0.4$	$4.1 \pm 0.2$	$-8.1 \pm 0.2$	$(1.1 \pm 0.4) \times 10^6$
25	0.21	$-2.7 \pm 0.1$	$6.8 \pm 0.2$	$-9.5 \pm 0.4$	$(9.5 \pm 5.8) \times 10^6$
30	0.13	$-1.8 \pm 0.2$	$8.0 \pm 0.2$	$-9.8 \pm 0.3$	$(1.2 \pm 0.6) \times 10^7$
37	0.11	$-1.6 \pm 0.4$	$6.5 \pm 0.3$	$-10.1 \pm 0.5$	$(1.4 \pm 1.0) \times 10^7$

Only a fraction of the interactions that occur elicit a measurable heat change by ITC and are represented by  $\alpha$ . Reprinted with permission from Goobes G et al. (2007) John Wiley and Sons

sites on the HAP surface ( $M'_i$ ) available for statherin adsorption (Fig. 3.15). As in the previous study, adsorption occurred through an initial exothermic event followed by a thermoneutral event. The apparent thermodynamic parameters of the interactions are shown in Table 3.7. The exothermic event was seen to decrease with an increase in temperature. The determined  $\Delta Cp$  and  $\Delta S$  of the interaction were positive and collectively suggest that electrostatic and not hydrophobic interactions dominated the interaction likely through the charge interactions of ionic HAP surface sites and the charged N-terminus of the protein (Goobes G et al. 2007).

The bottom-up hierarchical approach to material assembly using biomolecules to control growth and morphology of materials is increasingly applied with an aim of achieving programmable structures with superior functions. In our studies, we have applied ITC to study the interaction of ZnO-twinned hexagonal rods and synthetic inorganic binding peptides that have been shown to modify the morphology of the inorganic materials during synthesis studies in the presence and absence of the peptides (Liang et al. 2011; Tomczak et al. 2009). Data showing the interaction of GT-16 peptide (GLHVMHKVAPPR-GGGC) with ZnO crystals has been illustrated in Fig. 3.12a. We have also studied the interaction of ZnO with G-12 peptide (GLHVMHKVAPPR) and its alanine mutants using computational tools (Tripos SYBYL and Accelrys Materials studio) and ITC. Additionally, we have carried out synthesis of ZnO in the presence of wild-type G-12 peptide and some selected mutants. Interaction studies using peptide G-12 (GLHVMHKVAPPR) with uncalcined and calcined crystals show differences in the isothermal profiles highlighting the importance of surface characterization (Fig. 3.16).

In addition, for binding experiments conducted with single point mutants of G-12, differences in the features of the isothermal profiles can be observed (Fig. 3.17). From the ITC data, there is a clear participation of two interaction process of opposite heat change; an endothermic event followed by an exothermic event. The observed endothermic interaction may reflect changes in peptide conformational entropy influenced by the intrinsic properties of the peptide and by the structuring effect of water molecules. Endothermic interactions measured could also have resulted from displacement of water molecules that interact with the surface of ZnO thereby breaking hydrogen bonds before the peptide interacts. This may be the reason why less of the endothermic event is seen for the calcined

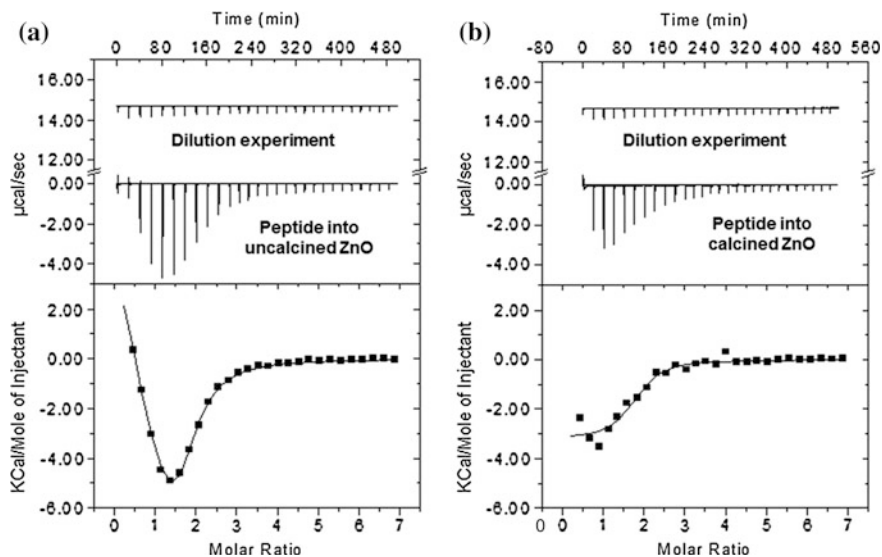


**Fig. 3.16** ITC isotherms representing the interaction of as prepared (uncalcined) ZnO rods and calcined ZnO rods with G-12 peptide. **a** Above, raw data profile of titrating 280  $\mu\text{l}$  of 3.125 mM G-12 peptide in 10  $\mu\text{l}$  aliquots into a cell containing 1.4 ml of ddH<sub>2</sub>O producing heats of dilution. Below is the raw data profile of titrating the peptide into a cell containing a suspension of 0.1 mM ZnO rods. **b** A similar experiment of G-12 interaction with calcined ZnO hexagonal crystal rods (Unpublished data)

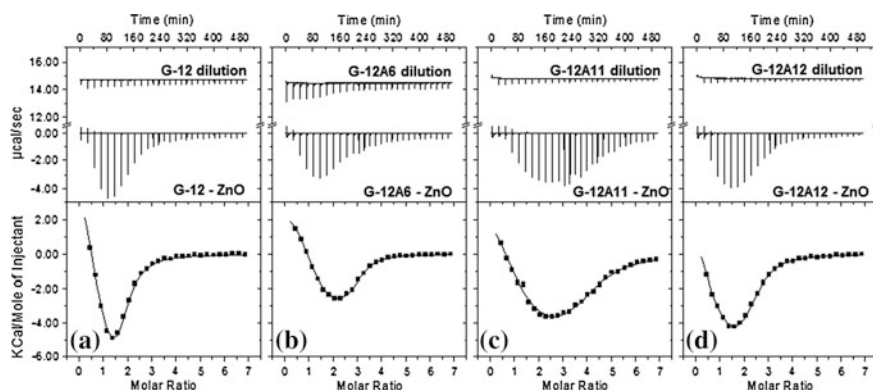


**Fig. 3.17** ITC isotherms showing interaction of G-12 peptide and mutants with ZnO rods. **a** G-12 peptide, **b** G-12A6 peptide, **c** G-12A11 peptide, **d** G-12A12 peptide. In all experiments, 3.125 mM peptide was added in 28 injections each with 10  $\mu\text{l}$  aliquots into a cell containing 1.4 ml ZnO rods suspension containing 0.1 mM Zn<sup>2+</sup>. A constant cell temperature of 298 K was maintained (unpublished data)

ZnO crystals. Exothermic heat changes observed may be as a result of the interaction occurring between the peptide and the inorganic surface via noncovalent interactions such as van der Waals interaction, electrostatic interactions, or hydrogen bonding.

Quantification of binding potency can be based on the amount of material that adsorbs to the surface. The amount of peptide needed to obtain saturation in all the interactions was found to be in excess of the amount required to form a monolayer of peptide on the surface of ZnO available. This may suggest that the peptides could have self-recognition properties allowing them to bind to each other thus forming multilayers on the surface of ZnO. Two saturation events could be taking place: peptide binding and saturating the surface of ZnO and peptide binding to peptide forming a multilayer until peptide-peptide binding site saturation is achieved. Each event produces a measurable heat change; however, there is no clear distinction between the saturation of the peptide layer directly adsorbing onto the inorganic surface and subsequent saturation of the peptide-peptide interaction events. It is likely that both events would occur simultaneously rather than sequentially as the peptides could have adsorbed in an aggregated form as evidenced from DLS experiments showing that peptides are polydisperse and aggregated in solution. From synthesis studies in the absence and presence of G-12 peptide and mutant peptides, structural modification was also found to be peptide dependent.

Nanoparticles are increasingly being developed and administered in products including medicine (Lindman et al. 2007; Lynch and Dawson 2008; Mahmoudi et al. 2011). They are of interest mainly because of their small size which enhances their chemical reactivity through increasing the number of surface atoms and in biomedical applications, allows them to infiltrate into target sites that were previously inaccessible as well as to interact more intimately with cellular machinery. Nevertheless, reservations on their use linger as there is insufficient knowledge on the biological responses they elicit including toxicity which is alarming. In biological fluids, nanoparticles are coated with proteins forming the nanoparticle-protein corona which is the entity that the cells recognize and interact with (Lindman et al. 2007; Lynch and Dawson 2008). Studying the plausible toxicological effects of nanoparticles requires a detailed account of its interaction with proteins to determine which proteins enrich the nanoparticle surface. ITC has been used to determine the thermodynamics of interaction of human serum albumin (HSA) to copolymer nanoparticles or varying sizes/curvature and hydrophobicity (Lindman et al. 2007). Exothermic events were registered for all the nanoparticles used and the more hydrophobic nanoparticles required a higher concentration of HSA to be saturated which the authors inferred to suggest a higher surface coverage. Higher affinity was observed for the more hydrophilic nanoparticles. MOLMOL which is a molecular graphics program was used to calculate the maximum number of protein molecules that adsorb to the nanoparticle by estimating the minimum cross-section area of HSA structure. The theoretical surface area of the particles were also calculated and divided by the cross-sectional area of HSA achieving theoretical 100 % coverage for each particle. The sparse or dense

nature of the adsorbed protein layer (monolayer or multilayers) can be determined from the degree of surface coverage (Lindman et al. 2007). The surface coverage of nanoparticles with the same hydrophobicity but different particle size was also investigated. The curvature of the nanoparticles was seen to affect surface coverage (Cedervall et al. 2007; Lindman et al. 2007). The smallest nanoparticles (70 nm) with the highest available surface area for interaction were found to have less bound protein which was attributed to the high degree of curvature which could have interfered with binding. The larger nanoparticles (700 nm) tended toward a flat surface hence the effect of surface curvature became more insignificant. Particles between 120 and 400 nm had the highest surface coverage. A dense adsorbed layer of protein was observed for nanoparticles of 120 nm diameters and larger. However, the shape of the isothermal profiles did not suggest the occurrence of multilayers normally represented by steps as each layer is completed. This was attributed to undetectable entropy changes of protein–protein interactions similar to previous reports on the interaction of statherin with HAP (Goobes R et al. 2007, Lindman et al. 2007). Possibly as in the previously discussed study by You et al. (2008), CD measurements could be used to confirm if multilayer formation occurred. The authors also studied the interaction of other proteins including lysozyme, fibrinogen, and calmodulin with copolymer nanoparticles using ITC but no signals were found (Lindman et al. 2007). They concluded that the lack of signals could be as a result of no measurable heat change of interactions if reactions were entirely entropy driven or because there was no interaction. SPR was used as a complementary technique which confirmed that interactions could not be ruled out with some of the studied proteins which were contrarily found to interact with the copolymer nanoparticles that were immobilized to a gold surface using a thiol group. This underlines the benefits of using complementary techniques (Lindman et al. 2007).

Lindman et al. (2007) further studied the interaction of nanoparticles with HSA bound to its endogenous ligand oleic acid. The interaction was endothermic which they thought could have resulted from initial dissociation of oleic acid from HSA before it binds to the nanoparticle or variations in the binding mode of oleic acid bound HSA or if instead, oleic acid bound to the nanoparticles. A negative  $\Delta Cp$  was observed in the interaction of HSA with copolymer particles at different temperatures which suggested that hydrophobic interactions were the driving force supported by the fact that HSA is a hydrophobic protein. However, because the observed interaction was exothermic, the authors were more inclined to think that more specific interactions may occur between the side groups of the nanoparticles and HSA. ITC was also used to study the interaction of 16 nm diameter quantum dots (functionalized using hydrophilic polymers) with proteins HSA and  $\alpha$ -lactalbumin. An exothermic interaction was observed with HSA and a biphasic interaction was observed with  $\alpha$ -lactalbumin (Fig. 3.18). Here ITC showed its ability to measure processes with positive  $\Delta H$  of interaction (Lindman et al. 2007).

Another emerging application of nanoparticles in biomedicine is in vaccine development for example in cancer immunotherapy (Cho et al. 2011). Nanoparticles with high surface area can be used as efficient carriers to deliver target



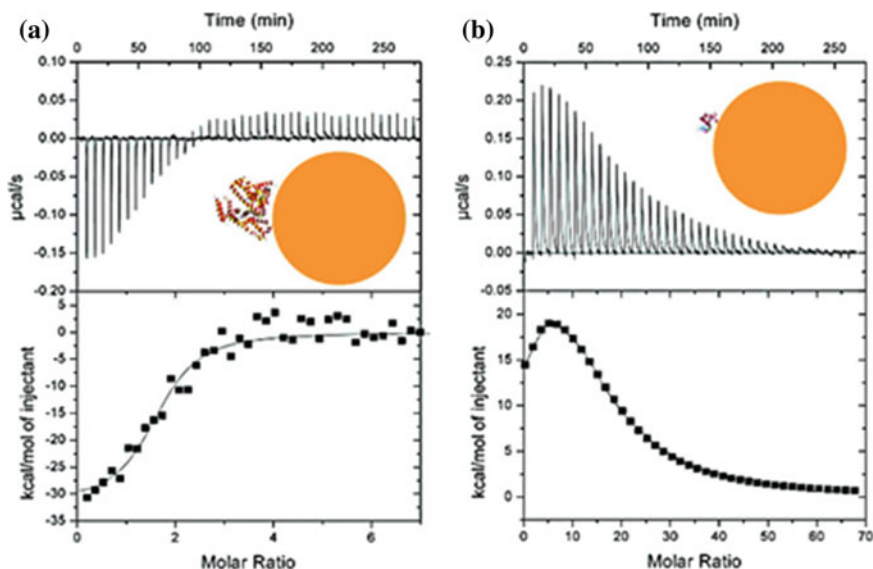


**Fig. 3.18** ITC profiles showing the interaction of **a** HSA (38 μM) with a solution of 800 nm quantum dots and **b** α-lactalbumin (230 μM) with solutions of 500 nm quantum dots in Hepes/NaOH, 0.15 M NaCl, 1 mM EDTA, pH 7.5, 25 °C. *Inset* the size comparisons of the proteins and nanoparticles are illustrated. Reprinted with permission from Lindman et al. (2007) American Chemical Society

antigens to dendritic cells (DC). These cells can migrate to lymph nodes to activate T-cells specific to the antigens thereby stimulating and regulating tumor antigenic responses (Cho et al. 2011). Imaging methods such as magnetic resonance imaging (MRI) are used to track DC migration. High resolution imaging in MRI requires the use of superparamagnetic iron oxide (SPIO) nanoparticles that are not biocompatible. By coating SPIO nanoparticles with a ZnO shell that is photonic for DC-based immunotherapy, biocompatibility was achieved (Cho et al. 2011). ZnO-binding peptide (ZBP) RPHPKGGDA bound to the ZnO surface served as carriers for tumor antigens into DCs. In the peptide sequence, RPHPK is the conserved binding motif while GGDA is the linker. ITC was used to determine the binding affinity of the ZBP and a triplicate tandem repeat of it ( $3 \times$  ZBP) to the ZnO coated nanoparticle (Fig. 3.19). The affinity of  $3 \times$  ZBP for the nanoparticles was higher than that of  $1 \times$  ZBP (Table 3.8). The authors deduced that the high affinity of  $3 \times$  ZBP peptide for the nanoparticle surface, may suggest that zinc ions are present on the surface of the nanoparticles (Cho et al. 2011). This immunotherapy approach was tested in vivo by immunizing mice and the results were promising (Cho et al. 2011).

ITC has equally proven to be useful in industrial advancements. An example is an investigation where ITC was used to probe metal–ligand interactions in the study of interactions between divalent copper cations and chitin fragments

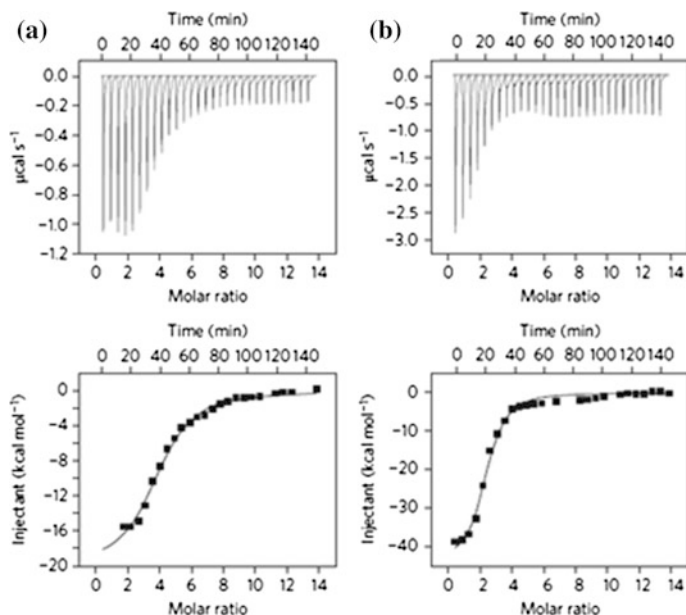


**Fig. 3.19** ITC isotherms showing the interaction of 0.25 mM of **a**  $1 \times$  ZBP and **b**  $3 \times$  ZBP with a  $4 \mu\text{M}$  nanoparticle suspension of ZnO coated SPIO nanoparticles at  $25^\circ\text{C}$ . Reprinted by permission from Macmillan Publishers Ltd: Nature Nanotechnology (Cho et al. 2011) Nature Publishing Group

**Table 3.8** Thermodynamic parameters for the interaction of ZnO-binding peptides and ZnO coated SPIO nanoparticles determined using ITC

	$K_a(\text{M}^{-1})$	$K_d(\text{M})$	$\Delta H^\circ$ (kcal/mol)	$\Delta S^\circ$ (kcal/mol)
$1 \times$ ZBP	$6.9 \pm 0.8 \times 10^5$	$1.5 \times 10^{-6}$	$-2.0 \times 10^4 \pm 757.7$	$-39.9$
$3 \times$ ZBP	$1.4 \pm 0.2 \times 10^6$	$6.9 \times 10^{-7}$	$-4.4 \times 10^4 \pm 1208.0$	$-119.0$

Reprinted by permission from Macmillan Publishers Ltd: Nature Nanotechnology (Cho et al. 2011) Nature Publishing Group

(Camci-Unal and Pohl 2010). Chitin is a nontoxic, naturally abundant insoluble and inexpensive polysaccharide that can be used for biosorption of heavy metal cations found in industrial water and as a biomaterial for medical applications (Kratochvil and Volesky 1998). In previous studies, the interaction of polymeric chitin with a number of metal cations was determined to be enthalpically driven and spontaneous (Camci-Unal and Pohl 2010). The authors carried out further investigations to determine if chitin possessed specific binding sites through which multiple ligands are able to chelate a metal cation. Interaction of copper with small fragments of chitin; N-acetyl-D-glucosamine (GlcNAc), its repeating units of different lengths (GlcNAc)<sub>2</sub> (GlcNAc)<sub>3</sub> (GlcNAc)<sub>5</sub> and D-glucosamine were studied using ITC to determine if the different segments would interact with different affinities

(Camci-Unal and Pohl 2010). Once more, the values of  $\Delta H$ ,  $\Delta S$ , and  $\Delta G$  were found to be negative and they established that the interactions were enthalpically driven and spontaneous (Camci-Unal and Pohl 2010). The strength of the interaction determined from binding affinity values increased with an increase in GlcNAc residues. The deacylated GlcNAc fragment, D-glucosamine, had a higher enthalpy value and greater affinity for copper compared to GlcNAc; therefore, the authors established that the amine group is important for the interaction. The occurrence of chelation-based multivalency was ruled out because addition of sugars to the polymer did not have a drastic effect on the binding affinity beyond statistical effects; therefore, a single copper atom was not bound by multiple amide groups. The authors concluded that the findings gave information that is useful to direct computational modeling for the design of metal- and carbohydrate-based materials (Camci-Unal and Pohl 2010).

In a similar study ITC was used to compare the thermodynamic interactions between toxic metals ions ( $\text{Al}^{3+}$ ,  $\text{Cr}^{3+}$ , and  $\text{Pb}^{2+}$ ) with activated carbon which is a high-cost sorbent commonly used for metal decontamination of water and the same metal ions with chitin which is a possible cheaper substitute of activated carbon (Karlsen et al. 2010). The integrated heat change in kcal/mol of injectant was plotted against the amount of metal ions used ( $\mu\text{mol}$ ) per gram of adsorbent chitin (Fig. 3.20). They then proceeded to fit data using the single set of identical sites or two sets of independent sites model to obtain thermodynamic parameters (Table 3.9). From the results, the authors deduced that there were two binding sites for the metal ions on chitin and the differences in thermodynamic signatures observed between the metal ions and chitin suggested that the metal ions may possibly bind to different functional groups found on chitin. High-cost activated carbon which is currently more commonly used to purify industrial waste water was seen to interact weakly with the metal ions at a single binding site (Karlsen et al. 2010). With this evidence, consumers can make an informed decision and may be encouraged to change from conventional use of high-cost activated carbon to low-cost chitin.

### 3.6 Summary, Recommendations, and Conclusions

In this chapter, we focused on the presentation of three different methods that can be used to experimentally determine thermodynamic properties that characterize the adsorption behavior of small peptides and proteins with material surfaces: SPR, AFM, and ITC. Each of these methods has its own specific set of advantages, disadvantages, and appropriate areas of application. In the preceding sections on each of these topics, we have sought to clearly identify these issues in order to provide direction for readers who may be interesting in applying these methods in their own studies to characterize peptide and protein interactions with material surfaces.

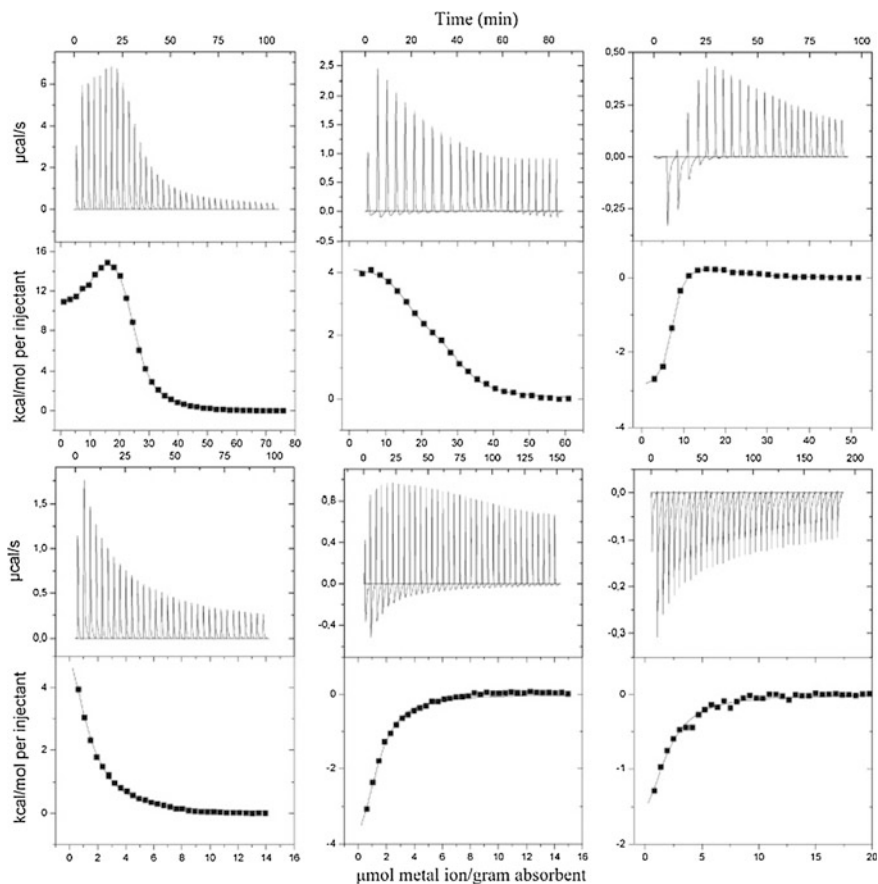


**Fig. 3.20** ITC isotherms showing the interaction of metal ions Al<sup>3+</sup>, Cr<sup>3+</sup>, and Pb<sup>2+</sup> (from left to right) with  $\beta$ -chitin (top three) and activated carbon (bottom three). Reprinted with permission from Karlsen et al. (2010) Elsevier

As a critical issue for any serious research project involving peptide/protein adsorption behavior, careful attention must be applied to ensure that the adsorbent surfaces are as clean and free from contamination as possible. Characterization methods should then be applied to document the chemical and physical properties of the adsorbent surface (e.g., chemical composition, surface energy, and surface roughness). These steps are important not only to ensure the quality of subsequent experimental results, but also so that others who wish to reproduce the results from a given study are able to closely match the conditions of the prior experiments.

As presented in Sect. 3.4, SPR spectroscopy can be used to determine the free energy of peptide adsorption to surfaces through the generation of adsorption isotherms and the application of the Langmuir model. It is important for readers to understand that the implementation of the Langmuir model is based on a set of

**Table 3.9** Thermodynamic parameters for the interaction of  $\text{Al}^{3+}$ ,  $\text{Cr}^{3+}$ , and  $\text{Pb}^{2+}$  with  $\beta$ -chitin and activated carbon at 25 °C determined using ITC

Metal ion	$K_a$ ( $\text{M}^{-1}$ )	$\Delta G$ (kJ/mol)	$\Delta H$ (kJ/mol)	$\Delta S$ (J/Kmol)	$n$ ( $\mu$ mol/g)
$\beta$ -Chitin					
$\text{Al}^{3*}$	$(4.0 \pm 2.4) \times 10^6$	-37.6	$17.6 \pm 3.6$	184	18
	$(2.3 \pm 0.5) \times 10^5$	-30.5	$75.3 \pm 5.0$	355	20
$\text{Cr}^{3+}$	$(6.0 \pm 1.4) \times 10^6$	-38.5	$16.3 \pm 2.9$	184	28
	$(3.6 \pm 2.8) \times 10^5$	-31.8	$8.2 \pm 2.1$	134	31
$\text{Pb}^{2+}$	$(2.0 \pm 1.4) \times 10^7$	-41.8	$-10.9 \pm 1.5$	105	7
	$(2.0 \pm 0.7) \times 10^5$	-30.1	$2.1 \pm 0.9$	109	31
Activated carbon					
$\text{Al}^{3*}$	$(5.0 \pm 0.9) \times 10^4$	-26.8	$38.5 \pm 3.4$	217	2
$\text{Cr}^{3*}$	$(6.5 \pm 1.5) \times 10^4$	-27.6	$-24.3 \pm 3.2$	12	3
$\text{Pb}^{2*}$	$(4/4 \pm 1.2) \times 10^4$	-26.3	$-14.2 \pm 22$	42	2

Reprinted with permission from Karlsen et al. (2010) Elsevier

specific conditions that must be present in order for the model to be used for the accurate determination of adsorption free energy. These conditions are that (i) the adsorption process must be fully reversible within the timeframe of the adsorption study (i.e., equilibrated conditions reached) (ii) all adsorption sites on the surface should be identical and bind only one solute molecule (i.e., homogeneous surface), (iii) solute–solute interactions do not influence the adsorption process, and (iv) the solute must adsorb as a monolayer without multilayer formation (Langmuir 1916; Everett 1964; Lan et al. 2001). Unfortunately, adsorption systems that strongly deviate from these conditions will often generate Langmuir-looking isotherms and it is therefore up to the individual user to determine that conditions i–iv are met for the adsorption process under consideration before the Langmuir model is applied. The adsorption behavior of small peptides (i.e., less than about 12 amino acid residues) onto a homogeneous material surface generally tends to follow these conditions with the exception of the influence of solute–solute interactions on the surface, which can substantially influence the amount of peptide that a surface will adsorb at saturation. The methods that we present in Sect. 3.4 enable this problem to be avoided through the use of a modified isotherm analysis approach that enables the adsorption behavior to be extrapolated to zero surface coverage, under which solute–solute interactions on the surface are minimized. The application of this analysis technique can thus provide an approach for the determination of standard-state adsorption free energy even for a system that exhibits solute–solute interactions that tend to influence the shape of the adsorption isotherm as surface saturation is approached.

One of the primary limitations of the SPR method is that the adsorbent surface must be synthesized as a thin film (i.e., <100 nm) over a metallic substrate (e.g., gold). Thus, materials that are not easily fabricated into such nano-thick layers are not amenable for use with SPR. To address this limitation, we have

developed a complementary AFM method that can be used in place of SPR. This combined set of methods is based on our findings that the force required to desorb simple unstructured peptides from a surface, as measured by a standardized AFM method, can be directly correlated to adsorption free energy measured by SPR. The critical aspect of this dual approach is the development of a correlation plot between these two methods through the use of a large set of peptide–surface systems that can be evaluated by both methods. Once this correlation plot is generated, then the same AFM protocol can be applied to measure peptide desorption forces for surfaces that are not amenable for use with SPR, with the correlation plot then used to provide estimates of adsorption free energies.

When used as a combined set, the presented SPR and AFM methods provide experimental methods that can be used to determine the change in standard-state free energy for peptide adsorption on any macroscopically flat surface. These methods, however, are not applicable to characterize the adsorption behavior of peptides with small particles that are suspended in solution. As addressed in [Sect. 3.5](#), ITC provides an excellent experimental method to characterize these types of adsorption processes.

From the discussed case studies and other studies reported in the literature it is clear that ITC is an invaluable tool for thermodynamic characterization of interfacial interactions with small particles. ITC has developed from its conventional use to study equilibrium processes to a universal tool that can be used to investigate irreversible processes of binding/adsorption of artificial molecules and biopolymers on surfaces or with each other ([Chiad et al. 2009](#); [Schmidtchen 2012](#)).

Like any other technique, ITC has limitations and challenges that need to be recognized. From the studies we have discussed we can already begin to understand some of these challenges. The importance of sample preparation and characterization especially of particles before carrying out ITC studies has been underlined. In an experiment, the user seeks to achieve a measurable heat change under optimum conditions to obtain a profile from which thermodynamic parameters can accurately be obtained. As thermodynamic parameters are calculated from concentrations, integrated heat change should be plotted against the molar ratio of interacting species for thermodynamic parameters to be determined. For interactions of peptides with surfaces, we agree with the proposed method to express the binding site for a ligand (i.e., protein) on a surface (i.e., inorganic particles) as the effective concentration of sites on the surface available for interaction so that data can be plotted as normalized integrated heat change in kcal/mole of injectant against the molar ratio of reactants ( $[\text{protein}]/[\text{inorganic surface sites}]$ ) ([Goobes R et al. 2007](#)) even though this information may be difficult to obtain in practice especially where multilayers of protein are adsorbed without a clear distinction between the saturation of the protein–surface and protein–protein adsorption event. The shapes of isothermal profiles from different interactions can vary dramatically and modeling of ITC data can become challenging especially if there are multiple binding sites involved and where there is no knowledge on

whether the sites are dependent or independent. Prior knowledge about the binding site of the interaction gives a clearer view as to which fitting model should be used. However, in many cases when studying interactions of molecules with inorganic particles, the exact binding site can be difficult to define (Ball and Maechline 2009). On detailed inspection of literature, one can begin to appreciate that there are uncertainties in using mathematical models when it comes to appropriate representation of an interaction being studied. In some studies, when unsure, authors have decided to fit data using more than one binding model and in many cases it is not clear why authors chose to use a particular model especially when there is no strong relation to the interaction being studied. Meaningful representation of data should be pursued. An expert in the use of ITC has even said that “All models are wrong, but some are useful” (Freyer and Lewis 2008). Mathematical expertise is valuable for developing additional useful models besides those provided in commercial software. Nonetheless using the simplest models with the fewest adjustable parameters are recommended (Schmidtchen 2012).

Data interpretation and deconvolution of individual events (i.e., van der Waals interactions, electrostatic interactions, hydrogen bonding, and hydrophobic interactions) occurring simultaneously and contributing to the global heat change is not always straightforward and cannot be described at the atomic level. Improvements in technology and methodology are needed especially where ITC experiments have to be simplified compared to the actual events they need to be correlated to (Cliff et al. 2004; Mahmoudi et al. 2011). For example in drug development it may only be possible to study interactions of individual proteins with nanoparticles using ITC to obtain information that can be assertively interpreted; however, in biological fluids, we know that there are several proteins of different affinities in coexistence and that cooperative effects must play an important role (Cliff et al. 2004; Mahmoudi et al. 2011). Complementary techniques are useful especially where more than one interaction occurs simultaneously and where interactions occur producing heat changes that are below the detection limit of the instrument (Goobes R et al. 2007; Lindman et al. 2007). Great prospects lie in using information obtained from ITC studies to advance design processes thereby creating novel materials. With continued improvements in instrumentation and methodology, the development of novel applications of ITC is far from being exhausted.

**Acknowledgments** R.A. Latour and Y. Wei would like to acknowledge support for this research from the Defense Threat Reduction Agency-Joint Science and Technology Office for Chemical and Biological Defense (Grant no. HDTRA1-10-1-0028). The facilities used were also supported by NIH Grants 5P20RR021949-04 and 8P20GM103444-04. We also would like to thank Ms. Megan Grobman, Dr. Lara Gamble, and Dr. David Castner of NESAC/BIO at the University of Washington for assistance with surface characterization with XPS under the funding support by NIH NIBIB (grant # EB002027). C.C. Perry and M.J. Limo would like to thank their collaborators at the Air force office of scientific research (AFOSR) for funding and support of their studies (FA9550-10-1-0024 and FA9550-13-1-0040).

## References

- Ababout A, Ladbury JE (2006) Survey of the year 2004: literature on applications of isothermal titration calorimetry. *J Mol Recogn* 19(1):79–89
- Allison DP, Hinterdorfer P, Han W (2002) Biomolecular force measurements and the atomic force microscope. *Curr Opin Biotechnol* 13(1):47–51
- Ball V, Maechling C (2009) Isothermal microcalorimetry to investigate non specific interactions in biophysical chemistry. *Int J Mol Sci* 10(8):3283–3315
- Biltonen R, Langerman N (1979) Microcalorimetry for biological chemistry: experimental design, data analysis, and interpretation. *Methods Enzymol* 61:287–318
- Blanchette CD, Loui A, Ratto TV (2008) Tip functionalization: applications to chemical force spectroscopy. *Handbook of Molecular Force Spectroscopy*, pp 185–203
- Blankschien MD, Pretzer LA, Huschka R et al (2013) Light-triggered biocatalysis using thermophilic enzyme-gold nanoparticle complexes. *ACS Nano* 7(1):654–663
- Bouchemal K, Mazzaferro S (2012) How to conduct and interpret ITC experiments accurately for cyclodextrin-guest interactions. *Drug Discov Today* 17(11):623–629
- Bramwell VW, Eyles JE, Oya Alpar H (2005) Particulate delivery systems for biodefense subunit vaccines. *Adv Drug Deliv Rev* 57:1247–1265
- Bryers JD, Giachelli CM, Ratner BD (2012) Engineering biomaterials to integrate and heal: the biocompatibility paradigm shifts. *Biotechnol Bioeng* 109(8):1898–1911
- Camci-Unal G, Pohl NLB (2010) Thermodynamics of binding interactions between divalent copper and chitin fragments by isothermal titration calorimetry (ITC). *Carbohydr Polym* 81(1):8–13
- Cedervall T, Lynch I, Lindman S, Berggard et al (2007) Understanding the nanoparticle-protein corona using methods to quantify exchange rates and affinities of proteins for nanoparticles. *Proc Natl Acad Sci USA* 104(7):2050–2055
- Charles MR, Abraham ML (2003) Quantitative modeling of protein adsorption. *Biopolymers at Interfaces*. M. M. Dekker, New York, pp 71–94
- Chen Y, Ming H (2012) Review of surface plasmon resonance and localized surface plasmon resonance sensor. *Photonics Sens* 2(1):37–49
- Chen K, Xu Y, Rana S et al (2011) Electrostatic selectivity in protein–nanoparticle interactions. *Biomacromolecules* 12(7):2552–2561
- Chiad K, Stelzig SH, Gropeanu R et al (2009) Isothermal titration calorimetry: a powerful technique to quantify interactions in polymer hybrid systems. *Macromolecules* 42(19):7545–7552
- Chilom CG, Craescu CT, Popescu AI (2004) Parameters of interaction between proteins and their specific ligands, deduced by isothermal titration calorimetry. In: Paper presented at the 5th International Balkan workshop on applied physics, pp 443–457
- Chiu CY, Li Y, Ruan L et al (2011) Platinum nanocrystals selectively shaped using facet-specific peptide sequences. *Nat Chem* 3(5):393–399
- Cho N, Cheong T, Min JH et al (2011) A multifunctional core-shell nanoparticle for dendritic cell-based cancer immunotherapy. *Nat Nanotechnol* 6(10):675–682
- Cliff MJ, Gutierrez A, Ladbury JE (2004) A survey of the year 2003 literature on applications of isothermal titration calorimetry. *J Mol Recogn* 17(6):513–523
- Crespo-Quesada M, Andanson J, Yarulin A et al (2011) UV–ozone cleaning of supported poly(vinylpyrrolidone)-stabilized palladium nanocubes: effect of stabilizer removal on morphology and catalytic behavior. *Langmuir* 27(12):7909–7916
- Davis SA, Dujardin E, Mann S (2003) Biomolecular inorganic materials chemistry. *Curr Opin Solid State Mater Sci* 7(4–5):273–281
- de Mol NJ, Fischer MJ (2010) Surface plasmon resonance: a general introduction. *Methods Mol Biol* 627:1–14
- De M, You C, Srivastava S et al (2007) Biomimetic interactions of proteins with functionalized nanoparticles: a thermodynamic study. *J Am Chem Soc* 129(35):10747–10753



- Dickerson MB, Sandhage KH, Naik RR (2008) Protein- and peptide-directed syntheses of inorganic materials. *Chem Rev* 108(11):4935–4978
- Dujardin E, Mann S (2002) Bio-inspired materials chemistry. *Adv Mater* 14(11):775
- Everett DH (1964) Thermodynamics of adsorption from solution. Part I. Perfect systems. *Trans Faraday Soc* 60:1803–1813
- Fears KP, Creager SE, Latour RA (2008) Determination of the surface pK of carboxylic- and amine-terminated alkanethiols using surface plasmon resonance spectroscopy. *Langmuir* 24(3):837–843
- Fenoglio I, Fubini B, Ghibaudi EM et al (2011) Multiple aspects of the interaction of biomacromolecules with inorganic surfaces. *Adv Drug Deliv Rev* 63(13):1186–1209
- Freyer MW, Lewis EA (2008) Isothermal titration calorimetry: experimental design, data analysis, and probing macromolecule/ligand binding and kinetic interactions. *Methods Cell Biol* 84:79–113
- Gandavarapu NR, Mariner PD, Schwartz MP et al (2013) Extracellular matrix protein adsorption to phosphate-functionalized gels from serum promotes osteogenic differentiation of human mesenchymal stem cells. *Acta Biomater* 9(1):4525–4534
- Garcia AJ (2006) Interfaces to control cell-biomaterial adhesive interactions. *Polymers for Regenerative Medicine*. C. Werner, J. H. Eisseff, C. Fischbacher al:171–190
- Geelhood SJ, Horbett TA, Ward WK et al (2007) Passivating protein coatings for implantable glucose sensors: evaluation of protein retention. *J Biomed Mater Res B* 81B(1):251–260
- Goobes G, Goobes R, Shaw WJ et al (2007) The structure, dynamics, and energetics of protein adsorption—lessons learned from adsorption of statherin to hydroxyapatite. *Magn Reson Chem* 45(S1):S32–S47
- Goobes R, Goobes G, Shaw WJ et al (2007) Thermodynamic roles of basic amino acids in statherin recognition of hydroxyapatite. *Biochemistry* 46(16):4725–4733
- Gourishankar A, Shukla S, Ganesh KN et al (2004) Isothermal titration calorimetry studies on the binding of DNA bases and PNA base monomers to gold nanoparticles. *J Am Chem Soc* 126(41):13186–13187
- Green RJ, Frazier RA, Shakesheff KM et al (2000) Surface plasmon resonance analysis of dynamic biological interactions with biomaterials. *Biomaterials* 21(18):1823–1835
- Gref R, Domb A, Quellec P et al (2012) The controlled intravenous delivery of drugs using PEG-coated sterically stabilized nanospheres. *Adv Drug Deliv Rev* 64:316–326
- Haruki M, Noguchi E, Kanaya S et al (1997) Kinetic and stoichiometric analysis for the binding of *Escherichia coli* ribonuclease HI to RNA–DNA hybrids using surface plasmon resonance. *J Biol Chem* 272(35):22015–22022
- Herr AE (2009). Protein microarrays for the detection of biothreats. In: Dill RHLK, Grodzinski P (eds) *Microarrays. Preparation, microfluidics, detection methods, and biological applications*. Springer, New York, pp 169–190
- Hoffmann F, Cornelius M, Morell J et al (2006) Silica-based mesoporous organic–inorganic hybrid materials. *Angew Chem Int Ed* 45(20):3216–3251
- Homola J, Yee SS, Gauglitz G (1999) Surface plasmon resonance sensors: review. *Sens Actuators B Chem* 54(1–2):3–15
- Horinek D, Serr A, Geisler M et al (2008) Peptide adsorption on a hydrophobic surface results from an interplay of solvation, surface, and intrapeptide forces. *Proc Natl Acad Sci U S A* 105(8):2842–2847
- Huang R, Carney R, Stellacci F et al (2013) Protein-nanoparticle interactions: the effects of surface compositional and structural heterogeneity is scale dependent. *Nanoscale* 5:6928–6935
- Jana NR, Gearheart L, Murphy CJ (2001) Seeding growth for size control of 5–40 nm diameter gold nanoparticles. *Langmuir* 17(22):6782–6786
- Jiang X, Ortiz C, Hammond PT (2002) Exploring the rules for selective deposition: Interactions of model polyamines on acid and oligoethylene oxide surfaces. *Langmuir* 18(4):1131–1143
- Joshi H, Shirude PS, Bansal V et al (2004) Isothermal titration calorimetry studies on the binding of amino acids to gold nanoparticles. *J Phys Chem B* 108(31):11535–11540

- Jung LS, Nelson KE, Campbell CT et al (1999) Surface plasmon resonance measurement of binding and dissociation of wild-type and mutant streptavidin on mixed biotin-containing alkylthiolate monolayers. *Sens Actuators B Chem* 54(1–2):137
- Karlsen V, Heggset EB, Sørli M (2010) The use of isothermal titration calorimetry to determine the thermodynamics of metal ion binding to low-cost sorbents. *Thermochim Acta* 501(1–2):119–121
- Kasemo B, Gold J (1999) Implant surfaces and interface processes. *Adv Dent Res* 13:8–20
- Kidoaki S, Matsuda T (2002) Mechanistic aspects of protein/material interactions probed by atomic force microscopy. *Colloids Surf B* 23(2–3):153–163
- Klein J (2007) Probing the interactions of proteins and nanoparticles. *Proc Natl Acad Sci* 104(7):2029–2030
- Knowles JR (1991) Enzyme catalysis: not different, just better. *Nature* 350:121–124
- Kratochvil D, Volesky B (1998) Advances in the biosorption of heavy metals. *Trends Biotechnol* 16(7):291–300
- Kröger N, Deutzmann R, Sumper M (1999) Polycationic peptides from diatom biosilica that direct silica nanosphere formation. *Science* 286(5442):1129–1132
- Kumar A, Mandal S, Pasricha R et al (2003) Investigation into the interaction between surface bound alkylamines and gold nanoparticles. *Langmuir* 19(15):6277–6282
- Ladbury JE, Doyle ML (2005) *Biocalorimetry 2: applications of calorimetry in the biological sciences*. Wiley, Chichester
- Lal R, John SA (1994) Biological applications of atomic force microscopy. *Am J Physiol Cell Physiol* 266(1):C1–C21
- Lan Q, Bassi AS, Zhu J-X et al (2001) A modified Langmuir model for the prediction of the effects of ionic strength on the equilibrium characteristics of protein adsorption onto ion exchange/affinity adsorbents. *Chem Eng J* 81:179–186
- Langmuir I (1916) The constitution and fundamental properties of solids and liquids. part i. solids. *J Am Chem Soc* 38:2221–2295
- Latour RA (2008) Molecular dynamics simulation of protein-surface interactions: benefits, problems, solutions, and future directions. *Biointerphases* 3:FC2–FC12
- Leavitt S, Freire E (2001) Direct measurement of protein binding energetics by isothermal titration calorimetry. *Curr Opin Struct Biol* 11(5):560–566
- Li X, Husson SM (2006) Adsorption of dansylated amino acids on molecularly imprinted surfaces: a surface plasmon resonance study. *Biosens Bioelectron* 22(3):336–348
- Liang Y (2008) Applications of isothermal titration calorimetry in protein science. *Acta Biochim Biophys Sin* 40(7):565–576
- Liang M, Deschaume O, Patwardhan SV et al (2011) Direct evidence of ZnO morphology modification via the selective adsorption of ZnO-binding peptides. *J Mater Chem* 21(1):80–89
- Lindman S, Lynch I, Thulin E et al (2007) Systematic investigation of the thermodynamics of HSA adsorption to N-iso-propylacrylamide/N-tert-butylacrylamide copolymer nanoparticles. Effects of particle size and hydrophobicity. *Nano Lett* 7(4):914–920
- Liu HN, Webster TJ (2010) Ceramic/polymer nanocomposites with tunable drug delivery capability at specific disease sites. *J Biomed Mater Res A* 93A(3):1180–1192
- Loomans E, Beumer TAM, Damen KCS et al (1997) Real-time monitoring of peptide-surface and peptide-antibody interaction by means of reflectometry and surface plasmon resonance. *J Colloid Interface Sci* 192(1):238–249
- Lynch I, Dawson KA (2008) Protein-nanoparticle interactions. *Nano Today* 3(1):40–47
- Mahmoud TA, Miot S, Frank O et al (2006) Modulation of chondrocyte phenotype for tissue engineering by designing the biologic-polymer carrier interface. *Biomacromolecules* 7(11):3012–3018
- Mahmoudi M, Lynch I, Ejtehadi MR et al (2011) Protein-nanoparticle interactions: opportunities and challenges. *Chem Rev* 111(9):5610–5637
- Martinez JC, Murciano-Calles J, Cobos ES et al (2013) Isothermal titration calorimetry: thermodynamic analysis of the binding thermograms of molecular recognition events by using equilibrium models. In: Elkordy AA (ed) Chapter 4, *Applications of Calorimetry in a Wide*

- Context-Differential Scanning Calorimetry, Isothermal Titration Calorimetry and Microcalorimetry. InTech—Open Access Company, pp 73–104
- Mazaheri M, Zahedi AM, Sadrnezhaad SK (2008) Two-step sintering of nanocrystalline ZnO compacts: effect of temperature on densification and grain growth. *J Am Ceram Soc* 91(1):56–63
- MicroCal L (2003) VP-ITC microcalorimeter user's manual. Microcal, Llc pp 1–94
- Monzó J, Koper M, Rodriguez P (2012) Removing polyvinylpyrrolidone from catalytic Pt nanoparticles without modification of superficial order. *ChemPhysChem* 13(3):709–715
- Naik RR, Brott LL, Clarson SJ et al (2002) Silica-precipitating peptides isolated from a combinatorial phage display peptide library. *J Nanosci Nanotechnol* 2(1):95–100
- Oka K, Shibata H, Kashiwaya S (2002) Crystal growth of ZnO. *J Cryst Growth* 237–239, Part 1:509–513
- Oren EE, Tamerler C, Sarikaya M (2005) Metal recognition of septapeptides via polypod molecular architecture. *Nano Lett* 5(3):415–419
- Perozzo R, Folkers G, Scapozza L (2004) Thermodynamics of protein-ligand interactions: history, presence, and future aspects. *J Recept Signal Transduct* 24(1–2):1–52
- Perry CC, Patwardhan SV, Deschaume O (2009) From biominerals to biomaterials: the role of biomolecule-mineral interactions. *Biochem Soc Trans* 37:687–691
- Pierce MM, Raman C, Nall BT (1999) Isothermal titration calorimetry of protein-protein interactions. *Methods* 19(2):213–221
- Pirzer T, Geisler M, Scheibel T et al (2009) Single molecule force measurements delineate salt, pH and surface effects on biopolymer adhesion. *Phys Biol* 6(2):25004
- Pitarke JM, Silkin VM, Chulkov EV et al (2007) Theory of surface plasmons and surface-plasmon polaritons. *Rep Prog Phys* 70(1):1
- Poon GM (2010) Explicit formulation of titration models for isothermal titration calorimetry. *Anal Biochem* 400(2):229–236
- Raj P, Johnsson M, Levine MJ et al (1992) Salivary statherin. dependence on sequence, charge, hydrogen bonding potency, and helical conformation for adsorption to hydroxyapatite and inhibition of mineralization. *J Biol Chem* 267(9):5968–5976
- Rautaray D, Mandal S, Sastry M (2005) Synthesis of hydroxyapatite crystals using amino acid-capped gold nanoparticles as a scaffold. *Langmuir* 21(11):5185–5191
- Rezwan K, Studart A, Vörös J et al (2005) Change of  $\zeta$  potential of biocompatible colloidal oxide particles upon adsorption of bovine serum albumin and lysozyme. *J Phys Chem B* 109(30):14469–14474
- Rioux R, Song H, Grass M et al (2006) Monodisperse platinum nanoparticles of well-defined shape: synthesis, characterization, catalytic properties and future prospects. *Top Catal* 39(3):167–174
- Ruan L, Ramezani-Dakhel H, Chiu C et al (2013) Tailoring molecular specificity toward a crystal facet: a lesson from biorecognition toward Pt {111}. *Nano Lett* 13(2):840–846
- Sabia R, Ukrainczyk L (2000) Surface chemistry of SiO<sub>2</sub> and TiO<sub>2</sub>-SiO<sub>2</sub> glasses as determined by titration of soot particles. *J Non-Cryst Solids* 277(1):1–9
- Sanford K, Kumar M (2005) New proteins in a materials world. *Curr Opin Biotechnol* 16(4):416–421
- Sarikaya M, Tamerler C, Jen AKY et al (2003) Molecular biomimetics: nanotechnology through biology. *Nat Mater* 2(9):577–585
- Schmidtchen, F.P. (2012) Isothermal titration calorimetry in supramolecular chemistry. *Supramolecular Chemistry: From Molecules to Nanomaterials*, 67-103
- Sigurskjold BW (2000) Exact analysis of competition ligand binding by displacement isothermal titration calorimetry. *Anal Biochem* 277(2):260–266
- Silin VV, Weetall H, Vanderah DJ (1997) SPR studies of the nonspecific adsorption kinetics of human IgG and BSA on gold surfaces modified by self-assembled monolayers (SAMs). *J Colloid Interface Sci* 185(1):94–103

- Snyder JA, Abramyan T, Yancey JA et al (2012) Development of a tuned interfacial force field parameter set for the simulation of protein adsorption to silica glass. *Biointerphases* 7(1–4):51–12 (article 56)
- Song H, Kim F, Connor S et al (2005) Pt nanocrystals: shape control and Langmuir-Blodgett monolayer formation. *J Phys Chem B* 109(1):188–193
- Stenberg E, Persson B, Roos H et al (1991) Quantitative determination of surface concentration of protein with surface plasmon resonance using radiolabeled proteins. *J Colloid Interface Sci* 143(2):513–526
- Tamerler C, Oren EE, Duman M et al (2006) Adsorption kinetics of an engineered gold binding Peptide by surface plasmon resonance spectroscopy and a quartz crystal microbalance. *Langmuir* 22(18):7712–7718
- Taylor AD, Ladd J, Homola J et al (2008) Surface plasmon resonance (SPR) sensors for the detection of bacterial pathogens. In: Zourob M, Elwary S, Turner A (eds) *Principles of bacterial detection: biosensors, recognition receptors and microsystems*, Springer, New York, pp 83–108
- Thomson JA, Ladbury JE (2004) Isothermal titration calorimetry: a tutorial. *Biocalorimetry* 2:37–58
- Thyparambil AA, Wei Y, Latour RA (2012) Determination of peptide-surface adsorption free energy for material surfaces not conducive to SPR or QCM using AFM. *Langmuir* 28(13):5687–5694
- Togashi T, Yokoo N, Umetsu M et al (2011) Material-binding peptide application—ZnO crystal structure control by means of a ZnO-binding peptide. *J Biosci Bioeng* 111(2):140–145
- Tomczak M, Gupta MK, Drummy LF et al (2009) Morphological control and assembly of zinc oxide using a biotemplate. *Acta Biomater* 5(3):876–882
- Velazquez-Campoy A, Kiso Y, Freire E (2001) The binding energetics of first- and second-generation HIV-1 protease inhibitors: implications for drug design. *Arch Biochem Biophys* 390(2):169–175
- Vellore NA, Yancey JA, Collier G et al (2010) Assessment of the transferability of a protein force field for the simulation of peptide-surface interactions. *Langmuir* 26:7396–7404
- Vernekar VN, Latour RA (2005) Adsorption thermodynamics of a mid-chain peptide residue on functionalized SAM surfaces using SPR. *Mater Res Innov* 9:337–353
- Wei Y, Latour RA (2008) Determination of the adsorption free energy for peptide-surface interactions by SPR spectroscopy. *Langmuir* 24(13):6721–6729
- Wei Y, Latour RA (2009) Benchmark experimental data set and assessment of adsorption free energy for peptide-surface interactions. *Langmuir* 25(10):5637–5646
- Wei Y, Latour RA (2010) Correlation between desorption force measured by atomic force microscopy and adsorption free energy measured by surface plasmon resonance spectroscopy for peptide-surface interactions. *Langmuir* 26(24):18852–18861
- Wei Y, Thyparambil AA, Latour RA (2012) Peptide–surface adsorption free energy comparing solution conditions ranging from low to medium salt concentrations. *ChemPhysChem* 13(17):3782–3785
- Whyburn GP, Li YJ, Huang Y (2008) Protein and protein assembly based material structures. *J Mater Chem* 18(32):3755–3762
- Wikiel K, Burke EM, Perich JW et al (1994) Hydroxyapatite mineralization and demineralization in the presence of synthetic phosphorylated pentapeptides. *Arch Oral Biol* 39(8):715–721
- Willemsen OH, Snel MM, Cambi A et al (2000) Biomolecular interactions measured by atomic force microscopy. *Biophys J* 79(6):3267–3281
- Wiseman T, Williston S, Brandts JF et al (1989) Rapid measurement of binding constants and heats of binding using a new titration calorimeter. *Anal Biochem* 179(1):131–137
- Wisniewski N, Moussy F, Reichert WM (2000) Characterization of implantable biosensor membrane biofouling. *Fresenius' J Anal Chem* 366(6):611
- Wu H, Zhang CH, Liang YP et al (2013) Catechol modification and covalent immobilization of catalase on titania submicrospheres. *J Mol Catal B-Enzym* 92:44–50

- You CC, Agasti SS, Rotello VM (2008) Isomeric control of protein recognition with amino acid- and dipeptide-functionalized gold nanoparticles. *Chem Eur J* 14(1):143–150
- You C, De M, Han G, Rotello VM (2005a) Tunable inhibition and denaturation of  $\alpha$ -chymotrypsin with amino acid-functionalized gold nanoparticles. *J Am Chem Soc* 127(37):12873–12881
- You C, De M, Rotello VM (2005b) Contrasting effects of exterior and interior hydrophobicities in the complexation of amino acid functionalized gold clusters with  $\alpha$ -chymotrypsin. *Org Lett* 7(25):5685–5688
- Zhang Z, Menges B, Timmons RB et al (2003) Surface plasmon resonance studies of protein binding on plasma polymerized di(ethylene glycol) monovinyl ether films. *Langmuir* 19(11):4765–4770

# Chapter 4

## Interfacial Structure Determination

Peter A. Mirau

**Abstract** The understanding of biomolecule structure at the nanoparticle interface is critical for the design of sensors containing nanoparticles and biological recognition elements. While many inorganic binding peptides have been identified from phage display and other experiments, the relationship between the peptide sequence, structure, and functional properties at the interface have not been identified. The structure of biomolecules at the interface can be determined with the tools (Circular Dichroism (CD), Fourier transform infra-red (FTIR), and nuclear magnetic resonance (NMR)) traditionally used for protein structure determination.

### 4.1 Introduction

Nanomaterials are of great interest for their unique, size-dependent electrical, magnetic, and mechanical properties that can be exploited as the active component in sensors and other devices. One of the most fundamental challenges limiting the use of nanomaterials in devices is creating active surfaces that respond to external stimuli, such as the binding of a target molecule. Peptides and proteins have great potential to for surface modification because they are well known to recognize chemicals and other biomolecules with great specificity and sensitivity. The grand challenge in peptide interfaces is to understand the relationship between the peptide primary sequence and its ability to bind and function at the nanostructured surface. This goal can be realized in part by solving the structure of peptides at the interface. The methods for peptide structure determination, including Fourier transform infra-red (FTIR), Circular Dichroism (CD) and nuclear magnetic resonance (NMR) spectroscopy, have the potential to greatly improve our understanding of structure-

---

P. A. Mirau (✉)

Soft Matter Materials Branch (AFRL/RXAS), Air Force Research Laboratories,  
Wright-Patterson AFB, 2941 Hobson Way, Bldg 654, Dayton, OH 45433, USA  
e-mail: Peter.Mirau@wpafb.af.mil

function relationships by providing structural information about the bound peptides. This field is currently in its infancy, but I believe it will grow to become a critical part of our ability to design the next generation of biomolecules at the nanomaterials interface.

It is well known in biology that proteins recognize and react with small molecules, other proteins and nucleic acids. The discovery of peptide sequences that interact with inorganic materials was initially recognized in organisms that synthesize proteins to interact with inorganic surfaces, including gold (Brown 1997) and silica (Kroger et al. 1999). More recently combinatorial phage-display methods have been used to identify peptide sequences that bind metals (Naik et al. 2002b), metal-oxides (Sano and Shiba 2003), semiconductors (Whaley et al. 2000), carbon-based nanomaterials (Wang et al. 2003), and synthetic polymers (Adey et al. 1995).

One means to understand structure-function relationships at the biotic-abiotic interface is to determine the structure of the bound biomolecules. FTIR, CD, and NMR have been extensively used for structure determination in proteins, and we can use these studies to develop tools for structure determination at the interface. It has long been recognized that elements of secondary structure in proteins ( $\alpha$ -helix,  $\beta$ -sheet,  $3_{10}$ -helix, and  $\beta$ -turns, etc.) have specific signatures in the FTIR (Surewicz et al. 1993), CD (Greenfield 2006) and NMR spectra (Wuthrich 1986). NMR has the potential to provide more precise structural detail because the chemical shifts and relaxation rates depend on the three dimensional structure and the distances between pairs of NMR-active nuclei (Cavalli et al. 2007; Wuthrich 1986).

## 4.2 Optical Characterization at the Nanomaterials Interface

Optical spectroscopy, including CD and FTIR spectroscopy, can provide important structural information about proteins and peptides at the inorganic interface. The optical signals often overlap but can provide information about the average structure of the entire biomolecule, rather than the conformation of individual residues. Both the CD and FTIR spectra can be used to identify and quantitate elements of secondary structure in peptides and proteins.

### 4.2.1 FTIR of the Nanomaterials Interface

The vibrational spectra of peptides and proteins are sensitive to local structure and can be used to study the structure of bound peptides. Like other optical methods, the signal has contributions from all residues, and cannot be used to determine the

**Table 4.1** The amide-I absorption bands for elements of secondary structure in peptides and proteins

Structure	Absorption ( $\text{cm}^{-1}$ )
$\alpha$ -helix	1656
$3_{10}$ helix	1660
$\beta$ -sheet	1633/1648
$\beta$ -turn	1672
Disordered	1647–1654

structure of individual amino acids. FTIR is particularly useful for identifying elements of secondary structure in peptides and proteins because the signals from the carbonyls can be usually resolved.

Amino acids give rise to a number of peaks in the vibrational spectra, but the most useful band for structure determination is the so-called amide-I band, which is assigned primarily to stretching vibrations of the carbonyl group and appears in the range of 1640–1680  $\text{cm}^{-1}$ . Hydrogen bonding is an important force stabilizing protein structure, and the hydrogen bonding strength and geometry can affect the intensity, frequency, and width of the amide-I band (Jackson and Mantsch 1995; Surewicz et al. 1993). Table 4.1 lists the FTIR frequencies for the amide-I band in secondary structures. The exact peak position varies with the length of the feature, solvent exposure and distance from the surface in nanoparticles (NPs). Note that  $\beta$ -sheets can be identified by two peaks in the amide-I region. Unfortunately the differences in frequency for the amide-I bands are typically less than the line widths, so the peaks overlap in most peptides and proteins. Secondary structural elements are often quantitated using curve fitting routines that are common on FTIR spectrometers. The amide-A band near 3300  $\text{cm}^{-1}$  from NH vibrations is also sensitive to the secondary structure.

The effect of covalent binding on the conformation of peptides has been studied for leucine-rich peptides (Ac-KTAL<sub>10</sub>NPC-NH<sub>2</sub>) linked by cystine residues to 5, 10 and 20 nm sized Au NPs (Mandal and Kraatz 2007). Figure 4.1 shows the amide-I and amide A bands for the peptide free and bound to 5, 10, and 20 nm Au NP and a flat Au surface. The pink bars show the frequencies for the two  $\beta$ -sheet peaks while the blue bars show the frequencies for the  $\alpha$ -helix. Two bars are shown from the  $\alpha$ -helix in the amide-I region because the frequency for the  $\alpha$ -helix (1659  $\text{cm}^{-1}$ ) is shifted by 15  $\text{cm}^{-1}$  on the Au surface due to the so-called optical effect (Miura et al. 1999) arising from the orientation of the carbonyl dipole relative to the Au surface. The free peptide shows a peak at 1659  $\text{cm}^{-1}$  that is consistent with an  $\alpha$ -helix formation. The peptides predominantly show a  $\beta$ -sheet structure when bound to the 5 nm Au NPs and a mixture of  $\alpha$ -helix and  $\beta$ -sheet when bound to the 10 nm NP, while the spectra for the 20 nm particle and the flat Au surface are consistent with the  $\alpha$ -helical conformation. These data demonstrate that FTIR can be effectively used to study peptide conformation at the surface, and that NP curvature and surface crowding can influence peptide conformation. NP size (and curvature) also affects the conformation of  $\beta$ -sheet forming peptides on Au NPs (Shaw et al. 2012). These studies also show that the NP properties can influence the amide-I frequencies as they do in flat Au surfaces.



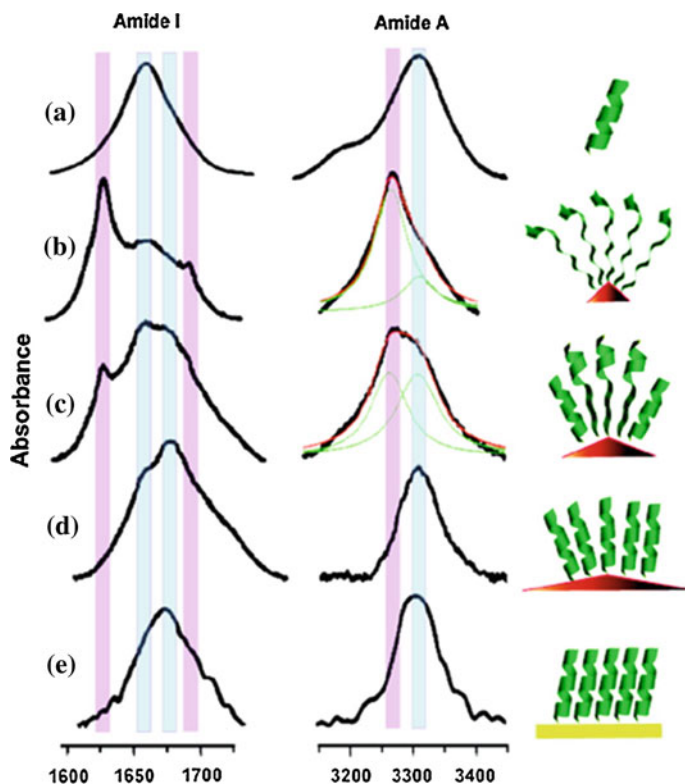


**Fig. 4.1** The FTIR spectra of the Leu<sub>10</sub> peptide **a** free and bound to **b** 5 nm **c** 10 nm **d** 20 nm Au NP and **e** flat Au surfaces. Reproduced from Mandal and Kraatz 2007

FTIR has also been used to probe the conformation of graphene-binding peptides both in solution and at the graphene surface (Katoch et al. 2012), and Fig. 4.2 compares the FTIR spectra of the peptide in solution with the peptide adsorbed on the graphene surface. The solution spectra are obtained in D<sub>2</sub>O to eliminate overlap of the amide-I band with the water signal, and is fit to two peaks at 1673 and 1648 cm<sup>-1</sup> that are assigned to trifluoroacetate ions and the peptide carbonyl. The peak at 1648 cm<sup>-1</sup> is consistent with some  $\alpha$ -helical content and is similar to the peak observed in solid powders. Since disordered peptides show an amide I band near 1640 cm<sup>-1</sup>, the peak at 1670 cm<sup>-1</sup> on the graphene surface is indicative of structure formation, although the structure cannot be definitively identified from the FTIR spectra.

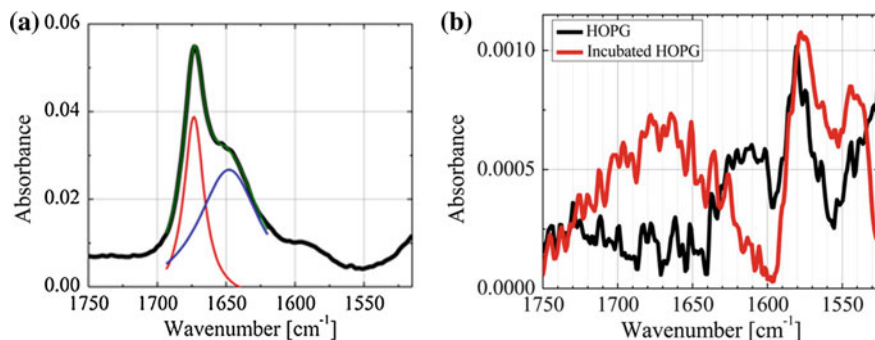


**Fig. 4.2** The FTIR spectra of the graphene binding peptide in **a**  $D_2O$  solution and **b** adsorbed on the graphene surface. The background spectrum for the graphene surface is shown in *black* in (b). Reproduced from Katoch et al. 2012

### 4.2.2 Circular Dichroism of the Nanomaterials Interface

Circular dichroism (CD) spectroscopy measures the relative absorption of right-handed versus left-handed circularly polarized light by peptides and proteins. CD is useful for structure determination because elements of secondary structure can be identified by the sign and frequency of the signal. The absorption occurs in the Far-UV region (190–230 nm) for the amide bonds and in the Near-UV region (250–350 nm) for the aromatic residues (Phe: 250–270 nm; Try: 270–290 nm; and Trp: 280–300 nm). The ratio of absorption by right-handed versus left-handed light is typically very small ( $10^{-4}$  to  $10^{-6}$ ), but is well within the range that can be measured experimentally.

The use of CD spectroscopy for measuring protein structure can be illustrated by comparing the spectra expected for structural elements with the spectra from proteins as shown in Fig. 4.3 (Greenfield 2006). The  $\alpha$ -helix can be identified by a double negative band with minima at 208 and 222 nm and a maximum at 208, while a random coil shows only a strong negative peak near 197 nm. The poly-proline II (PPII) conformation (not shown) shows a maximum at 222 nm and a minimum at 205 nm. Proteins typically contain several types of structures and the relative percentages are obtained by fitting the spectra (Surewicz et al. 1993), Fig. 4.3b shows that proteins with a large fraction of  $\rightarrow$ -helix, such as Myoglobin, can be easily identified from the CD spectra.

The CD spectra can be used to identify the structure of bound peptides at the abiotic interface as well as the structure of peptides in the absence of target to determine whether the peptide has a preferred conformation in solution that facilitates surface recognition. Figure 4.4 shows the CD spectra for a series of Au binding peptides identified by phase display (Hnilova et al. 2008). To study the sequence-structure relationship the authors compared the structure and binding of linear and constrained (cyclic) versions of a series of peptides (c-AuBP1: CGPWAGAKRLVLRREGPC; l-AuBP1: WAGAKRLVLRRE; c-AuBP2: CGPWALRRSIRRQSYGPC and

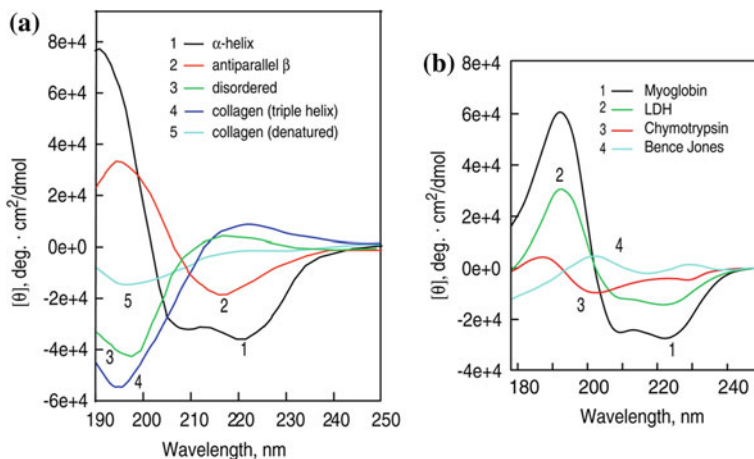


**Fig. 4.3** The CD spectra for **a** well-defined secondary structural elements in polypeptides and **b** proteins containing a mixture of secondary structural elements. Reproduced from Greenfield 2006

1-AuBP2: WALRRSIRRQSY) related to those discovered by phage display. The CD spectra differ significantly from the random coil conformation, particularly the 1-AuBP2, which shows a maximum at 222 nm. The authors conclude from a deconvolution analysis that the peptides are mixture of random coil and PPII conformations. The constraint of forming a cyclic peptide apparently does not allow the c-AuBP2 to adopt the PPII conformation. The PPII conformation has also been identified in the CD spectra for strong quartz-binding peptides (S1: PPPWLPYMPPWS; S2: LPDWPPPQLYH) but a random coil conformation was identified from the CD spectra of a weakly binding peptide (W1: EVRKEVVAVARN) (Oren et al. 2010).

CD spectroscopy has been used to measure the conformation of the Pd4 peptide (Pd4: TSNVHPTLRHL) bound to the surface of 2 nm sized Pd NP (Coppage et al. 2012). Figure 4.5 shows that the CD spectra of both the free and bound peptide are similar to those expected for a random coil conformation, although the magnitude of the peak at 200 nm is reduced for peptides prepared with a high ratio of Peptide:Pd<sup>2+</sup>. Fitting the spectra to identify elements of secondary structure shows that the bound peptide is predominantly disordered (45 %) with a low content of helical structures (6 %).

CD spectroscopy has also been used to compare the binding of noncovalent (Flg-A3: DYKDDDDKPAYSSGAPPMPF) and covalently attached (E5: CGGEVSALEKEVSALEKEVSALEKEVSALEKE VSALEK) helix-forming peptide to Au NPs (Slocik et al. 2011). These two peptides were chosen because FlgA3 is expected to lie flat on the Au surface while E5 is an end-linked structure expected to extend away from the Au surface. Figure 4.6 shows the CD spectra for E5 free and bound to 10 nm Au NPs. The spectrum for free E5 shows negative peaks at 208 and 222 nm, indicating the formation of an  $\alpha$ -helical structure. These

**Fig. 4.4** The CD spectra for Au-binding peptides in solution. Reproduced from (Hnilova et al. 2008)

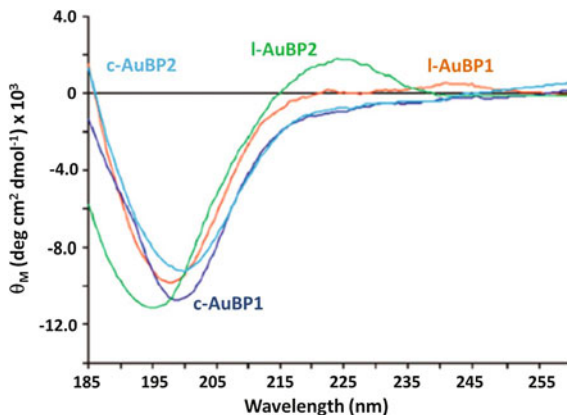


**Fig. 4.5** The CD spectra of free and bound Pd4 with Pd NPs prepared at different ratios of peptide: $\text{Pd}^{2+}$ . Reproduced from (Coppage et al. 2012)

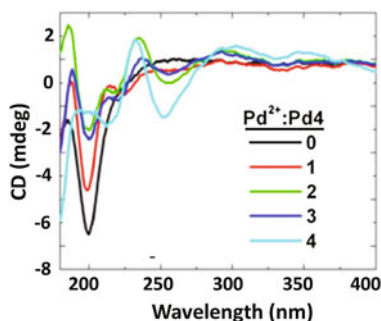
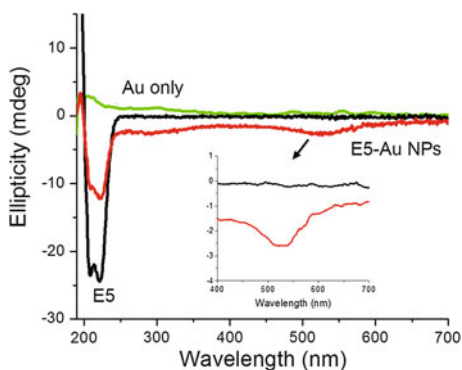


**Fig. 4.6** The CD spectra of free and bound E5 and Au NPs. The inset plot shows an expansion of the plasmonic band. Reproduced from (Slocik et al. 2011)



peaks are reduced in the Au-bound peptide and a new peak appears at 520 nm. The as-prepared 10 nm Au NPs show a plasmonic absorption at 520 nm, but no peaks in the CD spectra. The plasmonic band that appears in the CD spectrum for the E5-Au NP must therefore arise from coupling of the plasmonic band to the peptide

dipoles. The Flg-A3 peptide shows a random coil-like CD spectrum free in solution with a large negative peak near 200 nm. In comparison, the FlgA3-Au NP shows a smaller peak near 200 nm that is slightly shifted relative to the free peptide and a plasmonic peak near 520 nm. These experiments show that both covalent and noncovalent interactions of peptides with the Au NPs leads to optical coupling between the peptide and the inorganic NP. The plasmonic band also shifts in response to the addition of metal ions ( $\text{Ag}^+$  and  $\text{Pd}^{4+}$ ) that interact with the Flg (DYKDDDDK) sequence bound to the NP through the A3 (AYS-SGAPMPPF) Au binding sequence.

### 4.3 NMR Structure Determination at the Nanomaterials Interface

NMR is a powerful tool for structure determination because the NMR spectra and couplings can be directly related to the three dimensional structure. The parameters of most interest are the chemical shifts, the J coupling constants, relaxation rates, and peak intensities measured by multidimensional NMR. This information can be converted into a distance and angle constraints and input into a structure determination program to identify structures that are compatible with the experimental data (Schwieters et al. 2006).

The  $^1\text{H}$ ,  $^{13}\text{C}$  and  $^{15}\text{N}$  chemical shifts are sensitive to the primary sequence, as well as secondary and tertiary structure. The NH, H $\alpha$ , H $\beta$ , CO, C $\alpha$ , C $\beta$ , and amide nitrogen chemical shifts can be measured and compared with the random coil values (Wishart et al. 1995) to identify structured sections in peptides and proteins (Wishart and Sykes 1994). These can be further refined to identify elements of secondary structure (Wishart and Sykes 1994) and even the global conformations of proteins (Cavalli et al. 2007). Since the signals for peptides and proteins overlap, they are typically measured in 2D and 3D NMR experiments correlating chemical shifts from different nuclei (Cavanagh et al. 2007; Croasmun and Carlson 1994).

The through-bond scalar (J) coupling constants are important for structure determination because they can be directly related to the protein dihedral angles. The 3-bond coupling between the amide NH proton and the H $\alpha$  protons ( $^3J_{\text{HNH}\alpha}$ ) is correlated with the dihedral angle  $\phi$  between the amide and C $\alpha$  carbon the coupling between H $\alpha$  and H $\beta$  ( $^3J_{\text{H}\alpha\text{H}\beta}$ ) is related to the torsion angle  $\chi_1$  between the C $\alpha$  and C $\beta$  carbons (Cavanagh et al. 2007; Wuthrich 1986). These coupling constants are measured and converted to dihedral angle constraints for protein structure determination. The J coupling constants are also important for determining the residual dipolar couplings resulting from partial orientation of protein samples in low concentrations of liquid crystalline formers added to the NMR sample (Tjandra et al. 2000).

The most useful information for structure determination is contained in the dipolar couplings that are related to the distances between atoms. In solutions, we typically measure the nuclear Overhauser effects (NOEs) which depend on the inverse sixth power of the separation between NMR-active nuclei. The general strategy is to measure a large number of distances and find the family of structures consistent with the distance information. If the structures are very similar to each other, then the structure is considered well defined.

Solid-state NMR (ssNMR) most frequently uses  $^{13}\text{C}$  and  $^{15}\text{N}$  experiments to study peptide and protein structure. The ssNMR spectra can be obtained with unlabeled samples, but large amounts of sample (0.1 g) and long signal averaging times are required because of the low natural abundances of the  $^{13}\text{C}$  (1.08 %) and  $^{15}\text{N}$  (0.37 %) NMR-active isotopes. The proton lines in solids are broad because of strong (50 kHz) dipolar couplings, but recent advances in very fast (65 kHz) magic-angle spinning probes have made it feasible to use  $^1\text{H}$  NMR as a probe of protein structure in solids (Mafra et al. 2009).

The structural information from solid-state NMR (ssNMR) comes primarily from the chemical shifts and dipolar couplings that arise from the interactions between two or more NMR-active nuclei. Since the probability of having two  $^{13}\text{C}$  or  $^{15}\text{N}$  nuclei in close proximity is low because of the low natural abundances, isotopic labeling is required for most structural studies. Isotopic labeling greatly increases the sensitivity and enables a wide variety of two- and three dimensional NMR experiments for measuring dipolar couplings and determining the structure. (Andronesi et al. 2006; Renault et al. 2010).

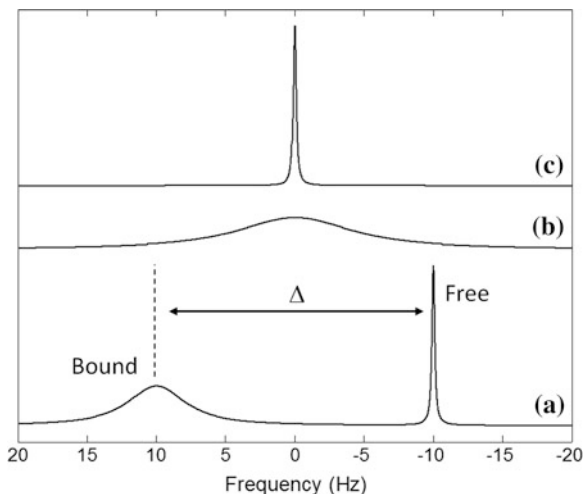
Spectral resolution is a key factor in determining the NMR methods suitable for the structure determination of peptides and proteins at the nanomaterials interface. Solution methods are easiest to use, but may not be applicable to all situations. One challenge for solution NMR is that the line widths depend on the rotational correlation time  $\tau_c$  for a molecule or nanoparticle complex which is given by

$$\tau_c = \frac{4\pi\eta r^3}{3kT}$$

where  $\eta$  is the viscosity,  $k$  is Boltzmann's constant,  $T$  is the temperature and  $r$  is the hydrodynamic radius. Note that  $\tau_c$  depends on the third power of the hydrodynamic radius, so larger particles have large line widths and poor resolution. It has been observed many times that the lines for proteins are much broader than for small molecules, but still within the range of solution NMR methods. Hen egg white lysozyme, for example, has a molecular weight of 14,307 g/mol and a hydrodynamic radius of 1.9 nm (Parmar and Muschol 2009), resulting in line widths on the order of 5–10 Hz. While lysozyme gives a well-resolved NMR spectrum, the line widths for a peptide bound to a 20 nm NP may be too large to observe by high-resolution solution NMR.

The spectral appearance (chemical shifts and line widths) of a peptide in the presence of NPs depends both on the size of the NP and the ligand binding kinetics. Figure 4.7 shows the schematic NMR spectra for a proton on a peptide

**Fig. 4.7** A diagram showing the NMR spectra for bound and free signals in the **a** slow **b** intermediate and **c** fast exchange limit



binding to a nanoparticle in the slow, intermediate and fast exchange limits. The peak positions and line widths depend on the difference in chemical shift between the free and bound state ( $\Delta$ ), the exchange rate ( $k_{ex}$ ), the free and bound line widths and the populations of free and bound peptide (Cavanagh et al. 2007). The exchange limits are defined by the relative ratio of the chemical shift separation to the exchange rate. The slow exchange limit is defined by a rate of exchange much less than the chemical shift separation ( $k_{ex} \ll \Delta$ ). In this case separate peaks are observed for the free and bound peptide, the line widths are much larger for the bound peptide and the peak intensities are proportional to the populations of free and bound peptide. The lines are greatly broadened in the intermediate exchange limit ( $k_{ex} \approx \Delta$ ) and are typically difficult to observe by high-resolution NMR. Sharp lines are observed in the fast exchange limit ( $k_{ex} \gg \Delta$ ) and the peak position is intermediate between the free and the bound chemical shift. The fast exchange limit is ideal for determining the structure of bound peptides because sharp lines are observed but the relaxation rates measured by 2D NMR are influenced by the conformation of the bound peptide.

### 4.3.1 Solid State NMR

In the last several years solid-state NMR (ssNMR) has emerged as an important tool for NMR structure determination in peptides and proteins (Andronesi et al. 2006; Tycko 2001) and has great potential for the study of biomolecules at inorganic surfaces. The lines are broader in solids but they can be narrowed with a combination of magic-angle sample spinning and proton decoupling (Schmidt-Rohr and Speiss 1994). The line widths in solids no longer depend on the

**Table 4.2** The carbon chemical shifts for poly-L-lysine in the  $\alpha$ -helical,  $\beta$ -sheet, and random coil conformations

Conformation	CO (ppm)	C $\alpha$ (ppm)
Random Coil	174.7	54.4
$\alpha$ -helix	176.1	57.4
$\beta$ -sheet	171.5	52.3

hydrodynamic radius, so ssNMR can be used to study the structure of peptides and proteins bound to larger nanomaterials that would likely have broad lines in the solution NMR spectra. One disadvantage of SSNMR is that isotopic labeling is typically required. It is possible to uniformly label biomolecules with  $^{15}\text{N}$  and  $^{13}\text{C}$ , but in many cases it is advantageous to site specifically label particular amino acids.

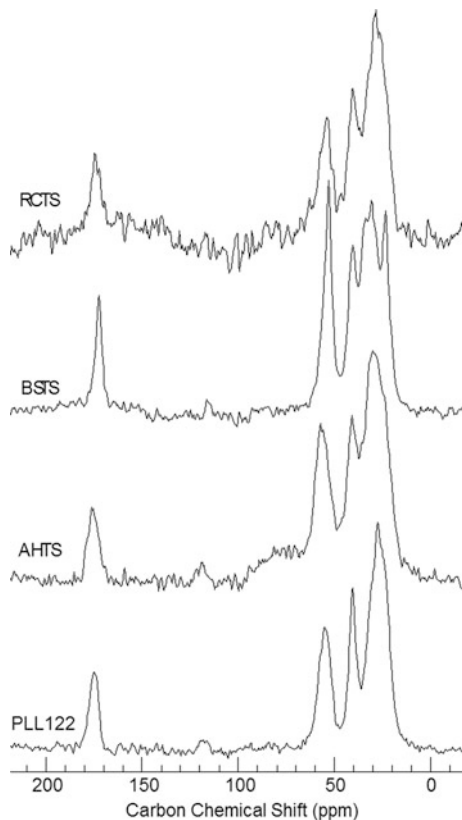
Among the earliest studies of biomaterials by ssNMR were the studies of polypeptides bound to silica and hydroxyapatite surfaces (Fernandez et al. 1992). These studies are possible without isotopic labeling because the signals arise from a single type of amino acid, and the chemical shifts for the C $\alpha$  and CO are particularly sensitive to the secondary structure. This is illustrated in Table 4.2 which compares the carbon chemical shifts for poly-L-lysine in the  $\alpha$ -helix,  $\beta$ -sheet, and random coil conformations (Mirau et al. 2008). While the resolution in SSNMR is not as high as for solutions, it is frequently possible to obtain line widths than 1 ppm. Table 4.2 shows that the change in chemical shift between the  $\alpha$ -helix and  $\beta$ -sheet conformation is 4.6 ppm for the CO and 5.1 ppm for the C $\alpha$  carbons, and that both conformations can be distinguished from the random coil. The differences in chemical shifts for the side chain carbons are not large enough to distinguish between elements of secondary structure.

Polyamino acids, including poly-L-lysine, and poly-L-glutamic acid, are well known to adopt a variety of conformations in solutions and solids that depend on the polymer chain length, ionic strength, pH, and relative humidity (Greenfield and Fasman 1969; Swanson and Bryand 1991). High molecular weight poly-L-lysine and poly-L-glutamic acid can adopt  $\alpha$ -helical conformations in the solid state, and these conformations have been confirmed from an analysis of the carbon chemical shifts (Fernandez et al. 1992). When these ionic polypeptides in solution are mixed with aqueous suspensions of silica or hydroxyapatite (HAP) they adsorb to the surface and can be separated from free polymer in solution by centrifugation. ssNMR studies show that while poly-L-lysine and poly-L-glutamic acid adopt an  $\alpha$ -helical conformation in the bulk solid, the polymers adopt a more extended conformation at the surface of silica and HAP (Fernandez et al. 1992).

The peptides identified as inorganic binders by phage display and other methods are frequently able to template the formation of inorganic nanoparticles (Dickerson et al. 2008), including silica (Kroger et al. 1999; Naik et al. 2002a), titania (Sano et al. 2005), gold (Slocik et al. 2005), and silver (Naik et al. 2002b). For silica and titania the templating peptides are incorporated into the growing nanostructures and are amenable to study by ssNMR.

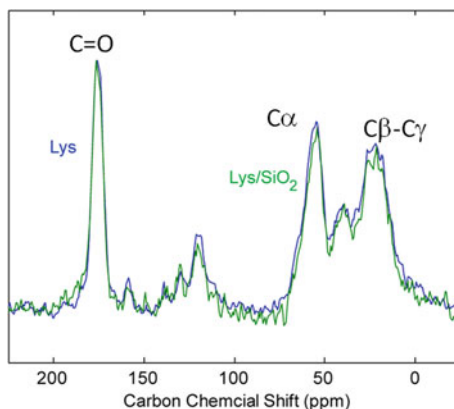


**Fig. 4.8** The 125 MHz carbon NMR spectra of poly-L-lysine in the bulk (PLL122) and in  $\alpha$ -helical-templated silica (AHTS),  $\beta$ -sheet-templated silica (BSTS) and random-coil-templated silica. Spectra were obtained with cross polarization and magic-angle sample spinning. Reproduced from Mirau et al. 2008



The conformation of peptides and proteins encapsulated in metal-oxide NPs can be determined from the carbon chemical shifts measured by ssNMR. Figure 4.8 compares the solid state carbon spectra for silica-encapsulated poly-L-lysine templated from the  $\alpha$ -helical,  $\beta$ -sheet, and random coil solution conformations (Mirau et al. 2008). The CO and C $\alpha$  chemical shifts for bulk poly-L-lysine are consistent with a random coil conformation. The close agreement between the expected and observed chemical shifts for the  $\alpha$ -helical and  $\beta$ -sheet-templated nanostructures show that the solution conformation of poly-L-lysine is retained upon encapsulation. A closer inspection of the CO peak for random coil-templated silica shows a mixture of random coil and  $\alpha$ -helix encapsulated in silica, demonstrating that the conformation of poly-L-lysine is changing during encapsulation. An additional advantage of ssNMR is that the relaxation times and proton line widths can be used to measure the molecular dynamics of the encapsulated peptide. The results show that the peptide backbone for the  $\alpha$ -helical poly-L-lysine is restricted relative to bulk poly-L-lysine, but the peptide side chain atoms are more dynamic.

**Fig. 4.9** The 125 MHz solid-state carbon NMR spectra of (*black*) crystalline lysozyme and (*blue*) silica-encapsulated lysozyme

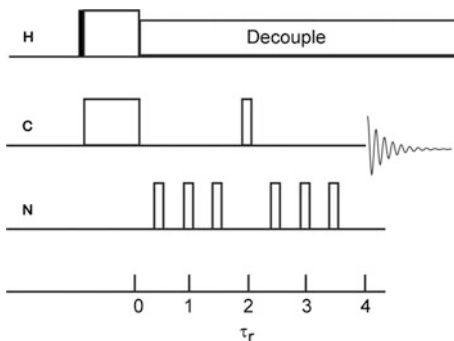


In addition to naturally occurring (Kroger et al. 1999) and genetically engineered peptides (Naik et al. 2002a), it has been reported that some enzymes are able to template silica and titania nanostructures (Luckarift et al. 2004). These nanostructured materials are porous, contain up to 20 wt % enzyme and show 90 % of the enzyme activity observed for the enzymes in solution. Figure 4.9 compares the carbon NMR spectra of crystalline lysozyme with the silica encapsulated enzyme. Lysozyme contains 128 amino acids so there is extensive overlap for the CO, C $\alpha$  carbons, and side chain carbons. However, because protein folding leads to large changes in chemical shifts (Cavalli et al. 2007), it is possible to identify the folded enzyme from the carbon spectra. The nearly identical spectra for the crystalline and silica-encapsulated enzymes show that the structure of lysozyme is retained in the silica-encapsulated nanostructure.

While it is possible to study the structure of some absorbed and encapsulated peptides and proteins by ssNMR, much more details can be obtained from experiments where the biomolecules are site-specifically or uniformly labeled with  $^{13}\text{C}$  and/or  $^{15}\text{N}$ . The power of site-specific labeling for NMR structure determination is illustrated in the results reported for the statherin, a 43 amino acid peptide (DpSpSEEKFLRRIGRFGYGYGPYQPVEQPLYPQPYQPQYQYTF) that controls crystallite size in dental materials by binding to the surface of the growing HAP crystals. CD and solution NMR studies show that statherin is disordered in solution, but shows a combination of  $\alpha$ -helix and polyproline II structures in 50 % trifluoroethanol/water mixtures (Elgavish et al. 1984; Naganagowda et al. 1998).

Dipolar couplings are important constraints for NMR structure determination because they are inversely related to the third power of the internuclear distances. The dipolar couplings are difficult to measure in peptides at natural abundance because the probability of having two  $^{13}\text{C}$  atoms or a  $^{13}\text{C}$  and  $^{15}\text{N}$  in close proximity is very low because of the low natural abundance ( $P(^{13}\text{C}-^{13}\text{C}) = 0.0108 \times 0.0108 = 1.1 \times 10^{-4}$ ;  $P(^{13}\text{C}-^{15}\text{N}) = 0.0108 \times 0.0037 = 3.9 \times 10^{-5}$ ). The structures can be determined by incorporating  $^{15}\text{N}$  or  $^{13}\text{C}$  isotopes at specific sites. In an  $\alpha$ -helix, for example, the distance between a carbonyl carbon at position  $i$  and a nitrogen atom at position  $i + 4$

**Fig. 4.10** The REDOR pulse sequence. Pulses on the  $^{15}\text{N}$  channel are applied in the middle of the rotor period



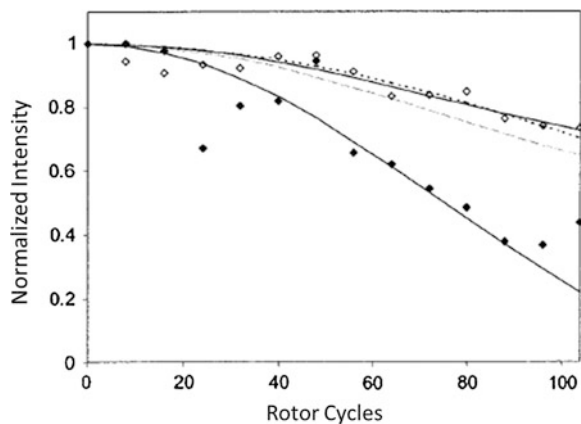
is 4.2 Å, while the distances in the  $3_{10}$ -helix and  $\beta$ -sheet are 5.2 Å and 10.6 Å (Long et al. 2001). In a similar way, the distances between labeled carbonyl carbons at positions  $i$  and  $i + 1$  are related to the torsion angle  $\phi$  which depends on the secondary structure. These measured distances and angles are important constraints for NMR structure determination.

The NMR spectra of isotopically labeled peptides provide information about the structure from the chemical shifts, but the dipolar couplings cannot be measured directly from the spectra. ssNMR spectra are typically acquired using cross polarization to enhance sensitivity and magic-angle sample spinning to average the chemical shift anisotropy and reduce the line width (Schmidt-Rohr and Speiss 1994). In addition to averaging out the chemical shift anisotropy, magic-angle spinning also averages the dipolar couplings, which are typically on the order of tens to hundreds of Hertz in peptides. The dipolar couplings can be observed in experiments where pulses are applied synchronously with sample spinning to reintroduce (recouple) the couplings averaged by sample spinning.

Rotational-Echo Double Resonance (REDOR) is one method used to measure intramolecular and peptide surface distances for NMR structure determination (Gullion and Schaefer 1989). The REDOR pulse sequence shown in Fig. 4.10 is used to measure the distances between carbon and nitrogen atoms. The  $180^\circ$   $^{15}\text{N}$  pulse applied in the middle of the rotor cycle reintroduces the  $^{13}\text{C}$ - $^{15}\text{N}$  dipolar coupling averaged by magic-angle sample spinning while the  $180^\circ$   $^{13}\text{C}$  pulses refocus the carbon magnetization after the second rotor cycle. The experiment is performed by taking the ratio of signal intensity as a function of rotor cycle with and without the  $^{15}\text{N}$  pulses. The signal intensity is fitted using a program to simulate the spin dynamics as a function of the dipolar coupling (Bak et al. 2000).

Figure 4.11 shows the REDOR dephasing curve for statherin with a  $^{13}\text{C}$  label on the carbonyl carbon of  $\text{S}_3$  and an  $^{15}\text{N}$  label on the amide nitrogen of  $\text{F}_7$  for hydrated and lyophilized statherin on the surface of HAP (Long et al. 2001). The best fit for the  $^{13}\text{C}$ - $^{15}\text{N}$  distance in the hydrated sample is 4.2 Å, a distance consistent with the  $\alpha$ -helical conformation. The average distance for the lyophilized sample is 5.2 Å, which can be simulated with a combination  $\alpha$ -helix and

**Fig. 4.11** The REDOR dephasing curve for  $S_3(^{13}\text{C})$ – $F_7(^{15}\text{N})$  labeled statherin. The open symbols are for the hydrated sample and the closed symbols for the dried sample. Reproduce from Long et al. 2001



$\beta$ -sheet. In a similar way  $^{31}\text{P}$ – $^{13}\text{C}$  REDOR can be used to measure distances between sites on the peptide and the phosphorus atoms in HAP (Ndao et al. 2009, 2010).

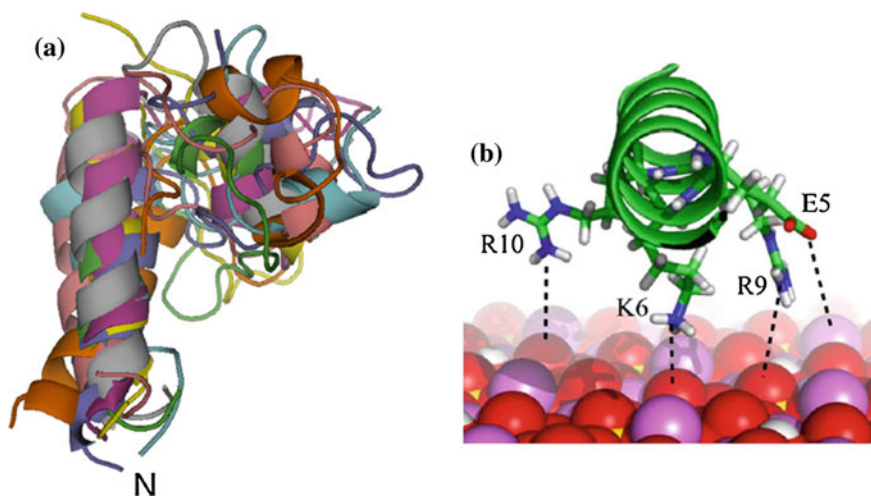
Double-quantum NMR is another important probe of peptides bound to nanomaterials. Double-quantum coherences are a property of coupled spin systems and can only be observed in isotopically labeled samples. As with REDOR, the goal of this experiment is to measure the dipolar coupling and infer the internuclear distance. This can be accomplished with pulse sequences such as Dipolar Recoupling with a Windowless Sequence (DRAWS) by again applying pulses with defined amplitudes and phases at specific points in the rotor cycle (Drobny et al. 2003). This experiment provides an important structural information because the distance between neighboring  $^{13}\text{C}$ -labeled carbonyl carbons depends on the dihedral angle ( $\phi$ ) between amide nitrogen and the  $\text{C}\alpha$  carbon which varies with secondary structure.

The strategy for NMR structure refinement is to make a large number of distance and angle measurements and calculate the family of structures consistent with the input constraints. Table 4.3 lists the distances and angles measured between isotopically labeled sites in the peptide and the HAP surface that are used to determine the structure. The distances and angle are used as input for the RosettaSurface structure determination program (Masica et al. 2010).

Figure 4.12 shows the structure of statherin and the N-terminal helix bound to the HAP surface (Masica et al. 2010). As shown in Table 4.3, a number of short (4–5 Å)  $i$  to  $i+4$  distances are measured at the N-terminal and C-terminal regions of statherin bound to HAP. These are consistent with  $\alpha$ -helix formation between residues 3–14 and residues 31–39. The structure in Fig. 4.12a shows an overlay of several structures calculated from the distance and angle constraints. The structures show an N-terminal and C-terminal  $\alpha$ -helix separated by a disordered region. The structure of statherin on the HAP surface in Fig. 4.12b is calculated from the  $^{31}\text{P}$ – $^{13}\text{C}$  REDOR experiments showing multiple contacts between HAP and the statherin side chains in the N-terminal  $\alpha$ -helix.

**Table 4.3** ssNMR distance and angle measurements for statherin on the surface of hydroxyapatite

Measurement	Label	Distance (Å) or Angle (°)	Reference
pS <sub>3</sub> $\varphi$	$^{13}\text{C}'_2$ - $^{13}\text{C}'_3$	$-60^\circ \pm 10$	Long et al. 2001
pS <sub>3</sub> -F <sub>7</sub>	$^{13}\text{C}'_7$ - $^{15}\text{N}$	$4.3 \pm 0.2 \text{ \AA}$	Long et al. 2001
K <sub>6</sub> -HAP	$^{15}\text{N}^\epsilon$ - $^{13}\text{C}$	$5.6 \pm 0.5 \text{ \AA}$	Gibson et al. 2005
F <sub>7</sub> -HAP	$^{13}\text{C}^\delta$ - $^{31}\text{P}$	$6.9 \pm 1.0 \text{ \AA}$	Gibson et al. 2005
L <sub>8</sub> $\varphi$	$^{13}\text{C}'_8$ - $^{13}\text{C}'_9$	$-60^\circ \pm 9$	Long et al. 2001
L <sub>8</sub> -G <sub>12</sub>	$^{13}\text{C}'_8$ - $^{15}\text{N}$	$4.8 \pm 0.4 \text{ \AA}$	Long et al. 2001
G <sub>12</sub> $\varphi$	$^{13}\text{C}'_{12}$ - $^{13}\text{C}'_{13}$	$-73^\circ \pm 3.6$	Long et al. 2001
P <sub>23</sub> -P <sub>33</sub>	$^{13}\text{C}'_\beta$ - $^{13}\text{C}'$	$8.8 \pm 0.8 \text{ \AA}$ or $10.5 \pm 1.0 \text{ \AA}$	Goobes et al. 2006
P <sub>23</sub> -Y <sub>34</sub>	$^{13}\text{C}'_\beta$ - $^{13}\text{C}'$	$8.8 \pm 0.8 \text{ \AA}$ or $10.5 \pm 1.0 \text{ \AA}$	Goobes et al. 2006
P <sub>33</sub> -Y <sub>34</sub>	$^{13}\text{C}'_{33}$ - $^{13}\text{C}'$	$3.12 \pm 0.13 \text{ \AA}$	Goobes et al. 2006
P <sub>33</sub> -Y <sub>38</sub>	$^{13}\text{C}'_{33}$ - $^{15}\text{N}$	$5.3 \pm 0.5 \text{ \AA}$	Goobes et al. 2006
Y <sub>34</sub> $\varphi$	$^{13}\text{C}'_{33}$ - $^{13}\text{C}'_{34}$	$-75^\circ \pm 15$	Goobes et al. 2006
Y <sub>34</sub> $\psi$	$^{13}\text{C}'_{33}$ - $^{13}\text{C}'_{34}$	$-40^\circ \pm 10$	Goobes et al. 2006
Y <sub>34</sub> -Y <sub>38</sub>	$^{13}\text{C}'_{34}$ - $^{15}\text{N}$	$4.0 \pm 0.5 \text{ \AA}$	Goobes et al. 2006
E <sub>4</sub> -HAP	$^{13}\text{C}^\delta$ - $^{31}\text{P}$	$>7.28$	Ndao et al. 2010
E <sub>5</sub> -HAP	$^{13}\text{C}^\delta$ - $^{31}\text{P}$	$4.2 \pm 0.3 \text{ \AA}$	Ndao et al. 2010
R <sub>9</sub> -HAP	$^{13}\text{C}^\zeta$ - $^{31}\text{P}$	$4.5 \pm 0.3 \text{ \AA}$	Ndao et al. 2010
R <sub>10</sub> -HAP	$^{13}\text{C}^\zeta$ - $^{31}\text{P}$	$4.4 \pm 0.2 \text{ \AA}$	Ndao et al. 2010
R <sub>13</sub> -HAP	$^{13}\text{C}^\zeta$ - $^{31}\text{P}$	$>7.28$	Ndao et al. 2010
F <sub>14</sub> -HAP	$^{13}\text{C}^\delta$ - $^{31}\text{P}$	$>7.28$	Masica et al. 2010
E <sub>26</sub> -HAP	$^{13}\text{C}^\delta$ - $^{31}\text{P}$	$>7.28$	Ndao et al. 2010
P <sub>28</sub> -HAP	$^{13}\text{C}'_{28}$ - $^{31}\text{P}$	$>7.28$	Masica et al. 2010

**Fig. 4.12** The a ssNMR structure of statherin and b the N-terminal helix of statherin adsorbed on the HAP surface. Reproduced from Masica et al. 2010

Similar ssNMR methods have been used to study the conformation of self-assembled monolayers of amyloid-derived peptides bound to 5, 10, and 25 nm Au NPs (Shaw et al. 2012). In the absence of Au NP the peptide (CFGAILSS) forms fibrils that are implicated in disease states, including Alzheimer's disease. The conformation of thiol-linked peptides at the Au NP surface was determined using the combination of carbon chemical shifts and  $^{13}\text{C}$ - $^{13}\text{C}$  dipolar couplings. The peptides form antiparallel  $\beta$ -sheets in fibers, but adopt a parallel  $\beta$ -sheet conformation on the Au NP surface where the orientation is restrained by end linking of the peptide to the Au NP surface. Intra- and intermolecular distances were distinguished by coating the Au NP with a 1:1 mixture of carbonyl-labeled ( $[^{13}\text{C}'\text{-A}]$ CFGAILSS) and  $\text{C}\alpha$ -labeled ( $[^{13}\text{C}\alpha\text{-A}]$ CFGAILSS) peptides. The higher fraction of  $\beta$ -sheet formation in the 25 nm NP compared to the 5 and 10 nm particles was linked to increased curvature and less crowding on the larger NP surface (Shaw et al. 2012).

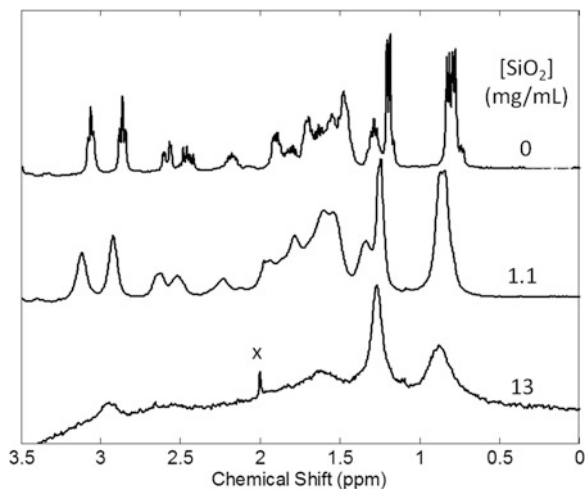
These examples show that ssNMR has emerged as an important tool for NMR structure determination at the inorganic interface. To date much of the information has been obtained using site-labeled peptides to extract the dipolar couplings and internuclear distances. Site-specific labeling not only simplifies the spectra, but also simplifies interpretation of the dipolar couplings, which can be affected by multispin effects. With the recent developments using proteins uniformly labeled with  $^{13}\text{C}$  and  $^{15}\text{N}$  (Andronesi et al. 2006; Baldus 2006; Cavalli et al. 2007), we anticipate that these new methods can be used to provide a high-resolution picture of the binding of peptides and proteins at the inorganic interface.

### 4.3.2 Solution NMR

In favorable cases, high resolution solution NMR can be used in place of ssNMR to determine the structure of peptides at inorganic surfaces. Solution NMR has a number of advantages, including a simpler experimental setup, since magic-angle sample spinning and high power proton decoupling is not required. In addition, many experiments are possible without isotopic labeling and the peptides identified as binders by phage display (12mers or 7mers) are small enough to be fully characterized on the relatively low field spectrometers (400 MHz) that are commonly available.

Progress on the solution structure determination of bound peptides has been slowed by the thought that nanomaterials much larger than proteins and will not give high-resolution NMR spectra. As noted above, the line widths depend on the rotational correlation time that scales with the third power of the particle radius. It was expected that peptides bound to particles with a radius of 10–20 nm would have lines too broad to study by high resolution NMR. More recent studies have shown solution NMR can be used for structure determination at the interface if the spectral parameters and exchange rates are favorable (Calzolari et al. 2010; Mirau et al. 2011).

**Fig. 4.13** The 400 MHz proton NMR spectra of RKLPGA in absence and presence of 14 nm SiO<sub>2</sub> NP at concentrations of 1.1 and 13 mg/mL. Reproduced from Mirau et al. 2011



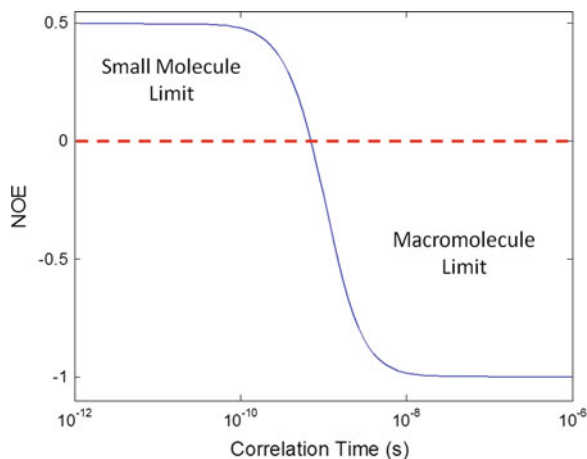
The peptide TBP1 (RKLPGAHPMPGW) has been identified by phage display as a binder of SiO<sub>2</sub>, TiO<sub>2</sub> and Ag, and alanine substitution experiments have shown that the first six amino acids (RKLPGA) are most important for surface recognition (Sano and Shiba 2003; Sano et al. 2005). Figure 4.13 shows the 400 MHz proton NMR spectra of the hexamer free and in the presence of increasing amounts of 14 nm SiO<sub>2</sub> NPs (Mirau et al. 2011). RKLPGA is a low molecular weight peptide that gives sharp lines in solution. The lines broaden and shift in the presence of 1.1 mg/mL SiO<sub>2</sub>, but a relatively high resolution spectrum can still be observed. This behavior is typical of that expected for peptides in the fast exchange limit. Broader lines are observed at 13 mg/mL SiO<sub>2</sub> NP because the peptide is all bound to the NP and slowly tumbling in solution. The slightly broadened and shifted lines observed at 1 mg/mL are optimal for structure determination of the bound peptide because sharp lines are detected but the cross relaxation rates measured by 2D NMR are dominated by the bound conformation.

As with solids, the structure of peptides at inorganic surfaces can be determined from the dipolar couplings. The dipolar couplings are most easily visualized by two dimensional NMR, since the cross peaks in 2D Nuclear Overhauser Effect Spectroscopy (NOESY) spectra are related to the internuclear distances and the molecular dynamics (Cavanagh et al. 2007; Wuthrich 1986). In the simplest case the cross relaxation rate  $\sigma_{ij}$  resulting in observable off-diagonal (cross) peaks is given by

$$\sigma_{ij} = \frac{\hbar^2 \gamma^4}{10r_{ij}^6} \left\{ \frac{6\tau_c}{1 + (2\omega\tau_c)^2} - \tau_c \right\}$$

where  $\gamma$  is the proton gyromagnetic ratio,  $r_{ij}$  is the internuclear distance,  $\omega$  is the NMR frequency and  $\tau_c$  is the rotational correlation time. The features to note are that the cross relaxation rates depend on the inverse sixth power of the internuclear

**Fig. 4.14** The nuclear Overhauser effect plotted as a function of the rotational correlation time at an observation frequency of 400 MHz



distance and the relaxation rate arises from a difference in terms that result in a change in sign for the cross peaks relative to the diagonal peaks as the correlation time changes from the fast motion regime (small molecule limit) ( $\tau_c \ll 0.3$  ns) to the slow motion regime (macromolecular limit) ( $\tau_c \gg 0.3$  ns) at 400 MHz. Figure 4.14 shows a plot of the NOE as a function of correlation time and illustrates how we can use the NOESY to probe the structure of the bound peptide. In the small molecule limit (free peptide) the cross relaxation rate is positive and the cross peaks are opposite in sign to the diagonal peaks. The peptide bound to the NP surface is greatly restricted relative to the free peptide, and the dynamics are in the macromolecular limit, giving rise to cross peaks with the same phase as those along the diagonal. In the fast exchange limit we detect the sharp, averaged line width, but the cross relaxation rates are much larger for the bound peptide compared to the free peptide. Thus, the cross relaxation rates (and NOESY cross peaks) are due predominantly to the bound conformation.

The effect of peptide binding on the 2D NOESY spectra is illustrated in Fig. 4.15, which shows a portion of the NOESY spectra for RKLPGA in the absence and presence of 25 nm  $\text{TiO}_2$  NPs (Mirau et al. 2011). The NOESY cross peaks for the free peptide are opposite in sign from the diagonal (red cross peaks), as expected for a peptide in the small molecule limit. In the presence of NPs the cross peaks have the same sign as the diagonal, and must therefore result from slowly tumbling peptide at the surface of the NP. This sample has good kinetics for NMR structure determination since sharp lines are detected and the peak intensities depend on the bound conformation.

Structure determination for peptides in fast exchange with inorganic interfaces follows the same general procedure developed for protein structure determination. The steps along the path of structure determination include sequence specific resonance assignment and measuring the NOESY cross peaks as a function of mixing time to estimate the internuclear distances that are used as input for a structure determination program (Cavanagh et al. 2007; Wuthrich 1986).



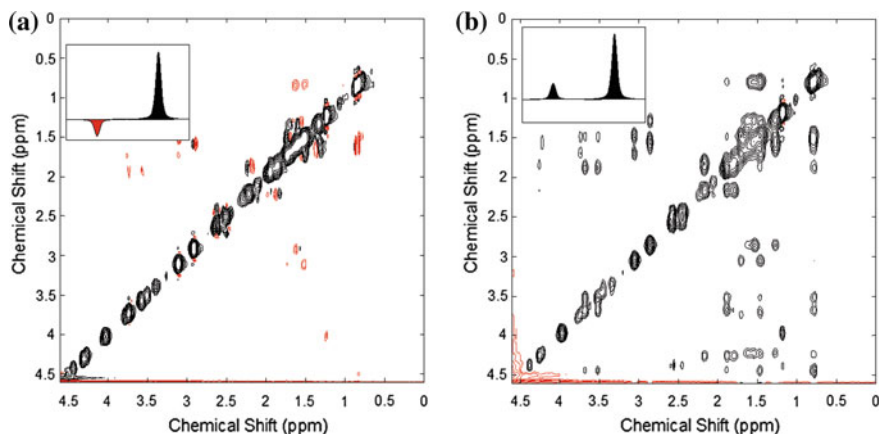


**Fig. 4.15** The 2D NOESY spectra of RKLPGA in the **a** absence and **b** presence of 1 mg/mL 25 nm TiO<sub>2</sub> NP. The inset plots show the relative sign of the diagonal and cross peak in the small molecule and macromolecular limit. Peaks opposite in sign to the diagonal are shown in *red*. Reproduced from Mirau et al. 2011

The sequence specific peak assignments are established using a combination of double-quantum filtered Correlation Spectroscopy (2Q COSY) and Total Correlation Spectroscopy (TOCSY) to identify the amino acid type using through-bond J coupling, and NOESY or Rotating-frame Overhauser Enhancement Spectroscopy (ROESY) to establish the sequence-specific assignments using through-space dipolar couplings (Cavanagh et al. 2007). For isotopically labeled peptides the Heteronuclear Multiple Quantum Coherence (HMQC) or Heteronuclear Single Quantum Coherence (HSQC) experiments are used to assign the carbon and nitrogen signals using the <sup>1</sup>H-<sup>13</sup>C or <sup>1</sup>H-<sup>15</sup>N through-bond correlations. The combination experiments (HMQC-NOESY, etc.) are useful both for establishing the assignments and measuring internuclear distances (Cavanagh et al. 2007).

The NMR structure determination for the peptides at the SiO<sub>2</sub> and TiO<sub>2</sub> surfaces relies primarily on NOESY distance restraints. The goal in any structure determination is to measure as many distances as possible identify the family of structures consistent with the input distances. As a general rule, the more restraints, the more refined the structure. Furthermore, not all peaks in the NOESY spectrum are useful for structure refinement. The inter-residue cross peaks are generally much more dependent on the structure than are the intra-residue cross peaks (Cavanagh et al. 2007). An exception to these rules are the cross peaks between the amide NH and H $\alpha$  protons which depend on the  $\phi$  torsional angle (Wuthrich 1986).

In favorable cases, information about the structure can be obtained directly from 2D spectra. This is illustrated in Fig. 4.16 which compares the 2D NOESY spectra for the alanine-substituted hexamer (RALPGA) and dodecamer (RALPDAHPMGPW) titanium binding peptides in the presence of 14 nm silica NPs.

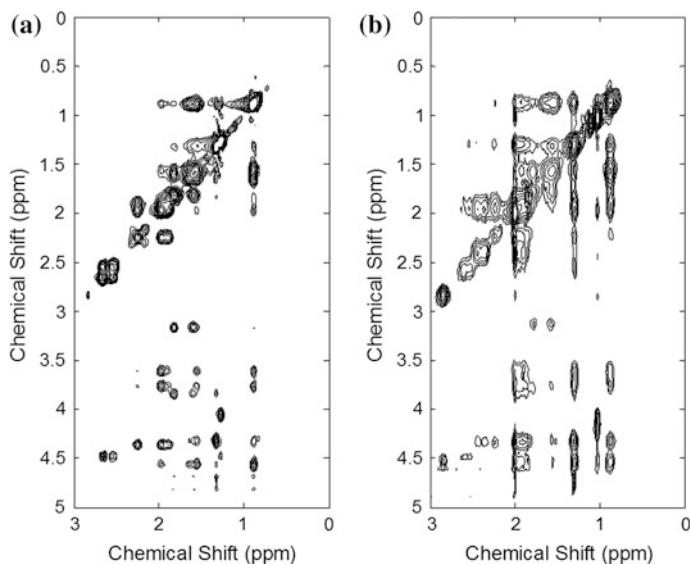


**Fig. 4.16** Comparison of the 2D NOESY spectra obtained with a 0.2 s mixing time for **a** RALPDA and **b** RALPDHPMGPW in the presence of 14 nm SiO<sub>2</sub> NP. Reproduced from Mirau et al. 2011

Note that there are not many more peaks in the dodecamer spectra compared to the hexamer. This supports the hypothesis from the alanine substitution experiments that only the first six amino acids are important for surface recognition (Sano and Shiba 2003).

The structure of the peptides bound to SiO<sub>2</sub> was determined by measuring the cross peak volumes from the NOESY spectra and converting the peak volumes to distance estimates. This is typically accomplished by comparing the peak volumes ( $A$ ) as a function of NOESY mixing time to a reference peak of a known distance as

$$r = r_{\text{ref}} \left[ \frac{A}{A_{\text{ref}}} \right]^{-1/6}$$

The commonly used reference distances are the tyrosine aromatic protons H $\delta$ -H $\epsilon$  (2.5 Å) or the alanine H $\alpha$ -H $\beta$  (2.5 Å). Measurement of the peak volumes as a function of mixing time is required because indirect magnetization transfer (spin diffusion) can result in cross peaks at long mixing times between pairs of protons that are not in close proximity (Cavanagh et al. 2007).

The structure of the bound peptide was obtained by inputting the measured distance estimates into the program XPLOR (Schwieters et al. 2006), which uses a simulated annealing algorithm starting from random coordinates to find structures that are compatible with the distance constraints. The refinement is

**Fig. 4.17** The structures of RALPDAHPMGPW calculated from the NMR derived distances. The N-terminal (R1) and C-terminal (W12) residues are shown. Reproduced from Mirau et al. 2011

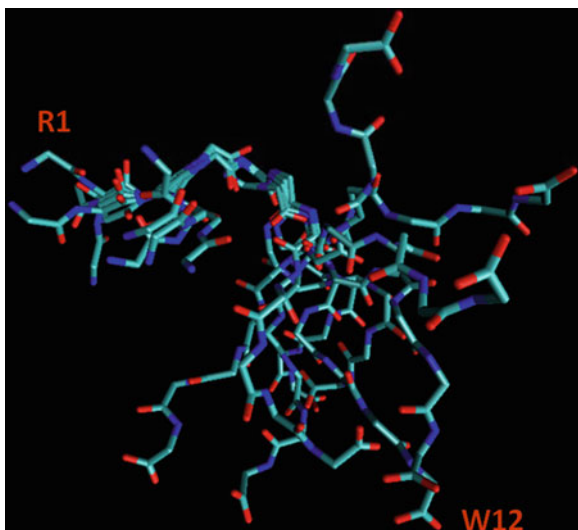
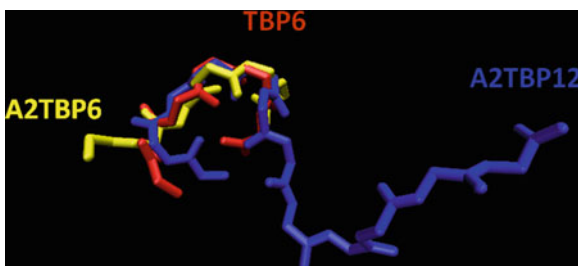


**Fig. 4.18** An overlay of typical structures for the titanium binding hexamer (TBP6), the A2-substituted hexamer (A2TBP6), and the A2-substituted dodecamer (A2TBP12). Reproduced from Mirau et al. 2011

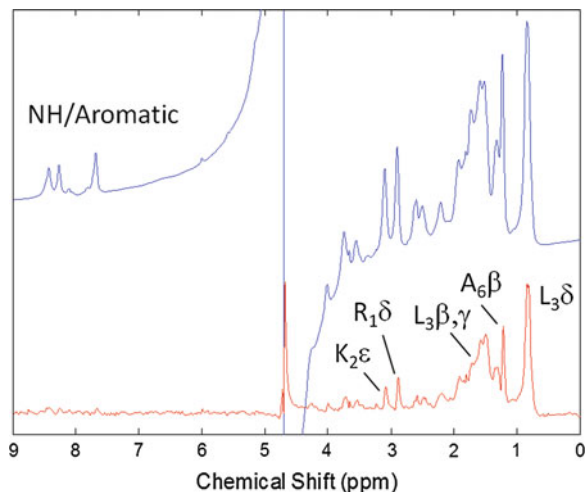


typically run many times and the output structures compared. If the structures are similar to each other, then the structure is considered well defined by the NMR data. If only parts of the structures are similar, then only parts of the structure are well defined.

Figure 4.17 compares 10 structures calculated from the distance restraints for the alanine-substituted dodecamer RALPDAHPMGPW bound to  $\text{SiO}_2$  NPs (Mirau et al. 2011). The overlay plot shows that similar structures are obtained for the first six amino acids. Few inter-residue cross peaks are observed for amino acids seven through twelve showing that this part of the peptide chain is not well defined by the NMR data.

A comparison of the NOESY spectra for the A2-substituted hexamer and dodecamer bound to silica and titania NP shows that many of the same inter-residue peaks are observed with similar intensities. Thus it appears from the raw data that the first six amino acids adopt a well-defined structure, and the structures are similar on both silica and titania. This conclusion is borne out in the refined structures as shown in Fig. 4.18, which overlays the first six amino acids for

**Fig. 4.19** The (*bottom*) saturation-transfer difference spectra (10x gain) for RKLPGA in the presence of SiO<sub>2</sub> NP and (*top*) the reference spectrum in H<sub>2</sub>O. Reproduced from Mirau et al. 2011



RKLPGA, RALPGA, and RALPGAHPMGPW bound to SiO<sub>2</sub> NPs (Mirau et al. 2011). These data show that the first six amino acids adopt a compact C-shaped conformation on the surface of the NPs.

The structures derived from the NOESY data show the conformation of the peptide on the NP surface, but do not provide an insight into peptide recognition of the NP surface. Saturation-Transfer Difference (STD) experiments have been successfully used to identify contacts between ligands and protein binding sites (Mayer and Mayer 2001), and similar experiments can be used to determine how peptides bind to NP surfaces. The experiment relies on a difference in line widths for the free and bound peptides and begins with a low-power saturation of a region of the spectrum that does not contain any signals from the free peptide ( $\sim -2$  ppm). The idea is that the protein (or NP) is reorienting slowly in solution and has a large line width which extends beyond the normal proton spectrum. In the silica and titania NP it is probably the spectra of the bound water or hydroxyl groups that extend into the high field portion of the spectra. The larger molecule is partially saturated by the low power irradiation and magnetization can be transferred to the exchanging peptide. The largest peaks in the difference spectra are those in closest proximity to the surface.

Figure 4.19 shows the STD spectra for RKLPGA in the presence of SiO<sub>2</sub> NP (Mirau et al. 2011). The difference spectrum shows peaks from several side chains, but not from the NH protons along the peptide main chain. This demonstrates that interactions with the NP surface occur predominantly as a consequence of side chain interactions with the NP surface.

The amino acids that stabilize interactions with the NP surface can be identified from the STD spectra. Silica NPs are hydrophilic, so it is expected that methylene protons near positively charged nitrogens (R1 H $\delta$  and K2 H $\epsilon$ ) would be in close proximity to the surface. However, peaks from hydrophobic residues (alanine and leucine) are also observed. The peaks close to the surface can be identified by

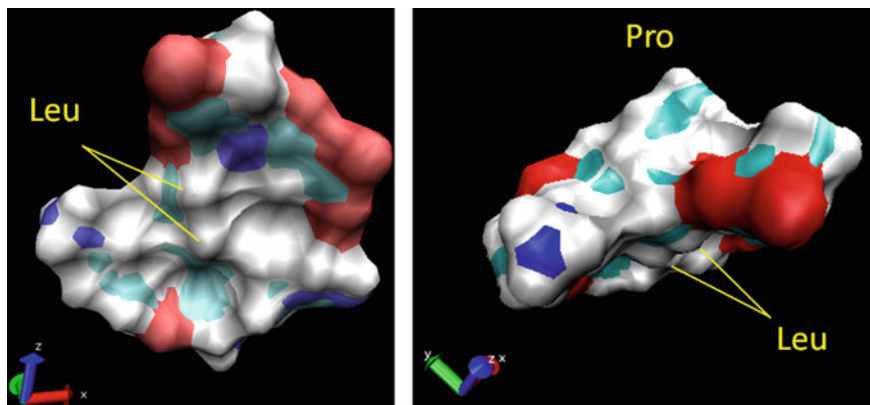


**Fig. 4.20** Surface views of RKLPGA bound to the surface of silica NP in two different orientations. Reproduced from Mirau et al. 2011

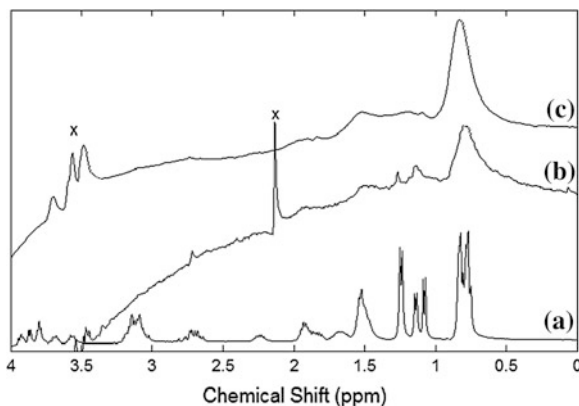
considering the compact C-shaped structure determined from the NOESY data shown in Fig. 4.20. These drawings show that one face of the peptide is relatively flat, and the leucine methyl groups project onto this face. The NMR data suggests that this face of the peptide lies flat on the silica surface. The proline protrudes from the other face of the peptide and may prevent the peptide from conformally binding the NP surface. We expect that the binding is due to both the shape of the peptide and the array of polar groups (shown in red and blue) that are able to interact with the surface.

In these examples we have considered how the size of the NP and the exchange rate affect the line width and the spectra, but we have not considered possible influence of the NP magnetic properties. It is well known from the Au NP literature that Au NPs can have a dramatic effect on the NMR spectra, and the effects depend on how far the signal of interest is separated from the Au NP surface (Badia et al. 1997; Zelakiewicz et al. 2003).

The magnetic effects of the NPs are illustrated in the NMR spectra of Pd4 (TSNAVHPTLRHL) bound to 2 nm Pd and 3 nm Pt NP shown in Fig. 4.21 (Mirau et al. 2014). Relatively sharp lines are expected for the free peptide, the peptide in the fast exchange limit and the bound peptide, since the size of the NP is about the same as lysozyme, an enzyme that gives well-resolved NMR spectra (Bartik et al. 1993). Control experiments show that the line widths are not affected by temperature and are therefore in the slow exchange limit. The large line widths observed in Fig. 4.21 must therefore be a consequence of the magnetic properties of the Pd and Pt NPs.

Pd4 was identified as a Pd binder from phage-display experiments using Pd NP (25 nm) as a target (Pacardo et al. 2009). In addition to surface binding, Pd4 has the ability to template the formation of small (2–3 nm) NPs from  $K_2PdCl_4/NaBH_4$  that are catalytically active in the Stille coupling reaction (Coppage et al. 2010,

**Fig. 4.21** The 400 MHz proton NMR spectra of **a** Pd4, **b** Pd4-Pd NP (2 nm), and **c** Pd4-Pt NP (3 nm). Reproduced from (Mirau et al. 2014)



2011, 2012; Pacardo et al. 2009). The Pd NP are stable in solution presumably because of a layer of passivating peptide at the surface.

There are several mechanisms that can potentially contribute to the broad lines observed for the peptide-passivated Pd and Pt NPs, including dipolar interactions, paramagnetic interactions and chemical exchange. In addition, the lines could be inhomogeneously broadened if the binding sites on the NP had different local magnetic environments, each leading to a slight difference chemical shift. If the shifts are less than the line width, then the lines are inhomogeneously broadened from the unresolved signals from the magnetically distinct binding sites.

Pd and Pt are both diamagnetic, and therefore not expected to broaden the spectra from paramagnetic interactions. In the Pd and Pt NPs the broad lines can be assigned to inhomogeneous broadening by comparison of the line widths  $\Delta\nu_{1/2}$  with those calculated from the spin-spin relaxation time  $T_2$  as given by

$$\Delta\nu_{1/2} = \frac{1}{\pi T_2}$$

The NMR experiments show that the measured  $T_2$  (0.24 s) is much longer than the  $T_2$  calculated from the apparent line width (0.012 s) for the leucine methyl protons (Mirau et al. 2014). This can only be observed when the lines are inhomogeneously broadened when the peptide binds on the surface and experiences a variety of local magnetic environments. It is well known from NMR studies of ligands covalently bonded to Au NP that the lines are inhomogeneously broadened (Badia et al. 1997; Zelakiewicz et al. 2003), and that the broadening extends about 0.5 nm from the surface. It has been proposed that the inhomogeneous broadening is a consequence of ligands binding on the faces and edges of faceted NP, as shown in Fig. 4.22a for peptides passivating a 2 nm Pd NP. Figure 4.22b shows a schematic diagram for a peptide broadening to the surface of a NP. The signals closest to the NP surface will experience inhomogeneous broadening, while signals further from the surface will show the sharper lines expected for a peptide bound to a 2 nm NP.

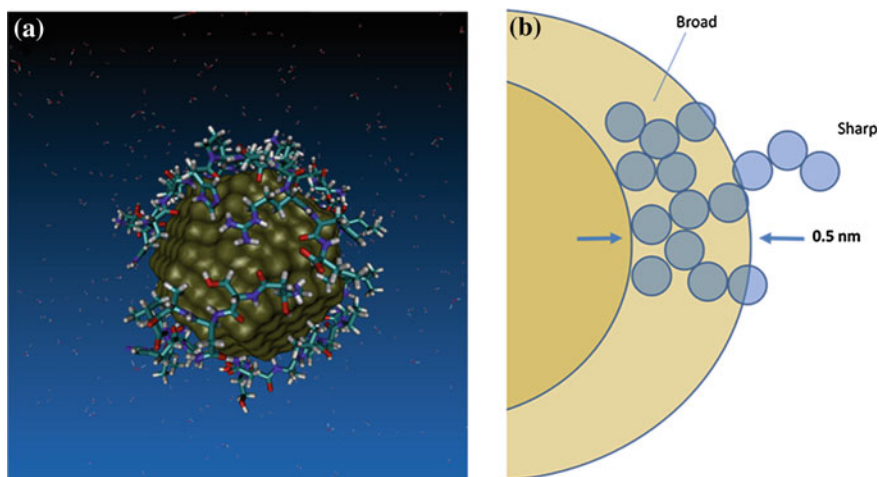


**Fig. 4.22** A schematic diagram of **a** Pd4 passivating a faceted 2 nm NP and **b** a diagram showing broadened lines for peptides constrained to within 0.5 nm of the NP surface

It has been proposed that the ability of Pd4 to recognize Pd surfaces is due in part to the histidines at positions six and eleven (Coppage et al. 2012). This hypothesis can be tested by comparing the NMR properties of Pd4 (TSNAVHPTLRHL) with the alanine-substituted A6 (TSNAVAPTLRHL), A11(TSNAVHPTLRAL) and A6,11(TSNAVAPTLRAL) analogs as shown in Fig. 4.23. This figure shows that all the peaks are broadened by NP binding, but the extent of the broadening depends on the peptide sequence. Note that the greatest broadening is observed for Pd4. This suggests that all of the protons in Pd4 are in close proximity to the NP surface, while the sharper lines in the A6,11 double mutant suggest that this peptide has residues that are more removed from the Pd surface. This effect can be quantified using 2D TOCSY NMR since the cross peaks in the through-bond correlation spectrum are greatly diminished as the line widths increase. By counting the number of cross peaks we can determine that the surface proximity of the peptide follows the order Pd4 < A6, A11 < A6,11. These data support the hypothesis that histidine interactions with the surface are a critical part of the Pd4 recognition of the Pd NP surface.

Solution NMR methods have also been used to identify proteins that interact with Au NPs, and Fig. 4.24a shows the HSQC spectrum of  $^{15}\text{N}$ -labeled ubiquitin (a 76 amino acid regulatory protein (8,564 g/mol)) in the absence (red) and presence of 10 nm Au NP (Calzolari et al. 2010). The  $^{15}\text{N}$ - $^1\text{H}$  correlation spectrum of ubiquitin is well resolved and the peaks can be assigned to individual amino acids. A high-resolution spectrum is also observed in the presence of Au NP. As with the  $\text{TiO}_2/\text{SiO}_2$  binding peptides (Mirau et al. 2011), only small changes in line width are observed in the presence of the NP. This can only arise if the protein is in fast exchange with the NP surface. The observation that only a fraction of the

**Fig. 4.23** The 400 MHz proton NMR spectra for **a** free Pd4 and the Pd NPs capped with **b** A6 **c** A11 **d** A6,11, and **e** Pd4. Impurities are marked (x). Reproduced from (Mirau et al. 2014)

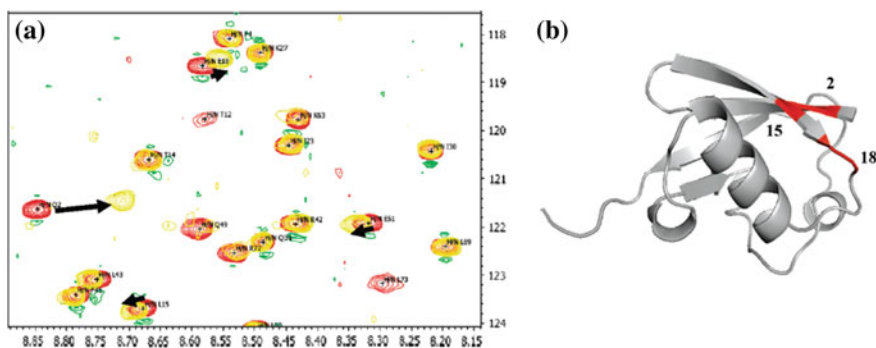
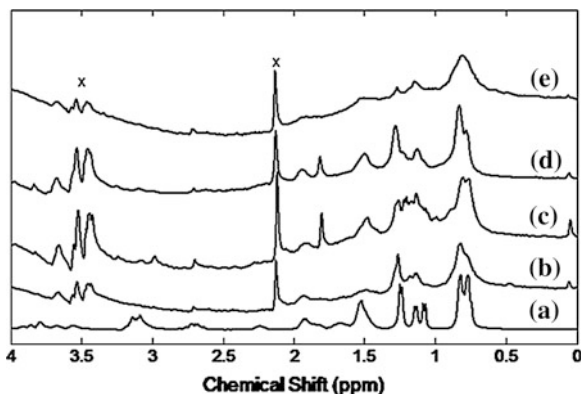


**Fig. 4.24** The **a**  $^{15}\text{N}$ - $^1\text{H}$  HSQC NMR spectrum of ubiquitin in the absence (*red*) and presence (*yellow*) of 10 nm Au NP and **b** a drawing of ubiquitin with the residues with large chemical shift changes shown in *red*. Reproduced from Calzolari et al. 2010

peaks are perturbed in the presence of the NP shows that ubiquitin interacts specifically with the Au NP surface. Figure 4.24b shows that the majority of perturbed peaks are on one face of ubiquitin (shown in red).

Similar experiments have been used to study the binding of recombinant human acid fibroblast growth factor (FGF1) with a hexa-histidine tag (typically used for protein purification) binding to 1.5 nm Au NP passivated with CAAKA (Kogot et al. 2009). The authors note that long incubation times are required, presumably due to competition between the His6-tag and the thiol-linked amino acids at the surface. High-resolution spectra can be obtained in this experiment since the small Au NPs do not greatly increase the rotational correlation time for the complex. The authors observed changes in both peak position and intensity and related the changes to interaction of the Au NP with the FGF1 surface.



## 4.4 Summary and Outlook

Peptides have emerged as important materials for the modification of inorganic surfaces and for the synthesis of monodisperse biocompatible NPs (Dickerson et al. 2008). The presence of peptides on inorganic surfaces allow for the functionalization of NP in devices, including sensors (Kuang et al. 2010; Slocik et al. 2008).

One strategy for using peptides at the nanomaterials interface is to use bifunctional peptides which contain a sequence for recognizing the nanomaterials surface linked to a peptide with another functionality, such as recognizing TNT (Kuang et al. 2010) or other metal ions (Slocik et al. 2008). Another strategy is to use peptides to passivate the surface of NP to control catalytic reactions (Coppage et al. 2010; Pacardo et al. 2009).

While peptides at the NP surface have been engineered for many applications, relatively little information is available about the molecular interactions of peptides with the NP surfaces. This arises in part because of the difficulty in characterizing the molecular level structures of the peptides at the interface. This problem can be solved in part through the application of the optical and NMR methods presented in this review to new peptide-NP systems so we can determine the molecular-level interactions and the forces that drive the binding of specific sequences at the nanomaterials interface. Our understanding will be greatly increased by combining these experimental methods with recent advances in computational materials science (Heinz et al. 2008, 2009) to understand the peptide NP interactions.

The applications of these methods to study the peptide-nanomaterials interface could enable significant progress toward the grand challenge of understanding sequence-functionality relationships in peptides. In phage display, for example, a few 12-mer peptide sequences out of  $10^9$  are able to recognize a particular inorganic surface. The challenge is to explore that small pool of binders so that we can understand the sequence-structure-function relationships and rationally design the next generation of biofunctionalized NP interfaces.

## References

- Adey NB, Mataragnon AH, Rider JE, Carter JM, Kay BK (1995) Characterization of phage that bind plastic from phage-displayed random peptide libraries. *Gene* 156(1):27-31. doi:[http://dx.doi.org/10.1016/0378-1119\(95\)00058-E](http://dx.doi.org/10.1016/0378-1119(95)00058-E)
- Andronesi OC, Heise H, Baldus M (2006) Determining protein 3D structure by magic angle spinning NMR. *Mod Magn Reson* 1:523-526
- Badia A, Cuccia L, Demers L, Morin F, Lennox RB (1997) Structure and dynamics in Alkanethiolate monolayers self-assembled on gold nanoparticles: a DSC, FT-IR, and deuterium NMR study. *J Am Chem Soc* 119(11):2682-2692
- Bak M, Rasmussen JT, Nielsen NC (2000) SIMPSIN: a general simulation program for solid-state NMR spectroscopy. *J Mag Reson* 147:296-330

- Baldus M (2006) Solid-state NMR spectroscopy: molecular structure and organization at the atomic level. *Angew Chem Int Ed* 45(8):1186–1188
- Bartik K, Dobson CM, Redfield C (1993) H-1-NMR analysis of turkey egg-white lysozyme and comparison with hen egg-white lysozyme. *Eur J Biochem* 215(2):255–266. doi:[10.1111/j.1432-1033.1993.tb18030.x](https://doi.org/10.1111/j.1432-1033.1993.tb18030.x)
- Brown S (1997) Metal-recognition by repeating polypeptides. *Nat Biotechnol* 15(3):269–272
- Calzolari L, Franchini F, Gilliland D, Rossi F (2010) Protein-nanoparticle interaction: identification of the ubiquitin-gold nanoparticle interaction site. *Nano Lett* 10(8):3101–3105. doi:[10.1021/nl101746v](https://doi.org/10.1021/nl101746v)
- Cavalli A, Salvatella X, Dobson CM, Vendruscolo M (2007) Protein structure determination from NMR chemical shifts. *Proc Natl Acad Sci* 104:9615–9620
- Cavanagh J, Fairbrother WJ, Parlmer AG III, Rance M, Skelton NJ (2007) *Protein NMR spectroscopy: principles and practice*. Elsevier Academic Press, Burlington
- Coppage R, Slocik JM, Sethi M, Pacardo DB, Naik RR, Knecht MR (2010) Elucidation of peptide effects that control the activity of nanoparticles. *Angew Chem Int Ed* 122(22):3855–3858. doi:[10.1002/ange.200906949](https://doi.org/10.1002/ange.200906949)
- Coppage R, Slocik JM, Briggs BD, Frenkel AI, Heinz H, Naik RR, Knecht MR (2011) Crystallographic recognition controls peptide binding for bio-based nanomaterials. *J Am Chem Soc* 133(32):12346–12349. doi:[10.1021/ja203726n](https://doi.org/10.1021/ja203726n)
- Coppage R, Slocik JM, Briggs BD, Frenkel AI, Naik RR, Knecht MR (2012) Determining peptide sequence effects that control the size, structure, and function of nanoparticles. *ACS Nano* 6(2):1625–1636. doi:[10.1021/nl204600d](https://doi.org/10.1021/nl204600d)
- Croasmun WR, Carlson MK (eds) (1994) *Two-Dimensional NMR. Applications for Chemists and Biochemists. Methods in Stereochemical Analysis*. VCH Publishers, Inc., New York
- Dickerson MB, Sandhage KH, Naik RR (2008) Protein- and Peptide-directed syntheses of inorganic materials. *Chem Rev* 108(11):4935–4978
- Drobny GP, Long JR, Karlsson T, Shaw W, Popham J, Oyler N, Bower P, Stringer J, Gregory D, Mehta M, Stayton PS (2003) Structural studies of biomaterials using double-quantum solid-state NMR spectroscopy. *Ann Rev Phys Chem* 54:531–571
- Elgavish GA, Hay DI, Schlesinger DH (1984) 1H and 31P nuclear magnetic resonance studies of human salivary statherin. *Int J Pept Protein Res* 23(3):230–234. doi:[10.1111/j.1399-3011.1984.tb02714.x](https://doi.org/10.1111/j.1399-3011.1984.tb02714.x)
- Fernandez VL, Reimer JA, Denn MM (1992) Magnetic Resonance Studies of Polypeptides Adsorbed on Silica and Hydroxyapatite Surfaces. *J Am Chem Soc* 114:9634–9642
- Gibson JM, Raghunathan V, Popham JM, Stayton PS, Drobny GP (2005) A REDOR NMR study of a phosphorylated statherin fragment bound to hydroxyapatite crystals. *J Am Chem Soc* 127(26):9350–9351
- Goobes G, Goobes R, Schueler-Furman O, Baker D, Stayton PS, Drobny GP (2006) Folding of the C-terminal bacterial binding domain in statherin upon adsorption onto hydroxyapatite crystals. *Proc Natl Acad Sci USA* 103(44):16083–16088
- Greenfield NJ (2006) Using circular dichroism spectra to estimate protein secondary structure. *Nat Protoc* 1(6):2876–2890
- Greenfield NJ, Fasman GD (1969) Computed circular dichroism spectra for the evaluation of protein conformation. *Biochemistry* 8(10):4108–4116
- Gullion T, Schaefer J (1989) Rotational-echo double resonance NMR. *J Magn Reson* 81:196–200
- Heinz H, Vaia RA, Farmer BL, Naik RR (2008) Accurate simulation of surfaces and interfaces of face-centered cubic metals using 12–6 and 9–6 Lennard-Jones Potentials. *J Phys Chem C* 112(44):17281–17290. doi:[10.1021/jp801931d](https://doi.org/10.1021/jp801931d)
- Heinz H, Farmer BL, Pandey RB, Slocik JM, Patnaik SS, Pachter R, Naik RR (2009) Nature of molecular interactions of peptides with gold, palladium, and Pd-Au bimetal surfaces in aqueous solution. *J Am Chem Soc* 131(28):9704–9714. doi:[10.1021/ja900531f](https://doi.org/10.1021/ja900531f)
- Hnilova M, Oren EE, Seker UOS, Wilson BR, Collino S, Evans JS, Tamerler C, Sarikaya M (2008) Effect of molecular conformations on the adsorption behavior of gold-binding peptides. *Langmuir* 24(21):12440–12445. doi:[10.1021/la801468c](https://doi.org/10.1021/la801468c)

- Jackson M, Mantsch HH (1995) The use and misuse of FTIR spectroscopy in the determination of protein-structure. *Crit Rev Biochem Mol Biol* 30(2):95–120. doi:[10.3109/10409239509085140](https://doi.org/10.3109/10409239509085140)
- Katoch J, Kim SN, Kuang Z, Farmer BL, Naik RR, Tatulian SA, Ishigami M (2012) Structure of a peptide adsorbed on graphene and graphite. *Nano Lett* 12(5):2342–2346. doi:[10.1021/nl300286k](https://doi.org/10.1021/nl300286k)
- Kogot JM, Parker AM, Lee J, Blaber M, Strouse GF, Logan TM (2009) Analysis of the Dynamics of assembly and structural impact for a histidine tagged FGF1–1.5 nm Au Nanoparticle Bioconjugate. *Bioconjug Chem* 20(11):2106–2113. doi:[10.1021/bc900224d](https://doi.org/10.1021/bc900224d)
- Kroger N, Deutzmann R, Sumper M (1999) Polycationic peptides from diatom biosilica that direct silica nanosphere formation. *Science* 286:1129–1132
- Kuang ZF, Kim SN, Crookes-Goodson WJ, Farmer BL, Naik RR (2010) Biomimetic chemosensor: designing peptide recognition elements for surface functionalization of carbon nanotube field effect transistors. *ACS Nano* 4(1):452–458. doi:[10.1021/nn901365g](https://doi.org/10.1021/nn901365g)
- Long JR, Shaw WJ, Stayton PS, Drobny GP (2001) Structure and dynamics of hydrated statherin on hydroxyapatite as determined by solid-state NMR. *Biochemistry* 40(51):15451–15455
- Luckarift HR, Spain JC, Naik RR, Stone MO (2004) Enzyme immobilization in a biomimetic silica support. *Nat Biotech* 22:211
- Mafra L, Siegel R, Fernandez C, Schneider D, Aussenac F, Rocha J (2009) High-resolution  $^1\text{H}$  homonuclear dipolar recoupling NMR spectra of biological solids at MAS rates of to 67 kHz. *J Magn Reson* 199:111–114
- Mandal HS, Kraatz H-B (2007) Effect of the surface curvature on the secondary structure of peptides adsorbed on nanoparticles. *J Am Chem Soc* 129(20):6356–6357. doi:[10.1021/ja0703372](https://doi.org/10.1021/ja0703372)
- Masica DL, Ash JT, Ndao M, Drobny GP, Gray JJ (2010) Toward a structure determination method for biomineral-associated protein using combined solid-state NMR and computational structure prediction. *Structure* 18(12):1678–1687. doi:[10.1016/j.str.2010.09.013](https://doi.org/10.1016/j.str.2010.09.013)
- Mayer M, Mayer B (2001) Group epitope mapping by saturation transfer difference NMR to identify segments of a ligand in direct contact with a protein receptor. *J Am Chem Soc* 123:6108–6117
- Mirau PA, Serres JL, Lyons M (2008) The structure and dynamics of Poly(L-lysine) in templated silica nanocomposites. *Chem Mater* 20(6):2218–2223. doi:[10.1021/cm702283u](https://doi.org/10.1021/cm702283u)
- Mirau PA, Naik RR, Gehring P (2011) Structure of peptides on metal oxide surfaces probed by NMR. *J Am Chem Soc* 133(45):18243–18248. doi:[10.1021/ja205454t](https://doi.org/10.1021/ja205454t)
- Miura Y, Kimura S, Imanishi Y, Umemura J (1999) Oriented helical peptide layer on the carboxylate-terminated alkanethiol immobilized on a gold surface. *Langmuir* 15(4):1155–1160. doi:[10.1021/la9803878](https://doi.org/10.1021/la9803878)
- Mirau PA, Naik RR, Coppage R, Knecht MR, Ramezani-DakHel H, Heinz H, Vaia RA, Kotlarchyk M (2014) The Structure of peptides at the palladium nanoparticle interface (submitted)
- Naganagowda GA, Gururaja TL, Levine MJ (1998) Delineation of conformational preferences in human salivary statherin by  $^1\text{H}$ ,  $^{31}\text{P}$  NMR and CD studies: sequential assignments and structure-function correlations. *J Biomol Struct Dyn* 16:91–107
- Naik RR, Brott LL, Clarson SJ, Stone MO (2002a) Silica-precipitating peptides isolated from a combinatorial phage display peptide library. *J Nanosci Nanotechnol* 2(1):95–100
- Naik RR, Stringer SJ, Agarwal G, Jones SE, Stone MO (2002b) Biomimetic synthesis and patterning of silver nanoparticles. *Nat Mater* 1(3):169–172
- Ndao M, Ash JT, Breen NF, Goobes G, Stayton PS, Drobny GP (2009) A  $^{13}\text{C}\{^{31}\text{P}\}$  REDOR NMR investigation of the role of glutamic acid residues in statherin-hydroxyapatite recognition. *Langmuir* 25(20):12136–12143
- Ndao M, Ash JT, Stayton PS, Drobny GP (2010) The role of basic amino acids in the molecular recognition of hydroxyapatite by statherin using solid state NMR. *Surf Sci* 604(15–16):L39–L42. doi:[10.1016/j.susc.2010.02.026](https://doi.org/10.1016/j.susc.2010.02.026)

- Oren EE, Notman R, Kim IW, Evans JS, Walsh TR, Samudrala R, Tamerler C, Sarikaya M (2010) Probing the molecular mechanisms of quartz-binding peptides. *Langmuir* 26(13):11003–11009
- Pacardo DB, Sethi M, Jones SE, Naik RR, Knecht MR (2009) Biomimetic synthesis of Pd nanocatalysts for the stille coupling reaction. *ACS Nano* 3(5):1288–1296
- Parmar AS, Muschol M (2009) Hydration and hydrodynamic interactions of lysozyme: effects of chotropic versus kosmotropic ions. *Biophys J* 97(2):590–598
- Renault M, Cukkemane A, Baldus M (2010) Solid-state NMR spectroscopy on complex biomolecules. *Angewandte Chemie Int Ed* 49(45):8346–8357. doi:[10.1002/anie.201002823](https://doi.org/10.1002/anie.201002823)
- Sano KI, Shiba K (2003) A hexapeptide motif that electrostatically binds to the surface of titanium. *J Am Chem Soc* 125:14234–14235
- Sano KI, Sasaki H, Shiba K (2005) Specificity and biomineralization activities of Ti-binding peptide-1 (TBP-1). *Langmuir* 21:3090–3095
- Schmidt-Rohr K, Speiss HW (1994) *Multidimensional solid-state NMR and polymers*. Academic Press, New York
- Schwietters CD, Kuszewski JJ, Clore G (2006) Using Xplor-NIH for NMR molecular structure determination. *Prog Nucl Mag Res Spectrosc* 48:47–62
- Shaw CP, Middleton DA, Volk M, Levy R (2012) Amyloid-derived peptide forms self-assembled mono layers on gold nanoparticle with a curvature-dependent beta-sheet structure. *ACS Nano* 6(2):1416–1426. doi:[10.1021/nn204214x](https://doi.org/10.1021/nn204214x)
- Slocik JM, Stone MO, Naik RR (2005) Synthesis of gold nanoparticles using multifunctional peptides. *Small* 1(11):1048–1052
- Slocik JM, Zabinski JS Jr, Phillips DM, Naik Rajesh R (2008) Colorimetric response of peptide-functionalized gold nanoparticles to metal ions. *Small* 4:548–551
- Slocik JM, Govorov AO, Naik RR (2011) Plasmonic circular dichroism of peptide-functionalized gold nanoparticles. *Nano Lett* 11:701–705. doi:[10.1021/nl1038242](https://doi.org/10.1021/nl1038242)
- Surewicz WK, Mantsch HH, Chapman D (1993) Determination of protein secondary structure by fourier transform infrared spectroscopy: a critical assessment. *Biochemistry* 32(2):389–394. doi:[10.1021/bi00053a001](https://doi.org/10.1021/bi00053a001)
- Swanson SC, Bryand RG (1991) The hydration response of Poly(L-Lysine) dynamics measured by <sup>13</sup>C NMR spectroscopy. *Biopolymers* 31:967–973
- Tjandra N, Tate S-i, Ono A, Kainosho M, Bax A (2000) The NMR structure of a DNA dodecamer in an aqueous dilute liquid crystalline phase. *J Am Chem Soc* 122(26):6190–6200
- Tycko R (2001) Biomolecular solid state NMR: advances in structural methodology and applications to peptide and protein fibrils. *Ann Rev Phys Chem* 52:575–606
- Wang SS, Hemphreys ES, Chung SY, Delduco DF, Lustig SR, Wang H, Parker KN, Rizzo NW, Subramoney S, Chiang YM, Jagota A (2003) Peptides with selective affinity for carbon nanotubes. *Nat Mater* 2:196
- Whaley SR, English DS, Hu EL, Barbara PF, Belcher AM (2000) Selection of peptides with semiconductor binding specificity for directed nanocrystal assembly. *Nature* 405:665–668
- Wishart DS, Sykes BD (1994) The <sup>13</sup>C chemical -shift index: a simple method for the identification of protein secondary structure using <sup>13</sup>C chemical-shift data. *J Biomol NMR* 4(2):171–180
- Wishart DS, Bigam CG, Holm A, Hodges RS, Sykes BD (1995) <sup>1</sup>H, <sup>13</sup>C and <sup>15</sup>N random coil NMR chemical shifts of the common amino acid. I. investigation of nearest neighbor effects. *J Biomol NMR* 5:67–81
- Wuthrich K (1986) *NMR of proteins and nucleic acids*. Wiley, New York
- Zelakiewicz BS, de Dios AC, Tong YY (2003) <sup>13</sup>C NMR spectroscopy of <sup>13</sup>C<sub>1</sub>-labeled octanethiol-protected Au nanoparticles: shifts, relaxations, and particle-size effect. *J Am Chem Soc* 125(1):18–19

# Chapter 5

## Understanding Biomineral Growth and Assembly for Engineering Novel Green Nanomaterials

Siddharth Patwardhan

**Abstract** Nanotechnology has great potential to make significant improvements in existing technologies. One such example is where learning from biology can help to develop bioinspired green nanomaterials. In this chapter, we will learn about uniqueness of biomineralisation. With the help of selected examples, we will discuss how we can take a step forward to design bioinspired technologies by understanding the controlled nucleation, growth and self-assembly typically displayed in biomineral formation. At the end of the chapter, a number of future avenues and challenges are outlined, which will help define future research directions.

### 5.1 Introduction

By 2015, nanotechnology markets are predicted to be \$1 trillion (Nel et al. 2006). Realisation of these estimates requires the development of innovative nanotechnologies. In the search for new nanomaterials, a wide range of approaches have been developed including mechanical methods (e.g. ball milling and attrition), physical techniques (e.g. sonochemical, sputtering and microwave-assisted), chemical routes (vapour phase synthesis, precipitation, micelles, solvothermal and sol-gel) and combination thereof (Gleiter 1989; Knauth and Schoonman 2002). However, these methods suffer from high energy demands, environmentally damaging conditions and/or a lack of sophistication in contrast to that exhibited by biominerals. Biology exerts a remarkable level of control over fabrication of more than 60 distinct nanomaterials (e.g.  $\text{CaCO}_3$ ,  $\text{Fe}_3\text{O}_4$ , silica) produced under environmentally-friendly conditions (Mann et al. 1989). It appears that biology has

---

S. Patwardhan (✉)

Department of Chemical and Process Engineering, University of Strathclyde,  
75 Montrose Street, Glasgow G1 1XJ, UK  
e-mail: Siddharth.Patwardhan@strath.ac.uk

identified 'clever' green routes to produce nanomaterials and an understanding of the secrets of biological nanomaterials formation could lead to materials with novel applications and/or new technologies for their production (Patwardhan 2011). Harnessing biological production of sophisticated nanomaterials has exciting prospects and it encompasses most of the twelve principles of green chemistry (Anastas and Kirchhoff 2002; Dahl et al. 2007).

Biomaterials are typically composed of polymers, such as polysaccharides and proteins, and simple insoluble oxides and salts. These organic and inorganic components can be assembled in a wide range of combinations to produce materials of desired properties and functions. In contrast, the range of available building blocks to us is vast (essentially the entire periodic table); however, it is not a simple matter to design *de novo* functional materials with desired properties. Nature still has a significant advantage over any scientist attempting to design materials to mimic those in living organisms. Evolution over millions of years has allowed biology to fabricate sophisticated natural materials that are ideally suited to their functions, such as sensing, protection or motion.

Earlier chapters have highlighted that in order to make progress in bioinspired technologies, it is imperative to gain a detailed understanding of nano-bio interactions. In this chapter, we aim to provide a background on and key features of biomineralisation in order to understand how nucleation and growth of biomaterials are controlled. A wide range of examples will be provided to illustrate. Towards the end of the chapter, with the aid of selected examples we will discuss strategies on how to progress in designing bioinspired technologies based on biomineralisation. This chapter should serve as an overview of the topics considered and readers are directed to some excellent references for seeking further detailed explanations and discussions.

## 5.2 Biomineralisation

Biomineralisation is a process by which biology produces minerals *in vivo*. Biomaterials are typically organic-inorganic composites of biopolymers and inorganic salts or oxides. Due to their unique assembly and composition, biomaterials often have physical and structural properties that are somewhat different from their synthetic counterparts. Another unique attribute of biomaterials is the hierarchical organisation of atoms all the way to macroscopic features. To date, over 60 types of biomaterials have been identified (Mann et al. 1989) which highlights the ability of biology to manipulate and synthesise inorganic nanomaterials. Biomaterials often contain proteins, glycoproteins, polysaccharides and other organic biomolecules which form the organic part of these spectacular hybrid materials. The most commonly occurring metals in biomineralisation are calcium, iron and silicon and the most common non-metals are oxygen in the form of carbonate, oxalate and phosphates, see Table 5.1. Other metals found in biomaterials, although in limited cases and often as sulphides, are Mn, Au, Ag, Pt, Cu, Zn, Cd and Pb, which are

**Table 5.1** Selected examples of major biominerals, their forms and functions, adapted from (Currie et al. 2007)

Mineral	Forms	Functions
Calcium carbonates	Calcite, aragonite, vaterite, amorphous	Exoskeleton, eye lens, gravity device
Calcium phosphates	Apatite, brushite, octa calcium phosphate, amorphous	Endoskeleton, calcium store
Calcium oxalates	Whewellite, whedellite	Calcium store, deterrent
Iron oxides/hydroxides	Magnetite, goethite, lepidocrocite, ferrihydrite	Magnet, teeth, iron store
Silica	Amorphous	Skeleton, deterrent

formed typically in bacteria. Calcium dominates the biomineral world—roughly half of biominerals are calcium based. From structural perspective, approximately a quarter of biominerals do not possess order at atomic length scales (i.e. they are amorphous in nature, e.g. amorphous calcium carbonate and biosilica).

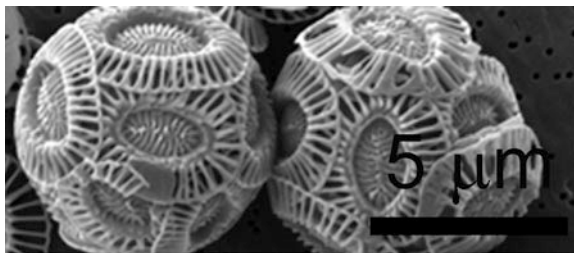
In the process of biomineralisation, organisms typically accumulate the precursors of biominerals from their environments. Prior to their conversion to biominerals and deposition into desired location, the precursors may be required to be stored and even transported *in vivo* to specialised compartments. There are two well-known forms of biomineralisation: controlled or uncontrolled. The former pertains to the minerals being formed for a specific biological function, which is strictly controlled (see examples in the section below). On the other hand, in uncontrolled biomineralisation process, biominerals are produced as by-products of other processes and these biominerals may be valuable, unfavourable or innocuous (e.g. kidney stones).

The compounds that are formed in biomineralisation are essentially simple salts and oxides. They occur as both crystalline and amorphous phases, except for silica, which has only been found in the amorphous form in living organisms. Despite the simplicity of the biominerals that are used by biology, the structures that result are highly sophisticated, complex and intricate as evident from Fig. 5.1 (Bauerlein 2000; Lowenstam and Weiner 1989; Mann 2001; Mann et al. 1989; Simkiss and Wilbur 1989). Table 5.1 provides a list of some of the important biominerals with their forms and functions.

### ***5.2.1 Functions, Properties and Selected Examples of Biominerals***

In most organisms, biominerals are produced for specific functions. Some of the known functions of biominerals include structural support, protection, motion, sensing, cutting and grinding, and buoyancy. In many organisms, deposited biominerals provide protection and therefore it is important in such biological

**Fig. 5.1** Coccolith skeleton composed of calcite, image adapted from (Leonardos et al. 2009) with permission of Wiley



systems to control the mechanical properties of these biominerals. This task is not a trivial one. For example with bones, the mineral content has been reported to differ between bone types and species. The end use of bones dictates their strength, stiffness and toughness, which can be modulated by the composition of bones (Wainwright 1976). The primary role of biosilica in plants such as rice and barley is to provide mechanical support to the plant thus allowing maximum exposure to sunlight, as well as offer resistance to biotic and abiotic stresses (Ma et al. 2006; Yamaji et al. 2012).

Biological systems have exploited biominerals as sensors. Magnetotactic bacteria precisely control the formation and assembly of single crystals of magnetite ( $\text{Fe}_3\text{O}_4$ ) (Moisescu et al. 2011). These magnetite crystals are typically identical to each other in terms of their sizes and shapes, and are patterned in a linear chain, see Fig. 5.2 (Arakaki et al. 2008; Mann et al. 1989). The bio-magnetite crystals help bacteria navigate using the Earth's magnetic field. Similarly, gypsum in jellyfish enables gravity sensing. Limpet and chiton teeth are biomineralised oxides or oxyhydroxides of iron ( $\alpha\text{-FeOOH}$ ,  $\gamma\text{-FeOOH}$  or  $5\text{Fe}_2\text{O}_3 \cdot 9\text{H}_2\text{O}$ ), Fig. 5.3. Marine molluscs and cephalopods use biomineralised aragonite ( $\text{CaCO}_3$ ) shells as buoyancy devices (Mann 2001). Organisms are also known to use biominerals as optical sensors. For example, sea urchins deposit a transparent layer of hemispherical calcite crystals, which appear to be a double-lens design (Fig. 5.4). It is these lenses that provide optical sensitivity due to the precisely uniform morphology of the calcite crystals (Aizenberg and Hendler 2004; Aizenberg et al. 2001).

These examples provide a flavour of the functions of biominerals, while an expanded list can be found in literature dedicated to types of biominerals (Lowenstam and Weiner 1989; Mann 2001; Mann et al. 1989; Simkiss and Wilbur 1989).

Biominerals are intriguing due to their unique characteristics such as chemical composition, structure, morphology and mechanical properties in comparison with the synthetic and geological minerals. Scientists have established that biological organisms control the chemical composition of the biominerals (discussed in subsequent sections). Very rarely biominerals are pure and often contain minor components (e.g. dopants). Doping biominerals with other ions and molecules enables the control over their chemical, physical and mechanical properties. The concentration of fluoride ions in teeth is known to regulate the chemical stability of enamel. Shark teeth, which contain a higher fluoride ion concentration (3.65 wt%),



**Fig. 5.2** Nano-magnets biomineralised in magnetotactic bacteria. Adapted from (Arakaki et al. 2008) with permission of the Royal Society of Chemistry

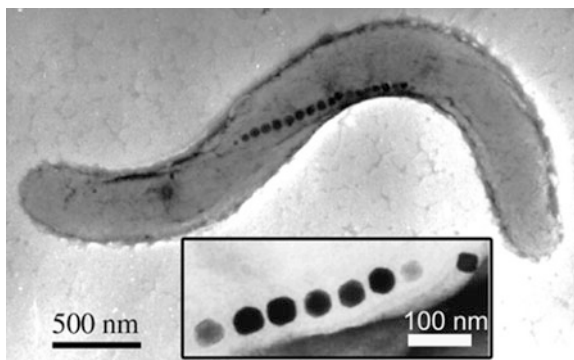
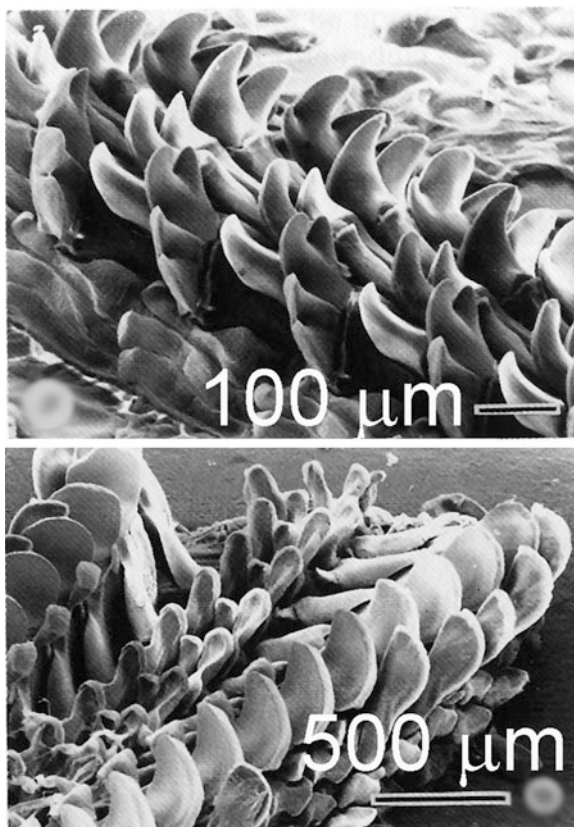
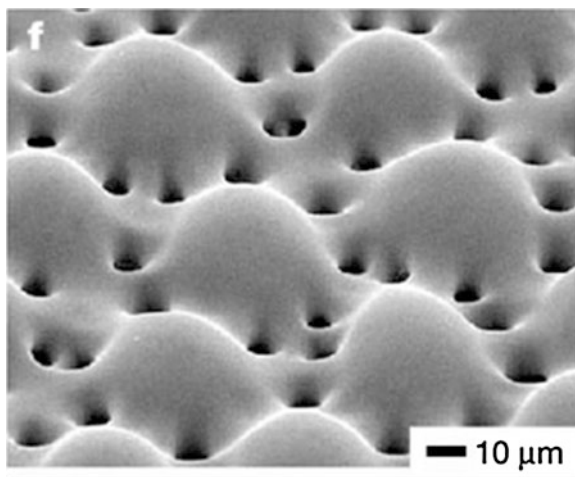


**Fig. 5.3** Scanning electron micrographs (SEM) of limpet (*top*) and chiton teeth. Reproduced from (Mann et al. 1989) with permission of Wiley-VCH and the authors



are highly resistant to dissolution when compared with human teeth with only 0.02 wt% fluoride ion content. In another example, it has been reported for calcite crystals that the presence of  $Mg^{2+}$  affects the growth, orientation, stability and morphology of calcite biominerals (Kwak et al. 2005; Politi et al. 2004).

**Fig. 5.4** Calcite lens from *O. wendtii*. Reprinted from (Aizenberg et al. 2001) with permission of Nature Publishing Group



Moreover, biominerals have been shown to occur as polymorphs—identical chemical composition but different crystalline structures. Calcium carbonate biominerals can be aragonite in the nacre plates, while they prefer calcite structure in coccolithophores (Addadi et al. 2003; Mann 2001).

In contrast to most other biominerals, biogenic silica ( $\text{SiO}_2 \cdot n\text{H}_2\text{O}$ ), which is deposited by microalgae, marine sponges and plants, is non-crystalline, i.e. lacks any atomic ordering. However, biosilica found in microalga (diatoms) typically possess regularly packed pores at tens and hundreds of nanometres length scales (Hildebrand 2008; Vrieling et al. 2004), Fig. 5.5. On the other hand, biosilica from sponges is essentially non-porous in the form of micro-needles, known as spicules (Müller 2003). This control over biomineral morphology becomes clearer when one considers the wide range of arrangements of silica nanoparticles reported in higher plants (Perry 1989).

### 5.3 Control of Nucleation and Growth in Biomineralisation

The section above has provided a background on some of the unique properties of biominerals and their biological functions. An outstanding attribute is the ability of biological systems to take simple components and manipulate them to produce functional biominerals which requires highest level of precision and control. In particular, both nucleation and growth of the mineral phases are regulated in biomineralisation. One of the most intriguing features of biological mineral formation is the regulation of the entire process of biomineralisation from the intake of simple components (ions and molecules) to the formation of ornate structures. It is this control that clearly separates the *in vitro* synthetic capabilities of mineralisation, that are presently far removed from the sophistication observed *in vivo*.

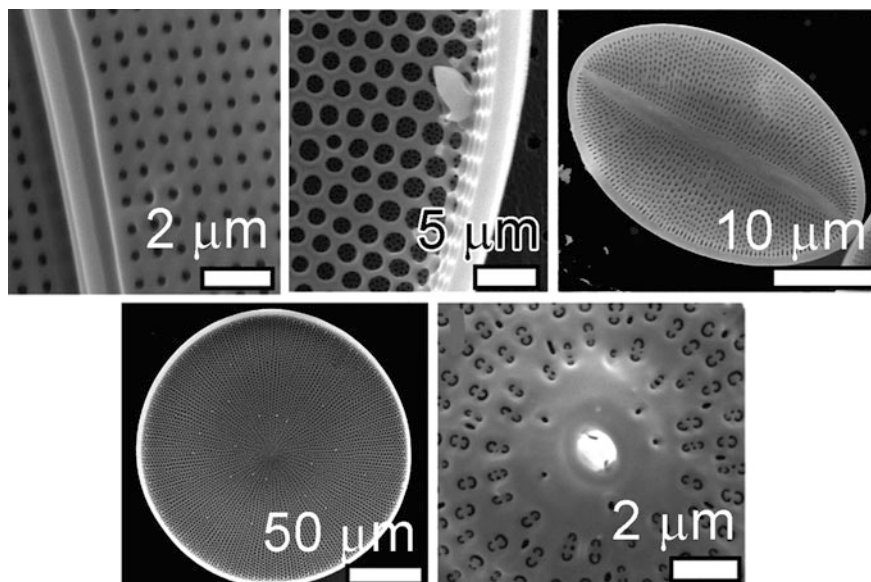


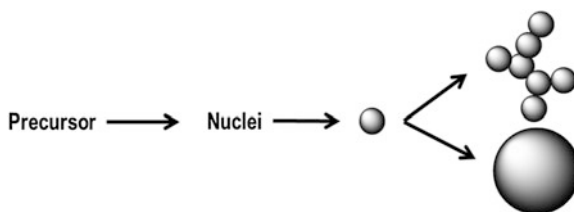
**Fig. 5.5** SEM of diatom biosilica, adapted from (Hildebrand 2008) with permission of American Chemical Society (Copyright 2008)

R. J. P. Williams clearly states—‘... inside [biological] space, the chemistry of the surface and/or of growth inhibiting compounds will control the precise compound which is precipitated’ (Mann et al. 1989). This suggests various control strategies involved in biomineralisation and these are discussed below.

Biomineral formation typically involves distinct nucleation, growth and ripening/maturation stages. When the concentration of biomineral precursors (ions/molecules) reaches supersaturation level, the formation of stable nuclei (a few angstroms in diameter) occurs (Fig. 5.6). Supersaturation is a function of the concentration of ions or molecular species and the solubility product for a given crystal phase. It is these solution properties that determine the structure of these nuclei, which in turn define the biomineral crystal structures. In the case of polymorphism, the solubility product values are specific to a given crystal, and hence the concentration of precursors at the nucleation stage can strongly influence the crystal structure (Nancollas 1982). The number of nuclei formed and the rate of their formation is dependent on supersaturation levels. Up to a certain supersaturation level the solution can be regarded as metastable where no nucleation occurs under fixed time. Once the supersaturation reaches its critical value, homogeneous nucleation takes place rapidly.

In biomineralisation, supersaturation can be chemically controlled through pH, ionic strength and/or the presence of biomolecules. pH is a powerful tool in initiating or inhibiting crystal formation and this is achieved through the pH dependent changes in ionic strengths of the precursors and the solubility product for a given crystal. Compartmentalisation allows biology to control the transport of

**Fig. 5.6** Nucleation, growth and maturation stages in biomineral formation are shown with the spheres representing building blocks, which can be crystals or amorphous cluster depending on the type of the biomineral and the conditions



certain ions and the local concentration of precursors, again regulating solubility product and hence biomineral formation. In addition to homogeneous nucleation, the presence of a surface offers reduced energy barrier for mineralisation and heterogeneous nucleation can occur. For example in bone formation, the adsorption of calcium ions onto glycoproteins offers increased local precursor concentrations and leads to localised bone formation.

Upon the formation of nuclei, a growth stage starts where these nuclei can undergo slow equilibrium or fast kinetic growth. In the former, the crystal size increases steadily, while the crystal morphology remains conserved (Fig. 5.6). In faster kinetic growth, the crystal face growth rates can differ for each face and as a result, changes in morphology can be observed during the growth phase. In the case of amorphous biomineralisation, the biomineral lacks in a fixed structure, and localised mineral formation, through compartmentalisation is typically observed. In order to regulate the growth rates, crystal phases and location for biomineral deposition, biology takes the advantage of specific adsorption of ions or biomolecules, which can affect the balance of interactions between biomineral-liquid and biomineral-surfaces.

The final stages of biomineral formation involve ripening, maturation and/or moulding. This stage is typically associated with very slow growth and restructuring of biominerals, and is caused by rapid depletion of the precursor and dissolution and re-precipitation of smaller particles. In some cases, remodelling and/or phase transformation of biominerals can also occur. Here the biomineral, which is initially formed in a transient phase, gets converted to their final functional form. Such remodelling has been observed during the sea urchin spicule formation where the initially formed amorphous calcium carbonate is converted into the final morphology and crystallises into calcite (Addadi et al. 2003; Politi et al. 2004).

## 5.4 The Role of the Organic Phase in Biomineralisation

In most stages of biomineralisation, organic biomolecules, such as peptides and proteins, lipids, polysaccharides, proteoglycans, etc., are involved and collectively, here they are termed organic phase. The organic phase is extremely crucial to

biomineral formation since it influences transport and storage of precursors, regulating mineral solubilities, catalysing reactions, templating biominerals and affecting biomineral stability. The organic phase can be functional, i.e. directly involved in regulating biomineralisation (Mann 2001), or it only acts as a framework. Their roles and effects include chemical, spatial, structural and morphological, and mechanical support. The organic phase is an effective tool used by organisms for controlling biomineralisation, and it can assemble in various forms. These include vesicles, networks, membranes, surfaces and at interfaces, and self-assembled structures.

Molecular recognition between biomolecules and biominerals is known to be important in biomineralisation (Mann 2001). These ‘nano-bio’ interactions can be viewed as chemical and/or physical interactions and they can occur at a range of length scales. As shown in Fig. 5.7, biomolecules, in soluble or self-assembled state, can interact with biomineral precursors, nuclei and/or larger building blocks. Such interactions can be driven by electrostatic forces, hydrophilic and/or hydrophobic effects, hydrogen bonding and van der Waals forces. Furthermore, the organic phase can catalyse biomineralisation. For example, it has been shown that in magnetotactic bacteria, the controlled formation of magnetite crystals occurs only in the presence of proteins that are tightly associated with the crystals (Galloway and Staniland 2012; Moisescu et al. 2011). Furthermore, the organic phase can also offer biomineral stabilisation by surface specific adsorption and inhibiting their dissolution, which is well known in the case of organic ‘casing’ found in diatoms.

Ultimately, biomineralisation is typically under strict biological/cellular control, which regulates all mechanisms discussed above. This helps to explain the significant dissimilarities observed between synthetic minerals and biominerals.

## 5.5 Bioinspired Nanotechnology

It appears that biology has identified ‘clever’ and green routes to produce ornate structures of nanomaterials (Sanchez et al. 2005) and an understanding of the secrets of biological mineral formation could lead to materials with novel applications and/or new technologies for nanomaterials production. It is clear that the implementation of the key features of biomineralisation into developing bioinspired nanotechnologies will be of great interest. This may allow the design of novel materials and technologies that are green and able to deliver sophisticated products. The question then is how do we transfer the knowledge obtained from biomineralisation into *in vitro* synthesis of nanomaterials in order to develop bioinspired materials technologies (Galloway et al. 2013). A number of ways are possible: *in vitro* model studies using biomolecules involved in biomineralisation in order to understand nano-bio interactions, and the use of bioinspired custom-made analogs of biomolecules (‘additives’) to produce cheaper and bespoke materials. These possibilities are discussed below with a representative example of

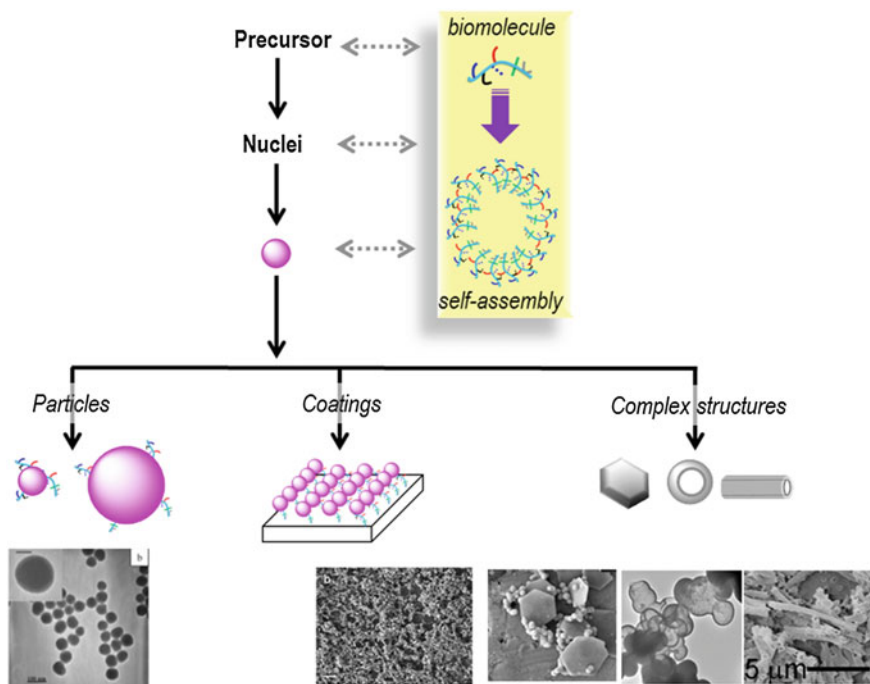


**Fig. 5.7** Schematic representation of possibilities of nano-bio interaction between mineral phases and biomolecules (both as individual molecules or self-assembled structures). These interactions can lead to the stabilisation of minerals or certain mineral phases, surface/site-specific growth and growth of complex structures. Such interactions can be exploited in bioinspired technologies in order to produce well-defined nanostructures such as particles, coatings and even more advanced nanomaterials. The electron micrographs in the bottom panel show representative examples of the fabrication of particles (Masse et al. 2008), coatings (Pogula et al. 2007), plates (Patwardhan 2011), hollow particles (Patwardhan 2011) and tubes (the micrograph kindly provided by Dr. T. Coradin) (Gautier et al. 2007). These micrographs have been reproduced with permission from respective publishers and remain copyright of the original publishers

silica, however, it is noted that research on bioinspired silica has also produced insights enabling synthesis and fabrication of valuable non-silicates such as ceramic, metallic and bimetallic materials (Dickerson et al. 2008; Patwardhan et al. 2007).

Biosilica is amorphous (no ordering below ca. 1 nm). Although the term ‘silica’ may lead to the impression of a single type of material, in reality, it consists of features such as the way in which the building blocks are assembled, the sizes of primary particles, secondary particles and aggregates, their porosities, the level of condensation/hydration (i.e. presence of silanol groups: Si-OH), and the surface chemistry (e.g. distribution of surface silanols and surface charge). These seemingly subtle differences which mainly arise from the processing conditions, can affect biodegradation (He et al. 2010) as well as nano-bio interactions (Patwardhan

et al. 2012). Biology produces silica, through biomineralisation, at scales  $>6.7 \times 10^9$  tonnes of silicon per year (Tacke 1999; Treguer et al. 1995), but all under mild conditions and achieves superior control over materials produced (Bauerlein 2000; Lowenstam and Weiner 1989; Mann 2001, Mann et al. 1989). The current industrial capacity for precipitated silica production is  $\sim 2.4 \times 10^6$  tonnes per annum, while silica-based materials form  $\sim \$3.6$  billion industry (Notch Consulting Group 2006). This industry covers a wide range of applications in catalysis, separations, food and drug technology, biomedical materials and paints (Flörke et al. 2000; Pagliaro 2009). The scale of biological silica deposition is orders of magnitude greater than the industrial capacity.

Researchers have unveiled mechanistic secrets of biosilica formation and it has become clear that through their chemistry and architecture, certain biomolecules play a crucial role in biomineral deposition. These biomolecules have been isolated, purified and used for *in vitro* mineralisation successfully. For example, biosilica forming biomolecules derived from diatoms, sponges, plants, and choanoflagellates have demonstrated the ability to control silica formation *in vitro* in aqueous systems and under mild conditions of pH and temperature (Cha et al. 1999; Currie and Perry 2007, 2009; Ehrlich et al. 2010; Gong et al. 2010; Harrison 1996; Krasko et al. 2000; Kröger and Poulsen 2008; Matsunaga et al. 2007; Perry and Keeling-Tucker 1998, 2003; Shimizu et al. 1998; Tesson and Hildebrand 2013; Zhou et al. 1999).

*In vitro* mineralisation experiments have developed bioinspired green routes by utilising a wide variety of ‘additives’ (analogs of biomolecules) (Patwardhan et al. 2005). As the understanding of the molecular interactions between additives and nanomaterials are beginning to become clear, control over green synthesis of nanomaterials and their properties is possible (Patwardhan 2011). Such investigations based on model systems afford the understanding of mechanisms underpinning biomineralisation, while simultaneously developing new bioinspired technologies as shown in Fig. 5.7 where a range of bioinspired nanomaterials have been obtained. For example, the rules that govern silica formation in the presence of additives have been identified and include the necessity of the presence of specific amino acids in a peptide; abundance of charged moieties; or the importance of self-assembly of additives prior to and during silica polymerisation.

In order to translate this knowledge into developing bioinspired technologies, further research has been directed towards the use of custom-made additives. These additives, which include synthetic polymers, block co-polymers, peptides, small molecules and dendrimers had been typically well-characterised in terms of their chemistry and their properties readily measured (Patwardhan 2011, Patwardhan et al. 2005). Furthermore, these tailored additives offer important advantages of controlling properties (e.g. structure and assembly) of silicas synthesised. *In vitro* experiments on silica formation have developed bioinspired or green routes to silica, whereby silica formation under mild conditions has been achieved (Coradin et al. 2004; Patwardhan 2011; Patwardhan et al. 2005), and a range of applications are envisaged, as discussed in subsequent chapters.

## 5.6 Summary and Future Outlook

Biology has mastered the fabrication of nanomaterials. Developing bioinspired strategies have completely changed the way scientists think of designing novel nanomaterials. These technologies have the ability to control material properties and synthetic methods such as nucleation and growth rates, structures and morphology, particles size, and porosity. One of the most important outcomes is the development of routes under mild synthetic conditions—all aqueous solutions, near-neutral pH, and ambient temperature. We now have a toolbox for developing novel bioinspired materials and their applications. More importantly, applications in areas ranging from biomedical materials to sensors and composite materials have started to appear. One could argue that learning from biology, ‘green’ routes to nanomaterials have been invented. If these advances are implemented in current industrial production, large savings, in addition to better control, could be achieved.

Without any doubts, the future challenges will be in demonstrating the versatility of this technology for generating applications that can make significant impacts. As reported recently (Matus et al. 2011), green nanotechnologies currently suffer from several barriers to their development. These include a lack of clear design rules for nanomaterials, incompatibility with existing manufacturing processes with the new bioinspired synthesis, lack of expertise spanning from green chemistry and engineering, and unclear end market demands. It is our job to address these shortcomings by carefully designing future research.

## References

- Addadi L, Raz S, Weiner S (2003) Taking advantage of disorder: amorphous calcium carbonate and its roles in biomineralization. *Adv Mater* 15:959–970
- Aizenberg J, Hendler G (2004) Designing efficient microlens arrays: lessons from nature. *J Mater Chem* 14:2066–2072
- Aizenberg J, Tkachenko A, Weiner S, Addadi L et al (2001) Calcitic microlenses as part of the photoreceptor system in brittlestars. *Nature* 412:819–822
- Anastas PT, Kirchhoff MM (2002) Origins, current status, and future challenges of green chemistry. *Acc Chem Res* 35:686
- Arakaki A, Nakazawa H, Nemoto M, Mori T et al (2008) Formation of magnetite by bacteria and its application. *J R Soc Interface* 5:977–999
- Baeuerlein E (ed) (2000) *Biomineralization: from biology to biotechnology and medical application*. Wiley, Chichester
- Cha JN, Shimizu K, Zhou Y, Christiansen SC et al (1999) Silicatein filaments and subunits from a marine sponge direct the polymerization of silica and silicones in vitro. *Proc Natl Acad Sci USA* 96:361–365
- Coradin T, Lopez PJ, Gautier C, Livage J (2004) From biogenic to biomimetic silica. *CR Palevol* 3:443–452
- Currie HA, Patwardhan SV, Perry CC, Roach P et al (2007) Natural and artificial hybrid biomaterials. In: KICKELBICK G (ed) *Hybrid materials—synthesis, characterization and applications*. Wiley, Weinheim



- Currie HA, Perry CC (2007) Silica in plants: biological, biochemical and chemical studies. *Ann Bot* 100:1383–1389
- Currie HA, Perry CC (2009) Chemical evidence for intrinsic ‘Si’ within equisetum cell walls. *Phytochemistry* 70:2089–2095
- Dahl JA, Maddux BLS, Hutchison JE (2007) Toward greener nanosynthesis. *Chem Rev* 107:2228
- Dickerson MB, Sandhage KH, Naik RR (2008) Protein- and peptide-directed syntheses of inorganic materials. *Chem Rev* 108:4935
- Ehrlich H, Deutzmann R, Brunner E, Cappellini E et al (2010) Mineralization of the metre-long biosilica structures of glass sponges is templated on hydroxylated collagen. *Nat Chem* 2:1084–1088
- Flörke OW, Graetsch HA, Brunk F, Benda L et al (2000) Silica. *Ullmann’s Encyclopedia of Industrial Chemistry*. Wiley, Weinheim
- Galloway JM, Bramble JP, Staniland SS (2013) Biomimetic synthesis of materials for technology. *Chem Eur J* 19:8710–8725
- Galloway JM, Staniland SS (2012) Protein and peptide biotemplated metal and metal oxide nanoparticles and their patterning onto surfaces. *J Mater Chem* 22:12423–12434
- Gautier C, Lopez PJ, Livage J, Coradin T (2007) Influence of poly-L-lysine on the biomimetic growth of silica tubes in confined media. *J Colloid Interface Sci* 309:44–48
- Gleiter H (1989) Nanocrystalline materials. *Prog Mater Sci* 33:223
- Gong N, Wiens M, Schroder HC, Mugnaioli E et al (2010) Biosilicification of loricate choanoflagellate: organic composition of the nanotubular siliceous costal strips of *Stephanocoa diplocostata*. *J Exp Biol* 213:3575–3585
- Harrison CC (1996) Evidence for intramineral macromolecules containing protein from plant silicas. *Phytochemistry* 41:37–42
- He QJ, Shi JL, Zhu M, Chen Y et al (2010) The three-stage in vitro degradation behavior of mesoporous silica in simulated body fluid. *Micropor Mesopor Mater* 131:314
- Hildebrand M (2008) Diatoms, biomineralization processes, and genomics. *Chem Rev* 108:4855–4874
- Knauth P, Schoonman J (2002) *Nanostructured materials*. Kluwer, Boston
- Krasko A, Lorenz B, Batel R, Schröder HC et al (2000) Expression of silicatein and collagen genes in the marine sponge *Suberites domuncula* is controlled by silicate and myotrophin. *Eur J Biochem* 267:4878–4887
- Kröger N and Poulsen N (2008) Diatoms—from cell wall biogenesis to nanotechnology. *Annu Rev Genet* 42:83–107
- Kwak SY, Dimasi E, Han YJ, Aizenberg J et al (2005) Orientation and Mg incorporation of calcite grown on functionalized self-assembled monolayers: a synchrotron X-ray study. *Cryst Growth Des* 5:2139–2145
- Leonardos N, Read B, Thake B, Young JR (2009) No mechanistic dependence of photosynthesis on calcification in the Coccolithophorid *Emiliana Huxleyi* (Haptophyta)1. *J Phycol* 45:1046–1051
- Lowenstam HA, Weiner S (1989) *On biomineralization*. Oxford University Press, New York
- Ma JF, Tamai K, Yamaji N, Mitani N et al (2006) A silicon transporter in rice. *Nature* 440:688–691
- Matus KJM, Hutchison JE, Peoples R, Rung S, et al (2011) Green nanotechnology challenges and opportunities. ACS Green Chemistry Institute
- Mann S (2001) *Biomineralization: principles and concepts in bioinorganic materials chemistry*. Oxford University Press, New York
- Mann S, Webb J, Williams RJP (eds) (1989) *Biomineralization*. VCH, Weinheim
- Masse S, Laurent G, Chuburu F, Cadiou C et al (2008) Modification of the Stober process by a polyazamacrocyclic leading to unusual core-shell silica nanoparticles. *Langmuir* 24:4026–4031
- Matsunaga S, Sakai R, Jimbo M, Kamiya H (2007) Long-chain polyamines (LCPAs) from marine sponge: possible implication in spicule formation. *Chem Bio Chem* 8:1729–1735

- Moiescu C, Bonneville S, Staniland S, Ardelean I et al (2011) Iron uptake kinetics and magnetosome formation by magnetospirillum gryphiswaldense as a function of pH, temperature and dissolved iron availability. *Geomicrobiol J* 28:590–600
- Müller WEG (2003) *Silicon biomineralization: biology, biochemistry, molecular biology, biotechnology*. Springer, Berlin
- Nancollas GH (1982) *Biological mineralization and demineralization*. Springer, Berlin
- Nel A, Xia T, Madler L, Li N (2006) Toxic potential of materials at the nanolevel. *Science* 311:622–627
- Notch Consulting Group (2006)
- Pagliaro M (2009) *Silica-Based Materials for Advanced Chemical Applications*. RSC Publishing, Cambridge
- Patwardhan SV (2011) Biomimetic and bioinspired silica: recent developments and applications. *Chem Commun* 47:7567–7582
- Patwardhan SV, Clarson SJ, Perry CC (2005) On the role(s) of additives in bioinspired silicification. *Chem Commun* 9:1113–1121
- Patwardhan SV, Emami FS, Berry RJ, Jones SE et al (2012) Chemistry of aqueous silica nanoparticle surfaces and the mechanism of selective peptide adsorption. *J Am Chem Soc* 134:6244
- Patwardhan SV, Patwardhan G, Perry CC (2007) Interactions of biomolecules with inorganic materials: principles, applications and future prospects. *J Mater Chem* 17:2875–2884
- Perry CC (1989) Biogenic Silica. In: Mann S, Webb J and Williams RJP (eds.) *Biomineralisation, chemical and biochemical perspectives*. VCH, Weinheim
- Perry CC and Keeling-Tucker T (1998) Crystalline silica prepared at room temperature from aqueous solution in the presence of intrasilica bioextracts. *Chem Commun* 9:2587–2588
- Perry CC, Keeling-Tucker T (2003) Model studies of colloidal silica precipitation using biosilica extracts from *Equisetum telmateia*. *Colloid Polym Sci* 281:652–664
- Pogula SD, Patwardhan SV, Perry CC, Gillespie JW et al (2007) Continuous silica coatings on glass fibers via bioinspired approaches. *Langmuir* 23:6677–6683
- Politi Y, Arad T, Klein E, Weiner S et al (2004) Sea urchin spine calcite forms via a transient amorphous calcium carbonate phase. *Science* 306:1161–1164
- Sanchez C, Arribart H, Guille MMG (2005) Biomimetism and bioinspiration as tools for the design of innovative materials and systems. *Nat Mater* 4:277–288
- Shimizu K, Cha J, Stucky GD, Morse DE (1998) Silicatein alpha: cathepsin L-like protein in sponge biosilica. *Proc Natl Acad Sci U.S.A* 95:6234–6238
- Simkiss K, Wilbur KM (1989) *Biomineralization*. Academic Press, San Diego
- Tacke R (1999) Milestones in the biochemistry of silicon: from basic research to biotechnological applications. *Angew Chem Int Ed* 38:3015–3018
- Tesson B and Hildebrand M (2013) Characterization and localization of insoluble organic matrices associated with diatom cell walls: insight into their roles during cell wall formation. *PLoS ONE* 8:e61675
- Treguer P, Nelson DM, Vanbennekorn AJ, Demaster DJ et al (1995) The Silica balance in the world ocean—a reestimate. *Science* 268:375–379
- Vrieling EG, Beelen TPM, Sun QY, Hazelaar S et al (2004) Ultrasmall, small, and wide angle X-ray scattering analysis of diatom biosilica: interspecific differences in fractal properties. *J Mater Chem* 14:1970–1975
- Wainwright SA (1976) *Mechanical design in organisms*. Edward Arnold, London
- Yamaji N, Chiba Y, Mitani-Ueno N, Ma JF (2012) Functional characterization of a silicon transporter gene implicated in silicon distribution in barley. *Plant Physiol* 160:1491–1497
- Zhou Y, Shimizu K, Cha JN, Stucky GD et al (1999) Efficient catalysis of polysiloxane synthesis by silicatein alpha requires specific hydroxy and imidazole functionalities. *Angew Chem Int Ed* 38:780–782

# Chapter 6

## Understanding Molecular Recognition on Metallic and Oxidic Nanostructures from a Perspective of Computer Simulation and Theory

Hendrik Heinz

**Abstract** In this chapter, surface properties of various solids at the nanometer scale and governing principles of the selective adsorption of molecules, surfactants, and biopolymers are reviewed and illustrated by examples. Clear distinctions emerge between elemental noble metal surfaces, polar pH-responsive surfaces, and ionic surfaces. Whereas the former are much simpler chemically and exhibit very attractive surfaces, many polar surfaces are prone to protonation/deprotonation equilibria and surface reactivity. These differences affect available options to control the assembly of surfactants, polymers, and biomacromolecules and grow nanomaterials from available precursors. Interestingly, we often encounter a wide variety of chemically different surfaces that originate from the “same” principal material. Our aim is to explain from the perspective of accurate atomistic models, simulation, and available results from experimentation the control mechanisms for selective binding to these different materials classes as far as they are known, as well as emerging concepts that play a role and warrant future investigation in detail.

### 6.1 Introduction

Hybrid materials containing various classes of compounds have become commonplace in all areas of life, including medical and communication devices, fabrics, automotive, building, and commodity materials (Sanchez et al. 2011; Osada and Sasaki 2012; Scrivener and Nonat 2011; Hagfeldt et al. 2010; Utracki et al. 2007). The challenge consists often in controlling the architecture from the nanometer scale to the macroscopic scale, i.e., from nanometers to millimeters or

---

H. Heinz (✉)

Department of Polymer Engineering, University of Akron, Akron,  
OH 44325-0301, USA  
e-mail: hendrik.heinz@uakron.edu

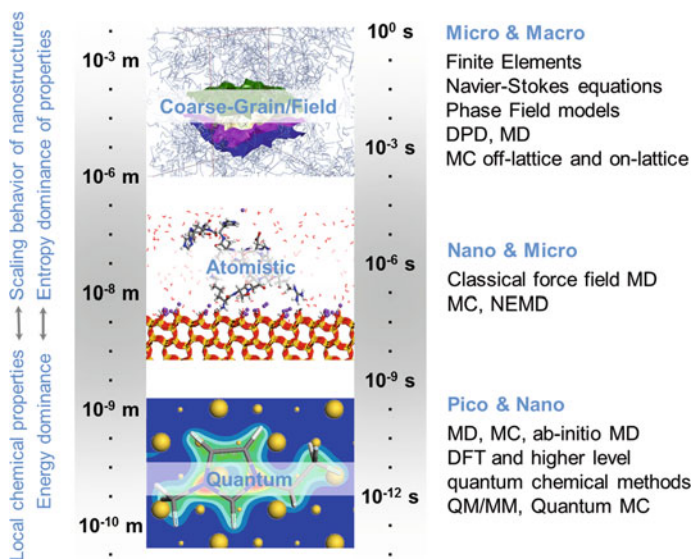


**Fig. 6.1** Different time and length scales of various current simulation methods (reproduced with permission from Ref. (Heinz et al. 2013))

even kilometers. Individual computational methods to examine structural, chemical, and physical properties typically span only a subsection of these length scales and can be combined or correlated with each other in multiscale approaches (Fig. 6.1) (Heinz et al. 2013). Similar to the coverage of different length scales, the coverage of common time scales of processes requires methods ranging from quantum mechanics, classical molecular dynamics to field-based and finite element simulations.

### 6.1.1 Surface Energies

Experimental, computational, and theoretical evidence has shown that control over self-assembly and morphology on the nanometer scale is influenced by the nature of the substrates, their chemistry, and inherent physical properties. For example, metal nanoparticles form crystalline structures at dimensions below 2 nm, oxidic minerals such as silica and titania often form larger amorphous structures with internal cavities from 10 nm to  $\mu\text{m}$  size, and many ionic minerals undergo hydration reactions and pH dependent chemical changes that result in a variety of structures and inorganic–organic composites such as seashells, bone, and teeth. Soft matter such as polymers and proteins also form particles through cross-linking, as well as domains through self-assembly. The definition and stability of nanostructures derived from these classes of materials decreases from metals to

**Table 6.1** Examples of cleavage energies for various classes of materials (data from Refs. (Tyson and Miller 1977; Wiederhorn et al. 1970; Ramaseshan 1946; Vigil et al. 1994; Zhuravlev 1993; Lewin et al. 2005; Heinz et al. 2005))

Compound	Lowest cleavage energy of ordered surfaces (mJ/m <sup>2</sup> )	Corresponding surface
Diamond	11300	{111}
Pt	2460	{111}
Pd	1980	{111}
Au	1540	{111}
Ag	1320	{111}
Tricalcium silicate	1300	{001}, {040}
Muscovite mica	375	{001}
Sodium chloride	330	{100}
Hydrated silica	80–250	NA
Nylon-4	49	NA
Polyethylene	30–37	NA
Polydimethylsiloxane	20–23	NA

soft macromolecules and it appears conceptually intriguing to relate these trends to the cleavage energy (or surface energy) of these materials (Table 6.1) (Tyson and Miller 1977; Wiederhorn et al. 1970; Ramaseshan 1946; Vigil et al. 1994; Zhuravlev 1993; Lewin et al. 2005; Heinz et al. 2005). The cleavage energy measures the cost to leave a surface bare and decreases in the same order as the definition of nanostructures and microstructures that can be obtained. The higher the surface energy, the better is the principally possible definition of a nanostructure.

A closer look reveals that the perhaps highest surface energies are found for diamond, boron nitride, and other strongly covalent solids (Table 6.1) (Ramaseshan 1946). The creation of surfaces then requires breaking strong covalent chemical bonds which is difficult to control due to high strength and chemical inertia. However, noble metals have some of the highest surface energies known, in excess of 2000 mJ/m<sup>2</sup>, and often pack in simple fcc and hcp structures (Tyson and Miller 1977; Heinz et al. 2008b). Metal nanostructures can be easily assembled by reduction of soluble precursors in solution and achieve a very high degree of crystallinity due to the high surface energy. Platinum, for example, can form small octahedra, cuboctahedra, and tetrahedra on the 5 nm scale using simple peptide ligands in reductive synthesis, which is more difficult for gold with lower surface energy (Chiu et al. 2011; Slocik et al. 2005). In comparison, the surface energy of ionic minerals is typically lower than for metals and only 375 mJ/m<sup>2</sup> for muscovite mica and even less for hydrated silica. This relative weakness of surface forces, as well as often higher surface reactivity, creates a barrier to obtain well-crystallized structures using bottom-up approaches. Polymers, proteins, DNA, and other soft molecules possess the lowest surface energies and weakest self-assembling forces, on the order of 20–70 mJ/m<sup>2</sup> (Lewin et al. 2005). Nevertheless, the range is widely tunable depending on pH, ionic strength, solvent, temperature, and involves highly residue-specific recognition as well as entropy contributions. As a result of weaker

cohesion, however, the stability of such structures is limited to certain conditions and perfect order rarely achieved by synthetic means. Examples for sensitive stabilization–destabilization processes are the denaturation of proteins, UCST, and LCST transitions of polymers, the phase behavior of micelles, and morphologies of multiblock copolymers.

The examples indicate that the interpretation of surface energies and surface chemistry may serve as a cornerstone to understand the feasible degree of order of nanostructures, dependence on chemical environment, and obtain guidance toward appropriate tools for tailoring structures at the nanometer scale.

### ***6.1.2 Chemical Bonding in Solids***

In addition to the overall attraction toward a nanoscale surface, surface and interfacial chemistry play a key role for the functionality. Unique chemical reactivity of different classes of materials involves, for example, catalytic hydrogenation reactions and formation of thiol bonds on metal nanoparticle surfaces, hydration reactions in cement, acid–base equilibria on apatite surfaces, and cross-linking of polymer chains. The unique differentiation in surface properties, which arises from specific differences in chemical bonding, thus translates into range of unique chemical reactivity. In the following, we will therefore more closely examine the specifics of processes such as (1) chemisorption of organic molecules on noble metal surfaces in vacuum and physisorption in the liquid phase, (2) condensation reactions and proton transfer equilibria on silica surfaces, (3) reversible ion pairing, hydrogen bonds, conformation transitions, and geometric fit of van-der-Waals interactions during binding of a drug molecule to a specific pocket of an enzyme.

The differences in molecular behaviors are directly related to the relative strength of covalent bonds, metallic bonds, ionic bonds, and intermolecular interactions (dipolar, hydrogen bond, van-der-Waals). These types of bonds can be seen as representatives of different classes of chemical bonding that can contribute to any partial degree in a given system and determine both thermodynamic and kinetic properties. Covalent bonds, for example, are often still associated with the textbook examples of C–C and H–H bonds with bond energies on the order of 100 kcal/mol (Lide 2008). However, covalent character is also associated with Au–S bonds in thiols and Au–H bonds in catalysts that are only around 10 kcal/mol strong, and even sulfur coordinates with epitaxial sites rather than with atoms in the topmost layer (Dubois et al. 1990; Heinz et al. 2008a). Also the closest Au–S and Au–H distances are on the order of 3 Å and 2 Å, almost twice the values for typical C–C or C–H bond length. These data indicate a different type of covalent bonding, up to an order of magnitude weaker than the well-known examples. This type of bonding only equals the strength of two to three hydrogen bonds and may well be considered as metal-coordinative bonding or weak covalent bonding.

On the other hand, the cohesive energy in metals is often quite large, on the order of 30–50 kcal/mol for noble metals, and thus similar to covalent bonding in

strength (Lide 2008). The nature of metal bonding allows surface reconstruction, reversible removal of single metal atoms in catalytic reactions, and etching by oxidation without strong ionic interactions. Strong bonding is consistent with high surface energies, high elastic moduli, and a strong preference for close-packed structures with long-range order.

Ionic interactions are primarily important in minerals, although very few compounds are more than 95 % ionic and many minerals are even predominantly covalent (Heinz and Suter 2004a). Fully ionic compounds include about half of the alkali halides and  $\text{CaF}_2$  and the actual balance between covalent versus ionic contributions to bonding for most other compounds determines many physical and chemical properties. The truthful representation of this balance is also detrimental for the quality of molecular models and force fields. For example, RbI is best described by a Rb charge of  $+0.8 \pm 0.1e$ ,  $\text{BeF}_2$  by a Be charge of  $+1.0 \pm 0.1e$ , and  $\text{SiO}_2$  by a Si charge of  $+1.1 \pm 0.1e$ . Similarly, charges in anions are far from formal charges, e.g., in  $\text{SO}_4^{2-}$  is best described by a S charge of  $+0.4 \pm 0.2e$  and O charges of  $-0.5$  to  $-0.6$  depending on the actual charge on the corresponding cation (Heinz et al. 2013; Heinz and Suter 2004a). The relationship of these covalent versus electrostatic contributions to bonding can be evaluated using cohesive energies, atomization, and ionization energies of the elements in an extended Born model. In addition, experimental data are available in the form of X-ray deformation electron densities for a significant range of compounds, as well as dipole moments for numerous molecules, physical data on melting points, solubility, as well as abundant data on chemical reactivity in heterolytic reactions (Lide 2008).

Among the nonbonded interactions, ion–ion and ion–dipole interactions are the strongest. The energy can amount to tens of kcal/mol, higher than weak covalent bonds. Further, hydrogen bonds play an ubiquitous role especially in biopolymers and are typically of a strength of 1–5 kcal/mol. Van-der-Waals interactions result from many weak pairwise interactions that individually are 0.05–0.2 kcal/mol strong per pair of atoms.

## 6.2 Soft Epitaxial Recognition on Metal Nanostructures

### 6.2.1 *Even Metal Surfaces and Coordination of Epitaxial Sites*

Molecular simulations of a more than 30 different peptides on extended gold, palladium, and platinum surfaces in aqueous solution using the CVFF-METAL and CHARMM-METAL force field have shown differences in the attraction to {111} and {100} facets (Heinz et al. 2009; Ruan et al. 2013; Feng et al. 2012; Coppage et al. 2013). These differences are relatively independent of the actual peptide sequence, whether identified as a strong binder by phage display or chosen as a random control sequence such as Pro-10 (Fig. 6.2). All peptides are strongly

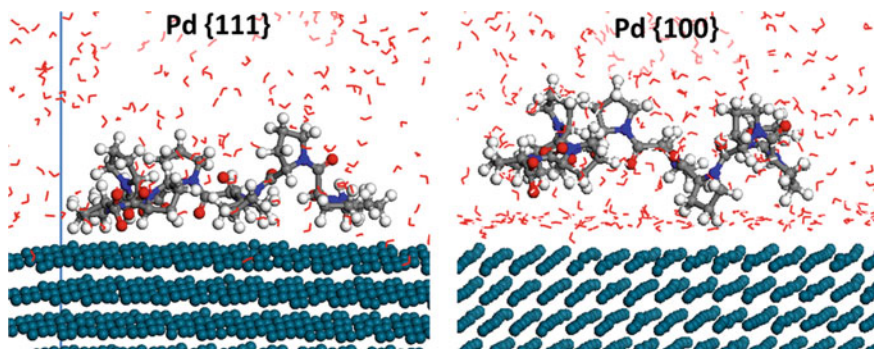


**Fig. 6.2** Snapshots of a proline decapeptide in contact with palladium {111} and {100} surfaces in aqueous solution. Direct contact with the {111} surface is seen, resulting in stronger adsorption and adaptation of the proline helix. A water interlayer persists on the {100} surface where adsorption is about an order of magnitude weaker (reproduced with permission from Ref. (Heinz et al. 2009))

attracted to {111} surfaces, up to  $-50$  kcal/mol for a 12-peptide on Au {111}, and much less attracted to {100} surfaces, typically with small negative or positive adsorption energies of  $\pm 5$  kcal/mol. The exact affinity to each surface and the binding differential between {111} and {100} surfaces varies notably depending on the peptide sequence even though the trend is universal. The type of fcc metal also makes no difference in the trend of strong attraction to {111} facets versus weak interaction with {100} facets, although the exact magnitude of attraction of the same peptide to {111} facets of different metals is roughly proportional to the surface energy, e.g., Pt > Pd > Au > Ag (Table 6.1). Further, it was noted that residues such as F, R, Y, W, H, as well as D spend more time in close contact with {111} surfaces than others while generally most residues are in direct contact with the {111} surface. In contrast, a water interlayer is maintained between most residues and the {100} surface, thus resulting in lower adsorption energy (Fig. 6.2).

At first, the observations in atomic resolution and the consistent trends in computed binding energies were surprising. Then, it did not take long to recognize the agreement with numerous observations. Peptides were repeatedly reported to bind to extended {111} facets in independent studies while no significant binding was reported to extended {100} facets. Apparently stronger binding of “gold binding peptides” (i.e., peptides combinatorially selected as binding to gold) to palladium and still considerable binding of the same peptides to silver were noticed experimentally as well. The mechanism of adsorption based on these simulation results and experimental data was thus concluded to involve soft epitaxial adsorption, which involve the coordination of polarizable atoms (C, N, O) in the peptides with epitaxial (fcc, hcp) sites on the metal surface (Fig. 6.3). This concept offers a unique explanation as common  $sp^2$  and  $sp^3$  hybridized groups in peptides exhibit a very good geometric fit to {111} metal surfaces (Fig. 6.3a), no matter what type of metal is present (Fig. 6.3b). In particular, the phenyl ring of



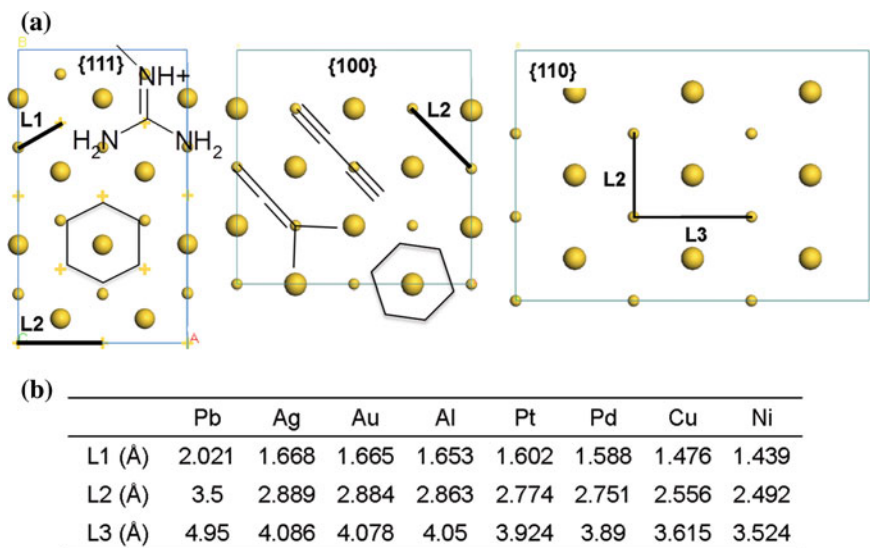


**Fig. 6.3** Concept of soft molecular epitaxy. **a** The hexagonal symmetry of the {111} surface provides epitaxial sites (*fcc* and *hcp*) that match the common geometry of  $sp^2$  and  $sp^3$  hybridized molecules such as benzene and guanidinium groups. {100} surfaces exhibit a square geometry of 2.88 Å spacing that is incommensurate with typical chain molecules, unless allenes or polyynes. The competition between solvent (water) and solutes will then be in favor of water and no significant attraction is achieved. {110} surfaces possess small and wide grooves that may be further enhanced by surface reconstruction. Adsorption is then less molecule specific. **b** The similarity in characteristic spacing of epitaxial sites (*L1*, *L2*, *L3*) leads to similar attraction of molecules and polymers on different noble metals. Differences in attraction, however, arise from unique surface energies and nonidentical characteristic spacing. According to the surface structure, matching molecules can be designed, aided by simulation for sampling and solvent effects (reproduced with permission from Ref. (Feng et al. 2011))

hexagonal symmetry could best coordinate {111} surfaces in contrast to {100} and {110} surfaces. On the latter surfaces, linear molecules have better probability to coordinate epitaxial sites. The strength of adsorption is finally a result of competition between the molecules and water molecules that are mobile and adjust to any type of {*h k l*} surface. Therefore,  $sp^2$  and  $sp^3$  groups cannot effectively compete with water molecules for epitaxial sites on {100} surfaces, thus leaving a water interlayer and small adsorption energies. The phenyl ring, for example, typically assumes tilted conformations relative to the {100} surface plane whereas a flat-on parallel conformation is observed on {111} surfaces. Of particular interest is also the characteristic lattice spacing *L1*, *L2*, *L3* of individual metal surfaces, which provides a measure of the goodness-of-fit to adsorbing molecules and a tool to rationally design entire molecules for binding to a given metal surface (Fig. 6.3).

The optimum coordination of epitaxial sites on {111} surfaces can be nicely seen in detail for arginine (Fig. 6.4). Polarizable atoms avoid proximity to metal

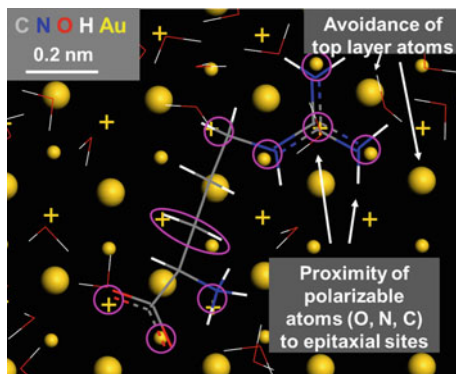


**Fig. 6.4** Illustration of soft epitaxial adsorption of arginine in aqueous solution on a gold {111} surface according to molecular dynamics simulation. Several epitaxial contacts are highlighted by *pink circles*. The molecule moves laterally on the surface by a hopping mechanism to other surface sites with similarly good epitaxial coordination in intervals on the order of 100 ps at room temperature (reproduced with permission from Ref. (Feng et al. 2011))

atoms in the top layer, and we have also computed the affinity of all 20 amino acids as well as some surfactants (single molecules) with the Au {111} surface in aqueous solution (Fig. 6.5) (Feng et al. 2011). Using the same thermodynamically consistent Lennard-Jones parameters for the metal (Heinz et al. 2008b), the trend depends somewhat on the force field parameters for the amino acids. The CHARMM-METAL results are preferred over CVFF-METAL, however, since CVFF is comparatively less validated and overestimates attraction of aromatic molecules. The results show the order of attraction approximately as:

$$\text{Arg} > \text{Trp} > \dots \text{Tyr} \dots > \dots \text{Phe} \dots \text{His} \dots \text{Ser} \dots > \text{Ala} \quad (6.1)$$

This trend indeed coincides with the relative strength of adsorption inferred from the abundance of amino acids in gold-binding peptides identified by phage display and other metal-binding peptides (Slocik et al. 2005; Hnilova et al. 2008; Fu et al. 2003; Naik et al. 2004; Slocik and Naik 1988; Slocik and Wright 2003). Further supporting evidence includes the attraction of metal-binding peptides such as A3 and GBPs in experiment to Ag {111}, Au {111}, and Pd {111} surfaces, which is explicable by the similar L1 spacing (Fig. 6.3b). Also, studies by several groups have shown that only peptides containing strongly binding amino acids, or such amino acids alone, could stabilize and control the shape of nanoparticles synthesized reductively from solutions of metal salts. Another interesting observation of amino acid sublattices on copper surfaces was made over 30 years ago by Low Energy Electron Diffraction (LEED) measurements (Fig. 6.6) (Atanasoska 1978). The likely arrangement of atoms due to the orientation of the sublattice also indicates avoidance of top layer atoms and possible epitaxial contacts. Also, adsorption data of alkane monolayers on Pt {111} surfaces suggest soft epitaxial order (Firmant and Somorjai 1977).

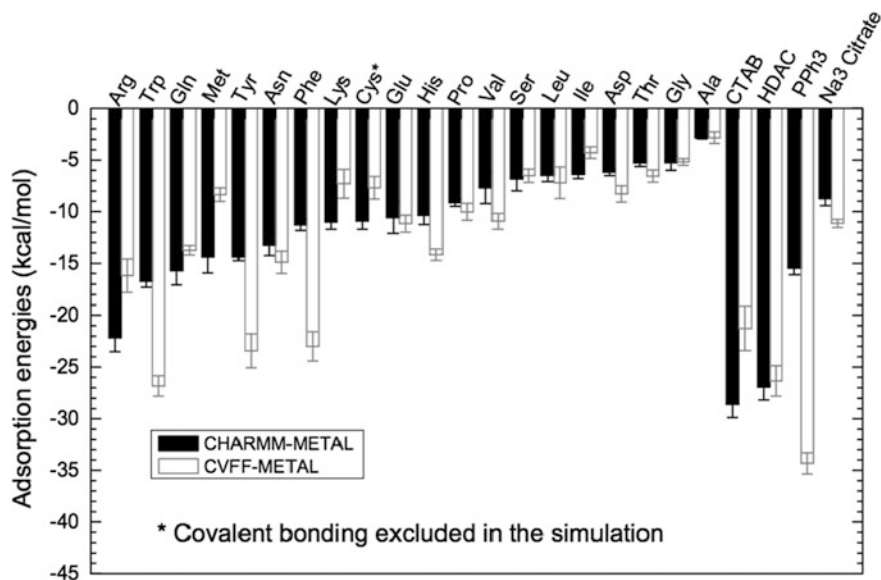


**Fig. 6.5** Computed adsorption energies of the natural amino acids and some surfactants on gold {111} surfaces in solution. Results of the CHARMM-METAL and the CVFF-METAL force field are shown, whereby CHARMM-METAL values are better supported by more accurate parameters for the amino acids. The data refer to single molecules in the limit of high dilution (reproduced with permission from Ref. (Feng et al. 2011))

## 6.2.2 Nanocrystals, Topographic Substrates, and Particles

An interesting application of the soft epitaxial concept is the selective stabilization of crystal facets during nanoparticle nucleation and growth from seed crystals. The stabilizing effect of phenyl rings toward {111} facets predicted from simulation could be applied during growth of platinum seed crystals upon reduction of hexachloroplatinic acid in the presence of ascorbic acid as a mild reducing agent (Fig. 6.7) (Ruan et al. 2013). Different phenylalanine containing peptides were employed as shape-directing templates. About 20 neutral, end-protected peptide sequences with and without F showed that the presence of the phenyl ring anywhere in the peptide sequence is sufficient as a molecular switch that converts cuboctahedra or cubic nanocrystals into tetrahedra during growth from seed crystals. Resulting tetrahedra are bounded exclusively by {111} facets, stabilized and slowed down from further growth by phenylalanine. The approach also functions for other molecules such as 3-Hydroxybutyric acid with phenyl substitution, as well as for Rh nanocrystals rather than Pt nanocrystals.

The main driving force for shape control according to simulation is the binding differential of the peptide to {111} versus {100} surfaces rather than the absolute binding strength to a specific facet (Fig. 6.8). The binding energy of all peptides, with or without F, is about equally high on {111} facets and shows no correlation

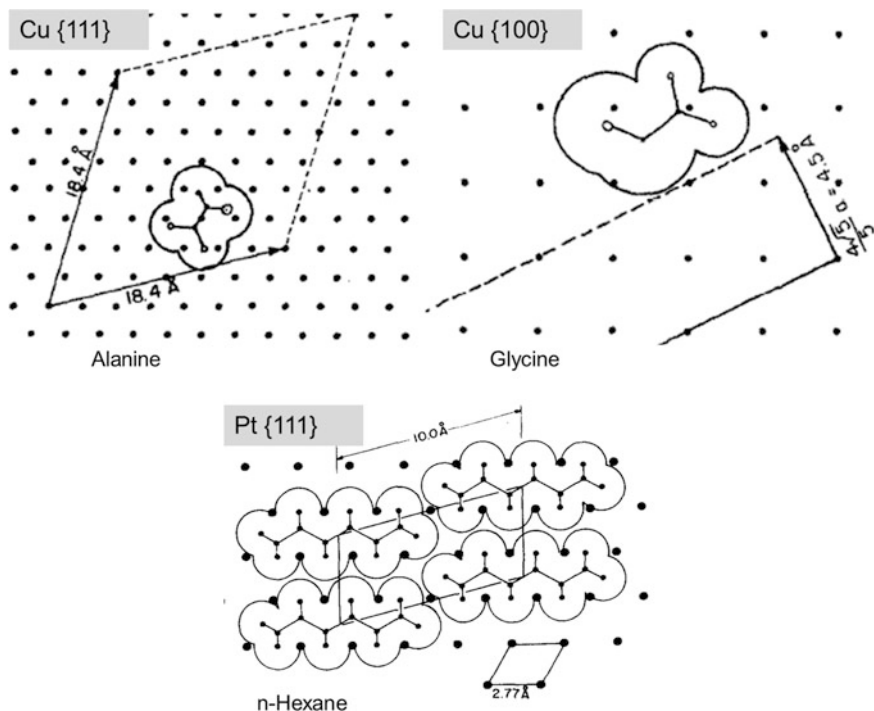


**Fig. 6.6** Suggested arrangement of amino acids at monolayer coverage on copper {111} and {100} surfaces, and of n-hexane on platinum {111} surfaces according to LEED measurements. The proposed arrangement of the molecules is consistent with the soft epitaxial mechanism by simulations (reproduced with permission from Refs. (Atanasoska LL 1978; Firment and Somorjai 1977))

with yield of tetrahedra (Fig. 6.8a). However, the binding energy of the peptides to {100} facets correlates well with the yield of tetrahedra, whereby the F-containing peptides (S7, S7-1, S7-2, SSF, FPQPN) show positive adsorption energy and the F-free peptides (S7-G, PQPN, S7-Y, SSY) show negative, attractive adsorption energy. Thus, the F-containing peptides leave the {100} facet more accessible to growth and complete {111} facets. On the contrary, the F-free peptides are slightly attracted to {100} surfaces and protect these facets from the exclusive growth of {111} facets. Particularly, we note the sensitivity of the models toward phenyl-alanine versus tyrosine (Fig. 6.8b). The phenyl ring in S7 is oriented parallel to the {111} surface and upright on the {100} surface as only two weak epitaxial contacts are feasible. The phenol ring in S7-Y, on the contrary, can form three epitaxial contacts on the {100} surface and position itself parallel. The addition of one hydroxyl group in Y versus F thus leads to loss of perfect hexagonal symmetry and stabilizes {100} surfaces.

The elucidation of mechanisms of shape control is also possible for different nanocrystal shapes such as cubes and twins aided by simulations, which will be

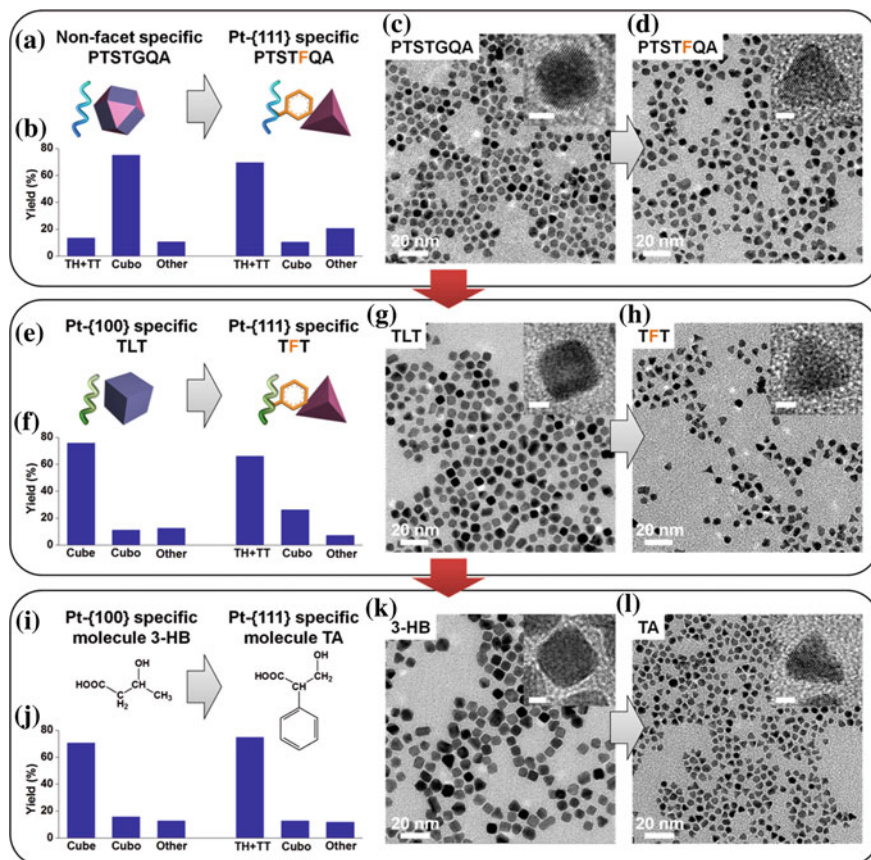


**Fig. 6.7** Application of epitaxial recognition of the phenyl ring by {111} facets to shape selective synthesis of Pt tetrahedra. **a–d** A cubooctahedron forming peptide sequence produces Pt tetrahedra upon substitution of one amino acid by phenylalanine. **e–h** A cube forming sequence also yields tetrahedra upon substitution of L by F. **i–l** A molecular shape-directing agent is transformed from cube-directing to tetrahedron-directing in an analogous way. High resolution TEM micrographs (**c,d,g,h,k,l**) indicate the shape changes (adapted and reproduced with permission from Ref. (Ruan et al. 2013))

soon explained in separate discussions. Thereby, the influence of nanoparticle shape on adsorption of solvents and solutes is quite substantial (Fig. 6.9) (Feng et al. 2012). We can distinguish geometric factors as well as factors related to the pattern of epitaxial sites. Even surfaces provide many metal atoms in the vicinity of the molecule of polymer to interact with and thus lead to strong epitaxial adsorption. Stepped surfaces contain inner edges and outer edges. Inner edges provide the highest number of metal atoms to interact with and lead to strongest adsorption, which is also shown in the surface potential. These sites are easily accessible by small solvent molecules and may not be sterically accessible by

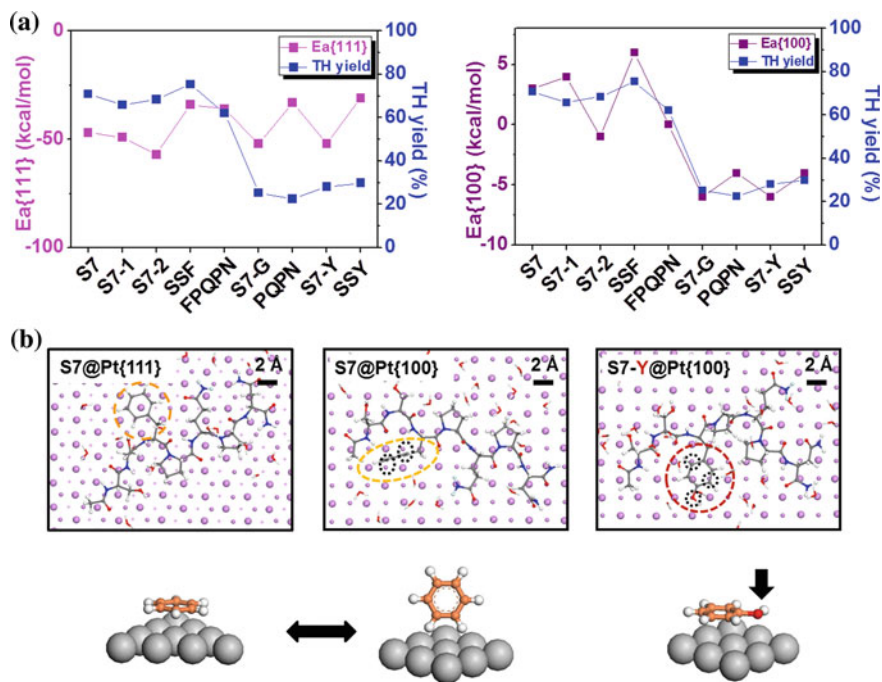


**Fig. 6.8** Relation of computed binding energies of various peptides, their conformations, and preferred nanocrystal shape in experiment. **a** The binding energy to the {111} surface is about equally strong among F-containing (S7 etc.) and F-free peptides (S7-G etc.). No correlation with the yield of tetrahedra is seen. The binding energy to the {100} surface is positive for F-containing and negative for F-free peptides. A direct correlation with yield of tetrahedral is seen, whereby F-containing peptides increase the unattractiveness of {100} facets. **b** Accordingly, the orientation of the phenyl ring in S7 is flat-on on {111} facets and upwards on {100} facets. A small substitution for phenol in S7-Y also leads to flat-on adsorption on {100} facets due to coordination of more epitaxial sites and helps protect {100} facets during growth (reproduced with permission from Ref. (Ruan et al. 2013))

larger molecules, however. Outer edges are least attractive sites for both peptides and solvent molecules. The differences in local dynamics can change the outcome of the competition between solvent and solute molecules, for example, faster solvent motion near the corners of nanocubes can improve adsorption of less mobile peptides. Therefore, adsorption is not only a facet-specific process but also depends on the local position of the solute on a finite-size facet. Finally, small nanoparticles with near-spherical geometry possess typically diminished adsorption of solvent and peptides, including less binding contrast among different peptides, as well as a reduced surface potential. Specific data have been reported by simulation (Feng et al. 2012) and experiment (Lacerda et al. 2010; Jiang et al. 2008) for various peptides in support of these arguments.

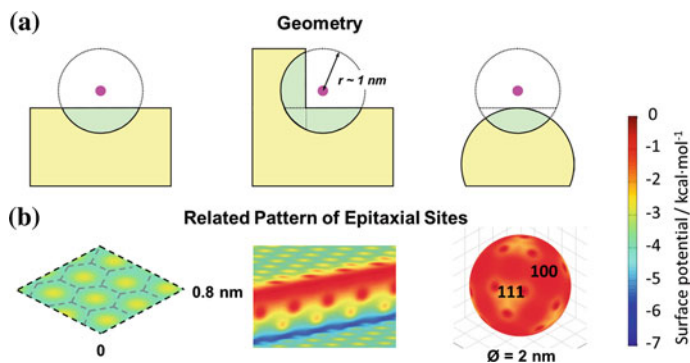


**Fig. 6.9** Dependence of adsorption of atom and molecules on the shape of a metal surface. **a** An atom (*red sphere*) or a molecule as a collection of such atoms is more attracted to even surfaces and inner edges, and less attracted to small near-spherical surfaces or outer edges (not shown). **b** The surface potential (= attraction of a carbon atom at 3 Å distance) reflects these general preferences and includes details of the pattern of epitaxial sites. The strength of adsorption of both solvents and solutes depends significantly on the local surface topology of a nanostructure. Adsorption and selectivity are weakest toward small nanoparticles (reproduced with permission from Ref. (Feng et al. 2012))

Often used near-spherical nanoparticles are also characterized by the presence of different facets, including {111}, {100}, and {110}. For thermodynamically stable particles, the ratio of these facets amounts to about 60:20:20 whereby the amount of {100} versus {110} may somewhat differ depending on size (Ramezani-Dakhel et al. 2013). The classification of the surface can also be further extended to atom types, which play a role in catalytic reactions such as Stille coupling (Fig. 6.10). The force field was shown to allow quantitative estimates of abstraction energies and reaction rates in Stille coupling (where such processes can be rate-determining).

### 6.2.3 Induced Charges and Weak Covalent Bonding

Further contributions to adsorption of organic molecules to metal surfaces may arise from induced charges and weak covalent bonding. Induced charges typically play a subordinate role in the first molecular layer of contact when epitaxial binding is strong, such as for peptides on {111} surfaces (Table 6.2) (Heinz et al. 2011). They can be primary contributions to adsorption, however, for charged molecules on epitaxially less attractive surfaces, e.g., charged peptides on {100} surfaces. For strongly ionic molecules such as CTAB surfactants or ionic liquids, the second molecular layer may experience more attraction due to induced charges than other attractive interactions independent of the strength of epitaxial matching

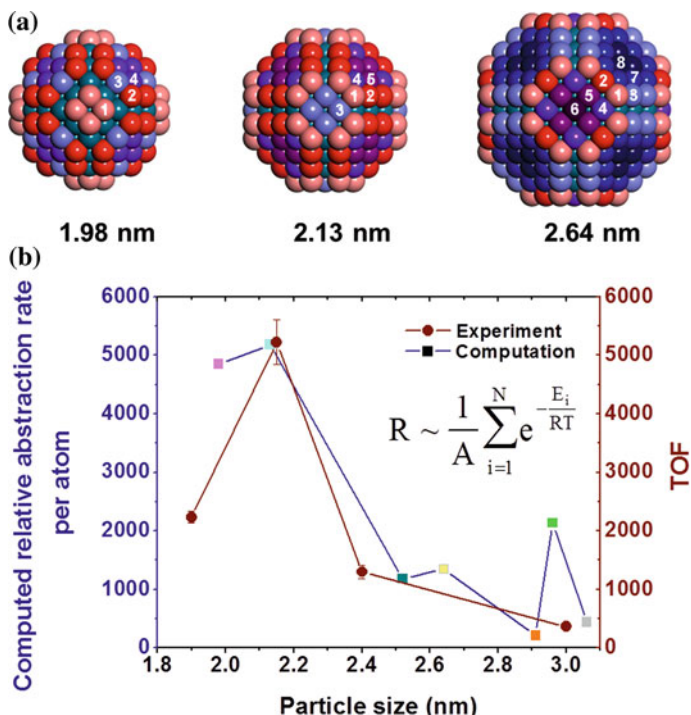


**Fig. 6.10** **a** Visualization of stable, near-spherical nanoparticles as a function of nanoparticle size. Atoms from lowest to highest abstraction energy are labeled by numbers and shown from *lighter* toward *darker color*. **b** Computed versus measured reaction rates in Stille coupling reactions as a function of particle size. The relative reaction rate was computed using a Boltzmann-weighted average of the abstraction energies of all surface atoms (reproduced with permission from Ref. (Ramezani-Dakhel et al. 2013))

(Jha et al. 2013). Overall, the strength of induced charges increases with the magnitude of charges and the distance between corresponding positive and negative charges in a surface-adsorbed molecule.

### 6.3 Ion Pairing and Hydrogen Bonding on pH-Responsive Oxide Surfaces

Adsorption is governed by a very different mechanism on oxide surfaces such as silica or apatites (Patwardhan et al. 2012). The surface energy is almost an order of magnitude lower than for metals (Table 6.1) and the surface structure dominated by a locally uneven pattern of silanol groups and ionized siloxide groups. As a consequence, soft epitaxy is not a possible adsorption mechanism. Further, silica and oxidic minerals are insulators rather than conductors and possess no



**Table 6.2** Contributions to adsorption by attractive polarization (induced charges) and soft epitaxy for a neutral peptide A3 and a charged peptide Flg–Na<sub>3</sub> on gold surfaces in aqueous solution

Surface	Peptide	Net attraction by polarization $E_{\text{Pol}}^N$ (kJ mol <sup>-1</sup> )	Net attraction by epitaxy $E_E^N$ (kJ mol <sup>-1</sup> )
Au {111}	A3	-28 ± 4 [-6 ± 16]	-260 ± 20
	Flg–Na <sub>3</sub>	-12 ± 4 [-10 ± 16]	-260 ± 20
Au {100}	A3	-16 ± 12 [+10 ± 16]	-38 ± 20
	Flg–Na <sub>3</sub>	-80 ± 20 [-69 ± 8]	0 ± 20

The contribution by polarization was evaluated by two approaches, direct calculation of the attractive image potential in the presence of water and peptide, though contributions from peptide and surface-replaced water (in square brackets, reproduced with permission from Ref. (Heinz et al. 2011))

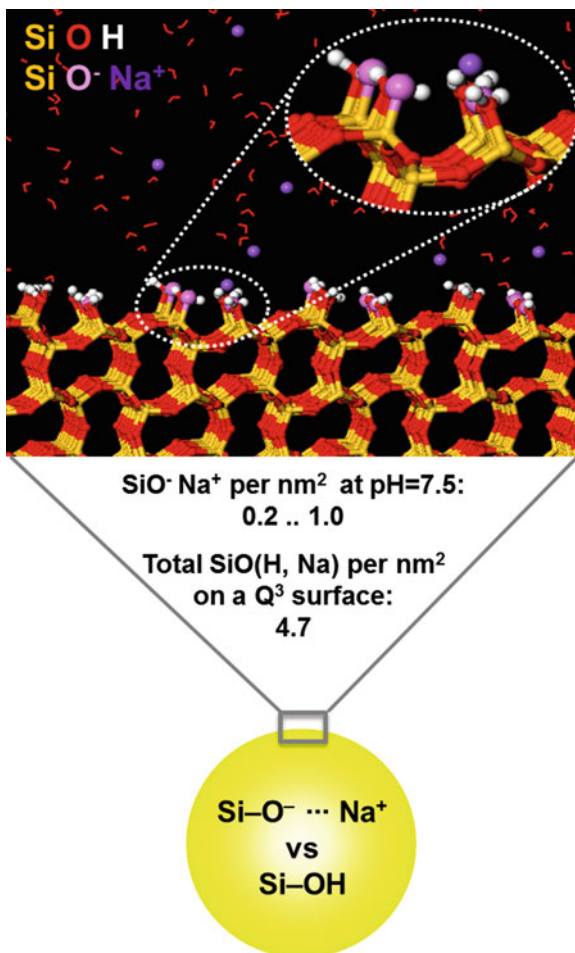
polarizable electron gas of valence electrons as found in strongly conducting metals. Therefore, induced charges do not occur and make no contribution to adsorption.

The reduced surface energy in comparison to metallic substrates leads to much weaker adsorption in the first molecular layer. For example, individual 12-mer peptides binding specifically to silica surfaces possess binding energies 1–10 kcal/mol while 12-mer peptides binding specifically to noble metal surfaces possess binding energies 10–100 kcal/mol according to adsorption isotherms and calculations (Heinz et al. 2009; Feng et al. 2012; Patwardhan et al. 2012; Perry et al. 2009; Oren et al. 2010; Corni et al. 2013). Oxide surfaces are also more polar, reactive, and pH sensitive. As a result, attraction of peptides and synthetic polymers is strongly dependent on conditions such as actual surface chemistry, pH, ionic strength, and particle surface features including porosity versus flat substrates.

### 6.3.1 The Wide Range of Silica Surface Chemistry and Surface Ionization

Silica surfaces are a great example for the variety in surface chemistry and the broad range of oxide chemistry in general (Iler 1979). Phage display techniques from one laboratory to another have shown less than 20 % in sequence similarity among peptides identified as strong binders under comparable pH conditions, owed to the differences in Q<sup>2</sup>, Q<sup>3</sup>, and Q<sup>4</sup> environments as well as in porosity of the silica surfaces as a function of particle size and synthesis method. The typical density of SiO(H,M) groups per nm<sup>2</sup> (M = Na, K, ...) varies between 0 and 9.4 per nm<sup>2</sup>, depending on cleavage plane, synthesis method, and thermal treatment (Zhuravlev 1993; Milonjić 1987; Tadros and Lyklema 1968; Yates and Healy 1976; Bolt 1957). Q<sup>3</sup> silica surfaces with 4.7 SiO(H,M) groups per nm<sup>2</sup> are most

**Fig. 6.11** Schematic of the surface structure of silica nanoparticles that includes silanol groups (SiOH) and a fraction of ionized groups such as sodium siloxide (SiONa). The presence of cations that can partly dissociate from the surface accounts for the observation on zeta potentials in the range of 0 to -40 mV. The typical area density of silanol groups and ionized groups per unit area is indicated (adapted and reproduced with permission from Ref. (Patwardhan et al. 2012))



common in glasses and nanoparticles at room temperature, however, the amount of ionized groups at pH 7.5 may still vary between 0.2 and 1.0 per nm<sup>2</sup> (Fig. 6.11). This range of variability over multiples causes a range of interactions to govern specific adhesion of surfactants and biomolecules. Also, simulations have just begun to take surface ionization into account while most previous models assumed neutral silica surfaces covered by SiOH groups. Such models are only suitable near the point of zero charge that corresponds to pH values between 2 and 4 depending on the type of silica surface. A substantial amount of experimental literature since the 1950s is available that characterizes the amount of ionized groups as a function of surface type, pH, and ionic strength, and type of cation (M) using potentiometric titration and zeta potential measurements (Zhuravlev 1993; Milonjić 1987; Tadros and Lyklema 1968; Yates and Healy 1976; Bolt 1957).

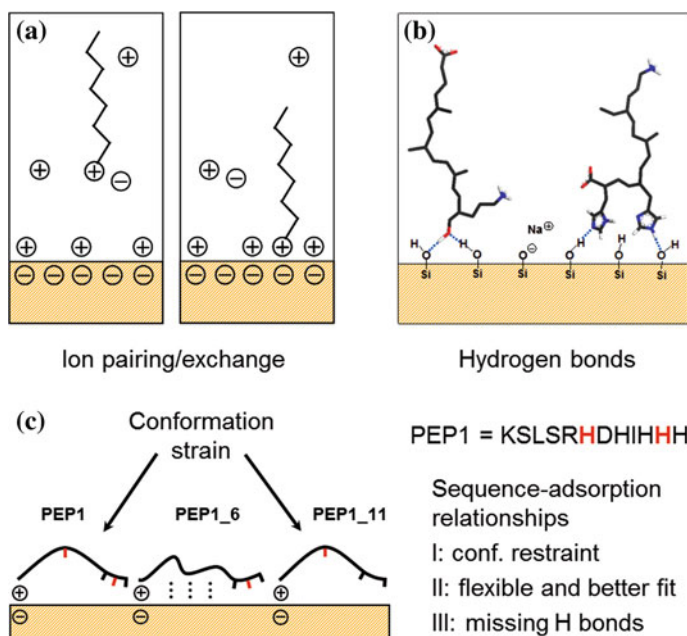


**Fig. 6.12** Main contributions to adsorption of peptides on silica surfaces. **a** Ion pairing and ion exchange (in case of washing procedures) **b** hydrogen bonds **c** conformation effects. Conformation analysis for three mutant peptides of the native peptide Pep1 on silica surfaces in molecular simulation shows that individual residues such as H6 may cause conformation strain that is relieved upon mutation to A6 in Pep1\_6. Other residues such as H11 can be essential for binding though protonation and hydrogen bonds, which is diminished upon mutation to A11 in Pep1\_11. Attraction of hydrophobic groups to the surface also contributes to adsorption at low surface ionization by fostering a continuous water structure

### 6.3.2 Adsorption of Peptides: Ion Pairing, Hydrogen Bonding, and Hydrophobic Interactions

The adsorption of peptides is accordingly determined through ion pairing, hydrogen bonds, hydrophobic interaction, and conformation preferences (Fig. 6.12). These contributions to binding were identified by molecular simulation in agreement with zeta potential measurements, IR and NMR spectroscopy, and adsorption isotherms for a series of several different peptides. The strongest adsorbing amino acids on negatively charged silica surfaces are protonated N termini, lysine (K), and arginine (R), which neutralize (or even reverse) the zeta potential (Fig. 6.12a). Molecular simulations with the Interface-PCFF and Interface-CHARMM force field have demonstrated that ammonium groups closely approach the silica surface and computed adsorption energies reach maximum negative values down to  $-7$  kcal/mol for 7-peptides and 12-peptides containing K

and R. Ion pairing is the dominant mechanism when the surface charge of silica is significant, i.e., at pH ranges near seven and above.

At the same time, hydrogen bonds are possible through silica oxygen atoms, siloxide ions, and silanol hydrogen atoms on the silica surface with alcohol groups (T, S), peptide groups, and aromatic heterocycles (H, W) in peptides (Fig. 6.12b). These interactions play a dominant role near the point of zero charge for all peptides. Peptides that contain suitable groups and possess no cationic groups can be primarily attracted to the silica surface through hydrogen bonds at any pH. In addition, it has been observed in simulations and in adsorption isotherms that peptides containing hydrophobic groups are also attracted to silica. Residues such as F, W, L, I, V can be effectively attracted to silica surfaces although these interactions are more the result of depletion forces that prevent the disruption of hydrogen bonds in the aqueous phase that would occur when the hydrophobic residues remain immersed (Puddu and Perry 2012). Thus, there is no intrinsic attraction of these groups to silica, it is rather the exclusion from water on less ionized silica surfaces that draws hydrophobic groups toward the surface. On increasingly ionized silica substrates, hydrophobic groups do not approach the surface because they would disrupt the hydration shell of siloxide ions and of the nondissociated surface cations.

Another contribution to adsorption arises from conformation preferences of the peptides (Figs. 6.12c, 6.13) (Patwardhan et al. 2012). Conformation effects are particularly important for longer chain molecules and play a role on all surfaces, whether metal or oxides alike. Simulation results have indicated the dynamic nature of the interfaces in which the peptides move on and off the surface, effectively spending a certain fraction of time in close contact with the surface ( $<3 \text{ \AA}$ ). In case of ion pair formation, the time in close contact can be over 90 % although it may only involve the N terminus or the lysine side chain. Other parts of the peptide are often quite detached from the surface for most of the time. A dynamic average that represents the superposition of many thousand equilibrium structures is shown in Fig. 6.13b and c for the peptide Pep1 (KSLSRHDHIIHHH), which binds to 82 nm particles from Stober synthesis. In the absence of ion pairing, the time in close contact with the surface by hydrogen bonds is only in the range 30–70 % and may often involve hydrophobic interactions as well. Residue-specific metrics can be derived from molecular simulation and the difference to isotropic orientation of the peptides in solution can be clearly seen (Fig. 6.13b).

Specific mutations in a peptide can also cause changes in conformation and binding. Such effects were investigated in detail for the mutation of H to A in the 6 and 11 positions in Pep1 (KSLSRHDHIIHHH). The native peptide is of a bent conformation related to some conformation stiffness in the middle of the sequence. In the mutation Pep1\_6, by replacement of H6 for A6, this stiffness is reduced and the binding strength increases in simulation and adsorption isotherm due to more hydrogen bonds with the surface throughout the backbone (Fig. 6.12c). In the mutation Pep1\_11, by replacement of H11 for A11, the higher stiffness of Pep1 is retained and the possibility of H bonding of H11 to the silica surface removed, as

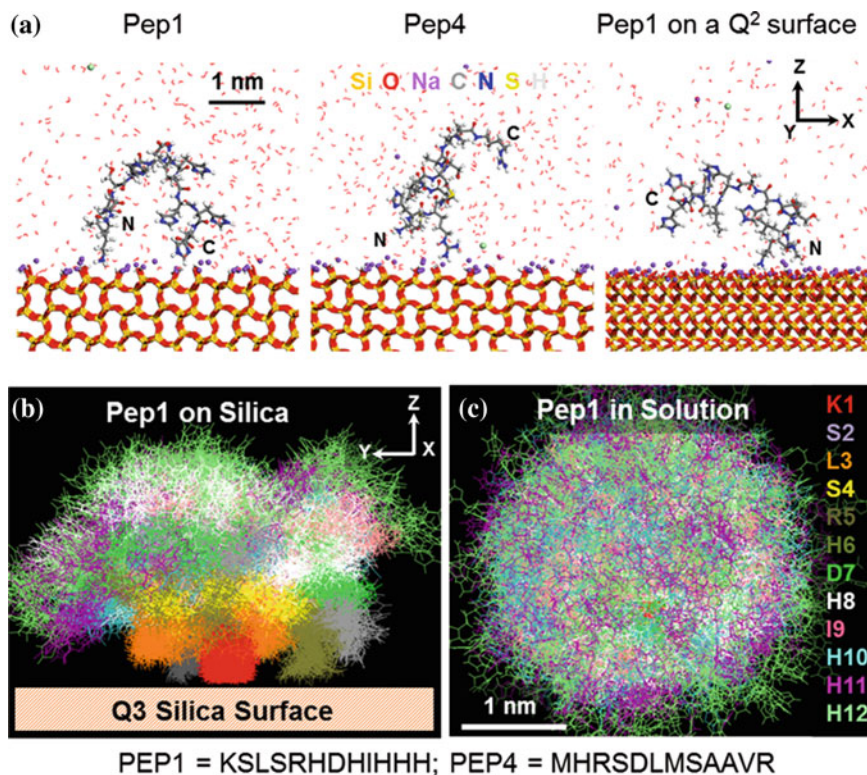


**Fig. 6.13** Representative snapshots and superposition of peptides adsorbed on silica surfaces and in solution. **a** Peptides pep1 and pep4 adsorbed on Q<sup>3</sup> silica surfaces (4.7 SiO<sub>2</sub>/Na groups per nm<sup>2</sup>) as well as on a Q<sup>2</sup> silica surface (9.4 SiO<sub>2</sub>/Na groups per nm<sup>2</sup>) with high ionization. The position of N and C termini is indicated. **b** Superposition of over 10000 peptide conformations during 20 ns simulation time in equilibrium on the Q<sup>3</sup> silica surface. The color code indicates the spatial distribution of amino acid residues, translated laterally to the same coordinate of K1. **c** Superposition of peptide structures in solution showing the isotropic orientation

well as the opportunity of H11 to accept protons and to form ion pairs with siloxide groups. Therefore, the binding of Pep1<sub>11</sub> is weaker in both measurement and molecular dynamics simulation.

### 6.3.3 Apatites: The Key Role of pH

Similar aspects can be observed in phosphates such as hydroxyapatite. The surface is very much pH sensitive and protonated between monohydrogen phosphate and dihydrogen phosphate under physiological conditions (Fig. 6.14). These important aspects have been only recently taken into account in molecular simulations, and very different behavior of peptides on the surface is seen for surfaces of different

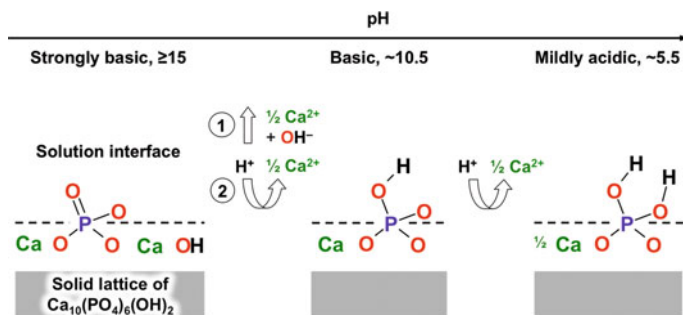


**Fig. 6.14** Termination of hydroxyapatite surfaces at different pH values. Cleavage energies decrease from  $\sim 1000 \text{ mJ/m}^2$  to  $\sim 250 \text{ mJ/m}^2$  upon decrease in pH for typical {001}, {010}, {020}, and {101} facets and adsorption patterns of peptides undergo drastic changes (reproduced with permission from Ref. (Lin 2013))

pH (Lin 2013). Current simulation tools such as the Interface force field allow very specific and accurate analysis of the interfacial interactions of apatites as a function of pH, including the reproduction of hydration energies and peptide specificity. The analysis of bone and dentin mineralization in extracellular environments, the action of drug molecules against osteoporosis, and processes such as the formation of atherosclerotic deposits are becoming accessible to investigations in atomic resolution using simulation and laboratory techniques in combination.

## 6.4 Surface Properties of Ionic Minerals in Clay and Cement and Their Modification

Clay and cement minerals are another class of compounds with ionic surfaces that often undergo surface reconstruction (Heinz 2012; Mishra et al. 2013; Taylor 1997). Clay minerals such as montmorillonite contain dissociable cations, although the surfaces are not prone to hydration–dehydration equilibria, pore formation, and dissolution as in the case of silica and apatites. Therefore, many layered silicates and clay minerals (layered silicates of lesser cation density) serve as model substrates to measure surface forces and conduct self-assembly processes. Layered silicates are also suited to analyze the influence of the type of cations and their area density on swelling, ion exchange, adsorption of organic molecules, and on the assembly of surfactants grafted by ion exchange reactions.

Cement minerals, on the other hand, share some of these properties but are typically exposed to hydration reactions and exhibit many possible nano and micromorphologies that are key for the stability and durability of building structures. Important minerals in this class include tricalcium silicate, dicalcium silicate, tricalcium aluminate, gypsum, ettringite, double layer hydroxides (LDH)

such as monosulfate (hydrocalumite), other Afm phases, tobermorites 9, 11, and 14 Å that may represent hydrated phases, and calcium silicate hydrate (CSH) gel with various calcium-to-silica-to-water (C/S/W) ratios (Taylor 1997; Nonat 2004). The quantitative simulation of structural and surface properties of these phases has recently become possible through the Interface force field, including quantitative insight into aqueous properties and polymer-stabilized phases using a single simulation platform (Heinz et al. 2013). The understanding of the interfaces, reactions, and structure formation on the nanometer scale has still not far progressed. However, large payoffs to sustainable development are anticipated due to global pressure to reduce the CO<sub>2</sub> footprint upon cement production, to increase the long-term stability of building structures, and practical requirements to tune setting properties. Achieving better control over concrete structures from nanometers to kilometers is thus an exciting future task in which advanced experimental characterization tools and simulation capabilities have a major stake.

### 6.4.1 Cation Exchange Mechanisms

For clay minerals, the substitution of surface cations by alkylammonium and alkylphosphonium surfactants is known for about a century. Ion exchange reverses the polarity from hydrophilic to hydrophobic and renders many clay minerals suitable for immersion in nonpolar solvents and polymer matrices for packaging materials, automotive and aerospace parts, commodity plastics, and coatings.

The exchange of cations such as sodium or lithium on clay mineral surfaces for alkylammonium ions may occur spontaneously or require prior exfoliation of the nanometer-thick clay mineral layers at high temperature using harsh reagents. At the end, the surfactants enter the galleries and arrange as homogeneous molecular layers or as islands, depending on the chain length, packing density, and stoichiometric amount (Fig. 6.15). The amount intercalated can be often determined by an increase in the gallery spacing  $d$ . At stoichiometric ion exchange, the arrangement of surfactants on the individual even surfaces depends on the packing density  $\lambda_0$  that has been defined as the ratio of the cross-sectional area of the surfactant chains  $A_{C,0}$  and the available surface area per cationic site  $A_S$  (Heinz et al. 2008a):

$$\lambda_0 = \frac{A_{C,0}}{A_S}. \quad (6.2)$$

The packing density also equals the cosine of the segmental tile angle of the surfactants and determines the occurrence of reversible melting transitions of flexible surfactants (e.g., alkyl chains) upon heating (Fig. 6.16). The order–disorder transitions of the surface-attached surfactants have been extensively studied by differential scanning calorimetry, IR spectroscopy, NMR spectroscopy, sum-frequency gener-

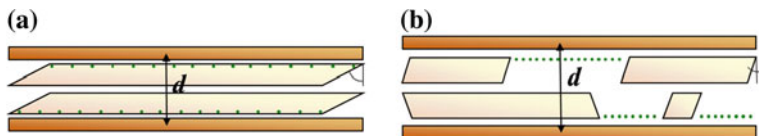


**Fig. 6.15** Schematic of clay mineral layers (*brown*) containing superficial alkali cations (*green dots*) and alkylammonium surfactants (*light color*) upon ion exchange. Partial ion exchange may lead to either **a** homogeneous structures containing surfactants and remaining alkali cations or **b** phase segregated structures containing islands of surfactants and portions of nonexchanged cations. Complete ion exchange may also consume all alkali cations and superstoichiometric ion exchange can lead to the intercalation of added surfactants, which further increases the basal plane spacing  $d$  (adapted from Refs. (Heinz et al. 2003; Heinz and Suter 2004b))

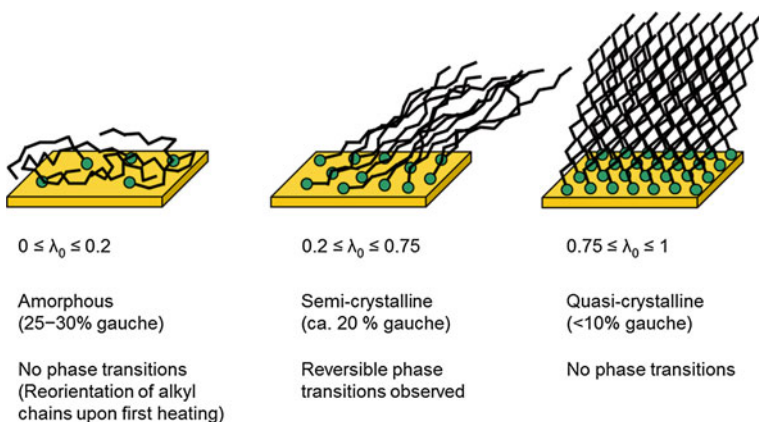


**Fig. 6.16** Range of homogeneous alkyl monolayers (chain length  $\geq C_{10}$ ) on flat substrates as a function of the packing density (reproduced with permission from ref. (Heinz et al. 2008a)). Significant reversible thermal transitions are only found at packing densities between 0.20 and 0.75

ation, and simulation. Such transitions are significant only at intermediate packing density  $\lambda_0$  between 0.2 and 0.75 and up to two reversible thermal transitions can be involved (Fig. 6.17) (Heinz et al. 2003). These correspond to the partial melting of the alkyl backbones, given a sufficient chain length  $> \sim C_{10}$ , and also to lateral rearrangements of the head groups on the clay mineral surface, which are often not immediately reversible upon cooling (Osman et al. 2000; Osman et al. 2004). The second type of transition occurs mostly for quaternary ammonium head groups due to a lower barrier for rearrangement on the surface, whereas primary ammonium head groups form additional hydrogen bonds that prevent such thermal transitions. Details of these processes can be found in review articles and in the primary literature.



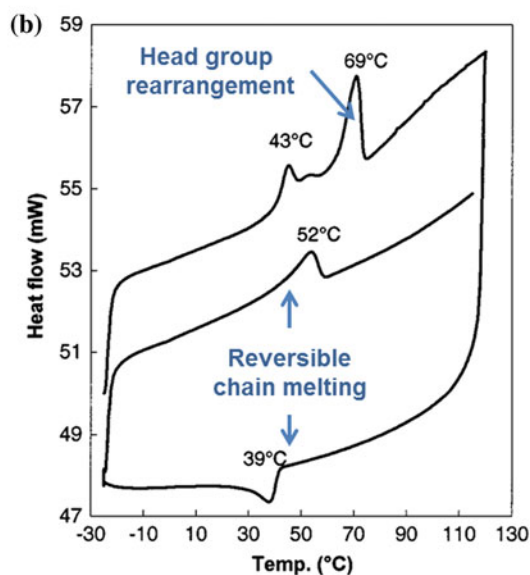
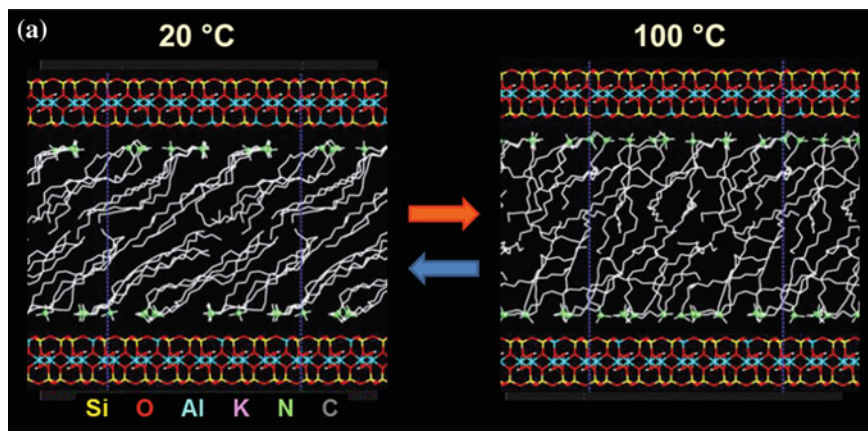


**Fig. 6.17** Reversible thermal transitions at the molecular level and in differential scanning calorimetry (DSC). **a** The transition of semi-ordered octadecyltrimethylammonium chains to random orientation on mica upon heating in molecular dynamics simulation. Order–disorder transitions of the backbone as well as lateral rearrangements of the quaternary ammonium head groups occur. **b** DSC data indicate the corresponding two transitions, of which the rearrangement of head groups is not immediately reversible (reproduced with permission from Refs. (Heinz et al. 2003; Osman et al. 2000))

### 6.4.2 Self-Assembly of Surfactants

The alkyl chains confined between such minerals layers are in a quasi liquid state (Heinz et al. 2005, 2007). The variety of conformations and their assembly between solid like with less gauche conformations and liquid-like with more

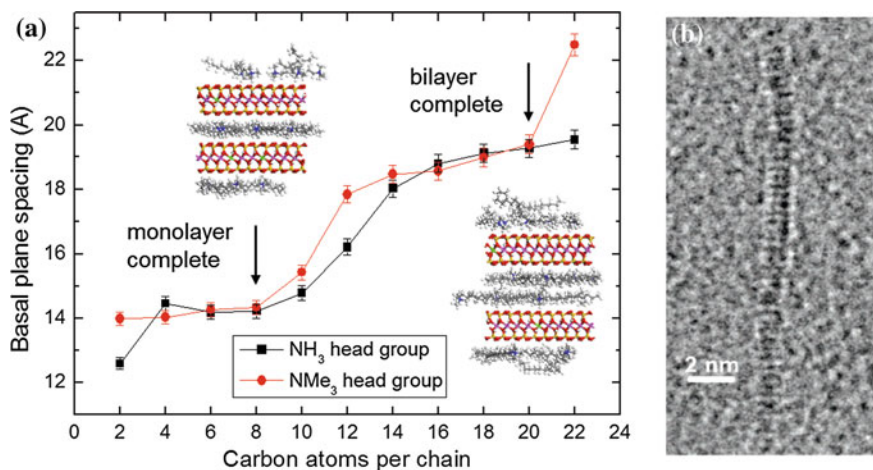


**Fig. 6.18** Gallery spacing and visualization of alkylammonium montmorillonites as a function of chain length. **a** Basal plane spacing of alkyl ammonium chains grafted to montmorillonite of low CEC (91 meq/100 g) as a function of head group and chain length at stoichiometric ion exchange. The successive formation of monolayers and bilayers is shown using atomistic models, and the computed basal plane spacing agrees better than 5 % with X-Ray data. **b** TEM micrograph of an organically modified montmorillonite lamella embedded in an epoxy polymer matrix (*upright orientation*). The visualization of the layered silicate appears similar to the simulation, however, the location of surfactant chains or of polymer cannot be traced (reproduced with permission from Refs. (Heinz et al. 2007; Drummy et al. 2005))

gauche conformations can be seen as a function of chain length and packing in the interlayer space. On substrates with low CEC and single chain surfactants, the packing density is 0.1–0.2 and the backbones orient themselves nearly parallel to the surface (Figs. 6.16, 6.18). The degree of conformational disorder is high and no reversible melting transitions are observed. On substrates with higher CEC or multi chain surfactants, such as trioctadecylmethylammonium, the packing density is higher and the chains orient with a regular tilt angle to the surface. In these systems, reversible melting transitions occur (Fig. 6.17a). For very high packing density  $>0.75$ , as also found for thiols on the surfaces of Ag, Au, and Cu, the quasi crystalline order leads to over 90 % anti conformations and allows no reversible melting transitions.

The case of low packing density leads to significant variation in interlayer packing. As the chain length of the surfactants increases, flat-on monolayers, bilayers, and multilayers are formed, as represented by stepwise increases in basal plane spacing as observed in X-ray diffraction (Fig. 6.18). The successive layer filling leads to maxima and minima in interlayer density as well as in the cohesive energy between the layers. For example, the cleavage energy fluctuates between 45 and 30 mJ/m<sup>2</sup>, the percentage of gauche conformations between 30 and 15 %, and the interlayer density between 800 and 600 kg/m<sup>3</sup> (Fu and Heinz 2010). The variation of cleavage energies is particularly interesting as a contribution to barriers for exfoliation of layered silicates in polymer matrices (Fig. 6.19).

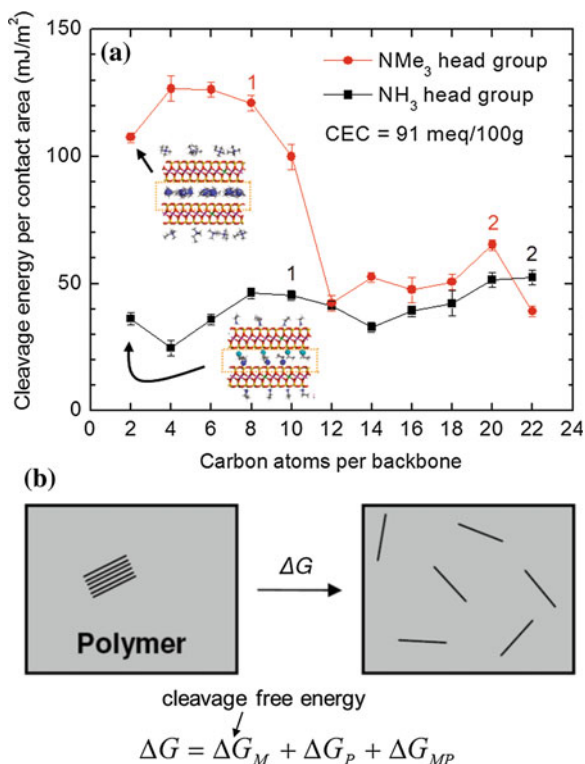


**Fig. 6.19** Computed cleavage energy of organically modified montmorillonite and the role in exfoliation in polymer matrices. **a** The cleavage energy of motnmorillonite (CEC = 91 meq/100 g) modified with alkylammonium surfactants of different chain length and head groups exhibits maxima and minima depending on completion of alkyl monolayers and bilayers (indicated by numbers). Residual strong Coulomb forces upon cleavage of quaternary ammonium surfactants at short chain length are found due to incomplete partition of the charged head groups between the two layers until a thickness of a partial bilayer is reached. **b** A thermodynamic model for the free energy of exfoliation  $\Delta G$  of mineral layers in a polymer. The cleavage energy of the filler lamellae is easier to adjust by choice specific surfactants choices than the cleavage energy of the host polymer ( $\Delta G_P$ ) or the interfacial forces ( $\Delta G_{MP}$ ) to lower the free energy of exfoliation (reproduced with permission from Ref. (Fu and Heinz 2010))

The organic material acts as a separator of interlayer Coulomb attraction that amounts to several  $100 \text{ mJ/m}^2$ . Some Coulomb attraction remains at monolayer thickness depending on the head group choice (Fig. 6.19a). For monolayer and bilayer coverage, the alternation in cleavage energies between high and low values can be seen. Interlayer properties such as gallery spacing, interlayer density, conformations including the percentage of anti and gauche conformations, associated changes in vibration spectra, as well as cleavage energies can be computed in near-quantitative agreement with measurements. The current upper size limit to monitor the time-resolved motion of atoms in predictive quality using classical molecular dynamics simulation is between 10 and 100 nm.

### 6.4.3 Agglomeration Forces and Reactivity of Calcium Silicates

An example for a strongly ionic and reactive surface is tricalcium silicate ( $\text{Ca}_3\text{SiO}_5$ , also called  $\text{C}_3\text{S}$ ), the main component of Portland cement. The mineral is composed of individual silicate tetrahedral, calcium, and oxide ions with a fair amount of isotropy, as demonstrated by similar cleavage energies of various crystal planes (Fig. 6.20) (Mishra et al. 2013). Cohesion is strong, caused to over 95 % by internal Coulomb interactions, and the cleavage energy of  $1340 \text{ mJ/m}^2$  is even comparable to noble metals (Table 6.1). Unhydrated portions of cement particles consist mainly of  $\text{C}_3\text{S}$  and the strength of  $\text{C}_3\text{S}$ , including a bulk modulus of 105 GPa, is a major contribution to the mechanical stability of concrete. It is also notable that tricalcium silicate is still a covalent and an ionic compound, as the atomic charges are only about 1.0e for Si,  $-1.0\text{e}$  for silicate oxygen, and  $\pm 1.5\text{e}$  for calcium ions and oxide ions, respectively. This special balance between covalent and ionic bonding is also innately connected to the reactivity of surfaces with water. In the first step of the hydration reaction, oxide ions are instantly hydrated to hydroxide ions, and also silicate tetrahedra experience hydration to silanol groups. The process of subsequent deposition of calcium hydroxide and dissolution of individual silicate species leads to condensation and formation of oligomeric silicates. Many current investigations by spectroscopy, imaging, and simulation aim at understanding such nanoscale processes better and achieving control over the complex interactions between multiple inorganic and added organic phases, both thermodynamically and kinetically.

We would like to pinpoint in more detail to the cation density on the surface and to interactions with organic molecules (Fig. 6.20). Alcohols and amines of low molecular weight such as glycerine and triethanolamine have been used as anti-agglomeration agents during grinding of cement to achieve energy savings in a ball mill (Fig. 6.20a). Computer simulations have helped to understand the effect of such modifiers in molecular detail to provide a rational basis for laboratory observations. The analysis of adsorption on representative low energy (040) surfaces by molecular simulation showed that adsorption can be rather strong on initially hydrated (as well as nonhydrated surfaces), on the order of  $-20$  to  $-50 \text{ kcal/mol}$ . The origin of the adhesion forces is the complexation of superficial Ca ions by hydroxyl groups in the alcohols as well as hydrogen bonds between superficial hydroxide groups of  $\text{C}_3\text{S}$  and amine or hydroxyl groups of the alcohols (Fig. 6.20b). The area density of calcium ions on the surface is very high, on the order of  $5.8 \text{ per nm}^2$  ( $3.2$  on the immediate outer surface layer and  $2.6$  accessible in the upper plane of silicon atoms). Due to the high charge of calcium and the high area density on the surface, the cations do not easily dissolve or swell although they induce very strong adsorption. At the same time, an organic layer of more than monolayer thickness reduces the strong Coulomb forces between cleaved surfaces very effectively (Fig. 6.20c, d). The adsorbed molecules thus function as a spacer, and the agglomeration energy is essentially the energy difference between

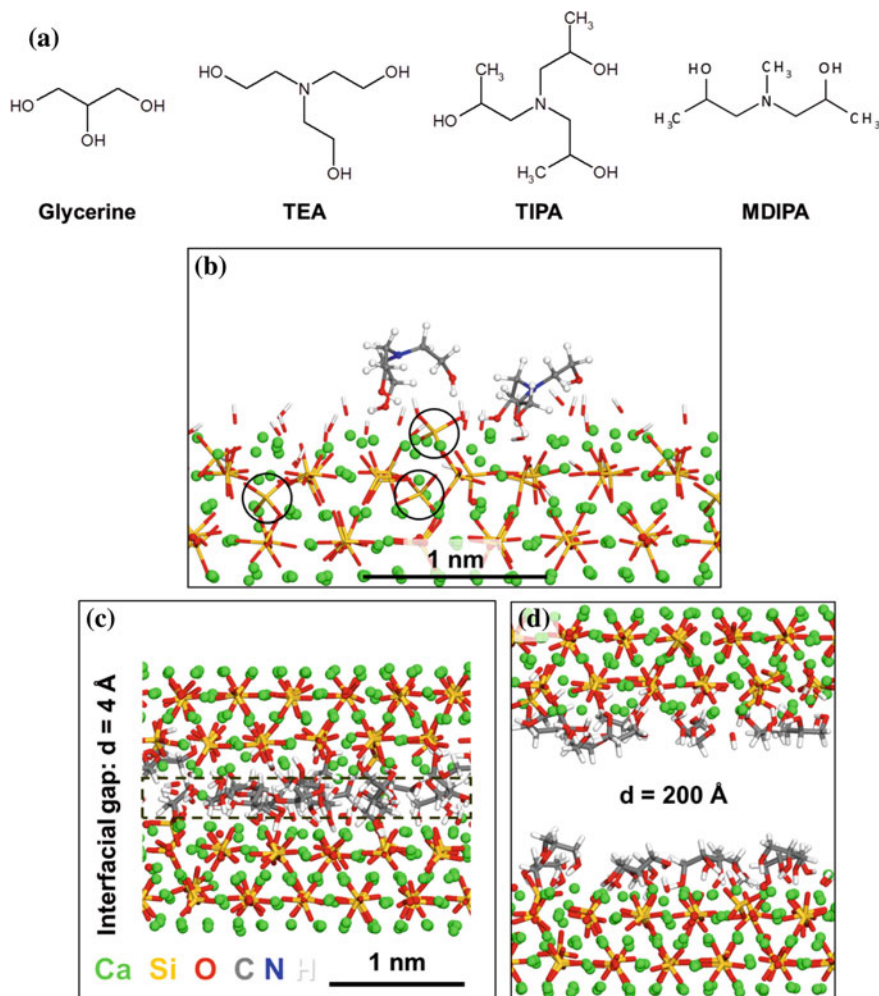
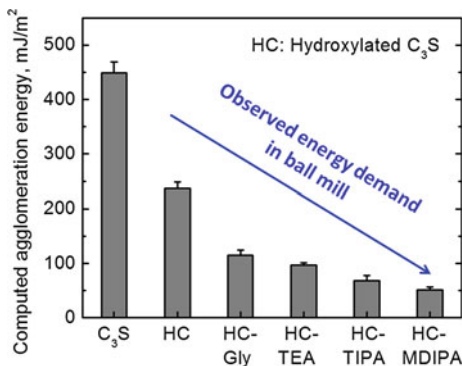


**Fig. 6.20** The interaction of small organic alcohols with surfaces of tricalcium silicate,  $\text{Ca}_3\text{SiO}_5$ . **a** Common alcohols and amines used as grinding aids in cement production. **b** Adsorption on the representative (040) surface involves complexation of  $\text{Ca}^{2+}$  ions and hydrogen bonds between hydroxyl groups of the alcohols with hydroxide and silicate groups on the mineral surface (shown for TEA at 383 K). Some disorder of the superficial silicate tetrahedra can be seen. **c, d** Origin of the reduction of agglomeration forces by multiple molecules above monolayer coverage in the agglomerated and separated state (shown for glycerine). The agglomeration energy corresponds to the difference in energy between state (c) and (d) (reproduced with permission from Ref. (Mishra et al. 2013))

the unified (Fig. 6.20c) and separated surfaces (Fig. 6.20d) in equilibrium. It was also found that the effectiveness as a spacer to reduce the agglomeration energy does not correlate with the trend in adsorption strength, for example, very flexible,

**Fig. 6.21** Computed agglomeration energy of  $C_3S$ , initially hydrated  $C_3S$ , and organically modified surfaces slightly below monolayer coverage in the separated state ( $0.20 \text{ mg/m}^2$ ). The trend correlates with the observed energy demand in ball mills



surface adaptive, and strongly adsorbing molecules such as glycerine do not effectively keep the surfaces apart. The reduction in agglomeration energy can be quantified assuming idealized even surfaces as a first approximation, and the identified trend agrees with observations in energy savings in the ball mill (Fig. 6.21). The efficiency of just one monolayer of organic molecules reduced the agglomeration energy over 95 % compared to the original cleavage energy of  $1340 \text{ mJ/m}^2$  and about 80 % compared to the agglomeration energy of  $250 \text{ mJ/m}^2$  of initially hydrated tricalcium silicate surfaces. The efficiency is due to the spacer effect and the neutralization of local dipole moments by molecule-specific complexation of surface ions.

## 6.5 Summary and Perspectives

The survey of various metallic, pH-responsive oxidic, and ionic surfaces has illustrated governing mechanisms of adsorption and assembly of surfactants and biomolecules. The different types of substrates possess unique and distinctive surface characteristics, such as (1) strong surface energy and epitaxial growth preferences on metal surfaces, (2) cation dissociation and hydrogen bonding on silica surfaces that changes strongly with pH, (3) a fixed cation density on clay minerals that results from defect substitution sites and allows grafting of surfactants layers with controllable properties by ion exchange, (4) strongly ionic surfaces on tricalcium silicate that do not undergo significant cation dissociation but hydration reactions with water and complexation of organic alcohols supported by hydrogen bonds. It becomes clear that the individual chemistry determines the interactions with solvents, polymers, and other organic templates to a far reaching extent so that no universal rules for the “design” of binding peptides, for example, can be formulated that apply to all materials classes.

Rather, it is possible to understand quantitative trends in interactions and design of binding molecules for each class of comparable materials and to formulate materials-specific concepts that have predictive character within each class. Such

concepts include (1) epitaxial matching of molecules to given metal surfaces and consideration of the role of induced charges if applicable (2) the quantification of the area density of dissociable ions on silica and clays, when applicable as a function of pH, and anticipation of ion pairing and cation exchange properties as well as hydrogen bonds and hydrophobic effects (3) the concept of pH and protonation states on pH-responsive surfaces to control specific adsorption of charged molecules (4) the concept of packing density and prediction of tilt angles and thermal behavior of alkyl chains on substrates where grafting can be controlled, and (5) the specific consideration of surface reactions and their effects on interfacial assembly. Some of these concepts are applicable by themselves and some benefit from added numerical evaluation using simulations. The design and understanding of materials with new properties ultimately necessitates laboratory synthesis and conceptual considerations. As these examples illustrate, there are still many unknowns and exciting opportunities to uncover nature's treasure box of nanoarchitectonics for human benefit.

## References

- Atanasoska LL, Buchholz JC, Somorjai GA (1978) Low-energy electron diffraction study of the surface structures of adsorbed amino acid monolayers and ordered films deposited on copper crystal surfaces. *Surf Sci* 72:189
- Bolt GH (1957) Determination of the charge density of silica sols. *J Phys Chem* 61:1166
- Chiu CY, Li YJ, Ruan LY, Ye XC, Murray CB, Huang Y (2011) Nanocrystals selectively shaped using facet-specific peptide sequences. *Nat Chem* 3:393
- Coppage R, Slocik JM, Ramezani-Dakhel H, Bedford NM, Heinz H, Naik RR, Knecht MR (2013) Exploiting localized surface binding effects to enhance the catalytic reactivity of peptide-capped nanoparticles. *J Am Chem Soc* 135:11048–11054
- Corni S, Hnilova M, Tamerler C, Sarikaya M (2013) Conformational behavior of genetically-engineered dodecapeptides as a determinant of binding affinity for gold. *J Phys Chem C* 117:16990–17003
- Drummy LF, Koerner H, Farmer K, Tan A, Farmer BL, Vaia RA (2005) High-resolution electron microscopy of montmorillonite and montmorillonite/epoxy nanocomposites. *J Phys Chem B* 109:17868
- Dubois LH, Zegarski BR, Nuzzo RG (1990) Fundamental studies of microscopic wetting on organic surfaces. 2. Interaction of secondary adsorbates with chemically textured organic monolayers. *J Am Chem Soc* 112:570
- Feng J, Pandey RB, Berry RJ, Farmer BL, Naik RR, Heinz H (2011) Adsorption mechanism of single amino acid and surfactant molecules to Au {111} surfaces in aqueous solution: design rules for metal-binding molecules. *Soft Matter* 7:2113
- Feng J, Slocik JM, Sarikaya M, Naik RR, Farmer BL, Heinz H (2012) Influence of the shape of nanostructured metal surfaces on adsorption of single peptide molecules in aqueous solution. *Small* 8:1049
- Firmit LE, Somorjai GA (1977) Surface structures of normal paraffins and cyclohexane monolayers and thin crystals grown on the (111) crystal face of platinum: a low-energy electron diffraction study. *J Chem Phys* 66:2901
- Fu YT, Heinz H (2010) Cleavage energy of alkylammonium-modified montmorillonite and relation to exfoliation in nanocomposites: influence of cation density, head group structure, and chain length. *Chem Mater* 22:1595

- Fu X, Wang Y, Huang L, Sha Y, Gui L, Lai L, Tang Y (2003) Assemblies of metal nanoparticles and self-assembled peptide fibrils—formation of double helical and single-chain arrays of metal nanoparticles. *Adv Mater* 15:902–906
- Hagfeldt A, Boschloo G, Sun LC, Kloo L, Pettersson H (2010) Dye-sensitized solar cells. *Chem Rev* 110:6595
- Heinz H (2012) Clay minerals for nanocomposites and biotechnology: surface modification, dynamics and responses to stimuli. *Clay Miner* 47:205
- Heinz H, Castelijns HJ, Suter UW (2003) Structure and phase transitions of alkyl chains on mica. *J Am Chem Soc* 125:9500
- Heinz H, Farmer BL, Pandey RB, Slocik JM, Patnaik SS, Pachter R, Naik RR (2009) Nature of molecular interactions of peptides with gold, palladium, and Pd-Au bimetal surfaces in aqueous solution. *J Am Chem Soc* 131:9704
- Heinz H, Jha KC, Luettmer-Strathmann J, Farmer BL, Naik RR (2011) Polarization at metal-biomolecular interfaces in solution. *J R Soc Interface / R Soc* 8:220
- Heinz H, Koerner H, Anderson KL, Vaia RA, Farmer BL (2005) Force field for mica-type silicates and dynamics of octadecylammonium chains grafted to montmorillonite. *Chem Mater* 17:5658
- Heinz H, Lin T-J, Mishra KR, Emami FS (2013) Thermodynamically consistent force fields for the assembly of inorganic, organic, and biological nanostructures: the INTERFACE force field. *Langmuir ACS J Surf Colloids* 29:1754
- Heinz H, Suter UW (2004a) Atomic charges for classical simulations of polar systems. *J Phys Chem B* 108:18341
- Heinz H, Suter UW (2004b) Surface structure of organoclays. *Angew Chem Int Ed* 43:2239
- Heinz H, Vaia RA, Farmer BL (2008a) Relation between packing density and thermal transitions of alkyl chains on layered silicate and metal surfaces. *Langmuir ACS J Surf Colloids* 24:3727
- Heinz H, Vaia RA, Farmer BL, Naik RR (2008b) Accurate simulation of surfaces and interfaces of face-centered cubic metals using 12-6 and 9-6 Lennard-Jones potentials. *J Phys Chem C* 112:17281
- Heinz H, Vaia RA, Krishnamoorti R, Farmer BL (2007) Self-assembly of alkylammonium chains on montmorillonite: effect of chain length, head group structure, and cation exchange capacity. *Chem Mater* 19:59
- Nilova M, Oren EE, Seker UO, Wilson BR, Collino S, Evans JS, Tamerler C, Sarikaya M (2008) Effect of molecular conformations on the adsorption behavior of gold-binding peptides. *Langmuir ACS J Surf Colloids* 24:12440
- Iler RK (1979) *The chemistry of silica: solubility, polymerization, colloid and surface properties, and biochemistry*. John Wiley and Sons, New York
- Jha KC, Liu H, Bockstaller MR, Heinz H (2013) Facet recognition and molecular ordering of ionic liquids on metal surfaces. *J Phys Chem C* 117:25969–25981
- Jiang W, Kim BY, Rutka JT, Chan WC (2008) Nanoparticle-mediated cellular response is size-dependent. *Nat Nanotechnol* 3:145
- Lacerda SHD, Park JJ, Meuse C, Pristiniski D, Becker ML, Karim A, Douglas JF (2010) Interaction of gold nanoparticles with common human blood proteins. *ACS Nano* 4:365
- Lewin M, Mey-Marom A, Frank R (2005) Surface free energies of polymeric materials, additives and minerals. *Polym Adv Technol* 16:429
- Lide DR (ed) (2008) *CRC handbook of chemistry and physics*, 89th edn. CRC Press, Boca Raton, FL
- Lin TZ (2013) Force field parameters and atomistic surface models for hydroxyapatite and analysis of biomolecular adsorption at aqueous interfaces. PhD thesis, University of Akron
- Milonjić SK (1987) Determination of surface ionization and complexation constants at colloidal silica/electrolyte interface. *Colloids Surf* 23:301
- Mishra RK, Flatt RJ, Heinz H (2013) Force field for tricalcium silicate and insight into nanoscale properties: cleavage, initial hydration, and adsorption of organic molecules. *J Phys Chem C* 117:10417



- Naik RR, Jones SE, Murray CJ, McAuliffe JC, Vaia RA, Stone MO (2004) Peptide templates for nanoparticle synthesis derived from polymerase chain reaction-driven phage display. *Adv Funct Mater* 14:25
- Nonat A (2004) The structure and stoichiometry of C-S-H. *Cem Concr Res* 34:1521
- Oren EE, Notman R, Kim IW, Spencer EJ, Walsh TR, Samudrala R, Tamerler C, Sarikaya M (2010) Probing the molecular mechanisms of quartz-binding peptides. *Langmuir ACS J Surf Colloids* 26:11003
- Osada M, Sasaki T (2012) Novel nanoelectronics from nanocrystal building blocks. *Adv Mater* 24:210
- Osman MA, Ploetze M, Skrabal P (2004) Structure and properties of alkylammonium monolayers self-assembled on montmorillonite platelets. *J Phys Chem B* 108:2580
- Osman MA, Seyfang G, Suter UW (2000) Two-dimensional melting of alkane monolayers ionically bonded to mica. *J Phys Chem B* 104:4433
- Patwardhan SV, Emami FS, Berry RJ, Jones SE, Naik RR, Deschaume O, Heinz H, Perry CC (2012) Chemistry of aqueous silica nanoparticle surfaces and the mechanism of selective peptide adsorption. *J Am Chem Soc* 134:6244
- Perry CC, Patwardhan SV, Deschaume O (2009) From biominerals to biomaterials: the role of biomolecule-mineral interactions. *Biochem Soc Trans* 37:687
- Puddu V, Perry CC (2012) Peptide adsorption on silica nanoparticles: evidence of hydrophobic interactions. *ACS Nano* 6:6356
- Ramaseshan S (1946) The cleavage properties of diamond. *Proc Ind Aca of Sci* 24:114
- Ramezani-Dakhel H, Mirau PA, Naik RR, Knecht MR, Heinz H (2013) Surface features, and atom leaching of palladium nanoparticles: toward prediction of catalytic functionality. *Phys Chem Chem Phys* 15:5488
- Ruan L, Ramezani-Dakhel H, Chiu C-Y, Zhu E, Li Y, Heinz H, Huang Y (2013) Tailoring molecular specificity toward a crystal facet: a lesson from biorecognition toward Pt{111}. *Nano Lett* 13:840
- Sanchez C, Belleville P, Popall M, Nicole L (2011) Applications of advanced hybrid organic-inorganic nanomaterials: from laboratory to market. *Chem Soc Rev* 40:696
- Scrivener KL, Nonat A (2011) Hydration of cementitious materials, present and future. *Cem Concr Res* 41:651
- Slocik JM, Naik RR (1988) Biologically programmed synthesis of bimetallic nanostructures. *Adv Mater* 2006:18
- Slocik JM, Stone MO, Naik RR (2005) Synthesis of gold nanoparticles using multifunctional peptides. *Small* 1:1048
- Slocik JM, Wright DW (2003) Biomimetic mineralization of noble metal nanoclusters. *Biomacromolecules* 4:1135
- Tadros TF, Lyklema J (1968) Adsorption of potential-determining ions at the silica-aqueous electrolyte interface and the role of some cations. *J Electroanal Chem Interfacial Electrochem* 17:267
- Taylor HFW (1997) *Cement chemistry*. Academic Press, London
- Tyson WR, Miller WA (1977) Surface free-energies of solid metals - estimation from liquid surface-tension measurements. *Surf Sci* 62:267
- Utracki LA, Sepehr M, Boccaleri E (2007) Synthetic, layered nanoparticles for polymeric nanocomposites (PNCs). *Polym Adv Technol* 18:1
- Vigil G, Xu ZH, Steinberg S, Israelachvili J (1994) Interactions of silica surfaces. *J Colloid Interface Sci* 165:367
- Wiederhorn SM, Moses RL, Bean BL (1970) Plastic deformation and fracture surface energy of sodium chloride. *J Am Ceram Soc* 53:18
- Yates DE, Healy TW (1976) The structure of the silica/electrolyte interface. *J Colloid Interface Sci* 55:9
- Zhuravlev LT (1993) Surface characterization of amorphous silica—a review of work from the former USSR. *Colloids Surf A* 74:71

# Chapter 7

## Bio-Inspired Nanocatalysis

Ryan Coppage and Marc R. Knecht

**Abstract** In response to increasing energy concerns, new materials are required that efficiently use and/or produce energy for a variety of applications. One specific and important area would be for catalytic applications that typically are energy intensive, but extremely important. In this regard, biomimetic methods have recently been studied for such reactivity, where the effects of the biointerface on the catalytic functionality have begun to be examined. This chapter focuses on these materials, typically prepared with peptides and viral templates, for a selection of important catalytic processes.

### 7.1 Introduction to Bio-Inspired Nanocatalysis

Projected petroleum and natural gas use is predicted to exhaust available supplies in ~40 years (Shafiee and Topal 2009). To that end, the continued consumption of these fuels and subsequent CO<sub>2</sub> production is anticipated to result in ecological damage, including global warming, (Joos et al. 1999) ocean acidification, (Doney et al. 2009) and air quality/pollution concerns. (Jenkinson et al. 1991). Additionally, this fuel exhaustion will result in an increase in energy costs, (Silvy 2003) as well as greatly impact the feed chemicals employed as the building blocks of current syntheses, including the production of bulk organic solvents. Taken together, these effects will lead to significantly higher costs associated with catalysis, resulting in a greater need for more energy-neutral synthetic pathways. As such, the exhaustion of fossil fuels could dramatically affect the chemical and materials industry over the next few decades. In light of this, the development of less intense practices could help reduce energy concerns and lower overall consumption. In this regard,

---

R. Coppage · M. R. Knecht (✉)  
Department of Chemistry, University of Miami, 1301 Memorial Drive, Coral Gables,  
FL 33146, USA  
e-mail: knecht@miami.edu

developing lower energy processes is one solution for the continued generation of organic solvents, pharmaceuticals, complex molecules, and molecular electronics.

The realization of new, sustainable catalytic standards could prove to be beneficial for projected energy consumption. Though advances in catalysis have targeted energy neutrality that does not require energy input for reactivity, the fabrication of efficient, low-energy catalysts with a wide range of reactivities remains difficult. Catalysis is a process through which alternate, lower energy pathways are followed for a chemical transformation, thus decreasing the activation energy (Voityuk 1987). Due to this lower activation energy, greater product yields are observed at lower temperatures (Temkin 2012). Current catalytic processes typically use large volumes of organic solvents, consume great amounts of energy, and produce byproducts and other wastes that require specialized separations and disposal (Astruc 1884; Stille 1986). While these issues can be addressed individually, green catalysis offers a way to simultaneously address these concerns (Armor 2000; Centi et al. 2002). Green catalysts function under energy-neutral and environmentally friendly conditions, including ambient temperatures and aqueous solvents. Replacing traditional catalysts with such ecologically and economically friendly materials would result in more efficient reaction processes, thereby significantly lowering production costs (Astruc 1884).

A wide variety of catalysts are commonly employed for different types of reactions, where these systems are generally classified as either homogeneous or heterogeneous (Widegren and Finke 2003). Homogeneous catalytic reactions are processed in a single phase where the catalytic species coexists in the same phase as the substrates. In contrast, heterogeneous catalysts are typically mounted onto a support or present in a different phase from the reactants, thus they are highly dependent on the diffusion of reagents and products to and from the reactive surface. Existing between these two types of catalysts are pseudo-homogeneous systems, in which the catalytic materials are dispersed in the reaction mixture, such as a colloidal distribution of particles (Wang et al. 2009). Most nonsupported nanocatalytic systems fall into this third state, making it difficult to characterize their structure/function relationship to determine the basis for their reactivity (Widegren and Finke 2003).

While catalysts can reduce the amount of energy input, thus lowering fuel consumption, current systems are not sustainable as fossil fuel supplies diminish. To this end, it would be advantageous to develop new long-term catalytic practices, including the development of more energy-neutral systems. Reflecting these standards, materials are needed that function at ambient temperatures and in aqueous solutions (Astruc 1884). The use of nanomaterials as active catalysts has demonstrated superior reactivity for a number of processes, which may be attractive alternatives to achieve such functionality (Braunstein 2004). Furthermore, these systems frequently employ the use of low temperature conditions and are often dispersible in aqueous systems. Due to the variety of metal compositions available and easily modulated surfaces, nanomaterials have received great attention as potential high-efficiency catalysts (Guo et al. 2007). To this end, nanocatalysts exhibit increased surface area exposure, based upon the maximized

surface-to-volume ratio, resulting in a more efficient display of the material surface for optimized catalytic reactivity. In general, such materials are difficult to classify as either fully homogenous or heterogeneous catalysts as the mechanism for many of the reactions driven by these materials remains unclear (Widegren and Finke 2003). Additionally, the ligands employed in the synthesis of nanomaterials, which are required to maintain particle stability in solution, have been demonstrated to control access to the inorganic surface (Polleux et al. 2005; Lynch and Dawson 2008). These ligands prevent bulk aggregation and they can be designed to modulate materials solubility, in addition to exposing active functional groups that may further enhance material reactivity for multifunctional use (Fang et al. 2009; Gref et al. 2003). These ligands include the use of biological molecules such as peptides, proteins, and DNA (Pasquato et al. 2005). In this regard, the biotic/abiotic interface of materials is significant for nanocatalyst activity, though a full understanding of biomolecule binding and ordering on inorganic surfaces is still not fully understood, which is likely to directly impact the catalytic reactivity.

Evolution has shaped biological processes for the production of inorganic structures with highly specific functions (Dickerson et al. 2008). These range from protection against predation, such as spicule formation in sponges, and direction sensing, including magnetite generation in magnetotactic bacteria, to the formation of highly complex inorganic architectures for structural support (e.g., bones), all of which are generated via biomineralization (Dickerson et al. 2008a, b; Lee et al. 2002). These inorganic structures are formed by proteins and peptides, which are highly versatile biomolecules that possess a wide range of biological activity and surface control over their intended materials. Though these biomineralization pathways and their resultant materials are complex and compositionally diverse, they typically do not possess many functions outside of their intended applications; however, the methods employed to fabricate such structures could be used as models to generate new materials with different functionalities.

In general, biomineralization has provided inspiration for the biomimetic synthesis of nanomaterials not present in the biosphere (Dickerson et al. 2008). Bionanomaterials are synthesized using biological ligands as surface passivants to create ligand-capped metal nanostructures, where noncovalent interactions are used to bind the biomolecules to the material surface (Dickerson et al. 2008a; Pacardo et al. 2009). These nanosystems can be both size-tunable and monodisperse, (Coppage et al. 2011) with control over the particle shape, (Li and Huang 1921) crystalline facet display, (Chiu et al. 2011), and material composition (Ataee-Esfahani et al. 2010). Bio-based inorganic nanomaterial systems have been employed in catalysis, (Pacardo et al. 2009; Guo and Wang 2011) assembly, (Slocik and Naik 1988; Kim et al. 2012; Carter and LaBean 2011), and biosensing applications (Wang 2005; Zhong 2009). Of these, the potential for the development of superior biomimetic nanocatalysts has received significant attention. The active surface area optimization, use of an aqueous solvent, ambient reaction temperatures, and extremely low concentrations of precious metal materials make these systems particularly desirable. These attributes position biomimetic nanomaterials as ideal catalyst candidates for use in many systems in which

reaction conditions have been improved with respect to temperature, (Costas et al. 2000) catalyst loading, (Chandra and Xu 2007) green solvents, (Sheldon et al. 2002), and shorter reaction times (Berner et al. 2006). In general, biomimetic nanoparticle-based systems have demonstrated significant catalytic activity for a range of reactions that could prove to be important for next generational systems (Cuenya 2010; Das et al. 2013; Debecker et al. 1806).

The bioligands on the particle surface can dramatically impact the overall nanomaterial reactivity. The biotic/abiotic interface must be designed to both expose the inorganic catalytic materials and maintain nanoparticle stability (Gref et al. 2003). A variety of ligands have been employed to synthesize these materials, including peptides, proteins, and oligonucleotides (Rana et al. 2010; Pengo et al. 2007; Samanta et al. 2008). Though surface-specific biomolecules have been demonstrated to passivate and support nanocatalyst functionality, the biotic/abiotic interface and binding effects are not fully understood. These peptides possess combinations of sequence-unique binding motifs, structures, and interfacial attributes that remain difficult to predict. Additionally, the orientation, sequence, concentration, and structural/binding motif of the biomolecule passivant has been demonstrated to greatly affect catalytic reactivities (Coppage et al. 2010, 2012, 2013). While bionanocatalytic systems are relatively new, they offer the potential to decrease reaction costs through lower energy requirements, where ambient reaction temperatures may prove to be optimal, opening the door for sustainable reactivity.

In this chapter, various biomimetic nanomaterial systems are outlined as potential catalysts that employ ambient conditions. Though the biotic/abiotic interface is still not fully understood, these studies reviewed herein demonstrate a catalytic efficiency that is highly desirable for next generation functionalities. To this end, the continued development of bionanomaterials for applied nanocatalytic systems could be both economically and ecologically advantageous.

## 7.2 Phage Display

The design and synthesis of bioinspired nanomaterials typically employs materials-directing peptides that can recognize and bind inorganic surfaces (Dickerson et al. 2008; Li and Huang 1921; Ruan et al. 2011). Ideally, these peptides should control the atomic arrangement of the metal atoms at the particle surface; however, such capabilities remain difficult to achieve. Since a majority of biomineralization processes are carried out through peptide interactions with inorganic materials, the rational design of such sequences could lead to nanomaterials of desired morphologies. These peptides can be isolated from random libraries through bio-combinatorial selection processes such as phage display (Naik et al. 2002; Petrenko 2008; Sidhu et al. 2000). For this, bacteriophages are employed, which are a virus that infects bacteria to replicate. Some phage possess single-stranded DNA, making them ideal candidates for genetic engineering to easily modify their coat proteins (Flynn et al. 2003). Most commonly used, the filamentous M13

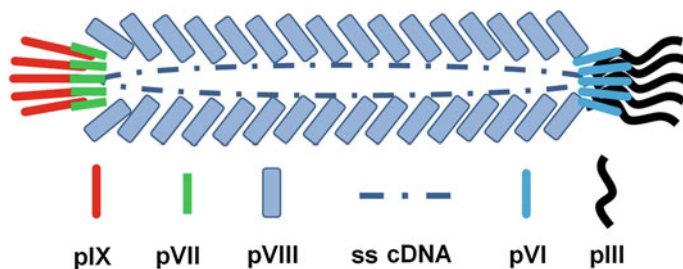


**Fig. 7.1** A diagram of the filamentous M13 bacteriophage and its corresponding coat proteins

phage, seen in Fig. 7.1, is composed of four minor and one major coat proteins: two minor coat proteins at the randomized end, a major capsid coat protein along the long axis of the virus, and two minor coat proteins at the opposite end (Huang et al. 2005). These viruses are  $\sim 900$  nm long and 6–8 nm wide, which can vary, depending upon the length of the enclosed cDNA and capsid sequence length (Sidhu 2001). Protein modifications and additions are typically performed at the opposing end pIII and pIX minor coat proteins (Fig. 7.1), in addition to the main capsid pVIII major coat protein; (Hess et al. 2012; Nam et al. 2006; Lee et al. 2012) however, the pVIII proteins are the least susceptible to modification, as large changes inhibit virus formation after cell infection (Li et al. 2003).

Commonly, the pIII minor coat protein genes are modified to display the randomized library of peptides at the viral terminus (Flynn et al. 2003). From this,  $\sim 1$  billion different peptide sequences can be presented to solution, generating a highly diverse combinatorial library. This library can be scanned for affinity to a target substrate by exposure of these random sequences to a material surface (Naik et al. 2004; Pande et al. 2010; Xiao et al. 2011). Based on this large number of sequences, it is likely that a subset of these peptides will specifically bind the intended target. To begin the biopanning process, the phage is incubated with the desired substrate to initiate binding (Fig. 7.2). The system is then washed to remove any unbound phage. Next, the bound phage are eluted from the target with a low pH elution step, which reverses the binding and allows for collection and amplification. These phage are then amplified by a bacterial host and then reintroduced to the target substrate. The process is repeated multiple times with increasingly stringent washes, resulting in only the most strongly bound phage remaining. Typically, phage collected after a fourth or fifth elution cycle are amplified and their DNA is sequenced (Sarikaya et al. 2003). This allows for gene identification and thus the pIII sequence identity of the substrate-binding peptide. Interestingly, those phage with the strongest substrate affinity may remain bound to the target surface and not identified. To account for this, Naik and coworkers have demonstrated that the bound phage can be ruptured directly on the surface, which releases their DNA (Naik et al. 2004). From this, the released DNA can be amplified and sequenced, elucidating peptides with the strongest surface affinities. This method and related selection processes (Naik et al. 2004; Wittrup 2001) allow

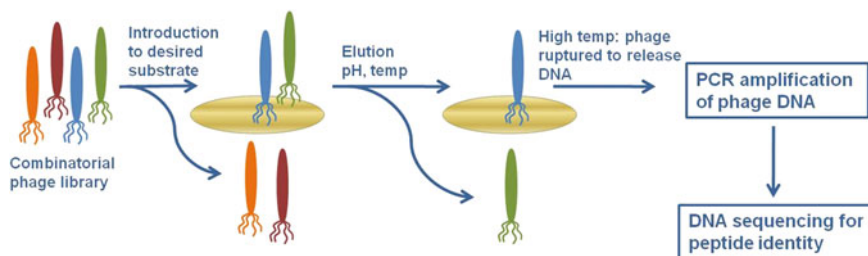


**Fig. 7.2** Phage display diagram of Naik et al. PCR-complemented procedure (Naik et al. 2004)

for the isolation of peptides with affinities for a variety of materials, including Pd, (Pacardo et al. 2009) Ag, (Naik et al. 2002) Au, (So et al. 2009) Fe<sub>2</sub>O<sub>3</sub>, (Laurent et al. 2008) TiO<sub>2</sub>, (Dickerson et al. 2008), and CdS (Lee et al. 2002; Mejare et al. 1998). Unfortunately, peptide sequences or binding motifs cannot be predicted at present; however, the phage-based isolation of surface-specific peptides may provide valuable sequence information in the pursuit of rational design principles for material-binding biomolecules.

### 7.3 Metallic Pt Bionanomaterials

Peptide sequences have been shown to possess an affinity for specific inorganic surfaces, potentially even showing facet selectivity (So et al. 2009; Tamerler et al. 2006). This is significant due to the high-energy edge and vertex atoms at the particle surface, which have been demonstrated to be highly active for catalytic applications (Rhee et al. 2009). Along these lines, nanomaterials have been designed by optimizing the exposure of these metallic features. Additionally, biological components have been demonstrated to direct catalytic processes and control inorganic surfaces (Vallee et al. 2010). By passivating a nanomaterial surface with biologically active moieties, this combination has the potential to lead to multifunctional catalytic materials (Zhou et al. 2004). These approaches have been incorporated into nanocatalyst production in various ways, with peptides coordinating metal ions prior to reduction, (Mlynarz et al. 2002) passivating the surface of the zerovalent materials, (Pacardo et al. 2009) facilitating growth along specific planes, (Li and Huang 1921) combining motifs for linking nanomaterials, (Slocik and Naik 1988) and functionalizing the surface of a nanomaterial with catalytically active groups and single atom metal-binding ligands (Pasquato et al. 2005; Manea et al. 2004).

Pt is a commonly used catalyst in catalytic converters, (De et al. 2000) olefin hydrogenation, (Ikeda et al. 2006) decomposition of H<sub>2</sub>O<sub>2</sub> into H<sub>2</sub>O and O<sub>2</sub>, (Hagiwara et al. 2010) and oxidation/reduction reactions (Gasteiger et al. 2005). Traditionally, these methods typically involve bulk Pt as a heterogeneous catalyst, which does not exploit the increased surface area possible via nanoscale materials.

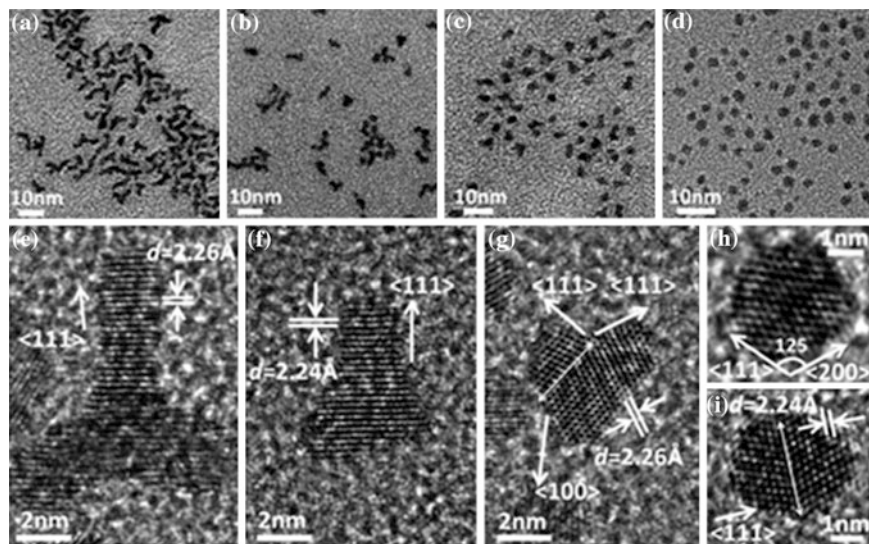


**Fig. 7.3** TEM analysis of Pt multipod structures with varying concentrations of BP7A (22.5–250  $\mu\text{g/mL}$ , **a–d**). Higher concentrations of peptide yielded more spherical particles, while lower peptide concentrations resulted in multipods. Reproduced from Diagne et al. (2002) with permission from Wiley-VCH, copyright 2010

The synthesis of exceptionally small Pt nanomaterials optimizes the exposed catalytic metal, which increases catalytic turnover. To that end, Huang and colleagues have developed Pt nanocrystals with electrocatalytic activity through the use of Pt-binding peptides (Li and Huang 1921). This peptide was obtained via phage display, through panning for sequences with an affinity for Pt metal (Li and Huang 1921). From this selection process, a septamer peptide, BP7A (Ac-TLHVSSY-CONH<sub>2</sub>, acylated on the N-terminus and with an amide functionality on the C-terminus), was obtained after the third biopanning cycle with an affinity for Pt wires. Pt nanocrystals were then synthesized in the presence of this peptide, with a controlled injection of NaBH<sub>4</sub>, followed by the addition of ascorbic acid for slow reduction and selective facet growth. By varying the peptide concentration, the particle shape was observed to be dependent on the BP7A concentration (Li and Huang 1921). Water-dispersible nanocrystals formed in the presence of the peptide results in nonspherical materials termed multipods, in which pod is a metallic growth along one facet. Of the materials produced in the presence of the BP7A peptide, linear growth occurs from the Pt crystal core along specific facets, resulting in single, bi, tri, or tetra-pod shapes (Fig. 7.3) (Li and Huang 1921). Most pods were observed to grow along the  $\langle 111 \rangle$  direction, while others were observed to grow in the  $\langle 100 \rangle$  direction. Strangely, the pods were not observed to grow in the  $\langle 110 \rangle$  direction, suggesting that the BP7A showed preferential binding to (110) facets. At lower peptide concentrations, growth was observed along the (111) and (100) facets, while at higher concentrations, all facets



were bound by the peptide, resulting in spherical shapes (Li and Huang 1921). TEM image analysis demonstrated that multipod nanocrystals showed distinctive (110) facets as compared to spherical Pt nanocrystals.

A correlation likely exists between the BP7A peptide sequence and the Pt nanocrystal pod growth, with facet selectivity driving the particle growth direction (Li and Huang 1921). This correlation between ligand and core material is likely responsible for the observed differences in nanocrystal size and shape. Due to the isolation of BP7A with affinity to Pt wires, some recognition of Pt facets (along the wire axis) may be engendered into the peptide sequence. Two amino acids, His and Tyr, are present that are known for their interaction with metals, (Rimola et al. 2006) such that their placement in a peptide may result in their ability to bind to a particular facet. At lower peptide concentrations, fewer peptides are available to bind to the surface, thus exposing the materials for continued growth, leading to pod formation. Conversely, at higher peptide concentrations, the metallic surface is fully saturated, resulting in inhibited growth and spherical shapes (Li and Huang 1921).

Electrochemical studies were performed via cyclic voltametry (CV) to evaluate the electrochemical surface area (ECSA) of the multipods (Li and Huang 1921). Of these materials, the Pt nanocrystals fabricated at a low-peptide concentration with a large number of pod growths were observed to possess the greatest ECSA of  $27.23 \text{ m}^2\text{g}^{-1}$ . This is significantly higher than the Pt black standard, which demonstrated a value of  $15.15 \text{ m}^2\text{g}^{-1}$ . When the more spherical structures were studied, lower ECSA values of  $23.67 \text{ m}^2\text{g}^{-1}$  and  $18.51 \text{ m}^2\text{g}^{-1}$  were obtained for the short pods and spherical nanocrystals, respectively (Li and Huang 1921). This difference was likely due to extensive peptide-based surface coverage.

Similar to the multipod structures, Huang and coworkers also isolated facet-specific peptides via phage display to generate Pt nanocrystals of varying and selectable shapes (Li and Huang 1921; Chiu et al. 2011; Ruan et al. 2011). These techniques are significant for potentially controlling surface structures, directing nanomaterial growth, and influencing the final shape of the materials. Shape-controlled nanomaterial growth can be both a kinetically directed process, which is dependent on concentrations, (Li and Huang 1921) and a thermodynamically directed process, based upon specific peptide/surface interactions (Zhang et al. 2012; Lisiecki 2005). While high-energy facets vanish, a particular shape is formed that is dominated by low-energy surfaces. This effect is controlled by the design and use of facet-specific ligands, which likely lower the overall facet energy to which they bind, thus preventing growth along this direction. This phenomenon results in selective particle growth with tunable shape control.

To isolate facet-specific peptides, Pt cubes with (100) facets, and Pt octahedra displaying (111) facets, were deposited onto a silicon wafer and used as single crystal target surfaces (Chiu et al. 2011). After three biopanning cycles, the remaining phage were eluted and sequenced for each system. Two peptides were obtained with an affinity for these facets: septamers T7 (TLTTLTN) for the (100) and S7 (SSFPEPD) for the (111) Pt interfaces (Chiu et al. 2011). By employing

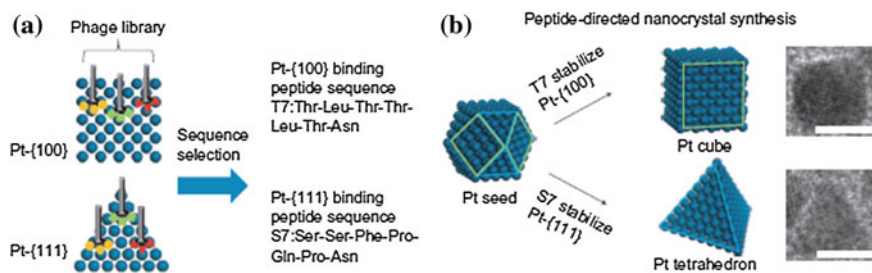


**Fig. 7.4** Shape-oriented Pt nanomaterials synthesis with **a** phage display for facet-selective peptide sequences and **b** shaped Pt nanomaterial synthesis with T7 and S7 peptides. Scale bars are 20 nm. Reprinted by permission from Macmillan Publishers Ltd: [Nature Chemistry] (Chiu et al. 2011), copyright (2011)

these sequences in the presence of  $\text{Pt}^{2+}$  ions, nonspherical Pt nanomaterials were synthesized in both cases. For each synthesis, first  $\text{NaBH}_4$  was added as an initial reductant, driving nucleation. Next, ascorbic acid was added as a slower reductant, allowing for controlled materials growth, as shown schematically in Fig. 7.4 (Chiu et al. 2011). This dual-reductant method was employed to help control the growth kinetics of the materials. To this end, a minor amount of  $\text{NaBH}_4$  is consumed for the production of small seed crystals ( $\sim 5$  nm) first. The ascorbic acid is then added to slowly reduce  $\text{Pt}^{2+}$  ions, which can be added to higher energy, unbound facets, not inhibited by peptide binding. As expected, the T7 sequence resulted in the formation of cube structures and the S7 peptide produced tetrahedral nanoparticles (Chiu et al. 2011).

Huang and coworkers have extended shaped nanomaterial synthesis employing selected single crystal and twinned seed particles (Ruan et al. 2011). This synthesis was repeated with Pt seeds generated with the multipod-forming BP7A peptide, to compare final material geometries (Li and Huang 1921). The BP7A peptide was observed to generate single-twinned seed crystals, which results in the production of different final materials (Fig. 7.5) (Ruan et al. 2011). To that end, the BP7A peptide assisted in formation of single-twinned seeds. These seeds were then shaped into right-bipyramids and (111)-bipyramids by stabilizing (100) and (111) facets, depending on the use of the T7 or S7 peptides, respectively (Ruan et al. 2011).

Similar to the multipod structures, the final particle shape was dependent on the presence of T7 or S7 used in the reaction (Ruan et al. 2011). To confirm this growth mechanism, the S7 peptide was added to a growth solution of T7-capped nanocubes, in which peptide concentrations were equivalent (Ruan et al. 2011). The T7-capped nanocubes were observed to change shape from cubic materials to tetrahedral geometries, enclosed with (111) facets. This phenomenon suggests that the S7 affinity to (111) facets is greater than the T7 affinity to (100) facets. Due to the observed change in shape, it is likely that the S7 peptide more strongly binds the (111) facet, directing growth to result in the formation of materials with the tetrahedral morphology.

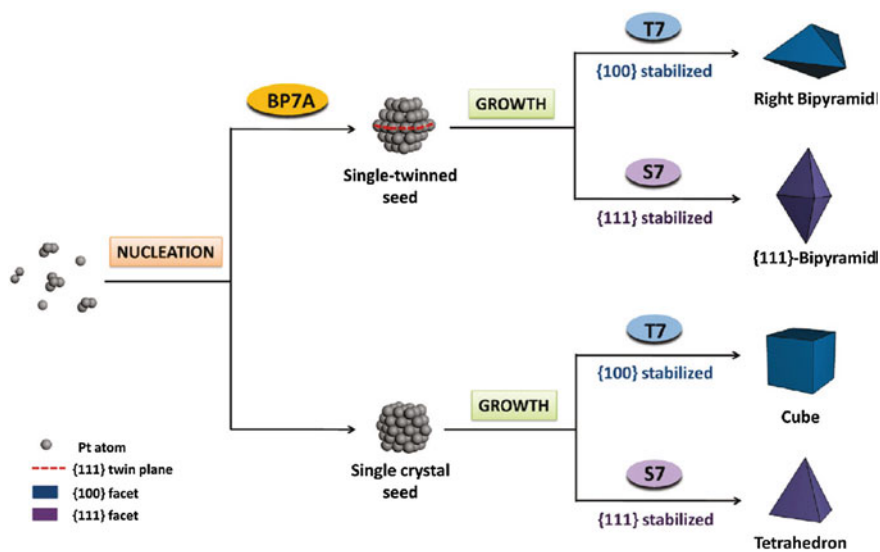
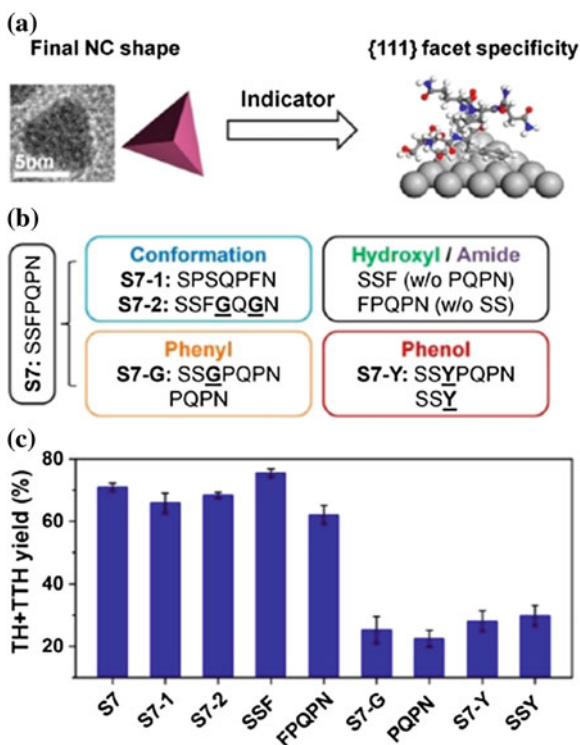


**Fig. 7.5** Scheme of shaped nanoparticle synthesis, which is dependent on the BP7A-influenced seeds and sequence-stabilized facets. Reprinted (adapted) with permission from (Ruan et al. 2013). Copyright (2011) American Chemical Society

Additional studies have been performed, which provided information toward understanding the surface-specific binding mechanism of peptides to (111) Pt facets (Ruan et al. 2013). This work was completed by manipulating the conformation and composition of the S7 sequence. Binding modifications were quantified by observing differences in nanocrystal shape with respect to sequence modification, which is indicative of a change in specific recognition. While S7 stabilizes tetrahedra, cuboctahedra are the thermodynamically favored shape for *fcc* metals (Ruan et al. 2013). The resulting structure using the modified S7 sequences indicated that the final material shape was due to the S7 peptide with (111)-binding affinity (Fig. 7.6a) (Ruan et al. 2013). For this study, a set of S7-variant peptides was prepared, which selectively exchanged binding residues, such that final material geometries could be observed. These sequence modifications were made to address both peptide conformations and chemical functional groups. As seen in Fig. 7.6b, the S7 peptide was retained as a reference and variants were prepared as follows: conformational changes were made in peptides S7-1 and S7-2, hydroxyl/amide changes in the SSF and FPQP trunctates, phenyl changes in the S7-G and PQPN, and phenol modifications in the SSYPQP and SSY sequences (Ruan et al. 2013). Shape results indicated that these sequences fell into two categories: sequences with or without phenylalanine. Peptide sequences that contained this residue were observed to produce significantly more tetrahedra and truncated tetrahedra (62.1–70.9 %), while those without phenylalanine were observed to fabricate mostly cuboctahedra (Fig. 7.6c) (Ruan et al. 2013). This suggests that the

**Fig. 7.6** Shape-selectivity analysis using peptides. Part **a** presents the study that examined the effect of particle shape using the materials-binding peptides of part **(b)**. Part **c** displays the material morphology analysis. Reprinted (adapted) with permission from (Ruan et al. 2013). Copyright (2013) American Chemical Society



presence of phenylalanine is mostly responsible for (111)-specificity, especially in the SSF fragment, which demonstrated the highest tetrahedra yields ( $70.9 \pm 1.4\%$ ) (Ruan et al. 2013).

To better characterize these binding differences, molecular dynamics simulations using the CHARMM-METAL force field were conducted, which demonstrated differences between adsorption energies for (100) and (111) facets (Fig. 7.7) (Ruan et al. 2013). As seen in Fig. 7.7a, the computed adsorption energies of the peptides with respect to tetrahedra materials demonstrated very negative values for the (111) facet for all sequences, indicative of epitaxial binding between the facet and multiple amino acid functional groups; however, slight positive binding adsorption values were observed for the (100) facet for sequences containing a phenylalanine (Fig. 7.7b). To this end, as opposed to (111)-facet affinity, a disaffinity to the (100) facet likely causes binding to be more energetically favorable on the (111) surface for tetrahedral materials (Ruan et al. 2013).

While these binding affinity value differences can be qualitatively observed, a full understanding of the shape selective biotic/abiotic interaction is not yet realized. Though phenylalanine was demonstrated to be important for the differential preference between (111) and (100) facets, other conformational and sequence-specific factors are likely to still control surface activity and resultant

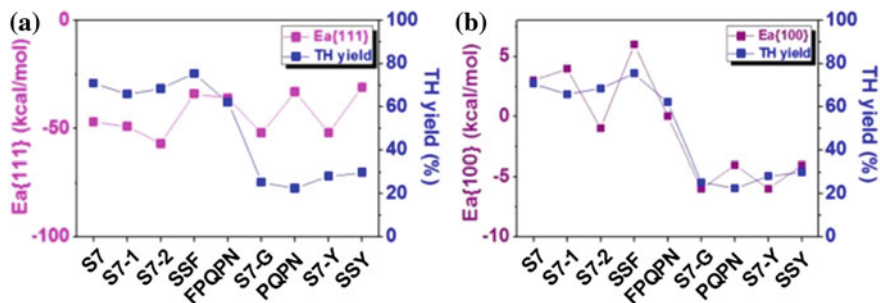


**Fig. 7.7** Comparison of the calculated binding energies and shape-selectivity of the selected Pt-binding peptides to the **a** (111) and **b** (100) facets. Reprinted (adapted) with permission from (Ruan et al. 2013). Copyright (2013) American Chemical Society

material size. A more in-depth understanding of these binding and facet-specific effects could lead to the development of superior materials-directing peptides with multifunctional and enhanced catalytic activity.

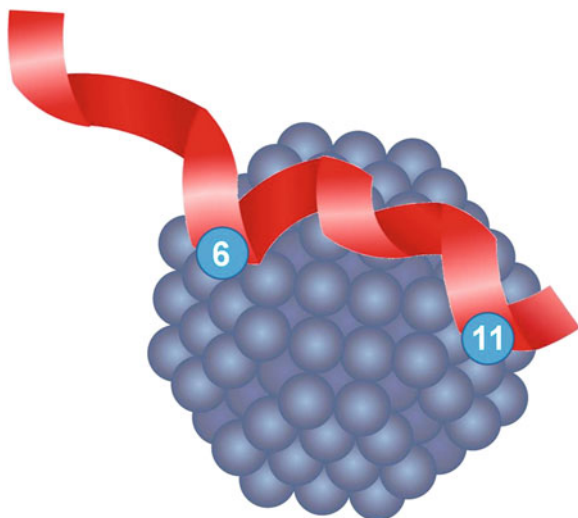
## 7.4 Pd Biomimetic Nanocatalysts

Aside from Pt, Pd is a noble metal catalyst heavily used in hydrogenation, (Huang et al. 2004) dehydrogenation, (Wang et al. 2004) C-C couplings, (Pacardo et al. 2009) and as an electrocatalyst for the oxidation of alcohols (Bianchini and Shen 2009). Even with a catalyst, these processes can sometimes require high reaction temperatures and harsh organic solvents. Due to its wide range of functionality, the development of Pd nanostructures that function under ambient conditions is highly desirable. To that end, Pd materials would need to be prepared that are sufficiently stable and soluble in water, but still possess particle surface accessibility for reactivity.

In pursuit of surface-specific biomimetic ligands, the Pd<sub>4</sub> peptide (TSNAVHPTLRHL) was isolated via phage display with affinity for Pd (Pacardo et al. 2009). Through Monte Carlo simulations, this sequence was modeled to bind most strongly via the histidines in positions 6 and 11 (Pandey et al. 1989). Other residues were also identified that bound the surface, such as asparagine and arginine; (Pandey et al. 1989) however, they were weaker binders. From this, it was suggested that the peptide likely forms a pinched structure on Pd surfaces (Fig. 7.8) (Pacardo et al. 2009). In this case, the catalytic reagents could ideally access the nanoparticle surface such that the reaction could be processed efficiently.

Using the Pd<sub>4</sub> sequence, Pacardo et al. synthesized nearly monodisperse  $1.9 \pm 0.3$  nm peptide-capped Pd nanoparticles by reducing  $K_2PdCl_4$  in the presence of the biomolecule (Pacardo et al. 2009). These materials were demonstrated to be stable at room temperature, in water, and were observed to be highly reactive for Stille C-C coupling (Stille 1986; Coppage et al. 2010; Pacardo et al. 2011).

**Fig. 7.8** Proposed pinched structure of the Pd4 peptide on a Pd nanoparticle in which the histidines at the 6 and 11 positions anchor to the surface



In this process, the Pd4 peptide passivates the Pd nanoparticles, from which Pd atoms can be leached during oxidative addition (Pacardo et al. 2011). Next in the coupling, transmetallation occurs via an organostannane, followed by reductive elimination to form the new C-C bond and release of a Pd<sup>0</sup> atom, as shown in Fig. 7.9 (Pacardo et al. 2009). For the coupling of 4-iodobenzoic acid with PhSnCl<sub>3</sub>, these nanocatalysts were able to generate quantitative product yields at Pd loadings of  $\geq 0.005$  mol% over 24.0 h, which was performed at room temperature in water. For this reaction, a rather high TOF value of  $3207 \pm 269$  mol product (mol Pd  $\times$  h)<sup>-1</sup> was reported. (Pacardo et al. 2009).

For the Stille coupling reaction, two distinctly different mechanisms have been proposed. First, a surface-based mechanism has been presented, in which the coupling takes place at the Pd nanoparticle surface (Lee et al. 2010). Additionally, a leaching mechanism has been suggested, in which Pd species are abstracted from the particle surface, process the coupling in solution, and then are redeposited onto the particle (Astruc et al. 2005). Of these two mechanisms, Pacardo et al. have obtained evidence that supports the leaching approach for the peptide-capped nanoparticle-driven Stille coupling reaction (Pacardo et al. 2011). This work employed the Pd4-stabilized Pd nanoparticles with a variety of aryl halides in aqueous solution and low temperatures (Fig. 7.10) (Pacardo et al. 2011). Through these studies, it was observed that the Stille couplings were sensitive to the Pd concentration, reaction temperature, and aryl halide composition.

Initially, a titration study demonstrated that increased Pd loadings resulted in lower overall yields for the Stille coupling of 4-iodobenzoic acid with PhSnCl<sub>3</sub> (Fig. 7.11). For this, at catalyst loadings of  $< 0.05$  mol% Pd, TOF values of  $\sim 2,400$  mol production (mol Pd  $\times$  h)<sup>-1</sup> were consistently observed (Pacardo et al. 2011). At higher Pd loadings, a decrease in reactivity was evident, suggestive of metal aggregation to form catalytically inactive Pd black. To complement this work,

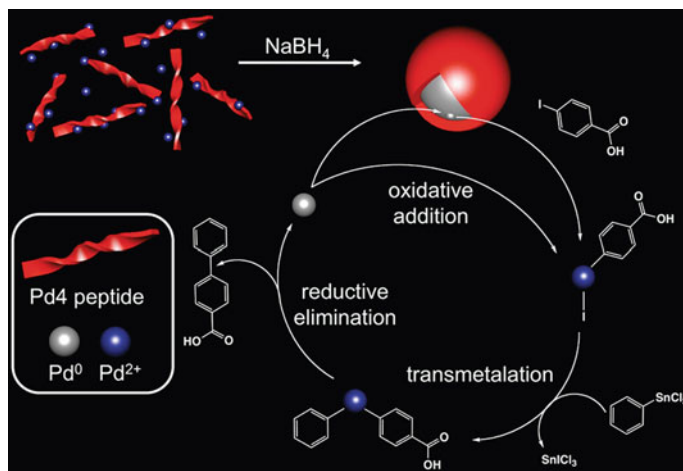


**Fig. 7.9** Synthesis of peptide-passivated Pd nanoparticles and their use as catalysts in the Stille coupling reaction. Reprinted (adapted) with permission from (Pacardo et al. 2009). Copyright (2009) American Chemical Society

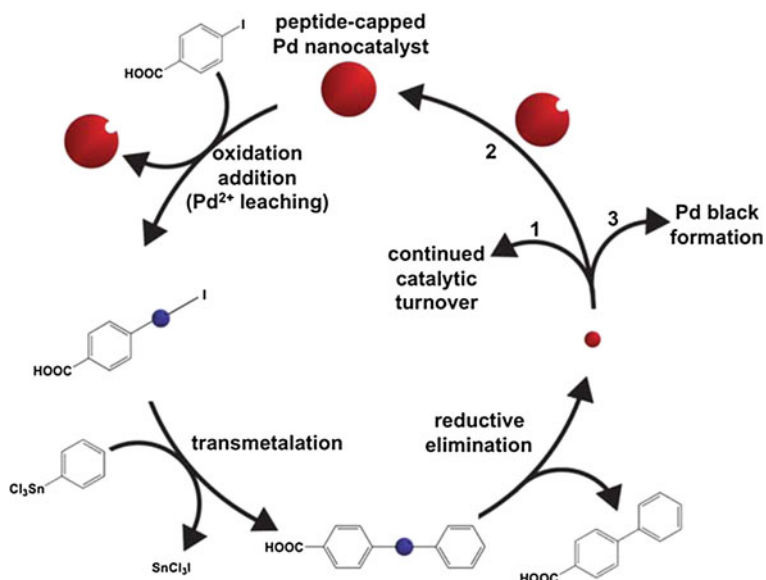


**Fig. 7.10** The atom-leaching Stille coupling of 4-iodobenzoic acid and  $\text{PhSnCl}_3$ . Reproduced ("Adapted") from (Pacardo et al. 2011) permission of the Royal Society of Chemistry

temperature studies were also performed that varied the starting reagents (Pacardo et al. 2011). For this, 4-bromobenzoic acid and 4-bromophenol were employed in the coupling, which are less reactive than their iodo-based counterparts. To increase their reactivity, elevated temperatures were studied with Pd loadings ranging from

**Fig. 7.11** Pd loading analysis of the Stille coupling reaction driven by the peptide-capped Pd nanoparticles Reproduced (“Adapted”) from (Pacardo et al. 2011) with permission of the Royal Society of Chemistry

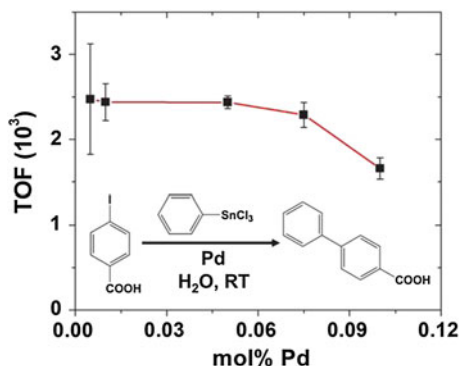
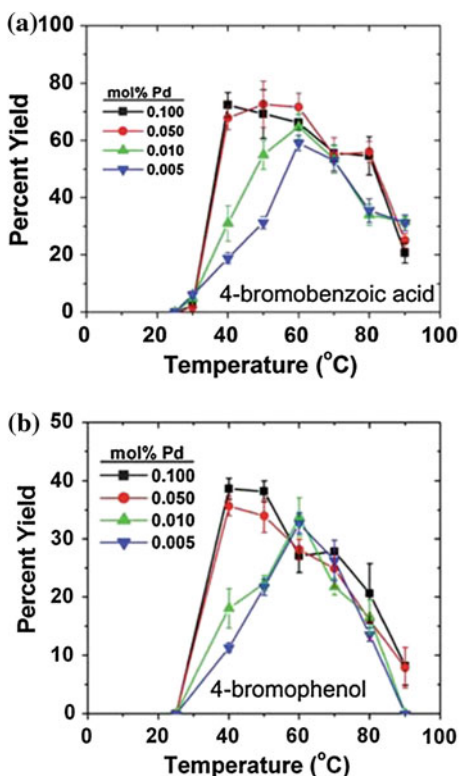


**Fig. 7.12** Temperature effects for the Stille coupling reaction using **a** 4-bromobenzoic acid and **b** 4-bromophenol. Reproduced (“Adapted”) from (Pacardo et al. 2011) with permission of the Royal Society of Chemistry



0.005 to 0.1 mol%, as shown in Fig. 7.12 (Pacardo et al. 2011). As is evident for 4-bromobenzoic acid, a maximum yield was achieved at 40 °C, which was maintained through 60 °C (Pacardo et al. 2011). At higher temperatures, the product yields continually decreased. Similar temperature effects were observed for the phenol-based aryl halide; however, lower degrees of reactivity were noted as anticipated (Pacardo et al. 2011). Control studies indicated no change in particle



morphology at higher temperatures, suggesting that the observed changes were not related to particle degradation, but rather to an effect of the reaction itself.

Taken together, the observed reactivity changes were directly attributed to a catalytic leaching mechanism driving the Stille C-C coupling process (Pacardo et al. 2011). For instance, at high temperatures, the rate of Pd black formation is anticipated to overcome the coupling rate, thus removing catalyst species from the reaction and lowering the amount of product generated. Since the particles are inherently stable at these temperatures, the mechanism itself is most likely responsible for such deactivation to occur via a leaching process. For the concentration studies, at high Pd loadings, extensive Pd atom leaching is present to generate a sufficiently concentrated solution of unstable Pd atoms that precipitate as Pd black, resulting in diminished TOF values (Pacardo et al. 2011). Finally, quartz crystal microbalance (QCM) studies of a Pd<sup>0</sup> surface confirmed that metal abstraction is possible using the aryl halide, (Pacardo et al. 2011) thus supporting the leaching-based mechanism using the peptide-capped materials.

In additional work, Pacardo et al. have performed complementary studies to probe the role of the Pd leaching mechanism with the Pd<sub>4</sub>-capped nanocatalysts (Pacardo and Knecht 2013). While it is likely that 4-iodobenzoic acid can abstract Pd atoms from the nanoparticle surface under ambient conditions, both bond distance and energy inhibit the same amount of reactivity for aryl-bromo bonds (Stille 1986; Pacardo and Knecht 2013). Should these metal atoms be preleached from the surface, coupling using the bromo species could potentially occur at lower temperatures. To probe this effect, Stille coupling reactions with aryl halide mixtures were employed at 0.05 mol% Pd loadings. From this, catalytic selectivity was noted, based upon the differences in the carbon-halogen bond strength (d Darwent 1970). For instance, as shown in Fig. 7.13, when employing mixtures of 4-iodobenzoic acid and 4-bromobenzoic acid, coupling at the iodo component occurred first at room temperature, with no coupling at the bromo substituent. When the reactivity was increased to 40 °C, consumption of the 4-bromobenzoic acid occurred, consistent with previous results (Pacardo et al. 2011). Furthermore, the degrees of catalytic selectivity were lost when the reaction was completely processed at 60 °C, suggesting that low temperature selectivity may be possible using the biomimetic materials. Such results were expanded to additional mixtures of aryl halides, including iodo-, bromo-, and chloro-based substrates, with preferential reactivity for iodo species over bromo species. No reactivity was evident from chlorinated aryl halides (Pacardo and Knecht 2013).

This low temperature reactivity was expanded to di-substituted aryl halides for Stille coupling at 25 °C, using 3-bromo-5-iodobenzoic acid (Pacardo and Knecht 2013). Under these conditions, the products were analyzed over 5.0 h, showing a decrease in the amount of starting materials with the production of both the intermediate, 3-bromo-5-phenylbenzoic acid, and a minor amount of the final product, 3,5-diphenylbenzoic acid (Fig. 7.14b). Note that no 3-iodo-5-phenylbenzoic acid was detected, suggesting that oxidative addition was dependent upon the halogen. Over the first 5.0 h, the main species generated was the intermediate; however, a small amount of the diphenyl final product was generated (Pacardo and

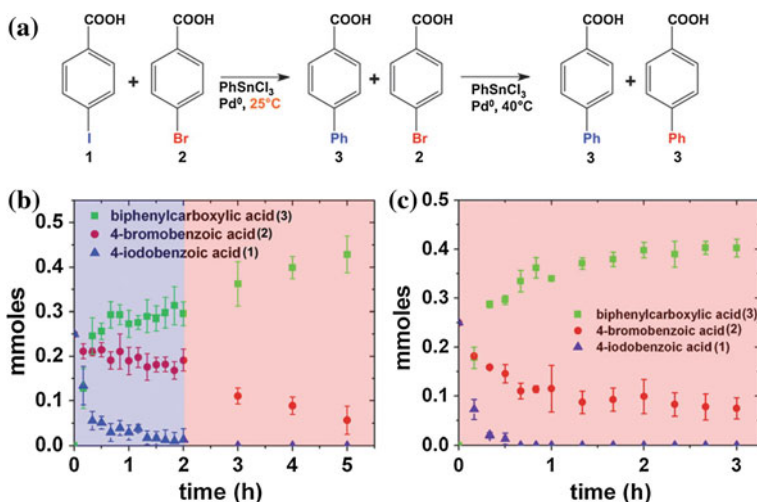
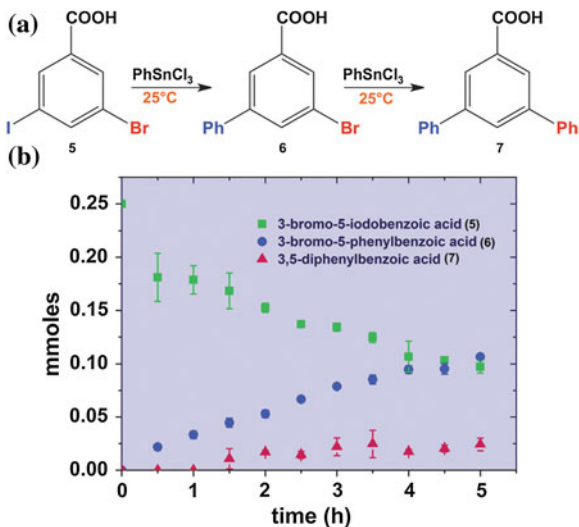


**Fig. 7.13** a The Stille coupling scheme under which the initial reaction takes place at 25 °C and is increased to 40 °C at 2.0 h (b). The reaction is also carried out at 40 °C (c) as a comparison. Reproduced (“Adapted”) from (Pacardo and Knecht 2013) with permission of the Royal Society of Chemistry

**Fig. 7.14** Aryl dihalide effects on the catalytic reactivity of the Pd4-capped Pd nanoparticles. Part a presents the reaction scheme, while part b presents the reaction analysis. Reproduced (“Adapted”) from (Pacardo and Knecht 2013) with permission of the Royal Society of Chemistry



Knecht 2013). This suggests that activation of the bromo group by the added phenyl ring may be possible. After allowing the reaction to proceed for 24.0 h, it was noted that  $70.8 \pm 0.9 \%$  of the intermediate was generated and  $22.1 \pm 2.5 \%$  of the 3,5-diphenylbenzoic acid product was prepared (Pacardo and Knecht 2013).

The amount of the final product can be increased should the reaction temperature or catalyst concentration be increased, which suggested a reactivity preference for the iodo over the bromo substituent.

Taken together, these studies suggest that Stille coupling using the peptide-capped materials may be selective under very low temperature conditions ( $<50\text{ }^{\circ}\text{C}$ ). This could prove to be quite important for the modification of thermally sensitive materials, such as proteins. Furthermore, this data provides important information concerning the catalytic reaction mechanism for Stille coupling. To this end, the Pd atoms can insert across the iodo-carbon bond at room temperature, while slight thermal activation is required for similar reactivity using bromo-based compounds. This effect is likely due to the bond strength difference of the two bonds (C-I>C-Br), (d Darwent 1970) which can directly affect their level of reactivity. In general, these peptide-capped materials are unique model systems to probe this degree of reactivity and the overall catalytic mechanism.

While initial studies indicated that Pd leaching was responsible for the reactivity using the Pd<sub>4</sub>-stabilized materials, the effects of the biotic/abiotic interface on both the material fabrication and catalytic functionality were unclear. To probe the binding effects, Coppage et al. synthesized three Pd<sub>4</sub> analogs by replacing the anchoring histidine residues with alanine substitutions at the 6 (A6), 11 (A11), and 6 and 11 (A6,11) positions (Table 7.1) (Coppage et al. 2010). From these peptides, stable Pd<sup>0</sup> nanoparticles were formed with sizes of  $2.2 \pm 0.4$ ,  $2.4 \pm 0.5$ , and  $3.7 \pm 0.9$  nm, respectively (Coppage et al. 2010). Circular dichroism (CD) studies indicated that the peptide surface structure of all of the materials was substantially different based upon the changes to the sequence at the residue level. Next, catalytic studies were processed for the coupling of 4-iodobenzoic acid with PhSnCl<sub>3</sub> using these materials, which demonstrated significant changes as compared to the Pd<sub>4</sub>-capped particles. For instance, the A6-capped materials displayed a TOF value of  $5224 \pm 381$  mol product (mol Pd  $\times$  h)<sup>-1</sup>, which was more than double the typical value observed for the native Pd<sub>4</sub>-capped materials ( $2234 \pm 99$  mol product (mol Pd  $\times$  h)<sup>-1</sup>) (Coppage et al. 2010). Conversely, a TOF decrease was observed for the Pd nanoparticles generated with either the A11 or A6,11 to values of  $1298 \pm 107$  mol product (mol Pd  $\times$  h)<sup>-1</sup> or  $361 \pm 21$  mol product (mol Pd  $\times$  h)<sup>-1</sup>, respectively. Taken together, these initial studies suggested that weak binding at the 6 position and strong binding at the 11 position would result in optimal reactivity.

While altered particle reactivities were noted as a function of the peptide sequence, unique information concerning the total structure of the materials became evident. In general, the peptide-capped Pd nanoparticles are prepared at a Pd:peptide ratio of 3.3:1 for all of the peptide sequences studied (Pacardo et al. 2009; Coppage et al. 2010). To explore the effect of reaction stoichiometry, this ratio was varied from 1 to 10; however, systems with a ratio  $\geq 5$  precipitated shortly after reduction. As a result, only the materials prepared at ratios  $\leq 4$  were analyzed (Coppage et al. 2011, 2012). Interestingly, regardless of the ratio employed for the stable materials, these systems produced particles of nearly equivalent sizes for each peptide. To this end, for the Pd<sub>4</sub>-based materials, a particle size of  $\sim 2$  nm was observed for all materials prepared at a Pd:peptide ratio  $\leq 4$ , as shown in Fig. 7.15a

**Table 7.1** List of the Pd4 alanine analog peptides studied

Peptide	Sequence	Size (nm)	TOF <sup>[a]</sup>
Pd4	TSNAVHPTLRHL	1.9 ± 0.3	2234 ± 99
A6	TSNAVAPTLRHL	2.2 ± 0.4	5224 ± 381
A11	TSNAVHPTLRAL	2.4 ± 0.5	1298 ± 107
A6, 11	TSNAVAPTLRAL	3.7 ± 0.9	361 ± 21

$$a = \frac{\text{mol BPCA}}{\text{mol Pd} \times h}$$

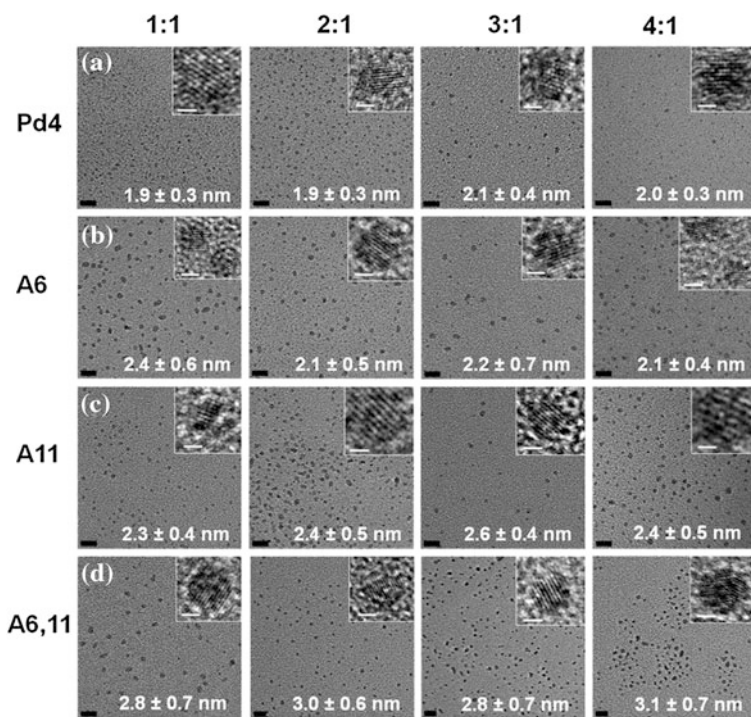
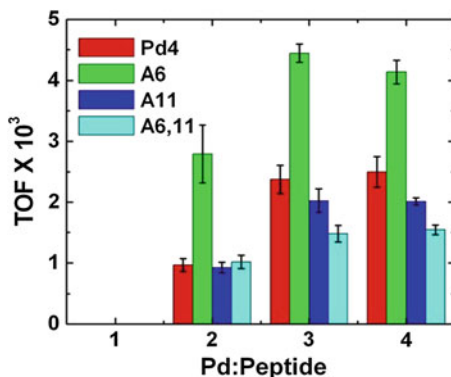


**Fig. 7.15** TEM analysis of materials generated using Pd:peptide ratio of 1–4, with peptides **a** Pd4 **b** A6 **c** A11, and **d** A6,11. Reprinted (adapted) with permission from (Coppage et al. 2012). Copyright (2012) American Chemical Society

(Coppage et al. 2011, 2012). In general, larger particles were observed for the alanine-modified peptide-capped materials, independent of Pd loading (Coppage et al. 2012). For instance, for the materials capped with the A6 peptide, particles of ~2.2 nm were generated, where the particle size further increased to ~2.4 and ~3.0 nm for the A11- and A6,11-capped Pd nanoparticles (Fig. 7.15) (Coppage et al. 2012). Such size effects are different from nanoparticles capped with standard alkyl thiol ligands, where the size varied based upon the ligand:metal ratio (Hussain et al. 2005; Brinas et al. 2008). Such effects for the peptide-based materials likely arises from biorecognition of the metallic surface, which is altered via the changes to the sequence for the A6, A11, and A6,11 peptides.

**Fig. 7.16** TOF analysis of nanoparticles capped with the Pd4 and alanine analog peptides prepared at Pd:peptide ratios of 1–4. Reprinted (adapted) with permission from (Coppage et al. 2012). Copyright (2012) American Chemical Society



Once characterized, the nanomaterials were employed in the Stille coupling reaction to compare their catalytic activities (Coppage et al. 2011, 2012). When considering the materials produced at the same Pd:peptide ratios, the resulting TOF values follow previously observed coupling trends (Coppage et al. 2010). To this end, for the materials prepared at a Pd:peptide ratio of 4, TOF values of  $2,496 \pm 252$  mol product  $(\text{mol Pd} \times \text{h})^{-1}$ ,  $4,314 \pm 190$  mol product  $(\text{mol Pd} \times \text{h})^{-1}$ ,  $2,010 \pm 59$  mol product  $(\text{mol Pd} \times \text{h})^{-1}$ , and  $1,565 \pm 66$  mol product  $(\text{mol Pd} \times \text{h})^{-1}$  were obtained for nanoparticles capped with Pd4, A6, A11, and A6,11, respectively (Fig. 7.16) (Coppage et al. 2012). The materials prepared at a Pd:peptide ratio of 3 demonstrated similar reactivity; however, at a ratio of 2, TOF values of  $965 \pm 105$  mol product  $(\text{mol Pd} \times \text{h})^{-1}$ ,  $2,793 \pm 473$  mol product  $(\text{mol Pd} \times \text{h})^{-1}$ ,  $1,026 \pm 191$  mol product  $(\text{mol Pd} \times \text{h})^{-1}$ , and  $1,009 \pm 78$  mol product  $(\text{mol Pd} \times \text{h})^{-1}$  were observed for the Pd4, A6, A11, and A6,11 peptide-capped particles, respectively (Coppage et al. 2012). Such a change represents a significant decrease in reactivity as compared to those samples prepared at higher ratios for all the four different systems. Finally, for the materials prepared at a Pd:peptide ratio of one, no C-C coupling product was observed over the 1.0 h timeframe of the TOF study (Coppage et al. 2012). These changes are likely based upon excess peptide available in solution, which can bind and sequester leached Pd atoms from the reaction medium. In this event, after the first coupling cycle, the liberated Pd atoms become unreactive, leading to diminished TOF values at lower ratios.

In addition to the alanine substitutions to the Pd4 sequence, a number of other substitutions have recently been made in an attempt to elucidate how localized surface binding events at the residue level affect the properties of the resultant nanomaterials (Coppage et al. 2013). For the alanine analogs, the greatest catalytic activity arose from the particles capped with the A6 peptide; however, modifications at the 11 position resulted in a substantial reactivity decrease. As such, weak binding at the 6 position and strong binding at the 11 position could provide for an optimal surface-bound peptide structure for catalytic reactivity. By substituting these binding sites with potentially stronger metal-binding residues, a

**Table 7.2** Cysteine- and alanine-substituted Pd4 analogs

Peptide	Sequence	Size (nm)	TOF <sup>[a]</sup>
Pd4	TSNAVHPTLRHL	2.0 ± 0.4	2,234 ± 99
C6	TSNAVCPTLRHL	2.2 ± 0.3	3,963 ± 28
C11	TSNAVHPTLRCL	2.4 ± 0.4	6,138 ± 55
C6, 11	TSNAVCPTLRCL	2.3 ± 0.4	3,974 ± 280
A6C11	TSNAVAPTLRCL	2.4 ± 0.4	6,097 ± 65
C6A11	TSNAVCPTLRAL	2.4 ± 0.4	4,147 ± 340

$$a = \frac{\text{mol BPCA}}{\text{mol Pd} \times \text{h}}$$

greater understanding of the peptide surface binding could be realized. To this end, the 6- and 11-position histidines were substituted with cysteine or alanine to create a set of five new peptides to probe these localized binding effects: C6, C11, C6,11, A6C11, and C6A11 (Table 7.2) (Coppage et al. 2013).

To quantify and compare the binding affinity of the cysteine-containing peptides to Pd, QCM analysis was employed, as shown in Fig. 7.17 (Coppage et al. 2013). Such a study was required in light of the thiolated residue that could dramatically change peptide binding affinities. Using previously described methods, (Tamerler et al. 2006) the association ( $k_a$ ) and dissociation ( $k_d$ ) constants can be determined, from which the equilibrium ( $K_{eq}$ ) constant and free energy ( $\Delta G$ ) of binding can be calculated. As shown in Fig. 7.13c, no trend was observed in the binding affinities of the cysteine-based peptides to the particle surface (Coppage et al. 2013). In general, higher affinity was noted from those sequences with the thiol group; however, the presence of cysteine did not automatically result in stronger surface binding. Together, this indicates that the positioning of the residues in the sequence plays an important role in the overall binding affinity to the target material (Fig. 7.18).

Once their binding strengths were confirmed, the peptides were employed in the synthesis of Pd nanoparticles (Coppage et al. 2013). For these peptides, Pd nanoparticles of nearly the same size were generated at a Pd:peptide ratio of 3.3. For instance, the Pd4-capped particles were noted to be  $2.0 \pm 0.4$  nm; however, the materials prepared with cysteine-substituted peptides were observed to be  $2.2 \pm 0.4$ ,  $2.4 \pm 0.3$ ,  $2.3 \pm 0.4$ ,  $2.4 \pm 0.4$ , and  $2.4 \pm 0.4$  nm for C6-, C11-, C6,11-, A6C11-, and C6A11-based structures, respectively (Fig. 7.14) (Coppage et al. 2013). This was surprising as the alanine analog capped materials were able to control the size of the generated particles (Coppage et al. 2012). The cysteine residue may play a different role in coordinating to the particle surface, which occurs through a covalent bond that may give rise to these differences. Additionally, the size of the particles did not correlate to the binding strength of the peptides, suggesting that the absolute affinity did not dictate the resultant particle size. Once prepared, CD studies of the Pd nanoparticles indicated that the structures for the C6 and C6A11 peptides were similar, while the structure of the

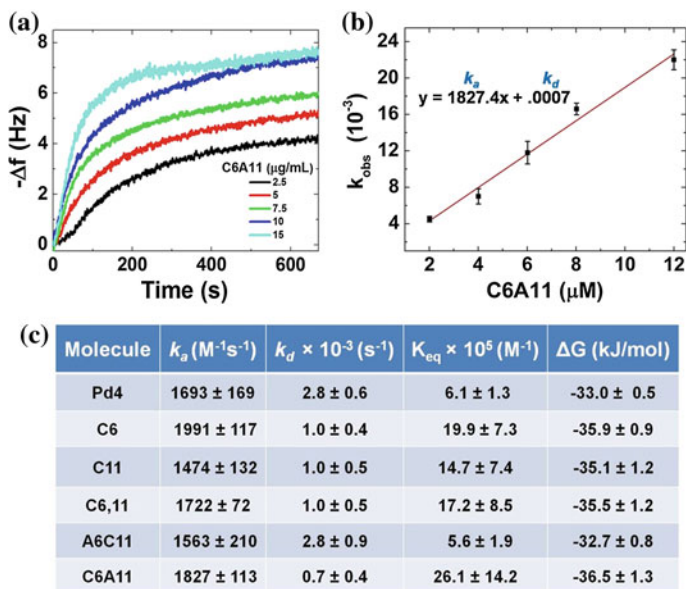


**Fig. 7.17** QCM analysis of Pd4 and cys-analogs. Part **a** presents the change in frequency as a function of time and peptide concentration, part **b** displays the linear fit of the  $k_{obs}$  values, and part **c** presents the  $k_a$ ,  $k_d$ ,  $K_{eq}$ , and  $\Delta G$  values. Reprinted (adapted) with permission from (Coppage et al. 2013) Copyright (2013) American Chemical Society

surface-bound C11 and A6C11 was also related (Coppage et al. 2013). As such, the surface structure of these two material sets is likely to be similar, which was consistent with the observed reactivity (described below).

To test and compare the catalytic activity of the Pd nanoparticles capped with the cysteine-containing peptides, the Stille coupling between 4-iodobenzoic acid and  $PhSnCl_3$  was studied (Coppage et al. 2013). Compared to previous catalytic results with Pd4-capped particles ( $2234 \pm 99$  mol product  $(mol Pd \times hr)^{-1}$ ), (Coppage et al. 2010) all the materials prepared with cys-substituted analogs showed an increase in reactivity based upon their TOF values. For the materials prepared with a 6-position cysteine, a nearly two-fold increase in activity was observed for C6, C6,11, and C6A11, resulting in TOF values of  $3963 \pm 28$  mol product  $(mol Pd \times hr)^{-1}$ ,  $3974 \pm 280$  mol product  $(mol Pd \times hr)^{-1}$ , and  $4147 \pm 340$  mol product  $(mol Pd \times hr)^{-1}$ , respectively (Fig. 7.19) (Coppage et al. 2013). Interestingly, for the materials with a peptide with an 11-position cysteine, an even greater increase in reactivity was noted with a value of  $6138 \pm 55$  mol product  $(mol Pd \times hr)^{-1}$  for the C11-capped particles and  $6097 \pm 65$  mol product  $(mol Pd \times hr)^{-1}$  for the A6C11-stabilized structures (Coppage et al. 2013).

Combined with the binding affinity values from the QCM analysis and the CD data, the catalytic information provides valuable insight into the nanoparticle

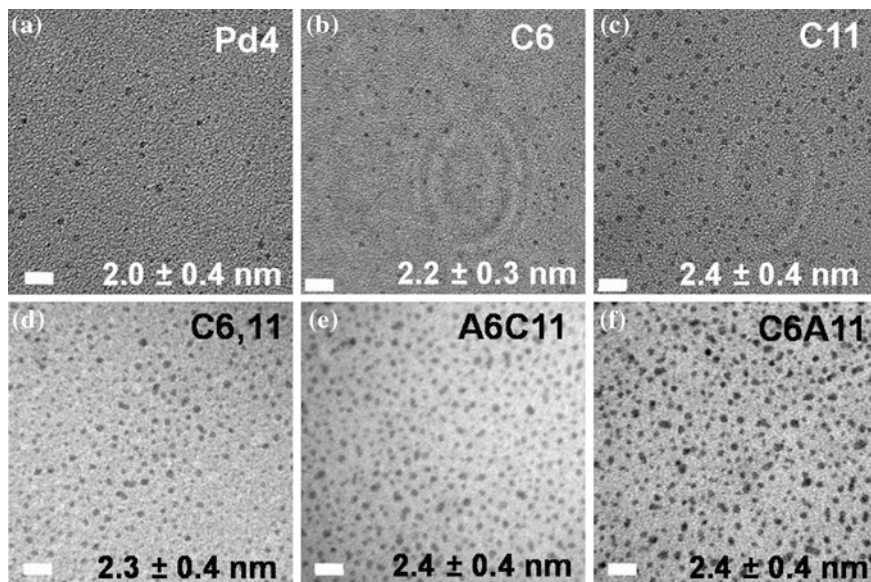
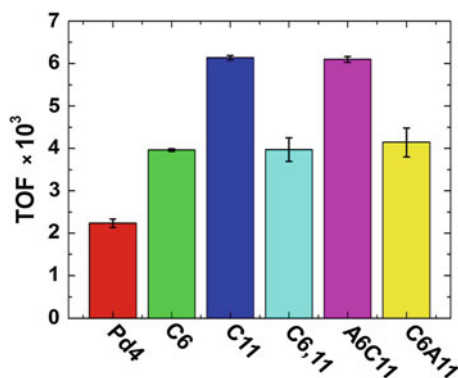


**Fig. 7.18** TEM images and sizing analysis of the Pd nanoparticles synthesized with the **a** Pd4 **b** C6 **c** C11 **d** C6,11 **e** A6C11, and **f** C6A11 peptide. Reprinted (adapted) with permission from (Coppage et al. 2013) Copyright (2013) American Chemical Society

**Fig. 7.19** TOF analysis of nanoparticles capped with the Pd4 and cys-substituted analog peptides. Reprinted (adapted) with permission from (Coppage et al. 2013) Copyright (2013) American Chemical Society



biointerface. This suggests that localized binding effects of the individual residues of peptides plays an important role in controlling material functionality. As such, peptide design could be employed in the future to isolate sequences with strong affinity that could direct the target affinity of the sequences, as well as the activity of the resultant materials.



## 7.5 Peptide-Capped Multicomponent Nanomaterials

Though monometallic nanoparticles possess well-known catalytic activity, select combinations of noble metals possess increased reactivity as compared to single-component systems (Slocik and Naik 1988; Slocik et al. 2008). Bimetallic catalysts have been demonstrated with AuPt, (Zhou et al. 2007) AuPd, (Hou et al. 2008) MnCu, (Stumpf et al. 1993) PdCu, (Xu et al. 2009), and CuRu (Sinfelt et al. 1980) materials with core-shell, (Wang et al. 2008) nanowire, (Lee et al. 2012) and other geometries (Han et al. 2007). This increase in activity is proposed to be a function of two different effects: electronic changes in the system and the geometric configuration of metal atoms in the material (Stamenkovic et al. 2007).

Bi-component PdAu nanocatalysts have been prepared using a multifunctional materials-binding peptide based upon two sequences known to bind noble metal nanoparticles (Slocik and Naik 1988). For this, the A3 peptide (AYS-SGAPPMPFF) isolated with an affinity to Ag and Au (Pandey et al. 1989) was integrated into a single sequence with the Flg (DYKDDDDK) peptide, which was known to bind noble metal particles (Pandey et al. 1989). With these two components, a single, multifunctional fusion peptide was generated to form the Flg-A3 sequence (Slocik and Naik 1988). Interestingly, the order of the sequences directly affected material binding, where positioning of the Flg and A3 regions at the N- and C-terminal portions, respectively, was required to optimize material binding for nanoparticle formation (Fig. 7.16). For this, the A3 region was anticipated to bind Au, thus displaying the Flg region that exposes multiple aspartic acids to bind Pd<sup>4+</sup> ions for eventual Pd<sup>0</sup> nanoparticle production.

Au nanoparticles were formed by mixing the Flg-A3 peptide with Au<sup>3+</sup> ions in a HEPES buffer and incubated for 30 min (Slocik and Naik 1988). To a solution of the resulting, purified Au nanoparticles, Pd<sup>4+</sup> was added, followed by sodium borohydride. This led to the generation of ~3.0 nm Pd nanoparticles attached to the surface of the Au materials via the Flg-A3. TEM analysis of the bimetallic materials revealed the formation of Au nanoparticles with smaller Pd particles incorporated at the surface, as shown in Fig. 7.16a (Slocik and Naik 1988). Prior to Pd nanoparticle production, the Flg-A3-capped Au nanoparticles were observed to be 10.7 ± 0.6 nm. The overall diameter increased to 15.5 ± 3.9 nm after Pd addition due to the presence of the smaller Pd particles (Slocik and Naik 1988). As shown in Fig. 7.20b, various lattices were distinguishable on the surface of the Au nanoparticle, indicative of the smaller Pd nanoparticles being included at the Au surface.

With this combination of metals, a catalytic increase was likely from the surface displayed Pd nanoparticles. To this end, the more electronegative Au component pulls electron density from the Pd particles, thus increasing their catalytic reactivity for olefin hydrogenation (Hou et al. 2008; Dash et al. 2008). To determine if such effects were observed from the biomimetic bimetallic materials, their activity was tested via the hydrogenation of 3-buten-1-ol to 1-butanol (Slocik and Naik 1988). With the peptide-capped materials, a TOF value of 1016 mol product (mol Pd × h)<sup>-1</sup> was noted, which is greater than double the value observed when

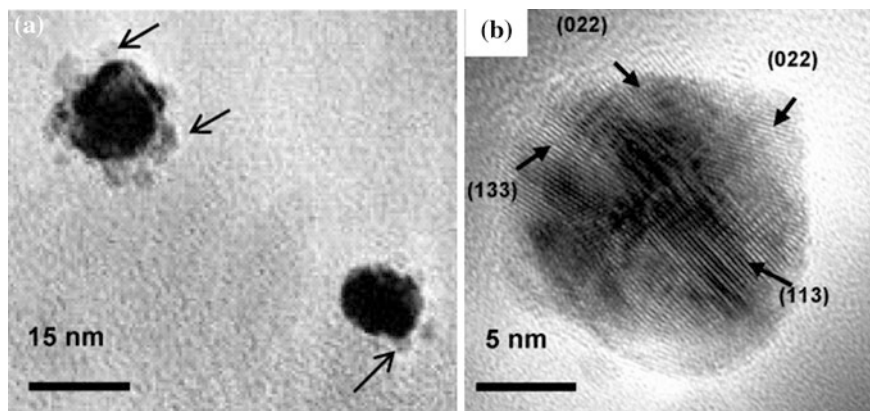


**Fig. 7.20** TEM images of the bimetallic PdAu nanoparticles prepared using the Flg-A3 peptide. Reproduced from Fang et al. (2009) with permission from Wiley-VCH, copyright 2006

using commercially available Pd nanoparticles under the same reaction conditions ( $501 \text{ mol product (mol Pd} \times \text{h)}^{-1}$ ) (Slocik and Naik 1988). As such, increased reactivity was observed, suggesting that sufficient contact between the two metallic components was present to allow for electronic changes that resulted in the enhanced functionality.

In a second study, the Flg-A3 peptide was employed by Slocik et al. for the synthesis of Pt-CdS nanomaterials as a biomimetic analog of the enzyme nitrate reductase (Slocik et al. 2008). This enzyme is known to reduce nitrate to nitrite, which has been emulated by metallodendritic catalysts (Mery and Astruc 1965) and exploited in the synthesis of silver nanoparticles (Kumar et al. 2007). For these studies, the Flg-A3 peptide was modified by the addition of a cysteine residue at the C-terminus, termed Flg-A3C (Slocik et al. 2008). The thiol functional group caps the growth of the CdS quantum dots, with the remainder of the peptide exposed to solution for Pt nanoparticle production. After introduction of  $\text{Pt}^{2+}$  ions and reduction, the multicomponent materials were generated, which displayed a unique chain-like structure (Slocik et al. 2008). At present, it is unclear why such a structure was generated; however, the materials were observed to be nearly monodisperse with sizes of 13 nm for the CdS quantum dots, 1.5 nm for the surface-bound Pt nanoparticles, and  $\sim 15$  nm for the nanoassemblies (Fig. 7.21) (Slocik et al. 2008). The organization of Pt nanoparticles on the surface of CdS was likely controlled by the fusion peptide. With the Pt and CdS components in close proximity, this could elicit rapid electron transfer upon exposure to UV light, which is required for nitrate reduction.

Once fully characterized, the Pt-CdS materials were employed as catalysts for nitrate reduction, which can be monitored via UV-vis. This was achieved by exciting at 370 nm and observing the fluorescent intensity at 431 nm, which is indicative of nitrite production (Slocik et al. 2008). From this study, the activity of the excited multicomponent Pt-CdS materials was observed to be at least 20 times

**Fig. 7.21** TEM analysis of the Pt-CdS nanomaterials prepared using the Flg-A3C peptide. Scale bars are 13 nm and 4 nm for the inset.

Reproduced with permission from Slocik et al. (2008) with permission from Wiley-VCH, copyright 2008

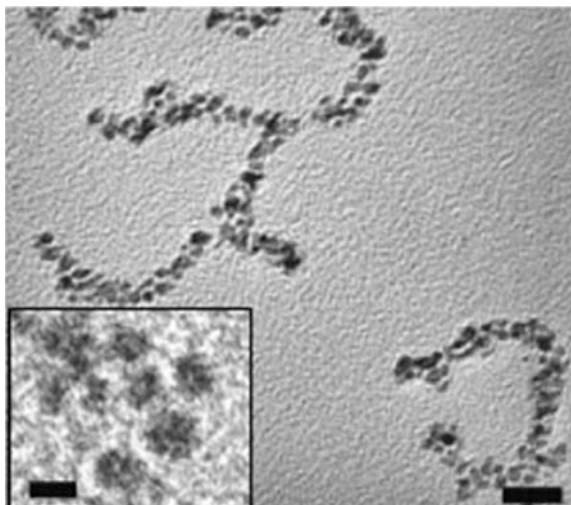
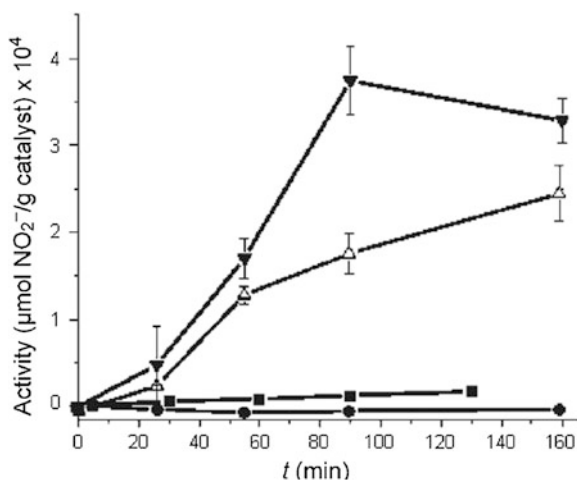


**Fig. 7.22** Activity comparison for various systems for the reduction of nitrate with Pt-CdS (▼), CdS nanoparticles (Δ) when excited at 250 nm, nitrate reductase (cofactor added) (■), and Pt-CdS nanoparticles without excitation (●). Reproduced with permission from Slocik et al. (2008)



greater than the activity of nitrate reductase. As controls, two other materials were tested for reactivity, including the excited CdS nanoparticles and the Pt-CdS system without excitation. Among these systems, the excited Pt-CdS nanoassemblies were observed to possess the highest activity with  $3.7 \times 10^4$  mol  $\text{NO}_2^-/\text{g}$  catalyst at 90 min, as shown in Fig. 7.22 (Slocik et al. 2008). At 90 min, almost no activity was observed for the enzyme (with cofactor) and the Pt-CdS quantum dots (without excitation). When the CdS materials were employed in the absence of the Pt component and excited at 250 nm, a lower activity was again observed ( $1.5 \times 10^4$  mol  $\text{NO}_2^-/\text{g}$  catalyst) (Slocik et al. 2008). The presence of the Pt provides a source of electron mediators between filling holes in the quantum dots, further increasing activity of the assemblies.

## 7.6 Peptide Template-Based Materials

Bhandari et al. have reported on the fabrication of nanoparticle networks (NPNs), templated by the R5 peptide (SSKKSGSYSGSKGSKRRIL) (Jakhmola et al. 2010; Bhandari and Knecht 2012a, b). This sequence was derived from the repeat units of the NatSil gene of the diatom *Cylindrotheca fusiformis* (Kroger et al. 1999). Known for the production of TiO<sub>2</sub> (Luckarift et al. 2006) and SiO<sub>2</sub>, (Knecht and Wright 2003) the R5 possesses an RRIL motif that facilitates self-assembly to form large scaffolds (Knecht and Wright 2003). With this peptide sequence, a variety of Pd nanoscale morphologies can be synthesized, ranging from spheres and ribbons to NPNs (Jakhmola et al. 2010). The Pd systems were observed to be loading-dependent, as shown in Fig. 7.23a–d. In this regard, at Pd:peptide ratios of 60, 90, and 120, stable nanostructured materials were observed; however, at ratios of 150 and above, bulk precipitation was noted (Jakhmola et al. 2010). These materials are defined as PdX, where X represents the Pd:peptide ratio employed during material synthesis. In solution, these bioscaffolds first self-assemble into larger constructs, which act as templates to control metallic material growth. First, the Pd<sup>2+</sup> ions are complexed within the bioscaffold through binding to the residues at the interior of the template. Second, addition of NaBH<sub>4</sub> results in metal ion reduction and the growth of zerovalent materials (Jakhmola et al. 2010). The peptide framework then acts as a template to guide the growth of the metallic components, in addition to stabilizing the final materials against aggregation via encapsulation. From this approach, spherical materials are observed at low Pd:peptide ratios that selectively aggregate in the template at higher ratios to form the linear NPN structures.

From TEM analysis of the Pd60 sample, spherical nanoparticles with a diameter of  $2.9 \pm 0.6$  nm were observed; however, for the Pd90 materials, nanoribbons with widths of  $3.9 \pm 0.8$  nm were noted, while for the Pd120 system, NPNs were discovered with an average width of  $4.1 \pm 1.2$  nm (Fig. 7.23a–c) (Jakhmola et al. 2010). HR-TEM imaging revealed that the ribbons and NPNs were polycrystalline, where single nanoparticles were initially formed and then fused together, based upon their close proximity within the template (Fig. 7.23d). Such results support a nanoparticle aggregation process inside the template, where those particles in close proximity can aggregate to form the linear materials.

Once the materials were characterized, they were employed as catalysts for the Stille coupling for 4-iodobenzoic acid with PhSnCl<sub>3</sub>. Here, the reactivities were found to be dependent on both the bioscaffold and metallic surface area, with TOF values of  $452.4 \pm 16.4$  mol product (mol Pd × h)<sup>-1</sup> for the spherical Pd60 materials, while the other systems demonstrated TOFs of  $334.3 \pm 38.3$  mol product (mol Pd × h)<sup>-1</sup> and  $437.1 \pm 14.3$  mol product (mol Pd × h)<sup>-1</sup> for the Pd90 and Pd120 samples, respectively (Fig. 7.23e) (Jakhmola et al. 2010). For each system, the metallic catalyst is contained within the peptide bioscaffold. Spherical particles were observed in the Pd60 materials, which are likely to possess the greatest surface area. For the Pd90 materials, a decrease in activity was

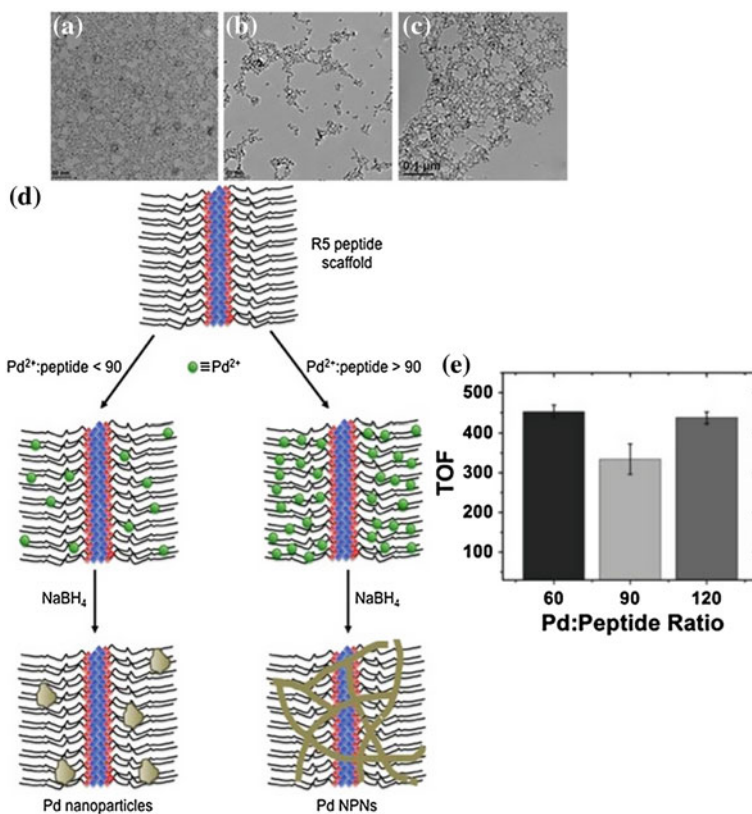


**Fig. 7.23** TEM images of the **a** Pd60 **b** Pd90, and **c** Pd120 materials. Part **d** presents the mechanism of nanostructure formation using the biotemplate, while part **e** displays the Stille TOF analysis of the materials. Reproduced (“Adapted”) from (Jakhmola et al. 2010) with permission of the Royal Society of Chemistry)

observed, which is expected as the surface area was diminished for the nanoribbons as compared to the nanospheres. Finally, an interesting increase in activity was observed for the Pd120 materials, even though they were anticipated to possess the lowest metallic surface area. This NPN reactivity effect was suggested to be a function of the overall structure of the materials (Jakhmola et al. 2010). For the NPNs, the greatest amount of metallic materials is present within the template, thus positioning the reactive components closer to the scaffold surface. As such, diminished reagent diffusion was required to reach the catalytic component, resulting in an increased TOF value.

While the R5 peptide formed a self-assembled template to encapsulate the Pd nanomaterials, the effect of the peptide sequence, and thus the scaffold structure, remained unclear. Two factors contribute to the catalytic activity of this system: the inorganic surface area and reagent diffusion through the bioframework. As such, modulation of these factors could be used to optimize the reaction efficiency.

To probe the effects of the template, Pd materials were synthesized employing four peptide truncates of the R5: T1 (SSKKSGSY), T2 (SGSKGSKRRIL), T1A (SSKKSGSYRRIL), and T2A (SGSKGSK). (Bhandari and Knecht 2012b) The first two peptides were obtained by cleaving the R5 peptide at the tyrosine residue, thus isolating the RRIL motif in the T2. Furthermore, both half sequences contain similar amino acids for metal ion coordination. Additionally, the T1A and T2A sequences were modifications of T1 and T2 that swapped the RRIL motif. Each of these peptides were employed to form stable materials at Pd:peptide ratios of 30, 60, and 90 (Bhandari and Knecht 2012b). These resulting Pd nanomaterials were characterized via TEM analysis and tested for Stille coupling reactivity.

For all four systems, at the lowest Pd:peptide ratio (30), the nanomaterials were observed to be spherical structures contained within the bioscaffold (Bhandari and Knecht 2012b). At ratios of 60, some elongated materials and nonspherical morphologies were observed, with larger dimensions as compared to the materials prepared with a ratio of 30. For the materials fabricated at a ratio of 90, mostly NPNs were noted (Bhandari and Knecht 2012b). In general, similar structures were prepared at the same Pd:peptide ratio, regardless of the bioscaffold employed to template the materials. TEM images of the Pd materials prepared with each peptide at Pd:peptide ratios of 30, 60, and 90, along with their individual sizing analysis, is shown in Fig. 7.24 (Bhandari and Knecht 2012b). Metallic materials prepared at higher Pd:peptide ratios aggregated, thus lower ratio materials were studied.

It was surprising that all of the truncates were able to generate nonspherical Pd materials, as the RRIL motif was missing from the T1 and T2A peptides. To probe the structure of the peptides in solution, DLS analysis was performed on both the free peptides and Pd<sup>2+</sup>-complexed biomolecular systems, which demonstrated an increasing size trend with respect to increased Pd<sup>2+</sup> loading (Bhandari and Knecht 2012b). These sizing results indicated that all peptides could assemble into bioscaffolds, independent of the RRIL motif; however, the peptides that contained the RRIL formed larger templates. As such, this motif appears to promote peptide self-assembly, but other factors within the sequence can also drive template formation.

To probe the reactivity of materials prepared with the truncated templates, the 12 different systems were employed as catalysts in the Stille coupling reaction of 4-iodobenzoic acid and PhSnCl<sub>3</sub> (Fig. 7.25) (Bhandari and Knecht 2012b). For the materials prepared with the T1 template at Pd:peptide ratios of 30 and 60, TOF values of  $1030 \pm 26$  mol product (mol Pd  $\times$  h)<sup>-1</sup> and  $1215 \pm 70$  mol product (mol Pd  $\times$  h)<sup>-1</sup>, respectively, were observed, while a lower TOF value of  $451 \pm 40$  mol product (mol Pd  $\times$  h)<sup>-1</sup> was noted for the T1-Pd90 NPNs (Bhandari and Knecht 2012b). For the T2 materials, TOF values of  $38 \pm 9$  mol product (mol Pd  $\times$  h)<sup>-1</sup>,  $530 \pm 49$  mol product (mol Pd  $\times$  h)<sup>-1</sup>, and  $437 \pm 46$  mol product (mol Pd  $\times$  h)<sup>-1</sup> were observed for ratios of 30, 60, and 90, respectively (Bhandari and Knecht 2012b). The T1A-Pd30, 60, and 90 materials demonstrated TOF values of  $166 \pm 23$  mol product (mol Pd  $\times$  h)<sup>-1</sup>,  $315 \pm 56$  mol product (mol Pd  $\times$  h)<sup>-1</sup>, and  $224 \pm 44$  mol product (mol Pd  $\times$  h)<sup>-1</sup>, respectively (Bhandari and Knecht 2012b). Finally, the T2A-Pd30 materials demonstrated TOF values of  $370.5 \pm 8.5$  mol product (mol Pd  $\times$  h)<sup>-1</sup>

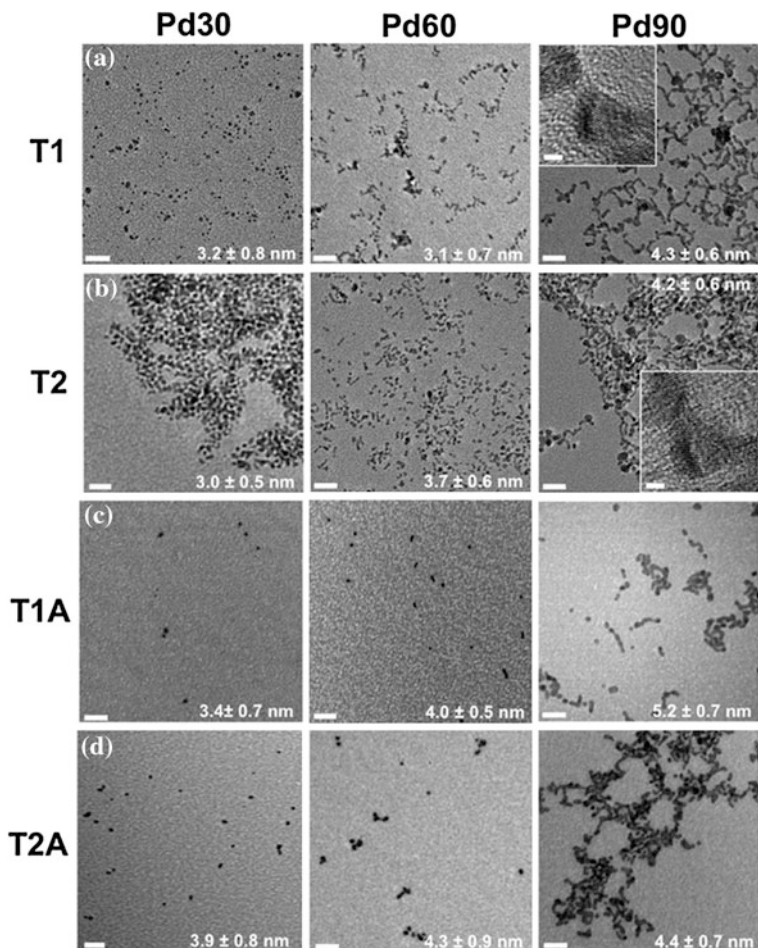
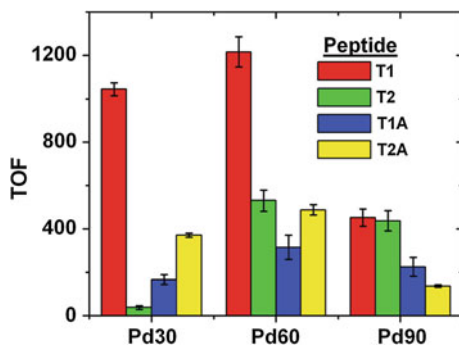


**Fig. 7.24** TEM analysis of materials prepared with the **a** T1 **b** T2 **c** T1A, and **d** T2A templates at Pd:peptide ratios of 30, 60, and 90. Scale bar is 20 nm and inset scale bar is 2 nm. Reprinted (adapted) with permission from (Bhandari and Knecht 2012b). Copyright (2012) American Chemical Society

**Fig. 7.25** TOF analysis of the materials prepared using the peptide truncates. Reprinted (adapted) with permission from (Bhandari and Knecht 2012b). Copyright (2012) American Chemical Society



for the spheres, while the T2A-Pd60 materials demonstrated a TOF average of  $487.3 \pm 24.2$  mol product  $(\text{mol Pd} \times \text{h})^{-1}$  for the nanoribbons, and the T2A-Pd90 materials showed a TOF value of  $137.5 \pm 4.9$  mol product  $(\text{mol Pd} \times \text{h})^{-1}$  (Bhandari and Knecht 2012b). Due to the structural similarity of the Pd components for each of the different materials, the variations in the peptide scaffold are likely responsible for the changes in the observed catalytic activity. To this end, similar Pd morphologies are present at each ratio; however, the templates must be different due to the differences in scaffold size and peptide sequence used to generate the framework. As such, this scaffolding effect may allow for greater access to the Pd materials for the T1 system over the other materials. Such bio-framework effects may open the door to rational template modifications to engender the materials with optimal functionality.

Beyond Pd-based materials, the R5 peptide has demonstrated the ability to form Au NPNs that are catalytically reactive (Bhandari and Knecht 2012a). Such material morphologies have become of interest due to their high metallic surface area, tunable optical properties, and large frameworks for a variety of applications such as nanoporous supports, (Lang et al. 2013) electrocatalysts, (Maye et al. 2000), and biosensing platforms (Sidhaye et al. 2005). Though these materials are traditionally prepared with ligands that bind directly to the metallic surface, (Chirea et al. 2011; Wang et al. 2006; Pei et al. 2004), (Sau and Murphy 2004a) recent biomimetic template synthesis approaches have allowed for their production with peptides (Bhandari and Knecht 2012a).

Au NPNs were prepared at  $\text{Au}^{3+}$ : peptide ratios of 30 and 60 using the R5 template (Bhandari and Knecht 2012a). Such ratios were selected due to the precipitation of bulk materials at higher ratios. This contrasts the synthesis of the Pd NPNs at ratios of 90 and 120, which were quite stable (Jakhmola et al. 2010). Such a difference in loading effects based upon the metal identity suggests different coordination environments within the bioscaffold. TEM analysis of the materials showed similarities between the Au30 and Au60 materials, as shown in Fig. 7.26. These materials consisted of highly branched NPNs, with individual widths of  $7.6 \pm 1.1$  and  $7.1 \pm 1.3$  nm, for the Au30 and Au60 systems, respectively (Bhandari and Knecht 2012a). The materials were observed to be polycrystalline, similar to the Pd nanostructures, with lattice spacings corresponding to the Au (111) plane, (Bhandari and Knecht 2012a) all of which is consistent with the template-based growth mechanism.

The catalytic activity of the templated Au NPNs was probed for the reduction of 4-nitrophenol to 4-aminophenol, which can be monitored via UV-vis (Bhandari and Knecht 2012a). For this, the substrate, 4-nitrophenol, absorbs at 400 nm, while the final 4-aminophenol product absorbs at 300 nm, as shown in Fig. 7.27a (Bhandari and Knecht 2012a). After a short lag period after reaction initiation, which likely is due to substrate surface adsorption, a decrease in the 400 nm peak was observed, correlating to reagent consumption (Fig. 7.27b). Concurrently, an increase was noted for the product at 300 nm. Of the Au30 and Au60 NPNs, a similar reaction rate was observed, which demonstrated comparable  $E_a$  values of  $29.0 \pm 1.4$  kJ/mol and  $27.7 \pm 1.6$  kJ/mol, respectively (Bhandari and Knecht



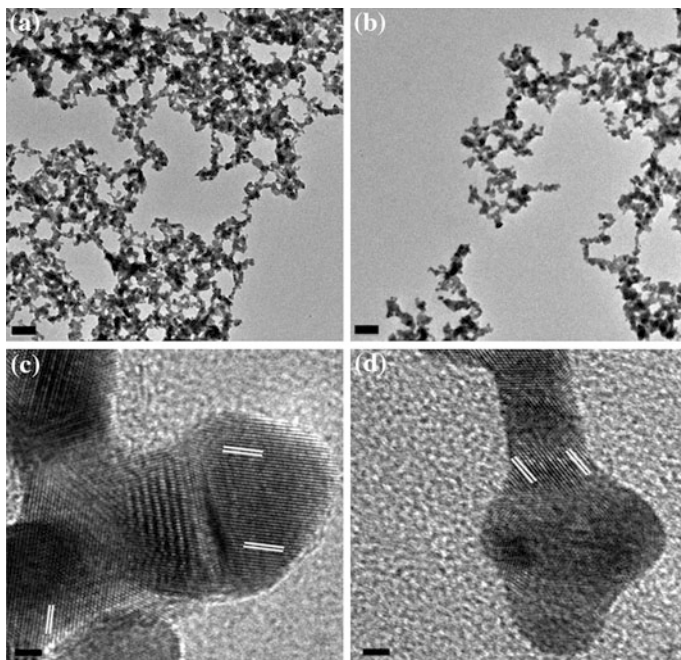


**Fig. 7.26** TEM analysis of the Au30 (**a** and **c**) and the Au60 (**b** and **d**) materials. Scale bars are 50 nm (**a** and **b**) and 2 nm (**c** and **d**). Reproduced (“Adapted”) from (Bhandari and Knecht 2012a) with permission of the Royal Society of Chemistry

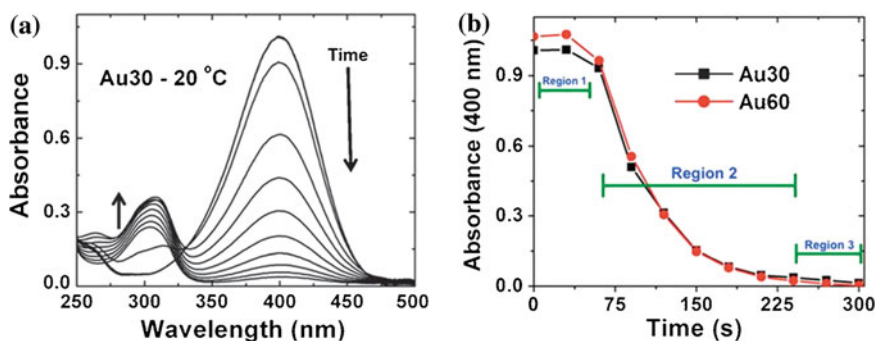


**Fig. 7.27** Reduction of 4-nitrophenol using Au NPNs. Part **a** presents the reaction analysis via UV-vis, where product consumption as a function of time is shown in part **b**. Reproduced (“Adapted”) from (Bhandari and Knecht 2012a) with permission of the Royal Society of Chemistry

2012a). Mechanistically, it was evident that adsorption of the substrate to the particle surface was required, based upon the initial lag period. Next, reduction of 4-nitrophenol occurs, which was saturated with hydrogen atoms from the  $\text{NaBH}_4$ .

Finally, the 4-aminophenol product desorbs, leaving an active site open for the reaction to continue (Bhandari and Knecht 2012a). Comparing the Au<sub>30</sub> and Au<sub>60</sub> materials, the two systems were observed to be basically equivalent for the reaction, within the limits of the error. This similarity between systems with very different loading quantities of metal suggests that the bioscaffold is highly flexible and does not inhibit the diffusion of the reagents to the metallic catalyst.

These networked materials are highly versatile systems, such that both the bioscaffold and the metallic structure direct the final catalytic reactivity. From these networked structures, the fusion of small particles seems to be controlled by the bioscaffold and metal loading, thus changing the surface area of the metallic materials; however, surface area does not necessarily control the material reactivity. Surface accessibility appears to be quite important as well, which was dependent on the effect of the metal component and the bioscaffold. Combined, these systems represent nanostructures that could provide new methods for material applications.

## 7.7 Virus-Templated Materials for Catalysis

In addition to their use in biocombinatorial selection methods described above, M13 bacteriophage have been exploited for a number of other applications, ranging from generation of complex frameworks to nanowire (NW) templating (Lee et al. 2006; Mao et al. 2004). For the former, binding motifs can be genetically programmed into the pIII and pIX coat protein at the virus' termini to drive their linear assembly, forming complex structures (Flynn et al. 2003). For the latter, modifications to the pVIII major coat protein allow for peptide additions along the entire length of the phage (Nam et al. 2006). Due to the difficulties with large changes to the pVIII coat protein, only small modifications are possible (Huang et al. 2005). From this, a simple addition that complexes metal ions has been demonstrated to be advantageous for the synthesis of phage-based nanomaterials.

Belcher and coworkers have demonstrated multiple pVIII-modified phage that have been demonstrated to bind metal ions and form complex NWs (Hess et al. 2012; Nam et al. 2006, 2010a). By employing this technique with a material-specific peptide, Au NWs have been generated using the M13 phage, which can then be coated in Pt to generate highly catalytically reactive materials (Lee et al. 2012). To achieve such structures, the M13 bacteriophage were genetically engineered to generate Au NWs at room temperature, as shown in Fig. 7.28. Previously selected with Au affinity, (Huang et al. 2005) the VSGSSPDS peptide was expressed on the pVIII coat proteins of a phage clone, termed p8#9. The capsid shell of this engineered virus allowed for the adsorption of both Au<sup>0</sup> and Au<sup>3+</sup> ions through complexation with the amino acids. After Au<sup>3+</sup> incorporation to the phage surface, the addition of a reductant resulted in the formation of Au nanoparticles that evolved to generate Au NWs (Lee et al. 2012). Unfortunately, some unwanted aggregation occurred, likely due to insufficient surface passivation. The formation of stable NWs was observed from the stepwise reduction of Au<sup>3+</sup> and Ag<sup>+</sup> by NaBH<sub>4</sub> and

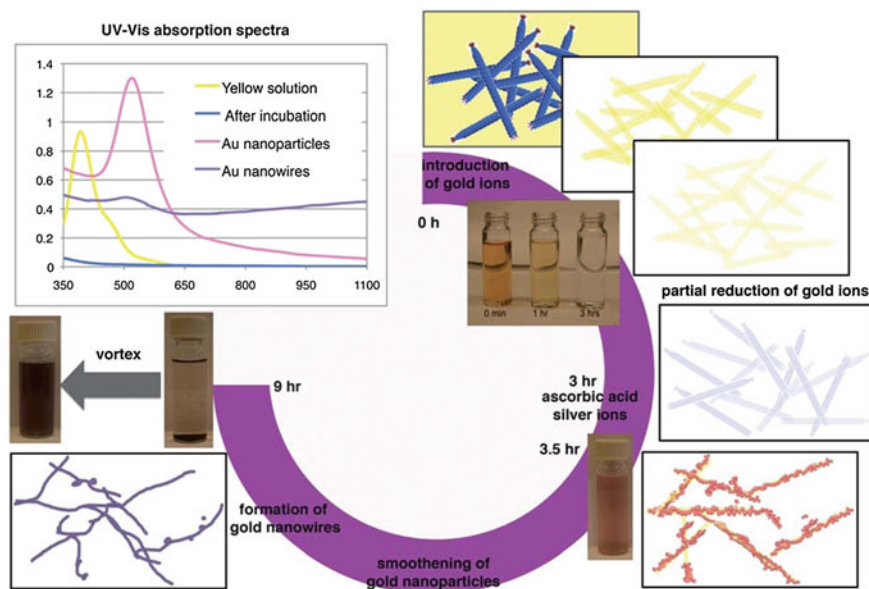


**Fig. 7.28** Synthesis steps for homogeneous Au-Ag NWs with the p8#9 M13 phage. This process results in NWs coated in surfactant, which can be redispersed upon mixing. Reproduced (“Adapted”) from (Lee et al. 2012) with permission of the Royal Society of Chemistry)

citrate in the presence of cetyltrimethylammonium bromide (CTAB) surfactant. The  $\text{Ag}^+$  ions were found as homogenous deposits within the Au as a 10 % alloy due to its low concentration in the reaction (Lee et al. 2012). By using this approach, more uniform Au NWs were prepared as compared to previous methods using the P8#9 phage that did not include  $\text{Ag}^+$  and CTAB (Seferos et al. 2007). To this end, the presentation of the Au-binding sequence bound the inorganic materials to the phage, while the surfactant stabilized the outer exposed Au surface, resulting in consistent NWs. Interestingly, the structures were  $\sim 5\times$  the length of the M13 phage precursor (Lee et al. 2012). This length difference was likely due to an end-growth mechanism caused by CTAB on the growing phage-nanowire surface, similar to previous Au nanorod-based synthetic methods (Sau and Murphy 2004b).

From these structures, core@shell materials were synthesized, in which the Au NWs were coated with Pt nanoparticles that fused to form a complete shell (Lee et al. 2012). This was performed by controlling the Pt concentration by varying amounts of  $\text{Pt}^{4+}$  titrated into the CTAB-stabilized Au NW solution. After incubation, ascorbic acid (a weaker reductant than  $\text{NaBH}_4$ ) was added to the solution and heated to  $50^\circ\text{C}$  overnight, resulting in Au@Pt core@shell structures (Fig. 7.29) (Lee et al. 2012). TEM imaging revealed that very fine Pt nanoparticles were present on the surface of the Au core, which were fused to give rise to the unique morphology (Fig. 7.30) (Lee et al. 2012). Using this approach, three systems were prepared where the Au:Pt ratio was varied at 2.6:1.0, 1.8:1.0, and 1.0:1.0 ratios. The resulting materials from these syntheses varied in diameter from

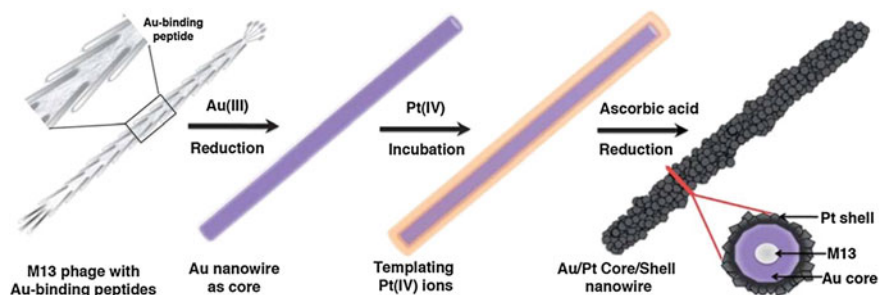


**Fig. 7.29** Synthesis of Au@Pt core@shell NWs. Reproduced (“Adapted”) from (Lee et al. 2012) with permission of the Royal Society of Chemistry

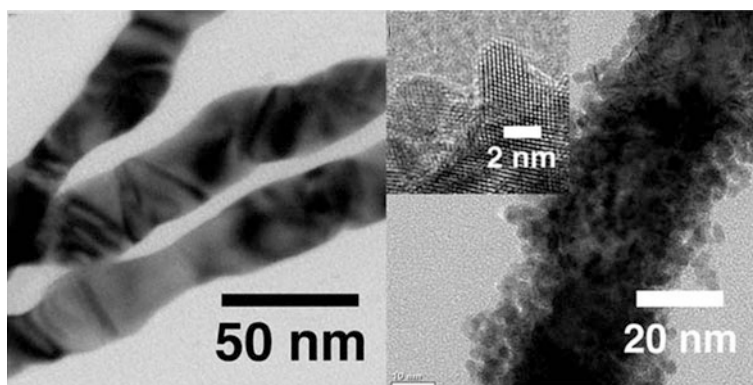


**Fig. 7.30** TEM images of the Au NWs on the *left* and then the Au@Pt core@shell NWs on the *right*. Reproduced (“in part”) from (Lee et al. 2012) with permission of the Royal Society of Chemistry

10–50 nm with changes in p8#9 phage, CTAB,  $\text{Au}^{3+}$ ,  $\text{Ag}^+$ , and ascorbic acid concentrations (Lee et al. 2012). The resulting NWs acted as supports for the deposition of small Pt nanoparticles. Though different Au:Pt ratios were employed, only a minimal increase in nanowire diameter was observed among these systems. As expected, the nanowire system with the most Pt surface coverage present was the 1.0:1.0 system (Fig. 7.30, right). Here, a greater quantity of available Pt is present, such that more surface coverage is possible. STEM analysis of the 1.0:1.0 materials revealed a Au-Ag core and an almost exclusively Pt surface coverage, as presented in Fig. 7.31.

Once characterized, the Au@Pt materials were tested for their activity for the ethanol oxidation reaction (EOR—Fig. 7.32). The EOR activities of the NWs with Au:Pt ratios of 2.6:1.0, 1.8:1.0, and 1.0:1.0 were observed to be  $0.72 \text{ mA cm}_{\text{Pt}}^{-2}$ ,  $0.60 \text{ mA cm}_{\text{Pt}}^{-2}$ , and  $0.65 \text{ mA cm}_{\text{Pt}}^{-2}$ , respectively (Fig. 7.32c) (Lee et al. 2012). Noticeably, the lowest ratio of Pt demonstrated the highest average EOR activity;

**Fig. 7.31** STEM analysis of Au@Pt core@shell NWs. Red corresponds to Au, blue to Ag, and green to Pt. Reproduced (“in part”) from (Lee et al. 2012) with permission of the Royal Society of Chemistry)

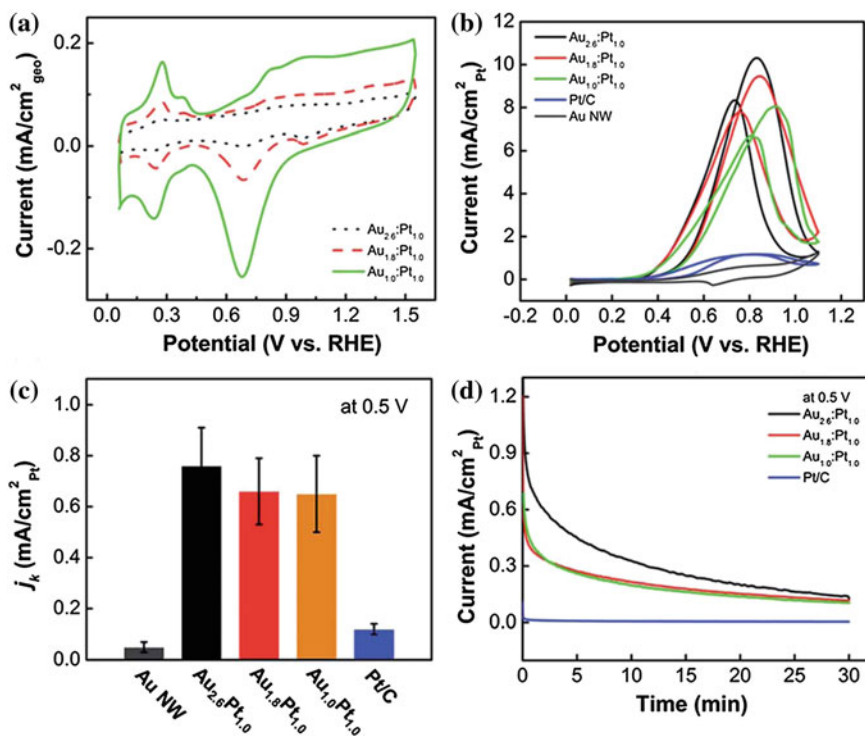
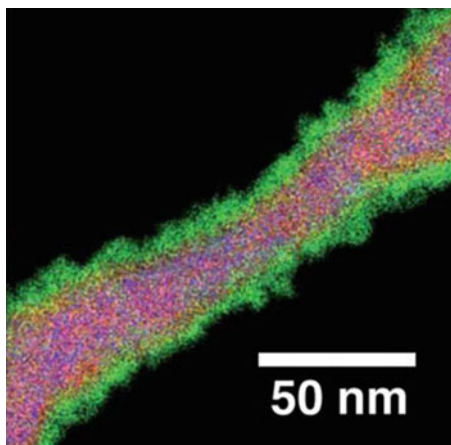


**Fig. 7.32** Catalytic activity of Au@Pt NWs. Part **a** compares the ethanol oxidation activity by CV measurements, while part **b** presents ethanol oxidation polarization curves of the Au@Pt NWs, Au NWs, and a commercial Pt on C catalyst. Finally, part **c** compares the materials reactivity, while part **d** displays chronoamperometry measurements of the materials. Reproduced (“Adapted”) from (Lee et al. 2012) with permission of the Royal Society of Chemistry)

however, these values were similar. Furthermore, these materials were observed to be  $>5$  times more reactive than a commercially available Pt on C catalyst ( $0.12 \text{ mA cm}_{\text{Pt}}^{-2}$ ) (Lee et al. 2012). It should be noted that the various materials were roughly similar in their catalytic activity. This suggests that the presence of Pt on the Au NW is necessary for enhanced activity, but not necessarily reflective of the material composition.

Beyond the Au@Pd NWs, phage-based  $\text{IrO}_2$  NWs have also been developed as catalysts for energy production via photochemical water splitting (Nam et al. 2010b). Belcher and coworkers developed multiple functional inorganic structures for this reaction by integrating a photosensitizer and metal oxide catalyst together on the M13 phage surface. For these materials,  $\text{IrO}_2$  was chosen as it is known to be highly stable and catalytically reactive for water splitting (Frame et al. 2011). For the development of a material with affinity to  $\text{IrO}_2$ , phage display was performed and the octameric sequence AGETQQAM was isolated with target affinity (Nam et al. 2010b). Subsequently, phage were engineered to be used as supports for nanoscale organization to include both  $\text{IrO}_2$  and the photosensitizer Zn(II) deuteroporphyrin IX-2,4-bis-ethylene glycol (ZnDPEG). The  $\text{IrO}_2$ -binding phage that displayed the peptide along the major coat protein were introduced to a ZnDPEG solution, yielding porphyrin nanoantennae structures. These materials were prepared by conjugation of the ZnDPEG to the pVIII coat protein on the M13 phage via a carbodiimide coupling reaction (Nam et al. 2010b). To prepare  $\text{IrO}_2$  material precursors,  $\text{Na}_2\text{IrCl}_6$  was first hydrolyzed to form Ir nanoclusters with citrate as a ligand. These nanoclusters were then added to the phage-porphyrin solution in the presence of  $\text{H}_2\text{O}_2$ , which yielded the final  $\text{IrO}_2$ -porphyrin NW product.

TEM studies were used to confirm the structure and composition of the hybrid materials (Nam et al. 2010b). From this study, compositional and structural differences were noted throughout the material synthesis. For this, materials were prepared with various  $\text{IrO}_2$ :nanoantennae loading ratios, which demonstrated morphologies ranging from NWs to networked materials. As shown in Fig. 7.33, materials prepared with an  $\text{IrO}_2$ :ZnDPEG ratio of 15:1 demonstrated more cluster-like morphologies, which resemble fused networks of particles (Nam et al. 2010b). As the ratio increased to 224:1, a greater amount of  $\text{IrO}_2$  is present in the system and available for binding to the phage surface (Nam et al. 2010b). This excess  $\text{IrO}_2$  results in morphologies that produce a more fully developed layer around the nanoantennae, resulting in recognizable, wire-like structures.

For comparison, materials were prepared at a ratio of 41 with both conjugated and free ZnDPEG as photocatalytic materials for water splitting. These include  $\text{IrO}_2$  particles with free ZnDPEG,  $\text{IrO}_2$  with the ZnDPEG-functionalized virus,  $\text{IrO}_2$  wires with free ZnDPEG, and  $\text{IrO}_2$ -ZnDPEG hybrid wires. For this analysis, the production of  $\text{O}_2$  was tracked and used to measure material reactivity. Of the systems prepared, the  $\text{IrO}_2$ -ZnDPEG hybrid NWs demonstrated the highest amount of  $\text{O}_2$  produced with respect to moles of catalyst, based upon the turnover number (TON) (Fig. 7.34a) (Nam et al. 2010b).  $\text{IrO}_2$ :ZnDPEG ratios of 15, 41, 72, and 224 were employed as catalysts in water splitting and demonstrated TON

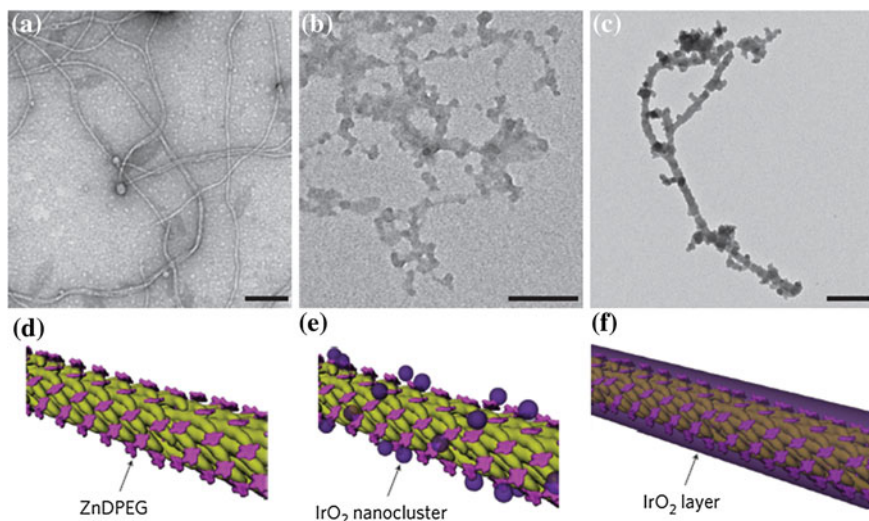


**Fig. 7.33** TEM images of the engineered M13 virus functionalized with **a** ZnDPEG **b** IrO<sub>2</sub> at 15:1 IrO<sub>2</sub>:ZnDPEG ratios, and **c** IrO<sub>2</sub> at 224:1 IrO<sub>2</sub>:ZnDPEG ratio. The graphic representations in **(d–f)** correspond to the materials in **(a–c)**. Scale bars are 200 nm. Reprinted by permission from Macmillan Publishers Ltd: [Nature Nanotechnology] (Nam et al. 2010b), copyright (2010)

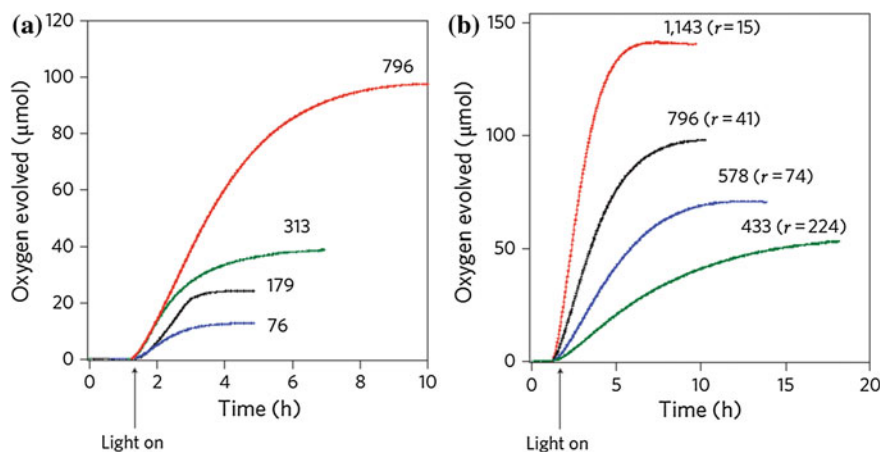


**Fig. 7.34** Water-splitting efficiency. Part **a** presents TON analysis for the following set of materials: IrO<sub>2</sub> with unconjugated ZnDPEG (*black*), IrO<sub>2</sub> with ZnDPEG-virus (*green*), IrO<sub>2</sub> wires with unconjugated ZnDPEG (*blue*), and IrO<sub>2</sub>-ZnDPEG hybrid wires (*red*). Note that the IrO<sub>2</sub>:ZnDPEG ratio was maintained at 41 for all of these samples. Part **b** displays the TON analysis for the IrO<sub>2</sub>-ZnDPEG NWs prepared at the indicated IrO<sub>2</sub>:ZnDPEG ratios (*r*). Reprinted by permission from Macmillan Publishers Ltd: [Nature Nanotechnology] (Nam et al. 2010b), copyright (2010)

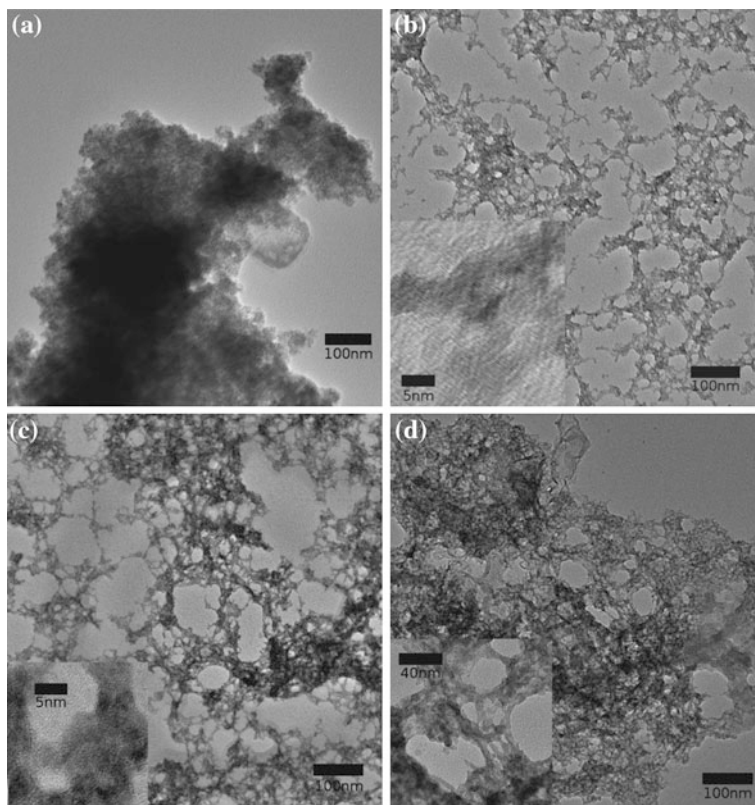


**Fig. 7.35** TEM analysis of AEEE-modified M13 phage-templated materials. Catalyst were prepared made at a 1 mM metal precursor concentration **a** without M13 **b** with  $10^7$  M13/mL **c** with  $10^{10}$  M13/mL, and **d** with  $10^{13}$  M13/mL. Insets show higher magnification images. Reprinted (adapted) with permission from (Neltner et al. 2010). Copyright (2010) American Chemical Society

values of 1143, 796, 578, and 433 mol product (mol catalyst) $^{-1}$  for the production of  $O_2$ , respectively (Fig. 7.34b) (Nam et al. 2010b). As such, the lowest  $IrO_2$ :ZnDPEG ratio NWs resulted in the highest activity, indicating that larger amounts of ZnDPEG increased the reactivity.

In addition to the  $IrO_2$ -based systems, similar virus-directed assemblies have been demonstrated to be efficient catalysts for the evolution of  $H_2$  from ethanol degradation (Neltner et al. 2010). Previously,  $Rh@CeO_2$  materials have been used for the conversion of water/ethanol mixtures into  $H_2$  for use as fuel (Diagne et al. 2002). While this is somewhat effective, the addition of Ni enhances their ability to oxidatively reform ethanol to generate the final  $H_2$  product (Kugai et al. 2005). To that end, C-C bond cleavage occurs, leading to degradation products ( $CH_4$  and  $CO$ ) that can then be reformed with  $H_2O$  to  $H_2$  and  $CO_2$  (Nam et al. 2010b; Shodiya et al. 2013). For the purpose of this reformation reaction, the M13 phage was expressed



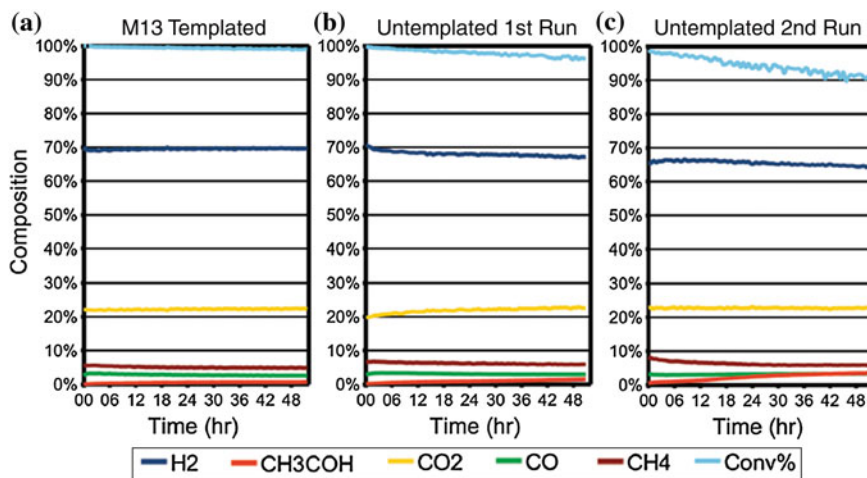


**Fig. 7.36** Steam reformation activity for the catalyst prepared **a** with and **b** without the M13 template. Part **c** presents the second run of the nontemplate materials. Reprinted (adapted) with permission from (Neltner et al. 2010). Copyright (2010) American Chemical Society

with an AEEE tetrapeptide addition to the major coat protein, which complexed metal ions to act as a nucleation site for the formation of  $\text{CeO}_2$  NWs with Ni/Rh dopants (Neltner et al. 2010). To a 1 mM metal precursor solution, materials were prepared first without M13 as a control and then with  $10^7$ ,  $10^{10}$ , and  $10^{13}$  M13/mL. This solution underwent oxide nucleation and growth by the addition of NaOH and  $\text{H}_2\text{O}_2$ , which formed Ni/Rh@ $\text{CeO}_2$  networks as observed via TEM (Fig. 7.35) (Neltner et al. 2010). Approximately 90 % of pores imaged were observed to be 4.5 nm for the templated materials. These networks also demonstrated a surface area of  $180 \text{ m}^2/\text{g}$ . This is quite important when compared to the control materials generated in the absence of the biomimetic template, which possessed 5.9 nm pore sizes with a surface area of  $143 \text{ m}^2/\text{g}$  (Neltner et al. 2010).

Once confirmed, these catalysts were employed for the steam reformation reaction with ethanol (Neltner et al. 2010). Prior to testing, the materials were heated to  $400 \text{ }^\circ\text{C}$  to burn off residual phage. For the reaction, a 1.7:1:10:11 air/ethanol/ $\text{H}_2\text{O}$ /Ar mixture was flowed over a 100 mg sample of the materials, where product generation was monitored via GC. Conversion rates were calculated as the ratio of ethanol consumed versus injected, with  $\text{N}_2$  as an internal standard. Conversion rates were calculated for both the M13-templated and nontemplated materials (Fig. 7.36). For the template materials, an initial 100 % conversion of ethanol was observed, with only a 1 % loss in activity after 52.0 h (Neltner et al. 2010). Additionally, steady degradation was observed for the other templated materials with yields of 70 %  $\text{H}_2$ , 5 %  $\text{CH}_4$ , 3 %  $\text{CO}$ , and 1 % acetaldehyde. The nontemplated structures showed similar initial rates that diminished over time. These structures were observed to regain some reactivity when exposed to air;

however, their rate diminishment increased after subsequent cycles (Neltner et al. 2010). To account for the high degree of reactivity for the virus-based structures, it is likely that the biotemplate allows for uniform network formation. This uniformity results in a more ordered structure to enhance the surface area. Furthermore, these structures demonstrated increased stability, decreased deactivation, smaller pore sizes, and higher catalytic activity as compared to nontemplated materials, (Neltner et al. 2010) suggesting an important role for biotemplates.

These engineered-phage materials provide significant progress toward the synthesis of biomimetic catalytic materials, in which the biological structures can direct the organization of the inorganic components for increased reactivity. These biomaterials generate highly efficient catalysts that minimize precious metal waste, with the ability to function at ambient and sustainable conditions. Furthermore, these viral-templated methods are critically important as NW precursors and NW-framework templates, thus providing a high catalytic surface area for reactivity. The M13 coat proteins allow for highly versatile modifications and assemblies, as well as the ability to interact with various metal precursors. Taken together, these effects make phage viruses incredibly valuable for the continued development of superior nanomaterials.

## 7.8 Conclusions

Despite the current development of biomimetic nanomaterial systems, the binding interactions that drive the synthesis and surface reactivity of these materials still remain unclear. While individual amino acids can be observed to possess specific binding effects, the binding interaction of longer sequences is significantly more complex and difficult to characterize. A delicate balance of passivating bioligand structure, binding, and surface assembly govern the final size, shape, and functionality of the nanomaterials. To that end, these properties can all potentially be modulated through rational peptide design. The selective tuning of these characteristics could lead to the development of optimized catalytic materials, with specific functionality obtained through size and surface effects. Additionally, the design of peptide-modulated activity on inorganic surfaces allows for selective shapes through directed facet growth and thus the exposure of high-energy atoms. The optimization of inorganic surfaces and sequence-controllable activity through biomimetic nanomaterial synthesis could lead to superior structures with functionality over a wide range of catalytic reactions. To that end, the continued pursuit of superior materials inspired from biology and their efficiency could prove to be beneficial for catalytic applications under sustainable conditions for long-term use.

## References

- Armor JN (2000) Energy efficiency and the environment—opportunities for catalysis. *Appl Catal A* 194:3–11
- Astruc D (2007) Palladium nanoparticles as efficient green homogeneous and heterogeneous carbon-carbon coupling precatalysts: a unifying view. *Inorg Chem* 46(6):1884–1894
- Astruc D, Lu F, Aranzas JR (2005) Nanoparticles as recyclable catalysts: the frontier between homogeneous and heterogeneous catalysis. *Angew Chem, Int Ed* 44(48):7852–7872
- Ataee-Esfahani H, Wang L, Nemoto Y, Yamauchi Y (2010) Synthesis of bimetallic Au@Pt nanoparticles with Au core and nanostructured Pt shell toward highly active electrocatalysts. *Chem Mater* 22(23):6310–6318
- Berner S, Biela S, Ledung G, Gogoll A, Backvall JE, Puglia C, Oscarsson S (2006) Activity boost of a biomimetic oxidation catalyst by immobilization onto a gold surface. *J Catal* 244(1):86–91
- Bhandari R, Knecht MR (2012a) Isolation of template effects that control the structure and function of nonspherical. Biotemplated Pd Nanomaterials. *Langmuir* 28(21):8110–8119
- Bhandari R, Knecht MR (2012b) Synthesis, characterization, and catalytic application of networked Au nanostructures fabricated using peptide templates. *Catal Sci Technol* 2(7):1360–1366
- Bianchini C, Shen PK (2009) Palladium-based electrocatalysts for alcohol oxidation in half cells and in direct alcohol fuel cells. *Chem Rev* 109(9):4183–4206
- Braunstein P (2004) Functional ligands and complexes for new structures, homogeneous catalysts and nanomaterials. *J Organomet Chem* 689(24):3953–3967
- Brinas RP, Hu MH, Qian LP, Lymar ES, Hainfeld JF (2008) Gold nanoparticle size controlled by polymeric Au(I) thiolate precursor size. *J Am Chem Soc* 130(3):975–982
- Carter JD, LaBean TH (2011) Organization of inorganic nanomaterials via programmable DNA self-assembly and peptide molecular recognition. *ACS Nano* 5(3):2200–2205
- Centi G, Ciambelli P, Perathoner S, Russo P (2002) Environmental catalysis: trends and outlook. *Catal Today* 75(1–4):3–15
- Chandra M, Xu Q (2007) Room temperature hydrogen generation from aqueous ammonia-borane using noble metal nano-clusters as highly active catalysts. *J Power Sources* 168(1):135–142
- Chirea M, Freitas A, Vasile BS, Ghitulica C, Pereira CM, Silva F (2011) Gold nanowire networks: synthesis, characterization, and catalytic activity. *Langmuir* 27(7):3906–3913
- Chiu CY, Li YJ, Ruan LY, Ye XC, Murray CB, Huang Y (2011) Platinum nanocrystals selectively shaped using facet-specific peptide sequences. *Nat Chem* 3(5):393–399
- Coppage R, Slocik JM, Sethi M, Pacardo DB, Naik RR, Knecht MR (2010) Elucidation of peptide effects that control the activity of nanoparticles. *Angew Chem, Int Ed* 49(22):3767–3770
- Coppage R, Slocik JM, Briggs BD, Frenkel AI, Heinz H, Naik RR, Knecht MR (2011) Crystallographic recognition controls peptide binding for bio-based nanomaterials. *J Am Chem Soc* 133(32):12346–12349
- Coppage R, Slocik JM, Briggs BD, Frenkel AI, Naik RR, Knecht MR (2012) Determining peptide sequence effects that control the size, structure, and function of nanoparticles. *ACS Nano* 6(2):1625–1636
- Coppage R, Slocik JM, Ramezani-Dakhel H, Bedford NM, Heinz H, Naik RR, Knecht MR (2013) Exploiting localized surface binding effects to enhance the catalytic reactivity of peptide-capped nanoparticles. *J Am Chem Soc* 135(30):11048–11054
- Costas M, Chen K, Que L (2000) Biomimetic nonheme iron catalysts for alkane hydroxylation. *Coord Chem Rev* 200:517–544
- Cuenya BR (2010) Synthesis and catalytic properties of metal nanoparticles: Size, shape, support, composition, and oxidation state effects. *Thin Solid Films* 518(12):3127–3150
- darwent B (1970) Bond dissociation energies in simple molecules. Washington: U.S. National Bureau of Standards; for sale by the Supt. of Docs., U.S. Govt. Print. Off.

- Das SK, Khan MMR, Guha AK, Naskar N (2013) Bio-inspired fabrication of silver nanoparticles on nanostructured silica: characterization and application as a highly efficient hydrogenation catalyst. [10.1039/C3GC40310F]. *Green Chem*
- Dash P, Dehm NA, Scott RWJ (2008) Bimetallic PdAu nanoparticles as hydrogenation catalysts in imidazolium ionic liquids. *J Mol Catal A: Chem* 286(1–2):114–119
- De DD, Englehardt JD, Kalu EE (2000) Electroreduction of nitrate and nitrite ion on a platinum-group-metal catalyst-modified carbon fiber electrode-Chronoamperometry and mechanism studies. *J Electrochem Soc* 147(12):4573–4579
- Debecker DP, Faure C, Meyre M-E, Derré A, Gaigneaux EM (2008) A new bio-inspired route to metal-nanoparticle-based heterogeneous catalysts. *Small* 4(10):1806–1812
- Diagne C, Idriss H, Kiennemann A (2002) Hydrogen production by ethanol reforming over Rh/CeO<sub>2</sub>-ZrO<sub>2</sub> catalysts. *Catal Commun* 3(12):565–571
- Dickerson MB, Sandhage KH, Naik RR (2008a) Protein- and peptide-directed syntheses of inorganic materials. *Chem Rev* 108(11):4935–4978
- Dickerson MB, Jones SE, Cai Y, Ahmad G, Naik RR, Kroger N, Sandhage KH (2008b) Identification and design of peptides for the rapid, high-yield formation of nanoparticulate TiO<sub>2</sub> from aqueous solutions at room temperature. *Chem Mater* 20(4):1578–1584
- Doney SC, Fabry VJ, Feely RA, Kleypas JA (2009) Ocean acidification: the other CO<sub>2</sub> problem. *Annual Review of Marine Science* 1:169–192
- Fang C, Bhattarai N, Sun C, Zhang MQ (2009) Functionalized nanoparticles with long-term stability in biological media. *Small* 5(14):1637–1641
- Flynn CE, Lee SW, Peelle BR, Belcher AM (2003) Viruses as vehicles for growth, organization and assembly of materials. *Acta Mater* 51(19):5867–5880
- Frame FA, Townsend TK, Chamousis RL, Sabio EM, Dittrich T, Browning ND, Osterloh FE (2011) Photocatalytic water oxidation with nonsensitized IrO<sub>2</sub> nanocrystals under visible and UV light. *J Am Chem Soc* 133(19):7264–7267
- Gasteiger HA, Kocha SS, Sompalli B, Wagner FT (2005) Activity benchmarks and requirements for Pt, Pt-alloy, and non-Pt oxygen reduction catalysts for PEMFCs. *Appl Catal, B* 56(1–2):9–35
- Gref R, Couvreur P, Barratt G, Mysiakine E (2003) Surface-engineered nanoparticles for multiple ligand coupling. *Biomaterials* 24(24):4529–4537
- Guo SJ, Wang EK (2011) Noble metal nanomaterials: controllable synthesis and application in fuel cells and analytical sensors. *Nano Today* 6(3):240–264
- Guo SJ, Fang YX, Dong SJ, Wang EK (2007) High-efficiency and low-cost hybrid nanomaterial as enhancing electrocatalyst: Spongelike AWN core/shell nanomaterial with hollow cavity. *J Phys Chem C* 111(45):17104–17109
- Hagiwara H, Kumagai K, Ishihara T (2010) Effects of nitrogen doping on photocatalytic water-splitting activity of Pt/KTa<sub>0.92</sub>Zr<sub>0.08</sub>O<sub>3</sub> perovskite oxide catalyst. *Chem Lett* 39(5): 498–499
- Han JG, Zhao RN, Duan YH (2007) Geometries, stabilities, and growth patterns of the bimetal Mo-2-doped Si-n (n=9–16) clusters: A density functional investigation. *J Phys Chem A* 111(11):2148–2155
- Hess GT, Cragolini JJ, Popp MW, Allen MA, Dougan SK, Spooner E, Guimaraes CP (2012) M13 Bacteriophage display framework that allows sortase-mediated modification of surface-accessible phage proteins. *Bioconjugate Chem* 23(7):1478–1487
- Hou WB, Dehm NA, Scott RWJ (2008) Alcohol oxidations in aqueous solutions using Au, Pd, and bimetallic AuPd nanoparticle catalysts. *J Catal* 253(1):22–27
- Huang J, Jiang T, Gao HX, Han BX, Liu ZM, Wu WZ, Zhao GY (2004) Pd nanoparticles immobilized on molecular sieves by ionic liquids: heterogeneous catalysts for solvent-free hydrogenation. *Angew Chem, Int Ed* 43(11):1397–1399
- Huang Y, Chiang CY, Lee SK, Gao Y, Hu EL, De Yoreo J, Belcher AM (2005) Programmable assembly of nanoarchitectures using genetically engineered viruses. *Nano Lett* 5(7):1429–1434

- Hussain I, Graham S, Wang ZX, Tan B, Sherrington DC, Rannard SP, Brust M (2005) Size-controlled synthesis of near-monodisperse gold nanoparticles in the 1-4 nm range using polymeric stabilizers. *J Am Chem Soc* 127(47):16398–16399
- Ikeda S, Ishino S, Harada T, Okamoto N, Sakata T, Mori H, Matsumura M (2006) Ligand-free platinum nanoparticles encapsulated in a hollow porous carbon shell as a highly active heterogeneous hydrogenation catalyst. *Angew Chem, Int Ed* 45(42):7063–7066
- Jakhmola A, Bhandari R, Pacardo DB, Knecht MR (2010) Peptide template effects for the synthesis and catalytic application of Pd nanoparticle networks. *J Mater Chem* 20(8):1522–1531
- Jenkinson DS, Adams DE, Wild A (1991) Model Estimates of CO<sub>2</sub> Emissions from Soil in Response to Global Warming. *Nature* 351(6324):304–306
- Joos F, Plattner GK, Stocker TF, Marchal O, Schmittner A (1999) Global warming and marine carbon cycle feedbacks: a future atmospheric CO<sub>2</sub>. *Science* 284(5413):464–467
- Kim DH, Lu NS, Ghaffari R, Rogers JA (2012) Inorganic semiconductor nanomaterials for flexible and stretchable bio-integrated electronics. *Npg Asia Materials* 4
- Knecht MR, Wright DW (2003) Functional analysis of the biomimetic silica precipitating activity of the R5 peptide from *Cylindrotheca fusiformis*. [10.1039/B309074D]. *Chem Commun* (24):3038–3039
- Kroger N, Deutzmann R, Sumper M (1999) Polycationic peptides from diatom biosilica that direct silica nanosphere formation. *Science* 286(5442):1129–1132
- Kugai J, Velu S, Song CS (2005) Low-temperature reforming of ethanol over CeO<sub>2</sub>-supported Ni-Rh bimetallic catalysts for hydrogen production. *Catal Lett* 101(3–4):255–264
- Kumar SA, Abyaneh MK, Gosavi SW, Kulkarni SK, Pasricha R, Ahmad A, Khan MI (2007) Nitrate reductase-mediated synthesis of silver nanoparticles from AgNO<sub>3</sub>. *Biotechnol Lett* 29(3):439–445
- Lang X-Y, Fu H-Y, Hou C, Han G-F, Yang P, Liu Y-B, Jiang Q (2013) Nanoporous gold supported cobalt oxide microelectrodes as high-performance electrochemical biosensors. *Nat Commun* 4
- Laurent S, Forge D, Port M, Roch A, Robic C, Elst LV, Muller RN (2008) Magnetic iron oxide nanoparticles: Synthesis, stabilization, vectorization, physicochemical characterizations, and biological applications. *Chem Rev* 108(6):2064–2110
- Lee SW, Mao CB, Flynn CE, Belcher AM (2002) Ordering of quantum dots using genetically engineered viruses. *Science* 296(5569):892–895
- Lee SK, Yun DS, Belcher AM (2006) Cobalt ion mediated self-assembly of genetically engineered bacteriophage for biomimetic Co-Pt hybrid material. *Biomacromolecules* 7(1):14–17
- Lee AF, Ellis PJ, Fairlamb IJS, Wilson K (2010) Surface catalysed Suzuki-Miyaura cross-coupling by Pd nanoparticles: an operando XAS study. [10.1039/C0DT00412J]. *Dalton Trans* 39(43):10473-10482
- Lee Y, Kim J, Yun DS, Nam YS, Shao-Horn Y, Belcher AM (2012) Virus-templated Au and Au-Pt core-shell nanowires and their electrocatalytic activities for fuel cell applications. *Energy Environ Sci* 5(8):8328–8334
- Li YJ, Huang Y (2010) Morphology-controlled synthesis of platinum nanocrystals with specific peptides. *Adv Mater* 22(17):1921
- Li ZP, Koch H, Dubel S (2003) Mutations in the N-terminus of the major coat protein (pVIII, gp8) of filamentous bacteriophage affect infectivity. *J Mol Microbiol Biotechnol* 6(1):57–66
- Lisiecki I (2005) Size, shape, and structural control of metallic nanocrystals. *J Phys Chem B* 109(25):12231–12244
- Luckarift HR, Dickerson MB, Sandhage KH, Spain JC (2006) Rapid, room-temperature synthesis of antibacterial bionanocomposites of lysozyme with amorphous silica or titania. *Small* 2(5):640–643
- Lynch I, Dawson KA (2008) Protein-nanoparticle interactions. *Nano Today* 3(1–2):40–47
- Manea F, Houillon FB, Pasquato L, Scrimin P (2004) Nanozymes: gold-nanoparticle-based transphosphorylation catalysts. *Angew Chem, Int Ed* 43(45):6165–6169

- Mao CB, Solis DJ, Reiss BD, Kottmann ST, Sweeney RY, Hayhurst A, Belcher AM (2004) Virus-based toolkit for the directed synthesis of magnetic and semiconducting nanowires. *Science* 303(5655):213–217
- Maye MM, Lou Y, Zhong C-J (2000) Core–Shell Gold Nanoparticle Assembly as Novel Electrocatalyst of CO Oxidation. *Langmuir* 16(19):7520–7523
- Mejare M, Ljung S, Bulow L (1998) Selection of cadmium specific hexapeptides and their expression as OmpA fusion proteins in *Escherichia coli*. *Protein Eng* 11(6):489–494
- Mery D, Astruc D (2006) Dendritic catalysis: Major concepts and recent progress. *Coord Chem Rev* 250(15–16):1965–1979
- Mlynarz P, Valensin D, Kociolek K, Zabrocki J, Olejnik J, Kozlowski H (2002) Impact of the peptide sequence on the coordination abilities of albumin-like tripeptides towards  $\text{Cu}^{2+}$ ,  $\text{Ni}^{2+}$  and  $\text{Zn}^{2+}$  ions. Potential albumin-like peptide chelators. *New J Chem* 26(2):264–268
- Naik RR, Brott LL, Clarson SJ, Stone MO (2002a) Silica-precipitating peptides isolated from a combinatorial phage display peptide library. *J Nanosci Nanotechno* 2(1):95–100
- Naik RR, Stringer SJ, Agarwal G, Jones SE, Stone MO (2002b) Biomimetic synthesis and patterning of silver nanoparticles. *Nature Materials* 1(3):169–172
- Naik RR, Jones SE, Murray CJ, McAuliffe JC, Vaia RA, Stone MO (2004) Peptide templates for nanoparticle synthesis derived from polymerase chain reaction-driven phage display. *Adv Funct Mater* 14(1):25–30
- Nam KT, Kim DW, Yoo PJ, Chiang CY, Meethong N, Hammond PT, Belcher AM (2006) Virus-enabled synthesis and assembly of nanowires for lithium ion battery electrodes. *Science* 312(5775):885–888
- Nam YS, Shin T, Park H, Magyar AP, Choi K, Fantner G, Belcher AM (2010a) Virus-templated assembly of porphyrins into light-harvesting nanoantennae. *J Am Chem Soc* 132(5):1462
- Nam YS, Magyar AP, Lee D, Kim JW, Yun DS, Park H, Belcher AM (2010b) Biologically templated photocatalytic nanostructures for sustained light-driven water oxidation. *Nature Nanotech* 5(5):340–344
- Neltner B, Peddie B, Xu A, Doenlen W, Durand K, Yun DS, Belcher A (2010) Production of hydrogen using nanocrystalline protein-templated catalysts on M13 phage. *ACS Nano* 4(6):3227–3235
- Pacardo DB, Knecht MR (2013) Exploring the mechanism of Stille C-C coupling via peptide-capped Pd nanoparticles results in low temperature reagent selectivity. *Catal Sci Technol* 3(3):745–753
- Pacardo DB, Sethi M, Jones SE, Naik RR, Knecht MR (2009) Biomimetic synthesis of Pd nanocatalysts for the stille coupling reaction. *ACS Nano* 3(5):1288–1296
- Pacardo DB, Slocik JM, Kirk KC, Naik RR, Knecht MR (2011) Interrogating the catalytic mechanism of nanoparticle mediated Stille coupling reactions employing bio-inspired Pd nanocatalysts. *Nanoscale* 3(5):2194–2201
- Pande J, Szcwzyk MM, Grover AK (2010) Phage display: Concept, innovations, applications and future. *Biotechnol Adv* 28(6):849–858
- Pandey RB, Heinz H, Feng J, Farmer BL, Slocik JM, Drummy LF, Naik RR (2009) Adsorption of peptides (A3, Flg, Pd2, Pd4) on gold and palladium surfaces by a coarse-grained Monte Carlo simulation. *PCCP* 11(12):1989–2001
- Pasquato L, Pengo P, Scrimin P (2005) Nanozymes: functional nanoparticle-based catalysts. *Supramol Chem* 17(1–2):163–171
- Pei L, Mori K, Adachi M (2004) Formation process of two-dimensional networked gold nanowires by citrate reduction of  $\text{AuCl}_4^-$  and the shape stabilization. *Langmuir* 20(18):7837–7843
- Pengo P, Baltzer L, Pasquato L, Scrimin P (2007) Substrate modulation of the activity of an artificial nanoesterase made of peptide-functionalized gold nanoparticles. *Angew Chem, Int Ed* 46(3):400–404
- Petrenko VA (2008) Evolution of phage display: from bioactive peptides to bioselective nanomaterials. *Expert Opinion on Drug Delivery* 5(8):825–836

- Polleux J, Pinna N, Antonietti M, Hess C, Wild U, Schlogl R, Niederberger M (2005) Ligand functionality as a versatile tool to control the assembly behavior of preformed titania nanocrystals. *Chem Eur J* 11(12):3541–3551
- Rana S, Yeh YC, Rotello VM (2010) Engineering the nanoparticle-protein interface: applications and possibilities. *Curr Opin Chem Biol* 14(6):828–834
- Rhee CK, Kim BJ, Ham C, Kim YJ, Song K, Kwon K (2009) Size effect of Pt nanoparticle on catalytic activity in oxidation of methanol and formic acid: comparison to Pt(111), Pt(100), and polycrystalline Pt electrodes. *Langmuir* 25(12):7140–7147
- Rimola A, Rodríguez-Santiago L, Sodupe M (2006) Cation– $\pi$  interactions and oxidative effects on Cu<sup>+</sup> and Cu<sup>2+</sup> binding to Phe, Tyr, Trp, and his amino acids in the gas phase. Insights from first-principles calculations. *J Phys Chem B* 110(47):24189–24199
- Ruan LY, Chiu CY, Li YJ, Huang Y (2011) Synthesis of platinum single-twinned right bipyramid and {111}-bipyramid through targeted control over both nucleation and growth using specific peptides. *Nano Lett* 11(7):3040–3046
- Ruan LY, Ramezani-Dakheel H, Chiu CY, Zhu EB, Li YJ, Heinz H, Huang Y (2013) Tailoring molecular specificity toward a crystal facet: a lesson from biorecognition toward Pt{111}. *Nano Lett* 13(2):840–846
- Samanta B, Yan H, Fischer NO, Shi J, Jerry DJ, Rotello VM (2008) Protein-passivated Fe<sub>3</sub>O<sub>4</sub> nanoparticles: low toxicity and rapid heating for thermal therapy. *J Mater Chem* 18(11):1204–1208
- Sarikaya M, Tamerler C, Jen AKY, Schulten K, Baneyx F (2003) Molecular biomimetics: nanotechnology through biology. *Nature Materials* 2(9):577–585
- Sau TK, Murphy CJ (2004a) Room temperature, high-yield synthesis of multiple shapes of gold nanoparticles in aqueous solution. *J Am Chem Soc* 126(28):8648–8649
- Sau TK, Murphy CJ (2004b) Seeded high yield synthesis of short Au nanorods in aqueous solution. *Langmuir* 20(15):6414–6420
- Seferos DS, Giljohann DA, Hill HD, Prigodich AE, Mirkin CA (2007) Nano-flares: probes for transfection and mRNA detection in living cells. *J Am Chem Soc* 129(50):15477
- Sheldon RA, Arends IWCE, Ten Brink GJ, Dijkstra A (2002) Green, catalytic oxidations of alcohols. *Acc Chem Res* 35(9):774–781
- Shafiee S, Topal E (2009) When will fossil fuel reserves be diminished? *Energy Policy* 37(1):181–189
- Shodiya T, Schmidt O, Peng W, Hotz N (2013) Novel nano-scale Au/ $\alpha$ -Fe<sub>2</sub>O<sub>3</sub> catalyst for the preferential oxidation of CO in biofuel reformat gas. *J Catal* 300:63–69
- Sidhaye DS, Kashyap S, Sastry M, Hotha S, Prasad BLV (2005) Gold nanoparticle networks with photoresponsive interparticle spacings. *Langmuir* 21(17):7979–7984
- Sidhu SS (2001) Engineering M13 for phage display. *Biomol Eng* 18(2):57–63
- Sidhu SS, Lowman HB, Cunningham BC, Wells JA (2000) Phage display for selection of novel binding peptides. *Appl Chimeric Genes Hybrid Proteins Pt C* 328:333–363
- Silvy RP (2003) World refining catalyst market update. *Oil Gas-European Magazine* 29(2):108–109
- Sinfelt JH, Via GH, Lytle FW (1980) Structure of Bimetallic Clusters-Extended X-Ray Absorption Fine-Structure (EXAFS) Studies of Ru-Cu Clusters. *J Chem Phys* 72(9):4832–4844
- Slocik JM, Naik RR (2006) Biologically programmed synthesis of bimetallic nanostructures. *Adv Mater* 18(15):1988
- Slocik JM, Govorov AO, Naik RR (2008) Photoactivated biotemplated nanoparticles as an enzyme mimic. *Angew Chem, Int Ed* 47(29):5335–5339
- So CR, Tamerler C, Sarikaya M (2009) Adsorption, diffusion, and self-assembly of an engineered gold-binding peptide on Au(111) investigated by atomic force microscopy. *Angew Chem, Int Ed* 48(28):5174–5177
- Stamenkovic VR, Mun BS, Arenz M, Mayrhofer KJJ, Lucas CA, Wang GF, Markovic NM (2007) Trends in electrocatalysis on extended and nanoscale Pt-bimetallic alloy surfaces. *Nature Materials* 6(3):241–247

- Stille JK (1986) The palladium-catalyzed cross-coupling reactions of organotin reagents with organic electrophiles. *Angew Chem, Int Ed* 25(6):508–523
- Stumpf HO, Pei Y, Kahn O, Sletten J, Renard JP (1993) Dimensionality of Mn(I)Cu(II) bimetallic compounds and design of molecular-based magnets. *J Am Chem Soc* 115(15):6738–6745
- Tamerler C, Oren EE, Duman M, Venkatasubramanian E, Sarikaya M (2006) Adsorption kinetics of an engineered gold binding peptide by surface plasmon resonance spectroscopy and a quartz crystal microbalance. *Langmuir* 22(18):7712–7718
- Temkin ON (2012) Kinetic models of multi-route reactions in homogeneous catalysis with metal complexes (A Review). *Kinet Catal* 53(3):313–343
- Vallee A, Humblot V, Pradier CM (2010) Peptide Interactions with Metal and Oxide Surfaces. *Acc Chem Res* 43(10):1297–1306
- Voityuk AA (1987) Mechanism of enzymatic catalysis-quantum chemical investigation of models of serine proteases (Brief Review). *Mol Biol* 21(4):729–733
- Wang J (2005) Nanomaterial-based electrochemical biosensors. *Analyst* 130(4):421–426
- Wang T, Hu X, Dong S (2006) Surfactantless synthesis of multiple shapes of gold nanostructures and their shape-dependent SERS spectroscopy. *J Phys Chem B* 110(34):16930–16936
- Wang YG, Shah N, Huffman GP (2004) Pure hydrogen production by partial dehydrogenation of cyclohexane and methylcyclohexane over nanotube-supported Pt and Pd catalysts. *Energy Fuel* 18(5):1429–1433
- Wang LY, Park HY, Lim SII, Schadt MJ, Mott D, Luo J, Zhong CJ (2008) Core@shell nanomaterials: gold-coated magnetic oxide nanoparticles. *J Mater Chem* 18(23):2629–2635
- Wang DS, Xie T, Li YD (2009) Nanocrystals: solution-based synthesis and applications as nanocatalysts. *Nano Research* 2(1):30–46
- Widegren JA, Finke RG (2003) A review of the problem of distinguishing true homogeneous catalysis from soluble or other metal-particle heterogeneous catalysis under reducing conditions. *J Mol Catal A: Chem* 198(1–2):317–341
- Wittrup KD (2001) Protein engineering by cell-surface display. *Curr Opin Biotechnol* 12(4):395–399
- Xiao N, Cheng DF, Wang Y, Chen L, Liu XR, Dou SP, Rusckowski M (2011) Identification of a high affinity TAG-72 binding peptide by phage display selection. *Cancer Biology & Therapy* 11(1):22–31
- Xu CX, Zhang Y, Wang LQ, Xu LQ, Bian XF, Ma HY, Ding Y (2009) Nanotubular mesoporous PdCu bimetallic electrocatalysts toward oxygen reduction reaction. *Chem Mater* 21(14):3110–3116
- Zhang DS, Du XJ, Shi LY, Gao RH (2012) Shape-controlled synthesis and catalytic application of ceria nanomaterials. *Dalton Trans* 41(48):14455–14475
- Zhong WW (2009) Nanomaterials in fluorescence-based biosensing. *Analytical and Bioanalytical Chemistry* 394(1):47–59
- Zhou B, Hermans S, Somorjai GA, American Chemical Society. Meeting (2004) Nanotechnology in catalysis. Kluwer Academic/Plenum Publishers, New York
- Zhou SH, Jackson GS, Eichhorn B (2007) AuPt alloy nanoparticles for CO-tolerant hydrogen activation: Architectural effects in Au-Pt bimetallic nanocatalysts. *Adv Funct Mater* 17(16):3099–3104



# Chapter 8

## Addressable Biological Functionalization of Inorganics: Materials-Selective Fusion Proteins in Bio-nanotechnology

Banu Taktak Karaca, Marketa Hnilova and Candan Tamerler

**Abstract** Biological systems have developed a wide range of ingenious solutions, which serve as valuable sources for inspiration in designing new materials and systems. The evolutionary pathways through which biological systems have been formed build upon the biomolecular machinery bridging multiple length scales to exhibit a multitude of diverse outstanding properties. With a growing understanding of the molecular processes involved, biological principles are regularly revisited for developing new bio-enabled approaches to materials engineering. A number of biomolecules play important roles in biological systems by performing various tasks based on their functional specificity and their precise molecular recognition capability. Proteins are specifically involved in both collecting and transporting raw materials and interacting with ions. Proteins systematically undergo self- and co-assembly to yield short- and long-range ordered nuclei, substrates and other cellular organelles, as well as to catalyze reactions. The precise molecular recognition and the self-assembly exhibited in these interactions are an outcome of evolutionary process, where proteins have undergone cycles of structural fittings that lead to improved specific interactions. In the last decade, peptides have been utilized as critical building blocks to mimic biomolecular capabilities of proteins and to develop unique novel hybrid materials for a variety of practical applications. Here in, we summarize the inspirations that allow engineers to

---

B. T. Karaca · C. Tamerler  
Bioengineering Research Center (BERC), Lawrence, KS, USA

C. Tamerler (✉)  
Department of Mechanical Engineering, University of Kansas,  
3114 Learned Hall, 66045 Lawrence, KS, USA  
e-mail: ctamerler@ku.edu

M. Hnilova  
Department of Materials Science and Engineering, University of Washington,  
98195 Seattle, WA, USA

B. T. Karaca  
Department of Molecular Biology and Genetics, Istanbul Technical University  
(ITU-MOBGAM), 34469 Istanbul, Turkey

mimic biomolecular processes and the utility of combinatorial biology-based library systems to screen peptides for materials. Finally, we provide examples of addressable assembly on a variety of surfaces leading to self-organized hybrid systems that employ peptides fused to different functional proteins as building blocks for materials specificity.

## 8.1 Biological Systems as Models for Design of Materials

The diverse properties of structural biological materials have been studied by many groups over a long period of time with at least one early example going back to Sir Thompson's book, i.e., "On Growth and Form" published in 1917 (Thompson 1917). Thompson pointed out the correlations between biological forms and mechanical properties. Today's accumulated knowledge on biological materials is continuing to attract the interest of materials engineers more than ever due to their exceptional properties resulting from Nature's inherent approach concealed in molecular scale design.

The exceptional mechanical properties of natural materials mainly providing protection and support have always been at the core of bioinspired materials (Wainwright 1976; Sarikaya and Aksay 1995; Mann 1996; Meyers et al. 2008). Biological materials are structured in a hierarchical way over multiple length scales, starting from nanometer-scale objects. Hierarchical structuring is one of the key features providing intricate architectures that ultimately inherit multifunctionality to adapt the survival needs of an organism. These intricate structures derive their function from controlled size, morphology and self-organization into two- and three-dimensional constructions (Berman et al. 1988; Sarikaya and Aksay 1995; Mann 1996; Aizenberg et al. 2002, 2005; Meyers et al. 2008;). Owing to their hierarchical structures, these intricate constructions are of great importance to provide conditions to adapt the survival requirements of a living organism (Alberts 2002). The variety of the materials is consequently an incredible inference of the natural evolution adaption to several environments and circumstances. These constructions are simultaneously dynamic and complex, and exhibit self-organization, selfregulation, and selfhealing characteristics that are difficult to achieve in purely synthetic systems. Based on their highly controlled diverse functions, biocomposites have properties of high-technological interest that surpass synthetic systems with similar phase compositions (Vincent 1990; Calvert and Mann 1988; Tirrell 1994; Aksay and Weiner 1998; Sanchez et al. 2005; Sarikaya 1999).

The striking difference in the design strategies used by Nature compared to today's engineering creates a significant barrier in translating the lessons learned from biological materials to the design of new materials. Many biological materials are structured in a highly organized-, hierarchical-manner at the nano-, meso-, and macro-scales over a long period of evolutionary adaptations (Calvert and Mann 1988; Sarikaya 1994; Aizenberg et al. 2002). The way Nature evolves the biological

systems serves to bring multiple distinguishing functions that are built upon biomolecular machinery. One of the unique features is probably their inherent ability to self-organize over both multiple times and multiple length scales. Among different biomolecules in the palette of life, proteins play an important role in biomolecular systems by performing diverse functions built into them due to their functional specificity and their precise molecular recognition properties. For a long time, the field of biotechnology has invested in using biological principles and components for medical and technological applications. In this endeavor, biomacromolecules, such as genes, proteins, enzymes, and antibodies have been the major components previously used for a variety of applications in materials science. While relying on biomacromolecules and cells, material science is currently integrating more biotechnology into its palette. Here, the ultimate aim is to bring more traditional engineered materials and the components of nanotechnology, toward achieving efficient, addressable, adaptable biologically-controlled, and multifunctional hybrid molecular materials and systems.

For instance, hard tissues, such as bones, teeth, spicules, shells, beaks, and bacterial nanoparticles, are examples that all have a high percentage of mineral that is integrated within a protein-rich matrix. This matrix can contain one or more protein-based organic components that control structural formation, as well as becoming an integral part of the biological composites (Lowenstam and Weiner 1989; Sarikaya and Aksay 1995; Meyers et al. 2008). Examples include silaffins and silicateins in silica-based structures, amelogenin in enamel, collagen in bone, calcite- or aragonite-forming proteins in mollusk shells and magnetite-forming proteins in magnetotactic bacteria (Berman et al. 1988; Cariolou and Morse 1988; Paine and Snead 1997; Schultzelam et al. 1992). Each of these functional biological systems has self-organization and selfregulation characteristics that are difficult to achieve in purely synthetic systems, even with the recently developed bottom-up processes that rely on the use molecules and nanocomponents.

Among many different biomacromolecules, proteins seem to function as the leading enablers for specific interactions between various cell and tissue components, as well as in cellular communications (Hanks et al. 1988; Yang et al. 1996; Sanchez et al. 2005; Tamerler and Sarikaya 2007b). For example, protein phosphorylation is one of the key mechanisms in the regulation of signal transduction pathways in both prokaryotes and eukaryotes (Hanks et al. 1988; Yang et al. 1996). Many essential biological interactions in living organisms are based on precise molecular recognition between individual proteins and other biomolecules (Fig. 8.1). It is apparent that the amino acid sequence of a given protein directly dictates its secondary and tertiary folding and which, in turn, dictates its interaction with other proteins, DNA and other biomacromolecules based on molecular recognition. For most of the protein systems, a biological activity necessitates the retained protein structure. However, adsorption-induced conformational changes can cause at least partial loss in the activity of the protein, such as enzymatic activity (in the case of enzyme) or molecular recognition (in the case of antibody). In fact, the biomineral-associated biological proteins can be considered to operate on the same basic principles of molecular recognition, i.e., sequence-related

molecular structure that recognizes the counterpart mineral and dictates its function. Understanding the molecular recognition elements in the hierarchical design and structural adaptability of biological composites continues to provide insights for designing new materials and systems (Sarıkaya and Aksay 1995; Sarıkaya et al. 2003; Tamerler et al. 2010). In the last decade, biomimetics, at the molecular scale, is considered a promising way for the realization of this concept toward solving nanotechnologic challenges by increasing the open-ended nano-scale revolution (Sarıkaya 1999; Ball 2001; Sarıkaya et al. 2003; Seeman and Belcher 2002).

Mimicking molecular scale interactions of biomolecules at the material interfaces was initiated with the search for control over directing molecular evolutions toward technologically relevant materials. Peptides, with specific materials recognition have been a major biocomponent in this approach. In the last decade many groups, including the authors, used combinatorial biology-based approaches to generate peptides with a specific affinity and selectivity for a material of technological interest. These new set of peptides have revealed that novel ways of addressing the biomolecular interfacial interactions can be generated by mimicking the natural evolution process. There is a continued interest to identify additional peptides and understand their lexicon for molecular level interactions with different materials such as metal, metal oxides, and ceramics. As the fundamental level of peptide-based interfacial interactions continues, peptides are making their ways into bio-enabled materials and systems assembly and synthesis processes.

Already there appears to be a path to follow in order to design peptide-based biomimetic systems: (1) The inorganic-specific peptides are identified by initiating a fast evolution toward the materials of interest, using combinatorial biology-based libraries; (2) These peptide building blocks can be further engineered to tailor their recognition and assembly properties using rational design or computational biology approaches, including bioinformatics and structural biology. This step is similar to natural evolution, where successive cycles of mutation and selection potentially leads to improved progeny; (3) The engineered peptides can be used to self- or co-assemble into an ordered functional biomolecular layer, building upon the controlled biomolecular-inorganic materials interface; and (4) Building upon the modularity of the peptide domains, a domain can be used as molecular building blocks to combine: (a) two-different materials binding functions to couple different materials within a close proximity, and (b) a biological cue to any type of materials with size, shape, and composition leading to the design of multifunctional hybrid materials (Sarıkaya et al. 2004). The outcome of this process will continue to have great impact on medical and technological applications, including self-assembled-, multi-functional-, molecular-structure constructs, from nanophotonics to nanomedicine, as well as to devise systems that can be built upon the multitude of selfregulatory operational modes intrinsic to proteins.

Our bio-enabled approach is being constructed in a way that future biomimetic system can include engineered biomolecules built upon the peptide-based, materials-specific function. The domain-by-domain design afforded by peptide and

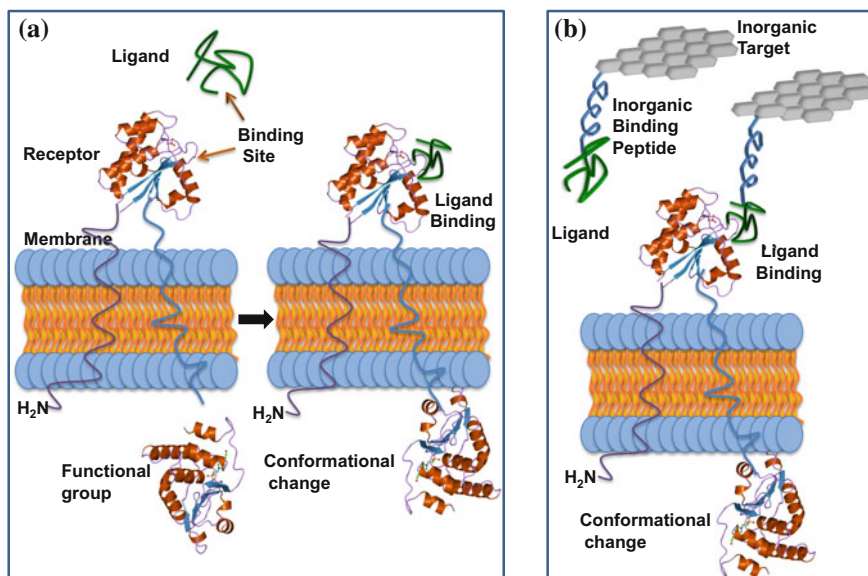


**Fig. 8.1** Biological Interactions and Molecular Recognition: **a** Examples of biological interactions in living organisms: Ligand binding induces the conformational change of molecule for functionalization **b** Peptide-enabled biofunctionalization of inorganic surfaces mimicking biological molecular recognition

protein constructs is next applied to obtain multifunctional biomolecular building blocks, each specifically designed for a material of interest. Here, we provide examples on the peptide-based assembly of multifunctional proteins and the use of enzymes on different set of inorganics that lead to the self-organized hybrid material systems.

## 8.2 Combinatorial Selection and Engineered Evolution of Inorganic-Binding Peptides

Progress in the development of combinatorial selection techniques created a major tool for a myriad of biotechnological applications including discovery antigen–antibody interactions, studying peptide–ligand interactions, and drug and vaccine development (Smith 1985; Brown 1997; Boder and Wittrup 1997). In the last decade, combinatorial biology-based molecular library protocols have been adapted from molecular biology to materials science and engineering, with the intention to select peptides that recognize and bind to an inorganic surface.

Among the combinatorial biology methods, phage display (PD) and cell surface display (CSD) are two well-adapted techniques used to screen peptides against an

inorganic target surface. The basic principle of each technique relies on the link between phenotype and genotype. DNA sequences corresponding to random peptides are inserted into the genome of microorganisms where they will express, within the context of proteins localized on the surface of phage or the cell. The random peptide sequences can be displayed on the target surface of the phage or bacterial cells within fimbria, lipoprotein, and flagellar protein of the cell or on the major or minor coat protein of phage (Smith 1985; Smith and Petrenko 1997; Lee et al. 2003). Among cell surface and phage display combinatorial approaches, the phage display system has risen to become more dominant owing to better efficiency than the cell surface technique.

The typical biopanning round that is applied in selecting inorganic-binding peptides is composed of multiple steps. The randomized peptide library displayed on phage or bacterial surfaces first interacts with the inorganic target having a specific material with a defined composition, shape, or size. Next, the nonbinding phage or cell clones are washed off the surface, followed by an elution protocol to recover the bound clones from the inorganic surface. Depending on the materials and solution properties, the elution process might involve physical and/or chemical methods. The recovered pooled clones are amplified for a subsequent panning round. Generally, a biopanning cycle is repeated 3–5 times (Fig. 8.2). In early rounds, low affinity binders can be retrieved if the selection is performed under mild conditions. In later rounds, as the elution conditions get harsher (more stringent), high-affinity binders are also recovered. Because the chimera is encoded within the phage genome or in a plasmid carried by the cell, the amino acid sequence information can be readily deduced by DNA sequencing (Fig. 8.2).

In contrast to biological targets, inorganic materials present many challenges, which may result in lack of consensus in the selected peptide sequences. Each peptide may also exhibit different binding levels for their inorganic targets (Tamerler et al. 2010). This probably reflects the heterogeneity of inorganic surfaces and various binding mechanisms applied in masses to the peptide–surface interactions during panning. Thus, in our group we developed a simple binding assay to gain insight into the relationship between amino acid composition of selected clones and their affinity levels using a fluorescence microscopy technique. In our approach, we test the binding affinity of 30–50 experimentally selected clones. The relative binding strength of selected individual phage or cell clones is estimated by enumerating either the surface coverage of the phage to the material surface or enumerating adhered cells on the materials surface through immunolabeling by fluorescently labeled anti-M13 antibodies or DNA-binding fluorescence dyes (Thai et al. 2004; Seker et al. 2007; Gungormus et al. 2008; Hnilova et al. 2008; Sedlak et al. 2012; Tamerler et al. 2010). The experimentally selected peptides showing promising binding affinity in these preliminary fluorescence microscopy experiments can be used directly or can be further engineered by either bioinformatics tools or mutagenesis approaches to produce second and higher generations of more functionally specific peptides (Oren et al. 2007).

Our, as well as other groups, have shown that improved selectivity can be achieved by integrating simple modifications into the biopanning protocol

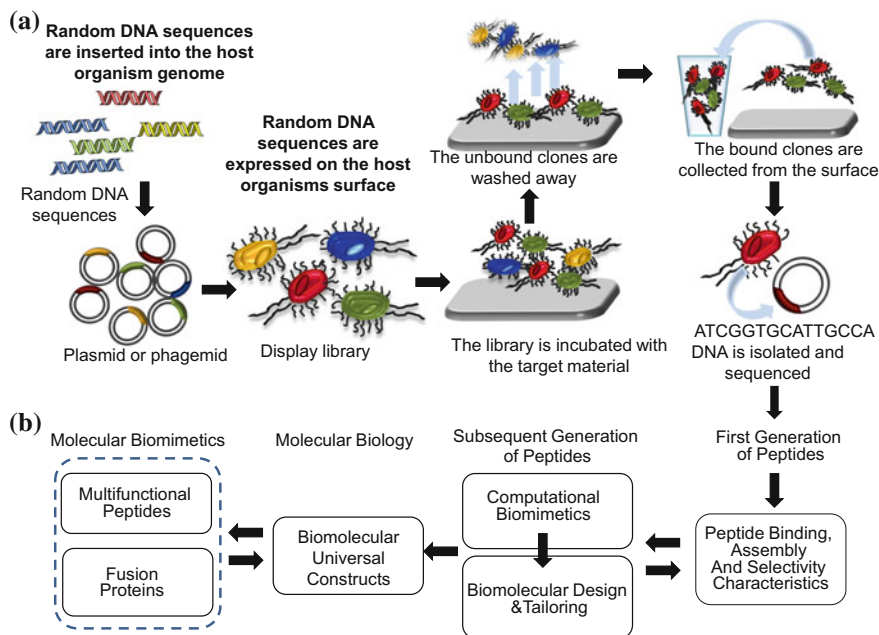


**Fig. 8.2** Selection and Engineering of Inorganic-binding Peptides and Fusion Proteins: **a** Schematic of experimental steps in biopanning process; **b** Schematic of engineering steps in materials specific fusion protein design

(e.g., counter selection step, material specificity testing, etc.) in order to isolate peptides with materials selective high affinity (Tamerler et al. 2006a, b, 2010; Hnilova et al. 2008; Hashimoto et al. 2011; Cui et al. 2012; Sedlak et al. 2012; Baneyx and Park 2013; Frascione et al. 2013; Coyle et al. 2013). Since proteins composed of diverse amino acids residues can nonspecifically interact with any surfaces through their side chains, material selectivity becomes an important parameter toward the integration of the desired molecular recognition properties into peptide-based materials and systems. Additionally, we note that special attention should be paid to adapting and continuously modifying the biopanning conditions for optimized selection of the inorganic-binding peptides, since each materials surface, with respect to its composition, surface properties, e.g., charge, topography, roughness, and reactivity in buffer environment, are very different from protein-to-ligands, from which the combinatorial selection techniques were originally developed (Sarıkaya et al. 2003; Tamerler and Sarıkaya 2007a, 2008; Evans et al. 2008).

So far, various peptide sequences for different inorganic materials, e.g., metals, Au (Brown 1997; Hnilova et al. 2008), Ag (Naik et al. 2002; Sedlak et al. 2012), Pt (Seker et al. 2007; Tao et al. 2013), SiO<sub>2</sub> (Brott et al. 2001; Oren et al. 2007), Cu<sub>2</sub>O (Thai et al. 2004), ZnO (Zhou et al. 2010; Rothenstein et al. 2012), TiO<sub>2</sub> (Sano et al. 2005; Puddu et al. 2013; Yazici et al. 2013), and ZrO<sub>2</sub> (Hashimoto et al. 2011),

minerals including hydroxyapatite, calcite, sapphire (Gaskin et al. 2000; Krauland et al. 2007; Gungormus et al. 2008), semiconductors including GaN, ZnS, and CdS (Whaley et al. 2000; Lee et al. 2002; Matmor and Ashkenasy 2012), graphite (So et al. 2012; Akdim et al. 2013), and diamond-like carbon (Gabryelczyk et al. 2013) have been isolated using combinatorial molecular biology procedures, e.g., phage and cell surface displays. The experimentally selected peptides that show promising affinity in preliminary binding experiments can be used directly or can be further engineered by either bioinformatics tools or rational engineering approaches to produce the next generation of engineered peptides.

The “know-how” in biological systems has been built throughout billions years of evolution. The laboratory imposed cycle of generations and mutations have been an important part of the improved progeny found in these screening exercises. However, to reach the next level of control, we introduced bioinformatics tools and computational approaches that are combined with experimental characterization to continue to generate peptides with improved properties (Oren et al. 2007, 2010; Evans et al. 2008; Notman et al. 2010) These properties can be dictated by the application area. For example, depending on the multi-material environments, peptides can be generated with specific material selectivity properties or they can be tuned toward catalytic ability enabling control over nucleation and growth of a desired material with a specific morphology. In the next paragraphs, we will provide examples of peptide self-assembly on various solid surfaces such as gold, silver, hydroxyapatite, and silica, as well as their utilization as fusion protein with multifunctional properties.

### **8.3 Inorganic-Binding Peptides as Fusion Partners in Recombinant Proteins for Bio-enabled Surface Functionalization**

An immediate practical application of inorganic-binding peptides is to use them as molecular linkers in displaying or immobilizing functional molecular entities via directed assembly approaches. One unique feature of these peptides is their relatively simple conjugation protocol with functional proteins via site-directed genetic recombination. Once a set of fully characterized inorganic-binding peptides is developed, they could be utilized as specific surface-binding ligands to functionalize the inorganic surfaces. Their surface-specific binding abilities may lead to formation of self-assembled biomolecular films at the inorganic interfaces. The inorganic-binding peptides bind to their respective materials with high affinity, with dissociation constant ( $K_D$ ) values in the  $\mu\text{M}$  to  $\text{nM}$  range, while also exhibiting desired material selectivity (Seker et al. 2007; Tamerler et al. 2006b; Hnilova et al. 2008; Kacar et al. 2009a; So et al. 2009). Moreover, several inorganic-binding peptides have already been shown to form densely packed monolayers, which is an advantage in surface engineering and modification applications.



The domain-by-domain integration of the peptides allows the coupling of diverse inorganic recognition ability with another biological cue. By taking advantage of molecular binding and recognition characteristics of inorganic-binding peptides, our group and others have pioneered the utility of the peptides in association with various fusion partners, such as proteins or peptides (Woodbury et al. 1998; Nygaard et al. 2002; Dai et al. 2005; Park et al. 2006; Krauland et al. 2007; Ishikawa et al. 2008; Kacar et al. 2009b; Sedlak et al. 2010; Yuca et al. 2011; Hnilova et al. 2012a, b).

The genetic insertion of the peptides can be located at either one of the termini, i.e., C-terminus (Krauland et al. 2007) and N-terminus (Kacar et al. 2009b), or within a permissive site identified on the protein (Dai et al. 2005). Following the cloning of the fusion proteins, proteins are produced using the most suitable bacterial or yeast expression systems and purified (Fig. 8.3). Table 8.1 summarizes the fusion protein examples that were explored for diverse engineering applications by our group.

Over the years, we have adapted various genetic fusion strategies (Fig. 8.3) and engineered a variety of model fusion proteins, such as maltose-binding protein, green fluorescent protein, DNA-binding protein (TraI), hybrid Thioredoxin 1 (TrxA) fused with tandem repeat of the B domain of protein A (BB) as well as multiple enzymes, including alkaline phosphatase (AP) and L-lactate dehydrogenase (LDH) (Table 8.1). In these genetic fusions, we utilized various inorganic-binding peptides, including CuO<sub>2</sub>-, ZnS-, Ag-, Au-, and hydroxyapatite-binding peptides, as specific tag partners enabling enhanced, controlled immobilization of fusion proteins. The engineering applications of these fusion proteins are diverse, ranging from the controlled hierarchical assembly of hybrid nanostructures, templating the nanoparticle synthesis, morphology, and decoration, as well as site-directed assembly of proteins for enhanced biosensing signal transduction and detection.

For examples, CuO<sub>2</sub>-binding motif in the produced fusion DNA-binding protein (TraI) facilitated the synthesis of CuO<sub>2</sub> nanoparticles, while TraI fusion partner templated the geometric control of formed CuO<sub>2</sub> nanoparticles resulting in decoration of protein-coated Cu<sub>2</sub>O nanoparticles on the circular plasmid DNA (Dai et al. 2005). ZnS-binding peptide, on the other hand, enabled the biofabrication of zinc sulfide quantum dots decorated with antibodies in single step via tandem repeat of the B domain of protein A (BB) fusion partner (Zhou et al. 2010). In other application, the morphology control over the silver nanoparticle growth using electrochemical deposition was achieved using Ag-binding motif fused to maltose binding protein demonstrated (Grosh et al. 2009). Recently, the engineered fusion proteins are shown to enhance the site-directed display of functional protein and enzyme entities on various metal surfaces via specific inorganic-binding tags. Thus, this bioenabled process has enhanced the control over the functional interface leading to the formation of addressable hierarchical architecture of hybrid assemblies (Sengupta et al. 2008; Tamerler et al. 2010; Hnilova et al. 2012a, b, c; Sedlak et al. 2012). The following sections provide a summary on some of the experimental designs and findings achieved by our group in detail.



**Table 8.1** Table of material-selective fusion proteins and their bionanotechnological applications

Peptide	Inorganics	Protein	Application	Reference
CN225	Cu <sub>2</sub> O	DNA-binding protein (TraI)	Decoration of protein-coated Cu <sub>2</sub> O nanoparticles on the circular plasmid DNA	(Dai et al. 2005)
Ag4	Ag	Maltose-binding protein (MBP)	Enhanced binding affinity and control of protein orientation on Ag nanoparticles	(Sengupta et al. 2008)
GBP	Au	Alkaline Phosphates (AP)	Protein-based control of silver growth using electrochemical deposition	(Grosh et al. 2009)
CT43	ZnS	Thioredoxin I (TrxA) & B domain of protein A (BB)	Directed self-Immobilization of alkaline phosphatase on micropatterned substrates	(Kacar et al. 2009b)
GBP	Au	DNA-binding protein (TraI)	Single-pot biofabrication of zinc sulfide immunoquantum dots	(Zhou et al. 2010)
AuBP2C			Engineered DNA-binding protein self-assembly on metallic nanostructures	(Sedlak et al. 2010)
HABP1	Hydroxy-apatite	Green fluorescent protein (GFP)	In vitro labeling of hydroxyapatite minerals by an engineered protein	(Yuca et al. 2011)
AuBP1	Au	Maltose-binding protein (MBP)	Fabrication of hierarchical hybrid structures using bioenabled layer-by-layer self-Assembly	(Hnilova et al. 2012a)
AgBP2C	Ag	Maltose-binding protein (MBP) & Green fluorescent protein (GFP)	Multifunctional protein enabled patterning on arrayed ferroelectric materials	(Hnilova et al. 2012c)
AgBP2C	Ag	Maltose-binding protein (MBP)	Promoting silver tolerance in E. coli bacteria	(Sedlak et al. 2012)
AuBP2C	Au	L-lactate dehydrogenase (LDH)	Addressable self-immobilization of lactate dehydrogenase across multiple length scales	(Cetinel et al. 2013)

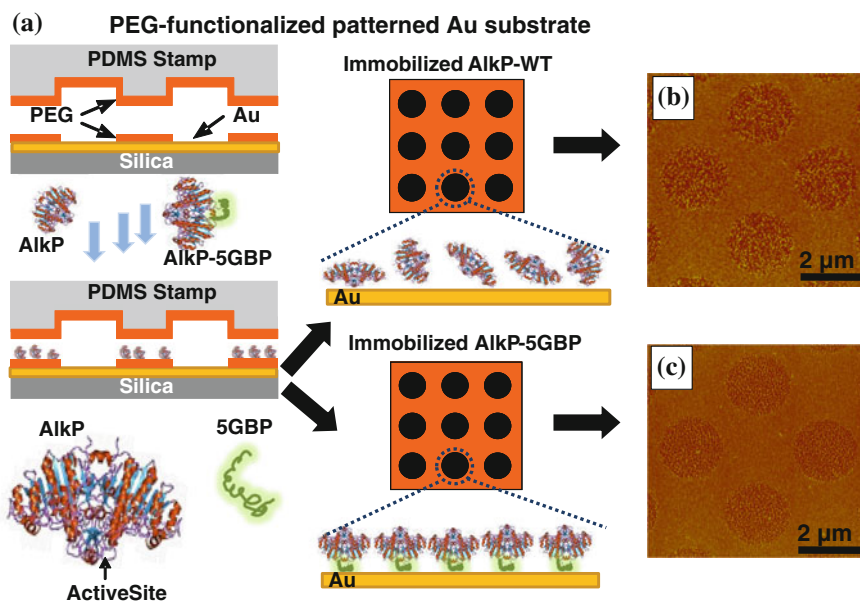


**Fig. 8.4** 2D Patterned Protein Immobilization: **a** Schematic representation of the experimental procedure to generate 2D arrays of immobilized proteins for enzymatic activity assays; (B-C) Topography images of the microarrays of immobilized AP-WT **b** and AP-5GBP; **c** taken in tapping mode (silicon cantilever, scan rate = 1.5 Hz, spring constant  $\approx$  40 N/m) at different resolution

formations of GBP-1 on atomically flat Au (111) surfaces resulting from a combination of forces involving intermolecular interaction as well as the lattice recognition of Au by GBP-1. Using the mutant strains of the bacteria supplied to us by Brown, the characterized oligonucleotides transferred from *lamB* gene encoding insoluble LamB protein to pSB2991 expression vector encoding soluble periplasmic alkaline phosphatase. Different numbers of multiple repeats ( $n = 5, 6, 7, 9$ ) containing gold-binding peptide constructs were genetically fused to alkaline phosphatase and resulting multifunctional enzymes were expressed in *E.coli* cells. Multifunctional and wild-type alkaline phosphatase (AP-WT) enzymes were purified through ion-exchange and gel filtration chromatography.

Phosphatase, as well as gold binding activities of hybrid construct, were studied using several biochemical and molecular imaging protocols. Alkaline phosphatase is a dimer, broad term associated with nonspecific metallo-phosphomonoesterases with activity optima at alkaline pH and an essential enzyme for regulating (preventing or enhancing) biomineralization via the control of extracellular phosphate concentration by catalyzing the pyrophosphate degradation. For example, in the dental pulp AP is responsible for dentin matrix formation. The AP-GBP bi-functional construct, therefore, is developed as a promising probe, especially in biomedical applications ranging from following the mineralization activity, as well

as providing bio-labeling of a tissue specific mineralization. In this application, the engineered construct provides excellent probing properties to follow the mechanism via the gold binding and enzymatic properties and, hence, may be utilized for providing a controlled and monitored delivery of AP to the desired locations. The idea here is to use the GBP-1 as molecular erector, and introduce multi-functionality to the hybrid construct, i.e., enzymatic and inorganic binding simultaneously.

Purified AP-WT and AP-nGBP constructs were tested for their bi-functional activities. Insertion of a peptide having an inorganic binding domain over different repeat numbers of the core peptide in the enzyme caused a decrease in the AP activity. Among the multifunctional AP constructs inserted with different repeats of GBP, AP-5GBP presented the highest activity (Fig. 8.4). The second function of the hybrid molecular constructs containing different numbers of inorganic binding recognition units were tested using bare gold substrates to prevent a bias from any other materials used to support a gold thin film. Protein solutions having either wild-type or hybrid constructs were left for overnight binding in the presence of the gold substrate and then the substrate was taken out of the solution and the solution without substrate was checked for the AP catalytic activity. While the wild-type protein solution retained its activity, no activity was observed in the supernatant of the hybrid construct ensuring the efficient self-immobilization of the AP via GBP domain on the gold substrate. Due to the orientation control provided with the site-specific insertion of GBP to AP, AP-5GBP also showed a 15-fold higher percentage of retained activity than AP-WT did. The hybrid construct with 5 repeats GBP presenting the highest bi-functional activity among all other constructs was chosen for the directed assembly experiments.

Additionally, two-dimensional arrays of AP-5GBP molecular constructs were generated, schematically represented in Fig. 8.4. It involves the initial patterning of oligo (ethylene glycol)-terminated alkanethiols (OH-(OCH<sub>2</sub>)<sub>3</sub>-SH) on a gold film using microcontact printing ( $\mu$ CP) and the subsequent self-assembly of AP-GBP onto bare gold regions. Due to its parallel nature,  $\mu$ CP has proven to be a very convenient technique to pattern a variety of biological molecules with sub-micron features over a large area ( $> 1 \text{ cm}^2$ ) without the need for expensive lithographic equipment (Sarikaya et al. 2003). In our previous work, we showed that the direct deposition of GBP by  $\mu$ CP onto a gold surface leads to reduction in its surface recognition and self-assembly characteristics as a result of forced immobilization (Sarikaya et al. 2004). Further, we showed that the spatial conformation of adsorbed GBP plays an important role in its binding with gold surfaces (Sarikaya et al. 2004). In this study we allowed the AP-GBP molecular constructs to self-assemble using GBP as the linker. The self-assembled monolayer (SAM) of OH-(OCH<sub>2</sub>)<sub>3</sub>-SH patterned by  $\mu$ CP served as a template to direct the adsorption of AP-5GBP from solution into a well-defined array and minimized the nonspecific binding of proteins onto the undesired regions of the array (Tamerler et al. 2006a, b). We performed a comparative study on the self-assembly and template-directed assembly of AP-5GBP and AP-WT based on AFM and activity assay. The effect of template directly self-assembled over self-assembled sample was highlighted

using percentages. In the case of self-assembly, the total amount of enzymes and corresponding activities for both AP-WT and AP-5GBP were higher than the directed self-assembly results.

Using the number of enzymes per surface area, we investigated the effect of GBP- and template-directed assembly individually. The AP-WT enzyme lacking the advantage of GBP was 1.7 times less than those having the GBP-directed assembly. Whereas the number of AP-5GBP enzyme also exhibiting the template effect was 2.2 times higher than the one having no template advantage. In the AP-5GBP case, this increase was contributed to by both GBP and its added localization effects. Additionally, if the template effect was kept constant number of AP-5GBP enzyme was approximately 30 times higher than AP-WT enzymes. Finally, the number of AP-WT having no GBP and the template effect was more than 50 times less than number of AP-5GBP enzyme having both GBP- and template-directed assembly effect.

This study served as one of the early examples on inorganic binding peptide controlled oriented protein immobilization on the planar solid surfaces. Overall, the genetic fusion of the gold binding peptide to AP provided an orientation control to direct the self-immobilization of the enzyme, which resulted in enhanced enzymatic activity on flat gold surfaces as illustrated in AFM micrograms in Fig. 8.4 (Kacar et al. 2009b). Furthermore, the results demonstrated the utility of a selective peptide tag as an enabler for the enhanced immobilization affinity and orientation of fusion constructs on planar gold surfaces, using the exceptional molecular recognition and binding characteristics of peptide tag. As shown here, these peptide tags can concurrently direct, control and enhance the protein immobilization onto defined and selective inorganic surfaces. In contrast to conventional chemical and physical methods for protein adsorption, the robust peptide-based approach is highly intriguing due to being relatively simple in that it provides a single step surface functionalization with site-directed control, and it is biologically and environmentally friendly. Overall the results demonstrate that peptides provide a viable alternative to the conventional chemical coupling to produce various protein assemblies with highly controllable organization and architecture.

### ***8.3.2 Layer-by-Layer Protein Self-organization***

Hierarchical layer-by-layer immobilization of the inorganic nanoparticles and proteins onto solid surfaces is one of the challenges in building up micro/nano-scaled optical and diagnostics devices (Endo et al. 2006; Park et al. 2008a). Predominantly used immobilization strategies rely on physical forces, e.g., electrostatic interactions (Wang et al. 2003; Xu et al. 2007), DNA base-pairing (Park et al. 2008b; Nykypanchuk et al. 2008) or covalent linkage between the particle and the inorganic surface through a bifunctional molecule as the linker (Nath and Chilkoti 2002; Chen et al. 2007). Self-assembled monolayers (SAM) of

these molecules, e.g., aminoalkylalkoxysilanes (Westcott et al. 1998) for silica and carboxyl-terminated alkanethiols (Mrksich and Whitesides 1996) for gold, provide an appropriate interface on which two different inorganic surfaces can be linked to each other. For example, a gold nanoparticle can be attached to the surface of a larger silica nanoparticle pretreated with 3-aminopropyl trimethoxysilane molecule, leading to a hybrid nanostructure which, in turn, is used to synthesize a gold shell around silica surface in the presence of  $\text{HAuCl}_4$  solution (Oldenburg et al. 1998). However, most of the interactions mentioned here are labile and sensitive to some conditional parameters such as chemical solvent, heat and pH. Furthermore, silane and thiol-based molecules are not suitable for most of the biological reactions. Additionally, their use may require complex reactions for efficient coupling (Norde 1986; Nath and Chilkoti 2002; Zhen et al. 2006). In particular, thiol linkage has been shown to be susceptible to oxidation and disassociation (Flynn et al. 2003; Park et al. 2006; Willey et al. 2005).

Recent developments in molecular scale approaches to control the bio-material interfaces have enabled the self-functionalization of biomolecules onto nanoparticles using inorganic-binding peptides as biosurface linkers (Sarikaya et al. 2003; Whaley et al. 2000; Brott et al. 2001). The previous studies have shown that inorganic-binding peptides could be used for the attachment of nanoparticles and biomolecules, as well as the synthesis of hybrid nanostructures that all could be utilized in electronics and optical devices. For example, a streptavidin-coated quantum dot that has a strong and narrow emission at 605 nm was successfully immobilized on both gold (Zin et al. 2007) and silica (Kacar et al. 2009a) surfaces using biotinylated gold- and quartz-binding peptides, respectively. Gold-binding peptide was employed to immobilize gold nanoparticles (Zin et al. 2005) and proteins (Park et al. 2006) on gold surface, as well. Furthermore, synthesis of Au, Ag,  $\text{SiO}_2$  nanoparticles as well as hybrid DNA-protein- $\text{Cu}_2\text{O}$  nanostructures was achieved in presence of inorganic-binding peptides (Brown et al. 2000; Naik et al. 2002; Dai et al. 2005). These examples demonstrated that these peptides can work under ambient conditions and carry their material selective property based upon tailored surface recognition and assembly (Park et al. 2006; Brown et al. 2000; Tamerler et al. 2006a; Kacar et al. 2009a).

In the last years, peptides have been also demonstrated to link two different inorganic-binding sequences in a single peptide domain, resulting in a bifunctional peptide. Our designed bi-functional peptide was composed of silica- and gold-binding peptide sequences (QBP and AuBP), having a flexible poly-glycine spacer sequence to ensure both functions remain active. QBP and AuBP components were selected in our laboratories using optimized combinatorial selection, as well as de novo approaches adapted by our group (Oren et al. 2007; Hnilova et al. 2008). Both peptide sequences were carefully selected for best binding functionalities (Oren et al. 2007; Hnilova et al. 2008; Tamerler and Sarikaya 2009; Kacar et al. 2009a). Additionally, we were careful to avoid sequences dominated by amino acids known to interact with gold, such as cysteine and histidine (Levy et al. 2004; Wang et al. 2005; Slocik et al. 2005a, b; Slocik and Naik 2006) and which might, in turn, promote nonspecific interactions with gold. The bifunctional peptide

sequences were synthesized via automated Fmoc peptide synthesis and subsequently purified by reversed-phase high-performance liquid chromatography. The patterned QBP-AuBP multi-functional peptide (Fig. 8.5) was then utilized as a molecular linker for direct immobilization of gold nanoparticles onto the silica surface via a soft lithography process. The resulting gold nanostructure arrays were characterized using dark field (DF) optical microscopy as well as atomic force microscopy (AFM) in tapping mode (Fig. 8.5). The dark field optical and the atomic force micrographs revealed preferential assembly of the pre-made gold nanoparticles on to the patterned peptide templates. The height of the features observed under AFM was consistent with the expected height of the construct: 50 nm gold nanoparticle plus a 1–2 nm thick peptide monolayer (Hnilova et al. 2012b).

In our subsequent work we demonstrated bio-enabled self-assembly technique for fabrication of hybrid nanostructures and protein arrays with hierarchical architecture at multiple layers. We used the combinatorially selected gold-binding peptide (AuBP1) applied in our previous example as a modular tag to genetically fused protein. This approach enabled the immobilization of nanostructures and fusion proteins onto gold surface using a combination of soft-lithography and self-assembly techniques and resulted in multiple peptide/protein-enabled assembled layers. We first produced a bi-functional protein construct by genetically inserting the AuBP1 peptide to the C'-terminus of maltose-binding protein (MBP) using two structurally different spacers, i.e., either a rigid (PGPGPG) or flexible (SGGG) spacer. We then performed quantitative binding assays, Surface Plasmon Resonance (SPR) and Localized Surface Plasmon Resonance (LSPR). Spectroscopic evaluations confirmed similar levels gold binding peptide functionality for both of the engineered MBP-AuBP1 derivatives, with  $K_D$  of 0.032 and 0.035  $\mu\text{M}$ , respectively. Moreover, both of these fusion proteins demonstrated considerable higher gold binding affinities compared to wild-type MBP, with  $K_D$  of 0.124  $\mu\text{M}$ . Next, we tested the effectiveness of the proposed bio-enabled layer by layer assembly process on a glass surface. To start building up our protein enabled hierarchical assembly on a glass surface, we first stamped the bi-functional peptide (AuBP1-QBP1), which was synthesized previously as a single molecule via soft lithography (Hnilova et al. 2012b). We next incubated the gold nanoparticles, which were allowed to self-assemble onto the formed peptide patterns. To form the third layer, MBP-AuBP1 was added and left to selforganize on gold nanoparticles. Finally, immobilized fusion protein localized on these assembled hybrid structures were detected using an anti-MBP-specific fluorophore (Fig. 8.5). Our studies demonstrate that designed multi-functional peptide-based molecular constructs have the capacity for controlling and directing protein and nanostructure self-assembly on solid surfaces. Thus, they can be successfully used to fabricate multilayer protein microarrays, as well as functional hybrid nanostructures, through simple single step self-assembly that is tunable for each layer (Hnilova et al. 2012a).

In another screening, we selected the silver-binding peptides (AgBPs) using the FLiTrx bacterial surface library (Lu et al. 1995) using modified combinatorial



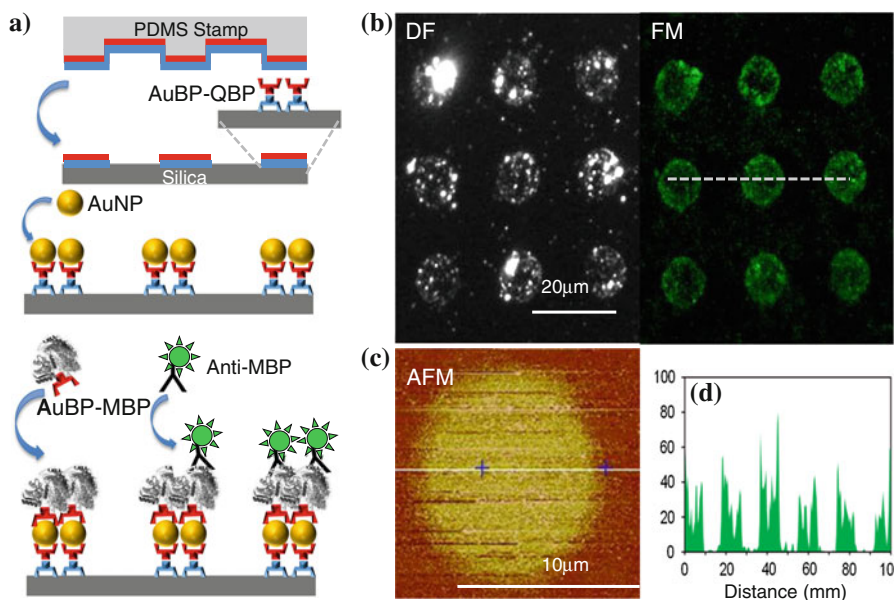


**Fig. 8.5** Layer-by-layer protein immobilization on patterned AuNP surfaces. **a** Schematic of layer-by-layer fusion maltose-binding protein (AuBP-MBP) immobilization on Au NP-arrayed surface; **b** Representative fluorescence and dark field images of MBP-(PG)3-AuBP1 proteins immobilized on Au NP arrays labeled with anti-MBP-Alexa-488 antibody; **c** Detail of atomic force microscopy scan of representative Au NP patterns immobilized on glass surface through QBP-PPP-AuBP bifunctional peptide; **d** Corresponding line scan plot of fluorescence images generated using ImageJ software (NIH, USA). The respective positions on fluorescence images used in ImageJ line scan analysis are indicated by dashed lines

selection procedures. Following the biopanning selection, we verified the binding characteristics of chemically synthesized AgBP1C and AgBP2C peptides onto Ag surface using surface plasmon resonance (SPR) spectroscopy, as an established technique from our earlier reports. The observed apparent binding constant  $k_{obs}$  and adhered peptide mass detected for both AgBP peptides tested at 0.66  $\mu\text{M}$  concentration and found to be within the generally observed peptide binding range (Tamerler et al. 2006a, b; Oren et al. 2007; Hnilova et al. 2008; Kacar et al. 2009a). The AgBP2C peptide exhibited a material selectivity by binding preferentially to Ag surface compared to Au. Only around 1.33  $\mu\text{M}$  AgBP2C peptide concentrations, we were able to detect a negligible peptide adhesion to Au surface approximately corresponding to over 10-fold reduction of adhered peptide mass compared to Ag surface.

Building upon the Ag binding ability of the selected peptides, we next demonstrated the efficient protein micro-patterning on spatially distributed arrays of AgNPs. In our approach, we used a combination of bio-enabled immobilization and ferroelectric lithographic technique on  $\text{LiNbO}_3$  substrates.  $\text{LiNbO}_3$  is a widely known ferroelectric material benefiting from its largest polarization existing only

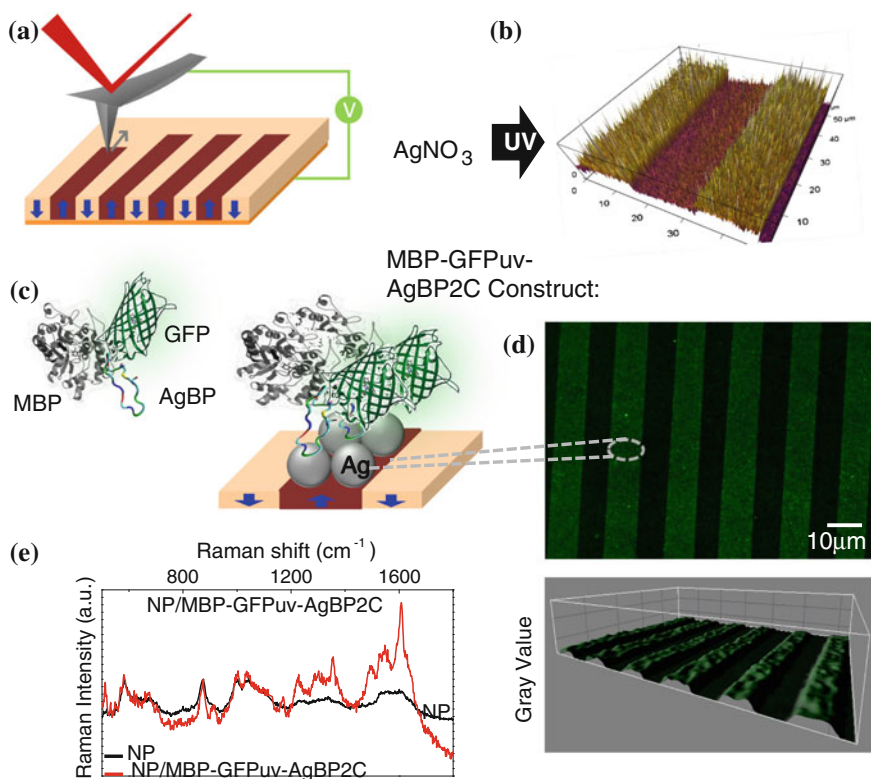


**Fig. 8.6** Multifunctional protein array on AgNPs patterned ferroelectric surface. **a** Depiction of ferroelectric domain manipulation and photochemical deposition of AgNPs; **b** AFM topographic image of the PPLN substrate after photochemical deposition; **c** Schematics of targeted protein immobilization on AgNPs pattern generated by photochemical deposition on LiNbO<sub>3</sub>; **d** Representative fluorescence images of 20 mM MBP-GFPuv-AgBP2C proteins immobilized on AgNPs pattern and corresponding 3D surface plots of fluorescence images generated by ImageJ imaging software; **e** SERS spectra taken from AgNP pattern with and without MBP-GFPuv-AgBP2C protein

along the crystallographic *c*-axis (Fig. 8.6). Polarization orientations can be manipulated by an external electric field (Fig. 8.6), which gives rise to the many applications based on ferroelectric materials (Myers et al. 1995; Kim et al. 2001). Inspired by the concept that spontaneous polarization in ferroelectrics has a strong effect on reactivity on surfaces; we combined polarization inversion with polarization-dependent photochemical reactions and fabricated AgNPs micro-patterns on the LiNbO<sub>3</sub> surface. Domain structures exhibiting anti-parallel polarizations along the *c*-axis were fabricated following a photolithographic step. Photochemical deposition was conducted by placing AgNO<sub>3</sub> solution over the substrate surface under light irradiation. Before deposition, the surface topography of

periodically poled lithium niobate (PPLN) substrate was examined by atomic force microscope (AFM) and domain structure was visualized through the phase image of piezoresponse force microscope (PFM). Domain-specific Ag deposition can be generated through a strong photovoltaic effect (Liu et al. 2007, 2008) of  $\text{LiNbO}_3$  crystals. The AgNPs pattern fabricated by the photochemical deposition was illuminated by a noncontact AFM topographic image.

Multifunctional protein-based surface functionalization was next studied on silver nanoparticles (AgNP) patterned on functional ferroelectric  $\text{LiNbO}_3$  substrates building upon the controlled interfacial interactions. Specifically, as a material-specific biolinker, we use a combinatorially selected silver-binding peptide (AgBP) fused to a maltose-binding protein (MBP) and a green fluorescent protein (GFPuv). The MBP fusion component was rationally selected based upon the lack of cysteine amino acid in order to prevent the sulfide-induced nonspecific protein interactions with metallic surface, ease of genetic manipulation, as well as its high expression protein yield in bacterial cells and straightforward purification. The second fusion partner, fluorescently active GFPuv protein, was chosen to visualize the model fusion protein immobilized on defined locations on silver surfaces. We separated the two functional domains; the silver-binding AgBP2C tag away the fluorescent GFPuv protein, by a flexible (SGGG) spacer, which, itself, is separated from the MBP protein by several amino acids encoded by the polylinker contained in the pMAL-c4x expression vector (Fig. 8.6).

Taking advantage of the multifunctional property of the designed MBP-GFPuv-AgBP2C protein, we fabricated protein arrays on AgNPs located on the PPLN substrate. The fluorescence microscopy results (Fig. 8.5b) confirm the material-selective robust self-assembly of MBP-GFPuv-AgBP2C fusion proteins onto AgNP array regions, resulting in fabrication of spatially controllable multilayered protein arrays. In contrast MBP-GFPuv protein did not reveal any protein binding in arrays and resulted in random nonspecific immobilization of MBP onto both solid surfaces (Fig. 8.6). Additionally, we confirmed the presence of MBP-GFPuv-AgBP2C protein adsorbed AgNPs patterned on the PPLN substrate by Surface Enhanced Raman Scattering (SERS).

Overall, these studies serve as an example for the formation of ordered hierarchical assemblies built upon hybrid nanostructures using modular and compatible peptide-based protocols built upon their tunable interactions at the material interfaces. Summarized bio-enabled paths are compatible with conventional patterning and microfabrication techniques to create different platforms including functional biosensing moieties. Furthermore, the described combination of specific bio-enabled immobilization technology with functional nanoscale and ferroelectric substrates opens a path to fabricate protein self-assemblies with arbitrary designs for applications in tunable biosensor systems. The bio-enabled self-assembly technology provides improved outcomes over conventional synthetic techniques. The engineered peptide tags can concurrently direct, control, and enhance protein immobilization onto specific solid surfaces in a relatively simple process while under biologically and environmentally friendly conditions (Hnilova et al. 2012c).

### ***8.3.3 Bio-enabled Protein Immobilization on Cyclic Voltametry-Based Biosensors***

Building upon our successful controlled self-assembly of functional proteins, we aimed to use the similar biomimetic approach to immobilize enzymes for biosensor applications. Enzyme immobilization has been studied extensively often in efforts to retain catalytic activity, operational stability and long term repeated use (Bornscheuer 2003; Rusmini et al. 2007; Sheldon 2007). Similar to proteins and other biomolecules, the common methods used for immobilization on inorganic surfaces include the physical adsorption such as ionic, hydrophobic, or polar interactions and chemical coupling using the reactive side chains of biomolecules (Rusmini et al. 2007) or chemical coupling by taking advantage of the reactive groups on the side chains of amino acids.

Oxidoreductases, often called dehydrogenases, catalyze biochemical redox reactions involving the transfer of electron pairs from organic substrates to carrier molecules such as nicotinamide adenine dinucleotide (NAD<sup>+</sup>). As biological catalysts, dehydrogenases play important roles in pharmaceutical, chemical, agriculture, and food processing industries (Hummel and Kula 1989). Lactate dehydrogenase (LDH) catalyzes the interconversion of pyruvate and lactate using the NADH/NAD<sup>+</sup> pair as a redox cofactor (Rasmussen et al. 1993). Since lactate is produced during normal metabolism and exercise, detection of lactate concentration plays an important role in clinical diagnostics, medicine validations and food analysis (Faridnia et al. 1993; Palleschi et al. 1994; Avramescu et al. 2002; Malhotra and Chaubey 2003). In the last couple of decades, redox enzymes have also been explored as bioactive matrices in amperometric biosensors or biofuel cells (Lobo et al. 1997; Chaubey et al. 2000; Willner 2002; Barton et al. 2004; Heller 2004; Zayats et al. 2008; Lee et al. 2009).

Despite the considerable progress that has been achieved in electrically contacted redox enzyme electrodes and biosensors devices, electronic communication efficiency is still far lower than the native electron transfer change. Random-oriented immobilization of the redox enzymes on the electrodes, as well as random substitution of the enzymes by the electron relay units, are considered the major causes (Zayats et al. 2008). There have been substantial research efforts directed to overcome the barrier of electron transfer while establishing electric contact between redox proteins and electrodes. All of these methods focused on shortening electron transfer distances and shuttling the electrons between the proteins and the electrodes. The use of mediators provide confinement control in the sol-gel matrixes, and reconstitution of apoenzymes on a relay co-factor monolayer over the thin film functionalized electrode surfaces (Marzouk et al. 1997; Palmisano et al. 2000; Parra et al. 2006; Suman et al. 2005; Lowinsohn and Bertotti 2007).

As demonstrated in our earlier examples, peptides with selective affinity for solid surfaces are good candidates as fusion partners with the target proteins due to their suitability for genetic insertion with the proteins (Kacar et al. 2009b; Yuca et al. 2011; Hnilova et al. 2012a, b, c). Recently, we demonstrated the efficient use

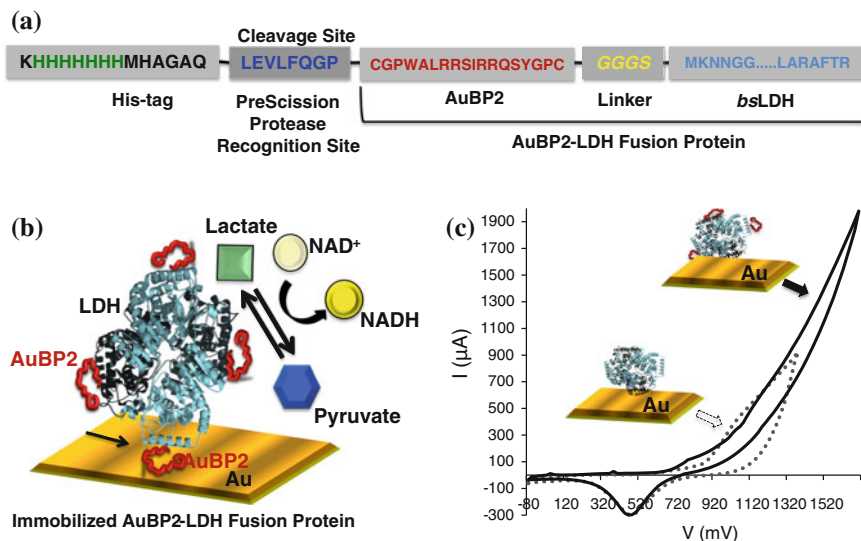


**Fig. 8.7** Bio-enabled enzyme immobilization for cyclic voltameter-based biosensor: **a** Schematic of design and production of material-selective, gold-binding lactate dehydrogenase enzyme (AuBP2-LDH) **b** Schematic of immobilized bsLDH-AuBP2 onto the Au (gold) surface **c** Cyclic voltammograms of (—) bsLDH-AuBP2 and (.....) bsLDH immobilized on gold working electrode following the addition of 10 mM NAD<sup>+</sup> and 2 M lactate. Experiments were performed in 50 mM Tris buffer pH 7.0, at 25 °C and a scan rate of 100 mM/s<sup>-1</sup>

of a gold binding peptide as a genetically conjugated tag for addressable self-attachment of L-lactate dehydrogenase (LDH) from *Bacillus stearothermophilus* (*bs*) on a variety of gold surfaces across multiple length scales ranging from nanoparticles to electrodes (Fig. 8.7). One of our previously selected and well-characterized gold binding peptide, AuBP2 (Hnilova et al. 2008), was exploited as the fusion partner to *bs*LDH. In our cloning and expression system, we introduced a his-tag cleavage region through the insertion of PreScission Protease recognition site between His-tag and the fusion proteins. The molecular weights of *bs*LDH and *bs*LDH-AuBP2 proteins expressed using *E. coli* DH5 $\alpha$ -T1 cells were confirmed. Surface binding kinetics data indicated that AuBP2-LDH have the ability to adsorb onto gold surface in relatively at low concentrations due to the AuBP insertion. Retained LDH activity also proved that the enzymatic activity was preserved in the fusion construct. We next demonstrated the enhanced enzyme stability once it is immobilized on the nanoparticle surfaces by using the AuBP tag over an extended period of time, i.e., 30 days, compared the *bs*LDH. Our results indicated that AuBP2 mediated immobilization is efficient not only for the retained activity but also for the enzyme stability. Finally, detection of the reduction reaction performed by immobilized enzyme on a cyclic voltammetry biosensor suggested that AuBP2 provides a new and efficient immobilization method for lactate

dehydrogenases. Providing better positioning to locate the enzyme at a close distance to the sensing surface resulting in efficient electron transfer between the enzyme and the electrode surface (Cetinel et al. 2013).

### ***8.3.4 Bio-enabled Protein Immobilization on LSPR-Based Biosensors***

Noble metal nanoparticles (gold, silver) exhibit a strong UV-visible absorption band that occurs when incident light is resonant with the collective excitation of surface electrons on nanoparticles. This phenomenon is known as localized surface plasmon resonance (LSPR) (Anker et al. 2008; Nath and Chilkoti 2004). LSPR is highly dependent on nanoparticle size, shape, interparticle spacing, and local dielectric environment (Anker et al. 2008; Prodan et al. 2003). The dependence of LSPR resonance on latter case allows one to design a sensor that targets molecule binding to the nanoparticle surface, which results in a shift in the LSPR peak (Endo et al. 2005). As a result, the LSPR sensor does not require any labeling steps for detection and in the literature both gold and silver nanostructures have been successfully utilized to detect various biomolecule interactions (Nath and Chilkoti 2004; Haes et al. 2004; Endo et al. 2005; Fujiwara et al. 2006; Willets and Van Duyne 2007).

Sensing through LSPR requires either attachment of metal nanostructures or deposition of noble metal atoms onto dielectric surface, e.g., glass. Conventionally, immobilization of gold nanoparticles on a glass substrate is accomplished by self-assembled monolayers (SAMs) of bifunctional molecules, such as amino terminated amonialkoxysilanes (Fujiwara et al. 2006). Similarly, the probe molecules can be attached to gold by different SAMs, e.g., carboxyl-terminated alkanthiols (Ostuni et al. 1999). One of the major drawbacks of these conventional techniques is the random immobilization orientation of the probe molecules and complexity of the process due to requirement of multiple step chemical reactions (Park et al. 2006; Fujiwara et al. 2006).

In our group, we took advantage of material selectivity of combinatorially selected inorganic-binding peptides and their tunable properties. As described in the previous sections, we linked chemically gold-binding and silica-binding peptide sequences (Oren et al. 2007; Hnilova et al. 2008) resulting in a single bifunctional peptide unit. Gold nanoparticles were immobilized onto glass substrate resulting in an LSPR-active surface. The attachment of gold nanoparticles onto the glass surface was verified by various techniques, such as dark field and atomic force microscopy. The LSPR band as a sensing platform without having any additional molecule present was established.

Similar to our previously summarized hierarchical protein self-assembly system, we genetically fused our gold-binding sequences with various probe molecules, such as alkaline phosphatase (AP). These probe molecules were then

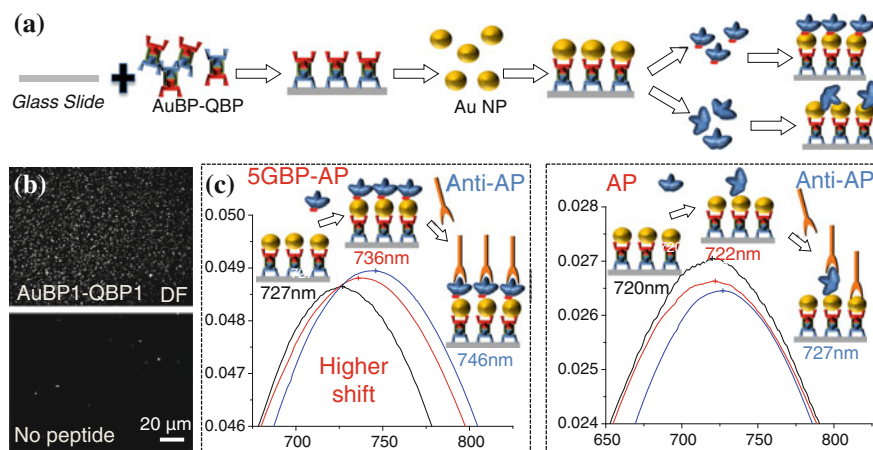


**Fig. 8.8** Bio-enabled localized surface plasmon resonance biosensor: **a** Schematic representation of gold nanoparticle immobilization using bifunctional AuBP-QBP peptide; **b** dark-field images of gold nanoparticle attachment on the glass slide preincubated with AuBP-QBP or no peptide (buffer); **c** Immunodetection of AP and fusion AP-GBP protein by anti-AP using LSPR-based biosensor composed of peptide-immobilized gold nanoparticles, transmission spectra were taken following nanoparticle, probe protein (AP, AP-GBP) and anti-AP immobilization

self-assembled onto the gold nanoparticles. Using LSPR spectroscopy, the assembly performance of the fusion AP protein was investigated and compared to AP wild-type. As evident in Fig. 8.8, the redshift at LSPR  $\lambda$  max of 5GBP-AP fusion protein was more than 3 times higher compared to the redshift recorded for AP wild-type assembly. This indicates that a higher number of molecules was assembled on the gold surface in the case of the fusion protein compared to wild-type probe.

In a subsequent step, we detected the probe molecules by adding anti-AP antibody following the LSPR shift. Since we recorded the LSPR signals from the biosensors before and after adding the probe molecules, we were able to quantify the LSPR shift corresponding to each assembly step shown in Fig. 8.8. Due to the change in local refractive index, the subsequent target anti-AP molecule assembly resulted in further redshift at the LSPR  $\lambda$  max. Since the number of assembled fusion protein molecules on gold surface was initially higher (due to presence of material selective peptide tag) the recorded shifts after 25  $\mu$ g/ml anti-AP resulted in higher shift compared to AP wild-type. Two control experiments were carried out by using the target molecule (anti-AP) incubated with bare biosensor platform and using an analog target molecule (anti-MBP) incubated with fusion AP-5GBP. The results revealed that the subsequent LSPR responses were due to the specific binding interactions between probe and target molecules.

This observation was also confirmed in other model systems using different probe and target molecules such as gold-binding fusion to maltose-binding protein as the probe and anti-MBP antibody as the target (data not shown). The results

demonstrated that inorganic-binding peptides could be used as alternative biological linkers for nanoparticle and biomolecule attachment in building up quantitative LSPR biosensors. We would like to note that utilization of inorganic-binding peptides as bi-functional molecular constructs and optically active noble metal nanoparticles can be successfully used to create hybrid biosensing active platforms for the detection of various important biomolecule targets.

### ***8.3.5 Material-Selective Fusion Proteins for Detection of Biomineralization***

Inorganic-binding peptides can provide a new platform for high performance of implants and hard tissue-engineering via immobilization of biomolecules with controlled attachment and assembly on solid surfaces. In this section, a fusion protein encoding both the fluorescence property of GFP and the hydroxyapatite binding is explained to provide another perspective for potential use of and hydroxyapatite-binding peptide in hard tissue engineering.

Biomineralization processes have attracted major interdisciplinary interest among diverse scientists as well as engineers whose goals have ranging from understanding the fundamentals, to mimicking mineralization processes to develop hybrid materials with controlled structures and functions for medical applications. Hydroxyapatite (HA) has been one of the most extensively studied biomineral, being the principal inorganic component of hard tissues such as bone and teeth in humans, in particular, and mammals, in general. The ability to track HA specifically, against the background of other calcium phosphates is important in biomedical area, such as bone and teeth formation/remodeling, gene/drug/cell delivery, regulation of cell bioactivity, and nano-technological implementations, such as nanoparticle composites (Dash and Cudworth 1998; Liu et al. 2005; Oh et al. 2005; Tan et al. 2007; Ma et al. 2008; Kasaj et al. 2008; Braux et al. 2009). The golden standards for in vitro staining of HA are alizarin red S, which stains calcium (Iipman 1935) and von Kossa stain, which stains phosphates and carbonates. Despite the potentially promising results reported so far, existing methods suffer either from the complex chemistries required for labeling or from the toxicity of the dopants or the composites. Even quantum dots, which have great potential in many research and diagnostic applications, are still considered toxic when they are used in living systems (Alivisatos et al. 2005; Hardman 2006). Likewise, bisphosphonates, used as a chemical linker, because of their high affinity to hard tissues, carry the risk of disrupting bone turnover due to their inhibitory effects on osteoblasts (Boonekamp et al. 1986; Weinstein et al. 2009).

In a previous study, we have reported phage display selected HA-binding peptides and provided their binding and molecular structural properties (Gungormus et al. 2008). Among these, a high affinity HA-binding heptapeptide, with the amino acid sequence of CMLPHHGAC, was also demonstrated to have mineral-forming capabilities. In the present study, we report a simple and versatile





**Fig. 8.9** Bio-enabled detection of hydroxyapatite biomineralization on tooth: **a** Schematic of design and production of material-selective, hydroxy-apatite-binding green fluorescent protein (HABP-GFP); **b** Schematic illustration of the labeling procedure of the teeth samples; **c** SEM micrograph of the surface of the root prior to protein labeling. Binding of GFPuv, GFPuv-HABP2, and GFPuv-HABP1 on the cementum of human incisors

method for biolabeling of minerals using a strong hydroxyapatite-binding peptide (HABP1) conjugated to a green fluorescent protein derivative (GFPuv) as a tag. The green fluorescent protein (GFP) from the bioluminescent jellyfish *Aequorea victoria* has been extensively used as a reporter molecule to monitor expression and localization of many proteins for a wide variety of studies in life sciences (Zimmer 2002). We demonstrated its utility here as an engineered molecular probe for fluorescent labeling of mineralized tissues (Fig. 8.9). The simultaneous formation and labeling of HA were performed under various conditions, including mineral formation on a solid substrate as well as on an existing biological hard tissue as a substrate.

Specifically, we engineered a fusion protein encoding the fluorescence activity of a GFP and the dual HA-binding and synthesis activity of a phage display selected heptapeptide. The hypothesis was that the genetic conjugation of GFP to HA-binding peptide would result in a multifunctional molecular probe, which provides targeted labeling and time-wise mineralization monitoring of HA via fluorescent signal. We demonstrated the applicability of this hypothesis on the synthesized HA mineral on a glass-surface mimicking a solid implant substrate and on a naturally mineralized tissue, namely the root of human incisor teeth, to mimic restoration. We built two different bi-functional constructs: GFPuv-HABP1 and GFPuv-HABP2, and prepared a GFPuv expression construct as control. Using fluorescence and circular dichroism studies we demonstrated that the fluorescent properties and structural traits of GFPuv were conserved upon the insertion of the

designed peptides. The binding properties of fusion proteins to HA surface were also examined using fluorescence microscopy and quartz crystal microbalance techniques. The equilibrium desorption constant, calculated from quantitative binding assays, of the GFPuv-HABP1 construct ( $6.6 \pm 0.3 \mu\text{M}$ ) is almost 70 times lower than that of the GFPuv-HABP2 ( $429 \pm 23 \mu\text{M}$ ) implying that GFPuv-HABP1 has a higher affinity to the HA substrate. Likewise, the free energy of adsorption ( $\Delta G_{\text{abs}}$ ), which is the change in the standard free energy of binding, of GFPuv-HABP1 is higher ( $-7 \text{ kcal/mol-K}$ ) than that of ( $-4.64 \text{ kcal/mol-K}$ ). This implies that binding of GFPuv-HABP1 on HA surface is thermodynamically favored compared to GFPuv-HABP2, consequently a high stability in the fusion protein–mineral system is achieved (Yuca et al. 2011).

The binding affinity of the GFPuv-HABP constructs on biological samples was also tested on human AAFC samples. The acellular cementum consists of a mineralized matrix but lacks collagen fibers and cementocytes. At identical imaging conditions under the fluorescent microscope, neither of the samples prepared with the incubation of GFPuv or GFPuv-HABP2 displayed any contrast on the teeth surfaces. Fluorescent contrast, however, was easily discerned on the teeth samples incubated with GFPuv-HABP1, due to its successful attachment to the surface. The fluorescent images demonstrated that the GFPuv-HABP1 construct can recognize biologically mineralized tissues as well as synthetically formed HA. Fluorescent intensity measurements from the samples indicated that GFPuv-HABP1 yields more than six times higher fluorescence on teeth compared to those using either GFPuv or GFPuv-HABP2. Our study demonstrates a simple and versatile application of inorganic-binding peptides conjugated with bioluminescence proteins in designing bioimaging molecular probes that can target mineralization, and which can be employed to a wide range of biomimetic processing and cell-free tissue engineering.

## 8.4 Future Perspectives on Bio-Enabled Functionalization

In the last decades, we have seen a wealth of new materials inspired by nature and applied in wide-ranging medical and technological areas. One of the key components underlying the structure and function in biological systems is their inherent hierarchical organization, which is a major challenge to achieve in engineering approaches. Nature's design uses biological self-assembly principles, the basis of which is precise recognition starting at the molecular scale. Biological machinery are inherently self-organized and self-regulated. Proteins are among the key players in this machinery. In mimicking the capabilities of proteins, peptides have been utilized as critical building blocks to develop unique novel hybrid materials for a variety of practical applications.

The inorganic binding peptides have been increasingly investigated as a novel bio-surface functionalization method, i.e., to couple different materials together or to bring biological cues to the material surfaces. Their modularity offers a unique

opportunity to link them with other functional proteins. Here we provided examples on their design and recombinant incorporation into functional proteins and enzymes to achieve addressable self-immobilization. The engineered multi-functional biomolecular constructs were demonstrated to self-organize to form hybrid hierarchical entities while preserving their original function. However, there is no all-encompassing solution for orientation control of the enzymes on surfaces using inorganic binding peptide tags. Each peptide and enzyme set need to be evaluated in detail once they are genetically conjugated; this will help achieve optimum performance for the both existing and additional functional domains.

Bio-functionalization of metallic or semiconductor surfaces has great potential in creating addressable and programmable biomolecular templates. Controlling the biological-materials interfaces will contribute to the developments of new generation biomolecule mediated devices and systems. These engineered biomolecular systems will serve as dynamic surface functionalization linkers providing functional biomolecules the ability to self-organize at the interfaces within a controllable proximity. This self-organization displays a great deal of potential in creating new materials and systems.

By mimicking natural evolution, inorganic binding peptides have already made their way into technological application, starting from material selective bio-functionalization of surfaces, to controlled synthesis of materials. With the progress in our understanding of biological pathways and the biomolecular mechanisms in the context of both physical and biological constraints for material formation, bio-enabled and biomimetic materials science and engineering will bring unique opportunities for designing new materials and systems with predictable and adaptable features. Mimicking the shapes and structures gifted to us by nature has resulted in the production of outstanding materials, it is rather exciting to think where mimicking the biological machinery will take us in materials assembly and synthesis.

**Acknowledgments** This research is supported by NIH 1R21AR062249-01 and University of Kansas School of Engineering and KU-BERC Funds, NSF-MRSEC Program through the University of Washington GEMSEC DMR 0520567, NSF-DMR BioMaterial Program, NSF-IRES and TUBITAK/NSF joint project (TBAG 107T250), TUBITAK-BIDEB program (B.T. Karaca).

## References

- Aizenberg J, Lambert G, Weiner S, Addadi L (2002) Factors involved in the formation of amorphous and crystalline calcium carbonate: a study of an ascidian skeleton. *J Am Chem Soc* 124 (1):32–39. doi: [10.1021/Ja0169901](https://doi.org/10.1021/Ja0169901)
- Aizenberg J, Weaver JC, Thanawala MS, Sundar VC, Morse DE, Fratzl P (2005) Skeleton of euplectella sp.: structural hierarchy from the nanoscale to the macroscale. *Science* 309 (5732):275–278. doi: [10.1126/Science.1112255](https://doi.org/10.1126/Science.1112255)
- Akdim B, Pachter R, Kim SS, Naik RR, Walsh TR, Trohalaki S, Hong GY, Kuang ZF, Farmer BL (2013) Electronic properties of a graphene device with peptide adsorption: insight from simulation. *Acs Appl Mater Interfaces* 5(15):7470–7477. doi:[10.1021/am401731c](https://doi.org/10.1021/am401731c)

- Aksay IA, Weiner S (1998) Biomaterials—is this really a field of research? *Curr Opin Solid St M* 3(3):219–220. doi:[10.1016/S1359-0286\(98\)80093-4](https://doi.org/10.1016/S1359-0286(98)80093-4)
- Alberts B (2002) *Molecular biology of the cell*, 4th edn. Garland Science, New York
- Alivisatos AP, Gu WW, Larabell C (2005) Quantum dots as cellular probes. *Annu Rev Biomed Eng* 7:55–76
- Anker JN, Hall WP, Lyandres O, Shah NC, Zhao J, Van Duyne RP (2008) Biosensing with plasmonic nanosensors. *Nat Mater* 7(6):442–453. doi:[10.1038/Nmat2162](https://doi.org/10.1038/Nmat2162)
- Avramescu A, Andreescu S, Noguier T, Bala C, Andreescu D, Marty JL (2002) Biosensors designed for environmental and food quality control based on screen-printed graphite electrodes with different configurations. *Anal Bioanal Chem* 374(1):25–32. doi:[10.1007/S00216-002-1312-0](https://doi.org/10.1007/S00216-002-1312-0)
- Ball P (2001) Life's lessons in design. *Nature* 409(6818):413–416. doi:[10.1038/35053198](https://doi.org/10.1038/35053198)
- Baneyx F, Park JK (2013) Editorial: nanobio versus bionano—what's in a name? *Biotechnol J* 8(2):158–159. doi:[10.1002/biot.201200407](https://doi.org/10.1002/biot.201200407)
- Barton SC, Galloway J, Atanassov P (2004) Enzymatic biofuel cells for implantable and microscale devices. *Chem Rev* 104(10):4867–4886. doi:[10.1021/Cr020719k](https://doi.org/10.1021/Cr020719k)
- Berman A, Addadi L, Weiner S (1988) Interactions of Sea-Urchin skeleton macromolecules with growing calcite crystals—a study of intracrystalline proteins. *Nature* 331(6156):546–548
- Boder ET, Wittrup KD (1997) Yeast surface display for screening combinatorial polypeptide libraries. *Nat Biotechnol* 15(6):553–557. doi:[10.1038/Nbt0697-553](https://doi.org/10.1038/Nbt0697-553)
- Boonekamp PM, Vanderweepals LJA, Vanwijkvanlennep MML, Thesing CW, Bijvoet OLM (1986) 2 Modes of action of bisphosphonates on osteoclastic resorption of mineralized matrix. *J Bone Miner Res* 1(1):27–39
- Bornscheuer UT (2003) Immobilizing enzymes: how to create more suitable biocatalysts. *Angew Chem Int Ed* 42 (29):3336–3337. doi: [10.1002/Anie.200301554](https://doi.org/10.1002/Anie.200301554)
- Braux J, Guillaume C, Jallot E, Nedelec JM, Laurent-Maquin D, Laquerriere P (2009) Effect of strontium treatment on human primary osteoblasts. hydroxyapatite: a drug delivery system?. *Int J Artif Organs* 32 (7):458
- Brott LL, Naik RR, Pikas DJ, Kirkpatrick SM, Tomlin DW, Whitlock PW, Clarson SJ, Stone MO (2001) Ultrafast holographic nanopatterning of biocatalytically formed silica. *Nature* 413(6853):291–293. doi:[10.1038/35095031](https://doi.org/10.1038/35095031)
- Brown S (1997) Metal-recognition by repeating polypeptides. *Nat Biotechnol* 15(3):269–272. doi:[10.1038/Nbt0397-269](https://doi.org/10.1038/Nbt0397-269)
- Brown S, Sarikaya M, Johnson E (2000) A genetic analysis of crystal growth. *J Mol Biol* 299(3):725–735. doi:[10.1006/Jmbi.3682](https://doi.org/10.1006/Jmbi.3682)
- Calvert P, Mann S (1988) Synthetic and biological composites formed by in situ precipitation. *J Mater Sci* 23(11):3801–3815. doi:[10.1007/Bf01106796](https://doi.org/10.1007/Bf01106796)
- Cariolou MA, Morse DE (1988) Purification and characterization of calcium-binding conchiolin shell peptides from the mollusc, *Haliotis rufescens*, as a function of development. *Journal of Comparative Physiology B-Biochemical Systemic and Environmental. Physiology* 157(6): 717–729
- Cetinel S, Caliskan HB, Yucesoy DT, Donatan AS, Yuca E, Urgan M, Karaguler NG, Tamerler C (2013) Addressable self-immobilization of lactate dehydrogenase across multiple length scales. *Biotechnol J* 8(2):262–272. doi:[10.1002/Biot00502](https://doi.org/10.1002/Biot00502)
- Chaubey A, Gerard M, Singhal R, Singh VS, Malhotra BD (2000) Immobilization of lactate dehydrogenase on electrochemically prepared polypyrrole-polyvinylsulphonate composite films for application to lactate biosensors. *Electrochim Acta* 46(5):723–729
- Chen Y, Munechika K, Ginger DS (2007) Dependence of fluorescence intensity on the spectral overlap between fluorophores and plasmon resonant single silver nanoparticles. *Nano Lett* 7(3):690–696. doi:[10.1021/NI062795z](https://doi.org/10.1021/NI062795z)
- Coyle BL, Rolandi M, Baneyx F (2013) Carbon-Binding Designer Proteins that Discriminate between sp(2)- and sp(3)-Hybridized Carbon Surfaces. *Langmuir* 29(15):4839–4846. doi:[10.1021/la4000846](https://doi.org/10.1021/la4000846)

- Cui Y, Kim SN, Naik RR, McAlpine MC (2012) Biomimetic peptide nanosensors. *Acc Chem Res* 45(5):696–704. doi:[10.1021/ar2002057](https://doi.org/10.1021/ar2002057)
- Dai HX, Choe WS, Thai CK, Sarikaya M, Traxler BA, Baneyx F, Schwartz DT (2005) Nonequilibrium synthesis and assembly of hybrid inorganic-protein nanostructures using an engineered DNA binding protein. *J Am Chem Soc* 127(44):15637–15643. doi:[10.1021/ja055499h](https://doi.org/10.1021/ja055499h)
- Dash AK, Cudworth GC (1998) Therapeutic applications of implantable drug delivery systems. *J Pharmacol Toxicol* 40(1):1–12. doi:[10.1016/S1056-8719\(98\)00027-6](https://doi.org/10.1016/S1056-8719(98)00027-6)
- Endo T, Kerman K, Nagatani N, Hiepa HM, Kim DK, Yonezawa Y, Nakano K, Tamiya E (2006) Multiple label-free detection of antigen-antibody reaction using localized surface plasmon resonance-based core-shell structured nanoparticle layer nanochip. *Anal Chem* 78(18):6465–6475. doi:[10.1021/Ac0608321](https://doi.org/10.1021/Ac0608321)
- Endo T, Kerman K, Nagatani N, Takamura Y, Tamiya E (2005) Label-free detection of peptide nucleic acid-DNA hybridization using localized surface plasmon resonance based optical biosensor. *Anal Chem* 77(21):6976–6984. doi:[10.1021/Ac0513459](https://doi.org/10.1021/Ac0513459)
- Evans JS, Samudrala R, Walsh TR, Oren EE, Tamerler C (2008) Molecular design of inorganic-binding polypeptides. *MRS Bull* 33(5):514–518. doi:[10.1557/mrs2008.103](https://doi.org/10.1557/mrs2008.103)
- Faridnia MH, Palleschi G, Lubrano GJ, Guilbault GG (1993) Amperometric biosensor for determination of lactate in sweat. *Anal Chim Acta* 278(1):35–40. doi:[10.1016/0003-2670\(93\)80082-V](https://doi.org/10.1016/0003-2670(93)80082-V)
- Flynn NT, Tran TNT, Cima MJ, Langer R (2003) Long-term stability of self-assembled monolayers in biological media. *Langmuir* 19(26):10909–10915. doi:[10.1021/La035331e](https://doi.org/10.1021/La035331e)
- Frascione N, Codina-Barrios A, Bassindale AR, Taylor PG (2013) Enhancing in vitro selection techniques to assist the discovery, understanding and use of inorganic binding peptides. *Dalton Trans* 42(28):10337–10346. doi:[10.1039/c3dt50541c](https://doi.org/10.1039/c3dt50541c)
- Fujiwara K, Watarai H, Itoh H, Nakahama E, Ogawa N (2006) Measurement of antibody binding to protein immobilized on gold nanoparticles by localized surface plasmon spectroscopy. *Anal Bioanal Chem* 386(3):639–644. doi:[10.1007/s00216-006-0559-2](https://doi.org/10.1007/s00216-006-0559-2)
- Gabryelczyk B, Szilvay GR, Salomaki M, Laaksonen P, Linder MB (2013) Selection and characterization of peptides binding to diamond-like carbon. *Colloids and Surf B* 110:66–73. doi:[10.1016/j.colsurfb.2013.04.002](https://doi.org/10.1016/j.colsurfb.2013.04.002)
- Gaskin DJH, Starck K, Vulfson EN (2000) Identification of inorganic crystal-specific sequences using phage display combinatorial library of short peptides: a feasibility study. *Biotechnol Lett* 22(15):1211–1216
- Grosh CD, Schwartz DT, Baneyx F (2009) Protein-Based control of silver growth habit using electrochemical deposition. *Cryst Growth Des* 9(10):4401–4406. doi:[10.1021/Cg9004196](https://doi.org/10.1021/Cg9004196)
- Gungormus M, Fong H, Kim IW, Evans JS, Tamerler C, Sarikaya M (2008) Regulation of in vitro calcium phosphate mineralization by combinatorially selected hydroxyapatite-binding peptides. *Biomacromolecules* 9(3):966–973. doi:[10.1021/bm701037x](https://doi.org/10.1021/bm701037x)
- Haes AJ, Zou SL, Schatz GC, Van Duyne RP (2004) A nanoscale optical biosensor: the long range distance dependence of the localized surface plasmon resonance of noble metal nanoparticles. *J Phys Chem B* 108(1):109–116. doi:[10.1021/Jp0361327](https://doi.org/10.1021/Jp0361327)
- Hanks SK, Quinn AM, T. H (1988) The protein kinase family: conserved features and deduced phylogeny of the catalytic domains. *Science* 241:42–52
- Hardman R (2006) A toxicologic review of quantum dots: toxicity depends on physicochemical and environmental factors. *Environ Health Perspect* 114(2):165–172
- Hashimoto K, Yoshinari M, Matsuzaka K, Shiba K, Inoue T (2011) Identification of peptide motif that binds to the surface of zirconia. *Dent Mater J* 30(6):935–940. doi:[10.4012/dmj.2011-161](https://doi.org/10.4012/dmj.2011-161)
- Heller A (2004) Miniature biofuel cells. *Phys Chem Chem Phys* 6(2):209–216. doi:[10.1039/B313149a](https://doi.org/10.1039/B313149a)
- Nilova M, Karaca BT, Park J, Jia C, Wilson BR, Sarikaya M, Tamerler C (2012a) Fabrication of hierarchical hybrid structures using bio-enabled layer-by-layer self-assembly. *Biotechnol Bioeng* 109(5):1120–1130. doi:[10.1002/bit.24405](https://doi.org/10.1002/bit.24405)

- Hnilova M, Khatayevich D, Carlson A, Oren EE, Gresswell C, Zheng S, Ohuchi F, Sarikaya M, Tamerler C (2012b) Single-step fabrication of patterned gold film array by an engineered multi-functional peptide. *J Colloid Interface Sci* 365(1):97–102. doi:[10.1016/j.jcis.2011.09.006](https://doi.org/10.1016/j.jcis.2011.09.006)
- Hnilova M, Liu X, Yuca E, Jia C, Wilson B, Karatas AY, Gresswell C, Ohuchi F, Kitamura K, Tamerler C (2012c) Multifunctional protein-enabled patterning on arrayed ferroelectric materials. *ACS Appl Mater Inter* 4(4):1865–1871. doi:[10.1021/Am300177t](https://doi.org/10.1021/Am300177t)
- Hnilova M, Oren EE, Seker UOS, Wilson BR, Collino S, Evans JS, Tamerler C, Sarikaya M (2008) Effect of molecular conformations on the adsorption behavior of gold-binding peptides. *Langmuir* 24(21):12440–12445. doi:[10.1021/La801468c](https://doi.org/10.1021/La801468c)
- Hummel W, Kula MR (1989) Dehydrogenases for the synthesis of chiral compounds. *Eur J Biochem* 184(1):1–13. doi:[10.1111/J.1432-1033.1989.Tb14983.X](https://doi.org/10.1111/J.1432-1033.1989.Tb14983.X)
- Iipman HJ (1935) Staining the skeleton of cleared embryos with alizarin red S. *Stain Technol* 10(2):61–63
- Ishikawa K, Yamada K, Kumagai S, Sano KI, Shiba K, Yamashita I, Kobayashi M (2008) Adsorption properties of a gold-binding peptide assessed by its attachment to a recombinant apoferritin molecule. *Appl Phys Express* 1 (3): 034006-1–034006-3. doi: [10.1143/Apex.1.034006](https://doi.org/10.1143/Apex.1.034006)
- Kacar T, Ray J, Gungormus M, Oren EE, Tamerler C, Sarikaya M (2009a) Quartz binding peptides as molecular linkers towards fabricating multifunctional micropatterned substrates. *Adv Mater* 21(3):295–299. doi:[10.1002/Adma01877](https://doi.org/10.1002/Adma01877)
- Kacar T, Zin MT, So C, Wilson B, Ma H, Gul-Karaguler N, Jen AKY, Sarikaya M, Tamerler C (2009b) Directed self-immobilization of alkaline phosphatase on micro-patterned substrates via genetically fused metal-binding peptide. *Biotechnol Bioeng* 103(4):696–705. doi:[10.1002/bit.22282](https://doi.org/10.1002/bit.22282)
- Kasaj A, Willershausen B, Reichert C, Gortan-Kasaj A, Zafiroopoulos GG (2008) Schmidt M (2008) Human periodontal fibroblast response to a nanostructured hydroxyapatite bone replacement graft in vitro. *Arch Oral Biol* 53(7):683–689. doi:[10.1016/J.Archoralbio.01.009](https://doi.org/10.1016/J.Archoralbio.01.009)
- Kim S, Gopalan V, Kitamura K, Furukawa Y (2001) Domain reversal and nonstoichiometry in lithium tantalate. *J Appl Phys* 90(6):2949–2963. doi:[10.1063/1.1389525](https://doi.org/10.1063/1.1389525)
- Krauland EM, Peelle BR, Witttrup KD, Belcher AM (2007) Peptide tags for enhanced cellular and protein adhesion to single-crystal line sapphire. *Biotechnol Bioeng* 97(5):1009–1020. doi:[10.1002/bit.21341](https://doi.org/10.1002/bit.21341)
- Lee JY, Shin HY, Lee JH, Song YS, Kang SW, Park C, Kim JB, Kim SW (2009) A novel enzyme-immobilization method for a biofuel cell. *J Mol Catal B-Enzym* 59(4):274–278. doi:[10.1016/j.molcatb.2008.10.008](https://doi.org/10.1016/j.molcatb.2008.10.008)
- Lee SW, Mao CB, Flynn CE, Belcher AM (2002) Ordering of quantum dots using genetically engineered viruses. *Science* 296(5569):892–895
- Lee SY, Choi JH, Xu ZH (2003) Microbial cell-surface display. *Trends Biotechnol* 21(1):45–52. doi:[10.1016/S0167-7799\(02\)00006-9](https://doi.org/10.1016/S0167-7799(02)00006-9)
- Levy R, Thanh NTK, Doty RC, Hussain I, Nichols RJ, Schiffrin DJ, Brust M, Fernig DG (2004) Rational and combinatorial design of peptide capping ligands for gold nanoparticles. *J Am Chem Soc* 126(32):10076–10084. doi:[10.1021/Ja0487269](https://doi.org/10.1021/Ja0487269)
- Liu TY, Chen SY, Liu DM (2005) Liou SC (2005) On the study of BSA-loaded calcium-deficient hydroxyapatite nano-carriers for controlled drug delivery. *J Control Release* 107(1):112–121. doi:[10.1016/J.Jconrel.05.025](https://doi.org/10.1016/J.Jconrel.05.025)
- Liu X, Kitamura K, Terabe K, Hatano H, Ohashi N (2007) Photocatalytic nanoparticle deposition on LiNbO<sub>3</sub> nanodomain patterns via photovoltaic effect. *Appl Phys Lett* 91(4):3. doi:[10.4401/110.1063/1.2759472](https://doi.org/10.4401/110.1063/1.2759472)
- Liu XY, Ohuchi F, Kitamura K (2008) Patterning of surface electronic properties and selective silver deposition on Linbo<sub>3</sub> template. *Funct Mater Lett* 1(3):177–182. doi:[10.1142/S1793604708000344](https://doi.org/10.1142/S1793604708000344)
- Lobo MJ, Miranda AJ, Tunon P (1997) Amperometric biosensors based on NAD(P)-dependent dehydrogenase enzymes. *Electroanal* 9(3):191–202. doi:[10.1002/Elan.1140090302](https://doi.org/10.1002/Elan.1140090302)

- Lowenstam HA, Weiner S (1989) *On biomineralization*. Oxford University Press, New York
- Lowinsohn D, Bertotti M (2007) Flow injection analysis of blood L-lactate by using a Prussian blue-based biosensor as amperometric detector. *Anal Biochem* 365(2):260–265. doi:[10.1016/J.Ab.2007.03.015](https://doi.org/10.1016/J.Ab.2007.03.015)
- Lu ZJ, Murray KS, Vancleave V, Lavallie ER, Stahl ML, Mccoy JM (1995) Expression of thioredoxin random peptide libraries on the escherichia-coli cell-surface as functional fusions to flagellin—a system designed for exploring protein-protein interactions. *Bio-Technol* 13(4):366–372. doi:[10.1038/Nbt0495-366](https://doi.org/10.1038/Nbt0495-366)
- Ma MY, Zhu YJ, Li L, Cao SW (2008) Nanostructured porous hollow ellipsoidal capsules of hydroxyapatite and calcium silicate: preparation and application in drug delivery. *J Mater Chem* 18(23):2722–2727. doi:[10.1039/B800389k](https://doi.org/10.1039/B800389k)
- Malhotra BD, Chaubey A (2003) Biosensors for clinical diagnostics industry. *Sensor Actuat B-Chem* 91(1–3):117–127. doi:[10.1016/S0925-4005\(03\)00075-3](https://doi.org/10.1016/S0925-4005(03)00075-3)
- Mann S (1996) *Biomimetic materials chemistry*. VCH, New York
- Marzouk SAM, Cosofret VV, Buck RP, Yang H, Cascio WE, Hassan SSM (1997) A conducting salt-based amperometric biosensor for measurement of extracellular lactate accumulation in ischemic myocardium. *Anal Chem* 69(14):2646–2652. doi:[10.1021/AC970020s](https://doi.org/10.1021/AC970020s)
- Matmor M, Ashkenasy N (2012) Modulating semiconductor surface electronic properties by inorganic peptide-binders sequence Design. *J Am Chem Soc* 134(50):20403–20411. doi:[10.1021/ja3078494](https://doi.org/10.1021/ja3078494)
- Meyers MA, Chen PY, Lin AYM (2007) Seki Y (2008) Biological materials: Structure and mechanical properties. *Prog Mater Sci* 53(1):1–206. doi:[10.1016/J.Pmatsci.05.002](https://doi.org/10.1016/J.Pmatsci.05.002)
- Mrksich M, Whitesides GM (1996) Using self-assembled monolayers to understand the interactions of man-made surfaces with proteins and cells. *Annu Rev Bioph Biom* 25:55–78. doi:[10.1146/Annurev.Bb.25.060196.000415](https://doi.org/10.1146/Annurev.Bb.25.060196.000415)
- Myers LE, Miller GD, Eckardt RC, Fejer MM, Byer RL (1995) Quasi-Phase-Matched 1.064- $\mu\text{m}$ -Pumped optical parametric oscillator in bulk periodically poled Linbo3. *Opt Lett* 20(1):52–54
- Naik RR, Stringer SJ, Agarwal G, Jones SE, Stone MO (2002) Biomimetic synthesis and patterning of silver nanoparticles. *Nat Mater* 1(3):169–172. doi:[10.1038/Nmat758](https://doi.org/10.1038/Nmat758)
- Nath N, Chilkoti A (2002) A colorimetric gold nanoparticle sensor to interrogate biomolecular interactions in real time on a surface. *Anal Chem* 74(3):504–509. doi:[10.1021/AC015657x](https://doi.org/10.1021/AC015657x)
- Nath N, Chilkoti A (2004) Label-free biosensing by surface plasmon resonance of nanoparticles on glass: optimization of nanoparticle size. *Anal Chem* 76(18):5370–5378. doi:[10.1021/AC049741z](https://doi.org/10.1021/AC049741z)
- Norde W (1986) Adsorption of proteins from solution at the solid-liquid interface. *Adv Colloid Interfac* 25(4):267–340. doi:[10.1016/0001-8686\(86\)80012-4](https://doi.org/10.1016/0001-8686(86)80012-4)
- Notman R, Oren EE, Tamerler C, Sarikaya M, Samudrala R, Walsh TR (2010) Solution study of engineered quartz binding peptides using replica exchange molecular dynamics. *Biomacromolecules* 11(12):3266–3274. doi:[10.1021/bm100646z](https://doi.org/10.1021/bm100646z)
- Nygaard S, Wendelbo R (2002) Brown S (2002) Surface-specific zeolite-binding proteins. *Adv Mater* 14(24):1853–1856. doi:[10.1002/Adma90019](https://doi.org/10.1002/Adma90019)
- Nykypanchuk D, Maye MM, van der Lelie D, Gang O (2008) DNA-guided crystallization of colloidal nanoparticles. *Nature* 451(7178):549–552. doi:[10.1038/Nature06560](https://doi.org/10.1038/Nature06560)
- Oh SH, Finones RR, Dariaio C, Chen LH, Jin SH (2005) Growth of nano-scale hydroxyapatite using chemically treated titanium oxide nanotubes. *Biomaterials* 26(24):4938–4943. doi:[10.1016/J.Biomaterials.01.048](https://doi.org/10.1016/J.Biomaterials.01.048)
- Odenburg SJ, Averitt RD, Westcott SL, Halas NJ (1998) Nanoengineering of optical resonances. *Chem Phys Lett* 288(2–4):243–247. doi:[10.1016/S0009-2614\(98\)00277-2](https://doi.org/10.1016/S0009-2614(98)00277-2)
- Oren EE, Notman R, Kim IW, Evans JS, Walsh TR, Samudrala R, Tamerler C, Sarikaya M (2010) Probing the molecular mechanisms of quartz-binding peptides. *Langmuir* 26(13):11003–11009. doi:[10.1021/la100049s](https://doi.org/10.1021/la100049s)

- Oren EE, Tamerler C, Sahin D, Hnilova M, Seker UOS, Sarikaya M, Samudrala R (2007) A novel knowledge-based approach to design inorganic-binding peptides. *Bioinformatics* 23(21):2816–2822. doi:[10.1093/bioinformatics/btm436](https://doi.org/10.1093/bioinformatics/btm436)
- Ostuni E, Yan L, Whitesides GM (1999) The interaction of proteins and cells with self-assembled monolayers of alkanethiolates on gold and silver. *Colloid Surface B* 15(1):3–30. doi:[10.1016/S0927-7765\(99\)00004-1](https://doi.org/10.1016/S0927-7765(99)00004-1)
- Paine ML, Snead ML (1997) Protein interactions during assembly of the enamel organic extracellular matrix. *J Bone Miner Res* 12(2):221–227. doi:[10.1359/Jbmr.12.2.221](https://doi.org/10.1359/Jbmr.12.2.221)
- Palleschi G, Volpe G, Compagnone D, Lanotte E, Esti M (1994) Bioelectrochemical determination of lactic and malic-acids in wine. *Talanta* 41(6):917–923. doi:[10.1016/0039-9140\(94\)e0044-r](https://doi.org/10.1016/0039-9140(94)e0044-r)
- Palmisano F, Rizzi R, Centonze D, Zambonin PG (2000) Simultaneous monitoring of glucose and lactate by an interference and cross-talk free dual electrode amperometric biosensor based on electropolymerized thin films. *Biosens Bioelectron* 15(9–10):531–539. doi:[10.1016/S0956-5663\(00\)00107-X](https://doi.org/10.1016/S0956-5663(00)00107-X)
- Park MH, Ofir Y, Samanta B, Arumugam P, Miranda OR, Rotello VM (2008a) Nanoparticle immobilization on surfaces via activatable heterobifunctional dithiocarbamate bond formation. *Adv Mater* 20 (21):4185–4188. doi: [10.1002/Adma.200801155](https://doi.org/10.1002/Adma.200801155)
- Park SY, Lytton-Jean AKR, Lee B, Weigand S, Schatz GC, Mirkin CA (2008b) DNA-programmable nanoparticle crystallization. *Nature* 451(7178):553–556. doi:[10.1038/Nature06508](https://doi.org/10.1038/Nature06508)
- Park TJ, Lee SY, Lee SJ, Park JP, Yang KS, Lee KB, Ko S, Park JB, Kim T, Kim SK, Shin YB, Chung BH, Ku SJ, Kim DH, Choi IS (2006) Protein nanopatterns and biosensors using gold binding polypeptide as a fusion partner. *Anal Chem* 78(20):7197–7205. doi:[10.1021/Ac060976f](https://doi.org/10.1021/Ac060976f)
- Parra A, Casero E, Vazquez L, Pariente F, Lorenzo E (2006) Design and characterization of a lactate biosensor based on immobilized lactate oxidase onto gold surfaces. *Anal Chim Acta* 555 (2):308–315. doi: [10.1016/J.Aca.2005.09.025](https://doi.org/10.1016/J.Aca.2005.09.025)
- Prodan E, Nordlander P, Halas NJ (2003) Effects of dielectric screening on the optical properties of metallic nanoshells. *Chem Phys Lett* 368 (1-2):94–101. [Pii] S0009-2614(02)01828-6. doi:[10.1016/S0009-2614\(02\)01828-6](https://doi.org/10.1016/S0009-2614(02)01828-6)
- Puddu V, Slocik JM, Naik RR, Perry CC (2013) Titania binding peptides as templates in the biomimetic synthesis of stable titania nanosols: insight into the role of buffers in peptide-mediated mineralization. *Langmuir* 29(30):9464–9472. doi:[10.1021/la401777x](https://doi.org/10.1021/la401777x)
- Rasmussen BA, Bush K, Tally FP (1993) Antimicrobial resistance in bacterioides. *Clin Infect Dis* 16:S390–S400
- Rothenstein D, Claasen B, Omiecienski B, Lammel P, Bill J (2012) Isolation of ZnO-Binding 12-mer peptides and determination of their binding epitopes by nmr spectroscopy. *J Am Chem Soc* 134(30):12547–12556. doi:[10.1021/ja302211w](https://doi.org/10.1021/ja302211w)
- Rusmini F, Zhong Z, Feijen J (2007) Protein immobilization strategies for protein biochips. *Biomacromolecules* 8(6):1775–1789. doi:[10.1021/bm061197b](https://doi.org/10.1021/bm061197b)
- Sanchez C, Arribart H, Guille MMG (2005) Biomimetism and bioinspiration as tools for the design of innovative materials and systems. *Nat Mater* 4(4):277–288. doi:[10.1038/Nmat1339](https://doi.org/10.1038/Nmat1339)
- Sano KI, Sasaki H, Shiba K (2005) Specificity and biomineralization activities of Ti-binding peptide-1 (TBP-1). *Langmuir* 21(7):3090–3095. doi:[10.1021/La047428m](https://doi.org/10.1021/La047428m)
- Sarikaya M (1994) An introduction to biomimetics— a structural viewpoint. *Microsc Res Techniq* 27 (5):360–375. doi: [10.1002/Jemt.1070270503](https://doi.org/10.1002/Jemt.1070270503)
- Sarikaya M (1999) Biomimetics: materials fabrication through biology. *P Natl Acad Sci USA* 96(25):14183–14185. doi:[10.1073/Pnas.96.25.14183](https://doi.org/10.1073/Pnas.96.25.14183)
- Sarikaya M, Aksay IA (1995) *Biomimetics: design and processing of materials*. IP Press, Woodbury
- Sarikaya M, Tamerler C, Jen AKY, Schulten K, Baneyx F (2003) Molecular biomimetics: nanotechnology through biology. *Nat Mater* 2(9):577–585. doi:[10.1038/Nmat964](https://doi.org/10.1038/Nmat964)



- Sarikaya M, Tamerler C, Schwartz DT, Baneyx FO (2004) Materials assembly and formation using engineered polypeptides. *Annu Rev Mater Res* 34:373–408. doi:[10.1146/Annurev.Matsci.34.040203.121025](https://doi.org/10.1146/Annurev.Matsci.34.040203.121025)
- Schultzelam S, Harauz G, Beveridge TJ (1992) Participation of a cyanobacterial S layer in fine-grain mineral formation. *J Bacteriol* 174(24):7971–7981
- Sedlak RH, Hnilova M, Gachelet E, Przybyla L, Dranow D, Gonen T, Sarikaya M, Tamerler C, Traxler B (2010) An engineered DNA-binding protein self-assembles metallic nanostructures. *ChemBioChem* 11(15):2108–2112. doi:[10.1002/Cbic00407](https://doi.org/10.1002/Cbic00407)
- Sedlak RH, Hnilova M, Grosh C, Fong H, Baneyx F, Schwartz D, Sarikaya M, Tamerler C, Traxler B (2012) Engineered escherichia coli silver-binding periplasmic protein that promotes silver tolerance. *Appl Environ Microbiol* 78(7):2289–2296. doi:[10.1128/aem.06823-11](https://doi.org/10.1128/aem.06823-11)
- Seeman NC, Belcher AM (2002) Emulating biology: building nanostructures from the bottom up. *P Natl Acad Sci USA* 99:6451–6455. doi:[10.1073/Pnas.221458298](https://doi.org/10.1073/Pnas.221458298)
- Seker UOS, Wilson B, Dincer S, Kim IW, Oren EE, Evans JS, Tamerler C, Sarikaya M (2007) Adsorption behavior of linear and cyclic genetically engineered platinum binding peptides. *Langmuir* 23(15):7895–7900. doi:[10.1021/la700446g](https://doi.org/10.1021/la700446g)
- Sengupta A, Thai CK, Sastry MSR, Matthaei JF, Schwartz DT, Davis EJ, Baneyx F (2008) A genetic approach for controlling the binding and orientation of proteins on nanoparticles. *Langmuir* 24(5):2000–2008. doi:[10.1021/La702079e](https://doi.org/10.1021/La702079e)
- Sheldon RA (2007) Cross-linked enzyme aggregates (CLEA (R) s): stable and recyclable biocatalysts. *Biochem Soc T* 35:1583–1587. doi:[10.1042/Bst0351583](https://doi.org/10.1042/Bst0351583)
- Slocik JM, Naik RR (2006) Biologically programmed synthesis of bimetallic nanostructures. *Adv Mater* 18 (15):1988-1992. doi: [10.1002/Adma.200600327](https://doi.org/10.1002/Adma.200600327)
- Slocik JM, Naik RR, Stone MO, Wright DW (2005a) Viral templates for gold nanoparticle synthesis. *J Mater Chem* 15(7):749–753. doi:[10.1039/B413074j](https://doi.org/10.1039/B413074j)
- Slocik JM, Stone MO, Naik RR (2005b) Synthesis of gold nanoparticles using multifunctional peptides. *Small* 1(11):1048–1052. doi:[10.1002/Sml100172](https://doi.org/10.1002/Sml100172)
- Smith GP (1985) Filamentous fusion phage—novel expression vectors that display cloned antigens on the virion surface. *Science* 228(4705):1315–1317. doi:[10.1126/Science.4001944](https://doi.org/10.1126/Science.4001944)
- Smith GP, Petrenko VA (1997) Phage display. *Chem Rev* 97(2):391–410. doi:[10.1021/Cr960065d](https://doi.org/10.1021/Cr960065d)
- So CR, Hayamizu Y, Yazici H, Gresswell C, Khatayevich D, Tamerler C, Sarikaya M (2012) Controlling self-assembly of engineered peptides on graphite by rational mutation. *ACS Nano* 6(2):1648–1656. doi:[10.1021/nn204631x](https://doi.org/10.1021/nn204631x)
- So CR, Kulp JL, Oren EE, Zareie H, Tamerler C, Evans JS, Sarikaya M (2009) Molecular recognition and supramolecular self-assembly of a genetically engineered gold binding peptide on Au{111}. *ACS Nano* 3(6):1525–1531. doi:[10.1021/Nn900171s](https://doi.org/10.1021/Nn900171s)
- Suman S, Singhal R, Sharma AL, Malthotra BD, Pundir CS (2005) Development of a lactate biosensor based on conducting copolymer bound lactate oxidase. *Sensor Actuat B-Chem* 107(2):768–772. doi:[10.1016/J.Snb.12.016](https://doi.org/10.1016/J.Snb.12.016)
- Tamerler C, Duman M, Oren EE, Gungormus M, Xiong XR, Kacar T, Parviz BA, Sarikaya M (2006a) Materials specificity and directed assembly of a gold-binding peptide. *Small* 2(11):1372–1378. doi:[10.1002/Sml100070](https://doi.org/10.1002/Sml100070)
- Tamerler C, Khatayevich D, Gungormus M, Kacar T, Oren EE, Hnilova M, Sarikaya M (2010) Molecular biomimetics: gepi-based biological routes to technology. *Biopolymers* 94(1): 78–94. doi:[10.1002/Bip.21368](https://doi.org/10.1002/Bip.21368)
- Tamerler C, Oren EE, Duman M, Venkatasubramanian E, Sarikaya M (2006b) Adsorption kinetics of an engineered gold binding peptide by surface plasmon resonance spectroscopy and a quartz crystal microbalance. *Langmuir* 22(18):7712–7718. doi:[10.1021/La0606897](https://doi.org/10.1021/La0606897)
- Tamerler C, Sarikaya M (2007a) Molecular biomimetics: utilizing nature's molecular ways in practical engineering. Elsevier, Canberra, pp 289–299. doi:[10.1016/j.actbio.2006.10.009](https://doi.org/10.1016/j.actbio.2006.10.009)
- Tamerler C Sarikaya M (2007b) Molecular biomimetics: utilizing nature's molecular ways in practical engineering. *Acta Biomater* 3(3):289–299. doi:[10.1016/J.Actbio.10.009](https://doi.org/10.1016/J.Actbio.10.009)

- Tamerler C, Sarikaya M (2008) Molecular biomimetics: genetic synthesis, assembly, and formation of materials using peptides. *MRS Bull* 33(5):504–510. doi:[10.1557/Mrs2008.102](https://doi.org/10.1557/Mrs2008.102)
- Tamerler C, Sarikaya M (2009) Molecular biomimetics: nanotechnology and bionanotechnology using genetically engineered peptides. *Philos T R Soc A* 367(1894):1705–1726. doi:[10.1098/Rsta.0018](https://doi.org/10.1098/Rsta.0018)
- Tan K, Cheang P, Ho IAW, Lam PYP, Hui KM (2007) Nanosized bioceramic particles could function as efficient gene delivery vehicles with target specificity for the spleen. *Gene Ther* 14(10):828–835. doi:[10.1038/Sj.Gt.3302937](https://doi.org/10.1038/Sj.Gt.3302937)
- Tao K, Wang JQ, Li YP, Xia DH, Shan HH, Xu H, Lu JR (2013) Short peptide-directed synthesis of one-dimensional platinum nanostructures with controllable morphologies. *Scientific Reports* 3. doi:[256510.1038/srep02565](https://doi.org/10.1038/srep02565)
- Thai CK, Dai HX, Sastry MSR, Sarikaya M, Schwartz DT, Baneyx F (2004) Identification and characterization of Cu<sub>2</sub>O- and ZnO-binding polypeptides by escherichia coli cell surface display: toward an understanding of metal oxide binding. *Biotechnol Bioeng* 87(2):129–137. doi:[10.1002/Bit9](https://doi.org/10.1002/Bit9)
- Thompson DAW (1917) *On growth and form*. Cambridge University Press, Cambridge
- Tirrell D (1994) *Hierarchical structures in biology as a guide for new materials technology*. Nmab, vol 464. National Academy Press, Washington
- Vincent JFV (1990) *Structural biomaterials*, Rev edn. Princeton University Press, Princeton
- Wainwright SA (1976) *Mechanical design in organisms*. Edward Arnold, London
- Wang Y, Tang ZY, Correa-Duarte MA, Liz-Marzan LM, Kotov NA (2003) Multicolor luminescence patterning by photoactivation of semiconductor nanoparticle films. *J Am Chem Soc* 125(10):2830–2831. doi:[10.1021/Ja029231r](https://doi.org/10.1021/Ja029231r)
- Wang Z, Levy R, Fernig DG, Brust M (2005) The peptide route to multifunctional gold nanoparticles. *Bioconjugate Chem* 16(3):497–500. doi:[10.1021/Bc0500471](https://doi.org/10.1021/Bc0500471)
- Westcott SL, Oldenburg SJ, Lee TR, Halas NJ (1998) Formation and adsorption of clusters of gold nanoparticles onto functionalized silica nanoparticle surfaces. *Langmuir* 14(19):5396–5401. doi:[10.1021/La980380q](https://doi.org/10.1021/La980380q)
- Weinstein RS, Roberson PK, Manolagas SC (2009) Giant osteoclast formation and long-term oral bisphosphonate therapy. *N Engl J Med* 360(1):53–62
- Whaley SR, English DS, Hu EL, Barbara PF, Belcher AM (2000) Selection of peptides with semiconductor binding specificity for directed nanocrystal assembly. *Nature* 405(6787):665–668
- Willetts KA, Van Duyne RP (2007) Localized surface plasmon resonance spectroscopy and sensing. *Annu Rev Phys Chem* 58:267–297. doi:[10.1146/Annurev.Physchem.58.032806.104607](https://doi.org/10.1146/Annurev.Physchem.58.032806.104607)
- Willey TM, Vance AL, van Buuren T, Bostedt C, Terminello LJ, Fadley CS (2005) Rapid degradation of alkanethiol-based self-assembled monolayers on gold in ambient laboratory conditions. *Surf Sci* 576(1–3):188–196. doi:[10.1016/J.Susc.12.022](https://doi.org/10.1016/J.Susc.12.022)
- Willner I (2002) Biomaterials for sensors, fuel cells, and circuitry. *Science* 298(5602):2407–2408. doi:[10.1126/Science.298.5602.2407](https://doi.org/10.1126/Science.298.5602.2407)
- Woodbury RG, Wendin C, Clendenning J, Melendez J, Elkind J, Bartholomew D, Brown S, Furlong CE (1998) Construction of biosensors using a gold-binding polypeptide and a miniature integrated surface plasmon resonance sensor. *Biosens Bioelectron* 13(10):1117–1126. doi:[10.1016/S0956-5663\(98\)00060-8](https://doi.org/10.1016/S0956-5663(98)00060-8)
- Xu H, Hong R, Wang XY, Arvizo R, You CC, Samanta B, Patra D, Tuominen MT, Rotello VM (2007) Controlled formation of patterned gold films via site-selective deposition of nanoparticles onto polymer-templated surfaces. *Adv Mater* 19(10):1383–1386. doi:[10.1002/Adma.200700124](https://doi.org/10.1002/Adma.200700124)
- Yang X, Kang CM, Brody M, Price CW (1996) Opposing pairs of serine protein kinases and phosphatases transmit signals of environmental stress to activate a bacterial transcription factor. *Genes Dev* 10(18):2265–2275

- Yazici H, Fong H, Wilson B, Oren EE, Amos FA, Zhang H, Evans JS, Snead ML, Sarikaya M, Tamerler C (2013) Biological response on a titanium implant-grade surface functionalized with modular peptides. *Acta Biomater* 9(2):5341–5352. doi:[10.1016/j.actbio.2012.11.004](https://doi.org/10.1016/j.actbio.2012.11.004)
- Yuca E, Karatas AY, Seker UOS, Gungormus M, Dinler-Doganay G, Sarikaya M, Tamerler C (2011) In vitro labeling of hydroxyapatite minerals by an engineered protein. *Biotechnol Bioeng* 108(5):1021–1030. doi:[10.1002/Bit.23041](https://doi.org/10.1002/Bit.23041)
- Zayats M, Willner B, Willner (2008) Design of amperometric biosensors and biofuel cells by the reconstitution of electrically contacted enzyme electrodes. *Electroanal* 20(6):583–601. doi:[10.1002/Elan04128](https://doi.org/10.1002/Elan04128)
- Zhen GL, Falconnet D, Kuennemann E, Voros J, Spencer ND, Textor M, Zurcher S (2006) Nitrilotriacetic acid functionalized graft copolymers: a polymeric interface for selective and reversible binding of histidine-tagged proteins. *Adv Funct Mater* 16(2):243–251. doi:[10.1002/Adfm00232](https://doi.org/10.1002/Adfm00232)
- Zhou W, Schwartz DT, Baneyx F (2010) Single-Pot biofabrication of zinc sulfide immuno-quantum dots. *J Am Chem Soc* 132(13):4731–4738. doi:[10.1021/ja909406n](https://doi.org/10.1021/ja909406n)
- Zimmer M (2002) Green fluorescent protein (GFP): Applications, structure and related photophysical behavior. *Chem Rev* 102(3):759–781. doi: [10.1021/cr010142r](https://doi.org/10.1021/cr010142r)
- Zin MT, Ma H, Sarikaya M, Jen AKY (2005) Assembly of gold nanoparticles using genetically engineered polypeptides. *Small* 1 (7):698–702. doi: [10.1002/Sml.200400164](https://doi.org/10.1002/Sml.200400164)
- Zin MT, Munro AM, Gungormus M, Wong NY, Ma H, Tamerler C, Ginger DS, Sarikaya M, Jen AKY (2007) Peptide-mediated surface-immobilized quantum dot hybrid nanoassemblies with controlled photoluminescence. *J Mater Chem* 17(9):866–872. doi:[10.1039/B615010a](https://doi.org/10.1039/B615010a)

# Chapter 9

## Environmental Interactions of Geo- and Bio-Macromolecules with Nanomaterials

Navid B. Saleh, Jamie R. Lead, Nirupam Aich, Dipesh Das  
and Iftheker A. Khan

**Abstract** Engineered nanomaterials (ENMs) are mostly synthesized with modified surfaces using various surfactants, polymeric, or biomolecule coatings to achieve desired functionality. When exposed to the environment, coatings on the ENMs will undergo the first set of interactions with natural geo- and bio-macromolecules pre-existing in aqueous and/or soil matrices. Such interfacial interaction will likely alter the conformation and extent of coverage of the synthetic ENM surface coatings via exchange, displacement, and/or overcoating by environmental macromolecules. The exchange kinetics and extent of replacement of the synthetic coatings will profoundly impact environmental fate, transport, transformation, and toxicity of the ENMs. This chapter discusses the state-of-the-art literature to identify key synthetic coating types, their interaction with the environmental and biological macromolecules, and illustrate the existing challenges to determine coating exchange kinetics and its environmental implications on ENMs.

---

Preparation for Submission to *Bioinspired Nanotechnology-From Surface Analysis to Applications*(August 30, 2013)

---

N. B. Saleh (✉) · I. A. Khan  
Civil, Architectural, and Environmental Engineering, Cockrell School of Engineering,  
The University of Texas at Austin, Austin, TX 78712-0273, USA  
e-mail: navid.saleh@utexas.edu

J. R. Lead  
Center for Environmental Nanoscience and Risk, Department of Environmental  
Health Sciences, Arnold School of Public Health, University of South Carolina,  
Columbia, SC 29208, USA

N. Aich · D. Das  
Nirupam Aich Civil, Architectural, and Environmental Engineering,  
Cockrell School of Engineering, The University of Texas at Austin,  
Austin, TX 78712-0273, USA

Department of Chemical Engineering, University of Rhode Island,  
Kingston, RI 02881, USA

## 9.1 Introduction

Nanotechnology is an emerging field of science and engineering, which enhances material properties by manipulation at the molecular scale. Incorporation of nanomaterials (NMs) enhances electrical, optical, mechanical, magnetic, reactive, and catalytic properties of products and devices in applications such as: optoelectronics (Avouris et al. 2008; Eda and Chhowalla 2010), photovoltaics (Gratzel 2001), solar cells (Gratzel 2003; Nozik 2002; Thompson and Frechet 2008), energy devices (Arico et al. 2005; Baughman et al. 2002), semiconductor industry (Allen et al. 2007; Burghard et al. 2009; Schwierz 2010), medical imaging (Bulte and Kraitchman 2004; Michalet et al. 2005), biomedical engineering (Gupta and Gupta 2005; Huang et al. 2009; Bianco et al. 2005), drug design and delivery (Bianco et al. 2005; Cho et al. 2008), personal care products (Aitken et al. 2006; Kokura et al. 2010), environmental pollution monitoring and management (Mauter and Elimelech 2008), sensing (Murphy et al. 2008; Pumera et al. 2010), etc. However, incorporation of NMs into such applications usually requires surface modifications with organic or inorganic chemical moieties that not only improve dispersibility but also enhance functionality within the products or devices (Gupta et al. 2007; Grubbs 2007). Such surface functionalities influence NM fate, transport, transformation, and biological interaction when released to the environment (Diegoli et al. 2008; Fabrega et al. 2009; Kim et al. 2013; Tejamaya et al. 2012). Thus fundamental understanding of the surface-coating properties and their interaction with the environmental matrices are key to accurately assess NM exposure and risk (Lowry et al. 2012).

The dispersibility required is often achieved by coating NM surfaces with synthetic surfactants (Bertrand et al. 2013; Matarredona et al. 2003), polymers (Saleh et al. 2005; Phenrat et al. 2008; Vaisman et al. 2006), and biological molecules (Zheng et al. 2003; Karajanagi et al. 2006). Moreover, specific functionality of NMs in medical devices and applications necessitates attachment of biological molecules, such as antibodies (Kim et al. 2008; Lee et al. 2002; McDevitt et al. 2007), DNA/RNA molecules (Kohli et al. 2004; Lee et al. 2007), proteins (Hernandez et al. 2004; Li et al. 2013; Bhattacharyya et al. 2005; Kurppa et al. 2007; Burt et al. 2004), enzymes (Besteman et al. 2003; Willner et al. 2007; Baron et al. 2007), and aptamers (So et al. 2005). Once in the environment, such coatings serve as the external surfaces to surrounding environment; hence their nature and interaction with environmental macromolecules are key to their behavior. Understanding NM interactions in environmental and biological systems demands thorough evaluation of the roles of surface coatings on their fate, transport, and toxicity (Lowry et al. 2012). A vast body of literature exists that studies coating morphology, layer properties, and their interaction in environmental and biological systems (Suresh et al. 2013; Lynch and Dawson 2008). Theoretical predictions of layer properties as well as their roles in aggregation,

deposition, and toxicity have been well studied as well. Experimental literatures have contributed in stability (Diegoli et al. 2008; Pallem et al. 2009; Gondikas et al. 2012) and toxicity (Kim et al. 2013) literature of coated NMs and have established a good, though incomplete, understanding of their interaction in natural and biological systems. However, given the complexity of manufactured nano- and environmental-systems, many uncertainties persist, which lead to greater unpredictability in environmental exposure and risk assessment.

Wide arrays of geo- and bio-macromolecules are present in most environmental and biological systems. Geomacromolecules include fulvic acids, humic acids with a range of chemical structure and hydrophobicity, polysaccharides, cellulosic materials, etc. (Ghabbour and Davies 2001) Due to their ubiquity and refractory nature, humic substances and polysaccharides are perhaps the most importance to NM behavior (Buffle et al. 1998). Biologically relevant macromolecules on the other hand include proteins, enzymes, lipids, peptides, etc. These complex macromolecules possess varied chemical structures and are present in a range of concentrations (Ghabbour and Davies 2001).

The recent literature has realized such complexities and directed research toward transformation processes of NMs (Lowry et al. 2012), although our understanding is at an early stage. During these processes, the mechanisms by which geo- and bio-macromolecules interact with the pristine and coated NM surfaces are mostly unknown. The following questions become critical to better address understanding of NM fate, transport, and toxicity in presence of these macromolecules: do the preexisting coatings on NM surfaces desorb during transformation? How do the geo- and bio-macromolecules interact with pristine versus coated NMs? Are there exchanges that take place between coatings and environmental macromolecules? What are the rates of exchange kinetics, layer conformation, soft layer composition, and resulting interaction due to such transformations? Does coexistence of multiple geo- and biomacromolecular species alter the exchange and soft layer behavior significantly? Addressing such questions will likely enhance understanding of essential soft layer (i.e., surface coating) interaction in environmental and biological systems.

This book chapter aims to identify potential interaction of geo- and bio-macromolecules with pristine and coated NM surfaces. The chapter is structured as follows. First, the common NM coatings are highlighted to better conceive their chemical nature. The following section reviews and identifies major macromolecules of geologic and biological origin and discusses their key physicochemical properties. The following section critically analyzes potential interaction of NMs during three stages of environmental interaction; i.e., fate and transport, transformation, and toxicity. The chapter ends with a discussion on environmental interaction of NMs in the presence of the macromolecules and identifies key research needs to address these issues.

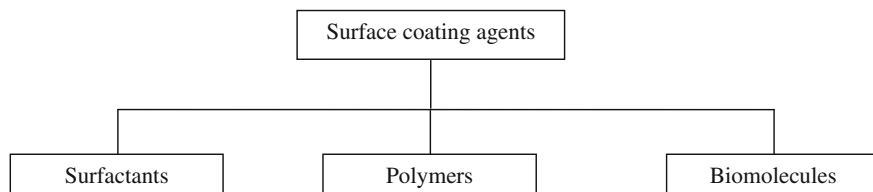


**Fig. 9.1** Classification of surface coating agents

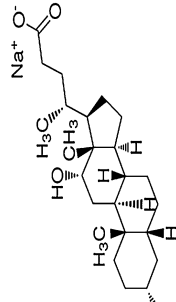
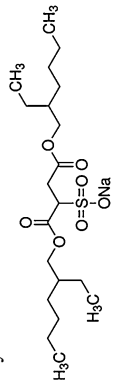
## 9.2 NM Surface Coatings

Modifying surfaces via surface engineering adds to the functionality of NMs, which maintains colloidal stability (Buffle et al. 1998). Surfactants, synthetic polymers, and biomolecules are commonly used to coat NMs (Fig. 9.1, Sperling and Parak 1915). Understanding surface coating properties is key to evaluate environmental processes of NMs (Lu et al. 2010). This section will discuss commonly used surface coatings for precoating NMs.

### 9.2.1 Surfactants

Surfactants are relatively smaller molecules with a hydrophobic nonpolar tail group and hydrophilic-charged head group. The charged group may possess positive or negative charge or may be uncharged. The common surfactants used as NM coatings typically possess an alkyl chain attached to single or multiple aromatic, cellulosic, or smaller ketone groups (Table 9.1). Surfactants are typically categorized based on their overall charge that include: anionic, cationic, zwitterionic, and nonionic surfactants. These are usually physisorbed onto NM surfaces via strong electrostatic (Zhao et al. 2008) or weak, nonspecific, short-ranged hydrophobic interactions (Islam et al. 2003). Typically, the physisorption takes place in the presence of a large concentration of surfactant molecules that directs ligand binding toward NM surfaces in quest of overall energy minimization (Usrey and Strano 2009). Mode of attachment depends on surfactant structure as well as inherent NM properties. The portion of the surfactants not attached to the NMs interacts with the surrounding matrices first and thus is key in controlling NM environmental interaction. Depending on the application and NM of concern, a choice of surfactants is made. For example, gold NMs can be used with anionic surfactants such as SDS (Mafuné et al. 2001), citrate (Brewer et al. 2005) as well as with cationic surfactants as CTAB (Sau and Murphy 2005). All these surfactants are used mainly for stabilization and size controlling purposes.

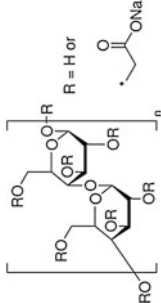
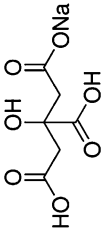
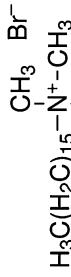
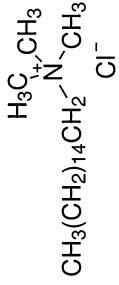

**Table 9.1** Example of surfactants used as NM coatings and their molecular structures

Commercial name	Category	Chemical name and structure	Coated nanomaterials	Reference
SDS	Anionic	Sodium dodecyl sulfate $\text{CH}_3(\text{CH}_2)_{10}\text{CH}_2\text{O}-\overset{\text{O}}{\parallel}{\text{S}}-\text{ONa}$	Ag Au Silica CNT TiO <sub>2</sub> fullerene	(Mafune et al. 2000) (Mafuné et al. 2001) (Kumar et al. 2012) (Vaisman et al. 2006) (Manzoori et al. 2009) (Moliner-Martínez et al. 2009)
SDBS	Anionic	Sodium dodecylbenzenesulfonate $\text{CH}_3(\text{CH}_2)_{10}\text{CH}_2-\text{C}_6\text{H}_4-\overset{\text{O}}{\parallel}{\text{S}}-\text{ONa}$	Ag, Au Fullerene	(Ma et al. 2004) (Todorović Marković et al. 2009)
SDOCO	Anionic	Sodium deoxycholate 	CNT sulfur Silicon nanocrystal	(Ju et al. 2012) (Chaudhuri and Paria 2011) (Froner et al. 2011)
AOT/DSS	Anionic	Dioctyl sodium sulfosuccinate 	Co CdS-Ag <sub>2</sub> S	(Behrens et al. 2006) (Hota et al. 2004)

(continued)

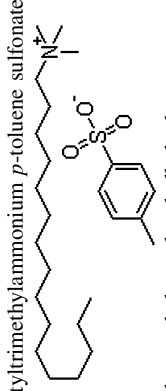
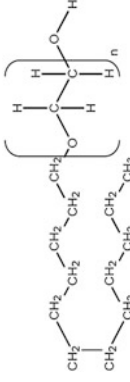
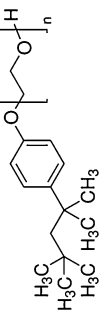
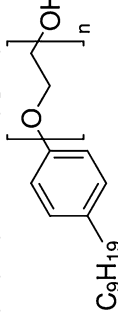


Table 9.1 (continued)

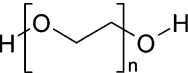
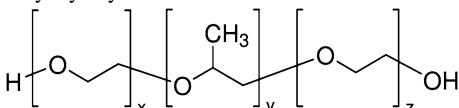
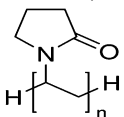
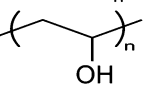
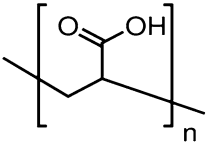
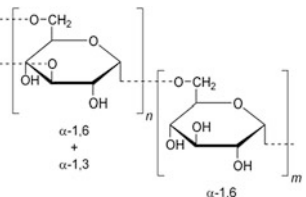
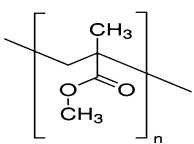
Commercial name	Category	Chemical name and structure	Coated nanomaterials	Reference
NaCMC	Anionic	<p>sodium carboxymethylcellulose</p> 	NZVI TiO <sub>2</sub>	(Phenrat et al. 2009) (Joo et al. 2009)
Citrate	Anionic	<p>Sodium citrate</p> 	Au Fe <sub>3</sub> O <sub>4</sub> Ag TiO <sub>2</sub>	(Brewer et al. 2005) (Da Silva et al. 2003) (Zhang et al. 2011) (Mudunkotuwa and Grassian 2010)
CTAB	Cationic	<p>Cetyltrimethylammonium bromide</p> 	ZnO Au Fe <sub>2</sub> O <sub>3</sub> Sulfur CNT CdS	(Tian et al. 2003) (Sau and Murphy 2005) (Liu et al. 1999) (Chaudhuri and Paria 2011) (Vaisman et al. 2006) (Tian and Fendler 1996)
CTAC	Cationic	<p>Cetyltrimethylammonium chloride</p> 		
CPyC	Cationic	<p>Cetyltrimethylpyridinium chloride</p> 	ZnS	(Mehta et al. 2009)

(continued)

Table 9.1 (continued)

Commercial name	Category	Chemical name and structure	Coated nanomaterials	Reference
TTAB	Cationic	tetradecyltrimethylammonium bromide $\text{CH}_3(\text{CH}_2)_{12}\text{CH}_2-\overset{\text{CH}_3}{\underset{\text{CH}_3}{\text{N}^+}}-\text{Br}^-$	Pt	(Aliaga et al. 2009)
CTAPTS	Zwitterionic	cetyltrimethylammonium <i>p</i> -toluene sulfonate 	Cu	(Salkar et al. 2000)
Brij	Nonionic	Polyoxyethylene glycol alkyl ether 	TiO <sub>2</sub>	(Sofís et al. 2008)
Triton™ X-100	Nonionic	Polyethylene glycol <i>tert</i> -octylphenyl ether 	Sulfur	(Chaudhuri and Paria 2011)
IGEPAL® CO-520	Nonionic	Polyoxyethylene (5) nonylphenylether 	ZnO-SiO <sub>2</sub>	(Bae et al. 2006)

**Table 9.2** Examples of polymers used as NM coating and their molecular structures

Commercial name	Chemical name and structure	Coated nanomaterials
PEG	Polyethylene glycol 	Au, Gd,
Pluronic	Polyoxyethylene-polyoxypropylene-Polyoxyethylene 	Fullerene, CNT, Au, Fe <sub>3</sub> O <sub>4</sub>
PVP	Polyvinylpyrrolidone 	Ag, Fe <sub>3</sub> O <sub>4</sub> , Pt
PVA	Polyvinyl alcohol 	Fe <sub>3</sub> O <sub>4</sub> , Au, Ag
PAA	Polyacrylic acid 	Au
Dextran		CNT, Fe <sub>2</sub> O <sub>3</sub> , Fe <sub>3</sub> O <sub>4</sub> , Au, Ag, Nanoceria
PMMA	Poly(methyl methacrylate) 	Au, Silica, Ag, CNT, nanoferrites

### 9.2.2 Polymers

Larger molecules synthesized by repeating smaller monomer units are known as polymers. Single or multiple monomer units are repeated to form a single polymer chain. Common polymers used to functionalize NMs can be categorized as polyelectrolytes, nonionic polymers, and block copolymers. Block copolymers also can have variations in positioning of the different chemical blocks along the backbone of the polymers. Commonly used polymers to coat NMs include alkanes and aromatic chains with alcohol, ketones, or cellulosic groups (Table 9.2), giving

a very large group of chemical moieties available to functionalize. Polymers with a wide range of molecular weight or size may also be used that can also alter NM properties and surface layer thicknesses.

Polymers can provide both electrostatic and steric interaction to stabilize NMs. These polymer-stabilized NMs can be used for different functions. As examples: PEG-coated AuNMs can be used as a contrast agent for in vivo X-ray computed tomography imaging (Kim et al. 2007), while PMPC and PDMA are used as AuNM stabilizers to produce highly biocompatible gold sols for biomedical application. The key functions extracted from these polymer layers include: steric stabilization (Lourenco et al. 1996), pH-responsive polymeric layers (Li et al. 2007), electrostatic (Veisoh et al. 2010), or functional-group-specific interaction (Breunig et al. 2008) for targeting, mobility, etc. Block copolymers can be tailored to obtain desired properties along the backbone of the polymers that can result in novel controllable NM properties (Saleh et al. 2005; Aich et al. 2013).

### 9.2.3 Biomolecules

Biomolecules used as coating agents include: nucleic acids (i.e., DNA/RNA/PNA/LNA as genes, oligomers, aptamers, ribozymes/DNAzymes), fatty acids, lipids, carbohydrates, all kinds of proteins, peptides, etc. (Sapsford et al. 2013). Some of these molecules may be functionally active, offering binding, catalytic, or therapeutic functionalities; while some of the other ones can serve as inert coatings on the NMs. These coatings may introduce biocompatibility to NMs. For example, placement and ordering of the coated NMs can be controlled in the biological media for targeted drug delivery. However, all these behaviors depend on the properties of both the biological molecule and the nanomaterial. The following Table 9.3, gives some examples of the biological molecules used as coating agents for nanomaterials.

Importantly, there is an increasing move toward multifunctionality and combined use of different types of coatings on the same NM surface. For instance, combined use of aptamers and polymers, such as PEG, offers decreased clearance from the body as well as site specific cellular recognition for drug delivery (Guo et al. 2011). Similarly, NMs with multicoatings are used to generate hierarchical nanohybrids; e.g., polymer-modified carbon nanotubes or graphene are conjugated with coated Ag nanoparticles (Pei et al. 2007; Zhang et al. 2013) to be used in antibacterial applications.

## 9.3 Geo- and Bio-Macromolecules

Geo- and bio-macromolecules play an important role in environmental and biological systems, as discussed below. In addition, NM suspensions are often prepared with geo- and bio-macromolecules to either invoke chemical functionality or

**Table 9.3** Example of biomolecules used as NM coating and relevant applications

Biological molecule	Coated nanomaterial	Application
Proteins	Au	Energy harvesting
	Pd	Biocatalysis
	Fe <sub>2</sub> O <sub>3</sub>	MRI imaging
	Semiconductor quantum dots (QD)	Pprobes
	NiO	Biocatalysis
Enzymes	CNT	Drug delivery
	Au	Bioelectronics
	Pt	Biosensing
	CNT	Drug delivery
DNA	ZrO <sub>2</sub>	Bioanalysis and sample capture
	Au	Gene therapy
	Au	Templated assembly/diagnostics/ DNA delivery to cells
	Fe <sub>2</sub> O <sub>3</sub>	Gene therapy
	SiO <sub>2</sub>	Drug and gene delivery/bioprobes
	Semiconductor QD	Biosensors
	TiO <sub>2</sub>	Subcellular organelle targeting
	CNT	Bioelectronics and bioanalysis
	CuS	Bioanalytical probe
	Carbohydrate	Au
Peptide	Au	Cellular labeling
	Fe <sub>2</sub> O <sub>3</sub>	Therapy
	Semiconductor QD	Cellular delivery
Lipid	Au	Gene therapy
Antibody	Ag	Cell surface detection
	SiO <sub>2</sub>	Bioanalysis
	Semiconductor QD	In vivo imaging/diagnostics/PDT
	semiconductor QD/iron oxide	Multimodal MRI/fluorescent imaging
Aptamers	PLA-PEG-COOH	Targeting prostate cancer cells

Source Adapted from (Sapsford et al. 2013)

to allow biocompatible interaction. These macromolecules are basic structural and functional units of cells. Geologically relevant macromolecules are decomposed fragments of cells and other living organisms, which typically show a wide range of chemical structures. Such macromolecules primarily include: humic substances (humic acids, fulvic acids) and polysaccharides; both of which are of primary importance due to their refractory and poorly degradable nature. Bio-macromolecules can be classified into three categories, namely: oligomers, polymers, and supramolecular assemblies (Fig. 9.2, Tsai 2007). This classification is essentially based on molecular weight, i.e., increasing from oligomers to supramolecular assemblies. Most NM surface coatings fall under the “polymer” category, however, larger ensemble molecules are recently used to generate NMs of medical interest. Understanding the chemical composition of these macromolecules can be

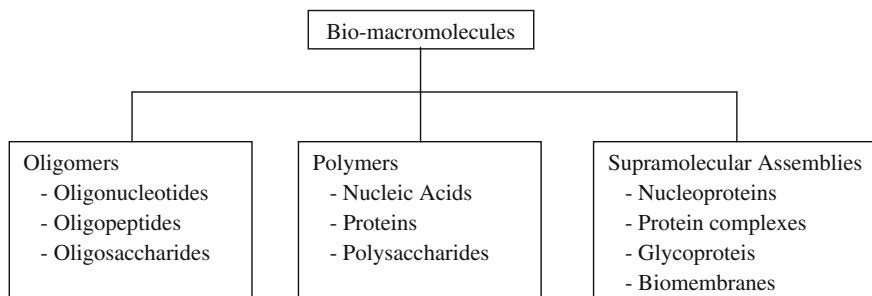


**Fig. 9.2** Possible classification of bio-macromolecules (Tsai 2007)

critical to evaluate NM interaction in natural and biological systems. The following section elaborates on the chemical structures of nucleic acids, proteins, and polysaccharides.

### 9.3.1 Humic Substances

Humic substances (HS) are major components of natural organic macromolecules (NOM) found in water and soil; where higher concentrations are found in soil. In natural waters, HSs are typically generated due to degradation of organisms, known as humification process. Concentrations in such cases are typically in the  $\mu\text{g L}^{-1}$  to  $\text{mg L}^{-1}$  range. Plants are the primary starting material in terrestrial and freshwater systems, while algae are in case of marine systems. HSs can be classified into different operationally defined categories that include humic acids (HAs) and fulvic acids (FAs).

One of the defining features of HSs is their chemical heterogeneity and polydispersity. Nevertheless, HAs typically have a higher molar mass than FAs and are more hydrophobic, with a lower charge and a higher C/O ratio. FAs on the other hand are relatively young and are more reactive, more easily leached from solid phases and more soluble in water. Many potential structures of HS exist. Representative, however not definitive structures of HSs are shown in Fig. 9.3. Different fractions, i.e., hydrophilic, hydrophobic, or transphilic, within one humic sample precludes production of a single exact structure (Lead and Wilkinson 2006).

### 9.3.2 Nucleic Acids

Nucleic acids are polymers of nucleotides which allow organisms to store and transfer genetic information from one generation to the next. They are considered as one of the most important bio-macromolecules alongside with proteins. Nucleic

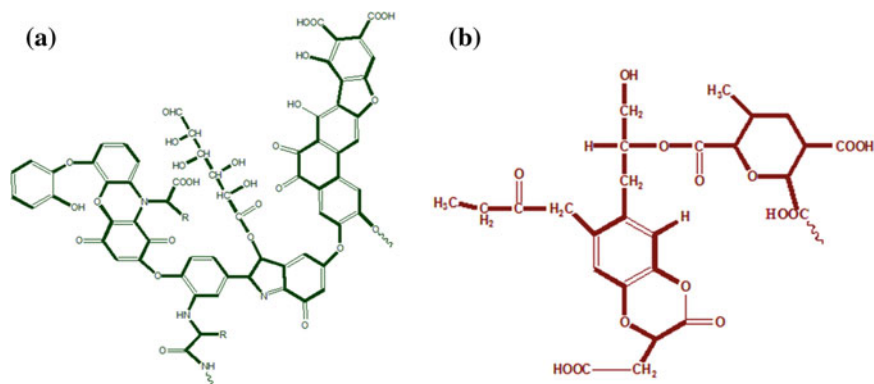


**Fig. 9.3** Representative structures of **a** humic acid (Stevenson 1994) and **b** fulvic acid (Leenheer et al. 1995). It is not suggested that these structures are unique or definitive

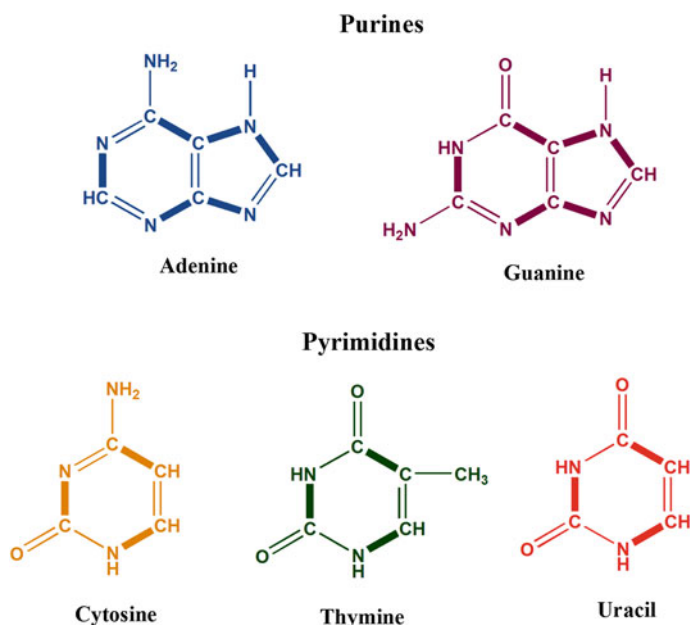
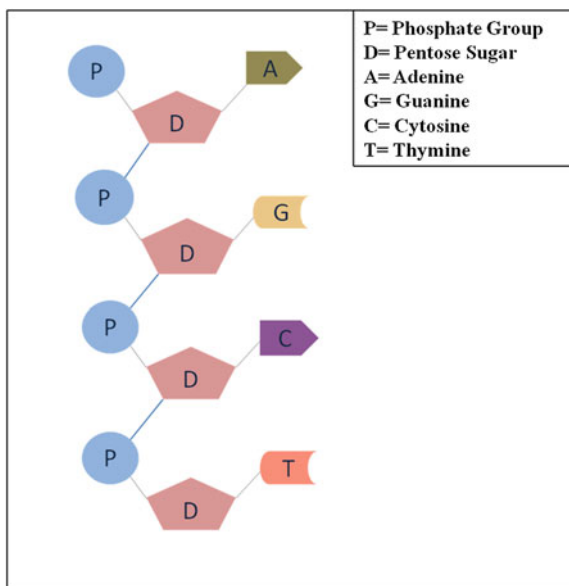


**Fig. 9.4** Nitrogen bases in nucleotides (Lodish 2008)

acids are divided into two classes, namely: deoxyribonucleic acid (DNA) and ribonucleic acid (RNA). The classification is based on the structure of the nucleotides. Each nucleotide has three components—a nitrogen base (purine or pyrimidine), a five-carbon pentose sugar, and a phosphate group. These structures are composed of pyrimidines—cytosine, thymine, and uracil and purines—adenine and guanine (Fig. 9.4).

**Fig. 9.5** Single DNA chain structure



DNA and RNA each contain two purine and two pyrimidine bases. For DNA, the nitrogen bases are cytosine, thymine, adenine, and guanine (shown in Fig. 9.5), while in RNA, thymines are replaced by uracil. In case of the five-carbon sugar, DNA contains a deoxyribose sugar while RNA contains a ribose sugar.

### 9.3.3 Proteins

Proteins are the most abundant and complex bio-macromolecules in cells and serve specific functions. Amino acids are the basic structural unit of proteins. These amino acids are bonded through peptide bonds that are created by attaching the carboxyl group of one amino acid to the amino group of the adjacent amino acid. A chain thus formed is called a peptide; short-length peptides are known as polypeptides and increase in length results in formation of proteins. Structure and biological functions of proteins depends on the physicochemical properties of the amino acids. Proteins are constructed from a set of 20 amino acids and have four levels of structural complexity:

- **Primary structure:** Primary structures refer to linear single chain structure with covalent linkage between amino acids.
- **Secondary structure:** This refers to specific geometric shapes (i.e., alpha helix and beta sheets) caused by intramolecular and intermolecular hydrogen bonding of amide groups.



- Tertiary structure: This type of structures refers to the final specific geometric shape determined by the noncovalent bonding between the side chains of the amino acids which might result into a number of folds, bends, and loops in the structure.
- Quaternary structure: Quaternary structures refer to a single, larger protein created by the same noncovalent bonding as in the tertiary structure among multiple polypeptides.

Proteins can be classified into three different categories based on their functionalities and correlating to their tertiary structures. They are globular and fibrous proteins. Enzymes and bovine serum albumin are soluble globular proteins that are often used in NM functionalization. These proteins facilitate biochemical reactions and work as catalysts in the organisms. Antibodies are special globular proteins (immunoglobulins) responsible for operating the immune system. These are Y-shaped macromolecules that are composed of combinations of 1,100–1,300 different amino acids (Wang et al. 2007). The combinatorial uniqueness results in antibody specificity to bind respective antigens. The tips of the Y-ends are light chains with lower molecular weight; whereas the straight legs possess high molecular weight heavy chains that usually anchor the NM surfaces (McDevitt et al. 2007). The heavy anchor chains are often composed of sugar-based fragments that join the lighter chained amino acid tips with disulfide junctions. Fibrous proteins provide the structural stability in the organism while membrane proteins usually serve as receptors or provide channels to relay signals between the cell's internal and external environment. NMs are often functionalized with fibrous proteins such as collagen and keratin for different purposes. Collagens are often used with semiconductor NMs for promoting biocompatibility of these semiconductor NMs (Sinani et al. 2003), while keratins are used as capping agents for silver NMs for improved handling properties of these NMs in the biological media (Martin et al. 2011).

### 9.3.4 Polysaccharides

Carbohydrate molecules bonded via glycosidic bonds form long-chained polysaccharides. These molecules possess either linear or branched structures and can be homogeneous or heterogeneous depending on their building blocks. If the monomers are of the same type they are called homosaccharides, however classified as heterosaccharides if composed of multiple unique monomers. Heterosaccharides are more common and are typically acidic or neutral where the former is composed of urinic acid and amino-sugars (may or may not be sulfated) while the latter contains urinic or sulfuric acid. Polysaccharides' chemical structure is represented by a general chemical formula  $C_x(H_2O)_y$ . Alternatively, the structure of polysaccharides (Fig. 9.6) can be expressed as  $(C_6H_{10}O_5)_n$  where  $40 \leq n \leq 3000$ .

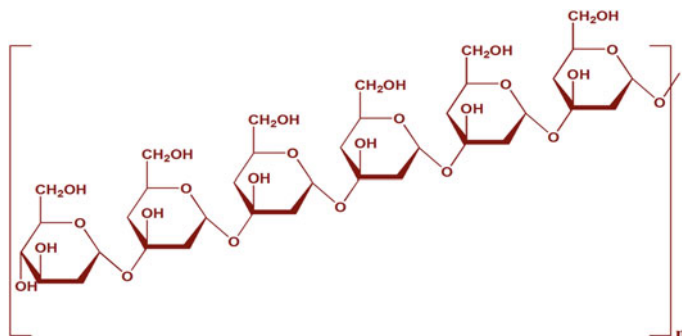


**Fig. 9.6** Structure of a polysaccharide

These are functional molecules serving plant and animal lives. Different types of polysaccharides demonstrate different functionality based on the structure and property of their monomer. For example: starch and glycogen serve as the main energy storage for plants and animals respectively. Cellulose, arabinoxylans, and chitin work as structural polysaccharides. Cellulose and arabinoxylans provide stability to plant cell walls while chitin does the same for many animal bodies. Large linear structures of polysaccharides are insoluble in water; e.g., cellulose, chitin, and similar molecules. Water solubility of polysaccharides increases with the increase in chain irregularity and branching.

## 9.4 Interaction of Coated Nanomaterials with Geo- and Bio-Macromolecules

NM release to the environment (Gottschalk and Nowack 2011; Nowack et al. 2012) and subsequent exposure to biological entities can occur during manufacturing (Bello et al. 2008; Yeganeh et al. 2008), use of consumer products (Farkas et al. 2011; Geranio et al. 2009; Kaegi et al. 2008, 2010; Benn and Westerhoff 2008; Benn et al. 2010; Hsu and Chein 2007), end-of-life degradation of nano-laden products (Köhler et al. 2008), as well as through waste-water facilities (Kiser et al. 2009, 2011). Modeling the release scenarios (Gottschalk et al. 2009; Mueller and Nowack 2008; Hendren et al. 2013) along the life cycle of NMs (Blaser et al. 2008) have realized the likelihood of significant NM release and environmental exposure. Interfacial interaction of NMs occurs when exposed to aqueous environment, where background chemistry and existing geo- and bio-macromolecules first interact with the soft coating layer (Gondikas et al. 2012). Particle-particle interaction and thus overlapping coating layers can also result in strong interfacial forces, influencing NM fate, transport, and toxicity (Tejamaya et al. 2012; Lowry et al. 2012; Qiu et al. 2010). Depending on the macromolecules present and the nature of existing surface coatings or lack thereof, such interaction can result into substantial transformation

of the outer surfaces of the NMs. Such transformation occurs via ligand exchange (Gupta et al. 2007; Diegoli et al. 2008) or overcoating with a secondary soft layer (Diegoli et al. 2008) and result in altered dissolution (Gondikas et al. 2012), reactivity (Li et al. 2008), and electron transport behavior (Fabrega et al. 2009). Similarly, NMs when exposed to biological fluids likely are going to interact with bio-macromolecules and result in similar surface alterations (Lynch and Dawson 2008; Huang et al. 2013). Moreover, biomacromolecule interaction, e.g., protein binding, is dynamic in nature; both from the ligand exchange as well as internal structural conformation (of proteins and other biomolecules) aspects (Lynch and Dawson 2008). Maintenance or changes in surface coatings are key factors controlling their subsequent environmental behavior and effects.

Further understanding of surface layer properties relies on the use of appropriate techniques to evaluate physicochemical properties of the surface ligands over appropriate temporal and spatial scales. Importantly, few such measurements that have been made are laboratory based. Plasmon resonance (Diegoli et al. 2008) and fluorescence-based (Pallem et al. 2009) studies had been used to identify ligand modification in presence of humic acids for coated AuNMs. Such characterization should be performed using a multimethod approach. For instance, Plasmon resonance (Diegoli et al. 2008) was used along with TEM, DLS, and other methods for detailed characterization of coating layers. Shift in Plasmon resonance and fluorescence quenching due to the interaction between coating and humics were described as key parameters discerning ligand-differences on AuNMs. Polymer layer analysis techniques include: ellipsometry (Brewer et al. 2005), total reflection infrared spectroscopy (Yang et al. 2005; Vargas et al. 2011), atomic force microscopy (Kim et al. 2003) combined with flow field fractionation (Baalousha and Lead 2007a, b), contact stylus instrument (Consiglio et al. 1998), and other optical techniques (Gole and Murphy 2005; Santra et al. 2001) that can be employed to measure layer thickness, ligand conformation, etc. Measured thicknesses and other properties can then be computed theoretically using, for example, Oshima's model of soft colloids (Phenrat et al. 2008), two-layer model for polymer thin films (Khlebtsov et al. 2003) or molecular dynamic simulation (Pinna et al. 2010). Such experimental and theoretical tools may be employed and likely require appropriate modification to capture the complex dynamics of ligand exchange during NM transformation processes. The following section outlines potential interaction of coated NMs with geo- and bio-macromolecules, based on commonly used ligands to surface functionalize.

### ***9.4.1 Interaction with Surfactant Coated NMs***

During environmental exposure of surfactant-coated NMs, the outer layer will likely encounter a strong lack of surfactant presence in the surrounding bulk and thus will be placed in a system with altered chemical potential. Thus the energetics will tend to favor desorption of those surfactant ligands from NM surfaces that are

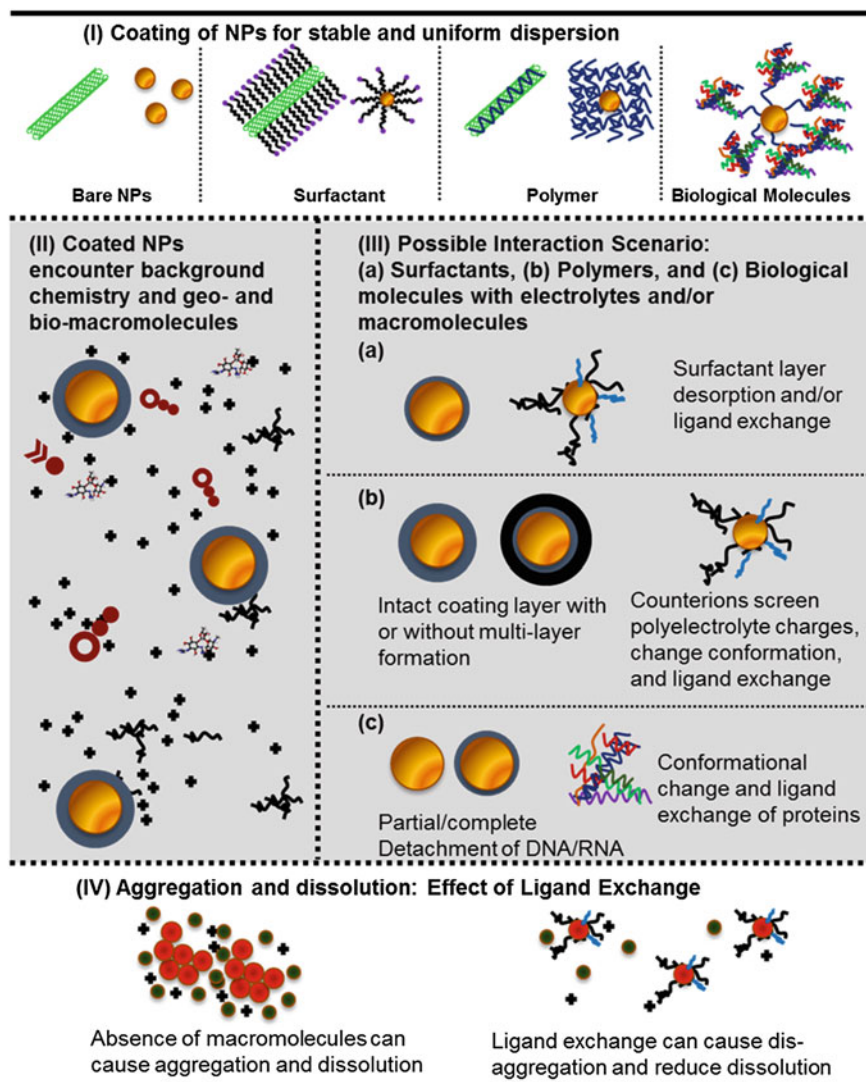


**Fig. 9.7** Interaction of NM with different surface coatings with geo- and bio-macromolecules. (I) Classes of NM coatings, (II) environmental interaction of NMs, (III) possible ligand exchange scenarios for NM coating classes, and (IV) effects of ligand exchange on aggregation and dissolution

attached mainly through weak interactions. Such entropic favorability can be overcome by relatively stronger electrostatic binding energies (Obata and Honda 2011). However, when nonionic or highly hydrophobic surfactants, are bound via weak forces, such tendencies will likely result in effective desorption of these ligands (Fig. 9.7). Thus, desorption will likely be controlled by the relative

strength of the binding energy between the surfactants and the NM surfaces as well as concentration gradient in the environment.

Moreover, most geo- and bio-macromolecules are often large compared to surfactant coatings and possess higher molar mass (Chin et al. 1994). During environmental and biological exposure, potential surfactant desorption and presence of such macromolecules will likely play a strong role in controlling the energetics of the system (Diegoli et al. 2008). It is well known that energy minimization for macromolecular systems occur by surface binding and acquired layer conformation of these molecules (O'Connell et al. 2002; Di Crescenzo et al. 2011; Saleh et al. 2010). Thus the tendency for surfactants to desorb combined with macromolecular surface binding propensity will cause ligand exchange to occur in these systems (Fig. 9.7). Ligand exchange rates, mechanisms of exchange, and thermodynamic (or steady state) conformation and chemistry are issues that deserve attention in these cases but have currently not been investigated in detail.

Examples of computational work on similar fields have recently shown displacement or overcoating of surfactants by NOM or biological molecules (Obata and Honda 2011). Computation with single-walled and multiwalled carbon nanotubes coated with tween 80 or lung surfactant surrogates dipalmitoylphosphatidylcholine (DPPC) presented differences in energetic stability, adsorption, and desorption time scales, and ligand exchange results as a function of the surface coatings of the nanotubes. This study demonstrated ligand–ligand interaction to be a dominant interaction mechanism, which will likely alter surface properties of carbonaceous nanomaterials prior to uptake via inhalation. Data gaps continue to persist that necessitate systematic studies on exchange of surfactants with geo- and bio-macromolecules as a function surfactant types (cationic, anionic, and non-ionic), density of bound surfactant molecules, macromolecules structures and variety, and a varied range of chemical conditions.

#### ***9.4.2 Interaction with Polymer-Coated NMs***

Compared to surfactants, polymers are larger ligands that can either be physisorbed to (Shenoy and Amiji 2005) or grafted from (Li and Ruckenstein 2004) the surfaces of NMs. Type of polymers plays a significant role on their surface density and conformation, thus results in controlling the overall energetics of the system (Corbierre et al. 2004). Polyelectrolytes, as an example, typically yield high surface density polymer brushes via electrostatic interaction along the polymer backbone (Tsujii et al. 2006). Thus displacement of such coatings requires a strong thermodynamic penalty to occur, which may not necessarily result from mere presence of larger molecular weight natural macromolecules (Lowry et al. 2012). However, polyelectrolyte brushes might collapse in presence of high concentration of electrolytes (Biesalski et al. 2004). Such counter ion presence can cause

electrostatic screening and will likely change the layer energetics to be favorable for possible ligand exchange with macromolecules (Fig. 9.7). Moreover, favorable electrostatic interaction with oppositely charged surface groups present in the polyelectrolytes and the macromolecules can result in multiple layer formation (Fig. 9.7, Xu et al. 2011; Boudou et al. 2010). Such layer-by-layer binding of counter-charged polymers has already been studied in simplified systems (Jaffar et al. 2004; Krass et al. 2002; Crespilho et al. 2005). Furthermore, sugar-based polysaccharides also have tendencies to form networks via molecular bridging (Rotureau et al. 2008), which are similar to such multilayered coronas.

On the other hand, nonionic polymers tend to display a higher surface footprint (Alexandridis et al. 1994), i.e., lower coverage, and thus have a different mode of interaction with the environmental and biological matrices. The larger surface footprint of these polymers indicate strong polymer–surface interaction, that are more insensitive to background electrolytes, will likely be difficult to displace via desorption. However, short-ranged polymer and geo- and biomacromolecule interaction is likely to occur, that may result in ligand exchange or multiple layer formation. Though it is hard to hypothesize potential layer conformation for such multilayered coatings, it is likely that nonionic polymer will yield thinner layers compared to charged polyelectrolytes (Louie et al. 2012). Moreover, network formation may also occur in presence of highly hydrophobic fractions of geomacromolecules or polysaccharides.

It is to be noted that some polymers can have moderate molecular weight and thus might interact similar to larger surfactant molecules. Ligand exchange, desorption from NM surfaces, as well as multilayer formation can occur for these cases as well. For example, SDS micelles when present in high concentrations can cause desorption of PVP polymer (present in low concentration) from the nanoparticle surfaces via stretching of the polymer chains (Cattoz et al. 2011). Some fraction of humic acids are known to possess surfactant like properties (Conte et al. 2005). Therefore, similar desorption mechanisms may exist in aquatic environment when low molecular weight polymer or low concentration of polymer is attached with NM.

There is evidence of polymer sorption and desorption in nanoscale zero-valent iron studies. Carboxymethyl cellulose, polystyrene sulfonate, and polyaspartate with a range of molecular weight were used to study desorption tendencies (Phenrat et al. 2008). The study presented molecular-weight-dependent desorption rate. Chemical moieties present in the polymers were also found to influence their desorption rates. However, data gaps persist in the systematic evaluation of such desorption and/or multilayer coating formation in the presence of geo- and biomacromolecules for most nanomaterials. Moreover, surface conformation, layer thicknesses, ligand exchange rates, and other important parameters are yet to be systematically evaluated to better understand the dynamic chemical structure of polymer-coated NM surfaces.

### 9.4.3 Interaction with Biomolecule-Coated NMs

Bio-macromolecules include antibodies, aptamers, DNA/RNA-related moieties, proteins, enzymes, etc. Most of such macromolecules are polypeptides or proteins that are relatively large possessing complex chemical functionalities (Tsai 2007). Such molecules have long-chained structures containing large fractions of carbon–nitrogen groups (Tsai 2007) (and phosphorous in DNA/RNA), and retain both cationic and anionic functional groups, distributed throughout. NMs coated with such biomolecules will undergo unique interaction when compared to the previous two classes of coatings. The uniqueness results from the complexity in the structure of such molecules as well as their inherent dynamism to evolve in response to environmental variables.

Antibody-coated NMs when exposed to geo- and bio-macromolecules may undergo multimode interaction; i.e., electrostatic (favorable and/or unfavorable) interaction depending on chemical moieties as well as short-ranged weak interaction with the sugar-based molecules. Thus multilayer formation is a possible outcome alongside with partial replacement of the antibodies with geo- and bio-macromolecules (Fig. 9.7). It is likely that the sugar moieties in anchor segments of antibodies will have weak short-range interaction with polysaccharides (Levy et al. 1981). However, the interplay between such favorable interactions will depend on chemical structure of the antibodies and the energetic balance of surface binding and interaction with such sugar-like molecules. Humics/fulvics might perform partial replacement, depending on the structure and surface coverage (Fig. 9.7). Proteins and other bio-macromolecules might result in similar ligand exchange, which will also depend on chemical identity of the antibody molecules.

DNA/RNA molecules are also combination of amino acids. Helical formation of these molecules allows for effective short-ranged interaction with anisotropic tube-like NMs; e.g., carbon nanotubes are often wrapped with DNA/RNA molecules to ensure drug delivery and targeting (Bianco et al. 2005; Cathcart et al. 2007; Prato et al. 2008). When released in the environment, such NMs will likely demonstrate stable surface composition, due to their interaction with large surface area. However, like-structured bio-macromolecules might favorably interact with these molecules and thus invoke their partial or complete detachment from the NMs (Fig. 9.7). Such occurrences will then be influenced largely by other geo- and bio-macromolecules.

Protein-stabilized NMs on the other hand will likely show dynamic behavior while exposed in environmental and biological systems. Conformation and layer folding of the existing protein molecules might get altered due to the background electrolyte conditions and thus will result in large changes in system energetic. Presence of other geo- and bio-macromolecules will cause further imbalance in the system (Bhan et al. 2013; Corsaro et al. 2010).

## 9.5 Interaction of NM with Protein Corona

The nano-bio literature focusing mostly on NM applications on medical processes and devices has been significantly ahead in understanding protein corona formation on coated NM surfaces. Thus interaction and exchange of surface coatings with biomolecules (such as proteins) have been advancing in this field. Protein binding occurs during NM exposure to biological fluids containing a complex mixture of proteins and other macromolecules. Such coronas can be single-layered or multilayered, comprising of hard and soft shells. Characterization of protein corona is performed using techniques such as circular dichroism (Treuel et al. 2012), surface Plasmon resonance (Cedervall et al. 2007), gel filtration (Cedervall et al. 2007), isothermal titration calorimetry (Cedervall et al. 2007), atomic force microscopy (Natte et al. 2013), x-ray photoelectron spectroscopy (Podila et al. 2012). It has been shown in the literature that protein binding can form either hard or soft corona, indicating relative transformation potential of the bound layer (Lynch and Dawson 2008). Moreover, a monolayer of irreversibly bound hard corona can be overcoated with a soft outer layer (i.e., soft corona) which can undergo dynamic exchange in the presence of other body fluids or plasma proteins (Milani et al. 2012). Recent literature on protein coronas thus shows the importance of ligand exchange (Lynch and Dawson 2008; Cedervall et al. 2007; Podila et al. 2012) studies as well as can shed light on coating–corona interaction to lead future studies on geomacromolecule interaction with NM coatings.

NM corona formation and their structures as well as subsequent interaction with cells and tissues are highly influenced by NM properties and coating characteristics. Cellular interaction and uptake of iron oxide nanoparticles are shown to be influenced by existing surface coating (Safi et al. 2011). Iron oxide particles coated with citrate were destabilized by protein replacement and corona formation and subsequently internalized into the cells, while PAA-coated ones showed higher stability and reduced uptake (Safi et al. 2011). Similarly, protein corona formation is shown to be a function of PEG molecular weight and surface density when silica nanoparticles interact with BSA molecules (Natte et al. 2013). Moreover, the structure of hard corona has been shown to be influenced by the nature of chemical functionality and polystyrene particle size (Lundqvist et al. 2008). These literature findings show role of coatings on protein corona formation.

The dynamic nature of soft protein corona is prone to cause change in conformation and also known to be influenced by surrounding chemistry. Large polymeric chains have been shown to suppress the dynamic evolution of protein corona in contrast to evolving corona in presence of lower molecular weight polymeric structures (Natte et al. 2013). Such corona formation processes are entropy driven where the interaction of polymer–NM interfaces play an important role (Lynch and Dawson 2008). The resistance to protein adsorption is derived from steric repulsions of polymer coatings that emanate from polymer composition, packing density, and polymer–NM attraction forces (Prime and Whitesides 1993; Carignano and Szleifer 2000; Satulovsky et al. 2000; Szleifer and Carignano



2000; Herrwerth et al. 2003). Moreover, conformational differences are reported to occur as protein coronas are formed with side-chain orientation compared to brush-conformation depending on polymeric coatings present (Natte et al. 2013). The rate of protein binding and corona formation is also reported to be influenced by NM coating type as shown in case of citric acid, PAA, and oleic acid-coated supermagnetic NMs (Jedlovsky-Hajdú et al. 2012). Thus, depending on the type of proteins used to decorate the NM surfaces and those that are present in the environmental systems, ligand exchange is plausible. The rate of exchange, conformation of the protein molecules before and after such transformations, extent of exchange will be the key parameters to be determined in such cases.

## 9.6 Environmental and Biological Implications

The environmental and biological processes that are appropriate to NMs are their fate, transport, transformation, and toxicity (Klaine et al. 2008). Each of these processes entails interfacial interactions that control NM exposure, transport, and ultimately risk to the environment and to human health. As discussed earlier, NM surfaces are decorated with synthetic and natural chemical moieties; which undergo transformation and thus influence subsequent environmental processes of these NMs. This section discusses roles of geo- and bio-macromolecules on possible alteration of these environmental processes, in light of the existing literature.

### 9.6.1 *Fate and Transport*

NM aggregation and deposition are interfacial processes that are controlled by inherent material properties, NM surface coatings, and environmental chemistry. Both of these processes are known to be heavily dependent on surface functionalities (Tian et al. 2010; Smith et al. 2009). Thus, likely ligand exchanges during environmental exposure and transformation stages will alter interfacial interaction and significantly influence aggregation and deposition behavior of NMs. These two interfacial processes are currently studied on both metallic (Baalousha et al. 2013; Afrooz et al. 2013) and carbonaceous (Saleh et al. 2010; Khan et al. 2013) NMs in presence of geo- and bio-macromolecules. However, most such studies either precoat the NMs with geo- or bio-macromolecules or evaluate interfacial behavior of pristine NMs in presence of these molecules. As an example, SWNT aggregation was studied in presence of humic acid, bovine serum albumin, and sodium alginate (Saleh et al. 2010). The study observed the effects of coatings on pristine SWNT surfaces and hypothesized mechanisms of interaction for the observed aggregation behavior. In another similar study, role of hydrophobic humic acid and hydrophilic acetic acid on SWNT transport was evaluated under

landfill conditions (Khan et al. 2013). Few recent studies acknowledged possibilities of humics and macromolecules exchange with preexisting coatings on NM, which resulted in alteration of aggregation behavior. Citrate and acrylate-coated AuNMs showed enhanced stabilization effects upon humic acid addition (Diegoli et al. 2008) and spectroscopic measurement confirmed likely coating substitution or possibly overcoating by humics (Diegoli et al. 2008). Also, Cumberland and Lead (Cumberland and Lead 2009) showed similar observations with citrate-coated Ag (Cumberland and Lead 2009). Similarly, the stability of citrate, PVP, and PEG-coated AgNMs were studied in biological media conditions for toxicity studies (Tejamaya et al. 2012). Electrostatically stabilized particles (citrate-AgNM) were found to be destabilized faster than sterically stabilized (PVP- and PEG-AgNM) ones. However, none of these studies presented exchange kinetics of coatings under realistic condition. Lack of such measurements and characterization thus leave a good deal of uncertainty in evaluation of aggregation and deposition of NMs, particularly when they are precoated with chemical functionalities.

### 9.6.2 Transformation

Transformation of NMs includes dissolution (for metallic NMs) (Zook et al. 2011), ligand binding (Li and Ruckenstein 2004), photocatalytic activities on surfaces (Kong et al. 2009; Hwang and Li 2010), and redox processes, e.g., oxidation (Lok et al. 2007; Phenrat et al. 2009), sulfidation, etc. (Levard et al. 2011; Lowry et al. 2012; Ma et al. 2013) All of these processes are influenced by surface coatings (Gondikas et al. 2012; Unrine et al. 2012); i.e., presence of soft layers on NM surfaces (e.g., gum Arabic vs. PVP coatings) will likely alter metal dissolution rate, as well as sulfidation. Ligand exchange is also likely to occur at this stage, which will further influence dissolution and subsequent redox processes. Moreover, photocatalytic reactions can alter the coating properties and thus influence the overall transformation process.

In addition, silver ion dissolution can be controlled by the surface coatings as shown by (Gondikas et al. 2012). Citrate (a low molecular weight surfactant) and PVP (larger polymer) were used to coat silver nanoparticles (Gondikas et al. 2012). Dissolution was monitored in presence of cysteine, an amino acid possessing thiol groups. Cysteine increased dissolution from both the coated particles, where the dissolution rate was higher for citrate-coated particles compared to PVP-coated ones. The study further analyzed surface chemistry with x-ray adsorption spectroscopy and argued that formation of silver-sulfhydryl bonds caused such dissolution behavior and that cysteine likely has displaced citrate molecules more than PVP.

Similarly, influence on photoactivity of SWNTs due to changes in the surface functionality has also been reported in the literature by Chen et al. (Chen and Jafvert 2011). Here photoirradiated transformation and resultant reactivity of PEG

and SDS modified SWNTs were compared with oxidized SWNTs. Photoirradiated PEGalated and oxidized SWNTs degraded furfural alcohol at a rate higher than SDS-SWNTs. Such coating-based differences in reactivity and phototransformation can also be translated in NM reactivity due to macromolecular transformations.

### 9.6.3 NM Toxicity and Biodistribution

Biological interaction of NMs involves cell viability, membrane interaction, organ, and higher trophic level species uptake, etc. NM coatings influence interfacial and uptake behavior, thus necessitate careful evaluation of ligand exchange and their roles on such processes. As an example: coating-dependent toxicity of NMs has been shown by Qiu et al. CTAB, PSS, and PDDAC were used as surface coatings for AuNMs (Blaser et al. 2008). CTAB showed higher toxicity compared to the other two coatings, whereas PDDAC showed higher uptake of the AuNMs. On the other hand, NOM has been shown to mask the toxic effect of NMs for both carbonaceous (Qiu et al. 2010) and metallic nanoparticles (Fabrega et al. 2009; Chen et al. 2011; Li et al. 2010). Such results indicate, that ligand exchange, particularly with geomacromolecules, can alter toxic response and uptake of NMs, significantly. Cellular uptake in biological and environmental settings can also be affected by NM coatings as well as by surface potential (Arvizo et al. 2010), hydrophobicity, coating conformation, etc. Nonionic PVA and anionic citrate-coated AuNMs have shown to associate less with cell surfaces compared to cationic poly(alkylamine hydrochloride)-coated ones (Cho et al. 2009). Hydrophobic functionalization of quantum dots (QDs) with olyel groups showed higher cellular uptake compared to hydrophilic carboxylated QDs (Tan et al. 2010). However, no differences were found on silver nanoparticle bioaccumulation or toxicity to earthworm *Eisnia Fetida* when coated with oleic acid and PVP (Shoults-Wilson et al. 2011); though both particles showed reproductive toxicity. Such results highlight the fact that not only surface coatings but also the material signature of the coated surfaces influence their toxic response and biodistribution. Thus ligand exchange as well as multilayer coating formation will also have significant role in altering toxicity behavior of NMs and necessitates systematic evaluation of these layer characteristics.

The environmental and biological processes showed that surface coatings of NMs significantly influence their behavior in aquatic systems. Careful evaluation of ligand exchange kinetics, ligand conformation, composition, as well as coating stability are essential for accurate and mechanistic determination of NM behavior in environmental and biological systems. Appropriate experimental and theoretical tools need to be developed to carefully measure and predict layer properties and exchange behavior. These coating properties can have strong influence on NM exposure and risk assessment.

## References

- Afroz A, Khan IA, Hussain SM, Saleh NB (2013) Mechanistic heteroaggregation of gold nanoparticles in a wide range of solution chemistry. *Environ Sci Technol* 47(4):1853–1860
- Aich N, Boateng L, Flora JRV, Saleh N (2013) Preparation of non-aggregating aqueous fullerenes in highly saline solutions with a biocompatible non-ionic polymer. *Nanotechnology* (in review)
- Aitken RJ, Chaudhry MQ, Boxall ABA, Hull M (2006) Manufacture and use of nanomaterials: current status in the UK and global trends. *Occup Med Oxf* 56(5):300–306
- Alexandridis P, Athanassiou V, Fukuda S, Hatton TA (1994) Surface-activity of poly(ethylene oxide)-block-poly(propylene oxide)-block-poly(ethylene oxide) copolymers. *Langmuir* 10(8):2604–2612
- Aliaga C, Park JY, Yamada Y, Lee HS, Tsung C-K, Yang P, Somorjai GA (2009) Sum frequency generation and catalytic reaction studies of the removal of organic capping agents from Pt nanoparticles by uv-ozone treatment. *J Phys Chem C* 113(15):6150–6155
- Allen BL, Kichambare PD, Star A (2007) Carbon nanotube field-effect-transistor-based biosensors. *Adv Mater* 19(11):1439–1451
- Arico AS, Bruce P, Scrosati B, Tarascon JM, Van Schalkwijk W (2005) Nanostructured materials for advanced energy conversion and storage devices. *Nat Mater* 4(5):366–377
- Arvizo RR, Miranda OR, Thompson MA, Pabelick CM, Bhattacharya R, Robertson JD, Rotello VM, Prakash YS, Mukherjee P (2010) Effect of nanoparticle surface charge at the plasma membrane and beyond. *Nano Lett* 10(7):2543–2548
- Avouris P, Freitag M, Perebeinos V (2008) Carbon-nanotube photonics and optoelectronics. *Nat Photonics* 2(6):341–350
- Baalousha M, Lead JR (2007a) Characterization of natural aquatic colloids (<5 nm) by flow-field flow fractionation and atomic force microscopy. *Environ Sci Technol* 41(4):1111–1117
- Baalousha M, Lead JR (2007b) Size fractionation and characterization of natural aquatic colloids and nanoparticles. *Sci Total Environ* 386(1–3):93–102
- Baalousha M, Nur Y, Romer I, Tejamaya M, Lead JR (2013) Effect of monovalent and divalent cations, anions and fulvic acid on aggregation of citrate-coated silver nanoparticles. *Sci Total Environ* 454:119–131
- Bae DS, Park K, Kim JW, Kim RH (2006) In fabrication and microstructure of ZnO–SiO<sub>2</sub> nanoparticles by a reverse micelle and sol-gel processing, materials science forum. *Trans Tech Publ* 2006:790–793
- Baron R, Willner B, Willner I (2007) Biomolecule-nanoparticle hybrids as functional units for nanobiotechnology. *Chem Commun* 4:323–332
- Baughman RH, Zakhidov AA, de Heer WA (2002) Carbon nanotubes—the route toward applications. *Science* 297(5582):787–792
- Behrens S, Bönemann H, Matussevitch N, Gorschinski A, Dinjus E, Habicht W, Bolle J, Zinoveva S, Palina N, Hormes J (2006) Surface engineering of Co and FeCo nanoparticles for biomedical application. *J Phys Condens Matter* 18(38):S2543
- Bello D, Hart AJ, Ahn K, Hallock M, Yamamoto N, Garcia EJ, Ellenbecker MJ, Wardle BL (2008) Particle exposure levels during CVD growth and subsequent handling of vertically-aligned carbon nanotube films. *Carbon* 46(6):974–977
- Benn TM, Westerhoff P (2008) Nanoparticle silver released into water from commercially available sock fabrics. *Environ Sci Technol* 42(11):4133–4139
- Benn T, Cavanagh B, Hristovski K, Posner JD, Westerhoff P (2010) The release of nanosilver from consumer products used in the home supplemental data file available online for this article. all rights reserved. no part of this periodical may be reproduced or transmitted in any form or by any means, electronic or mechanical, including photocopying, recording, or any information storage and retrieval system, without permission in writing from the publisher. *J Environ Qual* 39(6):1875–1882

- Bertrand F, German S-A, Anwar A, Irune V, Gemma B, Yolanda RDM, Lennart B (2013) Dispersion and surface functionalization of oxide nanoparticles for transparent photocatalytic and UV-protecting coatings and sunscreens. *Sci Technol Adv Mater* 14(2):023001
- Besteman K, Lee JO, Wiertz FGM, Heering HA, Dekker C (2003) Enzyme-coated carbon nanotubes as single-molecule biosensors. *Nano Lett* 3(6):727–730
- Bhan C, Brower TL, Raghavan D (2013) SPR studies of the adsorption of silver/bovine serum albumin nanoparticles (Ag/BSA NPs) onto the model biological substrates. *J Colloid Interface Sci* 402:40–49
- Bhattacharyya S, Sinturel C, Salvetat JP, Saboungi ML (2005) Protein-functionalized carbon nanotube-polymer composites. *Appl Phys Lett* 86(11)
- Bianco A, Kostarelos K, Partidos CD, Prato M (2005a) Biomedical applications of functionalised carbon nanotubes. *Chem Commun* 5:571–577
- Bianco A, Kostarelos K, Prato M (2005b) Applications of carbon nanotubes in drug delivery. *Curr Opin Chem Biol* 9(6):674–679
- Biesalski M, Johannsmann D, Ruhe J (2004) Electrolyte-induced collapse of a polyelectrolyte brush. *J Chem Phys* 120(18):8807–8814
- Blaser SA, Scheringer M, MacLeod M, Hungerbühler K (2008) Estimation of cumulative aquatic exposure and risk due to silver: contribution of nano-functionalized plastics and textiles. *Sci Total Environ* 390(2–3):396–409
- Boudou T, Crouzier T, Ren KF, Blin G, Picart C (2010) Multiple functionalities of polyelectrolyte multilayer films: new biomedical applications. *Adv Mater* 22(4):441–467
- Breunig M, Bauer S, Goepferich A (2008) Polymers and nanoparticles: intelligent tools for intracellular targeting? *Eur J Pharm Biopharm* 68(1):112–128
- Brewer SH, Glomm WR, Johnson MC, Knag MK, Franzen S (2005) Probing BSA binding to citrate-coated gold nanoparticles and surfaces. *Langmuir* 21(20):9303–9307
- Buffle J, Wilkinson KJ, Stoll S, Filella M, Zhang JW (1998) A generalized description of aquatic colloidal interactions: the three-colloidal component approach. *Environ Sci Technol* 32(19):2887–2899
- Bulte JWM, Kraitchman DL (2004) Iron oxide MR contrast agents for molecular and cellular imaging. *NMR Biomed* 17(7):484–499
- Burghard M, Klauk H, Kern K (2009) Carbon-based field-effect transistors for nanoelectronics. *Adv Mater* 21(25–26):2586–2600
- Burt JL, Gutierrez-Wing C, Miki-Yoshida M, Jose-Yacamán M (2004) Noble-metal nanoparticles directly conjugated to globular proteins. *Langmuir* 20(26):11778–11783
- Carignano MA, Szleifer I (2000) Prevention of protein adsorption by flexible and rigid chain molecules. *Colloids Surf B* 18(3–4):169–182
- Cathcart H, Quinn S, Nicolosi V, Kelly JM, Blau WJ, Coleman JN (2007) Spontaneous debundling of single-walled carbon nanotubes in DNA-based dispersions. *J Phys Chem C* 111(1):66–74
- Cattoz B, Cosgrove T, Crossman M, Prescott SW (2011) Surfactant-mediated desorption of polymer from the nanoparticle interface. *Langmuir* 28(5):2485–2492
- Cedervall T, Lynch I, Lindman S, Berggård T, Thulin E, Nilsson H, Dawson KA, Linse S (2007) Understanding the nanoparticle–protein corona using methods to quantify exchange rates and affinities of proteins for nanoparticles. *Proc Natl Acad Sci* 104(7):2050–2055
- Chaudhuri RG, Paria S (2011) Growth kinetics of sulfur nanoparticles in aqueous surfactant solutions. *J Colloid Interface Sci* 354(2):563–569
- Chen C-Y, Jafvert CT (2011) The role of surface functionalization in the solar light-induced production of reactive oxygen species by single-walled carbon nanotubes in water. *Carbon* 49(15):5099–5106
- Chen J, Xiu Z, Lowry GV, Alvarez PJJ (2011) Effect of natural organic matter on toxicity and reactivity of nano-scale zero-valent iron. *Water Res* 45(5):1995–2001
- Chin Y-P, Aiken G, O’Loughlin E (1994) Molecular weight, polydispersity, and spectroscopic properties of aquatic humic substances. *Environ Sci Technol* 28(11):1853–1858

- Cho K, Wang X, Nie S, Chen Z, Shin DM (2008) Therapeutic nanoparticles for drug delivery in cancer. *Clin Cancer Res* 14(5):1310–1316
- Cho EC, Xie J, Wurm PA, Xia Y (2009) Understanding the role of surface charges in cellular adsorption versus internalization by selectively removing gold nanoparticles on the cell surface with a I-2/KI etchant. *Nano Lett* 9(3):1080–1084
- Consiglio R, Randall NX, Bellaton B, von Stebut J (1998) The nano-scratch tester (NST) as a new tool for assessing the strength of ultrathin hard coatings and the mar resistance of polymer films. *Thin Solid Films* 332(1–2):151–156
- Conte P, Agretto A, Spaccini R, Piccolo A (2005) Soil remediation: humic acids as natural surfactants in the washings of highly contaminated soils. *Environ Pollut* 135(3):515–522
- Corbierre MK, Cameron NS, Lennox RB (2004) Polymer-stabilized gold nanoparticles with high grafting densities. *Langmuir* 20(7):2867–2873
- Corsaro A, Anselmi C, Polano M, Aceto A, Florio T, De Nobili M (2010) The interaction of humic substances with the human prion protein fragment 90-231 affects its protease K resistance and cell internalization. *J Biol Regul Homeost Agents* 24(1):27–39
- Crespilho FN, Zucolotto V, Siqueira JR, Constantino CJL, Nart FC, Oliveira ON (2005) Immobilization of humic acid in nanostructured layer-by-layer films for sensing applications. *Environ Sci Technol* 39(14):5385–5389
- Cumberland SA, Lead JR (2009) Particle size distributions of silver nanoparticles at environmentally relevant conditions. *J Chromatogr A* 1216(52):9099–9105
- Da Silva S, Melo T, Soler M, Lima E, Da Silva M, Morais P (2003) Stability of citrate-coated magnetite and cobalt-ferrite nanoparticles under laser irradiation: a Raman spectroscopy investigation. *IEEE Trans Magn* 39(5):2645–2647
- Di Crescenzo A, Aschi M, Del Canto E, Giordani S, Demurtas D, Fontana A (2011) Structural modifications of ionic liquid surfactants for improving the water dispersibility of carbon nanotubes: an experimental and theoretical study. *PhysChemChemPhys* 13(23):11373–11383
- Diegoli S, Manciuola AL, Begum S, Jones IP, Lead JR, Preece JA (2008) Interaction between manufactured gold nanoparticles and naturally occurring organic macromolecules. *Sci Total Environ* 402(1):51–61
- Eda G, Chhowalla M (2010) Chemically derived graphene oxide: towards large-area thin-film electronics and optoelectronics. *Adv Mater* 22(22):2392–2415
- Fabrega J, Fawcett SR, Renshaw JC, Lead JR (2009) Silver nanoparticle impact on bacterial growth: effect of pH, concentration, and organic matter. *Environ Sci Technol* 43(19):7285–7290
- Farkas J, Peter H, Christian P, Gallego Urrea JA, Hassellöv M, Tuoriniemi J, Gustafsson S, Olsson E, Hylland K, Thomas KV (2011) Characterization of the effluent from a nanosilver producing washing machine. *Environ Int* 37(6):1057–1062
- Froner E, D'Amato E, Adamo R, Prtljaga N, Larcheri S, Pavesi L, Rigo A, Potrich C, Scarpa M (2011) Deoxycholate as an efficient coating agent for hydrophilic silicon nanocrystals. *J Colloid Interface Sci* 358(1):86–92
- Geranio L, Heuberger M, Nowack B (2009) The behavior of silver nanotextiles during washing. *Environ Sci Technol* 43(21):8113–8118
- Ghabbour EA, Davies G (2001) Humic substances: structures, models and functions. Royal Society of Chemistry, Cambridge
- Gole A, Murphy CJ (2005) Polyelectrolyte-coated gold nanorods: synthesis, characterization and immobilization. *Chem Mater* 17(6):1325–1330
- Gondikas AP, Morris A, Reinsch BC, Marinakos SM, Lowry GV, Hsu-Kim H (2012) Cysteine-induced modifications of zero-valent silver nanomaterials: implications for particle surface chemistry, aggregation, dissolution, and silver speciation. *Environ Sci Technol* 46(13):7037–7045
- Gottschalk F, Nowack B (2011) The release of engineered nanomaterials to the environment. *J Environ Monit* 13(5):1145–1155

- Gottschalk F, Sonderer T, Scholz RW, Nowack B (2009) Modeled environmental concentrations of engineered nanomaterials (TiO<sub>2</sub>, ZnO, Ag, CNT, fullerenes) for different regions. *Environ Sci Technol* 43(24):9216–9222
- Gratzel M (2001) Photoelectrochemical cells. *Nature* 414(6861):338–344
- Gratzel M (2003) Dye-sensitized solar cells. *J Photochem Photobiol C-Photochem Rev* 4(2):145–153
- Grubbs RB (2007) Roles of polymer ligands in nanoparticle stabilization. *Polym Rev* 47(2):197–215
- Guo J, Gao X, Su L, Xia H, Gu G, Pang Z, Jiang X, Yao L, Chen J, Chen H (2011) Aptamer-functionalized PEG–PLGA nanoparticles for enhanced anti-glioma drug delivery. *Biomaterials* 32(31):8010–8020
- Gupta AK, Gupta M (2005) Synthesis and surface engineering of iron oxide nanoparticles for biomedical applications. *Biomaterials* 26(18):3995–4021
- Gupta AK, Naregalkar RR, Vaidya VD, Gupta M (2007) Recent advances on surface engineering of magnetic iron oxide nanoparticles and their biomedical applications. *Nanomedicine* 2(1):23–39
- Hendren CO, Badireddy AR, Casman E, Wiesner MR (2013) Modeling nanomaterial fate in wastewater treatment: Monte Carlo simulation of silver nanoparticles (nano-Ag). *Sci Total Environ* 449:418–425
- Hernandez RM, Richter L, Semancik S, Stranick S, Mallouk TE (2004) Template fabrication of protein-functionalized gold-polypyrrole-gold segmented nanowires. *Chem Mater* 16(18):3431–3438
- Herrwerth S, Eck W, Reinhardt S, Grunze M (2003) Factors that determine the protein resistance of oligoether self-assembled monolayers—internal hydrophilicity, terminal hydrophilicity, and lateral packing density. *J Am Chem Soc* 125(31):9359–9366
- Hota G, Jain S, Khilar KC (2004) Synthesis of CdS–Ag<sub>2</sub>S core-shell/composite nanoparticles using AOT/n-heptane/water microemulsions. *Colloids Surf A* 232(2):119–127
- Hsu L-Y, Chein H-M (2007) Evaluation of nanoparticle emission for TiO<sub>2</sub> nanopowder coating materials. In: Maynard A, Pui DH (eds) *Nanotechnology and occupational health*. Springer, Netherlands, pp 157–163
- Huang X, Neretina S, El-Sayed MA (2009) Gold nanorods—from synthesis and properties to biological and biomedical applications. *Adv Mater* 21(48):4880–4910
- Huang R, Carney RP, Stellacci F, Lau BLT (2013) Protein-nanoparticle interactions: the effects of surface compositional and structural heterogeneity are scale dependent. *Nanoscale* 5(15):6928–6935
- Hwang YS, Li Q (2010) Characterizing photochemical transformation of aqueous NC(60) under environmentally relevant conditions. *Environ Sci Technol* 44(8):3008–3013
- Islam MF, Rojas E, Bergey DM, Johnson AT, Yodh AG (2003) High weight fraction surfactant solubilization of single-wall carbon nanotubes in water. *Nano Lett* 3(2):269–273
- Jaffar S, Nam KT, Khademhosseini A, Xing J, Langer RS, Belcher AM (2004) Layer-by-layer surface modification and patterned electrostatic deposition of quantum dots. *Nano Lett* 4(8):1421–1425
- Jedlovsky-Hajdú A, Bombelli FB, Monopoli MP, Tombácz E, Dawson KA (2012) Surface coatings shape the protein corona of spions with relevance to their application in vivo. *Langmuir* 28(42):14983–14991
- Joo SH, Al-Abed SR, Luxton T (2009) Influence of carboxymethyl cellulose for the transport of titanium dioxide nanoparticles in clean silica and mineral-coated sands. *Environ Sci Technol* 43(13):4954–4959
- Ju L, Zhang W, Wang X, Hu J, Zhang Y (2012) Aggregation kinetics of SDBS-dispersed carbon nanotubes in different aqueous suspensions. *Colloids Surf A* 409:159–166
- Kaegi R, Ulrich A, Sinnet B, Vonbank R, Wichser A, Zuleeg S, Simmler H, Brunner S, Vonmont H, Burkhardt M, Bollner M (2008) Synthetic TiO<sub>2</sub> nanoparticle emission from exterior facades into the aquatic environment. *Environ Pollut* 156(2):233–239

- Kaegi R, Sinnet B, Zuleeg S, Hagendorfer H, Mueller E, Vonbank R, Boller M, Burkhardt M (2010) Release of silver nanoparticles from outdoor facades. *Environ Pollut* 158(9): 2900–2905
- Kaegi R, Voegelin A, Sinnet B, Zuleeg S, Hagendorfer H, Burkhardt M, Siegrist H (2011) Behavior of metallic silver nanoparticles in a pilot wastewater treatment plant. *Environ Sci Technol* 45(9):3902–3908
- Karajanagi SS, Yang HC, Asuri P, Sellitto E, Dordick JS, Kane RS (2006) Protein-assisted solubilization of single-walled carbon nanotubes. *Langmuir* 22(4):1392–1395
- Khan IA, Afrooz A, Flora JRV, Schierz PA, Sabo-Attwood T, Saleh NB (2013a) Chirality affects aggregation kinetics of single-walled carbon nanotubes. *Environ Sci Technol* 47(4):1844–1852
- Khan IA, Berge ND, Sabo-Attwood T, Ferguson PL, Saleh NB (2013) Single-walled carbon nanotube transport in representative municipal solid waste landfill conditions. *Environ Sci Technol*
- Khlebtsov NG, Dykman LA, Bogatyrev VA, Khlebtsov BN (2003) Two-layer model of colloidal gold bioconjugates and its application to the optimization of nanosensors. *Colloid J* 65(4):508–517
- Kim DK, Mikhaylova M, Zhang Y, Muhammed M (2003) Protective coating of superparamagnetic iron oxide nanoparticles. *Chem Mater* 15(8):1617–1627
- Kim D, Park S, Lee JH, Jeong YY, Jon S (2007) Antibiofouling polymer-coated gold nanoparticles as a contrast agent for in vivo X-ray computed tomography imaging. *J Am Chem Soc* 129(24):7661–7665
- Kim JP, Lee BY, Hong S, Sim SJ (2008) Ultrasensitive carbon nanotube-based biosensors using antibody-binding fragments. *Anal Biochem* 381(2):193–198
- Kim ST, Saha K, Kim C, Rotello VM (2013) The role of surface functionality in determining nanoparticle cytotoxicity. *Acc Chem Res* 46(3):681–691
- Kiser MA, Westerhoff P, Benn T, Wang Y, Pérez-Rivera J, Hristovski K (2009) Titanium nanomaterial removal and release from wastewater treatment plants. *Environ Sci Technol* 43(17):6757–6763
- Klaine SJ, Alvarez PJJ, Batley GE, Fernandes TF, Handy RD, Lyon DY, Mahendra S, McLaughlin MJ, Lead JR (2008) Nanomaterials in the environment: behavior, fate, bioavailability, and effects. *Environ Toxicol Chem* 27(9):1825–1851
- Köhler AR, Som C, Helland A, Gottschalk F (2008) Studying the potential release of carbon nanotubes throughout the application life cycle. *J Clean Prod* 16(8–9):927–937
- Kohli P, Harrell CC, Cao ZH, Gasparac R, Tan WH, Martin CR (2004) DNA-functionalized nanotube membranes with single-base mismatch selectivity. *Science* 305(5686):984–986
- Kokura S, Handa O, Takagi T, Ishikawa T, Naito Y, Yoshikawa T (2010) Silver nanoparticles as a safe preservative for use in cosmetics. *Nanomed Nanotechnol Biol Med* 6(4):570–574
- Kong LJ, Tedrow O, Chan YF, Zepp RG (2009) Light-initiated transformations of fullerene in aqueous media. *Environ Sci Technol* 43(24):9155–9160
- Krass H, Papastavrou G, Kurth DG (2002) Layer-by-layer self-assembly of a polyelectrolyte bearing metal ion coordination and electrostatic functionality. *Chem Mater* 15(1):196–203
- Kumar S, Aswal VK, Kohlbrecher J (2012) Size-dependent interaction of silica nanoparticles with different surfactants in aqueous solution. *Langmuir* 28(25):9288–9297
- Kurppa K, Jiang H, Szilvay GR, Nasibulin AG, Kauppinen EL, Linder MB (2007) Controlled hybrid nanostructures through protein-mediated noncovalent functionalization of carbon nanotube. *Angew Chem Int Ed* 46(34):6446–6449
- Lead JR, Wilkinson KJ (2006) Aquatic colloids and nanoparticles: current knowledge and future trends. *Environ Chem* 3(3):159–171
- Lee SB, Mitchell DT, Trofin L, Nevanen TK, Soderlund H, Martin CR (2002) Antibody-based bio-nanotube membranes for enantiomeric drug separations. *Science* 296(5576):2198–2200
- Lee J-S, Han MS, Mirkin CA (2007) Colorimetric detection of mercuric ion (Hg<sup>2+</sup>) in aqueous media using DNA-functionalized gold nanoparticles. *Angew Chem Int Ed* 46(22):4093–4096



- Leenheer JA, Wershaw RL, Reddy MM (1995) Strong-acid, carboxyl-group structures in fulvic acid from the Suwannee River, Georgia. 2. Major structures. *Environ Sci Technol* 29(2): 399–405
- Levard C, Reinsch BC, Michel FM, Oumahi C, Lowry GV, Brown GE Jr (2011) Sulfidation processes of PVP-coated silver nanoparticles in aqueous solution: impact on dissolution rate. *Environ Sci Technol* 45(12):5260–5266
- Levy DE, Horner AA, Solomon A (1981) Immunoglobulin-sulfated polysaccharide interactions. Binding of agarosectin and heparin by human IgG proteins. *J Exp Med* 153(4):883–896
- Li ZF, Ruckenstein E (2004) Water-soluble poly(acrylic acid) grafted luminescent silicon nanoparticles and their use as fluorescent biological staining labels. *Nano Lett* 4(8):1463–1467
- Li D, He Q, Cui Y, Li J (2007) Fabrication of pH-responsive nanocomposites of gold nanoparticles/poly (4-vinylpyridine). *Chem Mater* 19(3):412–417
- Li D, Lyon DY, Li Q, Alvarez PJJ (2008) Effect of soil sorption and aquatic natural organic matter on the antibacterial activity of a fullerene water suspension. *Environ Toxicol Chem* 27(9):1888–1894
- Li Z, Greden K, Alvarez PJJ, Gregory KB, Lowry GV (2010) Adsorbed polymer and NOM limits adhesion and toxicity of nano scale zerovalent iron to *E. coli*. *Environ Sci Technol* 44(9):3462–3467
- Li CX, Bolisetty S, Chaitanya K, Adamcik J, Mezzenga R (2013) Tunable carbon nanotube/protein core-shell nanoparticles with NIR- and enzymatic-responsive cytotoxicity. *Adv Mater* 25(7):1010–1015
- Liu T, Guo L, Tao Y, Wang Y, Wang W (1999) Synthesis and interfacial structure of nanoparticles  $\gamma$ -Fe<sub>2</sub>O<sub>3</sub> coated with surfactant DBS and CTAB. *Nanostruct Mater* 11(4):487–492
- Lodish H (2008) *Molecular cell biology*. Macmillan, London
- Lok C-N, Ho C-M, Chen R, He Q-Y, Yu W-Y, Sun H, Tam P-H, Chiu J-F, Che C-M (2007) Silver nanoparticles: partial oxidation and antibacterial activities. *J Biol Inorg Chem* 12(4): 527–534
- Louie SM, Phenrat T, Small MJ, Tilton RD, Lowry GV (2012) Parameter identifiability in application of soft particle electrokinetic theory to determine polymer and polyelectrolyte coating thicknesses on colloids. *Langmuir* 28(28):10334–10347
- Lourenco C, Teixeira M, Simões S, Gaspar R (1996) Steric stabilization of nanoparticles: size and surface properties. *Int J Pharm* 138(1):1–12
- Lowry GV, Gregory KB, Apte SC, Lead JR (2012a) Transformations of nanomaterials in the environment. *Environ Sci Technol* 46(13):6893–6899
- Lowry GV, Espinasse BP, Badireddy AR, Richardson CJ, Reinsch BC, Bryant LD, Bone AJ, Deonaraine A, Chae S, Therezien M, Colman BP, Hsu-Kim H, Bernhardt ES, Matson CW, Wiesner MR (2012b) Long-term transformation and fate of manufactured Ag nanoparticles in a simulated large scale freshwater emergent wetland. *Environ Sci Technol* 46(13):7027–7036
- Lu W, Senapati D, Wang S, Tovmachenko O, Singh AK, Yu H, Ray PC (2010) Effect of surface coating on the toxicity of silver nanomaterials on human skin keratinocytes. *Chem Phys Lett* 487(1–3):92–96
- Lundqvist M, Stigler J, Elia G, Lynch I, Cedervall T, Dawson KA (2008) Nanoparticle size and surface properties determine the protein corona with possible implications for biological impacts. *Proc Natl Acad Sci* 105(38):14265–14270
- Lynch I, Dawson KA (2008) Protein-nanoparticle interactions. *Nano Today* 3(1–2):40–47
- Ma H, Yin B, Wang S, Jiao Y, Pan W, Huang S, Chen S, Meng F (2004) Synthesis of silver and gold nanoparticles by a novel electrochemical method. *ChemPhysChem* 5(1):68–75
- Ma R, Levard C, Michel FM, Brown GE Jr, Lowry GV (2013) Sulfidation mechanism for zinc oxide nanoparticles and the effect of sulfidation on their solubility. *Environ Sci Technol* 47(6):2527–2534
- Mafune F, Kohno J-Y, Takeda Y, Kondow T, Sawabe H (2000) Formation and size control of silver nanoparticles by laser ablation in aqueous solution. *J Phys Chem B* 104(39):9111–9117

- Mafuné F, Kohno J-Y, Takeda Y, Kondow T, Sawabe H (2001) Formation of gold nanoparticles by laser ablation in aqueous solution of surfactant. *J Phys Chem B* 105(22):5114–5120
- Manzoori JL, Amjadi M, Hallaj T (2009) Preconcentration of trace cadmium and manganese using 1-(2-pyridylazo)-2-naphthol-modified TiO<sub>2</sub> nanoparticles and their determination by flame atomic absorption spectrometry. *Int J Environ Anal Chem* 89(8–12):749–758
- Martin JJ, Cardamone JM, Irwin PL, Brown EM (2011) Keratin capped silver nanoparticles—synthesis and characterization of a nanomaterial with desirable handling properties. *Colloids Surf B* 88(1):354–361
- Matarredona O, Rhoads H, Li ZR, Harwell JH, Balzano L, Resasco DE (2003) Dispersion of single-walled carbon nanotubes in aqueous solutions of the anionic surfactant NaDDBS. *J Phys Chem B* 107(48):13357–13367
- Mauter MS, Elimelech M (2008) Environmental applications of carbon-based nanomaterials. *Environ Sci Technol* 42(16):5843–5859
- McDevitt MR, Chattopadhyay D, Kappel BJ, Jaggi JS, Schiffman SR, Antczak C, Njardarson JT, Brentjens R, Scheinberg DA (2007) Tumor targeting with antibody-functionalized, radiolabeled carbon nanotubes. *J Nucl Med* 48(7):1180–1189
- Mehta S, Kumar S, Chaudhary S, Bhasin K (2009) Effect of cationic surfactant head groups on synthesis, growth and agglomeration behavior of ZnS nanoparticles. *Nanoscale Res Lett* 4(10):1197–1208
- Michalet X, Pinaud FF, Bentolila LA, Tsay JM, Doose S, Li JJ, Sundaresan G, Wu AM, Gambhir SS, Weiss S (2005) Quantum dots for live cells, in vivo imaging, and diagnostics. *Science* 307(5709):538–544
- Milani S, Bombelli FB, Pitek AS, Dawson KA, Radler J (2012) Reversible versus irreversible binding of transferrin to polystyrene nanoparticles: soft and hard corona. *ACS Nano* 6(3):2532–2541
- Moliner-Martínez Y, Cárdenas S, Simonet BM, Valcárcel M (2009) Recent developments in capillary EKC based on carbon nanoparticles. *Electrophoresis* 30(1):169–175
- Mudunkotuwa IA, Grassian VH (2010) Citric acid adsorption on TiO<sub>2</sub> nanoparticles in aqueous suspensions at acidic and circumneutral pH: surface coverage, surface speciation, and its impact on nanoparticle—nanoparticle interactions. *J Am Chem Soc* 132(42):14986–14994
- Mueller NC, Nowack B (2008) Exposure modeling of engineered nanoparticles in the environment. *Environ Sci Technol* 42(12):4447–4453
- Murphy CJ, Gole AM, Hunyadi SE, Stone JW, Sisco PN, Alkilany A, Kinard BE, Hankins P (2008) Chemical sensing and imaging with metallic nanorods. *Chem Commun* 5:544–557
- Natte K, Friedrich JF, Wohlrab S, Lutzki J, von Klitzing R, Österle W, Orts-Gil G (2013) Impact of polymer shell on the formation and time evolution of nanoparticle–protein corona. *Colloids Surf B* 104:213–220
- Nowack B, Ranville JF, Diamond S, Gallego-Urrea JA, Metcalfe C, Rose J, Horne N, Koelmans AA, Klaine SJ (2012) Potential scenarios for nanomaterial release and subsequent alteration in the environment. *Environ Toxicol Chem* 31(1):50–59
- Nozik AJ (2002) Quantum dot solar cells. *Physica E* 14(1–2):115–120
- Obata S, Honda K (2011) Dynamic behavior of carbon nanotube and bio/artificial surfactants complexes in an aqueous environment. *J Phys Chem C* 115(40):19659–19667
- O’Connell MJ, Bachilo SM, Huffman CB, Moore VC, Strano MS, Haroz EH, Rialon KL, Boul PJ, Noon WH, Kittrell C, Ma JP, Hauge RH, Weisman RB, Smalley RE (2002) Band gap fluorescence from individual single-walled carbon nanotubes. *Science* 297(5581):593–596
- Pallem VL, Stretz HA, Wells MJM (2009) Evaluating aggregation of gold nanoparticles and humic substances using fluorescence spectroscopy. *Environ Sci Technol* 43(19):7531–7535
- Pei XW, Hao JC, Liu WM (2007) Preparation and characterization of carbon nanotubes-polymer/Ag hybrid nanocomposites via surface RAFT polymerization. *J Phys Chem C* 111(7):2947–2952
- Phenrat T, Saleh N, Sirk K, Kim H-J, Tilton R, Lowry G (2008) Stabilization of aqueous nanoscale zerovalent iron dispersions by anionic polyelectrolytes: adsorbed anionic

- polyelectrolyte layer properties and their effect on aggregation and sedimentation. *J Nanopart Res* 10(5):795–814
- Phenrat T, Liu Y, Tilton RD, Lowry GV (2009a) Adsorbed polyelectrolyte coatings decrease Fe 0 nanoparticle reactivity with TCE in water: conceptual model and mechanisms. *Environ Sci Technol* 43(5):1507–1514
- Phenrat T, Long TC, Lowry GV, Veronesi B (2009b) Partial oxidation (“Aging”) and surface modification decrease the toxicity of nanosized zerovalent iron. *Environ Sci Technol* 43(1):195–200
- Pinna M, Hiltl S, Guo XH, Boker A, Zvelindovsky AV (2010) Block copolymer nanocontainers. *ACS Nano* 4(5):2845–2855
- Podila R, Chen R, Ke PC, Brown JM, Rao AM (2012) Effects of surface functional groups on the formation of nanoparticle-protein corona. *Appl Phys Lett* 101(26):263701–263704
- Prato M, Kostarelos K, Bianco A (2008) Functionalized carbon nanotubes in drug design and discovery. *Acc Chem Res* 41(1):60–68
- Prime KL, Whitesides GM (1993) Adsorption of proteins onto surfaces containing end-attached oligo(ethylene oxide): a model system using self-assembled monolayers. *J Am Chem Soc* 115(23):10714–10721
- Pumera M, Ambrosi A, Bonanni A, Chng ELK, Poh HL (2010) Graphene for electrochemical sensing and biosensing. *TrAC Trends Anal Chem* 29(9):954–965
- Qiu Y, Liu Y, Wang L, Xu L, Bai R, Ji Y, Wu X, Zhao Y, Li Y, Chen C (2010) Surface chemistry and aspect ratio mediated cellular uptake of Au nanorods. *Biomaterials* 31(30):7606–7619
- Rotureau E, Raynaud J, Choquet B, Marie E, Nouvel C, Six JL, Dellacherie E, Durand A (2008) Application of amphiphilic polysaccharides as stabilizers in direct and inverse free-radical miniemulsion polymerization. *Colloid Surf A* 331(1–2):84–90
- Safi M, Courtois J, Seigneuret M, Conjeaud H, Berret JF (2011) The effects of aggregation and protein corona on the cellular internalization of iron oxide nanoparticles. *Biomaterials* 32(35):9353–9363
- Saleh N, Phenrat T, Sirk K, Dufour B, Ok J, Sarbu T, Matyjaszewski K, Tilton RD, Lowry GV (2005) Adsorbed triblock copolymers deliver reactive iron nanoparticles to the oil/water interface. *Nano Lett* 5(12):2489–2494
- Saleh NB, Pfefferle LD, Elimelech M (2010) Influence of bio-macromolecules and humic acid on the aggregation kinetics of single-walled carbon nanotubes. *Environ Sci Technol* 44(7):2412–2418
- Salkar R, Jeevanandam P, Kataby G, Aruna S, Koltypin Y, Palchik O, Gedanken A (2000) Elongated copper nanoparticles coated with a zwitterionic surfactant. *J Phys Chem B* 104(5):893–897
- Santra S, Tapeç R, Theodoropoulou N, Dobson J, Hebard A, Tan WH (2001) Synthesis and characterization of silica-coated iron oxide nanoparticles in microemulsion: the effect of nonionic surfactants. *Langmuir* 17(10):2900–2906
- Sapsford KE, Algar WR, Berti L, Gemmill KB, Casey BJ, Oh E, Stewart MH, Medintz IL (2013) Functionalizing nanoparticles with biological molecules: developing chemistries that facilitate nanotechnology. *Chem Rev* 113(3):1904–2074
- Satulovsky J, Carignano MA, Szeleifer I (2000) Kinetic and thermodynamic control of protein adsorption. *Proc Natl Acad Sci USA* 97(16):9037–9041
- Sau TK, Murphy CJ (2005) Self-assembly patterns formed upon solvent evaporation of aqueous cetyltrimethylammonium bromide-coated gold nanoparticles of various shapes. *Langmuir* 21(7):2923–2929
- Schwierz F (2010) Graphene transistors. *Nat Nanotechnol* 5(7):487–496
- Shenoy DB, Amiji MA (2005) Poly(ethylene oxide)-modified poly(epsilon-caprolactone) nanoparticles for targeted delivery of tamoxifen in breast cancer. *Int J Pharm* 293(1–2):261–270
- Shoultz-Wilson WA, Reinsch BC, Tsyusko OV, Bertsch PM, Lowry GV, Unrine JM (2011) Effect of silver nanoparticle surface coating on bioaccumulation and reproductive toxicity in earthworms (*Eisenia fetida*). *Nanotoxicology* 5(3):432–444

- Sinani VA, Koktysh DS, Yun B-G, Matts RL, Pappas TC, Motamedi M, Thomas SN, Kotov NA (2003) Collagen coating promotes biocompatibility of semiconductor nanoparticles in stratified LBL films. *Nano Lett* 3(9):1177–1182
- Smith B, Wepasnick K, Schrote KE, Cho H-H, Ball WP, Fairbrother DH (2009) Influence of surface oxides on the colloidal stability of multi-walled carbon nanotubes: a structure-property relationship. *Langmuir* 25(17):9767–9776
- So HM, Won K, Kim YH, Kim BK, Ryu BH, Na PS, Kim H, Lee JO (2005) Single-walled carbon nanotube biosensors using aptamers as molecular recognition elements. *J Am Chem Soc* 127(34):11906–11907
- Solís D, Viguera-Santiago E, Hernández-López S, Gómez-Cortés A, Aguilar-Franco M, Camacho-López MA (2008) Textural, structural and electrical properties of TiO<sub>2</sub> nanoparticles using Brij 35 and P123 as surfactants. *Sci Technol Adv Mater* 9(2):025003
- Sperling R, Parak W (1915) Surface modification, functionalization and bio-conjugation of colloidal inorganic nanoparticles. *Philos Trans R Soc A* 2010(368):1333–1383
- Stevenson FJ (1994) Humus chemistry: genesis, composition, reactions. John Wiley and Sons, Hoboken
- Suresh AK, Pelletier DA, Doktycz MJ (2013) Relating nanomaterial properties and microbial toxicity. *Nanoscale* 5(2):463–474
- Szleifer I, Carignano MA (2000) Tethered polymer layers: phase transitions and reduction of protein adsorption. *Macromol Rapid Commun* 21(8):423–448
- Tan SJ, Jana NR, Gao S, Patra PK, Ying JY (2010) Surface-ligand-dependent cellular interaction, subcellular localization, and cytotoxicity of polymer-coated quantum dots. *Chem Mater* 22(7):2239–2247
- Tejamaya M, Römer I, Merrifield RC, Lead JR (2012) Stability of citrate, PVP, and PEG coated silver nanoparticles in ecotoxicology media. *Environ Sci Technol* 46(13):7011–7017
- Thompson BC, Frechet JMJ (2008) Organic photovoltaics—polymer-fullerene composite solar cells. *Angew Chem Int Ed* 47(1):58–77
- Tian Y, Fendler JH (1996) Langmuir-blodgett film formation from fluorescence-activated, surfactant-capped, size-selected CdS nanoparticles spread on water surfaces. *Chem Mater* 8(4):969–974
- Tian ZR, Voigt JA, Liu J, Mckenzie B, Mcdermott MJ, Rodriguez MA, Konishi H, Xu H (2003) Complex and oriented ZnO nanostructures. *Nat Mater* 2(12):821–826
- Tian Y, Gao B, Silvera-Batista C, Ziegler KJ (2010) Transport of engineered nanoparticles in saturated porous media. *J Nanopart Res* 12(7):2371–2380
- Todorović Marković B, Jakanović V, Jovanović S, Kleut D, Dramićanin M, Marković Z (2009) Surface chemical modification of fullerene by mechanochemical treatment. *Appl Surf Sci* 255(17):7537–7541
- Treuel L, Malissek M, Grass S, Diendorf J, Mahl D, Meyer-Zaika W, Epple M (2012) Quantifying the influence of polymer coatings on the serum albumin corona formation around silver and gold nanoparticles. *J Nanopart Res* 14(9):1–12
- Tsai CS (2007) Bio-macromolecules: introduction to structure, function and informatics. John Wiley and Sons, Hoboken
- Tsujii Y, Ohno K, Yamamoto S, Goto A, Fukuda T (2006) Structure and Properties of high-density polymer brushes prepared by surface-initiated living radical polymerization. In Jordan R (ed) *Surface-initiated polymerization I*, vol 197. Springer, Heidelberg, pp 1–45
- Unrine JM, Colman BP, Bone AJ, Gondikas AP, Matson CW (2012) Biotic and abiotic interactions in aquatic microcosms determine fate and toxicity of Ag nanoparticles. Part 1, aggregation and dissolution. *Environ Sci Technol* 46(13):6915–6924
- Usrey ML, Strano MS (2009) Controlling single-walled carbon nanotube surface adsorption with covalent and noncovalent functionalization. *J Phys Chem C* 113(28):12443–12453
- Vaisman L, Marom G, Wagner HD (2006a) Dispersions of surface-modified carbon nanotubes in water-soluble and water-insoluble polymers. *Adv Funct Mater* 16(3):357–363
- Vaisman L, Wagner HD, Marom G (2006b) The role of surfactants in dispersion of carbon nanotubes. *Adv Colloid Interface Sci* 128:37–46

- Vargas A, Shnitko I, Teleki A, Weyeneth S, Pratsinis SE, Baiker A (2011) Structural dependence of the efficiency of functionalization of silica-coated FeOx magnetic nanoparticles studied by ATR-IR. *Appl Surf Sci* 257(7):2861–2869
- Weiseh O, Gunn JW, Zhang M (2010) Design and fabrication of magnetic nanoparticles for targeted drug delivery and imaging. *Adv Drug Deliv Rev* 62(3):284–304
- Wang W, Singh S, Zeng DL, King K, Nema S (2007) Antibody structure, instability, and formulation. *J Pharm Sci* 96(1):1–26
- Willner I, Baron R, Willner B (2007) Integrated nanoparticle-biomolecule systems for biosensing and bioelectronics. *Biosens Bioelectron* 22(9–10):1841–1852
- Xu ZX, Hu CY, Hu GX (2011) Layer-by-layer self-assembly of multilayer films based on humic acid. *Thin Solid Films* 519(13):4324–4328
- Yang P, Meng XF, Zhang ZY, Jing BX, Yuan J, Yang WT (2005) Thickness measurement of nanoscale polymer layer on polymer substrates by attenuated total reflection infrared spectroscopy. *Anal Chem* 77(4):1068–1074
- Yeganeh B, Kull CM, Hull MS, Marr LC (2008) Characterization of airborne particles during production of carbonaceous nanomaterials. *Environ Sci Technol* 42(12):4600–4606
- Zhang W, Yao Y, Sullivan N, Chen Y (2011) Modeling the primary size effects of citrate-coated silver nanoparticles on their ion release kinetics. *Environ Sci Technol* 45(10):4422–4428
- Zhang Z, Zhang J, Zhang BL, Tang JL (2013) Mussel-inspired functionalization of graphene for synthesizing Ag-polydopamine-graphene nanosheets as antibacterial materials. *Nanoscale* 5(1):118–123
- Zhao XL, Shi YL, Ca YQ, Mou SF (2008) Cetyltrimethylammonium bromide-coated magnetic nanoparticles for the preconcentration of phenolic compounds from environmental water samples. *Environ Sci Technol* 42(4):1201–1206
- Zheng M, Jagota A, Semke ED, Diner BA, McLean RS, Lustig SR, Richardson RE, Tassi NG (2003) DNA-assisted dispersion and separation of carbon nanotubes. *Nat Mater* 2(5):338–342
- Zook J, Long S, Cleveland D, Geronimo C, MacCuspie R (2011) Measuring silver nanoparticle dissolution in complex biological and environmental matrices using UV–visible absorbance. *Anal Bioanal Chem* 401(6):1993–2002

# Chapter 10

## Mimicking Biomineral Systems: What have we Achieved and Where do we go from Here?

James J. De Yoreo

**Abstract** Biomimetic synthesis of inorganic crystals and composites has evolved dramatically since its inception. Advances in our understanding of matrix organization, templated nucleation, pathways of mineral formation via disordered precursor phases, mesocrystal formation, and the control of crystal shape have been paralleled by synthetic approaches to exploiting these discoveries. Resolution of current controversies concerning the early stages of nucleation and the mechanisms underlying both particle mediated crystal growth and matrix-directed nucleation will set the stage for further advances in the technology of biomimetic synthesis.

### 10.1 Introduction

The remarkable level of complexity and high level of function seen in biological systems has inspired a vast range of technologies, both mature and emerging. Examples range from sensors based on the architecture of cell membranes to self-assembling polymeric matrices that serve as scaffolds for tissue engineering. The landscape is far too large to summarize in a single paper. Consequently, here I focus on a single region of that landscape, namely biomimetic materials synthesis, which in itself constitutes an extensive field. Starting from the early work of Weiner, Addadi, Mann, and others (Weiner and Hood 1975; Addadi and Weiner 1985; Mann 1988), the realization that mimicking the ability of living systems to make hard materials would require a means to control both nucleation and crystal growth was abundantly clear. Moreover, achieving the unique properties of biominerals would depend upon the extent to which hierarchical organization

---

J. J. De Yoreo (✉)

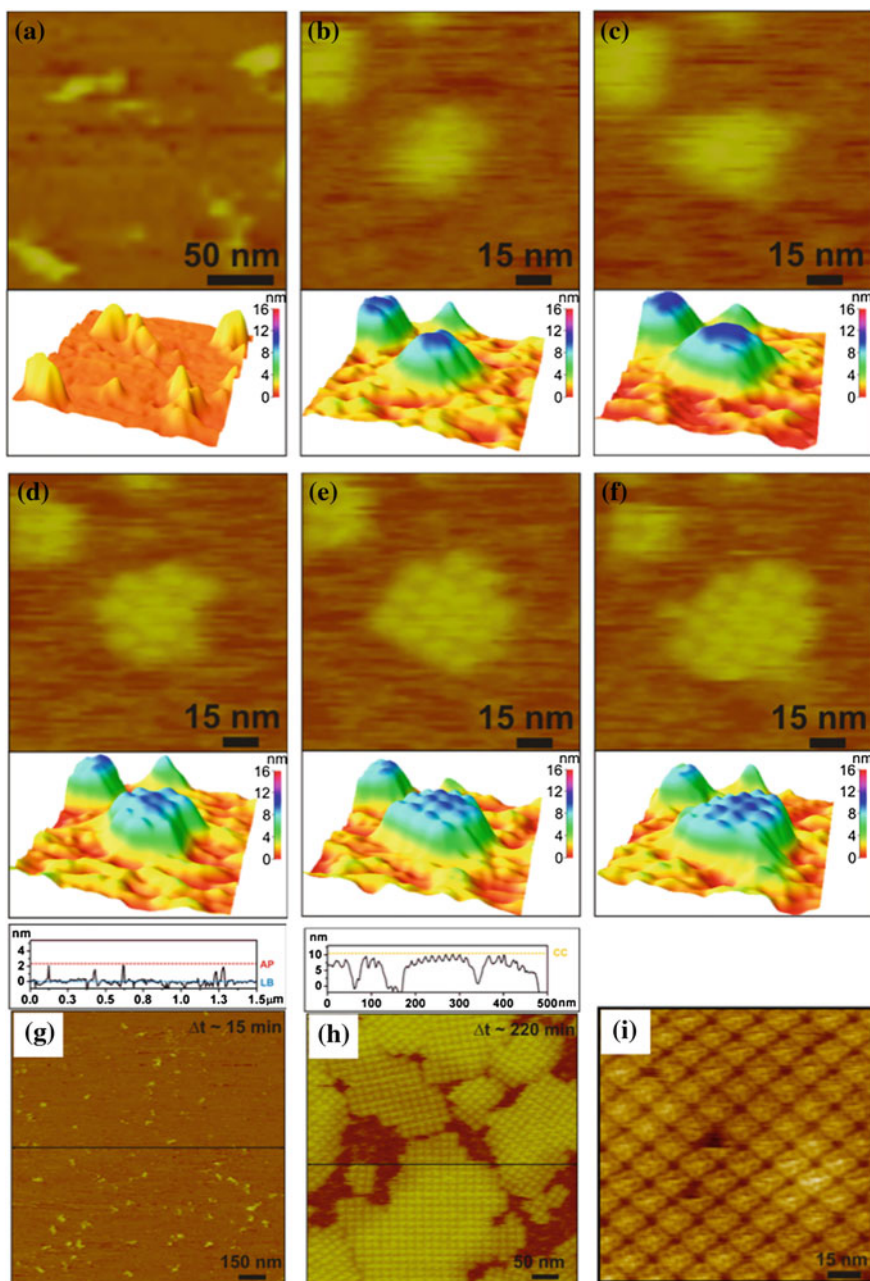
Physical Sciences Division, Pacific Northwest National Laboratory,  
Richland, WA 99352, USA

e-mail: James.DeYoreo@pnnl.gov

could be introduced (Mann 1993). Composites like bone illustrate the many levels of control from assembly of the collagen scaffold, to direction of initial hydroxyapatite (HAp) formation in terms of both spatial distribution and orientation, to control over the aspect ratio of the growing HAp platelets (Weiner et al. 1999; Landis et al. 1996). The common coalignment and precise location of crystal elements in biominerals (Mann 1993), and the isolation of acidic proteins from many carbonate biominerals (Berman et al. 1988) led researchers to exploit insoluble organic templates to direct nucleation (Berman et al. 1995) and introduce highly charged soluble polymers to control crystal shape (Albeck et al. 1996). However, the later discovery of amorphous precursor phases in immature biomineral structures (Beniash et al. 1997), the underlying nanoparticulate substructure of many single crystal biomineral elements (Addadi et al. 2006; Gong et al. 2012), and the realization that the stable phase of nanoparticles often differs from that of the bulk (Navrotsky 2004), led to a major change in the predominant view of how living systems make hard materials. This new knowledge, combined with the creation of polymer induced liquid precursors to calcium carbonate in the laboratory (Gower and Odom 2000), the development of the mesocrystal concept (Cölfen and Mann 2003), identification of clusters in supersaturated solutions prior to formation of solid precipitates (Gebauer and Cölfen 2008), and the prediction of polymeric and liquid-like states in the pure calcium carbonate solutions (Wallace et al. 2013), opened new approaches to biomimetic materials synthesis. Despite these advances, major questions about mineral nucleation, the role of organic matrices and soluble proteins, and the structure of solutions prior to nucleation are matters of intense debate. Moreover, the problem of how living systems create the macromolecular matrix, which is itself a highly organized structure and is the key to formation and properties of biocomposites, has barely been addressed. The purpose of this paper is, first, to highlight some of the advances made in both biomimetic approaches to synthesis based on our understanding of biomineral formation and second, frame the issues that are the key to further progress.

## 10.2 Matrix Organization

For biocomposites like bone, proper matrix organization is a requirement for tissue formation and function. *In vitro* investigations into protein assembly into extended ordered matrices have revealed an auto-catalyzed process by which proteins first aggregate into unstructured precursors out of which order emerges through reorganization and conformational transformation (Fig. 10.1) (Chung et al. 2010; Shin et al. 2012). As the first domains become ordered, the rate of new additions to the growing matrix increases nonlinearly, reflecting the greater ease of establishing the necessary specific bonds when the correctly organized matrix is presented to the incoming protein. This pathway of assembly through transient states of disorder or partial order is reminiscent of the dynamics seen in the related case of folding by an individual protein (Fig. 10.2). Often the proteins that comprise





◀**Fig. 10.1** Two-step pathway of protein matrix assembly illustrated by microbial membrane “S-layer” proteins. (a–f) Sequential *in situ* AFM height images and surface plots showing (a) S-layer adsorption onto a lipid bi-layer, followed by (b–c) condensation into amorphous or liquid-like clusters (d) transformation into an ordered domain of tetrameric units, and (e–f) subsequent growth through tetramer addition. (g, h) *In situ* AFM images and height profiles showing (g) initially adsorbed proteins and (h) fully crystalline clusters. Height profiles were measured along the horizontal black lines in each image and are labeled to denote the heights of the lipid bilayer (LB), adsorbed proteins (APs), and crystalline clusters (CCs). (i) A highly resolved image from mature CC reveals the tetrameric arrangement and submolecular details (Reproduced from De Yoreo et al. 2013)

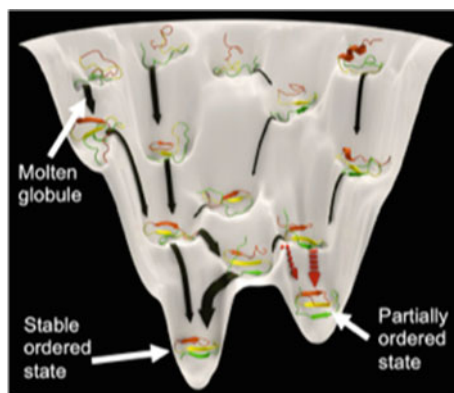


**Fig. 10.2** Adoption of protein folding funnel to description of protein matrix self-assembly showing unfolded, molten globule, partially ordered state, and fully ordered state. Barriers to forming partially ordered and fully ordered state from molten globule are small, but barriers to transformation from partially ordered to fully ordered states are large (Reproduced from De Yoreo et al. 2013)

mineral scaffolds contain hydrophobic and hydrophilic domains, which presumably aids in driving assembly, just as in the extreme case of block copolymers and other synthetic amphiphiles (Hartgerink 2001).

Numerous approaches to mimicking protein matrices have been pursued. Amphiphilic peptides have been used to create cylindrical micelles presenting charged groups to the surrounding solution to induce formation of calcium phosphates (Fig. 10.3) (Hartgerink 2001). Synthetic amphiphiles that form spherical micelles with acidic outer surfaces have been shown to bind to growing calcite crystals, become incorporated, and induce a high level of fracture toughness (Fig. 10.4) (Kim et al. 2011). Growth of calcite in hydrogels produces a similar result (Li et al. 2009). Small synthetic proteins exhibiting helical conformations with coil-to-coil binding have been developed for self-assembly into extended networks (Fletcher et al. 2013). Protein-like molecules called peptoids, which are polymer chains constructed from *n*-substituted glycines exhibiting high side chain diversity, have been shown to assemble into both sheets and helical ribbons (Fig. 10.5) (Nam et al. 2010). Viral capsids of the M13 bacterial phage, which are

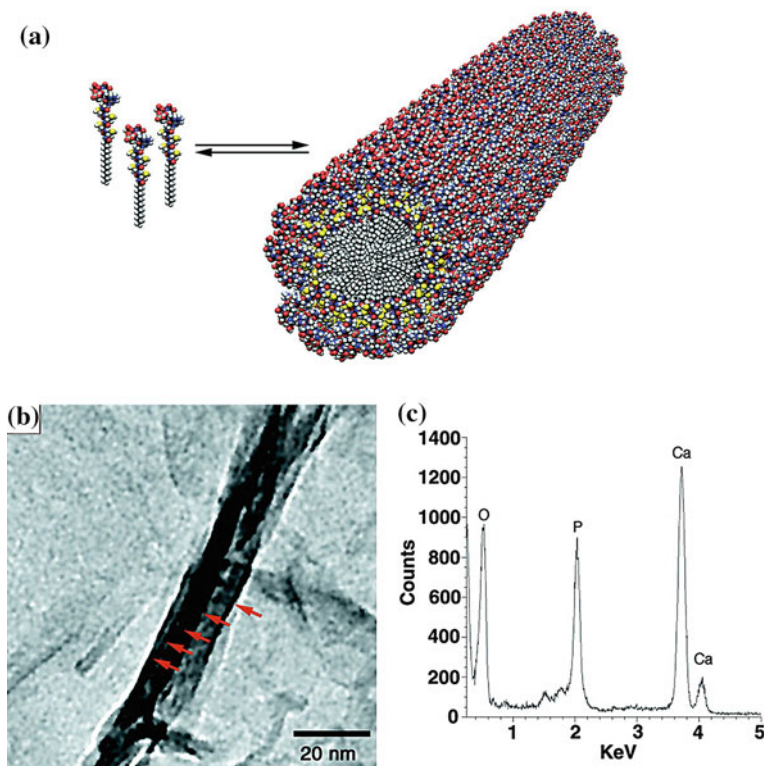
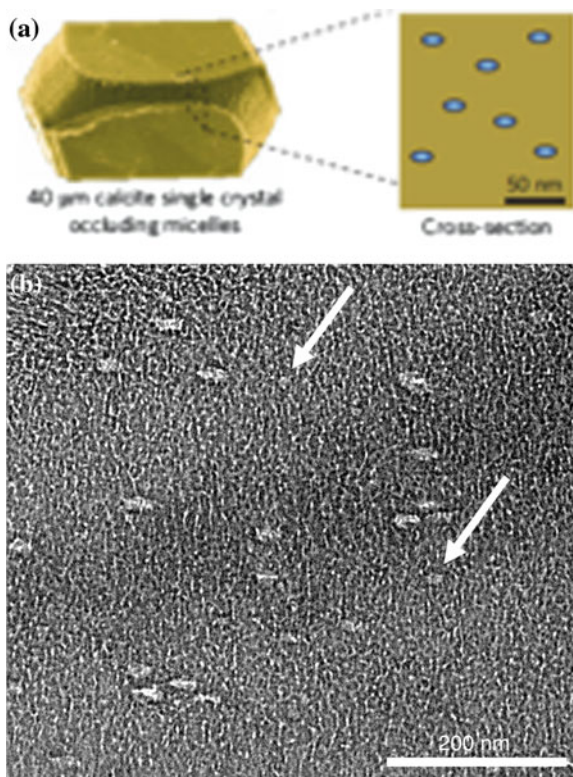


**Fig. 10.3** Self-assembly and mineralization of peptide-amphiphiles (PA) consisting of a long alkyl tail that conveys hydrophobic character to the molecule and a peptide headgroup. (a) Molecular model of PA and its self-assembly into a cylindrical micelle. Color scheme: C, black; H, white; O, red; N, blue; P, cyan; S, yellow. (b) TEM micrograph of the unstained, cross-linked peptide-amphiphile fibers incubated for 30 min in  $\text{CaCl}_2$  and  $\text{Na}_2\text{HPO}_4$  solution. Mature HA crystals (red arrows) completely cover the PA fibers. (c) EDS profile of mineral crystals after 30 min of incubation reveals a Ca/P ratio of 1.67, as expected for HA (Adopted from Hartgerink et al. 2001)

typically employed in phage display (see Sect. 10.3) (Whaley et al. 2000), can exhibit the behavior of liquid crystals and organize into layered structures, sometimes with a helical arrangement (Chung et al. 2011a). Because the coat proteins of the phage can be selected for their ability to form mineral phases, they have been successfully used to create highly organized composites (Chung et al. 2011a). Perhaps the ultimate self-assembling biomimetic matrix is DNA origami, which can be designed to assemble into virtually any pattern deterministically (Fig. 10.6) (Rothmund 2006), though its use as a matrix for mineralization has not been explored.

**Fig. 10.4** Schematic diagram of the encapsulation of copolymer micelles within calcite single crystals and TEM image of PSPMA30–PDPA47 copolymer micelles subsequent to incorporation in a calcite crystal as seen in a thin section cut through the nanocomposite crystal. The incorporation results in deformation of the micelles from spherical to ellipsoidal, producing a strain gradient that strengthens the crystal (Adopted from Kim et al. 2011)



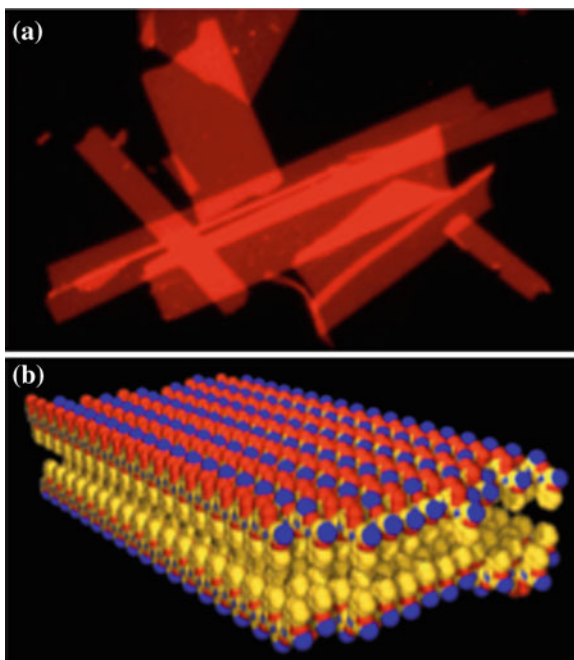
### 10.3 Directing Nucleation

Use of an organic matrix to direct nucleation has emerged as a widespread strategy in biomimetic crystallization. The conventional wisdom is that living systems create natural biocomposites like bone and dentin by exploiting interactions between the matrix and either solution-phase solutes or disordered, liquid-like, or amorphous precursor phases to control where, when, and with what crystallographic orientation crystallization of the matrix will occur. Regardless of the pathway, mineralization of the organic matrix requires the creation of a supersaturated state at least locally, whether on the matrix itself or inside a vesicle designed to deliver a precursor phase to the matrix. In both cases, nucleation of the crystalline phase is likely to be inhibited where and when it is undesirable. In fact, for sparingly soluble mineral phases like calcite and hydroxyapatite, the barrier to homogeneous nucleation is enormous (Fig. 10.7) (Hu et al. 2012). Consequently, once a supersaturation is created that is sufficient to drive nucleation, many polymorphs or other closely related phases become potential metastable products of nucleation. This is clearly demonstrated by the calcium carbonate system where titration experiments (Fig. 10.8a) show that a gradual but continual increase in

**Fig. 10.5** Two-dimensional crystalline sheets formed from two oppositely charged peptoid polymers: a negatively charged periodic amphiphilic peptoid (Nce–Npe)18, and a positively charged periodic amphiphilic peptoid (Nae–Npe)18.

**a** Fluorescent optical microscope image of individual sheets.

**b** Molecular model of the sheets assembled in which the hydrophobic groups face each other in the interior of the sheet and oppositely charged hydrophilic groups are alternating and surface-exposed. Atomic color scheme: carbon, *yellow*; nitrogen, *blue*; oxygen, *red* (Adopted from Nam et al. 2010)



supersaturation leads to nucleation well-above the solubility limit of all crystalline phases and that the first solid product is amorphous (Gebauer et al. 2008). Hence, both suppression of spurious homogeneous nucleation and enhancement of matrix-directed nucleation can be an important in both natural and biomimetic matrix-mineral composites.

Many soluble organic molecules are known to inhibit nucleation (Gebauer and Cölfen 2011). Examples include citrate and polyaspartate, which can be viewed as a mimic of naturally occurring biomineral-associated proteins, because these proteins commonly contain a large fraction of aspartic (or glutamic) acid residues (Addadi and Weiner 1985). These inhibitors can greatly extend induction times at constant supersaturation, as well as the  $\text{Ca}^{2+}$  concentration required to cause spontaneous nucleation during continual increase of supersaturation (Fig. 10.8b). Conversely, the presence of an insoluble organic matrix can enhance nucleation rates even at relatively low values of supersaturation (Hu et al. 2012; Habraken et al. 2013), control the orientation of the nucleus (Han and Aizenberg 2003), and drive formation of stable crystalline phases at concentrations below the solubility limit of less stable crystalline or amorphous phases (Hu et al. 2012).

While the underlying source of inhibition is still unclear—ignoring the obvious effect of ion complexation, which should be accounted for in estimating the supersaturation—the mechanism of enhancement has been clarified in recent years (Hu et al. 2012; Habraken et al. 2013; Giuffrè et al. 2013; Hamm et al. 2013). Formation of a heterogeneous nucleus (Fig. 10.9a) is aided by the decrease in

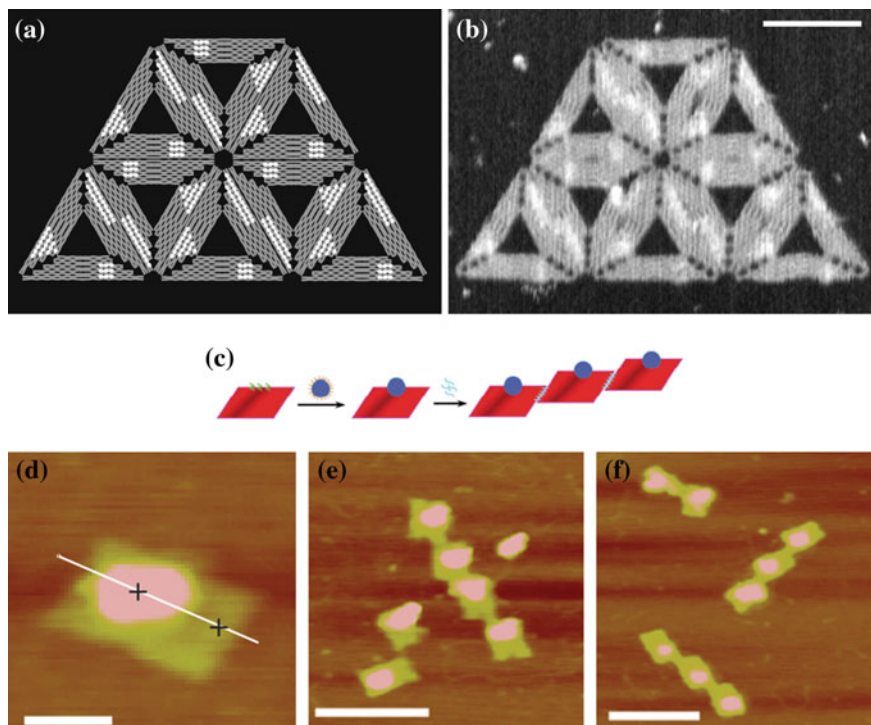
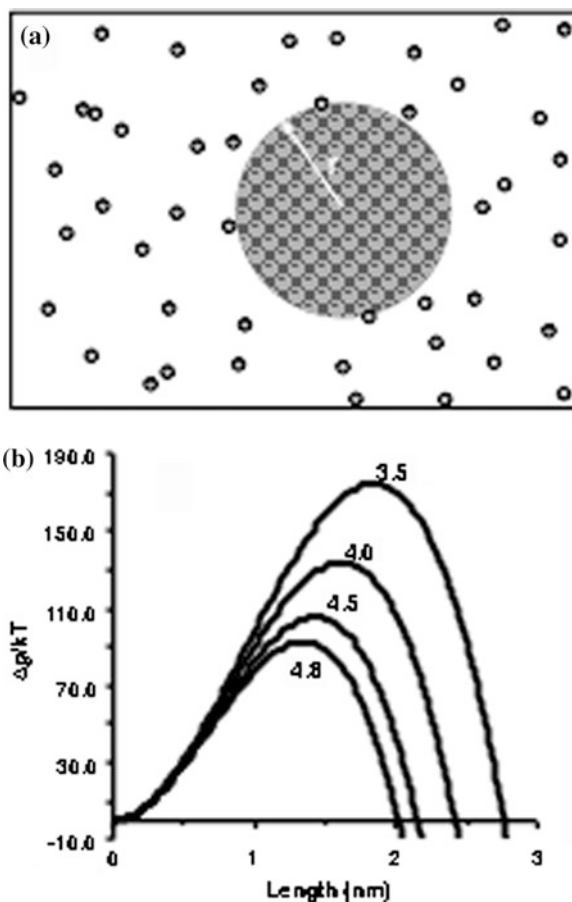


**Fig. 10.6** **a** Model of DNA origami and **b** AFM image of resulting origami tile. **c** Schematic showing linking of DNA-functionalized viral capsid to a DNA origami tile, as well as linking together of individual tile. **d–f** Realization of scheme in **c**. Scale bars: **b**—100 nm; **e**—50 nm; **d**, **e**—200 nm (**a**, **b** adopted from Rothemund 2006. **c–f**, adopted from Stephanopoulos et al. 2010)

interfacial energy brought about by the favorable interaction of the matrix with the mineral (De Yoreo and Vekilov 2003). Because the interfacial energy enters into the classical expression for the nucleation rate as a cubic term in an exponential, even small changes can have a dramatic impact on rates. Formation of calcite on self-assembled monolayers (SAMs) provides the classic example of matrix-directed—or templated—nucleation (Fig. 10.9b, c) (Aizenberg et al. 1999). Even for the same headgroup chemistry, the choice of a SAM monomer with an odd or even number of carbons in the alkyl chain influences both the crystallographic orientation of the nuclei (Fig. 10.9b, c) (Han and Aizenberg 2003) and their rate of formation (Fig. 10.9d) ((Hu et al. 2012). In the case of carboxyl terminated SAMs, the underlying source of the difference between the odd and even SAMs reveals a secondary, subtle aspect of templating (Freeman et al. 2013). The orientation of the SAM headgroups influences the degree to which the SAM monomers repel one another and, consequently, the average degree of order in the SAM. The terminating oxygen ions of the even SAM lie along a line parallel to the SAM surface,

**Fig. 10.7** **a** Formation of a spherical nucleus of radius  $r$  from a solution. **b** Classical dependence of free energy  $\Delta g$  on the length  $L$  of one side of an equilateral calcite rhombohedron for homogeneous nucleation from solutions formed from equal mixtures of  $\text{CaCl}_2$  and  $\text{NaHCO}_3$  for the indicated values of supersaturation  $\sigma$ . The corresponding final  $\text{Ca}^{2+}$  concentrations from top to bottom are: 10 mM; 15 mM; 23 mM; 28 mM (Reproduced from: **a**—De Yoreo and Vekilov 2003 and **b**—Hu et al. 2012)



while those of the odd SAM have an average orientation along a line tilted with respect to the SAM surface. This results in repulsive oxygen–oxygen interactions that periodically force one of the SAM monomers out of the pseudohexagonal arrangement seen in the even SAM. This element of disorder increases the interfacial energy with the forming calcite nucleus and, hence, reduces the nucleation rate and the degree of control over orientation.

Perhaps the most important technological approach to achieving template-directed nucleation is that of phage display (Whaley et al. 2000). The essential element of the technique is the exposure of a large library of M13 bacteriophage phenotypes to inorganic substrates of metals, semiconductors, or insulators. When the phage are cyclically cultured and eluted under increasingly harsh conditions, the peptides selected that bind most strongly to the substrate come to dominate the population. Subsequent genomic sequencing of these strong binders leads to identification of peptide sequences that can then be produced through synthetic

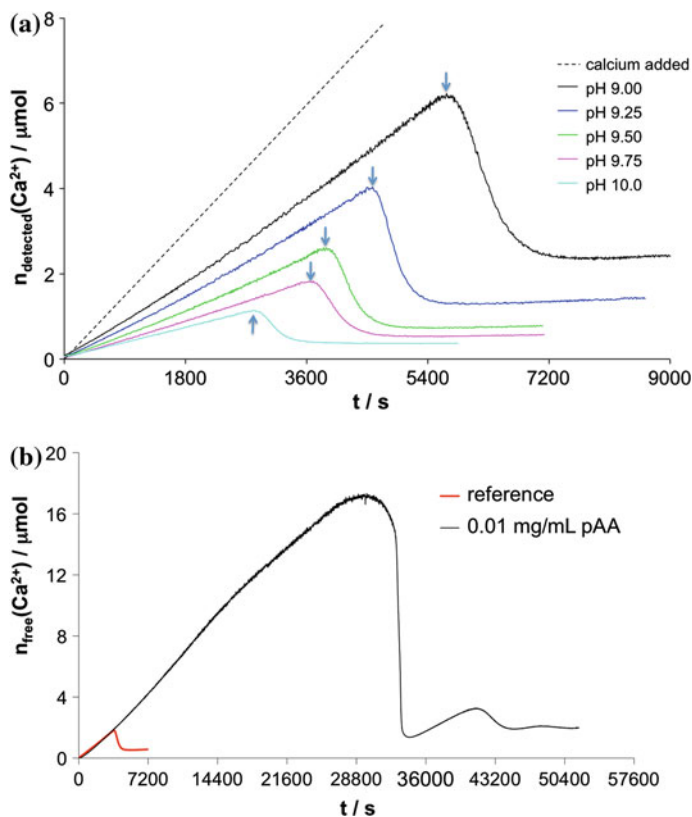


**Fig. 10.8** **a** Free calcium in 25 mL 10 mM carbonate buffer in a range between pH 9.00 and pH 10.0 during addition of 10 mM calcium chloride solution at a constant rate of 10  $\mu\text{L}/\text{min}$ . Arrows indicate the time of nucleation of calcium carbonate. **b** Time-developments of the free calcium amount in presence of poly(acrylic acid) (PAA), as compared to the PAA-free control at pH 9.75, showing large delay in the time of the nucleation event (Reproduced from Gebauer and Cölfen 2011)

means. In numerous cases, researchers have shown that these peptides can then be used to drive nucleation of the inorganic phase from aqueous precursors (Fig. 10.10) (Mao et al. 2004). Moreover, because these peptides can be patterned on substrates using micro-contact printing or nanolithographic techniques, they have numerous potential applications including bottom-up fabrication of nano-electronic circuitry, plasmonic devices, and tissue engineering.

The essential principle that underlies the use of phage display for discovery of nucleation templates can be simply stated: good binders are good nucleators. Why this statement is true was recently revealed in a careful study of nucleation rates and binding free energies for calcite on functionalized SAMs (Fig. 10.11) (Hamm et al. 2013). The key to the mechanistic link between binding and nucleation lies once again in the interfacial free energy. When the bond between an organic matrix and a

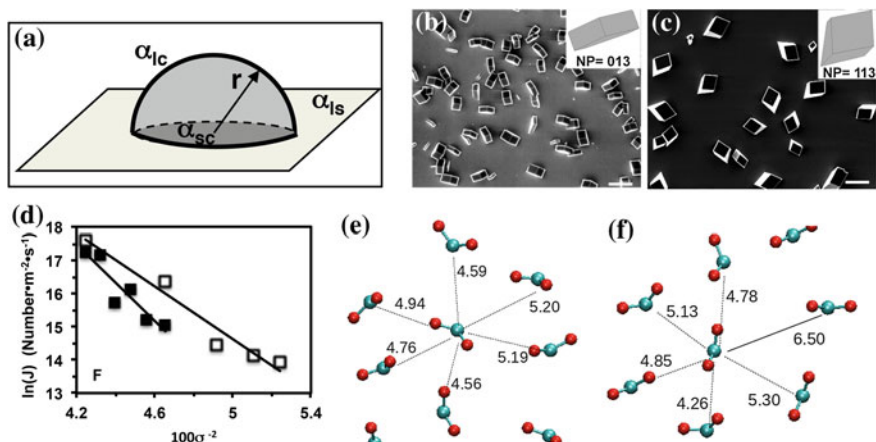


**Fig. 10.9** **a** Heterogeneous formation of a hemispherical nucleus at a foreign substrate. The interfacial free energies for the crystal-fluid, crystal-substrate and fluid-substrate interfaces are  $\alpha_{c-f}$ ,  $\alpha_{c-s}$ , and  $\alpha_{f-s}$ , respectively. **b** and **c** SEM micrographs of calcite crystals grown on carboxylate-functionalized self-assembled monolayers of **b** C<sub>15</sub>-Au, and **c** C<sub>10</sub>-Au. Scale bars: 20  $\mu\text{m}$ . Insets show computer simulations of similarly oriented calcite rhombohedra with the nucleating planes (NP) indicated. **d** Natural logarithm of the calcite nucleation rate  $J$  versus inverse supersaturation on even (mercaptohexadecanoic acid, MHA) and odd (mercaptoundecanethiol, MUA) SAMs. Shallower slope for the MHA film shows that interfacial energy is lower than for the MUA film. **e** and **f** Snapshot from simulations demonstrating different arrangement of headgroups as viewed from above the surface of **e** even and **f** odd carboxyl terminated SAMs. The nearest neighbor C–C separations are indicated with a dotted line while the increased separation between two carbons in the odd SAM is highlighted as a *solid line* (Reproduced from: **a**—De Yoreo and Vekilov 2003; **b**, **c**—Han and Aizenberg 2003; and **d**, **e**, **f**—Hu et al. 2012)

crystal face is ruptured, the change in free energy is given by the contact area times and the difference between the interfacial free energy of the final state minus that of the initial state. The interfacial energy of final state consists of a sum of the substrate-solution and crystal solution interfacial free energies, while that of the initial state consists of the crystal-substrate interfacial free energy. However, considering Fig. 10.9, one can see that these same terms enter into the net interfacial free energy of the heterogeneous nucleus. In fact, the free energy of binding should be proportional to the interfacial free energy of the heterogeneous nucleus, as indeed was shown to be the case for calcite on self assembled monolayers. The inevitable conclusion is that, indeed, good binders are good nucleators.

## 10.4 Stabilizing Disordered Phases

One of the lessons to emerge over the past decade or more is that living systems often use amorphous precursors to build complex biomineral structures (Beniash et al. 1997; Politi et al. 2004; Mahamid et al. 2008; Tao et al. 2009). However,



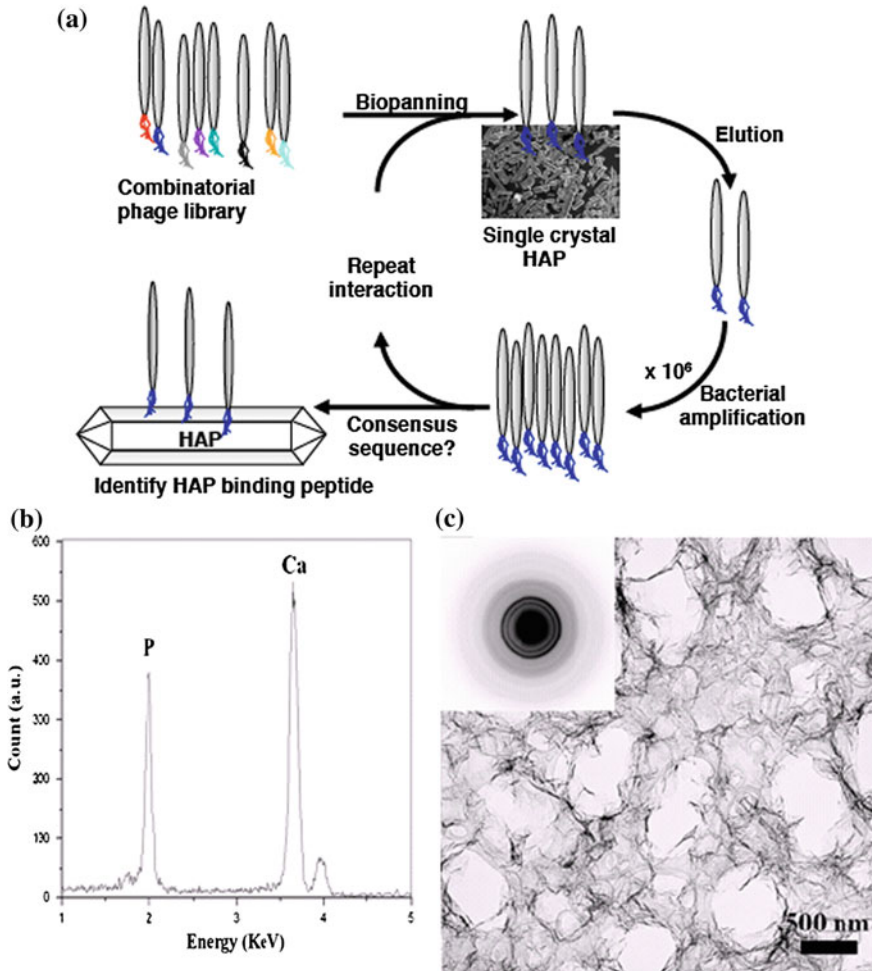


**Fig. 10.10** **a** Schematic diagram of the phage display process for discovery of peptides that bind to single-crystal HAP. **b** EDS spectrum with a Ca/P ratio of 1.67. **c** SEM micrograph of HAP crystals nucleated on a Au substrate using a peptide (CLP12) selected by phage display (Adopted from Chung et al. 2011b)

amorphous states of typical biominerals such as calcium carbonate or calcium phosphate are highly unstable when in contact with an aqueous phase and, hence, stabilization is critical until such time as transformation is required. A beautiful study of the stabilization and transformation process was performed on a land crustacean often referred to as the pill bug (Tao et al. 2009). The shell of the pill bug utilizes an interplay between the effects of Mg and aspartic acid-rich proteins to maintain an initial ACC phase that, over time, is transformed into a calcitic phase as the protein-to-Mg level increases (Fig. 10.12). While the use of

**Fig. 10.11** Interfacial energies ( $\alpha$ ) derived from nucleation rate measurements vs. free energies of binding ( $\Delta G_{ba}$ ) in units of  $kT$  for alkanethiol SAM molecules on calcite (104) surfaces as measured by dynamic force spectroscopy. Lower  $\alpha$  correlates with strong calcite-SAM interactions (large  $\Delta G_{ba}$ ) (Reproduced from Hamm et al. 2013)

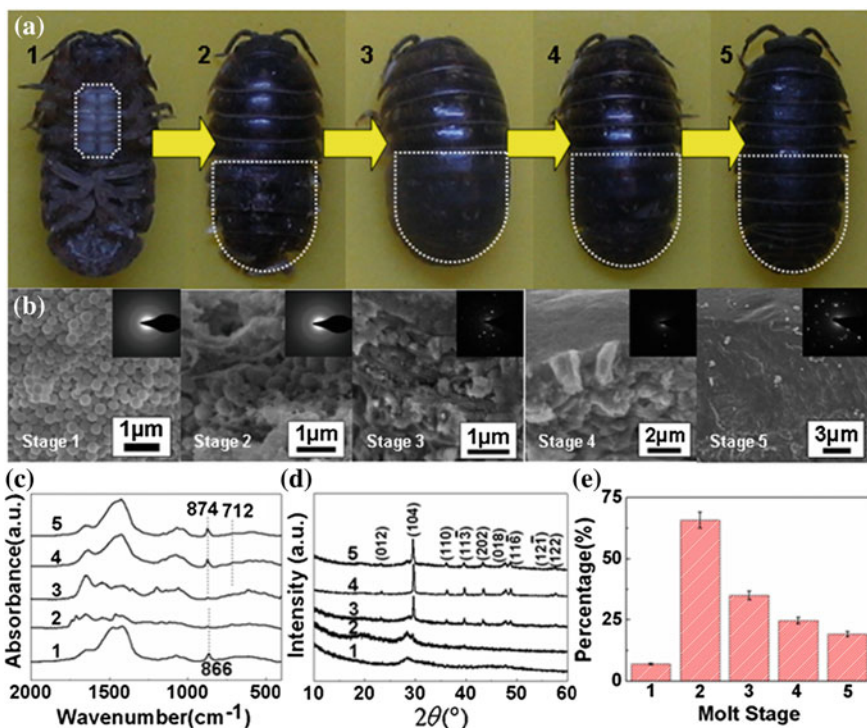
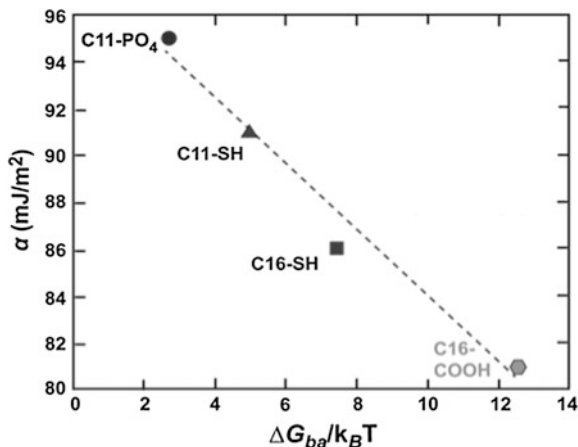


**Fig. 10.12** Morphology, phase, and composition of cuticles at different molt stages. **a** Photographs of *Armadillidium vulgare* in the different molt states (1–5). **b** SEM images and SAED patterns of the cross-sections of exocuticle layer in **a** showing initial amorphous nanoparticle stage and transformation to crystalline calcite. **c** and **d** XRD patterns and FT-IR spectra, respectively, documenting transformation from amorphous calcium carbonate to calcite. **e** Organic contents of the cuticles during the molt process showing the increase in aspartic acid rich protein with the onset of crystallization. Not shown is the high Mg content, which stabilizes the initial amorphous phase (Reproduced from Tao et al. 2009)

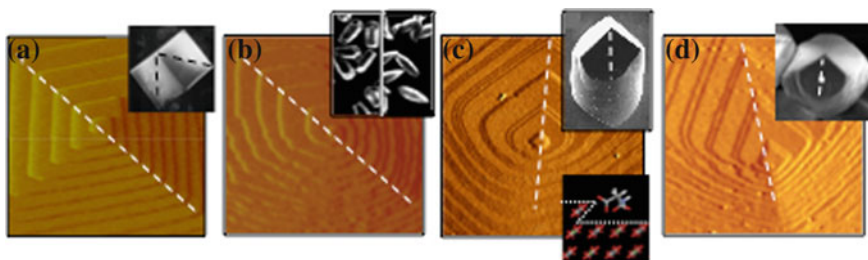


**Fig. 10.13** Change in crystal habit is directly related to modification of step morphology on natural crystal faces for a wide range of modifiers. **a–d** show AFM images of growth hillocks and SEM images of crystal habits. **a** pure calcite; **b** calcite plus  $\text{Mg}^{2+}$ ; **c** calcite plus D-aspartic acid; **d** calcite plus 8kD protein extracted from Abalone. Dashed lines show glide and mirror planes on calcite. **c** also shows minimum energy configuration for D-aspartic acid binding to acute step on calcite (104) face as predicted from molecular simulations (Reproduced from De Yoreo and Dove 2004)

amorphous precursors that can be triggered to transform into crystalline phases has not been widely adopted, the advantages of doing so in terms of building complex 3D architectures (Aizenberg et al. 2003) seems likely to drive future applications of this approach.

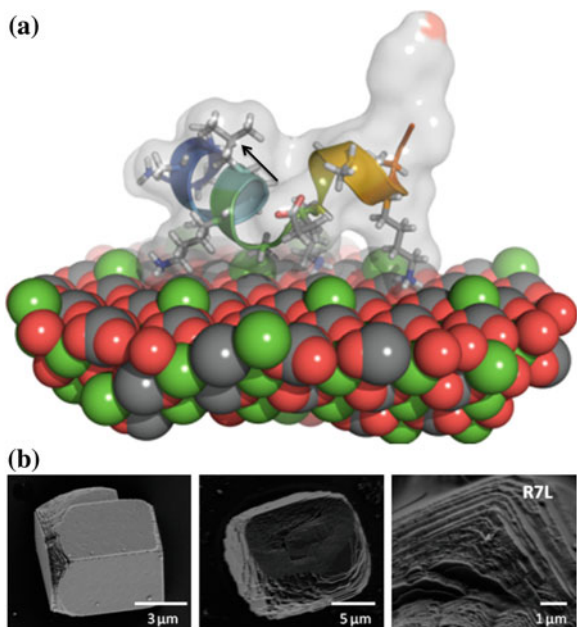
## 10.5 Controlling Crystal Shape

While many natural systems clearly utilize precursor materials that can be molded to create intricate 3D architectures, there are numerous examples that indicate growth of natural biominerals can also occur via traditional crystal growth mechanisms involving relatively flat crystal facets (See references in De Yoreo et al. 2007). Even in cases where the ultrastructure indicates formation occurs through an initial phase of nanoparticle aggregation or random matrix mineralization, the final shape often suggests a phase of single crystal growth and/or relaxation to a final faceted single crystal-like morphology (Mann 2001). In these cases, shape control emanates from the degree to which soluble organic molecules interact with atomic steps and terraces on crystal surfaces (De Yoreo and Dove 2004; De Yoreo et al. 2007). In essence, due to the self-replicating nature of crystal growth, the shape of the “so-called” growth hillock, where atomic steps are created at screw dislocations, is transferred into the shape of the facet and, eventually, the entire crystal (Fig. 10.13). The key to the observed control over shape is the strength and step-specificity of binding between the soluble organic molecules and the crystal (Fig. 10.13). Molecules that bind strongly to steps on a crystal face and block addition of solute ions to kinks, inhibit growth of that face, and thereby modify the overall crystal shape.

Determining whether a peptide or other organic molecule will bind to a particular face or step and modify crystal shape is a challenging endeavor without a

**Fig. 10.14 a** Representative low-energy molecular model characteristic of the observed motifs in secondary structure for the R7L peptide selected from de novo models for its ability to bind to the calcite (001) face. Arrows indicate mutation positions.

**b** Representative SEM images for calcite crystals grown in the presence of R7L (Reproduced from Schrier et al. 2011)



firm theoretical foundation. Nonetheless, recent work involving the Rosetta algorithm for calculation of equilibrium binding energies of peptide sequences to crystal faces has been used to identify sequences that might provide control over the kinetics of growth on a particular face and hence the final crystal shape (Schrier et al. 2011) (Fig. 10.14).

A related but purely synthetic approach to controlling growth kinetics and crystal shape that was recently reported relies on the side chain diversity of peptoids, the *n*-substituted glycine polymers described in the Sect. 10.2. Peptoids have been shown to exhibit dramatic levels of growth-rate acceleration and inhibition, as well as shape modification (Fig. 10.15) (Chen et al. 2011). As biomimetic materials technologies moves towards easily designed and synthesized polymers as substitutes for proteins, the use of high information content polymers such as peptoids will likely become increasingly more important.

## 10.6 Biomimetic Composites

Many—if not most—biominerals, even those that diffract as single crystals, are composites that exhibit an underlying nanoparticulate ultrastructure (Fig. 10.16). In some cases, the organic matrix is a predominant component of the composite, as in the case of bone (Landis et al. 1996; Weiner et al. 1999). However in other cases, an explicit insoluble matrix is missing, but there is some evidence for an

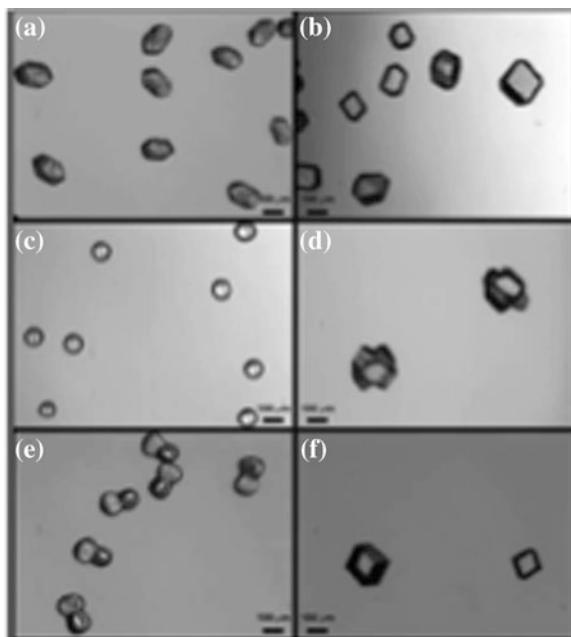


**Fig. 10.15** a–e Morphology of  $\text{CaCO}_3$  crystals grown in the presence of six different carboxyl-rich peptoids. f Morphology of peptoid-free control (Reproduced from Chen et al. 2011)

organic-rich region at the boundaries of the nanoparticle building blocks (Addadi et al. 2006; Gong et al. 2012). Thus these composites are “mesocrystals”, i.e., crystalline materials that diffract as single crystals but are, in fact, composed of nanoparticulate building blocks attached at organic-rich boundaries. Since the original mesocrystal concept was introduced (Cölfen and Mann 2003), many researchers have explored methods for growing them synthetically through the introduction of polyelectrolyte additives to growth solutions (Cölfen and Antonietti 2008 and references within). While in some cases, TEM images of distinct building blocks provide strong evidence for a mesocrystalline structure, more often, the characteristics used to conclude that the final products are indeed mesocrystals typically constitute indirect evidence. These characteristics include a rough, nanoparticulate-like surface, high porosity, and a pseudofaceted morphology. Nonetheless, the mesocrystal concept and the observation of a mesocrystalline nature in a number of biominerals have fueled efforts to develop synthetic approaches to producing mesocrystalline composites.

Development of artificial insoluble matrices as scaffolds for composite formation have also constituted a significant effort within the biomimetic synthesis community. One striking example that brings together crystal binding, functional selection, and surface templating comes from the technology of phage display (Fig. 10.17). Here, the inherent ability of M13 phage to form liquid crystalline

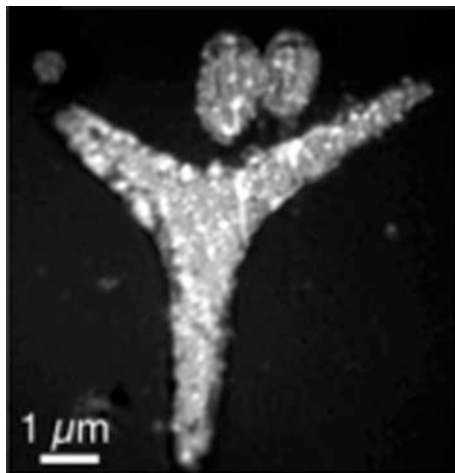


**Fig. 10.16** Component mapping of a 48-h old sea urchin spicules analyzed within 24 h of extraction from the embryo. Image shows XANES-PEEM image of three spicules embedded in epoxy, polished to expose a cross-section, and coated. The image is an average of all 121 images acquired across the Ca L-edge. The larger triradiate portion of a spicule at the center is polished in plane, whereas two other cylindrical spicules at the top have their long axes perpendicular to the plane of the image. The images reveal the mesocrystalline nature of the spicule through the percentage of the three calcium carbonate phases observed in each pixel of the image (Reproduced from Gong et al. 2012)

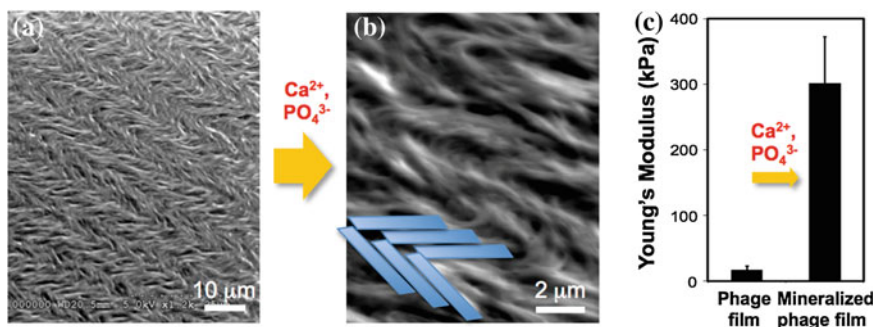


**Fig. 10.17** Growth of biomimetic soft/hard composite using self-assembly and template mineralization of M13 phage. **a** SEM image of self-assembled smectic helical phage film before biomineralization. **b** SEM image of the hard-tissue-like composite material following mineralization of the phage film in  $\text{Ca}^{2+}$  and  $\text{PO}_4^{3-}$  solutions. Blue overlay shows zig-zag structure of the composite, indicating that the hierarchical structures were preserved after biomineralization. **c** Increase in the Young's modulus of the phage films (about 20-fold) after biomineralization (Adopted from Chung et al. 2011a)

phases (Lee et al. 2002) was exploited to develop a 3D matrix, while the selection of the phage phenotype based on high binding affinity to the crystalline phase was used to create an effective crystallization template (Chung et al. 2011b). The result

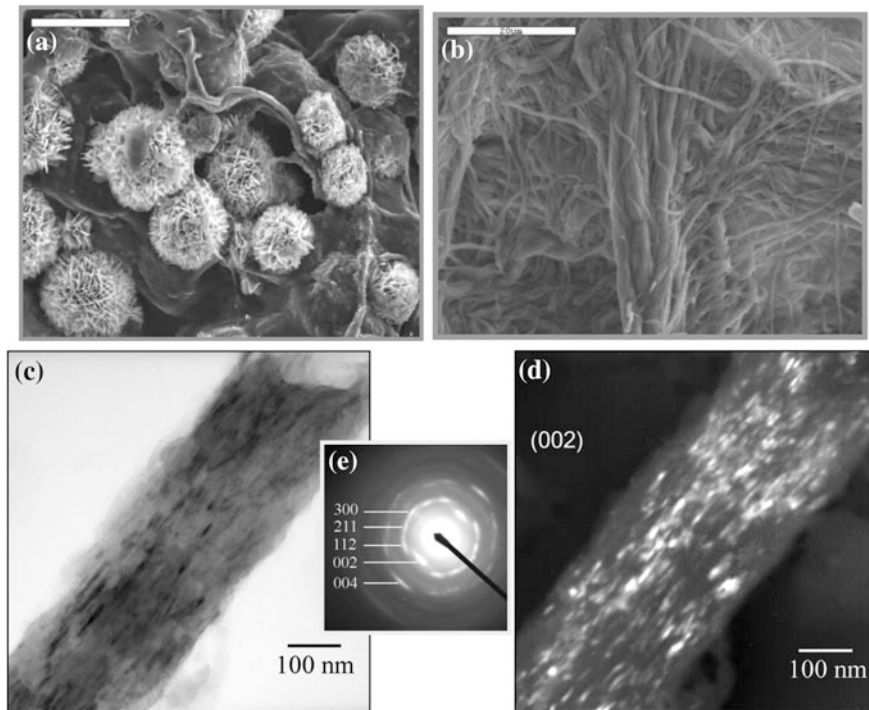


**Fig. 10.18** Intrafibrillar mineralization of type-I collagen scaffolds using the PILP process. **a** The control reaction, without polymer, leads to random spherulitic clusters of hydroxyapatite on the surface of the collagen fibrils, typical of the many reports in the literature. At the relatively high ion concentrations used, an amorphous CaP gel does form in the solution (which become cloudy), but this type of ACP does not lead to infiltration of the fibrils. **b** With the addition of polyaspartate, the collagen becomes well infiltrated with mineral, but no apparent clusters are seen on the surface. (EDS, XRD, and TGA all show a very high degree of mineralization with up to 70 wt % hydroxyapatite, as in bone). **c** After mineralization, thick dark crystallites can be seen in the TEM of this fibril. **d** Dark-field TEM of the same fibril, using the (002) reflection, shows the prevalence of oriented crystallites within the fibril. **e** Selected area electron diffraction of this fibril shows the crystallites are uniaxially oriented in the [001] direction, roughly parallel to the collagen fibril axis, with similar degrees of tilting and rotation disorder, as in bone (Adopted from Gower 2008)

is a true highly organized, organic–inorganic composite that mimics the hierarchical structure of biocomposites like bone.

An increasingly important discovery of relevance to creating biomimetic composites is that of the polymer-induced liquid precursor phase (PILP) (Gower and Odom 2000). Though initially discovered in the calcium carbonate system through its deposition on flat substrates, its utility in the creation of biomimetic composites was best demonstrated through the mineralization of collagen sponges and reconstituted collagen fibrils by calcium phosphate-based PILP (Fig. 10.18) (Olszta et al. 2007; Gower 2008). PILP appears able to readily infiltrate into dense

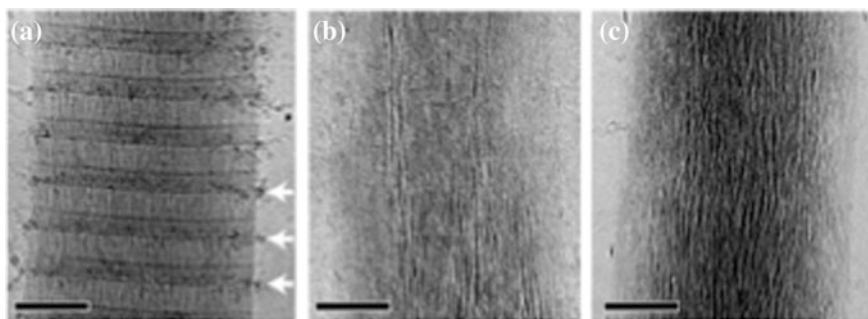


**Fig. 10.19** CryoTEM images of collagen at different stages of mineralization in the presence of  $10 \mu\text{g ml}^{-1}$  of polyAspartate. Mineralization was for **a** 24 h **b** 48 h, and **c** 72 h. Scale bars: 100 nm (Reproduced from Nudelman et al. 2010)

collagen scaffolds, coat the individual fibrils and then crystallize into coaligned HAp crystallites. This inferred pathway closely resembles the process seen subsequently in cryoEM experiments on collagen mineralization (Fig. 10.19) (Nudelman et al. 2010), though the latter did not come to a conclusion concerning the liquid-like character of the infiltrating mineral phase.

## 10.7 Future Directions

The most important aspect of biomineralization and biomimetic synthesis to emerge over the past decade or so is that of pathway. The importance of multi-step pathways, both in matrix organization and crystal formation is now irrefutable. However, there is still a great deal of controversy surrounding both the nature of the initial phases and the mechanisms by which they arise and transform. The experimental observation of clusters in calcium carbonate solutions prior to the nucleation event (Gebauer et al. 2008; Pouget et al. 2009; Habraken et al. 2013) has led to the idea that there is no true nucleation event in the classical sense, rather stable prenucleation clusters aggregate to form an amorphous precursor phase that then transforms into the crystalline solid through a dehydration reaction. However, formation of the bulk mineral phase in these experiments was observed at concentrations far in excess of the solubility of all calcium carbonate phases and molecular dynamics simulations suggest, under those conditions, the solutions undergo a barrier-less phase separation via spinodal decomposition that produces a dense liquid phase (Wallace et al. 2013), even without the addition of polymer to produce PILP (Gower and Odom 2000). In that scenario, broad distributions of clusters of many sizes, both large and small are expected as the spinodal is approached. Moreover, a number of studies of heterogeneous nucleation reported trends that are explained well by purely classical models and appear to produce calcite directly (Hu et al. 2012; Giuffrè et al. 2013; Hamm et al. 2013). Because many



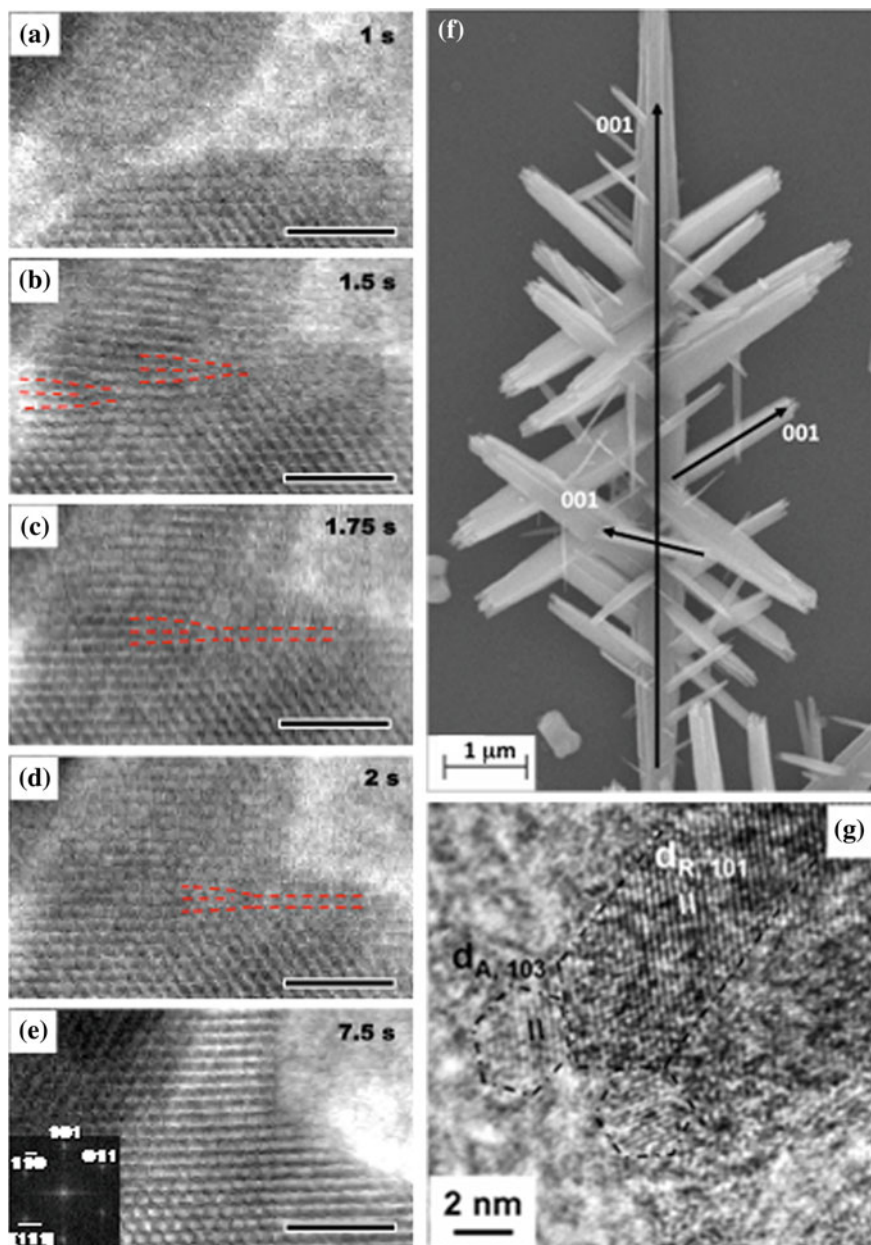


**Fig. 10.20** a–e Sequence of in situ TEM images showing oriented attachment of two ferrihydrite nanoparticles. Two edge dislocations denoted by the *dashed lines* translate to the right, leaving a defect-free structure in e. Scale bars are 2 nm. f, g Ex situ TEM images showing mature  $\text{TiO}_2$  branched nanowire and oriented attachment event of anatase nanoparticle to main branch of rutile nanowire during early stage of growth (Adopted from a–e Li et al. 2012 and f–g Li et al. 2013)

biominerals are composites in which the mineral forms in intimate contact with an organic matrix, heterogeneous nucleation may be commonplace. Thus perhaps the dynamics of homogeneous nucleation, whether via aggregation of stable prenucleation clusters or dense liquid phase droplets from spinodal decomposition are unimportant in the context biocomposites. Consequently, future progress in mimicking biomineral systems depends on our ability to sort out the role of these unexpected species and phases, as well as the role of the matrix in directing their formation or transformation.

Finally, the conclusion that many biominerals form through aggregation of nanoparticles (Addadi et al. 2006; Gong et al. 2012), whether amorphous, partially ordered, or fully crystalline, as well as the general observation of aggregation-based pathways in nanomaterials synthesis ((Penn and Banfield 1998; Banfield et al. 2000; Cölfen and Antonietti 2008; Zhang et al. 2010), has highlighted the critical role played by particle mediated growth (PMG) in defining crystal forms (Fig. 10.20). While ion-by-ion addition to both particles and their aggregates must play a role in growth when growth occurs in a supersaturated solution environment, numerous experiments show that particle addition can be dominant (Fig. 10.20a). Moreover, the complex, highly branched shapes that can result when a aggregation events occur through oriented attachment (OA) (Fig. 10.20b) (Li et al. 2012, 2013) highlight the technological value in developing a quantitative description of this type of growth. Once the underlying mechanisms of PMG and OA in are well understood, the pathways of nucleation are clearly defined, and the role of the matrix in directing these processes is firmly established, a predictive science of biomimetic synthesis will be within reach.

## References

- Addadi L, Weiner S (1985) Interactions between acidic proteins and crystals: stereochemical requirements in biomineralization. *Proc Nat Acad of Sci USA* 82:4110–4114
- Addadi L, Joester D, Nudelman F, Weiner S (2006) Mollusk shell formation: a source of new concepts for understanding biomineralization processes. *Chem Eur J* 12:980–987
- Albeck S, Weiner S, Addadi L (1996) Polysaccharides of intracrystalline glycoproteins modulate calcite crystal growth in vitro. *Chem Eur J* 2:278–284
- Aizenberg J, Black AJ, Whitesides GM (1999) Control of crystal nucleation by patterned self-assembled monolayers. *Nature* 398:495–498
- Aizenberg J, Muller DA, Graul JL, Hamann DR (2003) Direct fabrication of large micropatterned single crystals. *Science* 299:1205–1208
- Banfield JF, Welch SA, Zhang HZ, Ebert TT, Penn RL (2000) Aggregation-based crystal growth and microstructure development in natural iron oxyhydroxide biomineralization products. *Science* 289:751–754
- Beniash E, Aizenberg J, Addadi L, Weiner S (1997) Amorphous calcium carbonate transforms into calcite during sea urchin larval spicule growth. *Proc Royal Soc London B: Biol Sci* 264:461–465
- Berman A, Addadi L, Weiner S (1988) Interactions of sea-urchin skeleton macromolecules with growing calcite crystals—a study of intracrystalline proteins. *Nature* 331:546–548

- Berman A, Ahn DJ, Lio A, Salmeron M, Reichert A, Charych D (1995) Total alignment of calcite at acidic polydiacetylene films: cooperativity at the organic-inorganic interface. *Science* 269:515–518
- Chen C-L, Qi J, Zuckermann RN, DeYoreo JJ (2011) Engineered biomimetic polymers as tunable agents for controlling CaCO<sub>3</sub> mineralization. *J Am Chem Soc Commun* 133:5214–5217
- Chung S, Shin SH, Bertozzi CR, De Yoreo JJ (2010) Self-catalyzed growth of S layers via an amorphous to-crystalline transition limited by folding kinetics. *Proc Natl Acad Sci USA* 107:16536–16541
- Chung W-J, Oh J-W, Kwak K et al (2011a) Biomimetic self-templating supramolecular structures. *Nature* 478:364–368
- Chung W-J, Kwon K-Y, Song J, Lee SW (2011b) Evolutionary screening of collagen-like peptides that nucleate hydroxyapatite crystals. *Langmuir* 27:7620–7628
- Cölfen H, Mann S (2003) Higher-order organization by mesoscale self-assembly and transformation of hybrid nanostructures. *Angew Chem Int Ed* 42:2350–2365
- Cölfen H, Antonietti M (2008) Mesocrystals and nonclassical crystallization. Wiley, Chichester
- De Yoreo JJ, Vekilov P (2003) Principles of crystal nucleation and growth. In: Dove PM, De Yoreo JJ, Weiner S (eds) *Biomimetalization reviews in mineralogy and geochemistry*, vol 54. Mineralogical Society of America, Washington, pp 57–93
- De Yoreo JJ, Dove PM (2004) Shaping crystals with biomolecules. *Science* 306:1301–1302
- De Yoreo JJ, Wierzbicki A, Dove PM (2007) New insights into mechanisms of biomolecular control on growth of inorganic crystals. *CrysEngComm* 9:1144–1152
- De Yoreo JJ, Chung S, Friddle RW (2013) In situ AFM as a tool for investigating interactions and assembly dynamics in biomolecular and biomineral systems. *Adv Func Mat* 23:2525–2538
- Fletcher JM, Harniman RL, Frederick RH et al (2013) Self-assembling cages from coiled-coil peptide modules. *Science* 340:595–599
- Freeman CL, Hu Q, Nielsen MH, Tao J, De Yoreo JJ, Harding JH (2013) Surface selectivity of calcite on self-assembled monolayers. *J Phys Chem C* 117:5154–5163
- Gebauer D, Volkel A, Cölfen H (2008) Stable prenucleation calcium carbonate clusters. *Science* 322:1819–1822
- Gebauer D, Cölfen H (2011) Prenucleation clusters and non-classical nucleation. *Nanotoday* 6:564–584
- Giuffrè AJ, Hamm LM, Han N, De Yoreo JJ, Dove PM (2013) Polysaccharide chemistry regulates kinetics of calcite nucleation through competition of interfacial energies. *Proc Natl Acad Sci USA* 110:9261–9266
- Gong YUT, Killian CE, Olson IC et al (2012) Phase transitions in biogenic amorphous calcium carbonate. *Proc Natl Acad Sci USA* 109:6088–6093
- Gower LB, Odom DJ (2000) Deposition of calcium carbonate films by a polymer-induced liquid-precursor (PILP) process. *J Cryst Growth* 210:719–734
- Gower LB (2008) Biomimetic model systems for investigating the amorphous precursor pathway and its role in biomineralization. *Chem Rev* 108:4551–4627
- Habraken WJEM et al (2013) Ion-association complexes unite classical and non-classical theories for the biomimetic nucleation of calcium phosphate. *Nat Commun* 4:1507
- Hamm LM, Giuffrè AJ, Han N, De Yoreo JJ, Dove PM (2013) Reconciling disparate views of template-directed nucleation through measurement of calcite nucleation kinetics and binding energies. (Submitted)
- Han Y J, and Aizenberg J (2003) Face-selective nucleation of calcite on self-assembled monolayers of alkanethiols: effect of the parity of the alkyl chain. *Angew Chem Int Ed* 42:3668–3670
- Hartgerink JD, Beniash E, Stupp SI (2001) Self-assembly and mineralization of peptide-amphiphile nanofibers. *Science* 294:1684–1688
- Hu Q, Nielsen MH, Freeman CL, Hamm LM et al (2012) The thermodynamics of calcite nucleation: classical vs. non-classical pathways. *Faraday Disc* 159:509–523
- Kim Y-Y, Ganesan K, Yang P et al (2011) An artificial biomineral formed by incorporation of copolymer micelles in calcite crystals. *Nat Mater* 10:890–896

- Landis WJ, Hodgens KJ, Arena J, Song MJ, McEwen BF (1996) Structural relations between collagen and mineral in bone as determined by high voltage electron microscopic tomography. *Microsc Res Tech* 33:192–202
- Lee S-W, Mao C, Flynn CE, Belcher AM (2002) Ordering of quantum dots using genetically engineered viruses. *Science* 296:892–895
- Li H, Xin HL, Muller DA, Estroff LA (2009) Visualizing the 3D internal structure of calcite single crystals grown in agarose hydrogels. *Science* 326:1244–1247
- Li D, Nielsen MH, Lee JRI, Frandsen C, Banfield JF, De Yoreo JJ (2012) Direction-specific interactions control crystal growth by oriented attachment. *Science* 336:1014–1018
- Li D, Soberanis F, Fu J, Hou W, Wu J, Kisailus D (2013) Growth mechanism of highly branched titanium dioxide nanowires via oriented attachment. *Cryst Growth Des* 13:422–428
- Mahamid J, Sharir A, Addadi L, Weiner S (2008) Amorphous calcium phosphate is a major component of the forming fin bones of zebrafish: Indications for an amorphous precursor phase. *Proc Nat Acad Sci USA* 105:12748–12753
- Mann S (1988) Molecular recognition in biomineralization. *Nature* 332:119–124
- Mann S (1993) Molecular tectonics in biomineralization and biomimetic materials chemistry. *Nature* 365:499–505
- Mann S (2001) *Biomineralization: principles and concepts in bioinorganic materials chemistry*. Oxford University Press, Oxford 198 pp
- Mao C et al (2004) Virus-based toolkit for the directed synthesis of magnetic and semiconducting nanowires. *Science* 303:213–217
- Nam K-T, Shelby SA, Choi PH et al (2010) Free-floating ultrathin two-dimensional crystals from sequence-specific peptoid polymers. *Nat Mater* 9:454–460
- Navrotsky A (2004) Energetic clues to pathways to biomineralization: precursors, clusters, and nanoparticles. *Proc Nat Acad Sci USA* 101:12096–12101
- Nudelman F, Pieterse K, George A et al (2010) The role of collagen in bone apatite formation in the presence of hydroxyapatite nucleation inhibitors. *Nat Mater* 9:1004–1009
- Olszta MJ, Cheng X, Jee SS et al (2007) Bone structure and formation: a new perspective. *Mat Sci Eng R* 58:77–116
- Penn RL, Banfield JF (1998) Imperfect oriented attachment: dislocation generation in defect-free nanocrystals. *Science* 281:969–971
- Politi Y, Arad T, Klein E, Weiner S, Addadi L (2004) Sea urchin spine calcite forms via a transient amorphous calcium carbonate phase. *Science* 306:1161–1164
- Pouget EM, Bomans PHH, Goos JACM, Frederik PM, De With G, Sommerdijk NAJM (2009) The initial stages of template-controlled CaCO<sub>3</sub> formation revealed by Cryo-TEM. *Science* 323:1455–1458
- Rothmund PWK (2006) Folding DNA to create nanoscale shapes and patterns. *Science* 440:297–302
- Shin SH, Chung S, Sanii B, Comolli LR, Bertozzi CR, De Yoreo JJ (2012) Direct observation of kinetic traps associated with structural transformations leading to multiple pathways of S-layer assembly. *Proc Nat Acad Sci U S A* 109:12968–12973
- Schrier SB, Sayeg MK, Gray JJ (2011) Prediction of calcite morphology from computational and experimental studies of mutations of a de novo-designed peptide. *Langmuir* 27:11520–11527
- Stephanopoulos N, Liu M, Tong GJ et al (2010) Immobilization and one-dimensional arrangement of virus capsids with nanoscale precision using DNA origami nanoletters 10:2714–2720
- Tao J, Zhou D, Zhang Z, Xu X, Tang R (2009) Magnesium-aspartate-based crystallization switch inspired from shell molt of crustacean. *Proc Nat Acad Sci* 106:22096–22101
- Wallace AF, Hedges LO, Fernandez-Martinez A et al (2013) Liquid-liquid separation explains “non-classical” behavior during CaCO<sub>3</sub> crystallization. *Science* 341:885–889
- Weiner S, Hood L (1975) Soluble proteins of the organic matrix of mollusk shell: a potential template for shell formation. *Science* 190:987–989

- Weiner S, Traub W, Wagner HD (1999) Lamellar bone: structure-function relations. *J Struct Biol* 126:241–255
- Whaley SR, English DS, Hu EL, Barbara PF, Belcher AM (2000) Selection of peptides with semiconductor binding specificity for directed nanocrystal assembly. *Nature* 405:665–668
- Zhang J, Huang F, Lin Z (2010) Progress of nanocrystalline growth kinetics based on oriented attachment. *Nanoscale* 2:18–34